

Laboratory Course

Neutron Scattering

Lectures

Stephan Förster, Karen Friese, Margarita Kruteva, Shibabrata Nandi, Mirijam Zobel,
Reiner Zorn (Editors)

Schlüsseltechnologien / Key Technologies

Band / Volume 285

ISBN 978-3-95806-774-5

Forschungszentrum Jülich GmbH
Jülich Centre For Neutron Science (JCNS)

Stephan Förster, Karen Friese, Margarita Kruteva,
Shibabrata Nandi, Mirijam Zobel, Reiner Zorn (Editors)

Neutron Scattering

Lectures of the JCNS Laboratory Course held
at Forschungszentrum Jülich and at the
Heinz Maier-Leibnitz Zentrum Garching
In cooperation with
RWTH Aachen

Schriften des Forschungszentrums Jülich
Reihe Schlüsseltechnologien / Key Technologies

Band / Volume 285

ISSN 1866-1807

ISBN 978-3-95806-774-5

Bibliografische Information der Deutschen Nationalbibliothek.
Die Deutsche Nationalbibliothek verzeichnet diese Publikation in der
Deutschen Nationalbibliografie; detaillierte Bibliografische Daten
sind im Internet über <http://dnb.d-nb.de> abrufbar.

Herausgeber und Vertrieb: Forschungszentrum Jülich GmbH
Zentralbibliothek, Verlag
52425 Jülich
Tel.: +49 2461 61-5368
Fax: +49 2461 61-6103
zb-publikation@fz-juelich.de
www.fz-juelich.de/zb

Umschlaggestaltung: Grafische Medien, Forschungszentrum Jülich GmbH

Titelbild: Dr. Jennifer Fischer

Druck: Schloemer + Partner GmbH, Düren

Copyright: Forschungszentrum Jülich 2024

Schriften des Forschungszentrums Jülich
Reihe Schlüsseltechnologien / Key Technologies, Band / Volume 285

ISSN 1866-1807
ISBN 978-3-95806-774-5

Vollständig frei verfügbar über das Publikationsportal des Forschungszentrums Jülich (JuSER)
unter www.fz-juelich.de/zb/openaccess.



This is an Open Access publication distributed under the terms of the [Creative Commons Attribution License 4.0](https://creativecommons.org/licenses/by/4.0/),
which permits unrestricted use, distribution, and reproduction in any medium, provided the original work is properly cited.

Contents

1	Introduction: Neutron Scattering in Contemporary Research	Th. Brückel
2	Properties of the Neutron	P. Zakalek
3	Neutron Sources	U. Rucker
4	Diffraction/Elastic Scattering	S. Nandi
5a	Crystallography	M. Zobel
5b	Structural Analysis	S. Roth
6	Nanostructures Investigated by Small Angle Neutron Scattering	S. Jaksch
7	Macromolecules (structure)	J. Stellbrink
8	Spin-dependent and Magnetic Scattering of Polarized Neutrons	W. Schweika
9	Reflectometry and Grazing Incidence Small Angle Scattering	E. Kentzinger
10	Magnetic Nanostructures	U. Rucker
11	Inelastic Neutron Scattering	R. Zorn
12	Virtual Neutron Scattering Experiments	K. Lieutenant
13	Strongly Correlated Electrons	M. Angst
14	Dynamics of Polymers and Biological Macromolecules	R. Biehl
15	Applications of Neutron Scattering - an Overview	Th. Brückel

1 Introduction: Neutron Scattering in Contemporary Research

Th. Brückel

Jülich Centre for Neutron Science 2

Forschungszentrum Jülich GmbH

Contents

1.1	Introduction: Why Scattering?	2
1.2	X-Ray Scattering in Condensed Matter Research.....	3
1.3	Impact of Scattering in other Fields of Science.....	6
1.4	Why Neutrons?.....	7
1.5	The Social Practice of Neutron Scattering.....	11
	References	12
	Exercises	13

1.1 Introduction: Why Scattering?

In this chapter, we will start with a very gentle qualitative introduction entirely without formula to give you an idea what the course is all about. The details will follow in subsequent chapters.

Imagine you leave this lecture hall, some mean looking guys dressed entirely in black follow, kidnap and take you to the medieval castle of Nideggen in the close-by Eifel mountains. There you are being thrown into a pitch dark dungeon. You cannot see anything, but you hear some noises. Are there rats? Are there other prisoners? Are there dragons? Luckily you remember that you have some matches in your pocket. You light a match, you can see everything around you and everything becomes clear to you...

What I have just described is essentially like a scattering experiment: figuratively it sheds light into darkness and helps us understand the world around us. Let's analyse what you did in the dungeon: first when you light the match, you start a source of radiation. Here the radiation is light. This light then gets scattered (reflected, transmitted) from the surrounding objects. In a scientific scattering experiment, we will call this object a "sample". Back to the dungeon: some of this radiation gets scattered into your eye. Your eye serves as very special radiation detector: with its lens, it is able to even make an image of the objects on the retina, which in the language of a physicist would be called an "area position sensitive pixel detector". This image contains lots of information: the colour of the backscattered light tells you something about the absorption of certain components of the light and therefore gives information about the material the light is scattered from. The position of the signal on the retina gives you information about the spatial arrangement of the objects around you. And finally the time dependence of the signal tells you that the monster is actually crawling towards you, ready to attack. All this information has to be treated and interpreted. This is done by our brain, an extremely powerful computer to analyse this wealth of data.

This little example shows you the importance of scattering for our understanding of the world: nearly all information that we as individuals have about the world in which we live comes from light scattering and imaging through our eyes. It is only natural that scientists mimic this process of obtaining information in well controlled scattering experiments: they build a source of radiation, direct a beam of radiation towards a sample, detect the radiation scattered from a sample, i. e. convert the signal into an electronic signal, which they can then treat by means of computers. In most cases one wants an undisturbed image of the object under investigation and therefore chooses the radiation, so that it does not influence or modify the sample. Scattering is therefore a non-destructive and very gentle method, if the appropriate type of radiation is chosen for the experiment.

1.2 X-Ray Scattering in Condensed Matter Research

What other requirements must the radiation fulfill to be useful for scattering experiments? In condensed matter science we want to go beyond our daily experience and understand the microscopic atomic structure of matter, i. e. we want to find out where the atoms are located inside our samples and also how they move. This cannot be done by light scattering. Why? Well in general light is scattered from the surface and does not penetrate enough into many materials, such as metals, for example. On the other hand, if it penetrates like in the case of glass it is normally just being transmitted except if we have a very bad glass with lots of inhomogeneities, but the main reason is actually that light has too long of the wavelength, see figure 1.1.

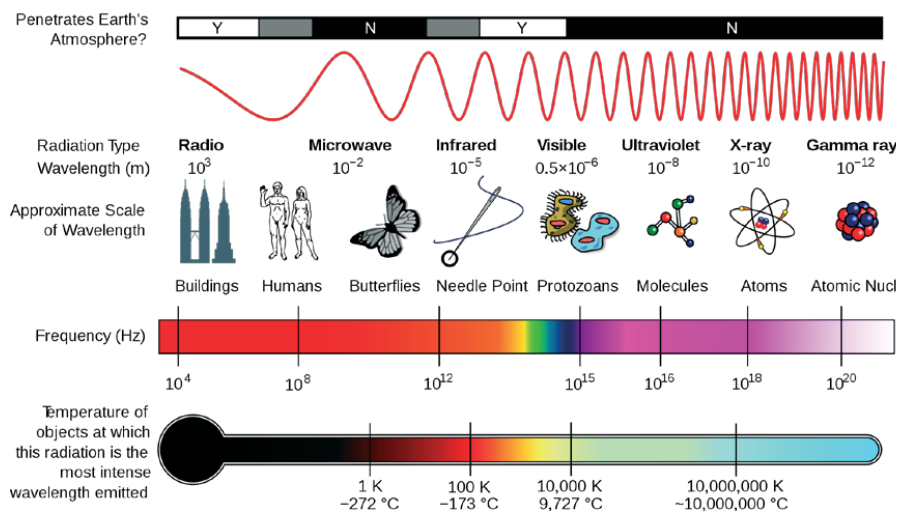


Fig. 1.1: *Electromagnetic spectrum; shown is the wavelength and frequency of electromagnetic waves, which have different names for different wavelength regions. Also given are examples for objects with sizes comparable to the wavelength. (from WIKIPEDIA)*

It is quite intuitive to understand that if we want to measure the distance between the atoms, we need a “ruler” of comparable lengths. Now the distance between atoms is in the order of $0.1 \text{ nm} = 10^{-10} \text{ m} = 0.0000000001 \text{ m}$. Since the distance between atoms is such an important length scale in condensed matter science, it has been given its own unit: $0.1 \text{ nm} = 1 \text{ \AA} = 1 \text{ \AA}$. If we compare the wavelength of light with this characteristic length scale, it is 4000 to 7000 times longer and therefore not appropriate to measure distances on an atomic lengthscale. In the electromagnetic spectrum, x-rays

have a well adapted wavelength of about 1 \AA for studies on such a microscopic scale. They also have a large penetration power as everybody knows from the medical x-ray images.

Classical physics describes electromagnetic radiation as propagation of electromagnetic waves. For a scattering experiment, we select waves of a certain wavelength and propagation direction, so-called plane waves, since all points on a plane in space have the same phase. If such a wave impinges on two point-like scattering centers (in a solid these could be atoms), spherical waves are being emitted from these scattering centers. This is nothing but Huygens principle for wave propagation. The emitted waves can superimpose and lead to either enhancement or cancellation of the signal in certain directions as depicted in figure 1.2.

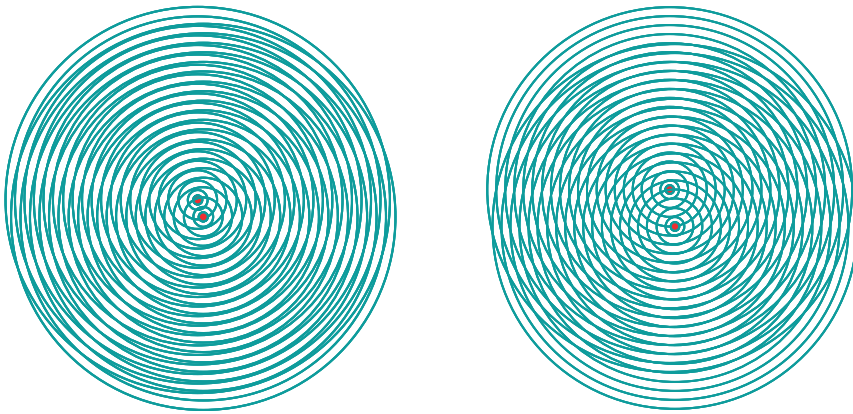


Fig. 1.2: *Moiré pattern for concentric circles with equal distances representing a planar cut through spherical waves emitted from two scattering centers. The circles represent surfaces of constant phase relationship. Linear superposition of the waves gives enhancement or cancellation of the wave amplitudes along certain directions. This interference effect is mimicked by the depicted Moiré pattern. If the distance between the scattering centers is increased, the distance in the interference maxima decreases and vice versa: distances in the image created by scattering are inverse proportional – or reciprocal - to distances in the original objects which motivates the introduction of a reciprocal space to describe scattering events compared to the real space of the object under investigation.*

As becomes clear from figure 1.2, scattering can be described as an interference phenomenon of the radiation waves. However, since de Broglie and Einstein, we know that quantum objects have a dual nature: the particle-wave-dualism. In the case of electromagnetic waves, the quanta carrying certain energy are called photons and in the detector, which registers the scattering pattern, we count single x-ray photons. This is characteristic for the quantum mechanical description: during propagation of radiation a wave picture is appropriate, while for the interaction with matter a particle is the

description of choice. Wave and particle picture are connected by the fact that the magnitude square of the wave at a certain position in space gives the probability density of finding the quantum particle at the corresponding position. Within this particle-wave-dualism it therefore becomes natural to use elementary particles as probes for scattering investigations of condensed matter systems. This was realised for the first time by Rutherford in 1909 in his famous experiment, where he directed a beam of α -particles onto a gold foil and registered the transmitted and scattered particles. He found that many particles were backscattered and from the ratio between transmitted and backscattered α -particles he could conclude on the model of an atom, which is now generally accepted, namely consisting of a positively charged nucleus of size about 10 femtometer = 10 fm = 10×10^{-15} m surrounded by a cloud of negatively charged electrons with an extension of about $1 \text{ \AA} = 10^{-10}$ m = 100000 fm, see figure 1.3.

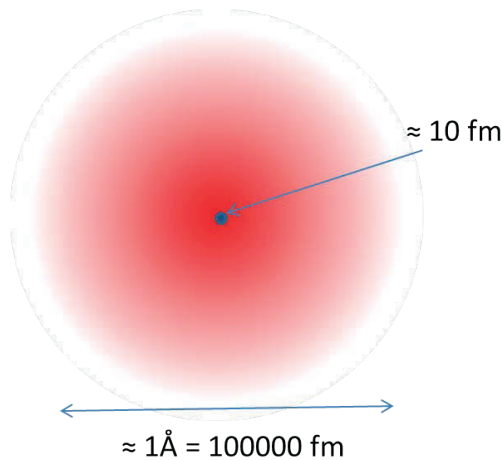


Fig. 1.3: Schematic model of an atom with the atomic nucleus consisting of neutrons and protons having a size of about 10 fm surrounded by electrons in a cloud of a size of about 1 \AA .

The real breakthrough for structure studies of condensed matter systems came with the idea of Max von Laue to use x-rays as scattering probes. Wilhelm Conrad Röntgen discovered x-rays in 1895 and soon it was concluded that x-rays were electromagnetic waves. Arnold Sommerfeld suggested that the wavelength of x-rays was about 1 \AA . At the time of Max von Laue, after the experiments of Rutherford, it was accepted that matter consisted of atoms but their periodic arrangement in crystals was maybe suggested by the regular facets of the crystals but could not be really proven by experiment. Max von Laue was a theoretician, who derived the famous Laue equation describing scattering from a regular three-dimensional periodic arrangement of scattering centers. He convinced the two experimentalists Friedrich and Knipping to perform an x-ray diffraction experiment. The result is shown in figure 1.4.

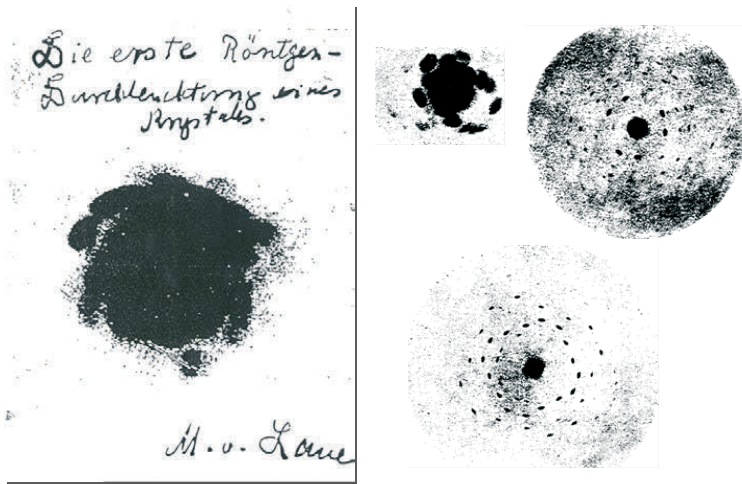


Fig. 1.4: Early x-ray diffraction diagrams recorded by a film from copper sulphite single crystals [1].

While the first transmission Laue photograph showed more or less just a fat plop, the quality of these images was soon refined and clear so-called Laue-spots could be identified. The impact of this discovery cannot be over-emphasized: it was the definite proof that solids consist of atoms, which are arranged in a regular three-dimensional periodic array and that x-rays were scattered as electromagnetic waves from such an arrangement of atoms. It is therefore natural that Max von Laue received the Nobel prize in 1914 for this breakthrough discovery. However, the experimentalists Friedrich and Knipping were left empty-handed.

Nearly everything we know today about the atomic structure of matter is based on this discovery which took place 100 years ago. Of course the techniques were significantly refined and nowadays x-ray diffraction is heavily being used to resolve complex structures of biological macromolecules in the field of protein crystallography. Such investigations need very intense and bright x-ray beams, which are provided from large accelerators, so-called synchrotron radiation sources. Many thousands of reflections are being recorded in a few seconds. As electromagnetic waves, x-rays are mainly scattered from the electronic charge distribution around the atoms and thus x-ray diffraction allows one to determine the electron density in solids.

1.3 Impact of Scattering in other Fields of Science

It should be pointed out that scattering is a much more general method in science, which is not only used by condensed matter scientists. The world's largest accelerator is located close to Geneva at the border between Switzerland and France in the CERN research center. CERN stands for *Centre Européenne pour la Recherche Nucléaire*, i. e.

the European organisation for nuclear research. Many accelerators are located on the CERN site of which the LHC, the Large Hadron Collider, is the world's largest and highest energy particles accelerator. The LHC lies in a tunnel 27 km in circumference as deep as 175 m beneath ground level. This huge accelerator serves nothing but a scattering experiment, where opposing particle beams e. g. protons at energy of 7 TeV collide in certain interaction points, which are surrounded by huge detectors built by large international collaborations. In inelastic scattering events, new particles can be created and the hope is that this huge investment helps us to address some of the most fundamental questions of physics advancing the understanding of the deepest laws of nature. At Research Centre Jülich we have a smaller version of such a particle accelerator, the so-called COSY synchrotron for Hadron physics. These large accelerators are needed to achieve high particles energies corresponding to short wavelengths, which allow one to study fine structures within nucleons. Large detectors are needed because at these scales no imaging is possible but if all scattered particles are being traced a reconstruction of the scattering event in the computer can take place. While at the LHC new particles are being created during deep inelastic scattering events, the connection to x-ray diffraction is more evident for the former HERA accelerator, which had been in operation at DESY in Hamburg until a few years ago. There, electrons were being scattered from protons in head-on collisions and the inner structure of the proton consisting of quarks and gluons could be resolved.

1.4 Why Neutrons?

Coming back to condensed matter science: if x-rays are so successful for structure determination, why do we need neutrons? Neutrons have some very specific properties which make them extremely useful for condensed matter studies:

1. Neutrons are neutral particles. They are thus highly penetrating, can be used as non-destructive probes and to study samples in severe environment such as cryomagnets or furnaces.
2. The wavelengths of neutrons are similar to atomic spacings - just as is the case for x-rays. Therefore they can provide structural information from the picometer to the 100 μm range.
3. The energies of thermal neutrons are similar to the energies of elementary excitations in solids. Therefore neutrons can determine molecular vibrations, lattice excitations and the dynamics of atomic motion.
4. Neutrons interact with the nuclei in contrast to x-rays or electrons which interact with the electron cloud, see Figure 1.5. They are very sensitive to light atoms like hydrogen, which is difficult to detect by x-rays since hydrogen in bonds has often less than one surrounding electron. They can also distinguish between neighbouring elements in the periodic table like manganese, iron and chromium, for which x-rays are insensitive since these elements have nearly the same number of electrons. Also one can exploit isotopic substitution. A famous example is contrast variation in soft matter or biological macromolecules by replacing deuterium for hydrogen in certain molecules or functional groups.

Similar to tinting in light microscopy, the location and movement of these functional groups can then be observed on the background of the other molecules.

- Neutrons have a magnetic moment. This dipolar moment is due to the nuclear spin. Therefore neutrons can be used to study microscopic magnetic structures but also the magnetic excitations in solids, which have similar energies than the neutrons.

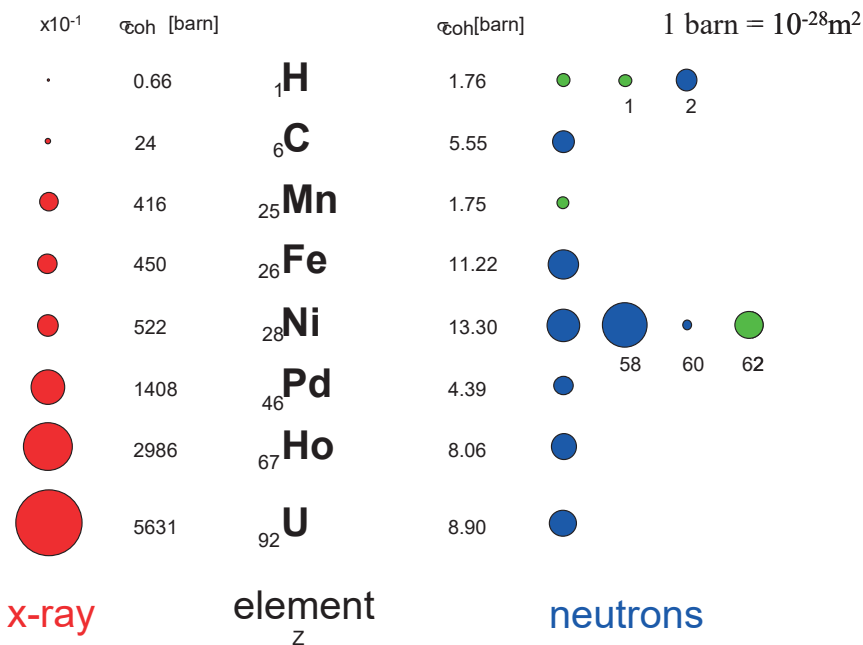


Fig. 1.5: Comparison of x-ray and neutron scattering from single atoms for a few elements of the periodic table. The filled circles represent a measure of the total cross section, i.e., of the probability for scattering. For x-rays, which are scattered from the electron cloud, this probability goes up with the number square of electrons. Therefore Hydrogen is hardly visible for x-rays in the presence of heavier atoms. The situation is quite different for neutrons, which are scattered from the atomic nucleus. Here the scattering varies not monotonically throughout the periodic table and is different for different isotopes of the same atom. Blue and green circles distinguish scattering with and without 180° phase shift, respectively.

Figure 1.6 shows the extreme range of applicability of neutrons for condensed matter studies based on these special properties. Different scattering techniques have to be used for different applications, as indicated in the figure.

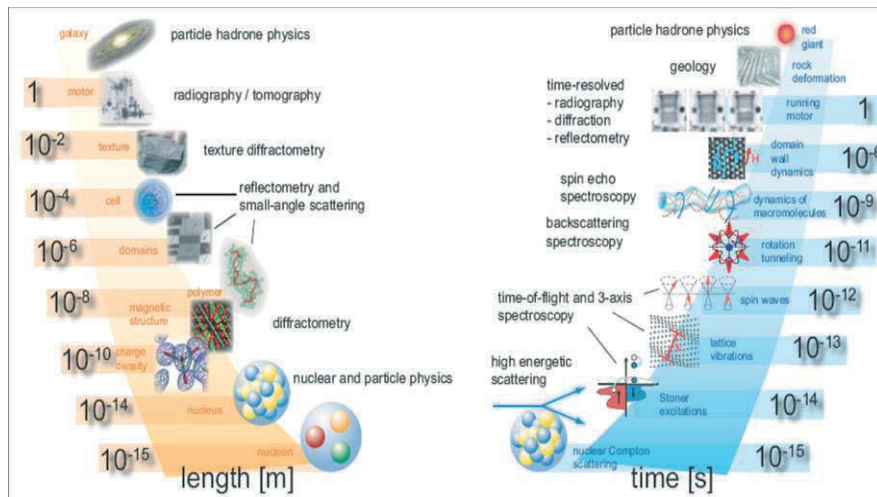


Fig. 1.6: Huge range of length (left side) and time (right side) scales covered by research with neutrons. Also indicated is the corresponding neutron technique.

Due to the huge impact of neutron scattering for condensed matter studies, it is no surprise that the Nobel prize in physics was awarded to two of the pioneers of neutron diffraction and inelastic neutron scattering, which Clifford G. Shull and Bertram Brockhouse received in 1994. The famous quote “neutrons tell us where atoms are and how they move” is due to Clifford Shull.

If you got the impression so far that neutrons are the ideal and most universal probe for condensed matter studies on an atomic scale, you are right in principle. However, as with everything in life, there are also some drawbacks. While neutrons are everywhere - without neutrons we would not exist - they are extremely difficult to produce as free particles not bound in nuclei. Free neutrons are produced by nuclear physics reactions, which require rather large and high-tech installations. Two main routes to produce free neutrons are being followed today:

- (1) **Fission** of the uranium 235 nuclei in a chain reaction; this process happens in research reactors.
- (2) Bombarding heavy nuclei with high energetic protons; the nuclei are “heated up” when a proton is absorbed and typically 20 - 30 neutrons are being evaporated. This process is called **spallation** and requires a spallation source with a proton accelerator and a heavy metal target station.

Since installations to produce free neutrons are rather expensive to build and to operate, there exist only a few sources worldwide. JCMS is present in some of the world best sources as shown in figure 1.7.



Fig. 1.7: Major neutron research centres worldwide which have sources of appreciable flux and a broad instrumentation suite for condensed matter research. JCNS instruments are located at four of the leading sources worldwide: the neutron research reactor FRM II in Garching, Germany, the Institut Laue-Langevin ILL in Grenoble, France, the Spallation Neutron Source SNS in Oak Ridge, USA and the Chinese Advanced Research Reactor CARR close to Beijing, China. JCNS also has a leading involvement in the European Spallation Source project, Lund, Sweden.

The fact that there are only a few sources worldwide implies that neutron scattering experiments have to be organised quite different from normal lab-based experiments. Users have to be trained in special schools (our JCNS school is one of them) and access to the experiments has to be organised (see below).

Not only the neutron research centres are rare but also free neutrons by themselves are rare. In a high flux reactor the neutron flux i. e. the number of neutrons passing through a given area in a given time is in the order of 10^{15} neutrons/cm²·s. If one compares this value with particle fluxes in gases, the neutron density in high flux sources corresponds to high vacuum conditions of about 10^{-6} mbar pressure. The neutrons have to be transported from the source to the experimental areas, which can either be done by simple flight tubes or so called neutron guides. These are evacuated tubes with glass walls (often covered with metal layers to increase the performance), where neutrons are transported by total reflection from the side, top, and bottom walls in a similar manner like light in glass fibers. The neutron flux downstream at the scattering experiments is then even much lower than in the source itself and amounts to typically $10^6 - 10^8$ neutrons/cm²·s. This means that long counting times have to be taken into account to achieve reasonable statistics in the neutron detector. Just for comparison: the flux of photons of a small Helium-Neon laser with a power of 1 mW (typical for a laser pointer) amounts to some 10^{15} photons/s in a beam area well below 1 mm².

However, it is not only the low flux that limits neutron scattering experiments, but also the fact that neutron sources are not very bright, i. e. neutron beams are rather large in the order of a few cm^2 and therefore require in general rather large samples. Typical sample sizes are again in the order of a few cm^2 and have masses of a few grams. However, this does not mean that we cannot study nanosized objects with neutrons as you will see in the subsequent lectures. However, for neutron scattering techniques, we have to have many of such objects and we will obtain ensemble averages.

1.5 The Social Practice of Neutron Scattering

The fact that neutron sources are rare leads to a particular social practice for neutron scattering: there are only a few major sources in Europe and worldwide and the operation of each one of these sources costs several million Euro per year. Therefore efforts have to be made to use the existing sources as efficient as possible. This means (i) continuous and reliable operation of the source during a large fraction of the year; (ii) many highly performing instruments, which can run in parallel, located around every source; (iii) professional instrument operation with highly qualified staff and a stringent risk management to keep the downtime of instruments and auxiliary equipment as low as possible; (iv) and access for as many scientists as possible.

There is no commercial market for neutron scattering instruments. Therefore these instruments are being built by research centres, where usually one or a few staff scientists work closely with engineers and technicians to realise an instrument for a certain application of research with neutrons. These highly experienced scientists will then later-on operate the instruments located at a certain neutron source. The Jülich Centre for Neutron Science JCNS has such staff scientists located at the outstations at FRM II, ILL. However, neutron facilities are way too expensive to be operated just for a small number of scientists. Beamtime is offered to external users from universities, research organisations (such as Max-Planck or Fraunhofer in Germany) and industry. In order for these users to obtain access to a neutron scattering instrument, the user will obtain information from the internet on available instruments, contact the instrument scientist and discuss the planned experiments with the instrument scientist. Once a clear idea and strategy for an experiment has been worked out, the user will write a beamtime proposal where he describes in detail the scientific background, the goal of the planned experiment, the experimental strategy and the prior work. The facility issues a call for proposals in regular intervals, typically twice a year. The proposals received are distributed to members of an independent committee of international experts, which perform a peer review of the proposals and establish a ranking. Typically overload factors between 2 to 3 on the neutron instruments exist, i. e. 2 to 3 times the available beam time is being demanded by external users. Once the best experiments have been selected, the beamtime will be allocated through the facility, where the directors approves the ranking of the committee, the beamline scientist schedules the experiments on her or his instrument and the user office sends out the invitations to the external users. Many facilities will pay travel and lodging for 1 up to 2 users per experiment. It is now up to the user to prepare his experiment as well as

possible. If the experiment fails because it was not well prepared, it will be very difficult to get more beamtime for the same scientific problem. Typical experiments last between 1 day and up to 2 weeks. In this time lots of data will be collected which users take home and usually spend several weeks or months to treat the data and model it.

A typical neutron scattering facility will run about 200 days a year with a few hundred visits of user from all over the world. This is also what makes research with neutrons so attractive to young scientists: early-on in their career they will learn to work in large international collaborations, get the opportunity to work on state-of-the-art high-tech equipment and learn to organise their research as efficient as possible. You have therefore chosen well to attend this laboratory course!

After this simple introduction, you can now look forward to many interesting lectures, where more details will be explained and where you will learn the basic principles to enable you to perform neutron experiments. Have lots of fun and success working with this special gift of nature, the free neutron!

References

- [1] W. Friedrich, P. Knipping, M. von Laue(1912). "Interferenz-Erscheinungen bei Röntgenstrahlen". Sitzungsberichte der Mathematisch-Physikalischen Classe der Königlich-Bayerischen Akademie der Wissenschaften zu München 1912: 303.

Some useful links for research with neutrons:

- [2] German Committee for Research with Neutrons: www.neutronenforschung.de
[3] European Neutron Portal: <http://www.neutron-eu.net/>
[4] Neutron scattering reference material: <http://www.neutron.anl.gov/reference.html>
[5] Neutron scattering web: <http://www.neutron.anl.gov/>
[6] Jülich Centre for Neutron Science: <http://www.fz-juelich.de/jcns/>

Exercises

E1.1 Multiple Choice

- Electromagnetic radiation with a wavelength of 500 nm corresponds to:
 - microwaves
 - visible light
 - ultraviolet
 - X-rays

- The typical distance between atoms in a solid amounts to:
 - 10 nm
 - 1 nm
 - 0.1 nm
 - 0.01 nm

- An atomic nucleus has a typical size of:
 - 1 Å
 - 0.1 nm
 - 1 pm
 - 10 fm

- The typical wavelength of thermal neutrons is:
 - 10 nm
 - 1 nm
 - 0.1 nm
 - 0.01 nm

- Which type of radiation would you use to distinguish iron and manganese atoms in a given compound?
 - X-rays
 - neutrons
 - electrons
 - light

- Which type of radiation would you use to determine the charge density distribution in a solid?
 - X-rays
 - neutrons
 - electrons
 - light

- How many neutrons per second impact on a sample with typical lateral dimensions of 1x1 cm in a typical neutron scattering experiment?
 - 10^3
 - 10^7
 - 10^{12}
 - 10^{16}

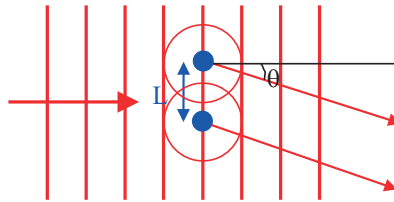
- Which type of radiation would you use to determine the magnetization density distribution in a solid?
 - X-rays
 - neutrons
 - electrons
 - light

E1.2 Comprehension

- a. What is the difference between a scattering and an imaging experiment? When would you choose one over the other?
- b. Why does one observe Laue spots when a “white” beam of X-rays is scattered from a single crystal? How about scattering from glass?
- c. Why are neutrons sensitive to the magnetic order in a crystal?
- d. Neutron scattering allows us to determine “where the atoms are and how the atoms move” in a condensed matter system. Other scattering probes include: light, x-rays, electrons, α -particles. Discuss qualitatively the strengths and weakness of these probes in comparison to neutron scattering.
- e. CO_2 has a bad reputation as green-house gas in the atmosphere. Could it, however, be useful as a scattering probe to replace neutrons? (A high flux of CO_2 molecules could e.g. be obtained by an expansion of pressurised CO_2 gas from a gas bottle through a nozzle - a flux many orders of magnitude higher than the neutron fluxes used in neutron scattering experiments!)

E1.3 Arithmetic Problem (optional): Huygens principle and coherence

A plane wave of wavelength λ is incident on a pair of identical scatterers, which are separated by a distance L perpendicular to the wave propagation, see figure:



According to the Huygens principle, spherical waves will be emitted from the two scatterers. In certain directions, these waves interfere constructively, i.e. the two scattered waves are in phase.

- Calculate the angles θ , where interference maxima occur in the far field limit.
- What happens to the interference maxima, if there is a broad distribution of wavelength in the incident wave, but the propagation direction remains well defined?
- What happens to the interference maxima, if the wavelength of the incident wave is well defined, but there are many waves of different directions impinging on our scatterers?
- How would you design an instrument to measure the distance L between the two scatterers, if light from a normal light bulb is being used as radiation? Which requirement does L have to fulfil in this case?
- According to b) and c) monochromatization and collimation are important to obtain well resolved interference pattern. The corresponding requirements for the radiation are called longitudinal (b) and transverse (c) coherence, respectively. Discuss qualitatively the relation between coherence and resolution, i.e. in our example the ability of the apparatus designed in d) to determine the distance L between the scatterers.

2 Properties of the neutron

P. Zakalek

Jülich Centre for Neutron Science 2

Forschungszentrum Jülich GmbH

Contents

2.1	Introduction	2
2.2	Nuclear interaction: Scattering and absorption	4
2.3	Neutron absorption.....	6
2.4	Coherent and incoherent scattering	8
2.5	Magnetic neutron scattering.....	12
2.6	Comparison of probes	12
	References	15
	Exercises	17

2.1 Introduction

The neutron with its unique properties as described here is used as a particularly useful probe for condensed matter investigations. The neutron is an elementary particle, a nucleon, consisting of three valance quarks, which are hold together by gluons (see Fig. 2.1). It thus has an internal structure, which, however, is irrelevant for condensed matter physics, since the energy scales involved in its internal excitations are much too high. Keeping in mind the difference in lengths scales (diameter of an atom: about $0.1 \text{ nm} = 10^{-10} \text{ m}$; diameter of a neutron: about $1 \text{ fm} = 10^{-15} \text{ m}$), we can safely consider the neutron as a point-like particle without internal structure for our purposes. Due to the weak interaction, the neutron is not a stable particle. A free neutron undergoes a β -decay into proton p , electron e^- and electron-antineutrino $\bar{\nu}_e$ after an average lifetime of about 15 minutes []:



This leaves ample time for scattering investigations. In contrast to the massless photon, the neutron has a mass m of about one atomic mass unit $\sim 1.675 \cdot 10^{-27} \text{ kg}$. The neutron has therefore a velocity well be low the speed of light and depending on its velocity can be significantly affected by gravity. The finite neutron mass is comparable to the mass of a nucleus and thus an appreciable amount of energy can be transferred during the scattering process. The neutron with the current measurement limit of 10^{-27} does not carry an neutron electric dipole moment and thus can be viewed as a neutral particle. It does not does not show the strong Coulomb interaction with matter which results in large penetration depths in mater. Finally, the neutron has a nuclear spin of 1/2 giving rise to a magnetic dipolar moment of

$$\mu_n = \gamma \mu_N \quad \text{with } \gamma = 1.91 \quad \text{and } \mu_N = 5.05 \cdot 10^{-27} \text{ J/T} \quad (2.2)$$

Due to this magnetic moment, the neutron can interact with the magnetic field of unpaired electrons in a sample leading to *magnetic scattering*. Thus, magnetic structures and excitations can be studied by neutron scattering.

To calculate the interference effects during the scattering process, a neutron has to be described as a matter wave with momentum

$$\mathbf{p} = m \cdot \mathbf{v} = \hbar \mathbf{k} \longrightarrow p = h/\lambda \quad (2.3)$$

and energy

$$E = \frac{1}{2} m v^2 = \frac{\hbar^2 k^2}{2m} = \frac{h^2}{2m\lambda^2} \equiv k_B T_{eq}, \quad (2.4)$$

where v is the velocity of the neutron and T_{eq} defines the temperature equivalent of the kinetic energy of the neutron. In practical units:

$$\lambda[nm] = \frac{400}{v[m/s]} \quad (2.5)$$

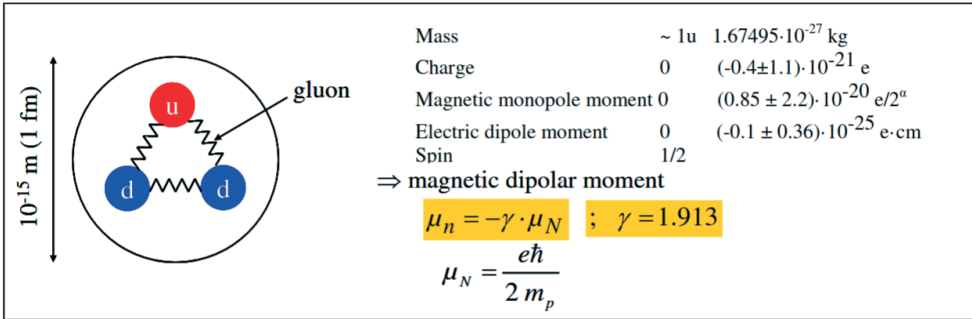


Fig. 2.1: Schematics of the neutron being composed of three quarks and gluons and the main quantities characterising the neutron as a particle.

$$E[\text{meV}] = \frac{0.818}{\lambda^2[\text{nm}]} \tag{2.6}$$

Let us consider the example of so-called thermal neutrons from a moderator at ambient temperature corresponding to a temperature equivalent of $T_{eq} \sim 300$ K. According to (2.4), their wavelength is 0.18 nm, matching perfectly the distance between atoms. The energy of thermal neutrons is around 25 meV, which matches well the energy of elementary excitations, such as spin waves (magnons) or lattice vibrations (phonons). Together with the usually large penetration depths (charge = 0) and the magnetic interaction, these properties make neutrons so extremely useful for condensed matter investigations.

In the elementary scattering theory of chapter <https://iffex.fz-juelich.de/project/628289bc4a86a300895dc7e92.3>, we saw that the relevant quantity is the interaction potential $V(\mathbf{r})$ of the probe with the system from which the probe is scattered. This potential enters in the cross-section in kinematical theory derived either from Born approximation or from Fermi's golden rule. To determine this interaction potential, we will look in more detail at the interaction of neutrons with matter. For neutrons there exist two dominant interactions: the interaction of the neutron with nuclei and its interaction with the magnetic field in the sample. The nuclear interaction results from the so-called strong interaction of particle physics, which is also responsible for the binding of neutrons and protons in the atomic nuclei. The interaction with the magnetic field is nothing but the magnetic dipole interaction of the neutron due to its dipolar moment with the magnetic field of unpaired electrons. There are other interactions, which are significantly weaker. One is the interaction of the neutron with the electric fields in the sample due to the neutrons magnetic dipole moment. This is a purely relativistic effect. Another is the magnetic dipole interaction of the neutron with the magnetic field produced by the nuclei. Since such interactions are several orders of magnitude weaker than the nuclear and magnetic interaction, they can usually be neglected and we will not discuss them further in this lecture.

2.2 Nuclear interaction: Scattering and absorption

To evaluate the cross section σ for nuclear scattering, we have to specify the interaction potential with the nucleus. To derive this interaction potential from first principles is one of the fundamental challenges of nuclear physics. Instead, Fermi has proposed a phenomenological potential based on the argument that the wavelength of thermal neutrons is much larger than the nuclear radius. This means that the nuclei are point-like scatterers which leads to isotropic, Q-independent, (so-called s-wave) scattering. We will therefore use the so-called *Fermi-pseudo-potential*

$$V(\mathbf{r}) = \frac{2\pi\hbar^2}{m} b\delta(\mathbf{r} - \mathbf{R}). \quad (2.7)$$

Despite the fact that the strong interaction of high energy physics is responsible for the scattering of the neutron with the nucleus, the scattering probability is small due to the small nuclear radius. Therefore, we can apply the first Born approximation. The quantity b introduced in (2.7) is a phenomenological quantity describing the strength of the interaction potential and is referred to as the *scattering length*. Tabulated values of b can be found in [8] or at <http://www.ncnr.nist.gov/resources/n-lengths/>. The total cross section of a given nucleus is $\sigma = 4\pi|b|^2$, corresponding to the surface area of a sphere with radius b . Since the interaction potential obviously depends on the details of the nuclear structure, b is different for different isotopes of the given element and also for different nuclear spin states. This fact gives rise to the appearance of so-called *coherent* and *incoherent scattering*, see section 2.4. Figure 2.2 shows the variation of the scattering amplitude as a function of atomic weight throughout the periodic table. The scattering length is mostly positive but can also adopt negative values. Since $-1 = \exp(i\pi)$ this negative sign corresponds to a phase shift of π (or 180°) during the scattering process. The scattering length roughly follows the dashed line labelled *potential scattering* contribution, despite the fact that there are rather large excursions from this line.

In the simplest one-dimensional model shown in Figure 2.3, we can describe the nucleus as a rectangular potential well with the radius of the well equal to the nucleus radius and the depth as V_0 . The kinetic energy of the neutrons is thus adjusted with the well potential. The wave function of the neutron being scattered from such a potential well can be written as

$$\Psi(r) \sim e^{ikr} + \frac{f}{r} e^{ikr}, \quad (2.8)$$

with f as the scattering amplitude, k as the wave vector of the neutron and r as the distance to the well center. Here the first term describes the incident plane wave and the second term describes a spherical wave emitted from the nucleus. In the limit of a hard sphere, the wave function on the surface of the nucleus has to vanish since the neutron cannot penetrate inside the hard sphere. Mathematically this is described by the condition $\Psi(R) = 0$ or $-f = R$. The scattering length is defined as $b := -f$, so that its value is positive for most nuclei. Therefore, for pure *potential scattering*, where the nucleus is assumed to be a hard sphere, b attains the value of the nuclear radius $b = R$, which is plotted in Figure 2.2 as a dashed line: the *potential scattering* contribution. The marked

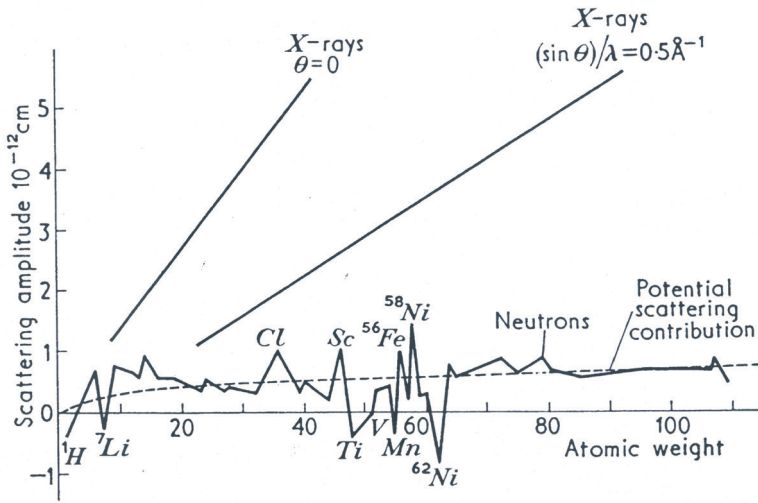


Fig. 2.2: Scattering length as a function of atomic weight throughout the periodic table (from *Research, London* 7 (1954), 257).

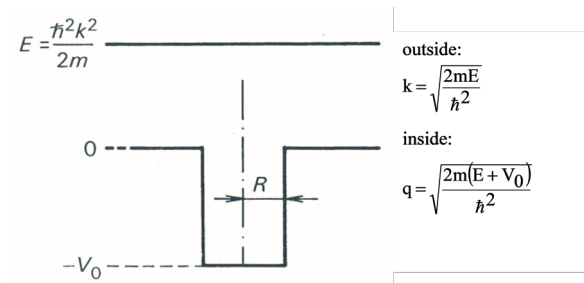


Fig. 2.3: The nucleus described as a potential well of radius R and depth $-V_0$, while the neutron has the kinetic energy $E = \frac{\hbar^2 k^2}{2m}$.

deviations from this overall behaviour are due to so-called *resonance scattering*. In a simplified picture, such resonances occur, when the neutron energy is such that absorption of the neutron in the nucleus produces a bound excited state. This can lead to a *resonant absorption* process, but it can also lead to *resonance scattering*, a typical second order perturbation process: in the initial state, the nucleus is in its ground state and the interaction with the neutron can be described as a virtual transition into an excited state of the compound nucleus and back with a re-emission of the neutron, where the nucleus decays back from the excited compound system into its ground state. This process $n + K \rightarrow C^* \rightarrow K + n$ has a cross-section given by the famous *Breit-Wigner-formula*

$$\sigma_R = 4\pi \left| R + \frac{const}{E - E_R + 1/2i\Gamma} \right|^2. \tag{2.9}$$

Here R is the radius of the nucleus, E the neutron energy, E_R the resonance energy and

Γ a damping term connected with the life-time of the excited state. As one can see, this formula describes a very strong energy dependence with a pronounced maximum when the neutron energy equals the resonance energy. Moreover, the resonance amplitude has an imaginary part, which describes the *resonance absorption*. In the *resonant absorption* process, the neutron is captured by the nucleus, leading to a compound nucleus in an excited state, containing one more neutron than the original nucleus. In a subsequent nuclear reaction, the compound nucleus gets rid of its excess energy. Examples for such absorption reactions will be given in the subsequent section. Finally, the Breit-Wigner-formula gives an indication that the scattering length can be negative whenever the resonant term is negative (i. e. $E < E_R$), and its magnitude is larger than the contribution from potential scattering.

2.3 Neutron absorption

As explained above, neutron absorption can occur during nuclear reactions. It can be divided into three regions depending on the neutron energy. These regions are the low energy named $1/v$ region, the intermediate energy named resonance region and the high energy region named smooth region.

Far away from the resonance at low neutron energies, the absorption cross section is given by

$$\sigma_a \sim \lambda \sim \frac{1}{v}. \quad (2.10)$$

This proportionality to the wavelength λ or the inverse velocity $1/v$ is a result of the density of states appearing in Fermi's golden rule. One can argue that wavelength and neutron velocity v are inversely proportional and thus, for longer wavelength i. e. smaller velocity, the neutron remains correspondingly longer close to the nucleus increasing the probability for a reaction, which leads to a higher absorption cross-section. Table 2.1 gives examples for neutron absorption processes connected with important nuclear reactions for neutron applications.

σ_a (25 meV) [barn]	
5333	$n + {}^3\text{He} \rightarrow {}^4\text{He}^* \rightarrow p + {}^3\text{T}$
940	$n + {}^6\text{Li} \rightarrow {}^7\text{Li}^* \rightarrow {}^3\text{T} + {}^4\text{He}$
3837	$n + {}^{10}\text{B} \rightarrow {}^{11}\text{B}^* \rightarrow {}^4\text{He} + {}^7\text{Li} + \gamma$
681	$n + {}^{235}\text{U} \rightarrow \text{fission}$

Table 2.1: Examples for neutron absorption processes due to nuclear reactions. The absorption cross-section is given for neutrons of energy 25 meV in barn = $10^{-28} \text{ m}^2 = 100 \text{ fm}^2$.

As an example, there is a high probability of neutrons to be absorbed by ${}^3\text{He}$ nuclei, because the ${}^4\text{He}$ or α -particle is very stable since it corresponds to a closed nuclear shell. However, during the absorption of the neutron, the ${}^4\text{He}$ nucleus is produced in an excited state. It gets rid of its surplus energy by decay into a proton and a triton ${}^3\text{T}$ (the

triton ${}^3\text{T}$ nucleus is a hydrogen isotope with one proton and 2 neutrons). Since these two particles have very high energies of about 0.5 MeV due to the nuclear reaction, charged particles are created during this decay, which can be used for neutron detection in a proportional counter. In a similar manner, the reaction with ${}^6\text{Li}$, ${}^{10}\text{B}$ or ${}^{235}\text{U}$ can be used to build neutron detectors. It should be mentioned, however, that the neutron absorption in ${}^3\text{He}$ is very strongly dependent on the relative orientation of the nuclear spins of both particles. While for antiparallel spin direction (singlet state), the absorption cross-section is ~ 6000 barn, it reduces to 2 barn for parallel spin direction (triplet state). This effect can be used to build efficient neutron polarization filters. By optical pumping with laser light, the nuclear moment of the ${}^3\text{He}$ nuclei can be aligned along one direction (so-called hyperpolarized ${}^3\text{He}$ gas). If an unpolarized neutron beam passes a filter cell filled with hyperpolarized ${}^3\text{He}$, the neutrons with spin moment antiparallel to the nuclear moment of the ${}^3\text{He}$ have a high probability to be absorbed, while neutrons with the other spin direction have a high probability to be transmitted. For an appropriate thickness of the filter cell, a very high neutron beam polarization can be achieved in this manner.

Another class of absorption processes are so-called (n, γ) -resonances at intermediate neutron energies. Examples are given in Table 2.2. In these processes, a nucleus is produced, which contains one additional neutron and this compound nucleus decays into the ground state by emission of γ -radiation. Prominent (n, γ) -resonances occur for Cadmium or Gadolinium where, depending on the isotope, the absorption cross-section can be very high, see Table 2.2. These metals are often used as neutron absorbers in shieldings or diaphragms, which define the size of the neutron beam. One should, however, be aware that in these reactions, γ -radiation of very high energy is being released, which requires additional lead shielding for radiation protection.

Nucleide	σ_γ [barn]	$E_{\text{resonance}}$ [meV]
${}^{113}\text{Cd}$	20600	178
${}^{151}\text{Eu}$	9200	321
${}^{155}\text{Gd}$	60900	26.8
${}^{157}\text{Gd}$	254000	31.4

Table 2.2: Examples for (n, γ) -resonances with the cross-section in barn and the resonance energy in meV.

As described by the Breit-Wigner-Formula, these resonance absorption cross-sections have very strong energy dependencies. The simple proportionality to the wavelength given in equation (2.10) no longer holds close to the resonance energies.

At high neutron energies, the resonances cannot be resolved anymore and thus the absorption cross-section appears to be smooth. Due to the high neutron energy, these cross-sections are typically small.

As an example, we show the energy dependence of the absorption cross-section for Cadmium and Gadolinium in Figure 2.4. Such data can be found JANIS Books provided by NEA [11].

Figure 2.4 shows that for lower energies, i. e. long wavelengths, the proportionality of the absorption cross-section to the wavelength holds to very good approximation. However,

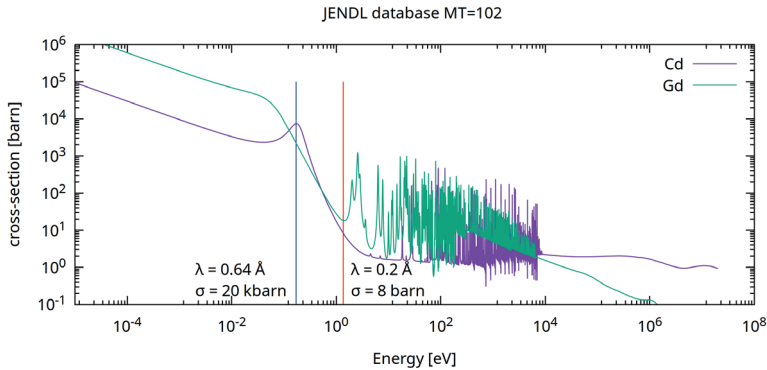


Fig. 2.4: Absorption cross-section of the element Cadmium and Gadolinium as a function of energy in a double logarithmic representation. The cross-sections for Cadmium at 0.64 Å and 0.2 Å are marked with lines. Tabulated values for the absorption cross-section MT = 102 were taken from the JENDL database [11].

there is a strong resonance for a wavelength of 0.64 Å, where the cross-section attains a maximum of about 20 kbarn. Above this energy, i. e. for shorter wavelengths, the absorption cross-section drops drastically. At a wavelength of 0.2 Å, it attains a value of only 8 barn. This shows that in the thermal energy range, Cadmium can be used as an efficient neutron absorber. However, one has to be careful and not use it for the same purpose in case of hot neutrons, where Cadmium becomes virtually transparent. There are many more resonances for higher neutron energies, which are not relevant for neutron scattering, where only hot ($T_{eq} = 2000$ K), thermal ($T_{eq} = 300$ K) and cold ($T_{eq} = 20$ K) neutrons are being used.

A similar strong energy dependence occurs for the element Gadolinium. Usually, neutron scatterers try to avoid samples containing Gadolinium since it is the most absorbing element, especially the isotope ^{157}Gd . However, the resonances lay right in the thermal neutron energy range. If the scattering experiment is performed with hot neutrons, the absorption cross-section of Gadolinium becomes much smaller and scattering experiments become feasible¹.

2.4 Coherent and incoherent scattering

As mentioned above, the nuclear interaction potential depends on the details of the nuclear structure and thus, the scattering length b is different for different isotopes of a given element and also for different nuclear spin states. In this section, we will discuss the effects of these special properties of the interaction of neutrons and nuclei for the scattering from condensed matter. Let us assume an arrangement of atoms with scatter-

¹ Another possibility is to use isotope enriched Gadolinium. While the isotope ^{157}Gd with natural abundance 15.7% has a thermal absorption cross section of 259000 barn, the isotope ^{158}Gd , which is the most abundant with 24.8%, has an absorption cross section of only 2.2 barn.

ing lengths b_i on fixed positions \mathbf{R}_i . For this case, the scattering potential writes

$$V(\mathbf{r}) = \frac{2\pi\hbar^2}{m_n} \sum_i b_i \delta(\mathbf{r} - \mathbf{R}_i). \quad (2.11)$$

The scattering amplitude is obtained from a Fourier transform

$$A(\mathbf{Q}) = \sum_i b_i e^{i\mathbf{Q}\mathbf{R}_i}. \quad (2.12)$$

When we calculate the scattering cross section, we have to take into account that the different isotopes are distributed randomly over all sites. Also the nuclear spin orientation is random, except for very low temperatures in high external magnetic fields. Therefore, we have to average over the random distribution of the scattering length in the sample

$$\frac{d\sigma}{d\Omega}(\mathbf{Q}) \sim |A(\mathbf{Q})|^2 = \langle \sum_i b_i e^{i\mathbf{Q}\mathbf{R}_i} \cdot \sum_j b_j^* e^{-i\mathbf{Q}\mathbf{R}_j} \rangle. \quad (2.13)$$

In calculating the expectation value of the product of the two scattering lengths at sites i and j , we have to take into account that according to the above assumption, the distribution of the scattering length on the different sites is completely uncorrelated. This implies that for $i \neq j$, the expectation value of the product equals to the product of the expectation values. Only for $i = j$ a correlation occurs, which gives an additional term describing the mean quadratic deviation from the average:

$$\langle b_i b_j \rangle = \begin{cases} \langle b \rangle \langle b \rangle = \langle b \rangle^2, & i \neq j \\ \langle b^2 \rangle = \langle (b - \langle b \rangle)^2 \rangle, & i = j \end{cases} \quad (2.14)$$

The line for $i = j$ results from the identity

$$\langle (b - \langle b \rangle)^2 \rangle = \langle b^2 - 2b\langle b \rangle + \langle b \rangle^2 \rangle = \langle b^2 \rangle - \langle b \rangle^2. \quad (2.15)$$

Therefore, we can write the cross section in the following form:

$$\begin{aligned} \frac{d\sigma}{d\Omega}(\mathbf{Q}) = \langle b \rangle^2 \left| \sum_i e^{i\mathbf{Q}\mathbf{R}_i} \right|^2 & \text{ "coherent"} \\ + N \langle (b - \langle b \rangle)^2 \rangle & \text{ "incoherent"} \end{aligned} \quad (2.16)$$

The scattering cross section is as a sum of two terms. Only the first term contains the phase factors $e^{i\mathbf{Q}\mathbf{R}_i}$, which result from the coherent superposition of the scattering from pairs of scatterers. This term takes into account interference effects and is therefore named *coherent scattering*. The scattering length averaged over the isotope- and nuclear spin-distribution enters this term. The second term in (2.16) does not contain any phase information and is proportional to the number N of atoms (and not to N^2 as for coherent scattering in fully constructive interference!). This term is not due to the interference of scattering from different atoms. As we can see from (2.15) (line $i = j$), this term corresponds to the scattering from single atoms, which subsequently superimpose in an

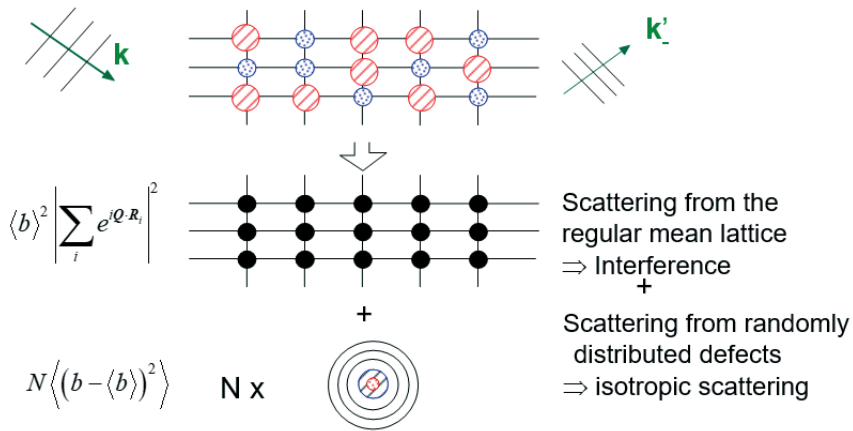


Fig. 2.5: Two-dimensional schematic illustration of the scattering process from a lattice of N atoms of a given chemical species, for which two isotopes (small dotted circles and large hatched circles) exist. The area of the circle represents the scattering cross section of the single isotope. The incident wave (top part of the figure for a special arrangement of the isotopes) is scattered coherently only from the average structure. This gives rise to Bragg peaks in certain directions. In the coherent scattering only the average scattering length is visible. Besides these interference phenomena, an isotropic background is observed, which is proportional to the number N of atoms and to the mean quadratic deviation from the average scattering length. This incoherent part of the scattering is represented by the lower part of the figure.

incoherent manner (adding intensities, not amplitudes!). This is the reason for the intensity being proportional to the number N of atoms. Therefore, the second term is called *incoherent scattering*. Coherent and incoherent scattering are illustrated in Figure 2.5.

The most prominent example for *isotope incoherence* is elementary nickel. The scattering lengths of the nickel isotopes are listed together with their natural abundance in Table 2.3 [8]. The differences in the scattering lengths for the various nickel isotopes are enormous. Some isotopes even have negative scattering lengths. This is due to resonant bound states, as compared to the usual potential scattering.

Isotope	Natural Abundance	Nuclear Spin	Scattering Length [fm]
^{58}Ni	68.27%	0	14.4(1)
^{60}Ni	26.10%	0	2.8(1)
^{61}Ni	1.13%	3/2	7.60(6)
^{62}Ni	3.59%	0	-8.7(2)
^{64}Ni	0.91%	0	-0.37(7)
Ni			10.3(1)

Table 2.3: The scattering lengths of the nickel isotopes and the resulting scattering length of natural $_{28}\text{Ni}$ [8].

Neglecting the less abundant isotopes ^{61}Ni and ^{64}Ni , the average scattering length is cal-

culated as

$$\langle b \rangle \approx [0.68 \cdot 14.4 + 0.26 \cdot 2.8 + 0.04 \cdot (-8.7)] \text{ fm} \approx 10.2 \text{ fm}, \quad (2.17)$$

which gives the total coherent cross section of

$$\Rightarrow \sigma_{coherent} = 4\pi \langle b \rangle^2 \approx 13.1 \text{ barn} \quad (\text{exact: } 13.3(3) \text{ barn}). \quad (2.18)$$

The incoherent scattering cross section per nickel atoms is calculated from the mean quadratic deviation:

$$\sigma_{incoherent}^{isotope} = 4\pi [0.68 \cdot (14.4 - 10.2)^2 + 0.36 \cdot (2.8 - 10.2)^2 + 0.04 \cdot (-8.7 - 10.2)^2] \text{ fm}^2 \quad (2.19)$$

$$= 5.1 \text{ barn} \quad (\text{exact: } 5.2(4) \text{ barn})$$

Values in parentheses are the exact values taking into account the isotopes ^{61}Ni and ^{64}Ni and the nuclear spin incoherent scattering (see below). From equations (2.18) and (2.19), we learn that the incoherent scattering cross section in nickel amounts to more than one third of the coherent scattering cross section.

The most prominent example for nuclear spin incoherent scattering is elementary hydrogen. The nucleus of the hydrogen atom, the proton, has the nuclear spin $I = 1/2$. The total nuclear spin of the system $\text{H} + n$ can therefore adopt two values: $J = 0$ and $J = 1$. Each state has its own scattering length: b_- for the singlet state ($J = 0$) and b_+ for the triplet state ($J = 1$) - compare Table 2.4.

Total Spin	Scattering Length	Abundance
$J = 0$ (singlet: $m_J = 0$)	$b_- = -47.5 \text{ fm}$	$\frac{1}{4}$ (one m_J state)
$J = 1$ (triplett: $m_J = -1, 0, +1$)	$b_+ = 10.85 \text{ fm}$	$\frac{3}{4}$ (three m_J state)
$\langle b \rangle = -3.739(1) \text{ fm}$		

Table 2.4: Scattering lengths for hydrogen [8].

Just as in the case of isotope incoherence, the average scattering length can be calculated

$$\langle b \rangle = \left[\frac{1}{4}(-47.5) + \frac{3}{4}(10.85) \right] \text{ fm} = -3.74 \text{ fm}. \quad (2.20)$$

This corresponds to a coherent scattering cross section of about ≈ 1.76 barn [8]

$$\Rightarrow \sigma_{coherent} = 4\pi \langle b \rangle^2 = 1.7568(10) \text{ barn}. \quad (2.21)$$

The nuclear spin incoherent part is again given by the mean quadratic deviation from the average

$$\sigma_{incoherent}^{nuclear\ spin} = 4\pi \left[\frac{1}{4}(-47.5 + 3.74)^2 + \frac{3}{4}(10.85 + 3.74)^2 \right] \text{ fm}^2 = 80.2 \text{ barn} \quad (2.22)$$

$$(\text{exact: } 80.26(6) \text{ barn}).$$

Comparing (2.21) and (2.22), it is immediately clear that hydrogen scatters mainly incoherently. As a result, we observe a large background for all samples containing hydrogen. We should avoid all hydrogen containing glue for fixing our samples to a sample stick. Finally, we note that deuterium with nuclear spin $I = 1$ has a much more favourable ratio between coherent and incoherent scattering:

$$\sigma_{coh.}^D = 5.592(7) \text{ barn}; \quad \sigma_{inc.}^D = 2.05(3) \text{ barn} \quad (2.23)$$

The coherent scattering lengths of hydrogen (-3.74 fm) and deuterium (6.67 fm) are significantly different. This can be used for contrast variation by isotope substitution in all samples containing hydrogen, i. e. in biological samples or soft condensed matter samples, see corresponding chapters. A further important element, which shows strong nuclear incoherent scattering, is vanadium. Natural vanadium consists to 99.75 % of the isotope ^{51}V with a nuclear spin $7/2$. By chance, the ratio between the scattering lengths b_+ and b_- of this isotope are approximately equal to the reciprocal ratio of the abundances. Therefore, the coherent scattering cross section is very small and the incoherent cross section dominates [8] with

$$\sigma_{coh.}^V = 0.01838(12) \text{ barn}, \quad \sigma_{incoh.}^V = 5.08(6) \text{ barn}. \quad (2.24)$$

For this reason, Bragg scattering from vanadium is difficult to observe above the large incoherent background. However, since incoherent scattering is isotropic, the scattering from vanadium can be used to calibrate multi-detector arrangements.

Here, we will not discuss scattering lengths for further elements and refer to the values tabulated in [8].

2.5 Magnetic neutron scattering

So far, we have only discussed the scattering of neutrons by the atomic nuclei. Apart from nuclear scattering, the next important process is the scattering of neutrons by the magnetic field created within the sample from the moments of unpaired electrons. This so-called magnetic neutron scattering comes about by the magnetic dipole-dipole interaction between the magnetic dipole moment of the neutron and the magnetic field of the unpaired electrons, which has spin and orbital angular momentum contributions. This magnetic neutron scattering allows us to study the magnetic properties of a sample on an atomic level, i. e. with atomic spatial- and atomic energy- resolution. Here we do not discuss magnetic neutron scattering any further and refer to the corresponding chapter on "Spin Dependent and Magnetic Scattering".

2.6 Comparison of probes

In this lecture, we have so far introduced the elementary formalism to describe the scattering process and discussed the interaction of neutrons with matter. We now want to

ask the question, for which problems in condensed matter research neutrons can be utilized successfully also in comparison to other probes, such as x-ray scattering or electron microscopy and electron scattering. To answer this question, we have to look at the ranges of energies, wavelengths or scattering vectors, which can be covered by various probes as well as the different contrast mechanisms.

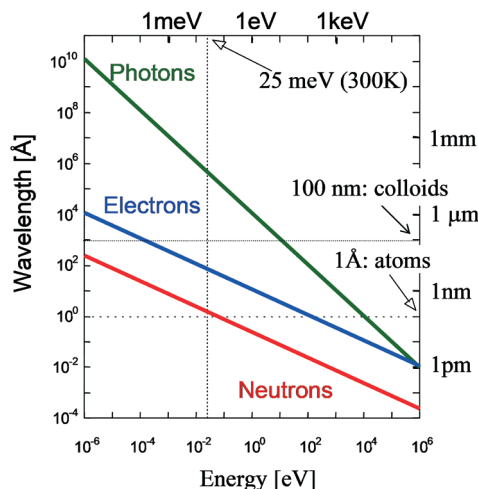


Fig. 2.6: Comparison of the three probes - neutrons, electrons and photons - in a double logarithmic energy-wavelength diagram.

Figure 2.6 shows a double logarithmic plot of the dispersion relation "wavelength versus energy" for the three probes neutrons, electrons and photons. The plot demonstrates how thermal neutrons of energy 25 meV are ideally suited to determine interatomic distances in the order of 0.1 nm, while the energy of x-rays or electrons for this wavelength is much higher. However, with modern techniques at a synchrotron radiation source, energy resolutions in the meV-region become accessible even for photons of around 10 keV corresponding to a relative energy resolution $\Delta E/E \approx 10^{-7}$. The graph also shows that colloids with a typical size of 100 nm are well suited for the investigation with light of energy around 2 eV. These length scales can, however, also be reached with thermal neutron scattering in the small angle region. While Figure 2.6 thus demonstrates for which energy-wave-length combination a certain probe is particularly useful, modern experimental techniques extend the range of application by several orders of magnitude.

It is therefore useful to compare the scattering cross sections as it is done in Figure 2.7 for x-rays and neutrons. Note that the x-ray scattering cross sections are in general a factor of 10 larger as compared to the neutron scattering cross sections. This means that the signal for x-ray scattering is stronger for the same incident flux and sample size. But caution has to be applied that the conditions for kinematical scattering are fulfilled. For x-rays, the cross section is proportional to the square of the number of electrons and thus varies in a monotonic fashion throughout the periodic table. Clearly it will be diffi-

cult to determine hydrogen positions with x-rays in the presence of heavy elements such as metal ions. Moreover, there is a very weak contrast between neighbouring elements as can be seen from the transition metals Mn, Fe and Ni in Figure 2.7. However, this contrast can be enhanced by anomalous scattering, if the photon energy is tuned close to the absorption edge of an element. For neutrons the cross section depends on the details of the nuclear structure and thus varies in a non-systematic fashion throughout the periodic table. For example, there is a very high contrast between Mn and Fe. With neutrons, the hydrogen atom is clearly visible even in the presence of such heavy elements as Uranium. Moreover there is a strong contrast between the two Hydrogen isotopes H and D. This fact can be exploited for soft condensed matter investigations by selective deuteration of certain molecules or functional groups. This will vary the contrast within the sample.

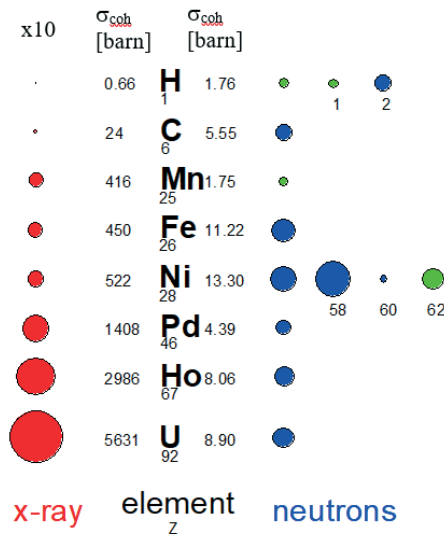


Fig. 2.7: Comparison of the coherent scattering cross-sections for x-rays and neutrons for a selection of elements. The area of the colored circles represent the scattering cross section, where in the case of x-rays a scale factor 10 has to be applied. For neutrons, the blue and green circles distinguish the cases where the scattering occurs with or without a phase shift of π . For ^1H and ^{28}Ni , scattering cross sections for certain isotopes are given in addition to the averaged values for the natural element.

Finally, both neutrons and x-rays allow the investigation of magnetism on an atomic scale. Magnetic neutron scattering is comparable in strength to nuclear scattering, while non-resonant magnetic x-ray scattering is smaller than charge scattering by several orders of magnitude². Despite the small cross sections, non-resonant magnetic x-ray Bragg scattering from good quality single crystals yields good intensities with the brilliant beams at modern synchrotron radiation sources. While neutrons are scattered from the magnetic induction within the sample, x-rays are scattered differently from spin and

² Typically between 6 to 9 orders of magnitude.

orbital momentum and thus allow one to measure both form factors separately. Inelastic magnetic scattering e.g. from magnons or so called quasielastic magnetic scattering from fluctuations in disordered magnetic systems is a clear domain of neutron scattering. Finally, resonance exchange scattering XRES of synchrotron x-rays allows one not only to get enhanced intensities, but also to study magnetism with element- and band sensitivity.

With appropriate scattering methods, employing neutrons, x-rays or light, processes in condensed matter on very different time and space scales can be investigated. Which scattering method is appropriate for which region within the "scattering vector Q - energy E plane" is plotted schematically in Figure 2.8. A scattering vector Q corresponds to a certain length scale, an energy to a certain frequency, so that the characteristic lengths and times scales for the various methods can be directly determined from the figure. Examples for applications and information on instrumentation will follow in subsequent lectures.

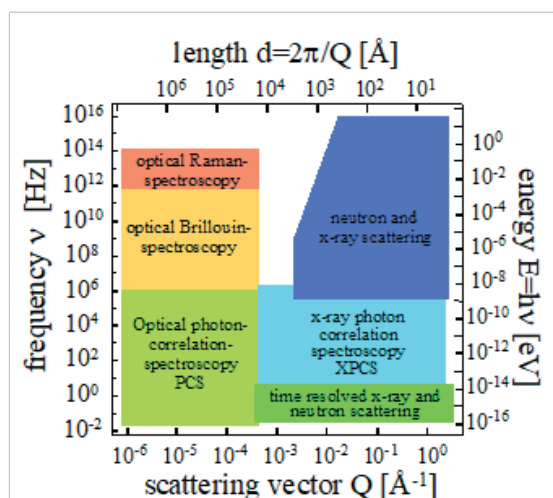


Fig. 2.8: Regions in frequency ν and scattering vector Q or energy E and length d , which can be covered by various scattering methods.

References

- [1] G. L. Squires, "Introduction to the Theory of Thermal Neutron Scattering" Dover (1997)
- [2] K. Sköld, D. Price (Eds.), "Methods of Experimental Physics" Neutron Scattering Part A-C, Academic Press (1987)
- [3] J. M. Cowley, "Diffraction Physics" North Holland, Amsterdam (1995)

-
- [4] S. W. Lovesey, "Theory of neutron scattering from condensed matter", Clarendon Press, Oxford (1987)
 - [5] A. Furrer, J. Mesot, T. Strässle, "Neutron Scattering in Condensed Matter Physics", World Scientific, London (2009)
 - [6] J. M. Carpenter, C.-K. Loong, "Elements of Slow-Neutron Scattering", Cambridge University Press (2015)
 - [7] B. W. Batterman, H. Cole, "Dynamical Diffraction of X-Rays by Perfect Crystals", Rev. Mod. Phys. 36, 681 - 717 (1964)
 - [8] A. Dianoux, G. Lander (Eds.), "Neutron Data Booklet", Institute Laue-Langevin (2002)
 - [9] D. E. Garber, R. R. Kinsey, "Neutron Cross-Section II", BNL-Report (1976), also: S. Mughabghab "Atlas of Neutron Resonances" Elsevier (2006)
 - [10] E. Price (Ed.), "International Tables for Crystallography, Volume C", International Union of Crystallography (2004)
 - [11] <https://www.oecd-nea.org/janisweb/book/neutrons>

Exercises

E2.1 Multiple choice

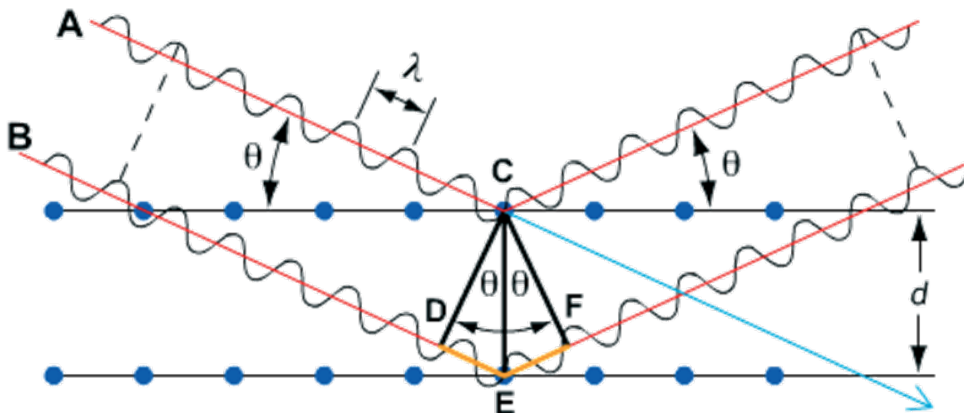
1. The typical diameter of an atom is closest to
 - 1 μm
 - 1 mm
 - 1 pm
 - 1 fm
2. The typical diameter of a neutron is closest to
 - 1 μm
 - 1 mm
 - 1 pm
 - 1 fm
3. Neutrons are neutral particles, neutron counting is done electronically, i.e. an electronic pulse has to be generated in a neutron detector. What would you use as counting gas in order to build a neutron detector:
 - ^3He
 - ^4He
 - H
 - D
4. You have to build a slit in order to define a beam size for neutrons of wavelength 1 \AA . Which material could you use:
 - Pb
 - Gd
 - Cd
 - Al
5. For a scattering experiment on Ni, you need a sample with strong coherent scattering, but as little background as possible. Which isotope mixture would you chose?
 - 100% ^{58}Ni
 - 100% ^{61}Ni
 - 100% ^{64}Ni
 - 57% ^{62}Ni + 43% ^{61}Ni

6. Kinematic scattering theory takes into account
- refraction
 - attenuation
 - multiple scattering
 - none of the above
7. You have measured the scattered intensity $I(\mathbf{Q})$ as a function of the scattering vector \mathbf{Q} . Which of the following statements are correct for kinematic scattering:
- The Fourier transform of $I(\mathbf{Q})$ is proportional to the scattering density.
 - $I(\mathbf{Q})$ is always described by the Laue function.
 - $I(\mathbf{Q})$ is the Patterson- or static pair correlation function.
 - The phase problem does not allow one to determine the atomic position directly by a simple mathematical procedure.

E2.2 Bragg scattering

Bragg had the idea to describe scattering from a three-dimensional periodic arrangement of scatterers (e.g. atoms in a crystal) by the interference of waves reflected from parallel atomic planes, see sketch below. For constructive interference, sharp intensity maxima appear as a function of scattering angle. These peaks are called “Bragg reflections”.

- a) After scattering, the waves reflected from the two planes show a path length difference. Which relation does this path length difference have to fulfil in order to achieve coherent superposition and thus an intensity maximum?
- b) Derive the condition for the occurrence of such a Bragg peak in terms of wavelength λ , scattering angle 2θ and distance between the planes d , the so-called Bragg equation.
- c) How does the Bragg equation relate to the Laue conditions?



E2.3 Neutron scattering from Ti-Zr alloys

Ti and Zr form a continuous alloy series with hexagonal crystal structure. Your task is to build a sample chamber from a $\text{Ti}_x\text{Zr}_{1-x}$ alloy for diffraction experiments with thermal neutrons. The chamber should produce as little background due to coherent Bragg reflections as possible.

- Which stoichiometry would you choose for the alloy? (It is sufficient to specify the condition, the actual calculation is optional)
- What is the disadvantage of such a sample chamber?

nuclid	natural abundance	scattering length b [fm]	nuclid	natural abundance	scattering length b [fm]
^{46}Ti	8.2%	4.93	^{90}Zr	51.45%	6.4
^{47}Ti	7.5%	3.63	^{91}Zr	11.32%	8.7
^{48}Ti	73.8%	-6.08	^{92}Zr	17.19%	7.4
^{49}Ti	5.4%	1.04	^{94}Zr	17.28%	8.2
^{50}Ti	5.2%	6.18	^{96}Zr	2.76%	5.5

E2.4 Neutron absorption

Aluminium has a face centred cubic crystal structure (cubic close packed lattice) with a lattice constant of $a_0 = 4.04959 \text{ \AA}$. The absorption cross section for neutrons of velocity 2200 m/s amounts to 0.231 barn.

- Calculate the absorption cross section of Aluminium for neutrons of wavelength $\lambda = 1 \text{ \AA}$.
- Besides pure absorption, do we have to take into account other processes when calculating the total attenuation?

The following exercise parts c and d are optional!

- Due to absorption, the neutron beam is attenuated according to $dI = -\mu \cdot I \cdot dx$ or $I = I_0 e^{-\mu \cdot x}$ where μ is the linear absorption coefficient. Calculate μ for neutrons of wavelength 1 \AA for Aluminium. (Hint: Calculate the absorption cross section per unit cell and compare to the unit cell dimensions).
- Determine the attenuation of a 1 \AA neutron beam in an Al slab of 10 cm thickness due to absorption only in percentage of the incident flux.

E2.5 Gravity

Due to the mass of the neutron and the low velocities at lower energies, the neutron experiences gravitational forces with $g = 9.8 \text{ m/s}^2$. Depending on the neutron energy, these disturbance might not be negligible.

- a) Calculate the velocity of neutrons with energies of 1 meV, 25 meV, 10 eV and 1 MeV.
- b) Typical instrument lengths for neutron scattering range from a few meters up to 150 m. What is the vertical deviation for instruments of 100 m length for the before specified energies?
- c) What impact could the deviation from the flight path have? How could this be compensated?

3 Neutron Sources

U. Rücker

Jülich Centre for Neutron Science

High Brilliance Source project group

Forschungszentrum Jülich GmbH

Contents

3.1	Introduction	2
3.2	Neutron Production	4
3.2.1	Radioactive neutron sources: (α ,n) reaction	4
3.2.2	Photoneutrons: (γ ,n) reactions	5
3.2.3	(p,n) and (d,n) reactions.....	5
3.2.4	Nuclear fusion: d+d or d+t reactions	7
3.2.5	Nuclear fission reactors	8
3.2.6	Spallation neutron sources.....	9
3.2.7	Efficiency of the neutron production.....	11
3.3	Manipulation of travelling neutrons	11
3.3.1	Moderation.....	11
3.3.2	Monochromatization.....	13
3.4	Neutron Transport.....	15
3.5	Neutron detectors	16
	References	17
	Exercises	18

Lecture Notes of the JCNS Laboratory Course Neutron Scattering. This is an Open Access publication distributed under the terms of the Creative Commons Attribution License 4.0, which permits unrestricted use, distribution, and reproduction in any medium, provided the original work is properly cited. (Forschungszentrum Jülich, 2024)

3.1 Introduction

The neutron is a baryon without electric charge. In contrast to the charged proton, it doesn't exist as a stable free particle, but only in bound states together with protons in atomic nuclei. The free neutron has been observed first in 1930 by W. Bothe and H. Becker. They found that if energetic α particles emitted from polonium impinge on certain light elements as e.g. beryllium, boron, or lithium, an unusually penetrating radiation was produced [1].

In 1932 J. Chadwick proved that this radiation consists of neutral particles with about the same mass as the proton. This particle had earlier been proposed as a part of atomic nuclei by E. Rutherford. Since then, it was named neutron. Chadwick has been awarded the nobel prize in physics in 1935 for the discovery of the neutron [2].

In contrast to the bound neutron, the free neutron experiences a β decay



into proton, electron, and electron antineutrino with a lifetime of almost 15 minutes. This lifetime is long enough to be able to use the neutron as a probe for the investigation of other objects as e.g. a solid material.

The mass m_n of the free neutron (compare: m_p of the free proton) is

$$\begin{aligned} m_n &= 1.6749 * 10^{-27} \text{ kg} = 1.008665 \text{ u} \\ (m_p &= 1.6726 * 10^{-27} \text{ kg} = 1.007277 \text{ u}) \end{aligned} \quad (3.2)$$

If the energy E of the neutron is taken into account, we always mean the kinetic energy.

$$E = \frac{1}{2} m_n \mathbf{v}^2 = \frac{\mathbf{p}^2}{2m_n} \quad (3.3)$$

with the velocity vector \mathbf{v} and the kinetic momentum \mathbf{p} . A temperature equivalent T of the kinetic energy can be defined using the Boltzmann constant k_B .

$$E = k_B T \quad (3.4)$$

The neutron's wavelength λ is obtained from the de Broglie relation

$$\lambda = \frac{h}{m_n |v|} = \frac{h}{|\mathbf{p}|} = \frac{h}{\sqrt{2m_n E}} \quad (3.5)$$

and the wave vector \mathbf{k} describes the propagation of the neutron wave

$$\hbar \mathbf{k} = \mathbf{p} \quad \text{with} \quad k = |\mathbf{k}| = \frac{2\pi}{\lambda} \quad (3.6)$$

A useful unit for the wavelength λ is the Ångström: $1 \text{ \AA} = 0.1 \text{ nm} = 10^{-10} \text{ m}$ and for the energy E it's the electron Volt: $1 \text{ eV} = e * 1 \text{ V} = 1.6022 * 10^{-19} \text{ J}$ with the electron's charge e .

Some useful conversions are

$$\lambda [\text{\AA}] = \frac{3956}{v [\text{m/s}]} \quad \text{and} \quad (3.7)$$

$$E [\text{meV}] = \frac{81.8}{\lambda^2 [\text{\AA}]} \quad (3.8)$$

The following table 3.1 shows the relations between energy, velocity, wavelength, and temperature of the neutron for a few examples which are commonly used. From these numbers, it immediately becomes obvious that neutrons with a temperature around room temperature have a wavelength comparable to interatomic distances, so they are useful to investigate the atomic order of condensed matter.

Energy E	Velocity v	Wavelength λ	Temperature T
1 MeV	$1.38 * 10^7 \text{ m/s}$	$2.86 * 10^{-4} \text{ \AA}$	$1.16 * 10^{10} \text{ K}$
1 eV	13800 m/s	0.286 Å	11600 K
230 meV	6600 m/s	0.6 Å	2700 K
82 meV	4000 m/s	1 Å	950 K
26 meV	2230 m/s	1.77 Å	300 K
10 meV	1380 m/s	2.86 Å	116 K
1.7 meV	570 m/s	6.9 Å	20 K

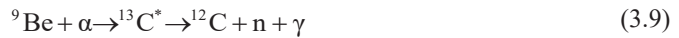
Table 3.1: Relation between energy, velocity, wavelength, and temperature of the neutron.

3.2 Neutron Production

Stable neutrons only exist in a bound state in atomic nuclei. A nuclear reaction is always needed to release a neutron from a nucleus. In most cases, energy is needed to release a free neutron, in all cases an activation barrier has to be overcome. Today, many reaction paths are known that yield free neutrons which are presented in the following.

3.2.1 Radioactive neutron sources: (α, n) reaction

The production of neutrons with α radiation has historically led to the discovery of the neutron [1,2]. The reaction



is still used today for small neutron sources used for detector calibration or constant activation purposes, e.g. in smoke detectors. Today's most common alpha emitter used in neutron sources is ${}^{241}\text{Am}$ (432 years half-life), artificially produced by Pu breeding in a nuclear reactor. Also ${}^{238}\text{Pu}$ or natural ${}^{226}\text{Ra}$ can be used together with Be to produce small neutron sources.



Fig. 3.1: *AmBe neutron source used for detector calibration. The source's α activity is 350 MBq, yielding a neutron production of 20000 n/s. The measured dose rate emitted by this source is about 10 $\mu\text{Sv/h}$.*

The neutron yield of an AmBe neutron source is about $6 * 10^4$ neutrons per GBq α activity. These neutron sources are hermetically sealed, so that the material can be handles safely and the α radiation is properly shielded. The strongly penetrating neutron and γ radiations are emitted.

Figure 3.1 shows an AmBe neutron source used in our laboratory to calibrate neutron detectors for the radiation safety interlock system. The white "pig" on the picture is a neutron detector encapsulated in a polyethylene thermal moderator making it possible to measure the intensity of thermal and fast neutron fields (see section 3.1) for radiation safety purposes.

3.2.2 Photoneutrons: (γ,n) reactions

The absorption of highly energetic γ photons can be used to excite a lot of nuclei to release a neutron. This works as well with light nuclei as Be as with heavy nuclei as W or Pb. A combination of ^{123}Sb (activated to ^{124}Sb as γ source) and Be (as neutron source) can be activated in a the neutron field of a nuclear reactor and emits monoenergetic neutrons with an energy of 24 keV [3]. The half-life of this source is 60 days. Because of its low neutron energy it is used to keep a residual neutron field in a nuclear reactor during shutdown.

Another application of (γ,n) reactions is a Compact Accelerator based Neutron Source (CANS) based on an electron accelerator and a thick heavy metal target. With an electron beam of some 100 MeV energy impinging on the target, a lot of highly energetic bremsstrahlung is produced whose energy is sufficient to release neutrons from the same target material. An example of this type of neutron source is the HUNS source at Hokkaido university, Japan [4]. The drawback of this kind of accelerator driven neutron source is the fact that the γ radiation produced by the electrons has an energy such high that is difficult to shield and that also in the shielding material neutrons are released by (γ,n) processes which again have to be shielded.

3.2.3(p,n) and (d,n) reactions

Accelerated protons or deuterons impinging on a metal target can be used to induce neutron production in a very efficient manner. Light ions can be accelerated in an electrostatic or a RF linear accelerator to energies in the range of a few MeV to a few 10 MeV. For most target materials the first neutron production channels open well below 20 MeV activation energy with additional contributions up to 100 MeV and higher. In case of deuteron beams, also the stripping of the deuteron's neutron increases the neutron production rate. Figure 3.2 shows the energy dependence of the probability of different neutron production reaction channels for deuterons impinging on Be. For the deuteron stripping, there is no energy threshold, the neutron emission from Be starts at about 2 MeV deuteron energy [5].

Due to the flexibility of the light ion accelerators, this kind of neutron source can be operated in pulsed mode at high intensities. The low energy protons or deuterons are stopped after a short penetration length in the target material. Therefore, the volume where primary neutrons are produced is small, so that the neutrons can efficiently be coupled into a thermal moderator. Based on this principle is the design of most of the Compact Accelerator based Neutron Sources (CANS), as they are being operated in many places in Asia and the United States.

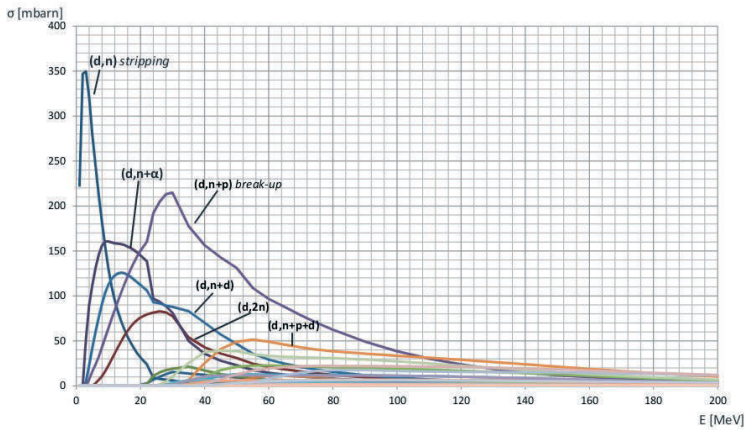


Fig. 3.2: Calculated energy dependence of the cross sections of different neutron emitting reactions for deuterons impinging on Be based on the TENDL nuclear data library [5].

This concept of low-energy accelerator driven neutron sources is well scalable from 100 W to 100 kW average proton beam power at the target. The smaller sources are suitable for laboratory characterization of samples along with the sample preparation or for quality control of industrial processes using dedicated instruments. The larger sources can be equipped with neutron scattering or analysis instrumentation that is competitive with the instruments installed at today's high flux research reactors.

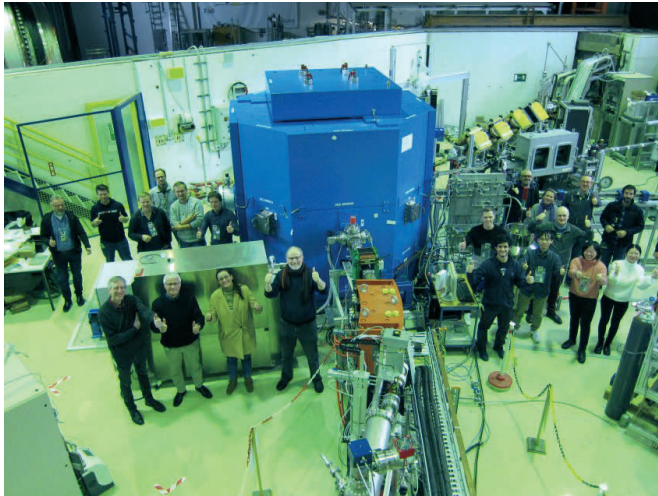


Fig. 3.3: JULIC Neutron Platform.

Here in Jülich and in several partner institutions in Europe, we have developed plans for High-Current Accelerator-driven Neutron Sources (HiCANS). The project of the High Brilliance neutron Source (HBS) comprises a pulsed 70 MeV proton accelerator that serves 3 target stations with different pulse schemes to provide the most suitable neutron beams for up to 36 instruments [6].

As a proof for the feasibility of the technology developed for the HBS neutron source, we have built a full-scale demonstrator at the pulsed JULIC proton accelerator of the Nuclear Physics Institute (IKP). Figure 3.3 shows the JULIC Neutron Platform which has been equipped with 6 beamlines for neutron imaging, reflectometry, moderator spectroscopy, diffraction, and detector tests and is in operation since 13.12.2022.

3.2.4 Nuclear fusion: d+d or d+t reactions

The neutron production by nuclear fusion of deuterium (d or ^2H) and tritium (t or ^3H) can be induced at a low ion energy (below 100 keV) that can easily be achieved with a small accelerator. The two reactions available yield monochromatic neutrons:



Technologically demanding is the fact that the target material is a gas. This is solved by using a metallic hydride as target. From time to time the target is burnt up and must be refreshed. Figure 3.4 shows a commercial neutron generator based on the reaction (3.10). It can produce up to 10^8 n/s in continuous or pulsed operation.

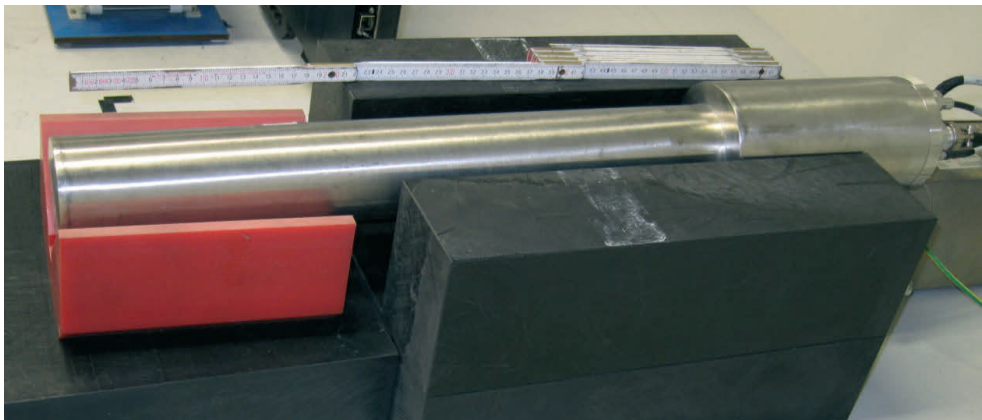


Fig. 3.4: A fusion neutron generator GENIE 16 GT commercially available from EADS Sodern. The tritium loaded metal hydride neutron production target is located 15 cm from the end of the long cylinder.

3.2.5 Nuclear fission reactors

Nuclear fission reactors are high-intensity neutron sources available since the 1940s. If ^{235}U is irradiated with thermal neutrons, the nucleus absorbs the neutron and breaks into typically two fission fragments. In this process neutrons are emitted with an average of 2.3 neutrons per fission process.

In a nuclear reactor, these fission neutrons are used to sustain a chain reaction. A sufficient amount of ^{235}U (more than the critical mass) together with a suitable thermal moderator (see section 3.3.1) that slows down the originally fast fission neutrons makes it possible that at least 1 of the 2.3 fission neutrons can again be absorbed by a ^{235}U nucleus. The remaining neutrons either escape from the core region (e.g. into a neutron beamline towards a neutron scattering experiment), or they are absorbed by the moderator or any structure material. The excess neutrons need to be absorbed by a reactor control system that can tune the chain reaction to a stable level or a slight deviation for an increase or decrease of the reaction speed, i.e. the reactor power.



Fig. 3.5: *A model of the fuel element of the FRM II research reactor. The inclined plates contain the fuel, the cooling water flows in between the fuel plates. The central channel is the position of the control rod. The core of FRM-2 is the most compact ^{235}U reactor core ever built. (Copyright W. Schürmann, TU Munich)*

For the reactor control it is important that a small fraction of the neutrons (0.65% in the case of ^{235}U) are not emitted immediately after the fission, but about 10 to 20 s later. If the chain reaction is leveled so that the prompt neutrons are not sufficient to sustain the chain reaction, the delayed neutrons can be used to control a slow change in reactor power. The reactor must never be operated in a state where the prompt neutrons alone sustain the chain reaction (“prompt critical reactor”) [7]. In this case, the reactor power rises exponentially in an uncontrollable manner. This happened for example at the Chernobyl accident.

In contrast to a nuclear power plant with an extended core for optimal cooling conditions, the fuel of a research reactor is arranged in a compact way to achieve high neutron fluxes that can be used for irradiation inside the moderator region or for the extraction of intensive neutron beams with relatively low thermal power. Figure 3.5 shows a model of the fuel element of the FRM II research reactor in Garching near Munich. The reactor core consists of this single fuel element loaded with highly enriched ^{235}U , a light water cooling circuit passing vertically through the fuel element and a heavy water moderator and reflector that brings back thermal neutrons to the core to sustain the chain reaction, and that feeds tangential beam tubes to extract neutrons from the reactor to use them in neutron beam lines outside the reactor vessel. The reactor power is controlled by a neutron absorber rod located in the centre of the fuel element.

Historically, and still today, nuclear reactors are the main source of high-intensity neutron beams for research applications. As most research reactors have been built in the years 1950 – 1970, they are aging and more and more of them are shut down. Their role as a supply of neutron beams for research is gradually taken over by CANS and by spallation neutron sources.

3.2.6 Spallation neutron sources

Spallation is the interaction of heavy nuclei with high-energy protons, i.e. protons with energy in the GeV range. In the collision of a nucleus with a proton at such high energy, the nucleus is completely disintegrated. At energies above 150 MeV the de Broglie wavelength of the proton is small enough that the proton interacts with the individual nucleons in the target nucleus. The nucleus is highly excited, up to 30 neutrons are evaporated from a single nucleus and several small nuclei are formed [8].

Spallation is most energy-efficient process of neutron production, but a lot of the energy is transferred onto the neutrons, so that neutrons with energies up to 500 MeV need a high effort to design a suitable shielding for the operation of such a source. Due to the large stopping length of the high energy protons, the neutron production zone is elongated to several 10 cm.

Today’s strongest pulsed neutron sources are spallation sources. The European Spallation Source ESS, which is currently being built in Lund (Sweden) will be the strongest research neutron source worldwide [9]. It is designed with a 600 m long linear proton accelerator to achieve 2000 MeV proton energy. The protons impinge on the target which is shown in figure 3.6. The wheel is 2.6 m in diameter and consists of hundreds of heavy metal Tungsten bricks encased in a disk of stainless-steel shielding. The unit weighs 11 tonnes and rotates at 23.3 rotations per minute to distribute the heat load to the entire tungsten volume, where it is removed by a He gas cooling circuit. Above and below of the target wheel are the moderators to convert the primary high-energy neutrons to a useful energy (see section 3.3.1).

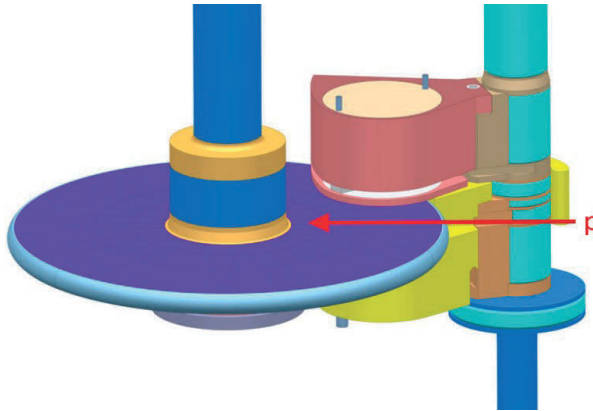


Fig. 3.6: Model of the ESS target wheel and moderator-reflector system (from [9]).

The ESS is designed as a long pulse spallation source which receives proton pulses of 2.86 ms length immediately from the linear accelerator. Other spallation sources, e.g. ISIS (UK) or SNS (USA), are constructed as short pulse spallation sources with pulse lengths down to 1 μ s. Figure 3.7 shows the schematic setup of such a source. The protons are accelerated in a linear accelerator in the form of H^- ions. The bunches coming from the linear accelerator are subsequently injected into a compressor ring for protons. At the point of injection (which is located inside a strong magnetic field) the electrons are stripped off by a carbon sieve, so that the injection of the H^- ions is performed with the opposite direction of curvature compared to the naked protons circulating in the ring.

The time of one revolution inside the ring is equal to the time distance between the bunches from the linear accelerator, so that the newly injected protons meet the already circulating protons in phase. With this technique, the length of the pulse can be reduced by ~ 1000 while the peak current is increased by the same factor.

For some instruments, the shorter neutron pulses have advantages for the energy and wavelength resolution of the measurements.

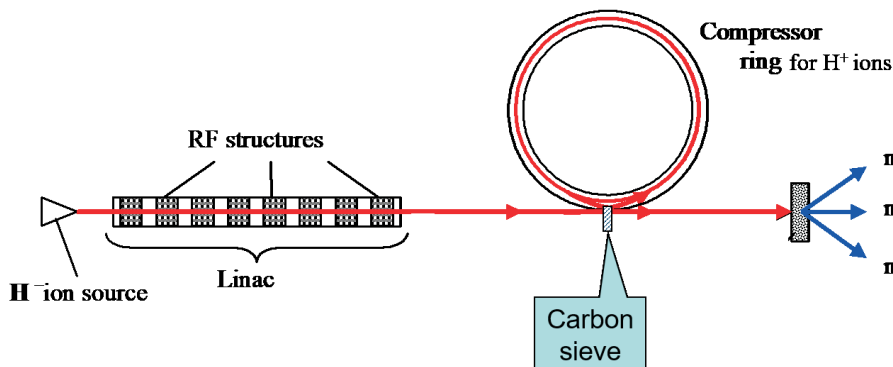


Fig. 3.7: Schematic of a short pulse spallation source with a compressor ring.

3.2.7 Efficiency of the neutron production

Table 3.2 shows the neutron yield and the heat deposition per neutron for different neutron production reaction. From this point of view, fusion is the most attractive opportunity, but the technology is not yet ready to use this for a high-flux neutron source.

Spallation is more attractive than fission, but the investments necessary for building a high energy proton accelerator are high, so that not many sources of that kind have been built yet. The (p,n) reactions seem to be not attractive, but the well confined neutron cloud emitted from the compact target compensates quite well the reduced neutron emission probability.

Reaction	Energy/event	Yield (neutron/event)	Deposited heat (MeV/neutron)
(d,t) fusion		~1 neutron/fusion	3
²³⁵ U fission		~1 neutron/fission	180
Pb spallation	1 GeV	~ 20 neutron/proton	23
Be (p,n)	25 MeV	0.006 neutron/proton	1200

Table 3.2: Efficiency of different neutron production reactions.

3.3 Manipulation of travelling neutrons

3.3.1 Moderation

Primary free neutrons that are produced in a nuclear reaction typically have an energy of a few MeV, in case of spallation it might be a lot higher. To make these neutrons useful to investigate atomic matter, this energy has to be reduced below 1 eV according to table 3.1. The useful neutron energies correspond to about room temperature, for crystallography maybe higher, for investigations of complex matter (e.g. macromolecules or layered structures) even lower. This neutron energy can be reached by bringing the neutron field into thermal equilibrium with something that has the proper temperature and that interacts strongly with the neutrons.

One important candidate to do so is hydrogen in any compound that has a high density. The hydrogen atom has approximately the same weight as the neutron, so collisions between a neutron and a hydrogen nucleus (i.e. a proton) can optimally transfer momentum from the neutron to the proton. In addition, the inelastic scattering cross section that describes the probability of an energy transfer between hydrogen nuclei and neutrons is high.

So, for neutron moderation to thermal temperatures water H₂O or heavy water D₂O are ideal. H₂O has the advantage that it is easily available and does not produce any radioactive waste, but the disadvantage of a non-negligible neutron absorption. Thermalization of a MeV neutron in H₂O needs about 7 collisions and 10 μs of time.

D₂O has the advantage that it hardly absorbs neutrons, but if it does, radioactive tritium is produced. In addition, the interaction between neutrons and D₂O is weaker compared to H₂O, so that the moderator volume needs to be bigger and the neutron field is diluted. If the thermal load is low, also solid polyethylene is a good thermal neutron moderator, but it cannot be cooled as efficiently as liquid water. Another useful thermal moderator is Be which is solid but with a high thermal conductivity and has almost no neutron absorption. A thermal moderator efficiently delivers neutrons in the wavelength range between 0.7 and 2.5 Å.

If neutrons with longer wavelengths are desired, a "cold neutron source" is used to moderate thermal neutrons to even lower temperatures. Liquid H₂, liquid D₂, solid methane CH₄ or solid mesitylene C₉H₁₂ are the most frequently used substances in a cold neutron source. A cold neutron source efficiently delivers neutrons in the wavelength range between 2 and 8 Å. Depending on the realization, sometimes neutrons with wavelengths up to 20 Å can be used for special applications.

In some research reactors specialized beamlines for crystallography and high-energy spectroscopy are fed by a hot neutron source. A hot neutron source is a graphite moderator heated (by the γ radiation close to the fuel element) to temperatures between 2500 and 3000 K. This moderator efficiently delivers neutrons with wavelengths down to 0.2 Å corresponding to an energy up to 2 eV.

Figure 3.8 shows the neutron spectra available at the FRM II reactor. This reactor has a large D₂O tank as thermal moderator where a cold source with liquid D₂ and a hot source with a graphite moderator are inserted.

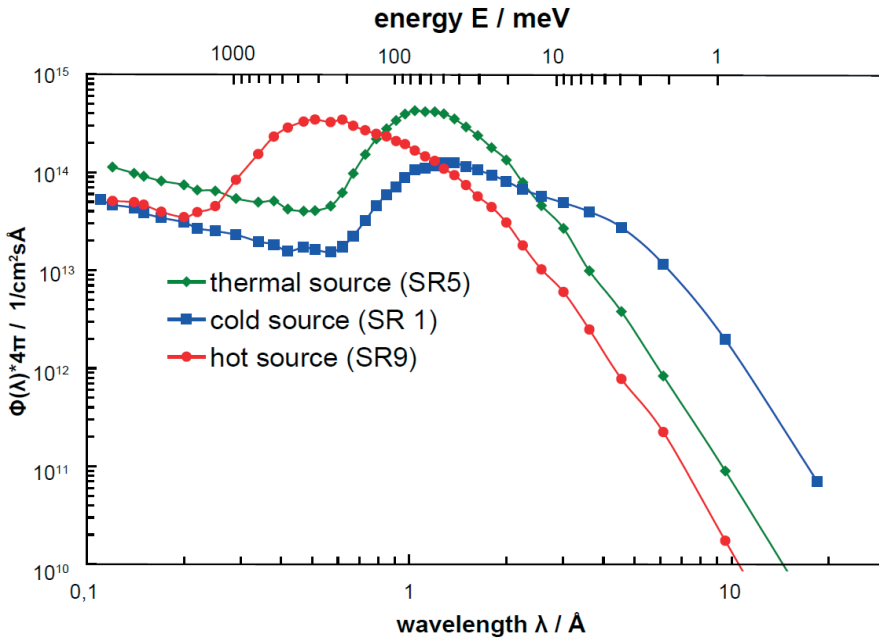


Fig. 3.8: Neutron spectra available at the beam tubes of FRM II.

3.3.2 Monochromatization

In a neutron scattering experiment it is in most cases necessary to know the neutron's wavelength or energy when it interacts with the sample. There are three methods of monochromatization commonly used:

Time-Of-Flight (TOF)

The TOF method uses the energy dependent velocity of the neutrons (eq. (3.5) and (3.7)). The neutron beam is structured in time by a rotating chopper that is transparent only for a short fraction or it is emitted from a pulsed source. When the neutron beam travels the distance between source / chopper to the detection system, the neutrons with shorter wavelength arrive earlier at the detector. With the control of the timing between source / chopper and the detector system, the wavelength of every neutron can be reconstructed from the arrival time. Figure 3.9 shows a schematic diagram of the definition of an instrument's band width and resolution in time-of-flight by several choppers. This instrument is located at a continuous source (i.e. at a research reactor).

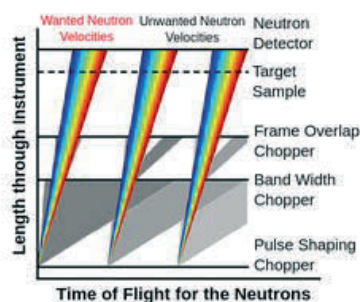


Fig. 3.9: Time-of-flight diagram for an instrument with three choppers.

It can be seen that the neutrons are only used during the opening time of the first chopper, all the remaining time the neutrons are discarded. In the case of an accelerator driven source this can be optimized so that neutrons are only produced when they can be accepted by the instruments. A duty cycle of some 2% of the source are sufficient to provide useful measurement data at the detector for some 95% of the time by just using one wavelength after the other.

Velocity selector

A velocity selector is a rotating turbine wheel with neutron absorbing channel walls, as can be seen in figure 3.10. The neutron beam impinges in a direction parallel to the turbine axis. If the speed of the neutrons matches the rotational motion of the channel, the neutrons of this speed can pass the velocity selector. This technique is used for instruments that need a monochromatic beam with moderate wavelength resolution (10-20%).



Fig. 3.10: Turbine wheel of the velocity selector used at KWS-3. The selector blades consist of a MgLi alloy with neutron absorbing ${}^6\text{Li}$.

Monochromator crystals

Bragg reflections on a single crystal happen only, if wavelength and angle of incidence on a suitable lattice plane match. Therefore, a neutron beam with well-defined direction can be monochromatized by Bragg reflection from a monochromator crystal. Depending on the quality of the crystal, a wavelength resolution between 0.05% and 1.5% can be achieved. Sometimes "too good" crystals are treated mechanically to disturb the perfection of the lattice to be able to reflect a wider wavelength band.

Fig. 3.11 shows a double focusing Cu monochromator. It is equipped with 105 single crystals that have been hammered to increase the reflectivity. This monochromator can be focused vertically to be able to illuminate small samples more strongly and it can be focused horizontally to be able to transport a larger wavelength band (due to different Bragg angles of the individual columns of the monochromator) to the sample on the expense of a higher beam divergence.



Fig. 3.11: Double focussing monochromator equipped with 105 Cu single crystals.

3.4 Neutron Transport

Originally, thermal or cold neutrons are emitted isotropically from the moderator. Instruments directly located at a beamtube of a nuclear reactor can use the entire solid angle that is illuminated through the opening of the reactor shielding. But, as space around the shielding is very limited, a way to bring neutrons efficiently to instruments at a larger distance is necessary.

Neutron guides based on the principle of total reflection (see lecture 9) are used to transport neutron beams with a limited divergence but with low losses over distances of up to 200 m. The walls of neutron guides are polished glass plates with a metal coating. A simple Ni coating offers total reflection up to the critical angle

$$\theta_c = \frac{0.1^\circ}{\text{\AA}} * \lambda \quad (3.12)$$

for neutrons with the wavelength λ . These neutrons are transported without losses. Today's supermirror technology has achieved to increase the reflection angles up to $m=6$ times θ_c with reflectivities between 95% (for $m=2$) down to 60% (for the highest angles with $m=6$). From eq. (3.12) it is obvious that neutron guides are more efficient for cold neutrons with long wavelengths than for thermal neutrons. Therefore, most cold neutron instruments are located at increased distance from the reactor surface while only thermal instruments are located directly at the beamtubes.

Fig. 3.12 shows the neutron guides serving all cold neutron instruments of the neutron guide hall at the former research reactor in Jülich. Straight and slightly curved guides allow to supply neutrons to instruments that have sufficient space to be operated independently.

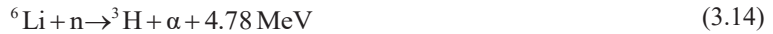
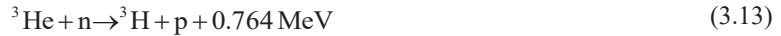


Fig. 3.12: Neutron guides serving the cold neutron instruments at the former FRJ-2 research reactor in Jülich.

3.5 Neutron detectors

Neutrons cannot be detected electronically because they carry no charge. Again, a nuclear reaction is necessary to produce charges that can be treated with electronic devices. The capture of the neutron in a suitable converter material releases charged secondary particles with high energy which are able to ionize detector material [10].

The most important nuclear capture reactions for neutron detection are



Gas detectors use the ionization of gas by particle radiation within an electrical field. The ions and electrons are moving to the electrodes and induce a charge signal that can be detected by electronics. Typical detector gases for the detection of thermal or slow neutrons are ${}^3\text{He}$ and ${}^{10}\text{BF}_3$.

In Scintillation detectors, the neutron converter is embedded in a transparent solid matrix and the energy of the secondary particles is converted into excited states of the matrix that decay with the emission of photons. These photons in a second step can be converted into electronic signals in a photomultiplier. A typical neutron scintillator material is glass with embedded ${}^6\text{LiF}$.

Both detector techniques can be used to build a position sensitive detector, where the charges are detected in a spatially resolved way. 1D or 2D spatial resolution can be achieved down to 50 μm .

References

- [1] <https://en.wikipedia.org/wiki/Neutron>
- [2] <https://www.nobelprize.org/prizes/physics/1935/chadwick/facts/>
- [3] <https://www.nrc.gov/docs/ML1122/ML11229A704.pdf>
- [4] <https://www.jcans.net>
- [5] U. Rucker et al., The Jülich high-brilliance neutron source project, *Eur. Phys. J. Plus* **131**, 19 (2016)
- [6] T. Brückel, T. Gutberlet (Eds.), Conceptual Design Report Jülich High Brilliance Neutron Source (HBS), ISBN 978-3-95806-501-7 (2020)
Free download at: go.fzj.de/hbs-tdr
- [7] M. Borlein, Kerntechnik, Vogel Buchverlag, Erlangen (2009), chapter 5
- [8] D. Filges, F. Goldenbaum, Handbook of Spallation Research, Wiley-VCH, Weinheim (2009), chapter 1.3
- [9] <https://europeanspallationsource.se/>
- [10] G. Kemmerling, lecture C5 in: 43rd IFF Spring School: Scattering Methods for Condensed Matter research, Forschungszentrum Jülich, Series Key Technologies, Vol. **33** (2012)

Exercises

E3.1 Basic relations *

Calculate the velocity (in m / s), the kinetic energy (in meV), and the temperature (in K) for

- hot neutrons ($\lambda = 0.5 \text{ \AA}$),
- thermal neutrons ($\lambda = 1.8 \text{ \AA}$),
- cold neutrons ($\lambda = 6 \text{ \AA}$).

$$\begin{aligned}m_n &= 1.675 * 10^{-27} \text{ kg} \\h &= 6.626 * 10^{-34} \text{ Js} \\e &= 1.602 * 10^{-19} \text{ As} \\k_B &= 1.38 * 10^{-23} \text{ J / K}\end{aligned}$$

E3.2 Neutron production in a fission reactor **

Calculate the neutron production of a 20 MW fission reactor (in 1 / s). What would be the neutron production of a hypothetical spallation source with the same thermal power?

Assuming that the reactor core is a point source and the neutrons just diffuse out of the core without absorption in the moderator: Calculate the neutron flux in 2 m, 10 m and 50 m distance from the core (in 1 / cm² s).

4 **Diffraction/ Elastic Scattering**

Shibabrata Nandi

Jülich Centre for Neutron Science 2

Forschungszentrum Jülich GmbH

Contents

4.1	Introduction	3
4.2	Elementary scattering theory: Elastic scattering	3
4.3	Fundamental scattering theory: The Born series	7
4.4	Coherence	12
4.5	Pair correlation functions	14
4.6	Form-factor	15
4.7	Scattering from a periodic lattice in three dimensions	16
4.8	Probes for scattering experiments in condensed matter science ..	18
4.9	Diffraction geometry	20
4.10	Diffraction intensities	26
4.11	Diffractometers	28
	References	32
	Exercises	34

Lecture Notes of the JCNS Laboratory Course Neutron Scattering. This is an Open Access publication distributed under the terms of the Creative Commons Attribution License 4.0,

which permits unrestricted use, distribution, and reproduction in any medium, provided the original work is properly cited. (Forschungszentrum Jülich, 2024)

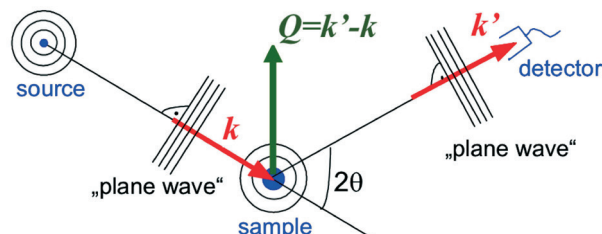


Fig. 4.1: A sketch of the scattering process for monochromatic radiation in the Fraunhofer approximation. It is assumed that plane waves are incident on sample and detector due to the fact that the distances source-sample and sample-detector, respectively, are significantly larger than the size of the sample.

4.1 Introduction

After the very qualitative introduction given in chapter 1, we now have to move to a more quantitative description of neutron scattering, giving the basic formulas for the simplest cases.

This lecture is organized as follows: First we give a very basic general introduction into elementary scattering theory for elastic scattering. Then a more rigorous derivation in the framework of the Born series follows. This section can be skipped by beginners but is provided for completeness.

We will introduce the concepts of coherence and pair correlation functions. Then we will discuss, which probes are most relevant for condensed matter investigations and present in some detail the interaction of neutrons with matter leading to the absorption and scattering cross-sections. More details can be found in [1–7]. Finally, we will discuss details of neutron diffraction experiments, in particular, how to calculate diffraction intensities and practical realizations of single and powder diffraction experiments.

We will frequently make use of the particle-wave dualism of quantum mechanics, which tells us that the radiation used in the scattering process can be described in a wave picture, whenever we are interested in interference phenomena, and in a particle picture, when the interaction with matter is relevant, e. g. for the detection process.

4.2 Elementary scattering theory: Elastic scattering

Throughout this lecture we assume that the atoms within our sample are rigidly fixed on equilibrium positions in space. Therefore we only look at those processes, in which the recoil is being transferred to the sample as a whole so that the energy change for the radiation is negligible and the scattering process appears to be elastic. In subsequent lectures, this restriction will be dropped and so-called inelastic scattering processes will be discussed. These are due to excitations or internal fluctuations in the sample, which give rise to an energy change of the radiation during the scattering process. A sketch of the scattering experiment is shown in Figure 4.1.

Here we assume the so-called *Fraunhofer approximation*, where the size of the sample is much smaller than the distance between sample and source and the distance between sample and detector, respectively. This assumption holds in all cases discussed in this lecture. In addition, we assume that the source emits radiation of one given energy, i. e. so-called *monochromatic radiation*. Then the wave field incident on the sample can be considered as a plane wave, which is completely described by a wave vector \mathbf{k} . The direction of \mathbf{k} indicates the propagation direction of the wave. The same holds for the wave incident on the detector, which can be described by a vector \mathbf{k}' . In the case of elastic scattering (diffraction) we have (-with λ as wavelength):

$$k = |\mathbf{k}| = |\mathbf{k}'| = k' = \frac{2\pi}{\lambda} \quad (4.1)$$

Let us define the so-called *scattering vector* by

$$\mathbf{Q} = \mathbf{k}' - \mathbf{k} \quad (4.2)$$

$\hbar\mathbf{Q}$ represents the momentum transfer during scattering, since according to de Broglie, the momentum of the particle corresponding to the wave with wave vector \mathbf{k} is given by $\mathbf{p} = \hbar\mathbf{k}$. The magnitude of the scattering vector can be calculated from wavelength λ and scattering angle 2θ as follows

$$Q = |\mathbf{Q}| = \sqrt{k^2 + k'^2 - 2kk' \cos 2\theta} \Rightarrow Q = \frac{4\pi}{\lambda} \sin \theta \quad (4.3)$$

A scattering experiment comprises the measurement of the intensity distribution $I(\mathbf{Q})$ as a function of the scattering vector \mathbf{Q} . The scattered intensity is proportional to the so-called *cross section*, where the proportionality factors arise from the detailed geometry of the experiment. For a definition of the scattering cross section, we refer to Figure 4.2. If n' particles are scattered per second into the solid angle $d\Omega$ seen by the detector under the scattering angle 2θ and into the energy interval between E' and $E' + dE'$, then we can define the so-called *double differential cross section* by:

$$\frac{d^2\sigma}{d\Omega dE'} = \frac{n'}{j d\Omega dE'} \quad (4.4)$$

Here j refers to the incident beam flux in terms of particles per area and time. If we are not interested in the change of the energy of the radiation during the scattering process, or if our detector is not able to resolve this energy change, then we will describe the angular dependence by the so-called *differential cross section*:

$$\frac{d\sigma}{d\Omega}(\theta) = \int_0^\infty \left. \frac{d^2\sigma}{d\Omega dE'} \right|_\theta dE' \quad (4.5)$$

Note that the integral has to be taken for the constant scattering angle of the detector. Finally, the so-called *total scattering cross section* gives us a measure for the total scattering probability independent of changes in energy and scattering angle:

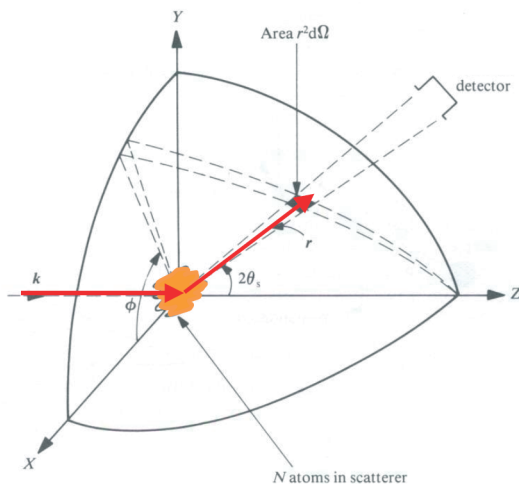


Fig. 4.2: Geometry used for the definition of the scattering cross section.

$$\sigma = \int_0^{4\pi} \frac{d\sigma}{d\Omega} d\Omega \tag{4.6}$$

For elastic scattering our task is to determine the arrangement of the atoms in the sample from the knowledge of the scattering cross section $d\sigma/d\Omega$. The relationship between scattered intensity and the structure of the sample is particularly simple in the so-called *Born approximation*, which is often also referred to as *kinematic scattering theory*. In this case, refraction of the beam entering and leaving the sample, multiple scattering events and the attenuation of the primary beam due to scattering within the sample are neglected. For simplicity, we assume that the incident beam is ideally collimated (i.e. has no angular spread) and monochromatized (i.e. has no wavelength spread) and describe it as a plane wave.

Following Figure 4.3, the phase difference between a wave scattered at the origin of the coordinate system (A) and at position \mathbf{r} (D) is given by

$$\Delta\Phi = 2\pi \cdot \frac{(\overline{AB} - \overline{CD})}{\lambda} = \mathbf{k}' \cdot \mathbf{r} - \mathbf{k} \cdot \mathbf{r} = \mathbf{Q} \cdot \mathbf{r} \tag{4.7}$$

Here we see the other meaning of the scattering vector \mathbf{Q} : besides the momentum transfer $\hbar\mathbf{Q}$ (“particle picture”), it determines the phase shift $\mathbf{Q} \cdot \mathbf{r}$ during scattering (“wave picture”).

The amplitude of the scattered beam at position \mathbf{r} depends on the type of radiation used and the interaction of this radiation with the sample. In fact, the probability for a scattering event to occur is directly proportional to the interaction potential V , as will be shown in paragraph 4.3. The total scattering amplitude is given by a coherent superposition (i.e. taking the phase $\Delta\Phi$ into account) of the scattering from all points within the sample, i. e. by the integral

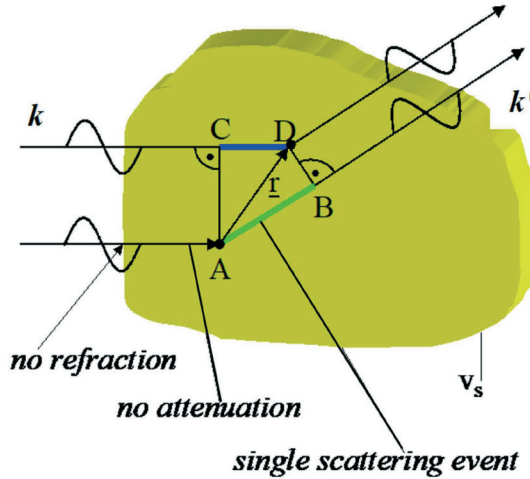


Fig. 4.3: A sketch illustrating the phase difference between a ray scattered at the origin of the coordinate system and a ray scattered at the position \mathbf{r} .

$$A(\mathbf{Q}) \sim A_0 \cdot \int_{V_s} V(\mathbf{r}) \cdot e^{i\mathbf{Q} \cdot \mathbf{r}} d^3r \quad (4.8)$$

Here A_0 denotes the amplitude of the incident wave field. Eqn. 4.8 demonstrates that the scattered amplitude is connected with the interaction potential $V(\mathbf{r})$ by a simple Fourier transform. Knowledge of the scattering amplitude A for all scattering vectors \mathbf{Q} allows us to determine via a Fourier transform the potential $V(\mathbf{r})$ uniquely. This is the complete information on the sample, which can be obtained by an elastic scattering experiment. Unfortunately, nature is not so simple. On one hand, there is the more technical problem that one is unable to determine the scattering cross section for **all** values of momentum transfer $\hbar\mathbf{Q}$. The more fundamental problem, however, is that normally the amplitude of the scattered wave is not measurable. Instead only the scattered intensity

$$I(\mathbf{Q}) \sim |A(\mathbf{Q})|^2 \quad (4.9)$$

can be determined. Therefore, the phase information is lost and the simple reconstruction of the scattering potential via a Fourier transform is no longer possible. This is the so-called *phase problem* of scattering. There are ways to overcome the phase problem, e. g. by use of reference waves (e. g. holography). Then the scattering potential becomes directly accessible. The question, which information we can obtain from a conventional scattering experiment despite the phase problem will be addressed below.

Which wavelength do we have to choose to obtain the required real space resolution? For information on a length scale L , a phase difference of about $Q \cdot L \approx 2\pi$ has to be achieved. Otherwise according to Eqn. 4.7, \mathbf{k}' and \mathbf{k} will not differ significantly. According to Eqn.

4.3, $Q \approx 2\pi/\lambda$ for typical scattering angles ($2\theta \sim 60^\circ$). Combining these two estimates, we end up with the requirement that the wavelength λ has to be in the order of the real space length scale L under investigation. To give an example: with the wavelength in the order of $1\text{\AA} = 0.1\text{ nm}$, atomic resolution can be achieved in a scattering experiment.

4.3 Fundamental scattering theory: The Born series

In this chapter, we will give a simple formulation of scattering theory. Our purpose is to derive 4.8 from fundamental principles. The conditions under which 4.8 holds and the limitations of kinematical scattering theory will thus become clearer. The derivation will be done for particle beams - in particular neutrons - for which the Schrödinger equation holds. This is bonus-material: Beginners can skip this chapter and continue with chapter 4.4 .

In quantum mechanics, neutrons are described as particle wave through the Schrödinger equation:

$$H\Psi = \left(-\frac{\hbar^2}{2m}\Delta + V \right) \Psi = i\hbar\frac{\partial}{\partial t}\Psi \quad (4.10)$$

ψ is the probability density amplitude, V the interaction potential. In case of purely elastic scattering $E = E'$, the time dependence can be described by the factor $\exp(-i\frac{E}{\hbar}t)$. Assuming this time dependence, a wave equation for the spatial part of the probability density amplitude ψ can be derived from 4.10:

$$\Delta\Psi + k^2(\mathbf{r})\Psi = 0 \quad (4.11)$$

In Eq. 4.11, we have introduced a spatially varying wave vector with the magnitude square:

$$k^2(\mathbf{r}) = \frac{2m}{\hbar^2}(E - V(\mathbf{r})) \quad (4.12)$$

Solutions of 4.10, in empty space (i. e. $V \equiv 0$) can be guessed immediately. They are given by plane waves $\Psi = \Psi_0 \exp[i(\mathbf{k} \cdot \mathbf{r} - \frac{E}{\hbar}t)]$ with $k^2 = \frac{2m}{\hbar^2}E$. The relations between magnitude of the wave vector k , wave length λ , and energy of the neutron E can be written in practical units:

$$k [\text{\AA}^{-1}] \approx 0.695\sqrt{E[\text{meV}]} \quad (4.13)$$

$$\lambda[\text{\AA}] \approx 9.045/\sqrt{E[\text{meV}]} \quad (4.14)$$

$$E[\text{meV}] \approx 81.8/\lambda^2[\text{\AA}] \quad (4.15)$$

To give an example, neutrons of wavelength $\lambda = 2.4\text{\AA} = 0.24\text{ nm}$ have an energy of $E = 14.2\text{ meV}$ with a magnitude of the neutron wave vector of $k = 2.6\text{\AA}^{-1}$.

To obtain solutions of the wave equation 4.11 in matter, we reformulate the differential equation by explicitly separating the interaction term:

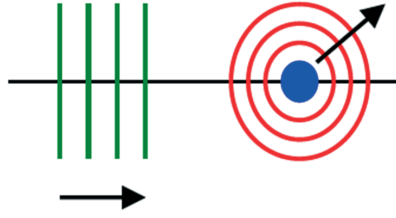


Fig. 4.4: The scattering from a point-like scatterer (δ -potential) gives an emitted spherical wave

$$(\Delta + k^2) \Psi = \frac{2m}{\hbar^2} V \cdot \Psi =: \chi \quad (4.16)$$

Here \mathbf{k} denotes the wave vector for propagation in empty space. The advantage of this formulation is that the solutions of the left-hand side are already known. They are the plane waves in empty space. Equation 4.16 is a linear partial differential equation, i.e. the superposition principle holds: the general solution can be obtained as a linear combination of a complete set of solution functions. The coefficients in the series are determined by the boundary conditions. To solve 4.16 one can apply a method developed for inhomogeneous linear differential equations. For the moment, we assume that the right-hand side is fixed (given as χ). We define a *Greens-function* by:

$$(\Delta + k^2) G(\mathbf{r}, \mathbf{r}') = \delta(\mathbf{r} - \mathbf{r}') \quad (4.17)$$

A solution of 4.17 is given by:

$$G(\mathbf{r}, \mathbf{r}') = \frac{e^{ik|\mathbf{r}-\mathbf{r}'|}}{4\pi|\mathbf{r}-\mathbf{r}'|} \quad (4.18)$$

The physical meaning of 4.18 is immediately clear: the scattering from a point-like scatterer (δ -potential) gives an emitted spherical wave. In a schematic graphical representation: Using the Greens-function $G(\mathbf{r}, \mathbf{r}')$, we can write down a formal solution of the wave equation 4.16:

$$\Psi = \Psi^o + \int G(\mathbf{r}, \mathbf{r}') \chi(\mathbf{r}') d^3 r' \quad (4.19)$$

Here, we have taken the initial conditions of an incident plane wave Ψ^o into account. Eqn. 4.19 is indeed a solution of Eqn. 4.16 as can be easily verified by substituting 4.19 into 4.16. If we finally substitute the definition of χ , one obtains the so-called *Lippmann-Schwinger* equation:

$$\Psi(\mathbf{r}) = \Psi^o(\mathbf{r}) + \frac{2m}{\hbar^2} \int_{V_s} G(\mathbf{r}, \mathbf{r}') V(\mathbf{r}') \Psi(\mathbf{r}') d^3 r' \quad (4.20)$$

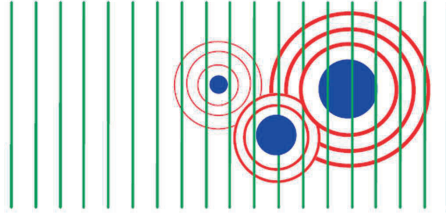


Fig. 4.5: *Physical interpretation of eqn. 4.20.*

Eqn. 4.20 has a simple interpretation: the incident plane wave $\Psi^o(\mathbf{r})$ is superimposed by spherical waves emitted from scattering at positions \mathbf{r}' . The amplitude of these spherical waves is proportional to the interaction potential $V(\mathbf{r}')$ and the amplitude of the wave field at the position \mathbf{r}' . To obtain the total scattering amplitude, we have to integrate over the entire sample volume V_s . However, we still have not solved 4.16: our solution Ψ appears again in the integral in 4.20. In other words, we have transformed differential equation 4.16 into an integral equation. The advantage is that for such an integral equation, a solution can be found by iteration. In the zeroth approximation, we neglect the interaction V completely.

This gives $\Psi = \Psi^o$. The next higher order approximation for a weak interaction potential is obtained by substituting this solution in the right-hand side of 4.20. The first non-trivial approximation can thus be obtained:

$$\Psi^1(\mathbf{r}) = e^{i\mathbf{k}\cdot\mathbf{r}} + \frac{2m}{\hbar^2} \int \frac{\exp(i\mathbf{k}|\mathbf{r} - \mathbf{r}'|)}{4\pi|\mathbf{r} - \mathbf{r}'|} V(\mathbf{r}') e^{i\mathbf{k}\cdot\mathbf{r}'} d^3r' \quad (4.21)$$

4.21 is nothing else but a mathematical formulation of the well-known *Huygens principle* for wave propagation.

The approximation 4.21 assumes that the incident plane wave is only scattered once from the potential $V(\mathbf{r}')$. For a stronger potential and larger sample, multiple scattering processes will occur. Again, this can be deduced from the integral equation 4.20 by further iteration. For simplification we introduce a new version of equation 4.20 by writing the integral over the "Greens function" as operator \widehat{G} :

$$\Psi = \Psi^o + \widehat{G}V\Psi \quad (4.22)$$

The so-called first *Born approximation*, which gives the *kinematical scattering theory* is obtained by substituting the wave function Ψ on the right hand side by Ψ^o :

$$\Psi^1 = \Psi^o + \widehat{G}V\Psi^o \quad (4.23)$$

This first approximation can be represented by a simple diagram as a sum of an incident plane wave and a wave scattered once from the potential V :

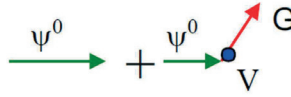


Fig. 4.6: This first approximation in Graphical representation.

The second approximation is obtained by substituting the solution of the first approximation 4.23 on the right-hand side of equation 4.22:

$$\Psi^2 = \Psi^o + \widehat{G}V\Psi^1 = \Psi^o + \widehat{G}V\Psi^o + \widehat{G}V\widehat{G}V\Psi^o \tag{4.24}$$

Or in a diagrammatic form:

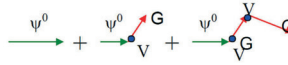


Fig. 4.7: This second approximation in Graphical representation.

I.e. in the second approximation, processes are being taken into account, in which the neutron is scattered twice by the interaction potential V . In a similar manner, all higher order approximations can be calculated. This gives the so-called *Born series*.¹ For weak potential and small samples, this series converges rather fast. Often, the first approximation, the *kinematic scattering theory*, holds very well. This is especially the case for neutron scattering, where the scattering potential is rather weak, as compared to x-ray or electron- scattering. Due to the strong Coulomb interaction potential, the probability for multiple scattering processes of electrons in solids is extremely high, making the interpretation of electron diffraction experiments difficult. But even for neutrons, the kinematic scattering theory can break down, for example in the case of Bragg scattering from large ideally perfect single crystals, where the Born series does not converge. The wave equation has to be solved exactly under the boundary conditions given by the crystal geometry. For simple geometries, analytical solutions can be obtained. This is then called the *dynamical scattering theory*. Since for neutrons, the kinematical theory holds in most cases, or multiple scattering events can often be corrected for, we will no longer discuss dynamical theory in what follows and refer to [3, 7].

Let us return to the first Born approximation 4.21. In a further approximation, the Fraunhofer approximation, we assume that the size of the sample is significantly smaller than the distance sample-detector. The geometry to calculate the far field limit of 4.21 is given in Figure 4.8 . Under the assumption $|R| \gg |r'|$, we can deduce from Figure 2.4 the following approximation for the emitted spherical wave:

$$\frac{\exp(ik|\mathbf{r} - \mathbf{r}'|)}{|\mathbf{r} - \mathbf{r}'|} \approx \frac{\exp(ik(R - \mathbf{r}' \cdot \mathbf{R}))}{R} \approx \frac{\exp(ikR)}{R} \cdot e^{-ik'\cdot\mathbf{r}'} \tag{4.25}$$

¹ Note that Born approximation or the Born series violates energy conservation: scattered waves are created without weakening of the incident plane wave. Born series can therefore only be applied in the limit of very weak scattering potentials.

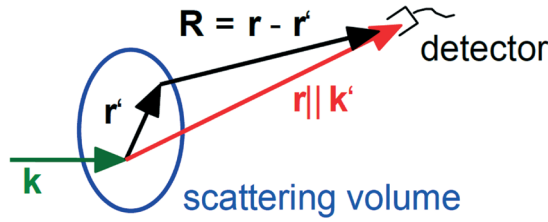


Fig. 4.8: Scattering geometry for the calculation of the far field limit at the detector. In the Fraunhofer approximation, we assume that $|\mathbf{R}| \gg |\mathbf{r}'|$.

The probability density amplitude for the scattered wave field in the limit of large distances from the sample is thus given by:

$$\Rightarrow \Psi^1(\mathbf{R}) = e^{i\mathbf{k}\cdot\mathbf{R}} + \frac{2m}{\hbar^2} \frac{e^{ikR}}{4\pi R} \int V(\mathbf{r}') e^{i\mathbf{Q}\cdot\mathbf{r}'} d^3r' \quad (4.26)$$

This is just the sum of an incident plane wave and a spherical wave emitted from the sample as a whole. The amplitude of the scattered wave is given according to 4.26:

$$A(\mathbf{Q}) = \frac{m}{2\pi\hbar^2} \int V(\mathbf{r}) e^{i\mathbf{Q}\cdot\mathbf{r}} d^3r \sim F[V(\mathbf{r})] \quad (4.27)$$

The integral in the above equation is nothing but the transition matrix element of the interaction potential V between the initial and final plane wave states, therefore:

$$\frac{d\sigma}{d\Omega} = \left(\frac{m}{2\pi\hbar^2} \right)^2 |\langle \mathbf{k}' | V | \mathbf{k} \rangle|^2 \quad (4.28)$$

This formula corresponds to *Fermi's Golden Rule* from time-dependent perturbation theory, where the transition probability per time interval from state \mathbf{k} to states \mathbf{k}' is given by:

$$W_{\mathbf{k}'\mathbf{k}} = \frac{2\pi}{\hbar} |\langle \mathbf{k}' | V | \mathbf{k} \rangle|^2 \cdot \rho(E_{\mathbf{k}'}) \quad (4.29)$$

Here, $\rho(E_{\mathbf{k}'})$ denotes the density of states for the final states \mathbf{k}' .

With this exact derivation of the scattering cross section, we can now confirm by comparison with 4.8 that the scattering probability in the simple derivation of chapter 4.2 is given by $\frac{m}{2\pi\hbar^2} V(\mathbf{r})$ for particle beams governed by the Schrödinger equation.

We now allow for inelastic processes, where the sample undergoes a change of its state from α to α' (α denotes a set of quantum numbers characterizing an eigenstate of the sample). In this case, due to the different length of the wavevectors for incoming and outgoing waves, we have to introduce factors k' and k , which arise from the density of states factor in 4.29.

Since the scattering event must fulfill energy and momentum conservation, we arrive at the double differential cross section (without detailed derivation):

$$\frac{d^2\sigma}{d\Omega d\omega} = \frac{k'}{k} \left(\frac{m}{2\pi\hbar^2} \right)^2 \sum_{\alpha} p_{\alpha} \sum_{\alpha'} |\langle \mathbf{k}', \alpha' | V | \mathbf{k}, \alpha \rangle|^2 \cdot \delta(\hbar\omega + E_{\alpha} - E_{\alpha'}) \quad (4.30)$$

The first summation is carried out over all possible initial states α of the system, weighted with their thermodynamic occupation probability p_{α} . The sum over α' is the sum over all final states allowed by energy conservation, which is guaranteed through the δ -function. $\hbar\omega$ denotes the energy transfer of the neutron to the system. This double differential cross section will be discussed in the following lectures on inelastic scattering.

4.4 Coherence

In the above derivation, we assumed plane waves as initial and final states. For a real scattering experiment, this is an unphysical assumption. In the incident beam, a wave packet is produced by collimation (defining the direction of the beam) and monochromatization (defining the wavelength of the incident beam). Neither the direction \mathbf{k} , nor the wavelength λ have sharp values but rather have a distribution of finite width about their respective mean values. This wave packet can be described as a superposition of plane waves. As a consequence, the diffraction pattern will be a superposition of patterns for different incident wavevector \mathbf{k} and the question arises, which information is lost due to these non-ideal conditions. This *instrumental resolution* is intimately connected with the *coherence* of the beam. Coherence is needed, so that the interference pattern is not significantly destroyed. Coherence requires a phase relationship between the different components of the beam. Two types of coherence can be distinguished.

- *Temporal or longitudinal coherence due to a wavelength spread.*

A measure for the longitudinal coherence is given by the length, on which two components of the beam with largest wavelength difference (λ and $\lambda + \Delta\lambda$) become fully out of phase.

According to the Figure 4.9, this is the case for $l_{\parallel} = n \cdot \lambda = \left(n - \frac{1}{2}\right) (\lambda + \Delta\lambda)$. From this, solving for n and assuming $\Delta\lambda \ll \lambda$, we obtain the *longitudinal coherence length* l_{\parallel} as:

$$l_{\parallel} = \frac{\lambda^2}{2\Delta\lambda} \quad (4.31)$$

- *Transversal coherence due to source extension*

Due to the extension of the source (transverse beam size), the phase relation is destroyed for large source size or large divergence. According to the Figure 4.10, a first minimum occurs for $\frac{\lambda}{2} = d \cdot \sin \theta \approx d \cdot \theta$.

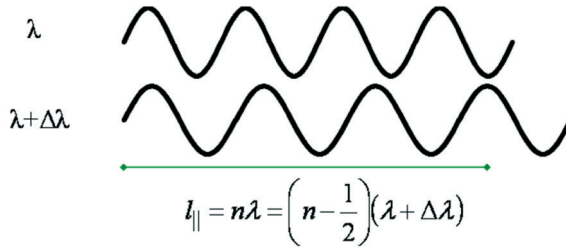


Fig. 4.9: A sketch illustrating the longitudinal coherence due to a wavelength spread.

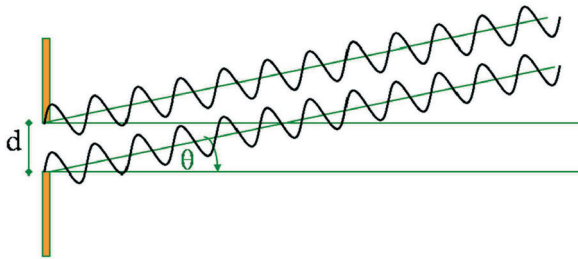


Fig. 4.10: A sketch illustrating the transverse coherence due to source extension.

From this, we obtain the *transversal coherence length* l_{\perp} as

$$l_{\perp} = \frac{\lambda}{2\Delta\theta} \tag{4.32}$$

Here $\Delta\theta$ is the divergence of the beam. Note that l_{\perp} can be different along different spatial directions: in many instruments, the vertical and horizontal collimations are different.

Together, the longitudinal and the two transversal coherence lengths (in two directions perpendicular to the beam propagation) define a *coherence volume*. This is a measure for a volume, in which the amplitudes of all scattered waves superimpose within the sample to produce an interference pattern. Normally, the coherence volume is significantly smaller than the sample size, typically a few 100 Å for neutron scattering, up to μm for synchrotron radiation. Scattering between different coherence volumes within the sample is no longer coherent, i.e. instead of the amplitudes the intensities of the contributions to the scattering pattern have to be added. This limits the real space resolution of a scattering experiment to the extension of the coherence volume.

4.5 Pair correlation functions

After having clarified the conditions under which we can expect a coherent scattering process, let us now come back to the question, which information is accessible from the intensity distribution of a scattering experiment. From 4.9 we see that the phase information is lost during the measurement of the intensity. For this reason the Fourier transform of the scattering potential is not directly accessible in most scattering experiments (note however that phase information can be obtained in certain cases).

Substituting 4.8 into 4.9 and applying the variable substitution $\mathbf{R} = \mathbf{r}' - \mathbf{r}$, we obtain for the magnitude square of the scattering amplitude, a quantity directly accessible in a scattering experiment:

$$I \sim |A(\mathbf{Q})|^2 \sim \int d^3r' V(\mathbf{r}') e^{i\mathbf{Q}\cdot\mathbf{r}'} \int d^3r V^*(\mathbf{r}) e^{-i\mathbf{Q}\cdot\mathbf{r}} = \iint d^3r' d^3r V(\mathbf{r}') V^*(\mathbf{r}) e^{i\mathbf{Q}\cdot(\mathbf{r}'-\mathbf{r})} \quad (4.33)$$

$$= \iint d^3R d^3r V(\mathbf{R} + \mathbf{r}) V^*(\mathbf{r}) e^{i\mathbf{Q}\cdot\mathbf{R}} \quad (4.34)$$

This shows that the scattered intensity is proportional to the Fourier transform of a function $P(\mathbf{R})$:

$$I(\mathbf{Q}) \sim \int d^3R P(\mathbf{R}) e^{i\mathbf{Q}\cdot\mathbf{R}} \quad (4.35)$$

This function denotes the so-called *Patterson function* in crystallography or more general the *static pair correlation function*:

$$P(\mathbf{R}) = \int d^3r V^*(\mathbf{r}) V(\mathbf{r} + \mathbf{R}) \quad (4.36)$$

$P(\mathbf{R})$ correlates the value of the scattering potential at position \mathbf{r} with the value at the position $\mathbf{r} + \mathbf{R}$, integrated over the entire sample volume. The Patterson function $P(\mathbf{R})$ vanishes, if no correlation exists between the values of the potential at position \mathbf{r} and $\mathbf{r} + \mathbf{R}$, when averaged over the sample. If, however, a periodic arrangement of a pair of atoms exists in the sample with a difference vector \mathbf{R} between the positions, then the Patterson function will have an extremum for this vector \mathbf{R} . Thus, the Patterson function reproduces all the vectors connecting one atom with another atom in a periodic arrangement. Quite generally, in a scattering experiment, pair correlation functions are being determined. In a coherent inelastic scattering experiment, we measure the *scattering law* $S(\mathbf{Q}, \omega)$, which is the Fourier transform with respect to space and time of the spatial and temporal pair correlation function:

$$\frac{d^2\sigma}{d\omega d\Omega} \sim S(\mathbf{Q}, \omega) = \frac{1}{2\pi\hbar} \int_{-\infty}^{+\infty} dt e^{-i\omega t} \int d^3r e^{i\mathbf{Q}\cdot\mathbf{r}} G(\mathbf{r}, t) \quad (4.37)$$

While the proportionality factor between the double differential cross section and the scattering law depends on the type of radiation and its specific interaction potential with the system studied, the spatial and temporal pair correlation function is only a property of the system studied and independent of the probe used:

$$G(\mathbf{r}, t) = \frac{1}{N} \sum_{ij} \int d^3r' \langle \delta(\mathbf{r}' - \mathbf{r}_j(0)) \cdot \delta(\mathbf{r}' + \mathbf{r} - \mathbf{r}_i(t)) \rangle = \frac{1}{N} \int d^3r' \langle \rho(\mathbf{r}', 0) \rho(\mathbf{r}' + \mathbf{r}, t) \rangle \quad (4.38)$$

Here, the pair correlation function is once expressed as a correlation between the position of N point-like particles (expressed by the delta functions) and once by the correlation between the densities at different positions in the sample for different times. In a magnetic system, we scatter from the atomic magnetic moments, which are vector quantities. Therefore, the scattering law becomes a tensor - the Fourier transform of the spin pair correlations:

$$\mathbf{S}^{\alpha\beta}(\mathbf{Q}, \omega) = \frac{1}{2\pi} \sum_l \int dt e^{i[\varphi(\mathbf{R}_l - \mathbf{R}_0) - \omega t]} \langle S_0^\alpha(0) S_l^\beta(t) \rangle \quad (4.39)$$

α, β denote the Cartesian coordinates x, y, z ; \mathbf{R}_0 and \mathbf{R}_l are the spatial coordinates of a reference spin 0 and a spin l in the system.

4.6 Form-factor

So far we have not specified the nature of our sample. Now we assume an assembly of N scatterers of finite size, see Figure 4.11. These could be atoms in a solid, or colloidal particles in a homogeneous solution. In what follows, we will separate the interference effects from scattering within one such a particle from the interference effects arising from scattering between different particles. With the decomposition of the vector \mathbf{r} into the centre-of-gravity-vector \mathbf{r}_j of particle number j and a vector \mathbf{r}' within the particle, the scattering amplitude can be written as (all particles are assumed to be identical):

$$A \propto \int_{V_s} d^3r V(\mathbf{r}) e^{i\mathbf{Q}\cdot\mathbf{r}} = \sum_{j=1}^N \int_{V_j} d^3r V(\mathbf{r}) e^{i\mathbf{Q}\cdot\mathbf{r}} \quad (4.40)$$

$$= \sum_{j=1}^N e^{i\mathbf{Q}\cdot\mathbf{r}_j} \int_{V_j^0} d^3r' V(\mathbf{r}') e^{i\mathbf{Q}\cdot\mathbf{r}'} =: \sum_{j=1}^N e^{i\mathbf{Q}\cdot\mathbf{r}_j} V_j^{tot} f_j(\mathbf{Q}) \quad (4.41)$$

With 4.41, we have separated the scattering from within the single particles from the interference between different particles. V_j^{tot} denotes the total scattering power of the particle. The *form-factor* $f(\mathbf{Q})$ is defined as the normalized amplitude of scattering from within one particle ² (it describes the "form" of the particle):

$$f(\mathbf{Q}) \equiv \frac{\int_{V_j^0} d^3r' V(\mathbf{r}') e^{i\mathbf{Q}\cdot\mathbf{r}'}}{\int_{V_j^0} d^3r' V(\mathbf{r}')} \quad (4.42)$$

For a homogeneous sphere

² For simplicity we now drop the index j

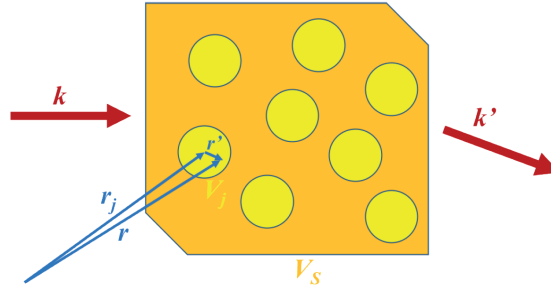


Fig. 4.11: Sketch showing the assembly of N scatterers of finite size and defining the quantities needed for the definition of the form factor.

$$V(\mathbf{r}) = \begin{cases} 0 & |\mathbf{r}| > R \\ C & |\mathbf{r}| \leq R \end{cases} \quad (4.43)$$

, the form-factor can be calculated by using spherical co-ordinates:

$$\Rightarrow f(Q) = 3 \cdot \frac{\sin QR - QR \cdot \cos QR}{(QR)^3} \quad (4.44)$$

The function in Eqn. 4.44 is plotted in Figure 4.12. In forward direction, there is no phase difference between waves scattered from different volume elements within the sample (note: we assume the Fraunhofer approximation and work in a far field limit): the form factor takes its maximum value of one. For finite scattering angles 2θ , the form-factor drops due to destructive interference from waves scattered from various parts within one particle and finally for large values of the momentum transfer shows damped oscillations around 0 as a function of QR .

4.7 Scattering from a periodic lattice in three dimensions

As an example for the application of 4.8 and 4.9, we will now discuss the scattering from a three dimensional lattice of point-like scatterers. As we will see later, this situation corresponds to the scattering of thermal neutrons from a single crystal. More precisely, we will restrict ourselves to the case of a Bravais lattice with one atom at the origin of the unit cell. To each atom we attribute a "scattering power"³ β . The single crystal is finite with N , M and P periods along the basis vectors \mathbf{a} , \mathbf{b} and \mathbf{c} . The scattering potential, which we have to use in 4.8 is a sum over δ -functions for all scattering centers:

³ We will later see that this "scattering power" is connected to the so-called scattering length of the atom.

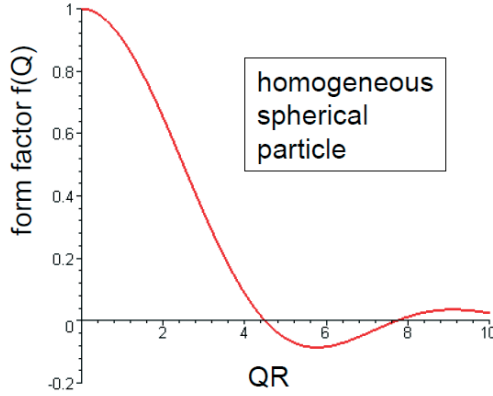


Fig. 4.12: Form-factor for a homogeneous sphere according to 4.44

$$V(\mathbf{r}) = \sum_{n=0}^{N-1} \sum_{m=0}^{M-1} \sum_{p=0}^{p-1} \beta \cdot \delta(\mathbf{r} - (n \cdot \mathbf{a} + m \cdot \mathbf{b} + p \cdot \mathbf{c})) \quad (4.45)$$

The scattering amplitude is calculated as a Fourier transform:

$$A(\mathbf{Q}) \sim \beta \sum_{n=0}^{N-1} e^{in\mathbf{Q} \cdot \mathbf{a}} \sum_{m=0}^{M-1} e^{im\mathbf{Q} \cdot \mathbf{b}} \sum_{p=0}^{p-1} e^{ip\mathbf{Q} \cdot \mathbf{c}} \quad (4.46)$$

Summing up the geometrical series, we obtain for the scattered intensity:

$$I(\mathbf{Q}) \sim |A(\mathbf{Q})|^2 = |\beta|^2 \cdot \frac{\sin^2 \frac{1}{2} N \mathbf{Q} \cdot \mathbf{a}}{\sin^2 \frac{1}{2} \mathbf{Q} \cdot \mathbf{a}} \cdot \frac{\sin^2 \frac{1}{2} M \mathbf{Q} \cdot \mathbf{b}}{\sin^2 \frac{1}{2} \mathbf{Q} \cdot \mathbf{b}} \cdot \frac{\sin^2 \frac{1}{2} P \mathbf{Q} \cdot \mathbf{c}}{\sin^2 \frac{1}{2} \mathbf{Q} \cdot \mathbf{c}} \quad (4.47)$$

The dependence on the scattering vector \mathbf{Q} is given by the so-called *Laue function*, which factorizes along to the three directions in space. One factor along one lattice direction \mathbf{a} is plotted in Figure 4.13.

The main maxima occur at the positions $Q = n \cdot 2\pi/a$. $Q = n \cdot 2\pi/a = h\mathbf{a}^*$, where \mathbf{a}^* is the reciprocal lattice vector (please see definition of reciprocal lattice at section 4.9, here, h , and n are integers.). The maximum intensity scales with the square of the number of periods N^2 , the half width is given approximately by $\Delta Q = 2\pi/(N \cdot a)$. The more periods contribute to coherent scattering, the sharper and higher are the main peaks. Between the main peaks, there are $N - 2$ side maxima. With increasing number of periods N , their intensity becomes rapidly negligible compared to the intensity of the main peaks. The main peaks are of course the well-known *Bragg reflections*, which we obtain for scattering from a crystal lattice. From the position of these Bragg peaks in momentum space, the metric of the unit cell can be

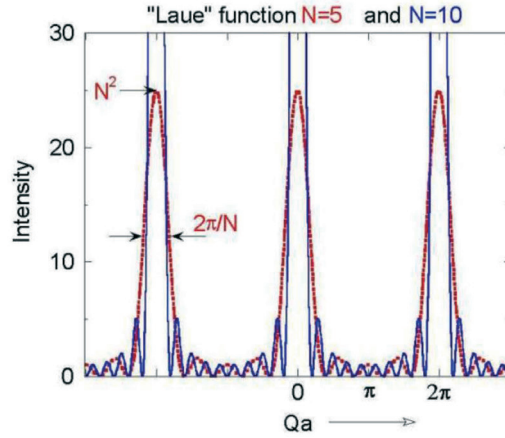


Fig. 4.13: Laue function along the lattice direction \mathbf{a} for a lattice with five and ten periods, respectively.

deduced (lattice constants a, b, c and unit cell angles α, β, γ). The width of the Bragg peaks is determined by the coherently scattering volume (parameters N, M , and P) - and some other factors for real experiments (resolution, mosaic distribution, internal strains, ...). For large N , the factors in 4.47, approaches a δ function, and the scattering intensity can be written as

$$I(\mathbf{Q}) \sim |A(\mathbf{Q})|^2 = N|\beta|^2 V_{BZ} \sum_h \delta(\mathbf{Q} - \mathbf{G}_h) \quad (4.48)$$

where V_{BZ} is the Brillouin zone volume. The physical meaning of the 4.48 is that the Bragg reflections occurs when momentum transfer (\mathbf{Q}) is equal to the reciprocal lattice vector (\mathbf{G}), which is precisely the Laue condition that will be discussed later.

4.8 Probes for scattering experiments in condensed matter science

In this chapter, we will discuss which type of radiation is suitable for condensed matter investigations. For neutron beams, we will then discuss the relevant interaction processes with matter in detail.

A list of requirements for the type of radiation used in condensed matter investigations looks as follows:

1. The achievable spatial resolution should be in the order of the inter-particle distances, which implies (see section 4.2) that the wavelength λ is in the order of the inter-particle distance L .

2. If we want to study volume effects, the scattering has to originate from the bulk of the sample, which implies that the radiation should be at most weakly absorbed within matter.
3. For a simple interpretation of the scattering data within the Born approximation (see section 4.2), multiple scattering effects should be negligible, i. e. the interaction of the radiation with matter should be weak.
4. For the sake of simplicity, the probe should have no inner degrees of freedom, which could be excited during the scattering process (i. e. avoid beams of molecules, which have internal vibrational or rotational degrees of freedom).
5. To study magnetic systems, we need a probe which interacts with the atomic magnetic moments in the sample.
6. If, in addition to structural studies, we want to investigate elementary excitations, we would like the energy of the probe to be in the order of the excitation energies, so that the energy change during the scattering process is easily measurable.

This list of requirements leads us to some standard probes in condensed matter research. First of all, electromagnetic radiation governed by the Maxwell equations can be used. Depending on the resolution requirements, we will use x-rays with wavelength λ of about 0.1 nm to achieve atomic resolution or visible light ($\lambda \sim 350 - 700$ nm) to investigate e. g. colloidal particles in solution. Besides electromagnetic radiation, particle waves can be used. It turns out that thermal neutrons with a wavelength ~ 0.1 nm are particularly well adapted to the above list of requirements. The neutron beams are governed by the Schrödinger equation of quantum mechanics. An alternative is to use electrons, which for energies of around 100 keV have wavelengths in the order of 0.005 nm. As relativistic particles, they are governed by the Dirac equation of quantum mechanics. The big drawback of electrons as a condensed matter probe is the strong Coulomb interaction with the electrons in the sample. Therefore, neither absorption, nor multiple scattering effects can be neglected. However, the abundance of free electrons and the relative ease to produce optical elements makes them very suitable for imaging purposes (electron microscopy). Electrons, but also atomic beams, are very powerful tools for surface science: due to their strong interaction with matter, both types of radiation are very surface sensitive. Low Energy Electron Diffraction LEED and Reflection High Energy Electron Diffraction RHEED are both used for in-situ studies of the crystalline structure during thin film growth, e.g. with Molecular Beam Epitaxy MBE. In what follows we will concentrate on neutron scattering as one of the probes, which is best suited for bulk studies on an atomic scale. We will introduce the properties of the neutron, discuss the absorption of neutrons in matter and derive the scattering cross sections for the main interaction processes with matter.

As mentioned earlier, each scattering experiment performed with any type of radiation - regardless of whether it involves massive particles like neutrons and electrons or electromagnetic waves like x-rays or visible light - has a total of four attributes which altogether characterize the type of the scattering experiment as well as the information that can be obtained from such an experiment. These attributes and their characteristics are:

Elastic scattering, which involves the conservation of the energy of the particle or quantum during the scattering process, **inelastic scattering**, corresponding to a loss or gain of parti-

cle or quantum energy during the scattering event, **coherent scattering** which involves the interference of waves (recall that, according to the particle-wave dualism first stated by de Broglie (1924), each particle may also be described by a wave which can interfere with other particle waves) and finally **incoherent scattering** which is scattering without interference.

In the following, we will deal exclusively with **neutron diffraction** which is, in the above nomenclature of a general scattering experiment, equivalent to **elastic, coherent scattering of neutrons**.

It is assumed that most of the readers of this chapter will be familiar with x-ray diffraction from crystals, which has been demonstrated for the first time by Laue in 1912 and, since then, has developed into the most powerful method for obtaining structural information on crystalline materials. Diffraction - in sharp contrast to imaging techniques like optical or electron microscopy - has no principal limitation as to the spatial resolution, expressed in units of the wavelength of the radiation used for diffraction or imaging: While the resolution of imaging is limited to half the wavelength (recall the Abbe diffraction limit) diffraction can yield useful information, for instance, on bond distances between atoms on a length scale that is by two to three orders of magnitude smaller than the wavelength. On the other hand, diffraction, other than imaging, requires 3-dimensional periodicity (see chapter 5).

This chapter will discuss the basics and some peculiarities of neutron diffraction from either single or polycrystalline matter. We will start by discussing the **geometry of diffraction** from crystals, treat the subject of **diffraction intensities** and end with a discussion of a few **experimental issues** connected to the instruments which will be used in the practical part of the course. Examples of applications of these methods will be given in a later chapter on “Structural Analysis”. The subject of magnetic neutron diffraction and scattering will be discussed in a separate chapter.

4.9 Diffraction geometry

For purely elastic scattering, the scattering function $S(\mathbf{Q}, \omega)$ reduces to the special case without energy transfer ($E_0 = E_1$ and $\hbar\omega = E_0 - E_1 = 0$) and equal length of the wave vectors of the incident and scattered beams ($|\mathbf{k}_0| = |\mathbf{k}_1|$). $S(\mathbf{Q}, \omega = 0)$. The scattering intensity then only depends on the scattering vector $\mathbf{Q} = \mathbf{k}_1 - \mathbf{k}_0$. The coherent elastic neutron scattering (\equiv neutron diffraction) yields information on the positions (distribution) of the atomic nuclei and the arrangement of the localized magnetic spins in crystalline solids, the pair correlation function of liquids and glasses, and the conformation of polymer chains.

Figure 4.14 shows a sketch of a **general diffraction experiment**. More specifically, it is a typical setup of a constant wavelength, angular dispersive diffraction experiment. There are other methods to perform a diffraction experiment (e.g. time of flight- (TOF), Laue-, energy-dispersive diffractometers etc.) but these are outside the scope of this introductory lecture.

For constant wavelength diffraction, the energy (wavelength) and direction (collimation) of the incident neutron beam needs to be adjusted. For that purpose, the diffractometer is equipped with a crystal monochromator to select a particular wavelength band ($\lambda \pm \Delta\lambda/\lambda$) out of the “white” beam. Collimators are used to define the beam direction and divergence

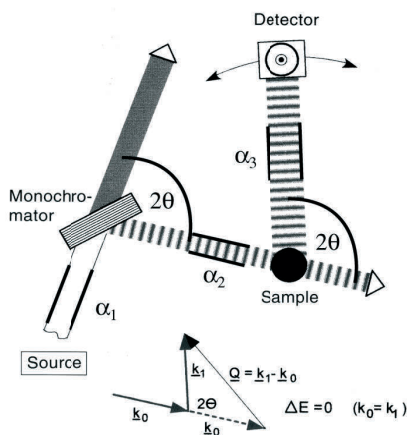


Fig. 4.14: Schematic representation of a constant wavelength diffractometer.

pretty much as it is done in x-ray diffraction.

In the case of a crystalline sample, the diffraction geometry is most conveniently described by the concepts of the *reciprocal lattice* and the *Ewald construction* which are both well-known from *x-ray-diffraction*.

Reciprocal lattice

The characteristic feature of the crystalline state (see chapter 5a) is its periodic order, which may be represented by a (translation) lattice. In the 3D case, *a*, *b*, and *c* being primitive lattice vectors of the direct lattice. Each lattice node of the crystal lattice can be addressed by a general lattice vector

$$\mathbf{R} = n_1\mathbf{a} + n_2\mathbf{b} + n_3\mathbf{c} \tag{4.49}$$

which results from a linear combination of the basis vectors with *n*₁, *n*₂, and *n*₃ integers (positive or negative integers, including 0). The position of atom *j* in the unit cell is given by the vector

$$\mathbf{r}_j = x_j\mathbf{a} + y_j\mathbf{b} + z_j\mathbf{c} \tag{4.50}$$

The coefficients *x*_{*j*}, *y*_{*j*}, and *z*_{*j*} are called atomic coordinates (0 ≤ *x*_{*j*} < 1; 0 ≤ *y*_{*j*} < 1; 0 ≤ *z*_{*j*} < 1). Given a (direct) lattice of points *R*, a point *G* is a point in the reciprocal lattice if and only if

$$e^{i\mathbf{G}\cdot\mathbf{R}} = 1 \tag{4.51}$$

for all points \mathbf{R} of the direct lattice.

We now make two key claims:

(1) We claim that the reciprocal lattice (defined by Eq. 4.51) is a lattice in reciprocal space (thus explaining its name).

(2) We claim that the primitive lattice vectors of the reciprocal lattice (which we will call \mathbf{a}^* , \mathbf{b}^* , and \mathbf{c}^*) are defined to have the following property:

$$\mathbf{a}_i \cdot \mathbf{a}_j^* = 2\pi\delta_{ij} \quad (4.52)$$

where δ_{ij} is the Kronecker delta.

We can certainly construct vectors \mathbf{a}_i^* to have the desired property of Eq. 4.52, as follows:

$$\begin{aligned} \mathbf{a}^* &= 2\pi \frac{\mathbf{b} \times \mathbf{c}}{\mathbf{a} \cdot (\mathbf{b} \times \mathbf{c})} \\ \mathbf{b}^* &= 2\pi \frac{\mathbf{c} \times \mathbf{a}}{\mathbf{a} \cdot (\mathbf{b} \times \mathbf{c})} \\ \mathbf{c}^* &= 2\pi \frac{\mathbf{a} \times \mathbf{b}}{\mathbf{a} \cdot (\mathbf{b} \times \mathbf{c})} \end{aligned}$$

It is easy to check that Eq. 4.52 is satisfied. For example,

$$\begin{aligned} \mathbf{a} \cdot \mathbf{a}^* &= 2\pi \frac{\mathbf{a} \cdot (\mathbf{b} \times \mathbf{c})}{\mathbf{a} \cdot (\mathbf{b} \times \mathbf{c})} = 2\pi \\ \mathbf{b} \cdot \mathbf{a}^* &= 2\pi \frac{\mathbf{b} \cdot (\mathbf{b} \times \mathbf{c})}{\mathbf{a} \cdot (\mathbf{b} \times \mathbf{c})} = 0 \end{aligned}$$

Now, given vectors \mathbf{a}^* , \mathbf{b}^* , and \mathbf{c}^* satisfying Eq. 4.52, we have claimed that these are in fact primitive lattice vectors for the reciprocal lattice. Let us write an arbitrary point in reciprocal space as

$$\mathbf{G} = m_1\mathbf{a}^* + m_2\mathbf{b}^* + m_3\mathbf{c}^* \quad (4.53)$$

In order to fulfill condition $e^{i\mathbf{G} \cdot \mathbf{R}} = 1$, m_1, m_2, m_3 need to be integers. Thus, points in reciprocal lattice are precisely given by equation 4.53. A plane with Miller indices h, k, l , is normal to the reciprocal lattice vector $\mathbf{G} = h\mathbf{a}^* + k\mathbf{b}^* + l\mathbf{c}^*$

Performing a **diffraction experiment** on a single crystal actually means doing a **Fourier transform** of the 3D-periodic crystal (see section 4.2) followed by taking the square of the resulting (complex) amplitude function. The Fourier transform of the (infinite) crystal lattice is essentially the reciprocal lattice derived above and yields directly the positions of the reflections in space (directions of the diffracted beams). The Fourier transform of the unit cell contents (kind and positions of all atoms) determines the reflection intensities. These reflection intensities may be envisaged as a weight attached to the nodes of the reciprocal lattice. Doing a (single crystal) diffraction experiment therefore corresponds to measuring the positions and weights of the reciprocal lattice points.

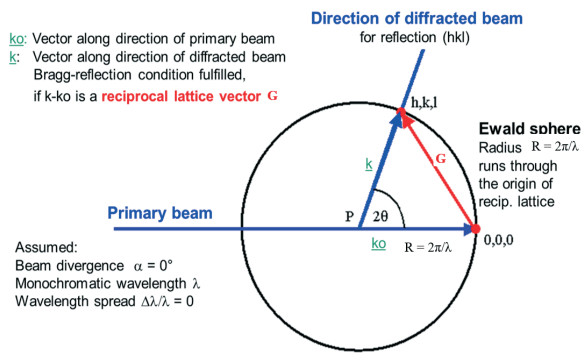


Fig. 4.15: Ewald construction in reciprocal space, showing the diffraction condition for reflection (hkl)

Ewald construction

The concept of reciprocal lattice (reciprocal space) also provides a handy tool to express geometrically the condition for Bragg diffraction in the so-called Ewald construction. In this way geometrical aspects of the different diffraction methods can be discussed. We consider the reciprocal lattice of a crystal and choose its origin (0, 0, 0). In Fig. 4.15 the wave vector \mathbf{k}_0 ($|\mathbf{k}_0| = 2\pi/\lambda$) of the incident beam is marked with its end at (0, 0, 0) and its origin at P. We now draw a sphere of radius $|\mathbf{k}_0| = 2\pi/\lambda$ around P passing through (0, 0, 0). Now, if any point hkl of the reciprocal lattice lies on the surface of this “Ewald sphere”, then the diffraction condition for the (hkl) set of lattice planes is fulfilled: The wave vector of the diffracted beam \mathbf{k} (with its origin also at P) for the set of planes (hkl) , is of the same length as \mathbf{k}_0 ($|\mathbf{k}| = |\mathbf{k}_0|$) and the resulting vector diagram satisfies $\mathbf{k} = \mathbf{k}_0 + \mathbf{G}$ ($\mathbf{Q} (= \mathbf{k} - \mathbf{k}_0) = \mathbf{G}$). Introducing the scattering angle 2θ (and hence the Bragg angle θ_{hkl} , we can deduce immediately from $2|\mathbf{k}| \cdot \sin \theta = |\mathbf{G}|$ the Bragg equation $2 d_{hkl} \cdot \sin \theta_{hkl} = \lambda$ (remember $d_{h,k,l} = \frac{2\pi}{|\mathbf{G}|}$). In the case of single crystal diffraction a rotation of the crystal and therefore also of the corresponding reciprocal lattice (which is rigidly attached to the crystal) is of often used to set the diffraction conditions for the measurement of intensities $I(\mathbf{G})$. If $|\mathbf{G}| > 4\pi/\lambda$ (then $d_{hkl} < \lambda/2\pi$) the reflection hkl cannot be observed. This condition defines the so called limiting sphere, with center at 000 and radius $4\pi/\lambda$: only the points of the reciprocal lattice inside the limiting sphere can be rotated into the diffraction position. Vice versa if $\lambda > 2 d_{\max}$, where d_{\max} is the largest interplanar spacing of the unit cell, then the diameter of the Ewald sphere is smaller than $|\mathbf{G}|_{\min}$. Under these conditions no node of the reciprocal lattice can intercept the Ewald sphere. That is the reason why diffraction of visible light (wavelength $\cong 5000\text{\AA}$) can never be obtained from crystals. λ_{\min} determines the amount of information available from a diffraction experiment. Under ideal conditions, λ_{\min} should be short enough to measure all points of the reciprocal lattice with significant diffraction intensities. For a real crystal of limited perfection and size the infinitely sharp diffraction peaks (delta functions) evolve into broadened reflections. One reason can be the local variation of the orientation of the crystal lattice (mosaic spread) implying some angu-

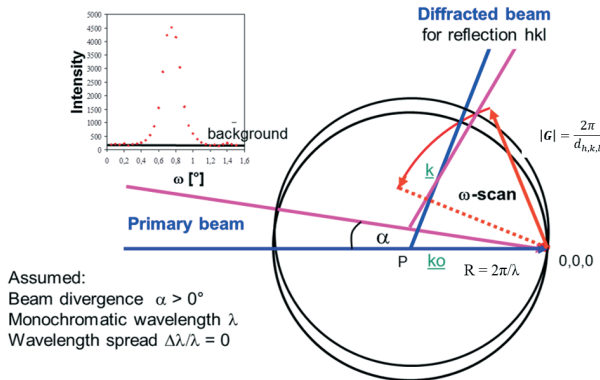


Fig. 4.16: Ewald-construction: Influence of the horizontal beam divergence on the experimental conditions for the measurement of Bragg-intensities. Inset: A typical ω -scan of a reflection.

lar splitting of the vector \mathbf{G} . A spread of interplanar spacings $\Delta d/d$, which may be caused by inhomogeneities in the chemical composition or by inhomogeneous strain in the sample, gives rise to a variation of its magnitude $|\mathbf{G}|$. The previously assumed ideal diffraction geometry also needs to be modified: In a real experiment the primary beam has a nonvanishing divergence and wavelength spread. The detector aperture is also finite. A gain of intensity, which can be accomplished by increasing the angular divergence and wavelengths bandwidth, has to be paid for by some worsening of the resolution function (see below) and hence by a limitation of the ability to separate different Bragg reflections.

All of these influences can also be studied by the Ewald construction. As an example, the influence of a horizontal beam divergence on the experimental conditions for a measurement of Bragg-intensities of a single crystal is illustrated in Fig. 4.16. Strictly monochromatic radiation (only one wavelength λ with $\Delta\lambda/\lambda = 0$) is still assumed. To collect the complete intensity contained in the spread out reflection, a so-called ω -scan, where the crystal is rotated around the sample axis perpendicular to the diffraction plane, needs to be used. The summation over the whole reflection profile yields the so-called integral diffraction intensities. As a final example, the geometry of powder diffraction experiments can also be discussed in terms of the Ewald-construction:

An ideal polycrystalline sample is characterized by a very large number of arbitrarily oriented small crystallites. Therefore, the reciprocal lattice points hkl are smeared out on a sphere and the 3D-information contained in vector \mathbf{G} is reduced to only 1D information contained in $|\mathbf{G}|$. In Figure 4.17 the corresponding sphere with radius $|\mathbf{G}| = 2\pi/d_{hkl}$ is drawn around the origin of the reciprocal lattice at $0, 0, 0$. For each Bragg reflection the circle of intersection of

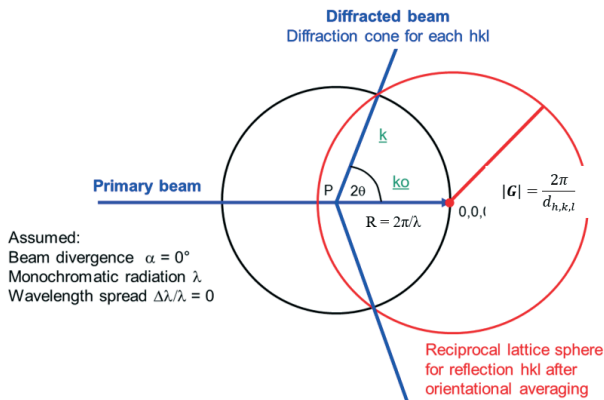


Fig. 4.17: Ewald construction for a powder diffraction experiment.

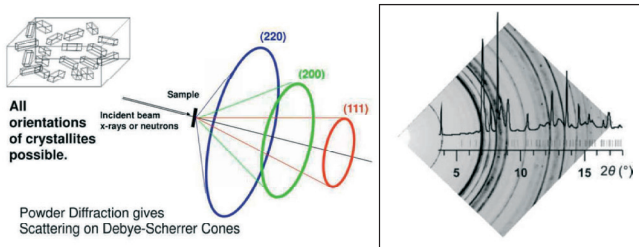


Fig. 4.18: Sketch of a powder diffraction experiment, diffraction cones are recorded on a 2D- or 1D-detector (reproduced from [9]).

the “reciprocal lattice sphere” with the Ewald sphere yields a diffraction cone. These cones (Fig. 4.18) are recorded on a point or position sensitive detector. The resulting information is plotted as an intensity vs. diffraction angle (or Q) diagram. All reflections with equal interplanar spacing d_{hkl} are perfectly superimposed and cannot be separated experimentally.

4.10 Diffraction intensities

Without the phase information, we need an approximate model of the crystal structure and a formula to calculate diffraction intensities from the model. In the kinematical scattering approximation we use the so called structure factor formula for that purpose (see below). The model is then iteratively improved to give an optimum match between observed and calculated intensities. This is referred to as the **structure refinement**.

Structure factor and Bragg intensities

In the **kinematical approximation**, which assumes that the magnitude of the incident wave is the same at all points in the specimen (this implies a small sample size, weak interaction between radiation and matter, no multiple diffraction and negligible absorption) and that the diffracted beams are much weaker than the primary beam, the diffracted intensity is proportional to the square of the amplitude of the scattered wave for each individual reflection; it can be regarded as a weight ascribed to the reciprocal lattice nodes.

$$I(\mathbf{G}) \sim |\mathbf{F}(\mathbf{G})|^2 \quad (4.54)$$

The structure factor $\mathbf{F}(\mathbf{G})$ is the Fourier transform of the scattering density within the unit cell. For a 3D-periodic scattering density function composed of discrete atoms (the crystal), the three fold spatial integral describing the Fourier transform in its most general form, simplifies to a sum over all atoms j in the unit cell. The structure factor $\mathbf{F}(\mathbf{G})$ contains the complete structural information, including the atomic coordinates $\mathbf{r}_j = x_j\mathbf{a} + y_j\mathbf{b} + z_j\mathbf{c}$ (see eqn. 4.50), site occupations and the thermal vibrations contained in T_j .

$$F(\mathbf{G}) = \sum_j b_j \exp[i(\mathbf{G} \cdot \mathbf{r}_j)] T_j \quad (4.55)$$

In the case of nuclear scattering of neutrons the structure factor has the dimension of a length, as has the scattering length $b_j(\mathbf{G}) = b_j = \text{const.}$ of nucleus j . $T_j(\mathbf{G})$ is the Debye Waller factor which takes into account dynamical and static displacements of the nucleus j from its average position \mathbf{r}_j in the unit cell.

$$T_j = \exp\left(-B_j \frac{\sin^2 \theta}{\lambda^2}\right)$$

Where $B_j = 8\pi^2 \langle u_j^2 \rangle$, is known as isotropic displacement parameter. Here, $u_j(t)$ is the displacement of atom of atom j from the equilibrium position at time t . With the fractional coordinates x_j, y_j and z_j , the scalar product in the exponential function can be written as

$$\mathbf{G} \cdot \mathbf{r}_j = 2\pi(hx_j + ky_j + lz_j) \quad (4.56)$$

In a diffraction experiment normally only relative Bragg intensities are measured. A scale factor SCALE takes into account all parameters which are constant for a given set of diffraction intensities. Additional corrections have to be applied, which are a function of the scattering angle. For nuclear neutron diffraction from single crystals the integrated relative intensities are given by

$$I(\mathbf{G}) = \text{SCALE} \cdot L \cdot A \cdot E \cdot |\mathbf{F}(\mathbf{G})|^2 \quad (4.57)$$

The Lorentz factor L is instrument specific. The absorption correction A depends on the geometry and linear absorption coefficient of the sample and the extinction coefficient E takes into account a possible violation of the assumed conditions for the application of the kinematical diffraction theory.

Information on the crystal system, the Bravais lattice type and the basis vectors \mathbf{a} , \mathbf{b} , \mathbf{c} of the unit cell (lattice parameters $a, b, c, \alpha, \beta, \gamma$) may be directly deduced from the reciprocal lattice. **Systematic absences** (zero structure factors) can be used to determine non-primitive Bravais lattices or detect the presence of symmetry operations with translation components (screw axes, glide planes).

As an example, consider a body centered cubic lattice with atoms at $(0,0,0)$ and $(1/2, 1/2, 1/2)$. Using eqn. 4.55 and dropping the Debye-Waller factor for the moment, the structure factor equation may be rewritten as:

$$\mathbf{F}(hkl) = \sum_j b_j \cdot \exp[2\pi i(hx_j + ky_j + lz_j)] \quad (4.58)$$

$$= b \cdot \exp[2\pi i(h \cdot 0 + k \cdot 0 + l \cdot 0)] + b \cdot \exp[2\pi i(h/2 + k/2 + l/2)] \quad (4.59)$$

For this simple structure, index j just runs over the two equivalent atoms with scattering length b within the unit cell. For a centrosymmetric structure, F is a real quantity (instead of being complex), the exponentials in (4.59) reduce to cosines and the phase factor assumes only the values + or -1 .

Thus we get:

$$F(hkl) = b \cdot \cos[2\pi(h \cdot 0 + k \cdot 0 + l \cdot 0)] + b \cdot \cos[2\pi(h/2 + k/2 + l/2)]$$

The first term $\cos(0) = 1$ and we therefore have:

$$F(hkl) = b + b \cdot \cos[2\pi(h/2 + k/2 + l/2)] = b \cdot (1 + \cos[\pi(h + k + l)])$$

If $h + k + l$ is even, the cosine term is +1 , otherwise it is -1 .

Reflections with $h + k + l = 2n + 1$ are therefore *systematically absent*.

These statements apply equally well to x-ray and neutron diffraction and to powder as well as to single crystal diffraction data.

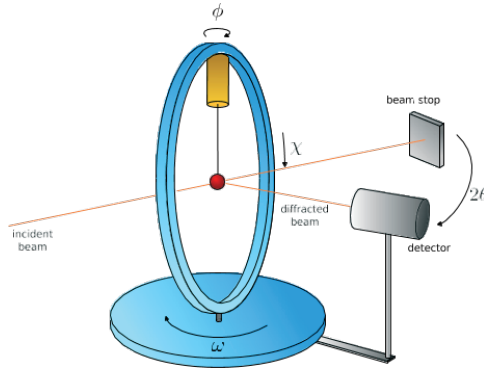


Fig. 4.19: Principle components of a constant wavelength single crystal diffractometer (Picture courtesy, Navid Qureshi (ILL, Grenoble)).

In the case of a **powder sample**, orientational averaging leads to a reduction of the dimensionality of the intensity information from 3D to 1D: Diffraction intensity I is recorded as a function $|\mathbf{G}| = 2\pi/d_{hkl}$ or, by making use of Bragg's law, of $\sin(\theta)/\lambda$ or just as a function of 2θ . For powders, two additional corrections (M and P in eqn. 4.60) need to be applied in order to convert between the measured intensities I and the squared structure factor magnitudes F^2 :

$$I(|\boldsymbol{\tau}|) = \text{SCALE} \cdot L \cdot A \cdot E \cdot M \cdot P \cdot |\mathbf{F}(\mathbf{G})|^2 \quad (4.60)$$

M is the multiplicity of the individual reflections and takes into account how many symmetrically equivalent sets of lattice planes correspond to a given hkl . In the cubic crystal system, for instance, $M_{111} = 8$ (octahedron) while $M_{100} = 6$ (cube). P is the so-called preferred orientation parameter which corrects the intensities for deviations from the assumption of randomly oriented crystals in the powder sample.

4.11 Diffractometers

Single Crystal Neutron Diffraction

Monochromator and collimator

For constant wavelength diffraction, the energy (wavelength) and direction (collimation) of the incident neutron beam needs to be adjusted. For that purpose, the diffractometer is equipped with a crystal monochromator to select a particular wavelength band ($\lambda \pm \Delta\lambda/\lambda$) out of the “white” beam according to the Bragg condition for its scattering plane (hkl)

$$2 d_{hkl} \cdot \sin \theta_{hkl} = \lambda \quad (4.61)$$

with the interplanar spacing d_{hkl} and the monochromator scattering angle $2\theta_{hkl} = 2\theta_M$. The width of the wavelengths band $\Delta\lambda/\lambda$, which is important for the Q -resolution, depends on the divergences of the beam before and after the monochromator (collimations α_1 and α_2), on the mosaic spread of the monochromator crystal, and on the monochromator angle $2\theta_M$. In order to increase the intensity of the monochromatic beam at the sample position the monochromator crystal is often bent in vertical direction perpendicular to the diffraction plane of the experiment. In this way the vertical beam divergence is increased leading to a loss of resolution in reciprocal space. The diffracted intensity from the sample is measured as a function of the scattering angle 2θ and the sample orientation (especially in case of a single crystal). 2θ is again defined by collimators.

As there is no analysis of the energy of the scattered beam behind the sample, the energy resolution $\Delta E/E$ of such a 2-axes diffractometer is not well defined (typically of the order of some %). In addition to the dominant elastic scattering also quasi-elastic and some inelastic scattering contributions are collected by the detector.

Neutron filters and the problem of $\lambda/2$ contamination

Unfortunately, the monochromator crystals not only “reflect” the desired wavelength λ by diffraction from the set of lattice planes (hkl) but also the higher orders of $\lambda/2$ or $\lambda/3$ etc. from 2h, 2k, 2l or 3h, 3k, 3l to the same diffraction angle:

$$\sin \theta = \lambda/d_{hkl} = (\lambda/2)/d_{2h\ 2k\ 2l} = (\lambda/3)/d_{3h\ 3k\ 3l} \quad (4.62)$$

The only requirement is, that the higher order reflection (2h, 2k, 2l) or (3h, 3k, 3l) has a reasonably large structure factor. Higher order contamination causes sizeable reflection intensities at “forbidden” reflection positions and in addition to that can modify intensities at allowed positions. Thus it can very much affect the correct determination of the unit cell as well of the space group symmetry (from systematically absent reflections). The solution to this problem is to minimize the $\lambda/2$ contamination by using filters which suppress the higher orders stronger than the desired wavelength. One such type of filters uses resonance absorption effects - completely analogous to the suppression of the K_β line in x-ray diffractometers. Another way to attenuate short wavelengths is to use the scattering from materials like beryllium or graphite. These filters use the fact that there is no Bragg diffraction if $\lambda > 2d_{max}$, where d_{max} is the largest interplanar spacing of the unit cell. As we have shown above, for such long wavelengths the Ewald sphere is too small to be touched by any reciprocal lattice point. Below this critical wavelength, the neutron beam is attenuated by diffraction and this can be used to suppress higher order reflections very effectively. Frequently used materials are polycrystalline beryllium and graphite. Due to their unit cell dimensions, they are particularly suitable for experiments with cold neutrons because they block wavelengths smaller than about 3.5 Å and 6 Å, respectively.

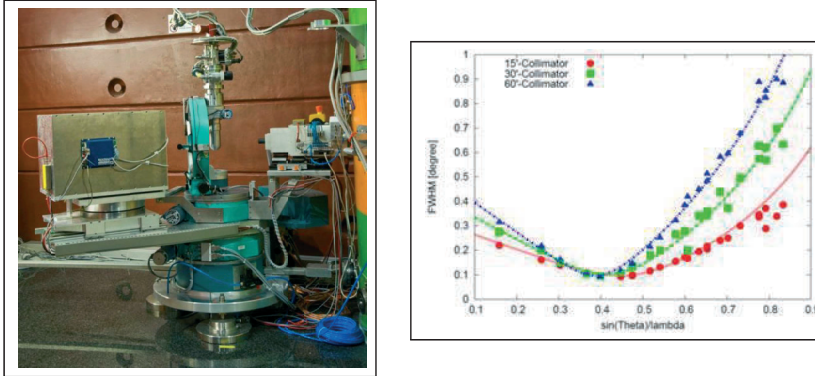


Fig. 4.20: *Left: Experimental setup of the four circle single crystal diffractometer HEiDi at FRM II. Right: Resolution function of HEiDi for different collimations, monochromator: Cu (220), $2\theta_{Mono} = 40^\circ \rightarrow \lambda = 0.873 \text{ \AA}$*

Resolution function:

An important characteristic of any diffractometer is its angular resolution. Fig. 4.20 shows (on the right) the resolution function (reflection half width as a function of scattering angle) for the four circle single crystal neutron diffractometer HEiDi at FRM II shown on the left. The resolution depends on a number of factors, among them the collimation, the monochromator type and quality, the 2θ and (hkl) of the reflection used for monochromatization etc.

Powder Neutron Diffractometry:

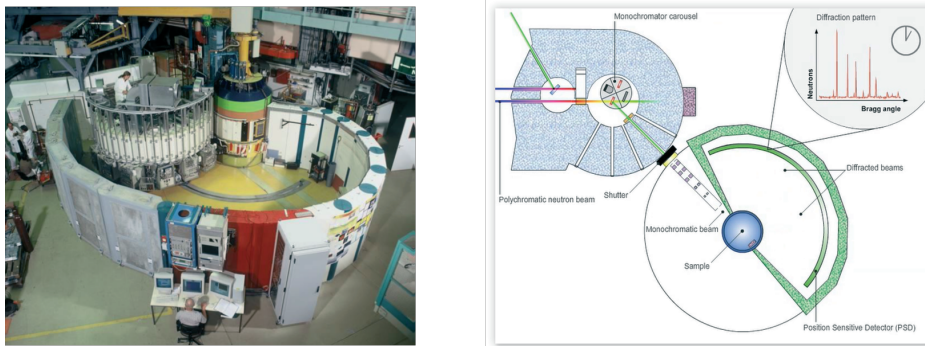


Fig. 4.21: *Left: Neutron powder diffractometer D20 at ILL, Grenoble. Right: Typical setup of a (constant wavelength) powder neutron diffractometer with position sensitive detector (PSD).*

Neutron Rietveld analysis:

The conversion from 3D- to 1D-intensity data caused by the averaging over all crystal-lite orientations in a powder sample severely restricts the informative value of powder neutron (or x-ray) diffraction experiments and makes the resolution function of the instrument even more important than in the single crystal case. Even with optimized resolution, the severe overlap of reflections on the 2θ -axis often prohibits the extraction of reliable integrated intensities from the experiment. Instead, the Rietveld method, also referred to as full pattern refinement, is used to refine a given structural model against powder diffraction data. The method, which is widely used in powder x-ray diffraction, has actually been invented by Hugo Rietveld in 1969 [10] for the structural analysis from powder neutron data. Full pattern refinement means that along with the structural parameters (atomic coordinates, thermal displacements, site occupations) which are also optimized in a single crystal structure refinement, additional parameters like the shape and width of the reflection profiles and their 2θ -dependence, background parameters, lattice parameters etc. need to be refined.

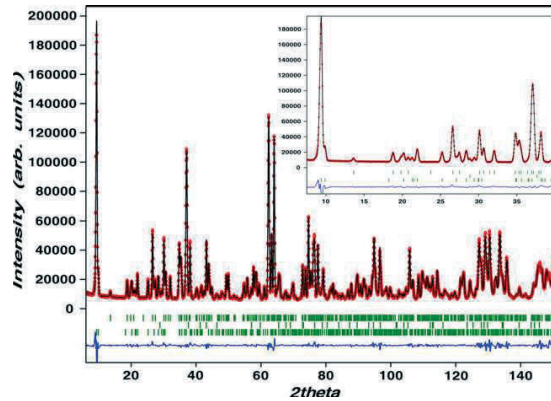


Fig. 4.22: Results of a Rietveld refinement at the magnetic phase transition of CoGeO_3 [8], red: measured intensity, black: calculated from model, blue: difference, green: tick-marks at allowed reflection positions. The figure shows the low-angle part of two diffractograms measured at SPODI at 35K and 30K. Note the strong magnetic reflection appearing below the magnetic ordering transition (in the inset).

References

- [1] K. Sköld, D. Price (Eds.) : "Methods of Experimental Physics" Neutron Scattering Part A-C" (Academic Press 1987).
- [2] G. L. Squires : "Introduction to the Theory of Thermal Neutron Scattering" (Cambridge University Press; Revised Edition (March 29, 2012)).
- [3] J. M. Cowley: "Diffraction Physics" North Holland, Amsterdam 1995
- [4] S. W. Lovesey "Theory of neutron scattering from condensed matter" Clarendon Press, Oxford, 1987
- [5] A. Furrer, J. Mesot, T. Strässle "Neutron Scattering in Condensed Matter Physics" World Scientific, London, 2009
- [6] J. M. Carpenter, C.-K. Loong "Elements of Slow-Neutron Scattering" Cambridge University Press (2015)
- [7] B. W. Batterman, H. Cole "Dynamical Diffraction of X-Rays by Perfect Crystals", *Rev. Mod. Phys.* **36**, 681 (1964).
- [8] G. Redhammer et al., *Phys. Chem. Min.* **37**, 311 (2010).
- [9] Reproduced from: Braggs world, talk by Th. Proffen <http://ebookbrowse.com/proffen-talk-bragg-pdf-d59740269> retrieved: 2015-05-05
- [10] H. M. Rietveld, *J. Appl. Cryst.* **2**, 65 (1969).

[11] The lecture note is adapted from Prof. G. Roth, RWTH Aachen and Prof. Th. Brueckel, JCNS lab course (Band/ Volume 255)

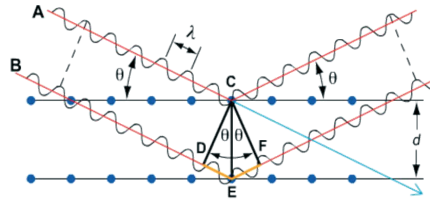


Fig. 4.23: Bragg scattering

Exercises

E4.1 Multiple choice

Kinematic scattering theory takes into account

- refraction
- attenuation
- multiple scattering
- none of the above

E4.2 Multiple choice

You have measured the scattered intensity $I(Q)$ as a function of the scattering vector Q . Which of the following statements are correct for kinematic scattering:

- The Fourier transform of $I(Q)$ is proportional to the scattering density.
- $I(Q)$ is always described by the Laue function.
- $I(Q)$ is the Patterson- or static pair correlation function.
- The phase problem does not allow one to determine the atomic position directly by a simple mathematical procedure.

E4.3 Bragg scattering

Bragg had the idea to describe scattering from a three-dimensional periodic arrangement of scatterers (e.g. atoms in a crystal) by the interference of waves reflected from parallel atomic planes, see sketch below. For constructive interference, sharp intensity maxima appear as a function of scattering angle. These peaks are called “Bragg reflections”.

1. After scattering, the waves reflected from the two planes show a path length difference. Which relation does this path length difference have to fulfill in order to achieve coherent superposition and thus an intensity maximum (See Figure 4.23) ?

2. Derive the condition for the occurrence of such a Bragg peak in terms of wavelength λ , scattering angle 2θ and distance between the planes d , the so-called Bragg equation.
3. How does the Bragg equation relate to the Laue conditions?

E4.4 Reciprocal lattice

A two-dimensional rectangular crystal has a unit cell with sides $a_1 = 0.468$ nm and $a_2 = 0.342$ nm.

- (a) Find out the reciprocal lattice vectors and Draw to scale a diagram of the reciprocal lattice.
- (b) Label the reciprocal lattice points for indices in the range $0 \leq h \leq 3$ and $0 \leq k \leq 3$.

E4.5 Types of Scattering Experiments

- a) Discuss/define the following terms: A. Elastic scattering, B. Inelastic scattering, C. Coherent scattering, D. Incoherent scattering
- b) What does the term “diffraction” correspond to in this context?

E4.6 Filtering

- a) What is the purpose of a beryllium (or graphite) filter for neutron diffraction?
- b) To discuss how it works: Use the Ewald construction for a given reciprocal lattice and a very short / very long wavelength.

E4.7 Structure factor equation

The structure factor equation is the central formula that allows us to calculate diffracted intensities from structural parameters. It corresponds to a Fourier-transform of the unit cell contents.

- a) Write down the structure factor equation
- b) Identify and discuss all parameters in the formula.
- c) Under which conditions does this formula hold (kinematical diffraction conditions)?
- d) Explain the difference in diffraction pattern (x-ray powder) although both have fcc NaCl type crystal structure (Figure 4.24).

E4.8 Neutron diffractometers

- a) What is the purpose of a monochromator?

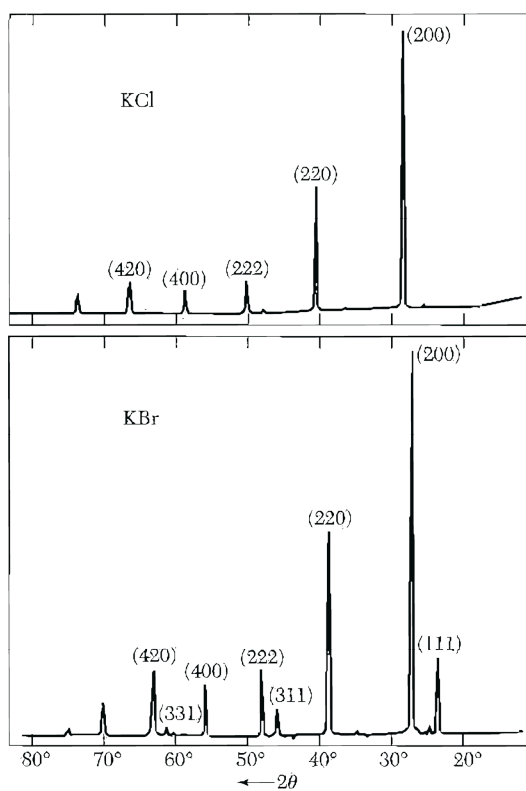


Fig. 4.24: X-ray powder diffraction of KCl and KBr.

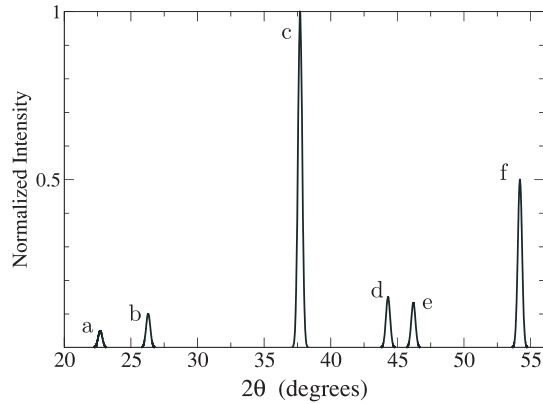


Fig. 4.25: Powder diffraction of neutrons from PrO_2 . The wavelength of the neutron beam is $\lambda = 0.123 \text{ nm}$. (One should assume that Lorentz corrections have been removed from the displayed intensities.). The approximate peak positions are: a: 22.7° , b: 26.3° , c: 37.7° , d: 44.3° , e: 46.2° , f: 54.2°

- b) How does it work?
- c) What does the term “collimation” mean?
- d) What is the resolution function of a diffractometer? (sketch)
- e) Why is it important?
- f) What is the purpose of a hot neutron source?
- g) How does it work?

E4.9 Calculation of lattice constant

Consider the powder diffraction data from PrO_2 shown in the above Figure (Fig. 4.25).

- a) Find out the lattice type (assume some sort of Cubic structure).
- b) Find out the lattice constant.

5a Crystallography

M. Zobel
Institute of Crystallography
RWTH Aachen University

Contents

5a.1 Introduction	2
5a.2 Crystal lattices	3
5a.3 Crystallographic coordinate systems	4
5a.4 Crystallographic symmetry operations and symmetry elements	6
5a.5 Crystallographic point groups and space groups	10
5a.6 Example: crystal structure description of $\text{YBa}_2\text{Cu}_3\text{O}_{7-8}$	12
Exercises Crystallography	16

5a.1 Introduction

The term “crystal” derives from the Greek κρύσταλλος, which was first used as a description of ice and later - more generally - of transparent minerals with regular morphology (regular crystal faces and edges), see Fig. 5a.1 as an example.



Fig. 5a.1: Example: Quartz (SiO_2), mineral specimen from the Gotthard-Massif.

Matter is usually classified into three states: gaseous – liquid – solid. Crystals are representatives of the solid state. **Crystalline solids** are **thermodynamically stable** in contrast to glasses and are characterised by a **regular three-dimensional periodic arrangement of atoms** (ions, molecules) in space. More than 90 % of matter are (partially) crystalline. In this chapter we discuss basic concepts which are used to describe the structure of crystals. The field of “Crystallography”, though, is not only limited to the concept of crystal symmetry, but further encompasses the techniques which allow us to characterize the structure and dynamics of matter, with X-ray and neutron scattering being the key techniques. The importance of this field is mirrored in a range of Nobel Prizes in relation to crystallography and structure characterization, see Fig. 5a.2.

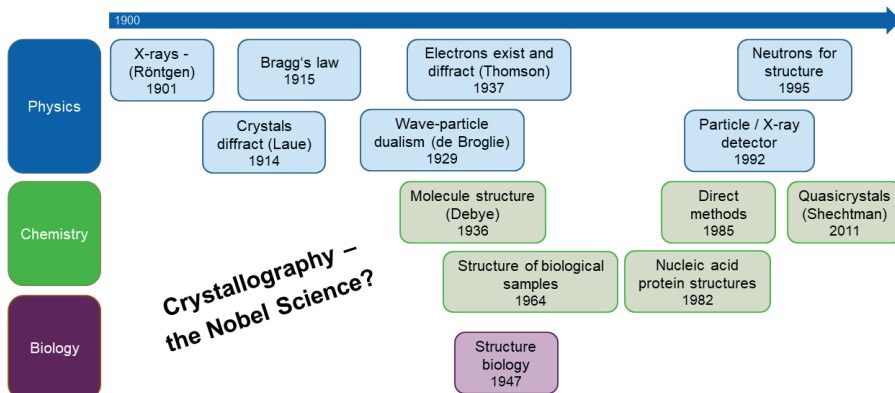


Fig. 5a.2: Nobel Prizes in relation to Crystallography

5a.2 Crystal lattices

The three-dimensional periodicity of crystals can be represented by the so-called crystal lattice. The repeat unit in form of a parallelepiped - known as the **unit cell** - is defined by three non-linear basis vectors \mathbf{a} , \mathbf{b} , and \mathbf{c} , whose directions form the reference axes X , Y , and Z of the corresponding right-handed crystallographic coordination system. The six lattice parameters are given as the lengths of the basis vectors $a = |\mathbf{a}|$, $b = |\mathbf{b}|$, $c = |\mathbf{c}|$ and the angles between the basis vectors: $\text{angle}(\mathbf{a}, \mathbf{b}) = \gamma$, $\text{angle}(\mathbf{b}, \mathbf{c}) = \alpha$, $\text{angle}(\mathbf{c}, \mathbf{a}) = \beta$. The faces of the unit cell are named as $\text{face}(\mathbf{a}, \mathbf{b}) = C$, $\text{face}(\mathbf{b}, \mathbf{c}) = A$, $\text{face}(\mathbf{c}, \mathbf{a}) = B$, see Fig. 5a.3

If the vertices of all repeat units (unit cells) are replaced by points, the result is the crystal lattice in the form of a **point lattice**. Each lattice point is given by a vector $\boldsymbol{\tau} = u\mathbf{a} + v\mathbf{b} + w\mathbf{c}$, with u , v , w being integers. \mathbf{a} , \mathbf{b} , \mathbf{c} act as the symmetry operation of parallel displacement also known as a **translation** and maps the atomic arrangement of the crystal (crystal structure) onto itself.

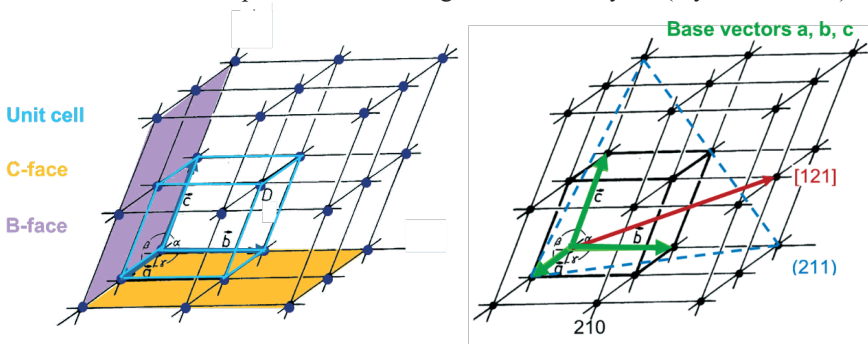


Fig. 5a.3: Point lattice with unit cell, basis vectors, B- and C-face, and notation for: lattice point 210, lattice direction [121] and lattice plane (211)

A **lattice point** is named “ uvw ”, according to the coefficients (integers) of the translation vector $\boldsymbol{\tau} = u\mathbf{a} + v\mathbf{b} + w\mathbf{c}$ from the origin to the lattice point. A **lattice direction** - given by the symbol $[uvw]$ - is defined by the direction of the corresponding translation vector. Nota: Watch out for the different brackets employed in crystallographic nomenclature.

A plane passing through three lattice points is known as a **lattice plane**. Since all lattice points are equivalent (by translation symmetry) there will be infinitely many parallel planes passing through all the other points of the lattice. Such a set of equally spaced planes is known as a **set of lattice planes**. If the first plane from the origin of a set of lattice planes makes intercepts a/h , b/k , c/l on the X , Y , Z axes, respectively, where h , k , l are integers, then the **Miller indices** of this set of lattice planes are (hkl) , the three factors h , k , l being enclosed in parentheses.

The equation of lattice planes can be written in intercept form as

$$\left(\frac{hx}{a}\right) + \left(\frac{ky}{b}\right) + \left(\frac{lz}{c}\right) = n, \quad 5a.1$$

where n is an integer. If $n = 0$ the lattice plane passes through the origin; if $n = 1$, the plane makes intercepts at a/h , b/k , c/l on the X , Y , Z axis respectively; if $n = 2$, the intercepts are $2a/h$, $2b/k$, $2c/l$; and so on.

The line of intersection of any two non-parallel lattice planes is a row of lattice points common to both planes. This lattice point row defines a lattice direction $[uvw]$ which is known as **zone**

axis. All lattice planes intersecting in a common lattice-point row are said to lie in the same **zone**. The condition for lattice planes to be parallel to a lattice vector $\tau = ua + vb + wc$ is the **zone equation**

$$uh + vk + wl = 0 \quad 5a.2$$

The zone axis symbol $[uvw]$ for the zone containing the two planes $(h_1k_1l_1)$ and $(h_2k_2l_2)$ is obtained by solving the simultaneous equations $uh_1 + vk_1 + wl_1 = 0$ and $uh_2 + vk_2 + wl_2 = 0$,

$$[uvw] = [k_1l_2 - k_2l_1, l_1h_2 - l_2h_1, h_1k_2 - h_2k_1] \quad 5a.3$$

5a.3 Crystallographic coordinate systems

The first step in the description of a crystal structure is to choose the basis vectors of a unit cell as the smallest repeat unit of the crystal. While in physics and chemistry, Cartesian coordinate systems are commonly used, crystallography uses symmetry adapted coordinate systems. In this way a **crystal-specific coordinate system** is defined which is then used to localize all the atoms in the unit cell. Crystal symmetry requires, in three dimensions, **7 different crystal systems** and hence 7 crystallographic coordinate systems to be defined:

name of system	minimum symmetry	conventional unit cell
triclinic	1 or $\bar{1}$	$a \neq b \neq c$; $\alpha \neq \beta \neq \gamma$
monoclinic	<u>one</u> diad, i.e. 2 or m (1Y)	$a \neq b \neq c$; $\alpha = \gamma = 90^\circ, \beta > 90^\circ$
orthorhombic	<u>three</u> mutually perpendicular diads, i.e. 2 or m (1X, Y and Z)	$a \neq b \neq c$; $\alpha = \beta = \gamma = 90^\circ$
tetragonal	<u>one</u> tetrad, i.e. 4 or $\bar{4}$ (1Z)	$a = b \neq c$; $\alpha = \beta = \gamma = 90^\circ$
trigonal (hexagonal cell)	<u>one</u> triad, i.e. 3 or $\bar{3}$ (1Z)	$a = b \neq c$; $\alpha = \beta = 90^\circ, \gamma = 120^\circ$
hexagonal	<u>one</u> hexad, i.e. 6 or $\bar{6}$ (1Z)	$a = b \neq c$; $\alpha = \beta = 90^\circ, \gamma = 120^\circ$
cubic	<u>four</u> triads, i.e. 3 or $\bar{3}$ (1 space diagonals of cube)	$a = b = c$; $\alpha = \beta = \gamma = 90^\circ$

The choice of the origin of the coordinate system is arbitrary, but for convenience it is usually chosen at a centre of symmetry (inversion centre), if present, otherwise at a point of high symmetry.

In order to complete the symmetry conventions of the coordinate systems, it is necessary to add to the **seven** so-called **primitive unit cells** of the crystal systems (primitive lattice types with only one lattice point per unit cell) **seven centred unit cells** with two, three or four lattice points per unit cell (centred lattice types). These centred unit cells are consequently two, three or four

times larger than the smallest repeat units of the crystal. The resulting **14 Bravais lattice types** with their centerings are compiled in figure 5a.4. Hereby the capital letters represent the type of centering: P = primitive (no centering); A, B, C = face-centered in A, B, C, respectively; F = face-centered on all faces; I = body centered; R = centering of the rhombohedral unit cell.

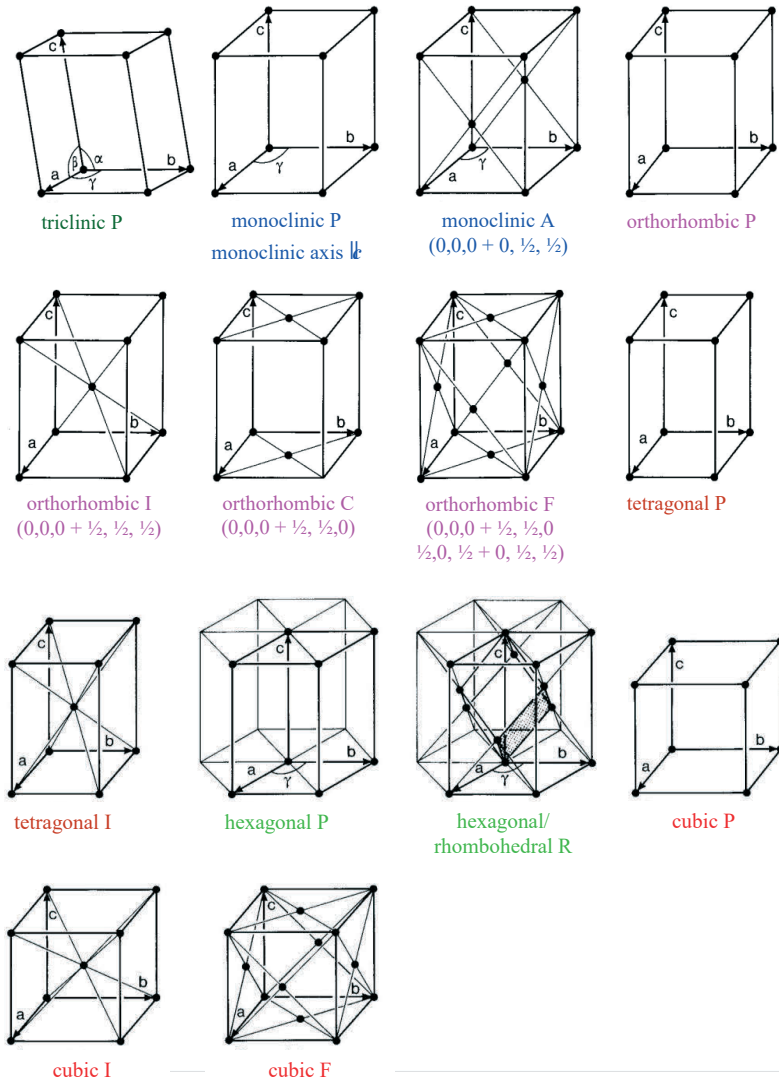


Fig. 5a.4: The 14 Bravais lattices consisting of the 7 primitive lattices P for the 7 crystal systems with only one lattice point per unit cell and the 7 centred (non-primitive) lattices A, B, C, I, R and F with 2, 3 and 4 lattice points per unit cell.

A set of lattice planes (hkl) is separated by a characteristic interplanar spacing $d(hkl)$. According to the different crystallographic coordinate systems these $d(hkl)$ values are calculated in a specific manner:

For the cubic lattice ($a = b = c$, $\alpha = \beta = \gamma = 90^\circ$)

$$d(hkl) = a \cdot (h^2 + k^2 + l^2)^{-\frac{1}{2}} \quad 5a.4$$

For the hexagonal lattice ($a = b$, c , $\alpha = \beta = 90^\circ$, $\gamma = 120^\circ$)

$$d(hkl) = \left(\frac{4}{3} \frac{h^2 + k^2 + hk}{a^2} + \frac{l^2}{c^2} \right)^{-\frac{1}{2}} \quad 5a.5$$

For the tetragonal lattice ($a = b$, c , $\alpha = \beta = \gamma = 90^\circ$)

$$d(hkl) = \left(\frac{h^2 + k^2}{a^2} + \frac{l^2}{c^2} \right)^{-\frac{1}{2}} \quad 5a.6$$

For the orthorhombic lattice (a , b , c , $\alpha = \beta = \gamma = 90^\circ$)

$$d(hkl) = \left(\frac{h^2}{a^2} + \frac{k^2}{b^2} + \frac{l^2}{c^2} \right)^{-\frac{1}{2}} \quad 5a.7$$

For the monoclinic lattice (a , b , c , $\alpha = \gamma = 90^\circ$, $\beta > 90^\circ$)

$$d(hkl) = \left(\frac{h^2}{a^2 \sin^2 \beta} + \frac{k^2}{b^2} + \frac{l^2}{c^2 \sin^2 \beta} - \frac{2hl \cos \beta}{ac \sin^2 \beta} \right)^{-\frac{1}{2}} \quad 5a.8$$

For the triclinic lattice (a , b , c , α , β , γ), the most general case,

$$d(hkl) = \left(1 - \cos^2 \alpha - \cos^2 \beta - \cos^2 \gamma + 2 \cos \alpha \cdot \cos \beta \cdot \cos \gamma \right)^{\frac{1}{2}} \left(\frac{h^2}{a^2} \sin^2 \alpha + \frac{k^2}{b^2} \sin^2 \beta + \frac{l^2}{c^2} \sin^2 \gamma + \frac{2kl}{bc} (c \cdot \cos^2 \beta - \cos \alpha) + \frac{2lh}{ca} (c \cdot \cos^2 \gamma - \cos \beta) + \frac{2hk}{ab} (c \cdot \cos^2 \alpha - \cos \gamma) \right)^{-\frac{1}{2}} \quad 5a.9$$

5a.4 Crystallographic symmetry operations and symmetry elements

The **symmetry operations** of a crystal are isometric transformations or motions, i.e. mappings in space which preserve distances and, hence, also angles and volumes. An object and its transformed object superpose in a perfect manner, they are indistinguishable.

The simplest crystallographic symmetry operation is the **translation**, which is a parallel displacement of the crystal by a translation vector τ (see chapt. 4.2). There is no fixed point, the entire lattice is shifted and, hence, the crystal lattice is considered to be infinite.

Crystallographic **rotations** n around an axis by an angle $\varphi = 360^\circ/n$ (n -fold rotations) and **rotoinversions** (combination of rotations and inversions) \bar{n} are called point symmetry operations because they leave at least one point in space invariant (at least one fixed point), see Fig. 5a.5. An important fact of crystallographic symmetry is the restriction of the rotation angles to $\varphi = 60, 90, 120, 180$ and 360° , resulting in the rotation axes 1, 2, 3, 4 and 6. This derives from the assumption of three-dimensional translational symmetry. Only for such crystallographic rotations the space can be covered completely without gaps and overlaps. The rotoinversion $\bar{n} = \bar{1}$ is an **inversion** at a point $\bar{n} = \bar{2} \equiv m$ (mirror plane) describes a **reflection** through a plane.

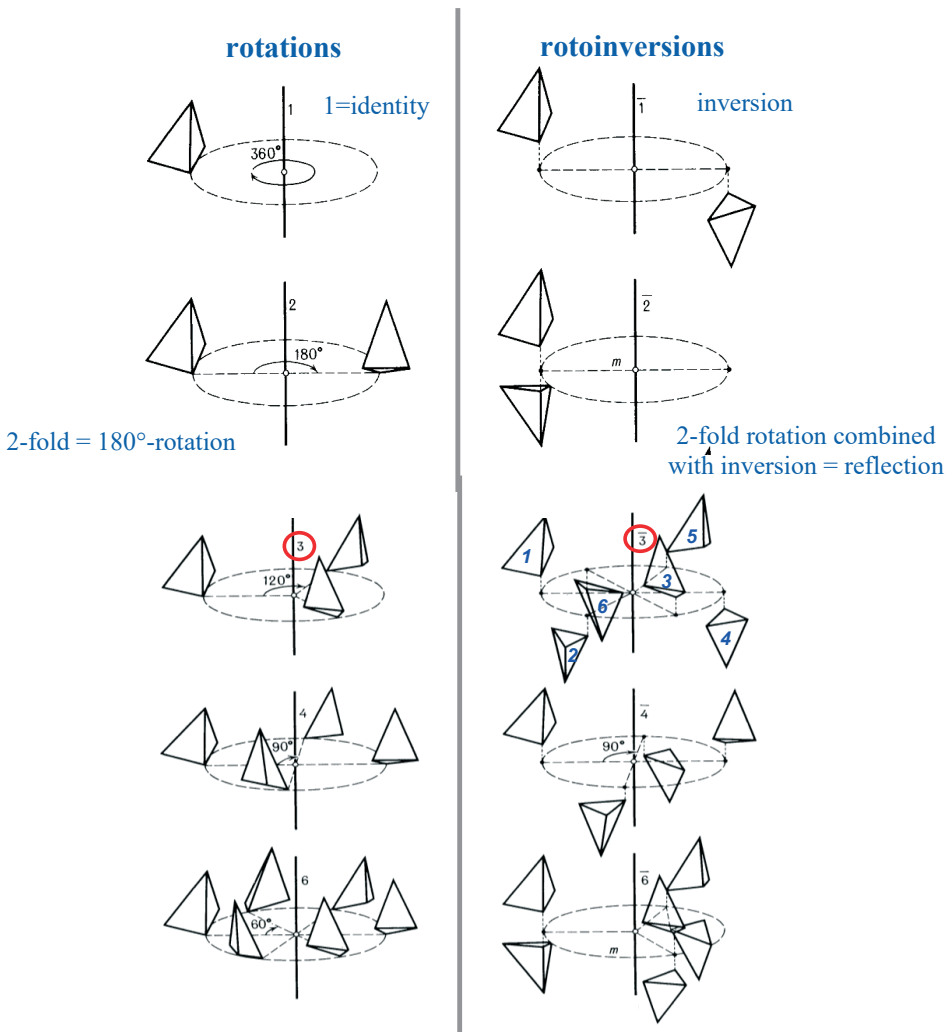


Fig. 5a.5: Rotations: $n=1$ (identity), $n=2$ (angle 180°), $n=3$ (120°), $n=4$ (90°), $n=6$ (60°).
 Rotoinversions: $\bar{1}$ (inversion), $\bar{2} \equiv m$ (reflection), $\bar{3} = 3 + \bar{1}$, $\bar{4}$, $\bar{6} = 3/m$.

The combination of n -fold rotations with $(m/n) \cdot a$ translation components ($m < n$) parallel (\parallel) to the rotation axis leads to the so-called **screw rotations** n_m , e.g. $2_1, 3_2, 4_2, 6_5$. These symmetry operations have no fixed points, see Fig. 5a.6.

The combination of a reflection through a plane (glide plane) with translation components (glide vectors) of $a/2, b/2, c/2, (a+b)/2, \dots \parallel$ to this plane are known as **glide reflections** a, b, c, n, \dots, d , see Fig. 5a.7. Again, no fixed points exist for these symmetry operations.

The objects which actually relate to the symmetry operations are the **symmetry elements**. They form the geometrical locus, oriented in space, of the symmetry operation (a line for a rotation, a plane for a reflection, and a point for an inversion) together with a description of this operation. Symmetry elements are mirror planes, glide planes, rotation axes, screw axes, rotoinversion axes and inversion centres. The geometrical descriptions of selected crystallographic symmetry operations are illustrated in Figs. 5a.4 - 5a.6.

A **symmetry operation** transforms a point X with coordinates x, y, z (corresponding to a position vector $X = xa_1 + ya_2 + za_3$) into a symmetrically equivalent point X' with coordinates x', y', z' mathematically by the system of linear equations

$$\begin{aligned} x' &= W_{11}x + W_{12}y + W_{13}z + w_1 \\ y' &= W_{21}x + W_{22}y + W_{23}z + w_2 \\ z' &= W_{31}x + W_{32}y + W_{33}z + w_3 \end{aligned} \quad 5a.10$$

Symmetry operation in matrix notation:

$$\begin{pmatrix} x' \\ y' \\ z' \end{pmatrix} = \begin{pmatrix} W_{11} & W_{12} & W_{13} \\ W_{21} & W_{22} & W_{23} \\ W_{31} & W_{32} & W_{33} \end{pmatrix} \circ \begin{pmatrix} x \\ y \\ z \end{pmatrix} + \begin{pmatrix} w_1 \\ w_2 \\ w_3 \end{pmatrix}; \quad X' = \mathbf{W} \circ X + \mathbf{w} = (\mathbf{W}, \mathbf{w}) \circ X \quad 5a.11$$

The (3×3) matrix \mathbf{W} is the rotation part and the (3×1) column matrix \mathbf{w} the translation part of the symmetry operation. The two parts \mathbf{W} and \mathbf{w} can be assembled into an augmented (4×4) matrix \mathbf{W} according to

$$\begin{pmatrix} x' \\ y' \\ z' \\ 1 \end{pmatrix} = \begin{pmatrix} W_{11} & W_{12} & W_{13} & w_1 \\ W_{21} & W_{22} & W_{23} & w_2 \\ W_{31} & W_{32} & W_{33} & w_3 \\ 0 & 0 & 0 & 1 \end{pmatrix} \circ \begin{pmatrix} x \\ y \\ z \\ 1 \end{pmatrix} = \mathbf{W} \circ X \quad 5a.12$$

Since every symmetry transformation is a "rigid-body" motion, the determinant of all matrices \mathbf{W} and \mathbf{W} is $\det \mathbf{W} = \det \mathbf{W} = \pm 1$ (+ 1: preservation of handedness; - 1: change of handedness of the object).

The sequence of two symmetry operations (successive application) is given by the product of their matrices \mathbf{W}_1 and \mathbf{W}_2 according to eq. 4.13, where \mathbf{W}_3 is again a symmetry operation.

$$\mathbf{W}_3 = \mathbf{W}_1 \circ \mathbf{W}_2 \quad 5a.13$$

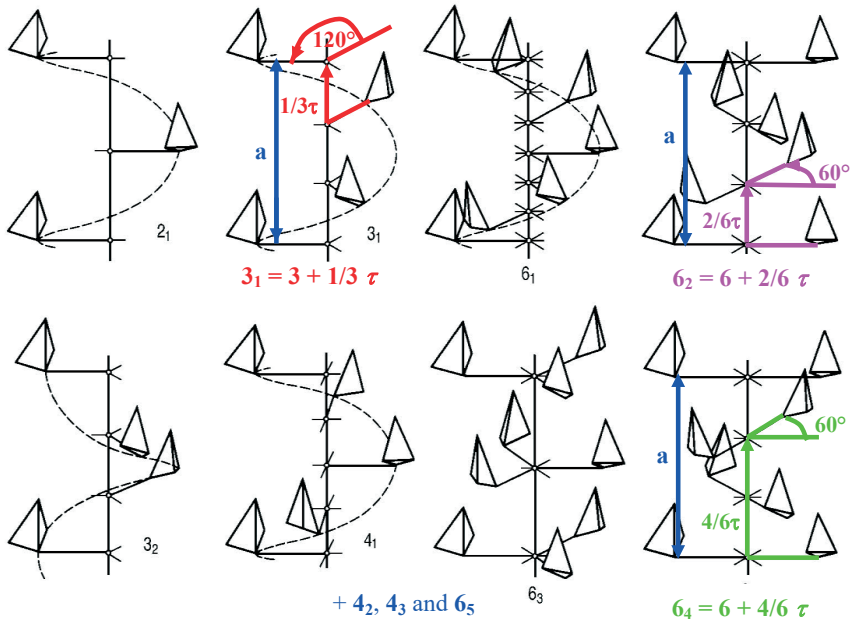


Fig. 5a.6: Screw rotations n_m : combination of rotations n and translation components $(m/n) \cdot a \parallel$ to the rotation axis.

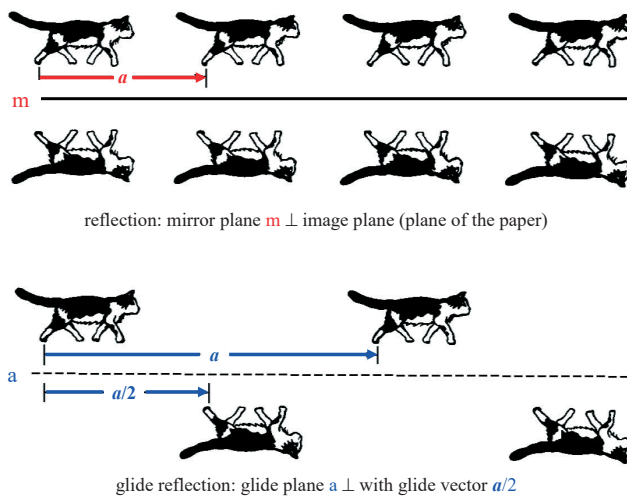


Fig. 5a.7: Examples of reflections and glide reflections.

5a.5 Crystallographic point groups and space groups

The symmetry of a macroscopic crystal and of its crystal structure relates to the different possibilities to fill 3D space and available point symmetry operations. All possible combinations of the crystallographic point symmetry operations in three-dimensional space lead to exactly **32 crystallographic point groups** (also called **crystal classes**).

Nota: The symmetry of the crystal structure can be described by mathematical group theory. The symmetry operations are the group elements of a crystallographic group G , and the combination of group elements is the successive execution of symmetry operations. The 32 point groups are each of finite order, with the order being the number of elements of the group (maximum order: 48 for the cubic crystal class).

If we now combine the 32 point groups with the 14 Bravais lattice types as well as the translation-containing symmetry operations of the screw axes and glide reflections and translational symmetry, we result in **230 space groups**. Fig. 5a.8 represents this schematically.

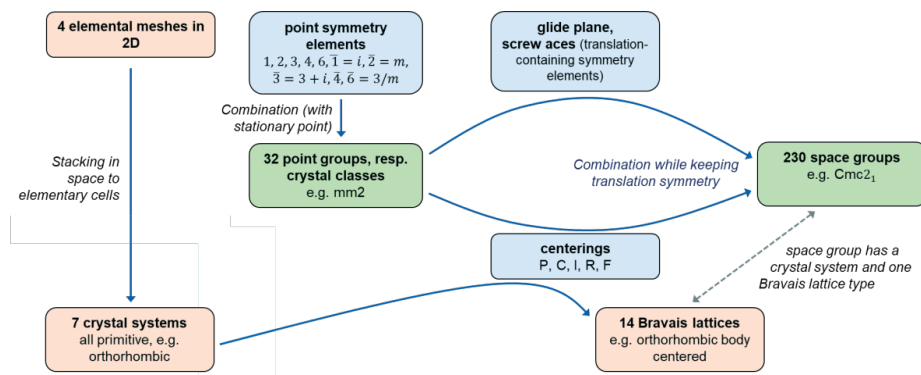


Fig. 5a.8: Going from elemental meshes to space groups by combining the concept of unit cells (with and without centering), point symmetry, translation-containing symmetry elements.

In Fig. 5a.8, an exemplary space group is given as “Cmc2₁”. This is the **Hermann-Mauguin symbol**, which is internationally employed in the field of crystallography to display in a compact form the symmetry information of the crystal. Three independent main **symmetry directions** (“Blickrichtungen”) describe the entire symmetry of a crystal. These Blickrichtungen are specifically defined for the seven crystal systems, and they define the sequence, in which the symmetries are listed in the Hermann-Mauguin symbols. As an example, the Blickrichtungen of the cubic system are shown in Fig. 5a.9.

Besides the Hermann-Mauguin symbol, the Schoenflies symbol is used alternatively to describe symmetry. Yet, the Schoenflies symbol only describes point group symmetry without containing information on translational symmetry. It is frequently used in chemistry to describe the symmetry of molecules, for instance in the fields of infrared and nuclear magnetic resonance spectroscopy.

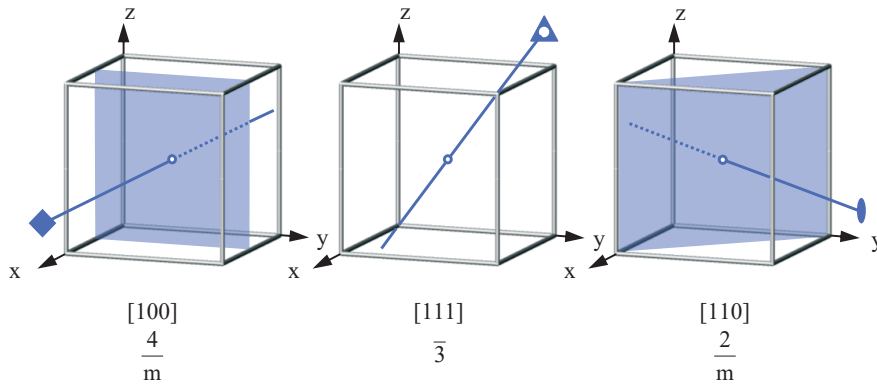


Fig. 5a.9: Symmetry directions (“Blickrichtungen”) of the cubic lattice ($a = b = c$, $\alpha = \beta = \gamma = 90^\circ$): $[100]$ with symmetry $4/m$, $[111]$ with $\bar{3}$, and $[110]$ with $2/m$.

The **point group symmetries** determine the anisotropic (macroscopic) **physical properties** of crystals, i.e. mechanical, electrical, optical and thermal properties. The crystal class can be deduced from a **diffraction experiment**. However, diffraction introduces an (additional) centre of symmetry, so that only the **11 centrosymmetric Laue classes** can be distinguished:

Crystal system	Laue class
triclinic	$\bar{1}$
Monoclinic	$1\ 2/m\ 1 = 2/m$
Orthorhombic	$2/m\ 2/m\ 2/m = m\ m\ m$
Tetragonal	$4/m$ $4/m\ 2/m\ 2/m = 4/m\ m\ m$
Trigonal	$\bar{3}$ $\bar{3}\ 2/m = \bar{3}\ m$
Hexagonal	$6/m$ $6/m\ 2/m\ 2/m = 6/m\ m\ m$
Cubic	$2/m\ \bar{3} = m\ \bar{3}$ $4/m\ \bar{3}\ 2/m = m\ \bar{3}\ m$

In three dimensions all possible combinations of the point symmetries of the **32 crystallographic point groups** with the lattice translations of the **14 Bravais lattices** lead to exactly **230 space groups**, all of infinite order. As already mentioned, the combination of point symmetry operations with translations results in new symmetry operations: screw rotations and glide reflections. The conventional graphical symbols for the three dimensional space group symmetry elements according to the International Tables for Crystallography Vol. A (ITA, 2002 [1]) are shown in figure 5a.9.

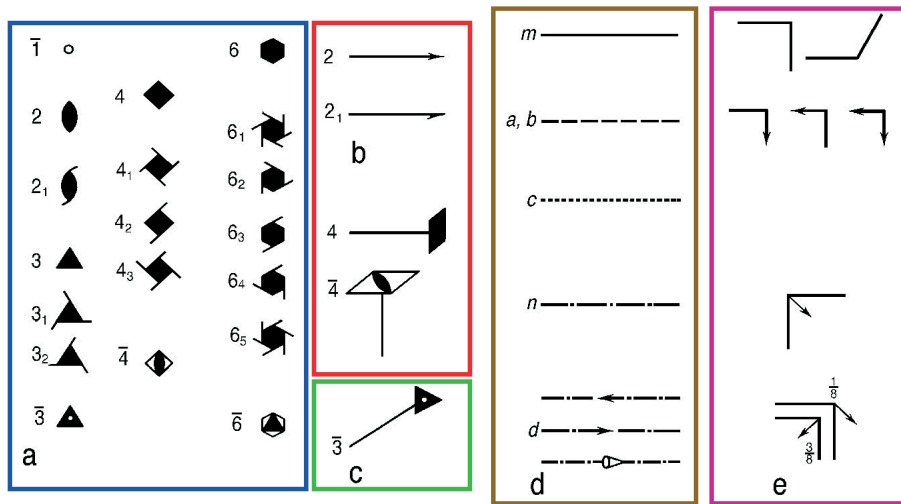


Fig. 5a.10: Conventional graphical symbols for symmetry elements: Left: axes (a) perpendicular, (b) parallel, and (c) inclined to the image plane; Right: planes: (d) perpendicular and (e) parallel to the image plane.

In the International Tables for Crystallography Vol. A [1] all space groups are described in detail with their Hermann-Mauguin symbols and corresponding crystal classes, the relative locations and orientations of the symmetry elements with respect to a chosen origin and the crystal-specific basis vectors, a listing of the general and all special positions (with their symmetrically equivalent points) and the related reflection conditions.

Side-note: It was the first institute director of the Institute of Crystallography, RWTH Aachen University, Prof. Theo Hahn, who served the International Union of Crystallography for 40 years as Chair of the Commission on *International Tables*, as editor of the *International Tables A* (five editions). The editions of the new *International Tables Volume A*, form a major part of his lifetime achievements.

5a.6 Example: crystal structure description of $\text{YBa}_2\text{Cu}_3\text{O}_{7-\delta}$

Crystal structure determination with atomic resolution is achieved by diffraction experiments with X-rays, electron or neutron radiation. As an example, the results of a structure analysis by neutron diffraction on a single crystal of the ceramic high- T_C superconductor $\text{YBa}_2\text{Cu}_3\text{O}_{7-\delta}$ with $T_C = 92$ K are presented. The atomic arrangement of the orthorhombic structure, space group Pmmm, and the temperature-dependent electrical resistivity is shown in figure 5a.10.

Information from ITA on the relative locations and orientations of the symmetry elements (symmetry operations $1, 2_z, 2_y, 2_x, \bar{1}, m_z, m_y, m_x$) of the orthorhombic space group Pmmm, together with the choice of the origin (in an inversion centre), is shown in figure 5a.11. The general position (site symmetry 1) of multiplicity 8 (symmetry produces 7 additional copies of this atom

in the unit cell) and all special positions with their site symmetries are listed in figure 5a.12. There are no special reflection conditions for this space group.

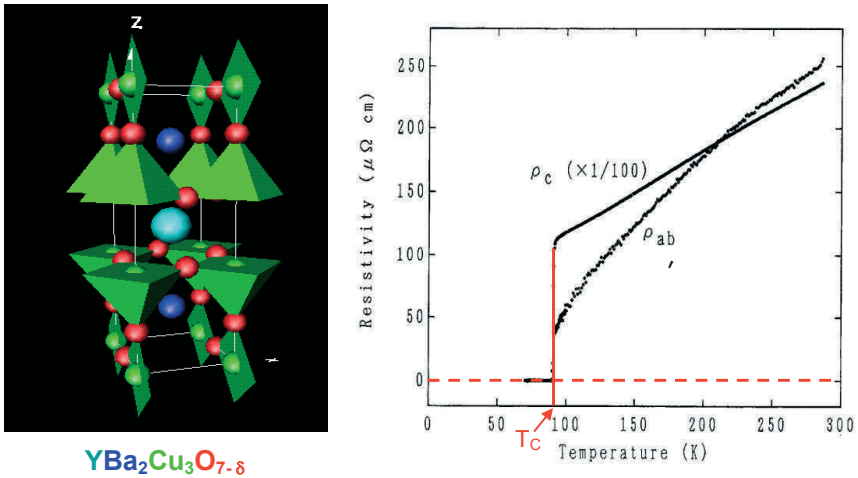


Fig. 5a.11: Unit cell of $YBa_2Cu_3O_{7-\delta}$ with CuO_x -polyhedra (left) and the electrical resistivity as a function of temperature \parallel and \perp to the $[001]$ direction (right).

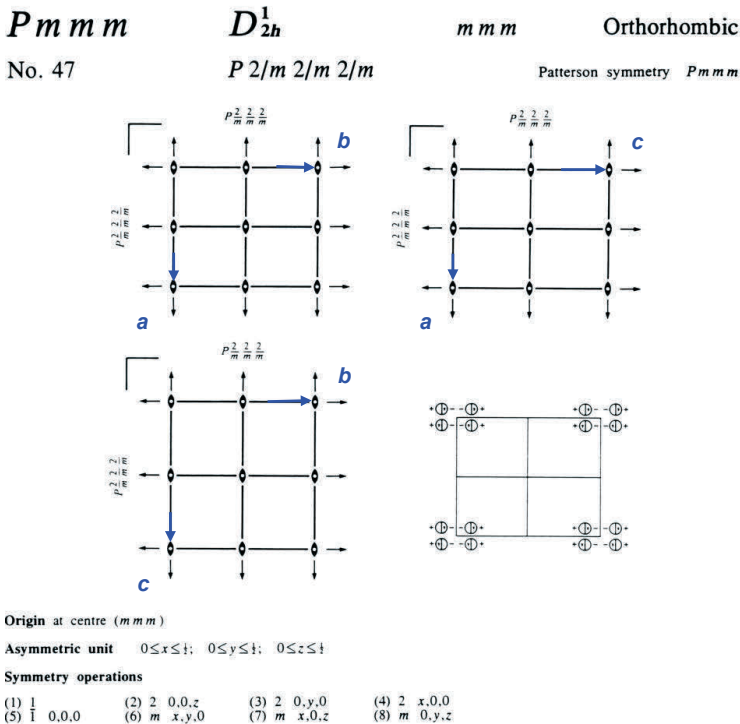


Fig. 5a.12: Description of the orthorhombic space group $P m m m$ in [1].

CONTINUED



No. 47

 Pmm Generators selected (1); $t(1,0,0)$; $t(0,1,0)$; $t(0,0,1)$; (2); (3); (5)

Positions

	Multiplicity	Wyckoff letter	Site symmetry	Coordinates	Reflection conditions		
8	α	1	(1) x, y, z (5) $\bar{x}, \bar{y}, \bar{z}$	(2) \bar{x}, \bar{y}, z (6) x, y, \bar{z}	(3) \bar{x}, y, \bar{z} (7) x, \bar{y}, z	(4) x, \bar{y}, \bar{z} (8) \bar{x}, y, z	General: no conditions Special: no extra conditions
4	z	$.m$	$x, y, \frac{1}{2}$	$\bar{x}, \bar{y}, \frac{1}{2}$	$\bar{x}, y, \frac{1}{2}$	$x, \bar{y}, \frac{1}{2}$	
4	y	$.m$	$x, y, 0$	$\bar{x}, \bar{y}, 0$	$\bar{x}, y, 0$	$x, \bar{y}, 0$	
4	x	$.m$	$x, \frac{1}{2}, z$	$\bar{x}, \frac{1}{2}, z$	$\bar{x}, \frac{1}{2}, \bar{z}$	$x, \frac{1}{2}, \bar{z}$	
4	w	$.m$	$x, 0, z$	$\bar{x}, 0, z$	$\bar{x}, 0, \bar{z}$	$x, 0, \bar{z}$	
4	v	$m..$	$\frac{1}{2}, y, z$	$\frac{1}{2}, \bar{y}, z$	$\frac{1}{2}, y, \bar{z}$	$\frac{1}{2}, \bar{y}, \bar{z}$	
4	u	$m..$	$0, y, z$	$0, \bar{y}, z$	$0, y, \bar{z}$	$0, \bar{y}, \bar{z}$	
2	t	$mm2$	$\frac{1}{2}, \frac{1}{2}, z$	$\frac{1}{2}, \frac{1}{2}, \bar{z}$			
2	s	$mm2$	$\frac{1}{2}, 0, z$	$\frac{1}{2}, 0, \bar{z}$			
2	r	$mm2$	$0, \frac{1}{2}, z$	$0, \frac{1}{2}, \bar{z}$			
2	q	$mm2$	$0, 0, z$	$0, 0, \bar{z}$			
2	p	$m2m$	$\frac{1}{2}, y, \frac{1}{2}$	$\frac{1}{2}, \bar{y}, \frac{1}{2}$			
2	o	$m2m$	$\frac{1}{2}, y, 0$	$\frac{1}{2}, \bar{y}, 0$			
2	n	$m2m$	$0, y, \frac{1}{2}$	$0, \bar{y}, \frac{1}{2}$			
2	m	$m2m$	$0, y, 0$	$0, \bar{y}, 0$			
2	l	$2mm$	$x, \frac{1}{2}, \frac{1}{2}$	$\bar{x}, \frac{1}{2}, \frac{1}{2}$			
2	k	$2mm$	$x, \frac{1}{2}, 0$	$\bar{x}, \frac{1}{2}, 0$			
2	j	$2mm$	$x, 0, \frac{1}{2}$	$\bar{x}, 0, \frac{1}{2}$			
2	i	$2mm$	$x, 0, 0$	$\bar{x}, 0, 0$			
1	h	mmm	$\frac{1}{2}, \frac{1}{2}, \frac{1}{2}$				
1	g	mmm	$0, \frac{1}{2}, \frac{1}{2}$				
1	f	mmm	$\frac{1}{2}, \frac{1}{2}, 0$				
1	e	mmm	$0, \frac{1}{2}, 0$				
1	d	mmm	$\frac{1}{2}, 0, \frac{1}{2}$				
1	c	mmm	$0, 0, \frac{1}{2}$				
1	b	mmm	$\frac{1}{2}, 0, 0$				
1	a	mmm	$0, 0, 0$				

Fig. 5a.13: General and special positions (coordinates of all symmetrically equivalent positions) of space group $Pmmm$ with their site symmetries and multiplicities as well as reflection conditions [1]. The special positions occupied in the $\text{YBa}_2\text{Cu}_3\text{O}_{7-\delta}$ -structure are indicated by frames.

The atomic parameters for $\text{YBa}_2\text{Cu}_3\text{O}_{6.96}$ obtained from the structure refinement of single crystal neutron diffraction data taken at room temperature [2] are given in the following Table:

Atomic positions of $\text{YBa}_2\text{Cu}_3\text{O}_{6.96}$					
orthorhombic, space group type P $2/m\ 2/m\ 2/m$					
$a = 3.858\ \text{\AA}$, $b = 3.846\ \text{\AA}$, $c = 11.680\ \text{\AA}$ (at room temperature)					
atom/ion	multiplicity	site symmetry	x	y	z
Cu1/Cu ²⁺	1	$2/m\ 2/m\ 2/m$	0	0	0
Cu2/Cu ²⁺	2	$m\ m\ 2$	0	0	0.35513(4)
Y/Y ³⁺	1	$2/m\ 2/m\ 2/m$	$\frac{1}{2}$	$\frac{1}{2}$	$\frac{1}{2}$
Ba/Ba ²⁺	2	$m\ m\ 2$	$\frac{1}{2}$	$\frac{1}{2}$	0.18420(6)
O1/O ²⁻	2	$m\ m\ 2$	0	0	0.15863(5)
O2/O ²⁻	2	$m\ m\ 2$	0	$\frac{1}{2}$	0.37831(2)
O3/O ²⁻	2	$m\ m\ 2$	$\frac{1}{2}$	0	0.37631(2)
O4/O ²⁻	1	$2/m\ 2/m\ 2/m$	0	$\frac{1}{2}$	0

References

- 1) *International Tables for Crystallography Vol. A, Space-group Symmetry*, edited by Th. Hahn, Dordrecht: Kluwer Academic Publishers (5. Edition, 2002)
- 2) *Crystallography: An Introduction*, Walter Borchardt-Ott, Springer Berlin Heidelberg (2011)
- 3) P. Schweiss, W. Reichardt, M. Braden, G. Collin, G. Heger, H. Claus, A. Erb, *Phys. Rev. B* **49**, 1387 – 1396 (1994)
- 4) G. Redhammer et al. *Phys. Chem. Min.* **37**, 311-332, (2010)
- 5) Interactive Structure factor and Ewald sphere tutorials: <http://www.ysbl.york.ac.uk/~cow-tan/>

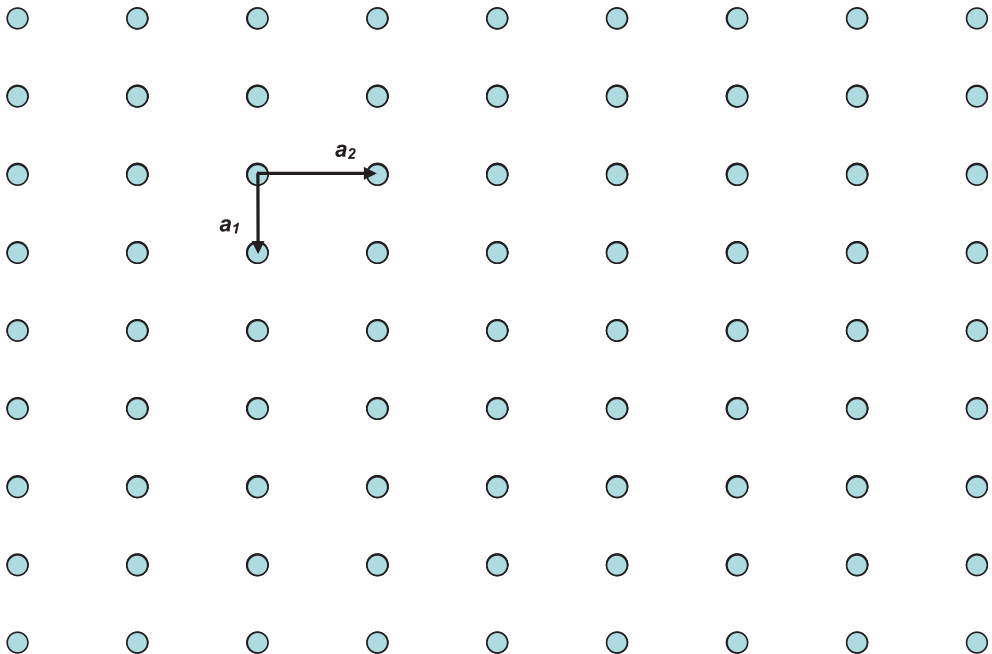
Exercises Crystallography

E5a.1 Lattice points, lattice directions and lattice planes

A projection of an orthorhombic lattice on the lattice plane (001) is given in the following figure (this means a projection parallel to the c -axis). The dots represent the lattice points (not atoms) according to the translational symmetry of a crystal with the general translation vector $\tau = ua + vb + wc$ (a , b , and c are the basis vectors of the unit cell and u , v , w being integers)

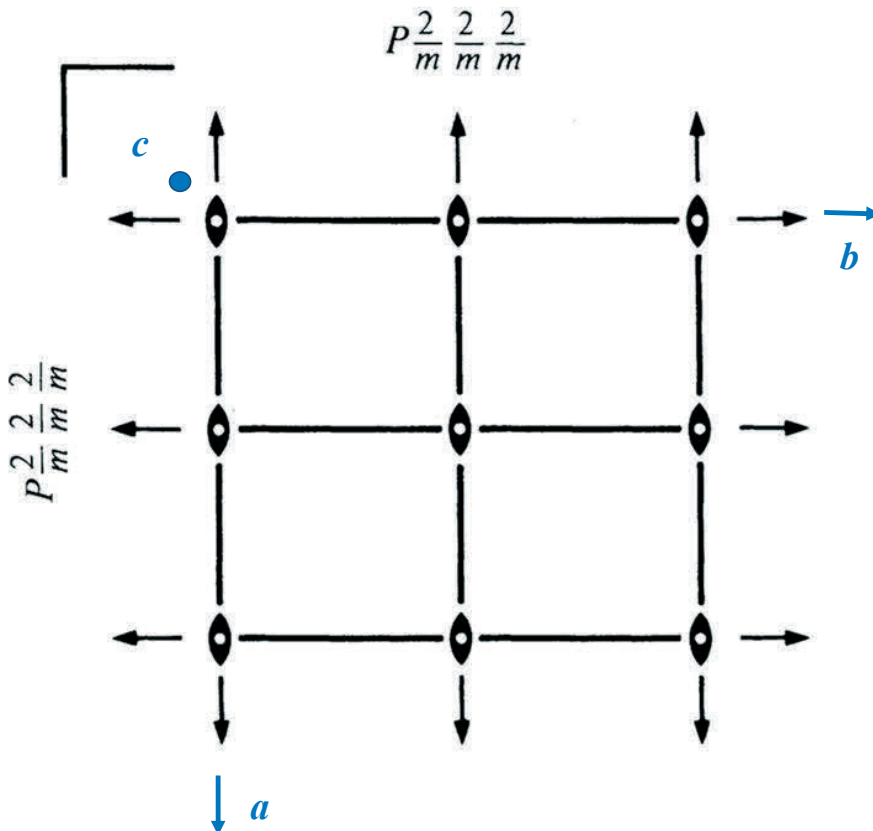
Please indicate in the figure

- The lattice points $uvw = 030$, $\bar{1}20$, $1\bar{2}0$, and 450 ,
- The lattice directions $[uvw] = [100]$, $[210]$, $[\bar{2}\bar{1}0]$ and $[\bar{2}50]$,
- The traces of the lattice planes $(hkl) = (100)$, (210) , (-210) , and (140) .



E5a.2 Crystal structure of $\text{YBa}_2\text{Cu}_3\text{O}_{7-\delta}$

The following figure reproduces the arrangement of the symmetry elements in the unit cell of $\text{YBa}_2\text{Cu}_3\text{O}_{7-\delta}$, see the upper left projection (of fig. 5a.12, taken from the international tables).



Make sure you understand the meaning of the symbols for the symmetry elements.
(see fig. 5a.10)

a) Draw the positions of all atoms (Y, Ba, Cu, O) into the above given projection.
(Take the coordinates from the table of the atomic positions given in the lecture book; mark the heights (z -coordinates) of the atoms along the projection direction by attaching the corresponding coordinates to the atoms.)

b) Given the space group $P2/m2/m2/m$: What is the crystal system (*refer to the conditions for the lattice parameters on page 4.17*) and the Bravais lattice type (*see the space group symbol*) of $\text{YBa}_2\text{Cu}_3\text{O}_{7-\delta}$?

c) How many formula units are in one unit cell of $\text{YBa}_2\text{Cu}_3\text{O}_{7-\delta}$? (*refer to fig. 4.10*)

d) Give the coordination numbers and describe the polyhedra of oxygen around atoms Cu1 and Cu2 (*refer, for simplicity, to fig. 5a.10*).

e) For all atoms: Check if the atom sits on an inversion centre (*either from the above plot or from fig. 5a.10 or from the table on page 4.17.*)

Cu1: Cu2: Y: Ba: O1: O2: O3: O4:

f) Calculate the interplanar spacings $d(hkl)$ (*choose the appropriate formula on page 4.6*) for the lattice planes (100), (200), (020), (002), (00-2).

g) List all symmetry equivalent lattice planes with identical d-spacing (*including all different orientation possibilities*) for the following types of lattice planes of $\text{YBa}_2\text{Cu}_3\text{O}_{7-\delta}$:

$(h00)$, $(00l)$, $(0kl)$, and (hkl)

Example for $(h0l)$ in the orthorhombic crystal system: $d(h0l) = d(\bar{h}0l) = d(\bar{h}0\bar{l}) = d(h0\bar{l})$.

h) How many symmetry-equivalent lattice planes result in each case? (*This is the multiplicity factor M of reflections needed as a correction factor in powder diffraction.*)

5b Structural Analysis

G. Roth
Institute of Crystallography
RWTH Aachen University

Contents

5b.1 Introduction.....	2
5b.2 Diffraction Contrast Variation	2
5b.3 The hydrogen problem in structural analysis	4
5b.4 Atomic coordinates and displacement parameters	7
5b.5 Magnetic structures from neutron diffraction	9
5b.6 Electron densities from x-rays and neutrons.....	12
5b.7 Magnetization densities from neutron diffraction	14
References	15
Exercises.....	16

5b.1 Introduction

The analysis of crystal structures and magnetic ordering is usually based on diffraction phenomena caused by the interaction of matter with x-rays, neutrons or electrons. Even though modern electron microscopy (HRTEM) can achieve atomic resolution, more detailed and quantitative information on the 3D atomic arrangement in crystals and on 3D magnetic structures and spin densities requires diffraction methods. In a more general nomenclature, diffraction is equivalent to coherent, elastic scattering. The basic theory of diffraction used for structural analysis (the so called kinematical theory) is similar for all types of radiation. Due to the different properties of x-rays, neutrons and electrons and their specific interaction with matter, complementary information is obtained from experiments with different types of radiation.

Considering only x-rays and thermal neutrons one finds that their wavelengths are similar ($0.5 \text{ \AA} < \lambda < 2.4 \text{ \AA}$) but they are scattered very differently by matter: While the electromagnetic x-radiation is scattered from the electrons and yields the total electron density distribution in the crystal, the nuclear scattering of neutrons is sensitive to the density distribution of the nuclei and the magnetic neutron scattering probes the magnetisation density of unpaired electrons.

x-ray diffraction using conventional laboratory equipment and/or synchrotron installations is the most frequently used method for structure analysis. Neutrons are, however, indispensable in a number of applications. The purpose of this chapter is to discuss a few typical examples of structural analysis, for which, instead of or complementary to x-rays, neutrons are required to solve structural problems.

5b.2 Diffraction Contrast Variation

A great advantage of neutrons over x-rays in the context of structural analysis is the very much different variation of the scattering length of atoms within the periodic system of the elements: The contrast in conventional x-ray diffraction is directly related to the ratio of the number of electrons Z_j of the different atoms or ions j involved. The atomic scattering factor f_j in the structure-factor formula, which represents the Fourier transform of the atomic electron density distribution, is proportional to Z_j ($f_j = Z_j$ for $\sin\theta/\lambda = 0$). Standard x-ray techniques can hardly differentiate between atoms/ions with a similar number of electrons (like Si and Al or Cr and Mn). Even if the atoms are fully ordered on different sites, x-ray diffraction just ‘sees’ the average structure.

For neutrons the atomic scattering factor f_j is replaced by the nuclear scattering length (or coherent scattering amplitude) b_j , which is of the same order of magnitude for all nuclei but varies from nucleus to nucleus in a non-systematic way. b_j values can be either positive or negative and depend on the isotopes and nuclear spin states of the element j (see previous chapters).

Crystal structure and site occupation of $(\text{Mn}_{1-x}\text{Cr}_x)_{1+\delta}\text{Sb}$.

As an example of contrast variation, the combination of x-ray and neutron diffraction information is demonstrated for the intermetallic compounds $(\text{Mn}_{1-x}\text{Cr}_x)_{1+\delta}\text{Sb}$, with $0 \leq x \leq 1$ [1]. This solid solution system is interesting for its magnetic properties: One end member of the solid solution series ($\text{Mn}_{1+\delta}\text{Sb}$) shows isotropic ferromagnetic behaviour while the other one ($\text{Cr}_{1+\delta}\text{Sb}$) is a uniaxial antiferromagnet. Intermediate compositions are characterized by competing magnetic interactions leading to a complex magnetic phase diagram. The crystal structure is closely related to the hexagonal NiAs-type structure (space group: $P6_3/mmc$) with some additional partial occupation (≤ 0.14) of the interstitial site 2(d) (see Fig. 5b.1):

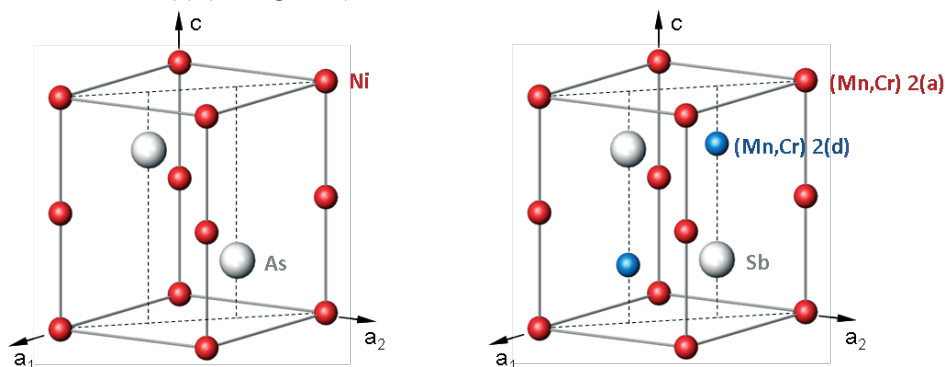
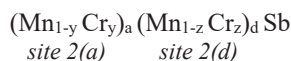


Fig. 5b.1: Left: NiAs structure, right: $(\text{Mn}_{1-x}\text{Cr}_x)_{1+\delta}\text{Sb}$ structure

Conventional x-ray diffraction can hardly differentiate between chromium ($Z_{\text{Cr}} = 24$) and manganese ($Z_{\text{Mn}} = 25$) but still yields information on the overall occupation probabilities by (Mn,Cr) for site 2(a) (denoted as a) and site 2(d) (denoted as d). The Sb position is assumed to be fully occupied, thus serving as an internal standard for the scattering power. The compound formula can now be reformulated site-specifically as:



corresponding to a chemical composition of $\text{Mn}_{[(1-y)a + (1-z)d]} \text{Cr}_{[ya + zd]} \text{Sb}$.

On the other hand, the nuclear scattering lengths of Cr and Mn for neutron diffraction are extremely different with $b_{\text{Cr}} = +3.52$ fm and $b_{\text{Mn}} = -3.73$ fm (see also chapter 4).

In the structure analysis of the neutron data, site-specific effective scattering lengths $b_{\text{eff}}(2a)$ and $b_{\text{eff}}(2d)$ are refined, which in turn are expressed as:

$$b_{\text{eff}}(2a) = a \cdot [(1-y) \cdot b_{\text{Mn}} + y \cdot b_{\text{Cr}}] \quad \text{and} \quad b_{\text{eff}}(2d) = d \cdot [(1-z) \cdot b_{\text{Mn}} + z \cdot b_{\text{Cr}}]$$

solving for the unknown parameters y and z gives:

$$y = [b_{\text{eff}}(2a)/a - b_{\text{Mn}}] / [b_{\text{Cr}} - b_{\text{Mn}}] \quad \text{and} \quad z = [b_{\text{eff}}(2d)/d - b_{\text{Mn}}] / [b_{\text{Cr}} - b_{\text{Mn}}].$$

The combination of the overall occupation probabilities a and d - from conventional x-ray studies - with the effective scattering lengths $b_{\text{eff}}(2a)$ and $b_{\text{eff}}(2d)$ determined in a

neutron diffraction experiment allows the evaluation of the Cr and Mn concentrations on the different sites 2(a) and 2(d).

It is evident, that the individual (Cr,Mn) distributions on the two crystallographically different sites 2(a) and 2(d) are not accessible merely by a chemical analysis. For most of the samples studied, the site 2(a) was found to be fully occupied: $a \approx 1.0$. But the formula $(\text{Mn}_{1-x}\text{Cr}_x)_{1+\delta}\text{Sb}$ used normally is only correct for the special case of equal Cr : Mn ratios on both sites:

$$x = y = z \quad \text{and} \quad 1 + \delta = a + d.$$

Note that, in general, a statistical occupation of one crystallographic site with three kinds of scatterers - e.g. Mn, Cr and "vacancies" - requires at least two independent experiments with sufficiently different relative scattering power of the atoms involved to determine the fractional occupancies.

The detailed information on the (Cr,Mn) distribution is needed to explain the magnetic properties of these intermetallic compounds, but we will not further elaborate on this.

5b.3 The hydrogen problem in structural analysis

The determination of the structural parameters (coordinates, displacement parameters) of hydrogen atoms in crystals is a special problem involving again the different properties of x-rays and neutrons. It is obvious that H or D atoms with $Z = 1$ give only a small contribution to the electron density and, therefore, they are hardly visible in x-ray structure analysis, particularly if heavy atoms are also present in the structure. However, there is an even more fundamental problem: The single electron of H or D is engaged in the chemical bonding and is by no means localised at the proton/deuteron position. Therefore, bond distances from x-ray diffraction involving hydrogen are notoriously wrong and any comparison with quantum mechanical calculations is quite hard to perform. This lack of sound experimental information is in sharp contrast to the importance of hydrogen bonding in solids, particularly in biological molecules like proteins, where hydrogen bonds govern to a large extent structures and functionalities of these 'bio-catalysts'. A combination with neutron diffraction experiments is important to determine the structural parameters of the H/D atoms properly. More generally, the structure analysis by neutron diffraction yields separately and independently from the x-ray data the structure parameters of all atoms including the mean square displacements due to static and dynamic (even anharmonic) effects.

H/D ordering in ferroelectric RbH_2PO_4 (RDP):

The hydrogen problem in crystal structure analysis is of special importance for structural phase transitions driven by proton ordering. KH_2PO_4 (KDP) is the most well-known representative of hydrogen-bonded ferroelectrics. Here, we discuss the isotypic RbH_2PO_4 (RDP). The crystal structure consists of a three-dimensional network of PO_4 -groups linked by strong hydrogen bonds (Fig. 5b.2).

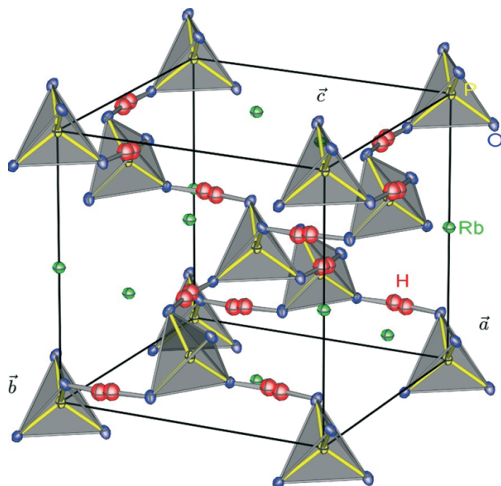


Fig. 5b.2: *Crystal structure of the paraelectric phase of RDP (RbH_2PO_4) with a split-model representation of the hydrogen disorder [3].*

In the paraelectric phase at room temperature KDP as well as RDP crystallise in the tetragonal space group $I\bar{4}2d$, where the H-atoms are dynamically disordered in symmetric $\text{O}\cdots\text{H}\cdots\text{O}$ bonds, which are almost linear with short O–O distances, typically in the range of 2.5 Å. The disordered H-distribution may be interpreted as corresponding to a double-well potential [2].

Figures 5b.3 and 5b.4 show the corresponding results for RDP, obtained from single crystal neutron diffraction [3].

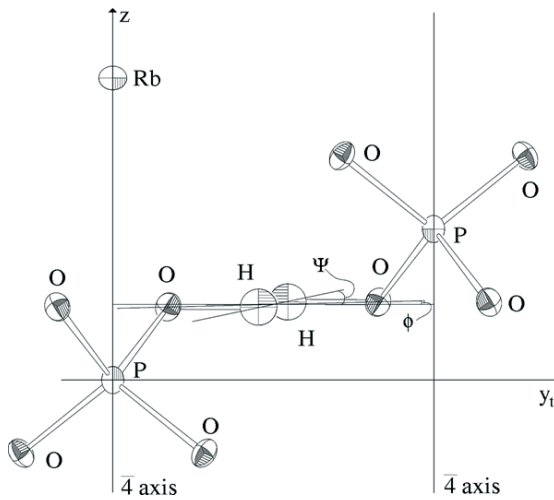


Fig. 5b.3: Local configuration of two PO_4 -tetrahedra in the paraelectric phase of RDP (RbH_2PO_4) at $T_c + 4$ K) linked by a strong, disordered hydrogen bond [3].

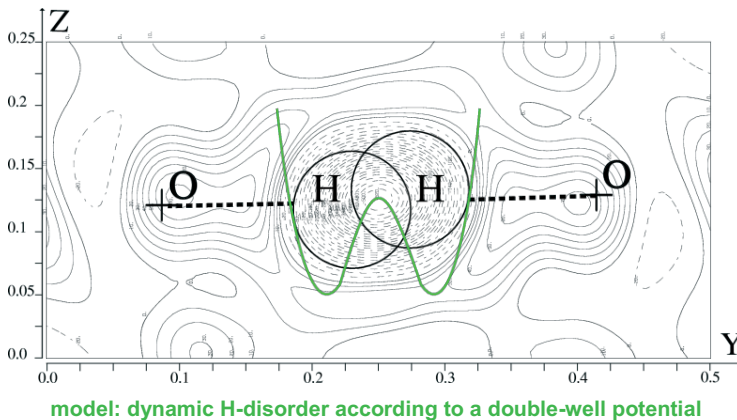


Fig. 5b.4: Difference-Fourier-plot of the negative proton density in the hydrogen bond of paraelectric RDP indicated by broken contour line [3]. The double-well potential model used to describe this density is inscribed in green.

The two very close hydrogen positions with 50% occupation probability are, of course, an artefact of the time-space averaging that is inherent to diffraction. In this case, the hydrogen disorder is assumed to be a dynamic hopping process between the two energetically degenerate sites.

At $T_c = 147$ K, RDP transforms to a ferroelectric phase of orthorhombic symmetry (space group: $Fdd2$) in which the protons order in short asymmetric $O-H \cdots O$ bonds (Fig. 5b.5). The PO_4 -tetrahedra show a characteristic deformation with two shorter and two longer P-O distances due to a transfer of electron density to the covalent O-H

bonds. The electrical dipole moments are oriented $\parallel z$ which give rise to a polarisation along the c -direction.

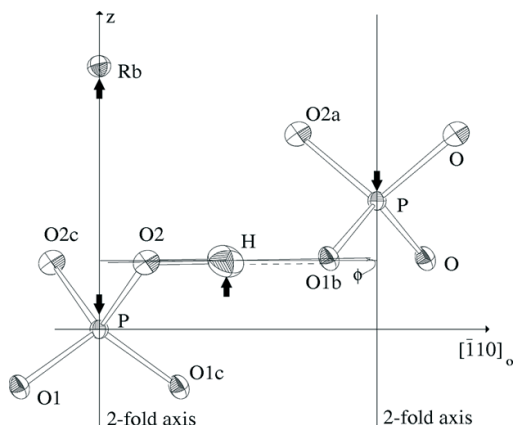


Fig. 5b.5: *Ferroelectric, hydrogen-ordered structure of RDP close to the phase transition at $T_C - 1$ K (major changes indicated by arrows, presentation as in Figure 5b.3) [3].*

The phase transition temperatures of KDP-type compounds change drastically when H is substituted by D. For $\text{K}(\text{H},\text{D})_2\text{PO}_4$, for instance, the para- to ferroelectric T_C changes from 122 K in the protonated to 229 K in the deuterated compound. This huge H/D-isotope effect proves that hydrogen-ordering and -dynamics is the major factor controlling this phase transition. Another type of H/D-isotope effect was found for $\text{Tl}(\text{H},\text{D})_2\text{PO}_4$ (TDP/DTDP) and $\text{Rb}(\text{H},\text{D})_2\text{PO}_4$ (RDP/DRDP), where a different polymorphism between the protonated and deuterated phases exists.

Clearly, the use of neutron diffraction is detrimental to a better understanding of these compounds and their interesting physical properties.

5b.4 Atomic coordinates and displacement parameters

As discussed above, neutron diffraction is very useful for obtaining precise atomic coordinates and displacement parameters. The improved accuracy (compared to x-rays) stems mainly from the absence of the form-factor fall-off. We will use measurements on Cobalt-olivine, Co_2SiO_4 , (crystal size $3 \times 2 \times 2$ mm) taken at the four-circle diffractometer HEiDi at the hot-neutron source of the FRM II reactor ($\lambda = 0.552 \text{ \AA}$) for demonstrating this advantage for the thermal displacements:

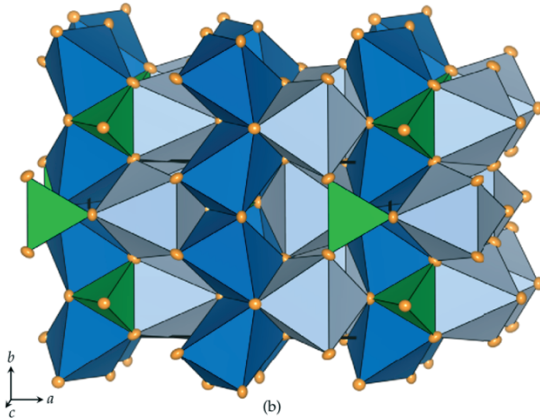


Fig. 5b.6: Structure of Co_2SiO_4 olivine at room temperature, projected along c . Green: SiO_4 -tetrahedra, Dark blue: $\text{Co}(1)\text{O}_6$ -octahedra, light blue: $\text{Co}(2)\text{O}_6$ -octahedra. Displacement ellipsoids are plotted at the 95% probability level (from [4]).

The olivine structure (fig. 5b.6) consists of chains of two types of edge-sharing CoO_6 -octahedra connected by SiO_4 -tetrahedra. A large data set with 1624 independent reflections up to $\sin \theta/\lambda = 1.05 \text{ \AA}^{-1}$ had been measured. The data were then successively cut off in shells of $\sin \theta/\lambda$ and the resulting partial data sets were used to analyse the displacement parameters. Figure 5b.7 shows two interesting observations: First of all, the precision improves significantly with increasing $(\sin \theta/\lambda)_{\text{max}}$, as is evident from the decreasing size of the error bars. In the x-ray case, high angle reflections are usually very weak and their measurement does often not lead to improved precision. Secondly, there is a systematic change of the displacement values themselves, resulting from systematic errors that vary with $(\sin \theta/\lambda)_{\text{max}}$.

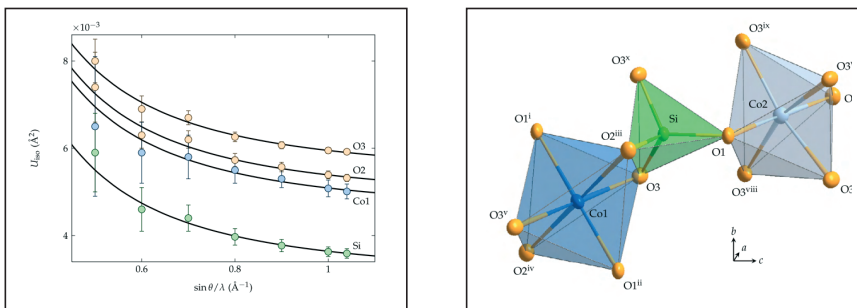


Fig. 5b.7: Left: Statistical (error bars) and systematic errors of isotropic displacements parameters in Co_2SiO_4 as a function of measured $\sin \theta/\lambda$ range from single-crystal neutron diffraction data at room temperature [4]. Right: Clinographic view of the CoO_6 and SiO_4 polyhedra in Co_2SiO_4 at room temperature [4].

High d_{hkl} -value resolution data from neutron diffraction is also useful to derive precise temperature dependent displacement parameters (fig. 5b.8):

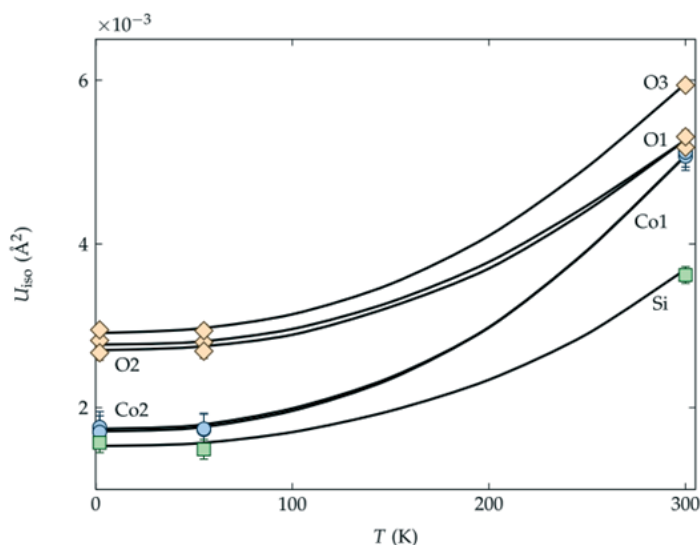


Fig. 5b.8: Temperature dependence of the isotropic displacement parameters of Co_2SiO_4 [4].

Just as in the case of high quality single crystal x-ray diffraction data, anisotropic displacement parameters can be determined as well. In addition to that, the quality of single crystal neutron data also often allows refining anharmonic displacement parameters. Anharmonic oscillations of atoms in crystals occur if the atoms are vibrating in a non-parabolic potential well. In such cases, the harmonic approximation, which is the basis of the description of thermal displacements by the Debye-Waller factor, fails. Analysis of the anharmonic displacements allows to reconstruct the non-parabolic potential at the site of the vibrating atom.

5b.5 Magnetic structures from neutron diffraction

Cobalt-Olivine, Co_2SiO_4 , orders magnetically below about 50 K. The magnetic moments of the Co^{2+} -ions turn from a paramagnetic phase with no long range order of the magnetic moments into an antiferromagnetically ordered arrangement. We use Co_2SiO_4 again to briefly demonstrate the application of neutron diffraction to the structural analysis of magnetic structures. This time, a powder neutron diffraction experiment has been performed at the diffractometer D20 (ILL, France) in its high-resolution mode, at temperatures between 70K and 5K, with a neutron wavelength of $\lambda = 1.87 \text{ \AA}$ and approximately 2 g of powdered Co_2SiO_4 [4].

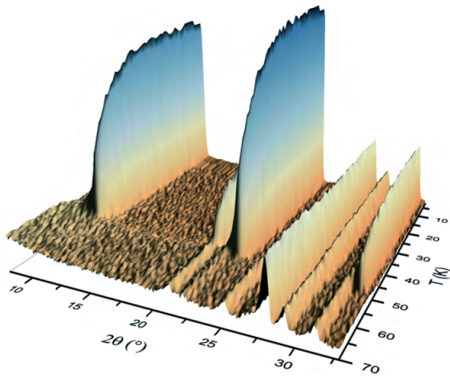


Fig. 5b.9: Thermal evolution of the neutron powder diffraction pattern (low angle part) of Co_2SiO_4 [4].

At about 50 K, new magnetic reflections (001), (100), (110), (300) etc. appear (fig. 5b.9). The nuclear reflections don't change much at the magnetic phase transition. The new reflections can be indexed with the same unit cell as the nuclear reflections, but they were forbidden in the paramagnetic phase with space group $Pnma$. Obviously, the symmetry has changed at the magnetic ordering transition. The task is then - just as in 'ordinary' structure determination - to find a structural model (that is: magnetic moments and their orientation on the magnetic ions, here Co^{2+}) that fits the observed positions and intensities of the magnetic Bragg peaks. Magnetic structure determination is outside the scope of this chapter, but assumed such a model has been constructed, it can be refined - in the case of powder data by the Rietveld method (fig. 5b.10).

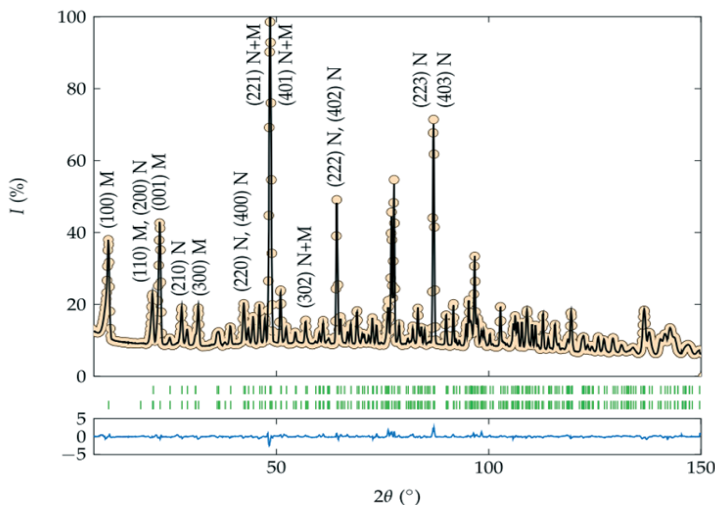


Fig. 5b.10: Neutron powder diffraction pattern (dots), Rietveld fit (black line) and allowed Bragg reflections (green marks) at 5 K of Co_2SiO_4 [4].

The lower trace (blue) is the difference $I_{obs} - I_{calc}$ on the same scale. The upper row of the green marks shows Bragg reflections corresponding to the nuclear phase and the lower row represents the allowed positions of the magnetic peaks. Some of the Bragg peaks are indexed. ‘N’ and ‘M’ denote the nuclear and magnetic contributions, respectively [4]. Note that the magnetic Bragg peaks are only visible at low diffraction angles.

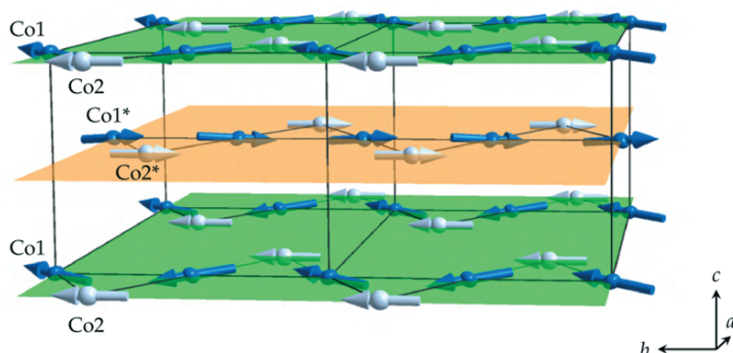


Fig. 5b.11: Graphical representation of the magnetic structure of Co_2SiO_4 below 50 K. The non-magnetic atoms (Si and O) are excluded for simplicity. The figure shows the zigzag chains of Co(1) and Co(2) in layers perpendicular to the c axis [4].

From the Rietveld refinements, one can derive the exact spin orientation (fig. 5b.11) as well as parameters describing quantitatively the magnetic moments on the two symmetrically non-equivalent Co^{2+} -sites (see table below). However, magnetic neutron diffraction from single crystals often gives additional and more accurate information:

	Co1 (0,0,0)	Co2 ($x,1/4,z$)
M_x (μ_B)	1.18 ± 0.05	—
M_y (μ_B)	3.61 ± 0.04	3.37 ± 0.04
M_z (μ_B)	0.66 ± 0.18	—
M (μ_B)	3.86 ± 0.05	3.37 ± 0.04
ϕ ($^\circ$)	71.9 ± 0.7	90
θ ($^\circ$)	80.2 ± 2.7	90

$\chi^2 = 2.23$, $R[F^2 > 2\sigma(F^2)] = 0.033$, $wR(F^2) = 0.044$.

The table shows cartesian (M_x , M_y and M_z) and spherical (M , ϕ and θ) components of the Co1 and Co2 magnetic moments according to the single-crystal neutron diffraction data at 2.5 K. The directions of the magnetic moments for other cobalt ions in the unit cell can be obtained by applying the symmetry operations of the magnetic space group (Schubnikov group) Pnma .

5b.6 Electron densities from x-rays and neutrons

Another advanced application of neutron diffraction in structural analysis is the determination of 3-dimensional high resolution maps of the electron density in the unit cell to study, for instance, details of the chemical bonding. The most involved method of electron density studies (called x-N-synthesis) uses a combination of high quality single crystal neutron and x-ray diffraction experiments. In the present case, a single crystal of Co_2SiO_4 with dimensions $3 \times 2 \times 2$ mm, was measured on the four-circle diffractometer HEiDi at the hot-neutron source of the FRM II reactor (Garching) at $\lambda = 0.552 \text{ \AA}$, the single crystal x-ray (synchrotron) experiment was performed on Diffractometer D3 at the synchrotron facility HASYLAB/DESY (Hamburg) with a Co_2SiO_4 -sphere, diameter $150 \mu\text{m}$ as the sample and an x-ray wavelength of $\lambda = 0.5 \text{ \AA}$.

The next step is to take the x-ray-data, do a Fourier-transform (Fourier-synthesis) to obtain the electron density map:

$$\rho(\mathbf{r}) = 1/V \cdot \sum_{\tau} F(\tau) \cdot \exp[2\pi i(\tau \mathbf{r})], \quad \text{with } F(\tau) = |F(\tau)| \cdot \exp[i\varphi(\tau)].$$

The phases $\varphi(\tau)$ are calculated from the atomic model (structure factor equation, see ch. 4), the moduli $|F(\tau)|$ are taken from the measured x-ray intensities. The result is a 3-dimensional map of the total electron density $\rho(\mathbf{r})$ within the unit cell:

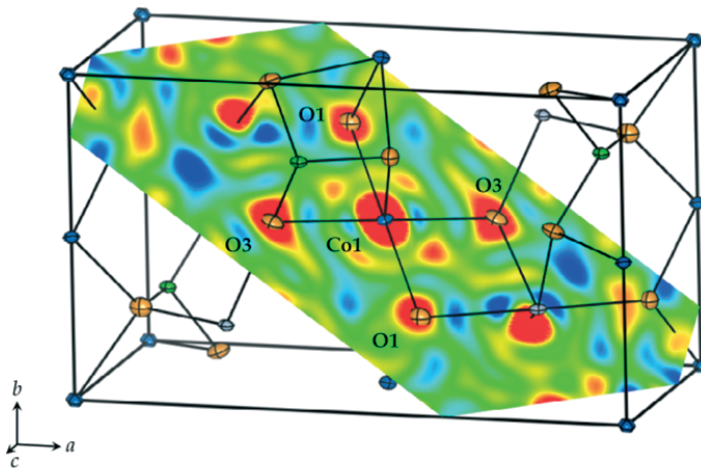


Fig. 5b.12: Electron density distribution $\rho(\mathbf{r})$ of Co_2SiO_4 at 12 K from Fourier synthesis of x-ray data. Contours range from -8 e/\AA^3 (blue) to 10 e/\AA^3 (red). A plane which intersects the Co1O_6 octahedron and contains the Co1, O1 and O3 atoms is shown together with a sketch of the crystal structure [4].

In favourable cases, such a map already shows interesting features of the (anisotropic) bonding electron density, however, the information content of the map can be very significantly improved by taking the coordinates and displacement parameters from the more accurate neutron diffraction experiment (see above for the reasons) and calculate, in a second step, the so called deformation density. This is done by subtracting from the total electron density $\rho(\mathbf{r})$ the density $\rho(\mathbf{r})_{\text{spherical}}$ corresponding to a superposition of spherical atoms at the nuclear positions. More specifically: atomic positions x_j, y_j, z_j and thermal displacements T_j of atoms j derived from the neutron experiment, ‘decorated’ with the calculated spherical single atom electron densities.

$\rho(\mathbf{r})_{\text{deform}} = \rho(\mathbf{r}) - \sum \rho(\mathbf{r})_{\text{spherical}}$, where the sum runs over all atoms in the unit cell.

$\rho(\mathbf{r})_{\text{spherical}}$ corresponds to the expectation value of the electron density within the unit cell without any effects which are due to chemical bonding. The deformation density then represents the deformation of the charge distribution as a result of the formation of chemical bonds. Figure 5b.13 shows such a deformation density map for Co_2SiO_4 . In favourable cases, the electron density in the hybridized bonding orbitals (in this case of Co3d- and O2p character) can be directly observed.

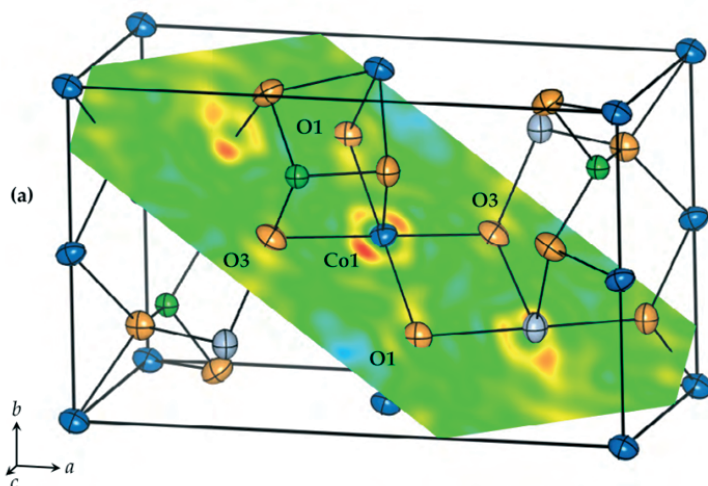


Fig. 5b.13: Deformation density from the x - N -difference Fourier map of Co_2SiO_4 at 300 K: Section through the O1–Co1–O3 plane. The difference density varies from $-1.25 \text{ e}/\text{\AA}^3$ (blue) to $1.15 \text{ e}/\text{\AA}^3$ (red) [4].

5b.7 Magnetization densities from neutron diffraction

As a final example for the application of neutron diffraction in structural analysis, we briefly sketch how a 3-dimensional map of the magnetization density, that is: the density of magnetic moments (spin- as well as orbital-moments) within the unit cell can be determined. These maps are sometimes lucidly called ‘spin density maps’, but in systems with non-vanishing orbital moments, the term magnetization density is really the correct one.

The experiment is performed by polarized neutron diffraction on a single crystal using the flipping ratio method. For details on the experimental method see the chapter on magnetic scattering. The flipping ratio method allows to separate nuclear and magnetic contributions to the diffracted intensities. It is performed *above* the magnetic phase transition in the paramagnetic state (in the case of Co_2SiO_4 above $T_N=50\text{K}$) and the sample is in a strong external magnetic field (here: 7 T). 207 Bragg reflection flipping ratios were measured at diffractometer 5C1 of the ORPHÉE reactor (Laboratory Léon Brillouin, CEA Saclay, France) for Co_2SiO_4 at 70K up to $\sin \theta/\lambda \approx 0.62 \text{ \AA}^{-1}$ at a neutron wavelength of $\lambda = 0.845 \text{ \AA}$. Given the flipping ratios and the nuclear structure factors, the magnetic structure factors can be calculated which are then Fourier transformed to give the spatially resolved magnetization density shown in figure 5b.14 in a section through the unit cell of Co_2SiO_4 .

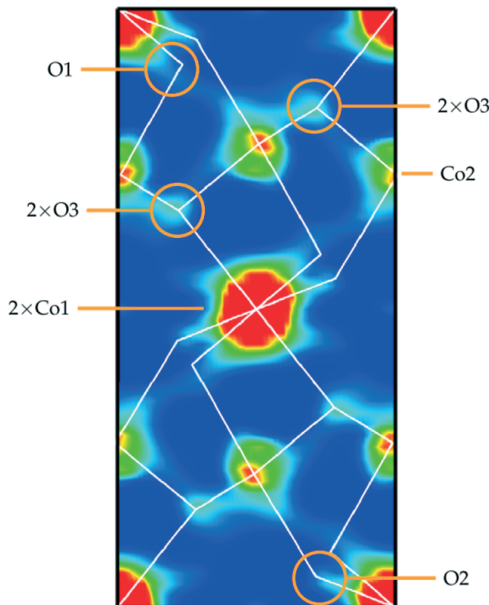


Fig. 5b.14: Reconstruction of the density (projected along the b axis) corresponding to the observed magnetization distribution of Co_2SiO_4 at 70 K with contours ranging from $0 \mu_B/\text{\AA}^3$ (blue) to $2 \mu_B/\text{\AA}^3$ (red) [4].

Among the interesting features of this map is the observation of magnetization density on the, nominally non-magnetic, oxygen atoms coordinating the Co^{2+} -ions. These ‘transferred moments’ are direct experimental evidence for the hybridization of the oxygen 2p- with Co-3d-orbitals which is not only responsible for covalent bonding but also for the magnetic exchange interaction along the Co-O-Co-bond network.

References

- [1] W. Reimers, E. Hellner, W. Treutmann and G. Heger, *J. Phys. C: Solid State Phys.* **15**, 3597 (1982).
- [2] R. J. Nelmes, W. F. Kuhs, C. J. Howard, J. E. Tibballs and T. W. Ryan, *J. Phys. C: Solid State Phys.* **18**, L711 (1985).
- [3] S. Mattauch, G. Heger, and K. H. Michel, *Cryst. Res. Technol.* **39**, 1027 (2004)
- [4] A. Sazonov, Ph.D.-thesis, RWTH Aachen (2009)
A. Sazonov et al., *Acta Cryst.* **B65**, 664-675 (2009).

Exercises

E5b.1 Displacement Parameters

The Debye-Waller-factor $T_j(\tau)$ enters the structure factor formula as the exponential factor $\exp [B \cdot (\sin^2\theta/\lambda^2)]$.

- a) Discuss the physical origin of this factor.
- b) Describe the overall effect of this displacement factor on the diffracted intensities.
- c) It is generally said, that neutron diffraction yields much more precise displacement parameters than x-ray diffraction. Is that statement correct? If so: Why?
- d) What are anisotropic displacement parameters and how can they be visualized?
- e) Is it correct, that all atoms in cubic crystals have to vibrate isotropically? (*Yes/No, Why?*)
- f) Discuss the non-zero values of the displacements parameters in fig.5b.8 for $T \Rightarrow 0$ K: (*Is it real? An artefact? Why?*)

E5b.2 Diffraction contrast & site occupancies

- a) Assume you have grown a compound containing both Pb and Bi. Which kind of diffraction experiment is better suited to distinguish Pb and Bi: X-ray or neutron? Why?

Check <http://webster.ncnr.nist.gov/resources/n-lengths/> for the coherent neutron scattering lengths and use your knowledge of the PSE for the x-ray scattering lengths.

- b) Assumed Bi and Pb sit on the same site in your structure and this site is also supposed to contain vacancies. Is one diffraction experiment sufficient to uniquely determine the occupation probabilities? (*Yes/No, Why?*)

E5b.3 Choice of neutron wavelengths

- a) Magnetic neutron diffraction experiments are usually done with rather long wavelengths (*see chapter 8.7: $\lambda = 1.87 \text{ \AA}$*): Why?
- b) Diffraction experiments aiming at obtaining precise atomic coordinates and displacements are done with much shorter wavelengths (*see chapter 8.8: $\lambda = 0.552 \text{ \AA}$*): Why?
- c) Powder diffraction experiments usually use longer wavelengths than single crystal experiments: Why?

Discuss this issue in terms of the competition between angular resolution (separation of reflections) and direct space resolution (separation of atoms).

E5b.4 Hydrogen bonded crystals

Assume you have grown a new hydrogen-bonded compound in the form of a single crystal and you want to know how the hydrogen bonds are arranged within the structure.

- a) Collect arguments Pro & Con the usage of a single crystal x-ray- vs. single crystal neutron diffraction experiment to study your new crystal.

Consider, for instance, factors like: Availability / costs of the experiment; time and effort required to get beam time; required size of the crystal; scattering power of hydrogen; expected precision of the H- position; absorption & incoherent scattering; additional effort needed for deuteration etc.

E5b.5 Density maps from diffraction experiments

- a) How can one obtain (from diffraction) the bonding electron density map? (*discuss briefly the experiment(s), the necessary calculations and the information obtained*)
- b) Discuss the difference between the bonding electron density map and a magnetization density map. (*kind of data used, specific information the experiment will yield?*)

6 Small-Angle Neutron Scattering – SANS

Sebastian Jaksch

Jülich Centre for Neutron Science 1

Forschungszentrum Jülich GmbH

Contents

6.1	Introduction	3
6.1.1	General concept	3
6.2	SAXS instruments	5
6.2.1	Laboratory SAXS setup	6
6.2.2	Synchrotron SAXS setups	7
6.3	SANS setups	9
6.4	Indirect space and Small-Angle Scattering	11
6.5	Resolution limits	12
6.6	Fourier Transform and Phase Problem	12
6.7	Scattering Efficiency	14
6.7.1	Scattering with x-rays	14
6.7.2	Scattering with neutrons	15
6.7.3	Scattering Cross Section and Contrast Matching	18
6.8	Form factors	20
6.8.1	Sphere	22
6.8.2	Thin Rod	24
6.8.3	Circular Disc	24
6.8.4	Non-particulate scattering from a flexible chain	24

6.8.5 Polydispersity	25
6.9 Structure Factors	25
6.9.1 Hard Sphere Structure Factor	26
6.10 Reading a curve	28
6.10.1 Forward scattering	28
6.10.2 Guinier regime	29
6.10.3 Debye regime	30
6.10.4 Porod regime	30
6.10.5 Estimation of particle and feature Size	31
6.11 Further Reading	31
6.11.1 A. Guinier: X-ray diffraction in crystals, imperfect crystals, and amorphous bodies	31
6.11.2 R.J. Roe: Methods of x-ray and neutron scattering in polymer science	31
6.11.3 G. Strobl: The physics of polymers	32
References	33
Exercises	34

6.1 Introduction

Small-Angle Scattering (SAS) investigates structures in samples that generally range from approximately 0.5 nm to a few 100 nm. This can both be done for isotropic samples such as blends and liquids, as well as anisotropic samples such as quasi-crystals. In order to obtain data about that size regime scattered intensity, mostly of x-rays or neutrons, is investigated at angles from close to zero, still in the region of the primary beam up to 10° , depending on the wavelength of the incoming radiation.

The two primary sources for SAS experiments are x-ray (small-angle x-ray scattering, SAXS) sources and neutron (small-angle neutron scattering, SANS) sources, which shall be the two cases discussed here. Also scattering with electrons or other particle waves is possible, but not the main use case for the purpose of this manuscript.

For most small-angle scattering instruments, both SAXS and SANS, the science case covers the investigation of self-assembled polymeric and biological systems, multi-scale systems with large size distribution of the contained particles, solutions of (nano-)particles and soft-matter systems, protein solutions, and material science investigations. In the case of SANS this is augmented by the possibility to also investigate the spin state of the sample and hence perform investigations of the magnetic structure of the sample.

In the following sections the general setup of both SAXS and SANS instruments shall be discussed, as well as data acquisition and evaluation and preparation of the sample and the experiment in general. The information contained herein should provide sufficient information for planning and performing a SAS experiment and evaluate the gathered data.

6.1.1 General concept

All SAS experiments, irrespective of the setup used in any specific case, rely on the concept of pinhole cameras to work. Fig.6.1 illustrates the geometric concept of the interplay between pinhole cameras and SAS.

In the usual case, pinhole cameras map every point of the sample (object) to a discrete point on the screen (film or detector). The smaller the hole, the better the point-to-point mapping works, since in the ideal case only a single path between object and image is available. However, this of course comes with a penalty in intensity, since the smaller hole lets less light pass through. Due to the geometry, an image taken with a pinhole camera is always upside down. While the mathematical implications shall be discussed later on in this manuscript at this point we only want to grasp the underlying concept. The information about the object is at the beginning stored in real space. Colors (wavelength) and locations are given as points on the surface of the object. When all beams have converged to the single point that is ideally the pinhole, the information is then encoded in direction of the path (or light-beam) and the wavelength of the light. This is the change between direct and indirect space, locations and directions. When the light falls onto the screen the information is reversed again, to location and color of a spot on the screen, into direct space.

This concept is exploited by SAS. Since we are looking at very small objects (molecules and atoms) the determination of the location with the naked eye, or even a microscope, and

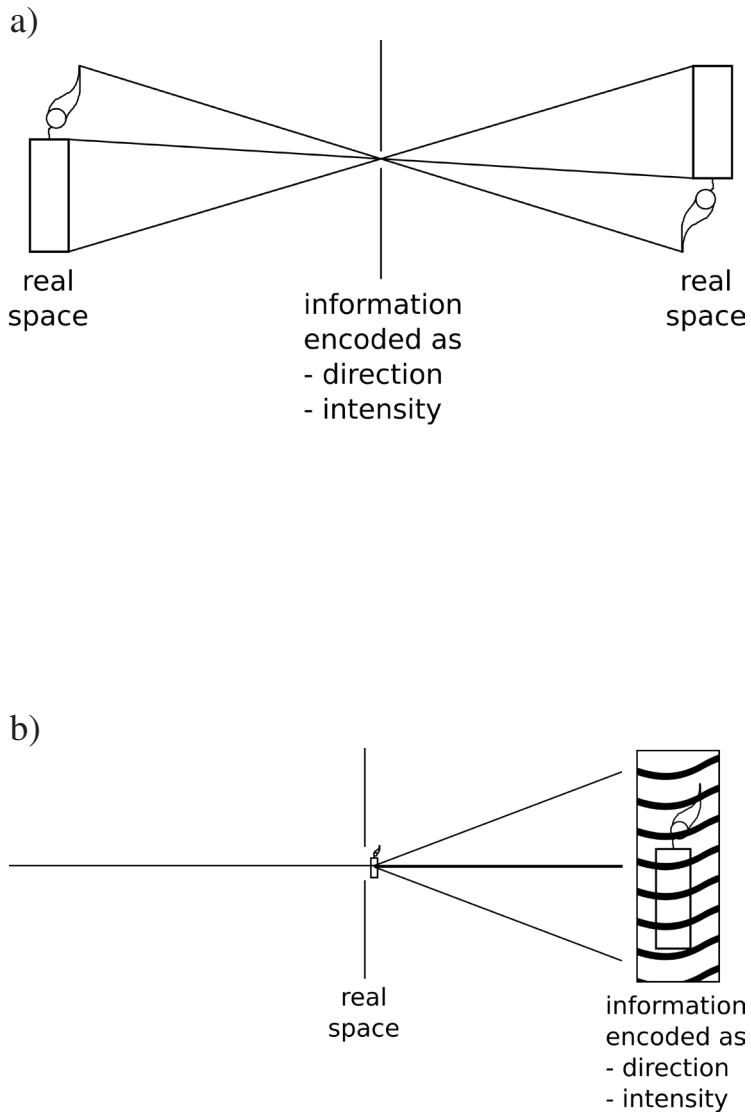


Fig. 6.1: a) Sketch of a pinhole camera and b) a simplified SAS instrument. The encoding of the real space information is in one case done inside the pinhole, in the other case the direction (and wavelength) encoded information is directly displayed on the screen (shaded area with waves). Positioning of the screen farther away improves the angular resolution and therefore the encoded information.

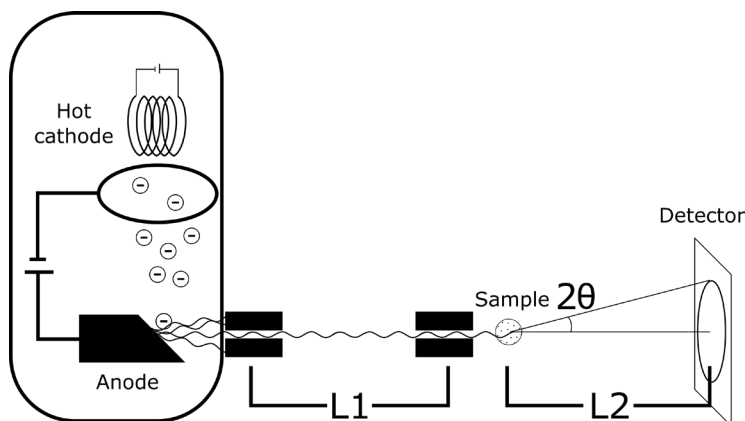


Fig. 6.2: *Laboratory SAXS setup. The left box is a sketch of a x-ray tube, all the components are in vacuum. The flight path is also usually evacuated. L1 and L2 are the collimation and sample detector distance (SDD) respectively. In the case of laboratory setup those range usually from about 20 cm up to 1-2 m in modern setups. The collimation blocks for L1 and L2 are usually set up in both x and y direction to constrict the flight path, widely used openings are around 1 mm×1 mm or below. In some setups, also a slit collimation instead of a point collimation is realized to increase the intensity.*

encoding of direction is easily achievable by increasing the distances and adjusting the size of the pinhole. However, instead of using the information that has been transferred to real space again, this time the object in real space is put close to the window. This way, the information about the location of atoms and molecules in the sample is encoded into direction or indirect space. Since there should be no information about the light before the pinhole, the light needs to be collimated down to a small, point-like source with no angular divergence.

6.2 SAXS instruments

In general there are two classes of SAXS instruments. One is the laboratory type setup that can be set-up in a single laboratory with a conventional x-ray tube, or more general any metal anode setup, while the other one is a large-scale facility setup at a synchrotron that can provide higher intensities. Since the setup of both instruments differs, and also the use case is not fully identical, we shall discuss both setups separately. One thing that should be kept in mind is that the fundamental principle is identical, i.e. any experiment that can be performed at a synchrotron can also in principle be performed at a laboratory SAXS setup and is only limited in intensity. This is important for the preparation of beamtimes at a synchrotron, which in general should be thoroughly prepared in order to fully exploit all capabilities offered there.

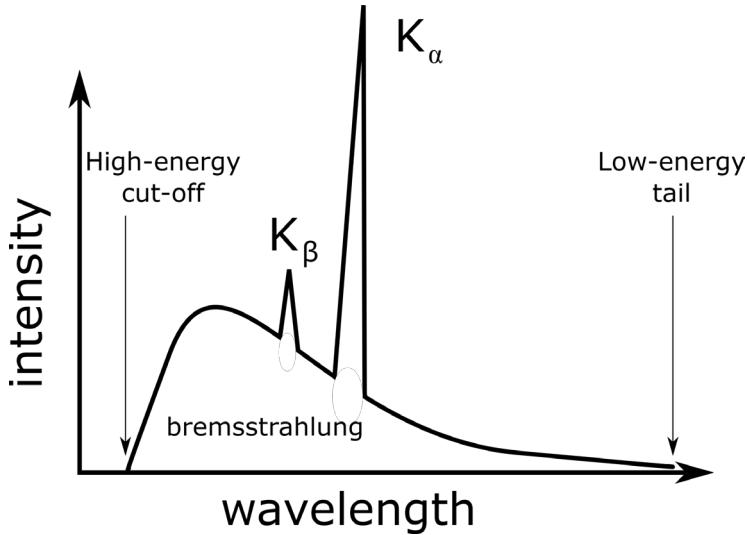


Fig. 6.3: Characteristic x-ray spectrum from a metal anode x-ray tube. The high-energy cut-off wavelength is given for the case that a single electron, fully accelerated by the voltage in the x-ray tube, deposits all its kinetic energy in a single photon. In an optimal setup this distribution is very narrow. Then the K_α line fully dominates the spectrum and gives a clean wavelength to perform a SAXS instrument.

6.2.1 Laboratory SAXS setup

Over the years a wide range of specialized SAXS instruments has become commercially available. The oldest concepts date back to the early 20th century, right after the discovery of x-rays. [1] Most of them offer specific advantages in certain use cases, such as the measurement of isotropic samples in a Kratky Camera [2], or highly adaptable sample environments. Here we shall only concentrate on the basic principle of operation. A general sketch of a SAXS instrument is shown in Fig.6.2. The x-rays are produced in an x-ray tube and then collimated by a set of slits. Here the collimation as such is already sufficient to obtain a coherent beam, since most of the intensity of standard x-ray tubes (and essentially all metal target x-ray sources) is concentrated into the characteristic spectral lines of the target material (see Fig.6.3). Common materials for the target anode are copper and molybdenum, delivering wavelengths of the most intensive K_α lines of 1.54 \AA and 0.71 \AA respectively. Under the assumption of a usual characteristic spectrum for the anode material the x-ray tubes can be considered monochromatic sources.

In order to achieve spatial as well as wavelength coherence most x-ray tubes work with a focused beam that is as small as technically feasible. This allows very narrow collimation slits, since it is not improving the coherence, and therefore the signal-to-noise ratio, to narrow the slit further than the initial beam spot or the pixel size of the detector, whichever be smaller. This however leads to a very high energy density, why some x-ray tube designs forgo a solid anode all together and either opt for a rotating anode, where the energy of the beam spot is distributed over a larger surface or a metal-jet anode, where the material is

Parameter	value
SDD	0.8-4 m
Pixel resolution	$172 \times 172 \mu\text{m}$
Flux	10^7 photons s^{-1}
wavelength λ	1.35 \AA
Q-range	$4 \cdot 10^{-3} - 8 \cdot 10^{-1} \text{ \AA}^{-1}$

Table 6.1: Performance parameters for state of the art laboratory SAXS setups, in this case with a liquid metal jet anode at the GALAXI instrument. [3]

refluxed and can therefore not heat up beyond the point of deformation and therefore also defocussing of the beam.

Some performance figures of current laboratory SAXS setups are given in Tab.6.1. It is worth noting that with the last generation of metal-jet anode setups even laboratory setups can achieve intensities comparable to what was achievable one or two decades ago at a world-class synchrotron. While this of course allows for faster measurements and smaller beam, it also means that beam damage to the sample has to be taken into account.

6.2.2 Synchrotron SAXS setups

While the setup in general is similar to that of a laboratory setup there are some key differences between a synchrotron and a laboratory SAXS setup. Most of the differences are based on radio protection needs and are therefore immaterial to this description in terms of the SAXS measurement itself. The other main difference is in the production of the x-rays itself. Current setups at synchrotrons use undulators in order to periodically accelerate charged particles (usually electrons/positrons) perpendicular to the direction of propagation of the particle beam. This creates a very brilliant, nearly perfectly monochromatic x-ray beam along the direction of the electron beam. The monochromaticity can further be improved by a monochromator crystal. Fig.6.4 shows an example of a synchrotron SAXS setup. After that, the collimation is very similar to that of a laboratory SAXS setup, only the materials are chosen to be thicker in most cases to improve the absorption characteristics. Due to the monochromaticity the brilliance, coherence and signal-to-noise ratio are significantly better than that of a laboratory SAXS setup, since there is no bremsstrahlung spectrum to contribute to the background. In terms of achievable wavelength there is no limitation to use a specific $K-\alpha$ line of any specific material. Often common wavelengths are chosen to better correspond to laboratory measurements on identical samples. One option that is also available in some synchrotrons is the tunability of the wavelength in order to measure resonance effects in the atomic structure of the sample (anomalous SAXS, ASAXS) [4] or better chose the accessible Q-space. Tab.6.2 summarizes some of the performance figures of current synchrotron SAXS setups. For most synchrotron SAXS beamlines beam damage, especially for organic samples, is an issue and has to be taken into account when planning an experiment.

Parameter	value
SDD	0.8-4 m
Pixel resolution	$172 \times 172 \mu\text{m}$
Flux	$10^{18} \text{ photons s}^{-1}$
wavelength λ	0.54 - 1.38 Å

Table 6.2: Performance parameters for a state of the art synchrotron SAXS beamline, here P03 at DESY. [5]

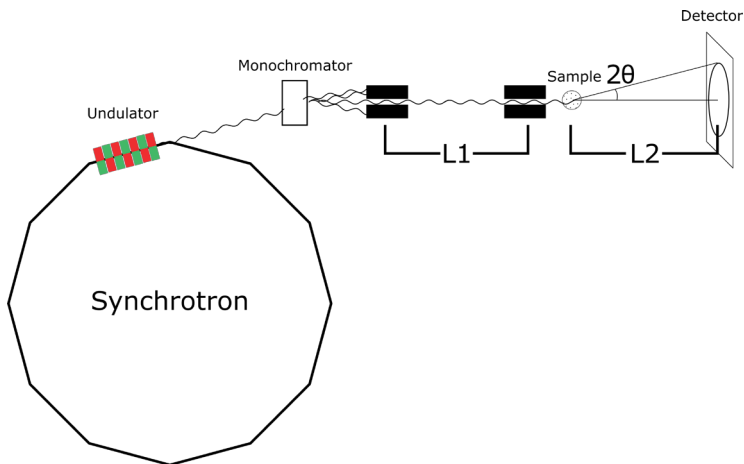


Fig. 6.4: Synchrotron SAXS setup. Here the radiation is produced in the storage ring of a synchrotron. In earlier designs, the x-rays were produced at the bending magnets in the ring (kinks in the ring here). This however lead to a wide spread of the produced wavelength and a high angular distribution of the radiation. An undulator from a magnet array as depicted here produces a narrow distribution of wavelength and angular divergence. The rest of the setup is comparable to the laboratory setup, albeit the intensity of the radiation is orders of magnitude higher, which allows for finer collimation slits and longer collimation distances and SDDs.

6.3 SANS setups

In contrast to x-rays, sufficient numbers of free neutrons can only be obtained by nuclear processes, such as fission, fusion and spallation. As large-scale facilities are needed to create the processes at a suitable rate to perform scattering experiments with them, the only facilities where neutron scattering today can be performed is at fission reactor sources and spallation sources. This of course also leads to larger efforts in terms of biological shielding.

It is an inherent feature of those reactions that the reaction products show a wide distribution of energies, with peak energies ranging up to 3 MeV kinetic energy per neutron. This leads to deBroglie wavelengths in the fermi meter region, which is unsuitable for SANS scattering experiments. Thus, in order to obtain a coherent beam it is not only necessary to collimate the neutrons but also to moderate and monochromatize them. Both processes result in losses in usable flux, since the phase space of neutrons cannot be compressed by lenses, as is the case for photons.

The moderation process is performed by collision processes in a moderator medium. The moderator is a material at temperatures around 25 K or below and the resulting neutron spectrum is a Maxwell-Boltzmann spectrum of the corresponding temperature. This results in peak wavelengths around 4 Å for the neutron beam. Neutron scattering instruments can be run both in time-of-flight mode or monochromatic mode.

A schematic of a SANS instrument is shown in Fig.6.5. Both cases with a monochromator and a chopper setup for time-of-flight are presented. In a continuous source the neutron flux has to be interrupted for the timing of time-of-flight mode while for pulsed sources there is an inherent interruption of the neutron flux.

This moderation and collimation process in consequence means that neutrons always show an albeit small distribution of wavelengths and therefore a lower signal to noise level than x-ray sources. Spin and isotopic incoherence add to that. Beam damage however is high on impossible with the weakly interacting neutrons.

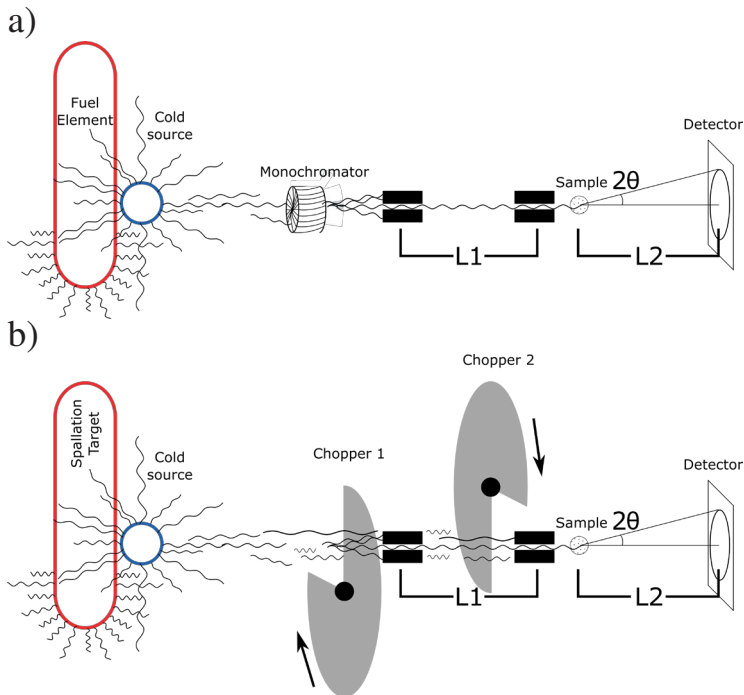


Fig. 6.5: a) Continuous source SANS setup and b) pulsed source SANS Setup. In both cases the neutron source (red) creates hot neutrons of a short wavelength. A cold source (blue) vessel (usually filled with cold ^2H or ^2D) is moderating the neutrons down to slower speeds, i.e. longer wavelengths. In both cases the collimation distance and SDD is widely adjustable for most instruments, with lengths between 1 m up to 30 m. In a SANS instrument at a continuous source a monochromator (a turbine with slightly inclined channels) selects a certain wavelength (usually between 3 and 15 Å) and afterwards the setup is very much like the one shown for SAXS setups, except that the whole instrument is larger. In case of a pulsed source choppers (rotating discs with transparent openings for neutrons) define a start and an end time for each pulse. Since neutrons, different from x-rays, are particle waves, their wavelength determines their speed. Thus, the wavelength is determined by measuring the time of arrival at the detector for each neutron. For an optimized neutron transport all components are usually evacuated.

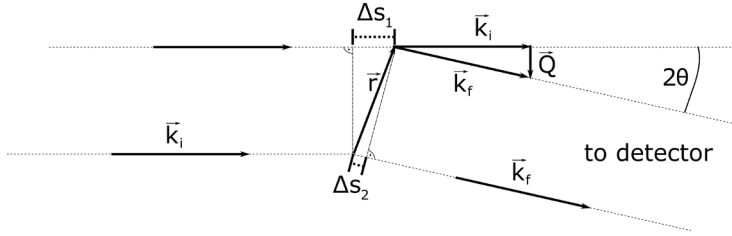


Fig. 6.6: Construction of \mathbf{Q} . The incoming and final wavevectors \mathbf{k}_i and \mathbf{k}_f define both the scattering vector \mathbf{Q} as well as the path length difference $\delta = \Delta s_1 - \Delta s_2$. Here it is important to note that the selection of the center of origin is arbitrary and thus can be chosen to be at the center of the construction. The calculation of the length of \mathbf{Q} is then given by Eq.6.2.

6.4 Indirect space and Small-Angle Scattering

The need for the resolution of small angles can be directly derived from Bragg's equation

$$n\lambda = 2d \cdot \sin \theta \quad (6.1)$$

with n being the order of the diffraction, d being the distance between two scatterers, θ as the scattering angle and λ the wavelength of the incoming beam. In order to get interference the incoming beam has to have a wavelength that corresponds to the investigated size regime, which in both cases is on the order of a few Angstroms. Using Bragg's equation with $n = 1$, $d = 50\text{\AA}$ and $\lambda = 1\text{\AA}$ we arrive at $0.01 = \sin \theta \approx \theta$. Thus, the largest structures to be resolved are determined by the smallest achievable angle.

In order to allow for a setup and wavelength independent data evaluation the data is recorded in terms of \mathbf{Q} or indirect space. The construction of that \mathbf{Q} -space from two scattering points is shown in Fig.6.6. From that the magnitude of \mathbf{Q} , which here for simplicity is $|\mathbf{Q}| = Q$, can be derived as

$$Q = \frac{4\pi}{\lambda} \sin \theta. \quad (6.2)$$

Even though \mathbf{Q} is strictly speaking a vector, for most small angle problems only the absolute value Q is of interest, hence this simplification is reasonable. This is due to the isotropic scattering picture of a majority of small-angle scattering data. Another simplification that is often used is the small-angle approximation for the sine with $\sin \theta = \theta$, which is very well valid for small angles. Combining Eqs.6.1 and 6.2 also delivers a useful expression for the approximation of inter-particle distances or correlation lengths

$$d = \frac{2\pi}{Q}. \quad (6.3)$$

6.5 Resolution limits

SAS is working based on the interference of coherent radiation. That in itself imposes some limitations on the samples and properties that can be investigated.

In term of size, the object under observation has to be of the same order of magnitude as the wavelength of the incoming radiation, analogous to light interference at a double slit. Concerning the analysis in indirect space, also the limited size of the detector and coherence volume of the sample has to be taken into account.

The second limitation that should always be considered is that only elastic scattering renders useful results, i.e. any change in speed or wavelength of the incoming radiation will render unusable results.

Finally, multiple scattering is usually not considered for the evaluation of SAS data. This means, mostly thin samples, or those with a high transmission (usually 90% or higher), can be investigated.

6.6 Fourier Transform and Phase Problem

Considering the spacing of only two scattering centers as in the last section needs to be extended to an arrangement of scattering centers for evaluation of macroscopic samples, where each atom/molecule can contribute to the scattered intensity. Since the incoming wave at location \mathbf{x} can be considered to be an even wave it can be described by

$$A(\mathbf{x}, t) = A_0 \exp\left(i2\pi\left(\nu t - \frac{\mathbf{x}}{\lambda}\right)\right) \quad (6.4)$$

With a A being the amplitude as a function of position \mathbf{x} and time t . A_0 is the modulus of the amplitude, ν the frequency and λ the wavelength.

In order to calculate the correct phase shift $\Delta\phi$ after scattering from two centers as in Fig.6.6 we need to know the differences in travelled distance between the two waves δ . This then yields

$$\Delta\phi = \frac{2\pi\delta}{\lambda} = \mathbf{Q}\mathbf{r}, \quad (6.5)$$

which is equivalent to the expression $2\pi x/\lambda$ in Eq.6.4. Here also the relation $\mathbf{Q} = \mathbf{k}_f - \mathbf{k}_i$ was used. This then leaves us with the spherical wave scattered by the first scattering center

$$A_1(\mathbf{x}, t) = A_0 b \exp(i2\pi(\nu t - \mathbf{x}/\lambda)) \quad (6.6)$$

and the corresponding scattered wave from the second scattering center

$$A_2(\mathbf{x}, t) = A_1(\mathbf{x}, t) \exp i\Delta\phi \quad (6.7)$$

$$= A_0 b \exp(i2\pi(\nu t - \mathbf{x}/\lambda)) \exp i\mathbf{Q}\mathbf{r} \quad (6.8)$$

This can then be combined into the full description of the amplitude with both contributions to

$$A(\mathbf{x}, t) = A_1(\mathbf{x}, t) + A_2(\mathbf{x}, t) \quad (6.9)$$

$$= A_0 b \exp(i2\pi(\nu t - \mathbf{x}/\lambda))(1 + \exp i\mathbf{Q}\mathbf{r}) \quad (6.10)$$

here an arbitrary scattering efficiency b for each scattering center has been introduced, which will later be discussed for both x-rays and neutrons.

Since only intensity can be observed at the detector, we need to consider the square, calculated with the complex conjugate of the expression itself

$$I(\mathbf{Q}) = A(\mathbf{x}, t)A^*(\mathbf{x}, t) \quad (6.11)$$

$$= A_0^2 b^2 (1 + \exp(i\mathbf{Q}\mathbf{r}))(1 + \exp(-i\mathbf{Q}\mathbf{r})). \quad (6.12)$$

Here the time and absolute location dependencies in Eq.6.10 have cancelled each other out, so we can neglect them and are left with a function that solely depends on the scattering vector \mathbf{Q} and the location of the particles \mathbf{r} . Neglecting those dependencies allows us to generalize Eq. 6.10 to the case of N identical scattering centers with

$$A(\mathbf{Q}) = A_0 b \sum_{i=1}^N \exp(i\mathbf{Q}\mathbf{r}_i). \quad (6.13)$$

The \mathbf{r}_i here signify the relative locations of all scattering centers in the sample, relative to either simply the first scattering center or any arbitrary center chosen. Indeed all arrangements are mathematically identical. Replacing the sum by a weighed integral allows also the calculation for the case of a (quasi)continuous sample with number density $\rho(\mathbf{r})$:

$$A(\mathbf{Q}) = A_0 b \int_V \rho(\mathbf{r}) \exp i\mathbf{Q}\mathbf{r} d\mathbf{r} \quad (6.14)$$

This is the Fourier transform of the number density of scattering centers with scattering efficiency b , it can also be applied for numerous scattering efficiencies.

However, since the phase information got lost while obtaining the intensity as an absolute square of the amplitudes, there is no direct analytic way of performing an inverse Fourier transform. This is why this is called the phase problem. Also, as described above, in a wide range of cases it is enough to investigate the modulus of \mathbf{Q} , neglecting its vector nature.

6.7 Scattering Efficiency

Since the physical scattering event is very dissimilar for x-rays and neutrons they shall be discussed separately here. However, it should be noted, that the nature of the scattering process does not impact on the method of data evaluation in general. Only in very specific cases, such as contrast matching or polarized scattering there is any discernible difference.

6.7.1 Scattering with x-rays

X-rays, as photons, interact with the sample via electromagnetic interaction. For the purpose of this manuscript it is sufficient to note that the vast majority only interact with the electron shell around the atoms and thus effectively map the electron density within the sample. Interactions with the nucleus would only occur at very high energies, which are not usually used in elastic scattering. In a rough approximation the strength of the electromagnetic interaction scales with Z^2 , meaning that heavy elements, such as a wide range of common metals, scatter considerably stronger than light ones, like hydrocarbon compounds. For element analyses there is also the possibility of resonance scattering, where the chosen x-ray energies are close to the resonance gaps in the absorption spectrum of specific elements (ASAXS). [4]

Based on Thomson scattering the scattered intensity at angle 2θ is

$$I(2\theta) = I_0 \left(\frac{e^2}{mc^2} \right) \frac{1 + \cos^2 2\theta}{2} \quad (6.15)$$

$$\frac{I}{I_0} = \left(\frac{d\sigma}{d\Omega} \right)_2 = r_e^2 \frac{1 + \cos^2 2\theta}{2} \quad (6.16)$$

Here we also introduced the differential scattering cross section $\frac{d\sigma}{d\Omega}$ for a single electron and r_e being the radius of an electron. This means that the total probability for a scattering event to occur into a solid angle $d\Omega$ is exactly that value for a single, isolated electron. This probability is in units of an area. Thus, the scattering length for a single electron b_e is defined as the square root of that:

$$b_e = r_e \sqrt{\frac{1 + \cos^2 2\theta}{2}} \quad (6.17)$$

With those previous equations it is again important to note that small-angle scattering is mainly concerned with small angles, thus that $\cos 2\theta \approx 1$ is a very good approximation. This is also, together with backscattering, the location of the highest intensity and negligible polarization effects. The numeric values for the constants used here are $r_e = 2.818 \times 10^{-15}$ m and the scattering cross section for a single electron $\sigma_e = 6.65 \times 10^{-29}$ m² = 0.665 barn after integration over the full solid angle. As apparent with integration over the full solid angle, the relation is $\sigma = 4\pi b_e^2$.

Since usually the goal is to find the distribution of scattering centers in a volume, the density of scattering length per unit volume is of interest. This is the scattering length density (SLD)

$$\rho(\mathbf{r}) = \frac{b_e(\mathbf{r})}{V}. \quad (6.18)$$

A very common way of expressing scattering efficiency is using electron units. As can be seen in Eq.6.13 the scattering amplitude is only determined by the SLD of a single electron apart from the Fourier transform of the local density. This means the scattering intensity in electronic units can be expressed as

$$I_{eu}(Q) = \frac{I(Q)}{I_0 b_e^2} \quad (6.19)$$

This means, with appropriate calibration, if there is an intensity of $I_{eu} = 200 b_e^2$ at a certain Q , that the size scale corresponding to that Q vector has 200 electrons per unit volume.

Since photons interact mainly with the electron shell, there is also an angle dependency accounting for the time averaged location probability of the electrons in the shell, which may or may not be spherical, depending on the electronic configuration of that specific atom. This would then lead to a SLD in terms of $b_e(Q) = b_e f_s(Q)$ with f_s being the atomic scattering factor for any specific element. This important to take note of, when there is a structure or form factor on the same size scale as a single atomic distance $Q = \frac{2\pi}{1.54 \text{ \AA}} = 4.08 \text{ \AA}^{-1}$. This is usually not in the regime of interest for small-angle scattering and will mostly vanish in the incoherent background.

Another incoherent background effect is Compton scattering, where inelastic processes change the wavelength during the scattering process. This is however again strongly suppressed at small angles. The wavelength shift occurring based on Compton scattering is following this expression

$$\Delta\lambda = \frac{h}{mc} 2 \sin^2 \theta \quad (6.20)$$

The prefactor is $\frac{h}{mc} = 0.02426 \text{ \AA}$. It is also obvious that at large angles $2\theta = 180^\circ$ the energy transfer is maximal. Since we are always investigating angles close to $\theta = 0$ the wavelength shift and hence the incoherent background is negligible compared to other experimental factors, such as slits and windows scattering.

6.7.2 Scattering with neutrons

Neutrons interact with the nuclei directly, which results in the atomic form factor being always spherically symmetric (billiard balls) and them being sensitive to different isotopes and spin-spin coupling. In contrast to x-rays, there is no simple expression for scattering strength as a function of isotope or atomic number. Directly neighboring elements and isotopes may have vastly different cross sections.

This is due to the fact that the Schrödinger equation has to be solved for each combination of incoming neutron and nucleus. The solution for the problem is illustrated by Hammouda or Tong [6, 7] in more detail. For here it is sufficient to note that Schrödinger's equations

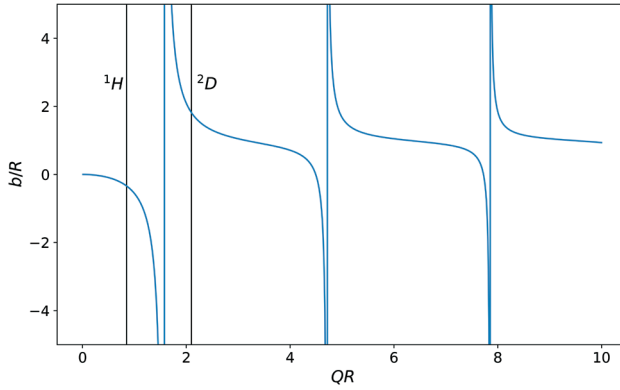


Fig. 6.7: Behavior of scattering length b as a function of nuclear radius R and momentum transfer Q . Using representative values for example for hydrogen ($R = 8.5 \cdot 10^{-16} \text{ m}$) and deuterium ($R = 2.1 \cdot 10^{-15} \text{ m}$) and reasonable Q -values for small angle scattering (such as forward scattering with $Q = 1 \cdot 10^{-5} \text{ \AA}^{-1}$) it becomes apparent how those strong differences in scattering length happen, and also why this has an especially strong impact for light elements, where the radius strongly changes by adding or removing one nucleon. Values for hydrogen and deuterium are marked.

is solved by taking into account an approximately MeV deep square well for the nucleus with a free particle outside the well. This results in an approximate solution for the relation between the radius of the atomic nucleus R and the scattering length b :

$$\frac{b}{R} = 1 - \frac{\tan qR}{qR} \quad (6.21)$$

A representation of this is given in Fig. 6.7. The strong variation due to minute changes in the numerical value make it clear, why tabulated values are used in most cases.

Based on that we usually rely on tabulated values for the cross sections and scattering lengths of different elements and isotopes (see Tab.6.3) and can then write the cross section and scattering length relation as

$$\frac{d\sigma}{d\Omega} = b^2 \quad (6.22)$$

That said, only coherent scattering can form interference patterns, i.e. no change of the nature of the radiation can take place during the scattering process. However, since the neutron can change its spin orientation through spin-spin coupling during the scattering process that may happen, depending on the spin orientation of the sample nuclei. Those are completely statistical processes.

As neutrons are fermions, which have spin $1/2$ the possible outcomes after a scattering process with a nucleus of spin i are $i + 1/2$ and $i - 1/2$, and the associated possible spin states

Element	scattering length $b_{coh}/10^{-14}m$
^1H	-0.374
^2D	0.667
C	0.665
N	0.936
O	0.580
Si	0.415
Br	0.680

Table 6.3: Coherent scattering length of several elements and isotopes.

are

$$\text{number of states } i + 1/2 : 2(i + 1/2) + 1 = 2i + 2 \quad (6.23)$$

$$\text{number of states } i - 1/2 : 2(i - 1/2) + 1 = 2i \quad (6.24)$$

$$\text{total number of states} : 4i + 2. \quad (6.25)$$

This immediately shows, that only for the case $i = 0$ there can be only two states. Since it is impossible to know the spin state of non-zero spin nuclei under ambient conditions, the differential cross section becomes a two-body problem of the form:

$$\frac{d\sigma}{d\Omega} = \sum_{i,j} \langle b_i b_j \rangle \exp -i\mathbf{Q}(\mathbf{r}_i - \mathbf{r}_j) \quad (6.26)$$

Here $\langle b_i b_j \rangle$ is the expectation value of the SLD for each $b_i b_j$ combination possible given isotope and spin variability. For this there is only one coherent outcome, where $b_i = b_j$, which then results in

$$\langle b_i b_i \rangle = \langle b_i^2 \rangle = \langle b^2 \rangle. \quad (6.27)$$

All other cases result in $b_i \neq b_j$ and therefore

$$\langle b_i b_j \rangle_{i \neq j} = \langle b_i \rangle \langle b_j \rangle = \langle b \rangle^2. \quad (6.28)$$

This then results in

$$\frac{d\sigma}{d\Omega} = \langle b^2 \rangle \cdot \sum_{j,k} \exp(-i\mathbf{Q}(\mathbf{r}_i - \mathbf{r}_j)) + N(\langle b^2 \rangle - \langle b \rangle^2). \quad (6.29)$$

Here $\sqrt{\langle b^2 \rangle} = b_{coh}$ signifies the coherent scattering length density, since it contains information about the structure of the sample via \mathbf{r}_{ij} and $\sqrt{\langle b^2 \rangle - \langle b \rangle^2} = b_{inc}$ is the incoherent cross section not containing any information about the sample structure. This cannot be suppressed

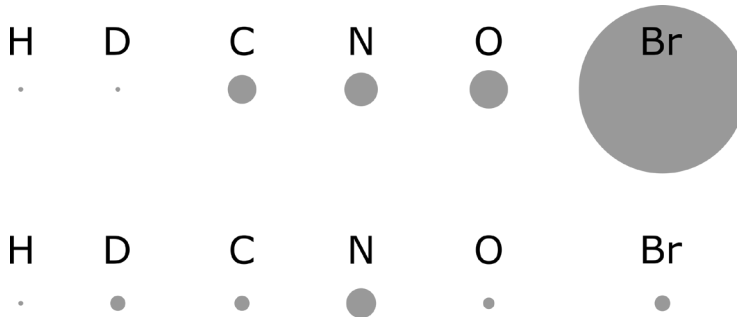


Fig. 6.8: Coherent cross-sections for selected elements for x-rays (top) and neutrons (bottom). The coherent scattering cross section scales linearly with the diameter of the circles. It is apparent, that the Z^2 dependency strongly emphasizes heavy elements in x-ray scattering, whereas for neutrons even single isotopes can be distinguished. However, for neutrons there is no simple analytic expression for the scattering cross-sections.

instrumentally, therefore often isotopes with low incoherent scattering length are chosen in neutron scattering to suppress the incoherent background. Both coherent and incoherent scattering lengths can separately used together with Eq.6.18 to obtain the corresponding scattering length densities.

6.7.3 Scattering Cross Section and Contrast Matching

As described above there is a Z^2 dependency of the cross section of atoms in case of x-rays and the cross section values for neutrons are taken from tabulated values. The resulting differences in cross section are illustrated in Fig.6.8. Because different isotopes have very different cross sections for neutron scattering, in some cases it is possible to replace certain isotopes in order to arrive at desired contrast conditions.

One of the most important examples for that technique, called contrast matching, is replacing hydrogen by deuterium. This leaves the chemical composition of the sample unchanged, and hydrogen is extremely abundant in most organic compounds. The concept can in some cases be extended to be used as the Babinet principle, in order to suppress background scattering, since it is extremely preferable to have a solvent with a low background and a solute with a higher background than vice versa. A sketch of the concept is shown in Fig.6.9.

This method allows highlighting otherwise hidden features of the sample or suppressing dominant scattering in order to better determine a structure with a lower volume fraction and therefore less scattering contribution. Examples for that application are highlighting the shell of a sphere, by matching the core or vice versa. Also for protein samples certain structures can be matched, so that only distinct features are visible.

In order to apply contrast matching, mostly the solvent is changed. In some rare cases also the polymer or other sample is synthesized with a different isotope composition. Here the finding of the correct H/D fraction of the solvent shall be shown. Fig.6.10 gives an example of how to find the correct H/D fraction in a semi-analytic way. The underlying principle is

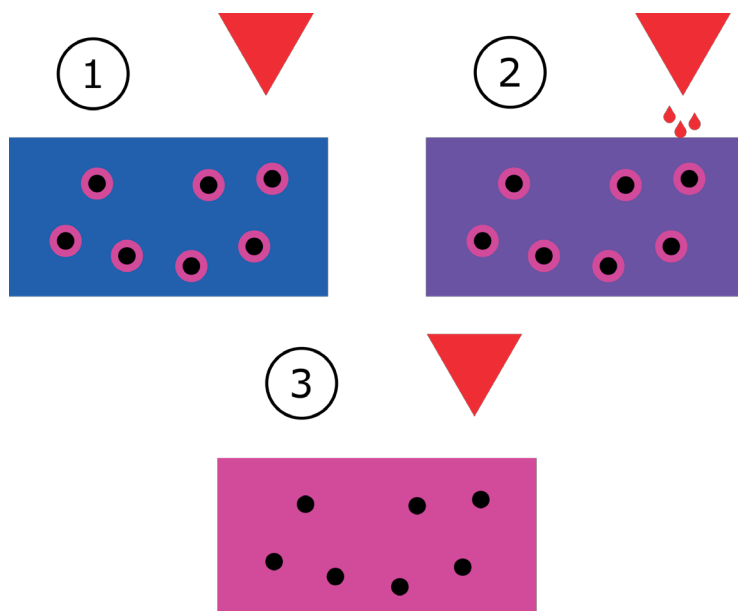


Fig. 6.9: Illustration of the concept of contrast matching. In step ① there are micelles with a corona (pink) dissolved in a solution (blue). The scattering length density of the corona is between the SLD of the solvent and its deuterated counterpart (red). In step ② the deuterated solvent is added to the solution, which changes the contrast conditions. Finally, in step ③ a sufficient amount of deuterated solvent has been added, so the contrast between the corona and the solvent has vanished. Now the micellar cores can be measured directly.

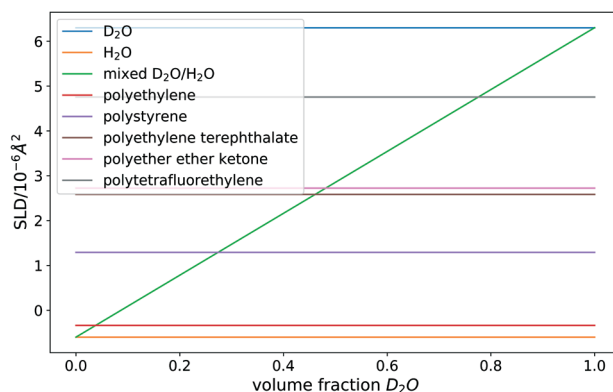


Fig. 6.10: Semi-analytic way to determine the necessary solvent deuteration for contrast matching. The concentration at the matching point, where the solvent has the same SLD as the polymer particles, is determined by the crossing of the mixed $\text{D}_2\text{O}/\text{H}_2\text{O}$ SLD line and the SLD line of the respective polymer. For the calculation the scattering length density of water is calculated to $-0.6 \cdot 10^{-6} \text{ \AA}^{-2}$ and the SLD of heavy water is calculated to $6.3 \cdot 10^{-6} \text{ \AA}^{-2}$.

expressed by

$$SLD_{sample} = SLD_{H_2O} \times H + SLD_{D_2O} \times D \quad (6.30)$$

$$H \equiv 1 \quad (6.31)$$

$$D = \frac{SLD_{sample} - SLD_{H_2O}}{SLD_{D_2O}}. \quad (6.32)$$

This way the volume of heavy water for each unit volume of protonated (usual) water can be calculated. It is also apparent from that calculation that only mixtures with a scattering length density between water and heavy water can be matched, and that the equations above only cover the non-trivial cases, where pure water or heavy water is not suitable. The actual volumes can then be calculated with $V_{water} = \frac{H}{H+D}$ and $V_{heavy\ water} = \frac{D}{H+D}$.

A prominent example for contrast matching is the matching out of the shell or core of a micelle. The contrast behavior and the resulting scattering curves are shown in Fig.6.11. Essentially contrast matching can improve the fitting procedure, if well known parts of the structure are matched out or emphasized by the contrast matching. This then delivers two or more different data sets that all should return comparable results. Another option is the reconstruction of embedded particles in a larger structure. Also here, the overall fitting procedure can profit from two fits with mutually corroborating results.

One concept that shall also be mentioned here is magnetic (spin-) contrast. In this context Fig.6.9 can be understood to be particles with a magnetic shell. As long as the spins are not aligned there is no contrast between the shell and the solvent (step ③). When an external magnetic field aligns the spins in the shell, a contrast between the shell and the solvent emerges (①). Several other possibilities with and without polarization analysis are possible, however that is beyond the scope of this manuscript.

6.8 Form factors

As described above, the phase problem usually prevents an analytic reconstruction of the structure from the scattered intensity by an inverse Fourier transform. There are approaches attempting the direct reconstruction of direct space information [8] or reconstruction from bead model annealing / Monte Carlo simulation [9, 10]. All these approaches have in common that a direct analytic expression for the scattering is not foreseen, and can therefore not be used as a starting point of the analysis. In the past, the model based analysis has been the most applied approach for the analysis of small-angle scattering data. Here, predetermined structures undergo a Fourier transform, whose result is then used to calculate a scattering pattern. This results in the most cases in analytic expressions that can be directly fitted to the data and are often used in a catalog-like manner in order to determine the structure of the sample. As most geometric forms can be approximated either as a sphere, a disk or a rod (see Fig.6.12) these are the forms that are going to be discussed here. More elaborate structures are available and can in principle be calculated for any structure where the form can be described by an analytic expression. A short,

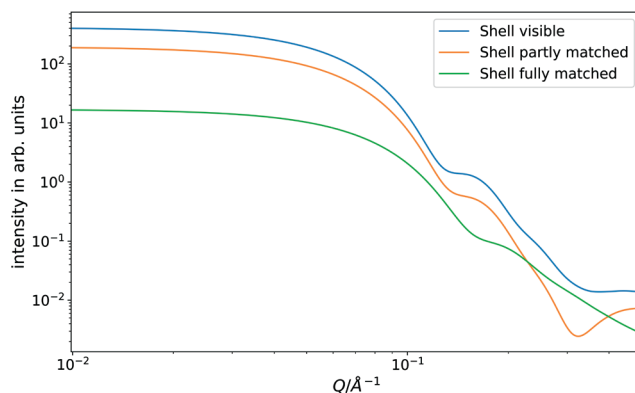


Fig. 6.11: Scattering curves for micelles with unmatched, partially matched and completely matched corona. The curves correspond to the scenarios ①, ② and ③ in Fig.6.9. Here two effects can be observed. The corona is only 50% of the radius of the core, hence it influences the scattered intensity at higher angles than the core itself, the scattering feature at $Q=0.15\text{\AA}^{-1}$ corresponding to the micellar core is therefore quite stable, while the intensity at higher Q changes drastically. Considering the forward scattering the dependence of the scattering contrast between solvent and core is directly visible. The matched out corona shows the least contrast, and therefore the lowest forward scattering intensity, while the unmatched corona has the highest contrast and the highest intensity. This approach is also used, when an analytic approach to find the matching D_2O/H_2O concentration cannot be found. Several concentrations are tested and where a minimum in the scattered intensity is found, the contrast can be assumed to be matched.

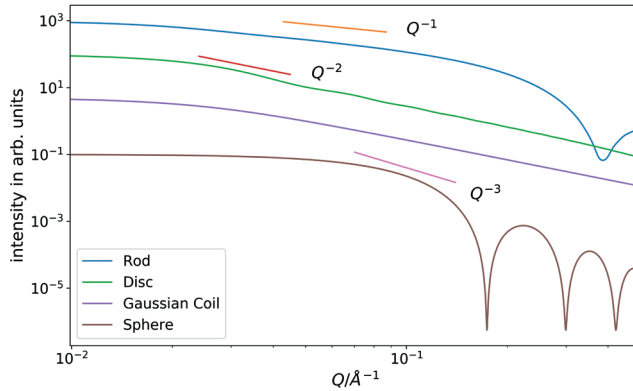


Fig. 6.12: Form factors for several scattering geometries. The slopes at the onset of the form factor after the plateau are shown, which is mostly determined by the fractal dimension of the scattering object. Here it also becomes apparent that solely relying on that slope may lead to misinterpretation between similarly scaling objects, here Gaussian coils and discs.

and by no means complete, list of programmes for the evaluation of SAS data is SasView (<https://www.sasview.org>), SasFit (<https://kur.web.psi.ch/sans1/SANSSoft/sasfit.html>) and Scatter (<http://www.esrf.eu/UsersAndScience/Experiments/CRG/BM26/SaxsWaxs/DataAnalysis/Scatter#>).

6.8.1 Sphere

The analytic expression for the scattering created by a sphere of radius R is

$$I(Q) = N \left[3V\rho_0 \cdot \frac{\sin(QR) - QR \cos(QR)}{(QR)^3} \right]^2 \quad (6.33)$$

with N being the number of the scattering particles, V being the volume of a single sphere and ρ_0 being the SLD contrast between the sphere and the solvent.

This expression can be reached by using a SLD description like a step function as depicted in Fig.6.13. As a sphere is already spherically symmetric this can be directly put into the Fourier transform

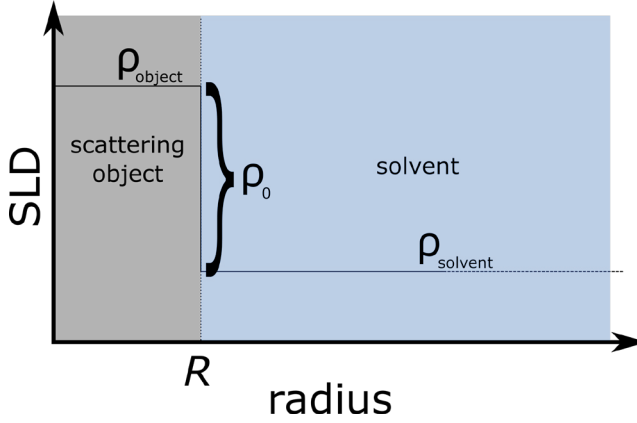


Fig. 6.13: Depiction of the SLD distribution along the radius of a sphere. ρ_0 is the SLD contrast, i.e. the SLD difference between the scattering particle and the solvent. R is the radius of the sphere.

$$A(\mathbf{Q}) = \mathcal{F}(\rho(\mathbf{r})) \cdot (2\pi)^3 \quad (6.34)$$

$$= \int_V \rho(\mathbf{r}) \exp(-i\mathbf{Q}\mathbf{r}) dV \quad (6.35)$$

$$= \int_{\phi=0}^{2\pi} \int_{\theta=0}^{\pi} \int_{r=0}^R \rho(\mathbf{r}) \exp(-i\mathbf{Q}\mathbf{r}) r^2 \sin\theta dr d\theta d\phi \quad (6.36)$$

$$= \int_{\phi=0}^{2\pi} \int_{\theta=0}^{\pi} \int_{r=0}^R \rho(r) \exp(-iQr \cos\theta) r^2 \sin\theta dr d\theta d\phi \quad (6.37)$$

$$= \int_{\phi=0}^{2\pi} \int_{u=-1}^1 \int_{r=0}^R \rho(r) \exp(-iQru) r^2 dr du d\phi \quad (6.38)$$

$$= 4\pi \int_{r=0}^R \rho(r) \left(\frac{\exp(iQru) - \exp(-iQru)}{iQr} \right) r^2 dr \quad (6.39)$$

$$= 4\pi \int_{r=0}^R \rho(r) \left(\frac{\sin Qr}{Qr} \right) r^2 dr \quad (6.40)$$

$$= 4\pi\rho_0 \int_{r=0}^R \frac{\sin Qr}{Qr} r^2 dr \quad (6.41)$$

$$= 4\pi\rho_0 \frac{\sin QR - QR \cos QR}{Q^3} \quad (6.42)$$

$$= 4\pi\rho_0 \frac{\sin QR - QR \cos QR}{Q^3} \quad (6.43)$$

$$= V\rho_0 \frac{3\sin QR - QR \cos QR}{R^3 Q^3} \quad (6.44)$$

Here Eq.6.37 used the identity of $\mathbf{Q}\mathbf{r} = Qr \cos\theta$ with theta being the enclosed angle and in Eq. 6.38 $\cos\theta$ was replaced by u . In addition, spherical symmetry was exploited for the

integration over the solid angle. The factor $(2\pi)^3$ is to correct for scaling differences during the Fourier transform.

This corresponds exactly to the squared term in Eq.6.33 which is nothing else than the squared amplitude that we calculated here. As this is only the scattering for a single, isolated sphere, the number density needs to be included to reflect the absolute scattered intensity. In case of neutron scattering this is the case for most of the instruments. X-ray instruments are often not calibrated to absolute scattering intensities and therefore need an arbitrary scaling factor. Similar approaches can be used for other analytic representations of form factors.

6.8.2 Thin Rod

The scattered intensity by a dilute solution of thin rods of length L is given by

$$I(Q) = \rho_0^2 v^2 \left(\frac{2}{QL \cos \theta} \right) \sin^2 \left(\frac{QL}{2} \cos \theta \right) \quad (6.45)$$

$$\rightarrow \rho_0^2 v^2 \frac{2}{QL} \left(\text{Si}(QL) - \frac{1 - \cos QL}{QL} \right). \quad (6.46)$$

Here v is the volume of the particle and the average over all orientations has been performed in the second step. The substitution $\text{Si}(QL) = \int_0^{QL} \frac{\sin u}{u} du$ was used.

6.8.3 Circular Disc

An infinitely thin circular disk of radius R scatters the incoming intensity as follows:

$$I(Q) = \rho_0 v^2 \frac{2}{Q^2 R^2} \left(1 - \frac{J_1(2QR)}{QR} \right) \quad (6.47)$$

J_1 here is the first order Bessel function.

6.8.4 Non-particulate scattering from a flexible chain

A flexible chain in solution cannot be described by a simple analytic form, since one needs to integrate over all possible conformations of the chain. Nevertheless, an analytic expression, the Debye scattering, can be found:

$$I(Q) = \rho_0^2 v^2 \frac{2(\exp(-Q^2 R_g^2) + Q^2 R_g^2 - 1)}{Q^2 R_g^2} \quad (6.48)$$

Here $R_g = \frac{1}{V} \int_V \mathbf{r}^2 \rho_0 d\mathbf{r}$ is the radius of gyration (in this case for constant SLD). A very important aspect of that scattering curve is, that it essentially scales with Q^2 .

For better comparison the radius of gyration for a solid sphere of radius R is $R_g = \sqrt{\frac{3}{5}}R$, the one for a thin rod of length L is $R_g = \frac{1}{\sqrt{12}}L$ and the one for a very thin circular disc with radius R is $R_g = \frac{1}{\sqrt{2}}R$

6.8.5 Polydispersity

All analytic form factors, that deliver the scattered intensity, are determining the scattered intensity for particles of one exact size. In real systems, however, there are mostly distributions of different sizes. This leads to a superposition of scattering from different particle sizes. Since most particle sizes follow a Gaussian distribution, this is also a good way to fold in the particle size distribution analytically. For extremely long, or very polydisperse, particles then Schulz-Zimm distribution is used, which looks very similar to the Gaussian distribution, however has a cut-off at zero to prevent negative sizes of the particles. For specialized problems also other distributions, such as La-Place, multi-modal or other size distribution functions can be used.

The general idea is that the scattered intensity $I(Q, r)$ is folded with the size distribution function $f(r)$

$$I_{\text{real}}(Q, r) = I_{\text{ideal}}(Q, r) * f(r). \quad (6.49)$$

Here the subscripts real and ideal identify the real measured intensity or the ideal intensity for any calculated particulate size and form.

The effects of the convolution can be seen in Fig.6.14. Most notably, the minima are smeared out, and in some cases vanish completely, so they can only be estimated. Another important effect is that the slopes of inclinations cannot be completely reproduced anymore, which is especially important to distinguish scattering from different contributions. The magnitude of the polydispersity is described by the polydispersity index $PDI = \sigma(f(r))/\mu(f(r))$ where $\sigma(f(r))$ is the standard deviation of the size distribution function and $\mu(f(r))$ is the mean of the size distribution function. Values of $PDI \geq 0.3$ are usually discarded during fitting, as then the results become unreliable in such a polydisperse sample.

In addition to this, the usual polydispersity (approximated by a Gaussian distribution) is by its very nature similar to a resolution smearing of the instrument itself. Therefore, it can easily happen to overestimate the polydispersity. If the resolution function of the instrument is known, it should be used for deconvolution before performing the fits.

6.9 Structure Factors

Structure factors in general describe the scattered intensity due to the arrangement of single particles. This can be because the solution is becoming to dense, and therefore the particles arrange following a nearest neighbor alignment or because the particles are attractive to each other and form aggregates. Thus, more generally a structure factor $S(Q)$ is a measure of interaction between the single particles in the solution and connected with the correlation

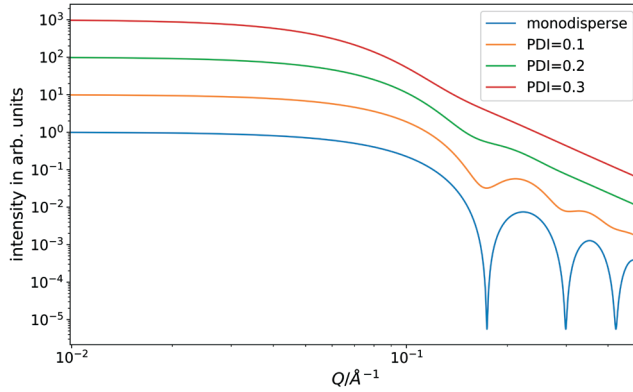


Fig. 6.14: *Effect of polydispersity. While the positions of the minima can still be found at higher polydispersity, the higher order undulations of the form factor vanish.*

function $c(r)$ (the probability to find a particle at a certain distance) with the relation

$$S(Q) = \frac{1}{1 - nc(Q)}. \quad (6.50)$$

Since the structure factor and the form factor need to be convolved in real space, in indirect space this converts to a multiplication, following the convolution theorem. Therefore the scattered intensity, described by form factor $F(Q)$ and structure factor $S(Q)$

$$I(Q) = F(Q) \cdot S(Q). \quad (6.51)$$

From this equation it also follows, that for a system of uncorrelated, identical particles the structure factor must be $S(Q) = 1$. Since the correlation between particles usually leads to either an aggregation or repulsion of particles over long length scales the contribution of the structure factor is most prominent at low Q -values. Also, this means that for large distances the structure factor has to level out to unity, to preserve the fact that at large Q only the inner structure of the particle is visible, not its arrangement in space. A few instructive examples for the structure factor are shown in Fig.6.15.

6.9.1 Hard Sphere Structure Factor

The hard sphere structure factor assumes an infinitely high potential below a radius R and a zero potential at higher radii. This can be described by

$$V(r) = \begin{cases} \infty & \text{for } r \leq R \\ 0 & \text{for } r > R. \end{cases} \quad (6.52)$$

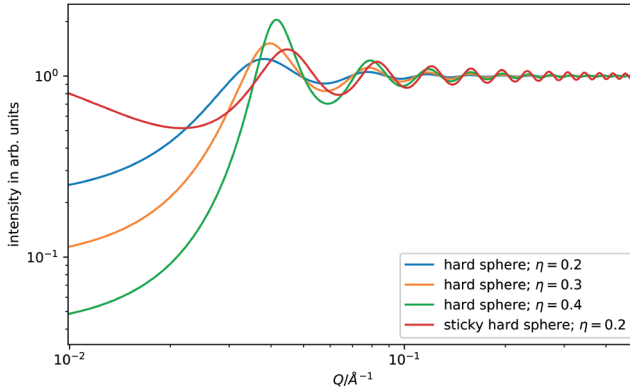


Fig. 6.15: Examples for structure factors. The intensity of the peaks roughly scales with the volume fraction η of the particles. Also the position of the peaks is slightly dependent on that volume fraction, which makes a direct calculation of $R = \frac{2\pi}{Q_{max}}$ invalid (The hard sphere radius used here was 60 Å). A distinct difference can be noted at low Q . Here, in general, attractive interaction (sticky hard spheres) leads to an increase in scattering, while repulsive interaction leads to a decrease in intensity.

Using Eq.6.50 this can be rewritten as

$$S(Q) = \frac{1}{1 + 24\eta_{HS}G(2QR)/2QR}. \quad (6.53)$$

Here $G(x)$ is defined as

$$G(x) = \alpha \frac{(\sin(x) - x\cos(x))}{x^2} + \quad (6.54)$$

$$= \beta \frac{(2x \sin(x) + (2 - x^2) \cos(x - 2))}{x^3} + \quad (6.55)$$

$$= \gamma \frac{(-x^4 \cos(x) + 4[(3x^2 - 6) \cos(x) + (x^3 - 6x) \sin(x) + 6])}{x^5} \quad (6.56)$$

with these definitions for α , β and γ :

$$\alpha = \frac{(1 + 2\eta_{HS})^2}{(1 - \eta_{HS})^4} \quad ; \quad \beta = \frac{6\eta_{HS}(1 + \eta_{HS}/2)^2}{(1 - \eta_{HS})^4} \quad ; \quad \gamma = \frac{\eta_{HS}/2(1 + 2\eta_{HS})^2}{(1 - \eta_{HS})^4}. \quad (6.57)$$

In all equations the volume fraction that is occupied by hard spheres of radius R is designated η_{HS} .

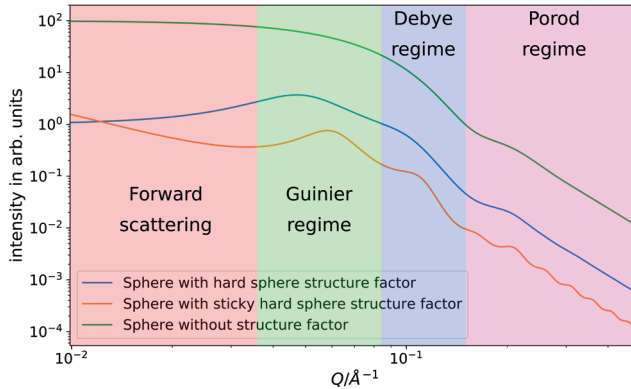


Fig. 6.16: Diverse scattering curves from identical spherical form factor and different structure factors.

6.10 Reading a curve

In an experimental environment it can be useful to determine the fundamental features in a preliminary fashion without computer aided data evaluation, also known as fitting. In addition, this helps determining good starting parameters for fits. In order to do so, we are going to look at the curves shown in Fig.6.16. There we can determine different regions of the scattered intensity (forward scattering, Guinier regime, Debye regime and Porod regime) and determine several properties of the sample from that intensity. When applying the described techniques for directly reading a curve it has to be kept in mind that most of them are either restricted in their validity concerning the Q -space or are very general and rough descriptions of the sample.

6.10.1 Forward scattering

As pointed out in the discussion of the structure factor, large aggregates mostly show their presence by an increased scattering intensity at low Q . This also becomes apparent when taking Eq.6.3 into account. This means, in general, an increased scattering at low Q is indicative of large aggregates being present in the sample. This also correlates with an attractive potential between the single particles.

Another possibility is strongly suppressed scattering at low Q . This can be the case for strongly repulsive interaction potentials between the particles, close to what is described for the hard sphere factor above.

A leveling out of the intensity at low Q is indicative of an either dilute solution or a very weak potential between the particles. Then there is no influence at low Q and only the structure factor of the single particles is visible.

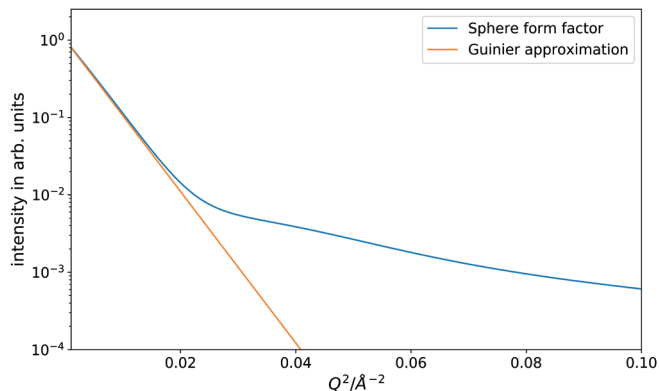


Fig. 6.17: Sphere form factor and Guinier approximation from Eq.6.58 in a Guinier plot. The radius of gyration is 25.8 \AA . The estimated slope by eye was $m = -185$. With $R_g = \sqrt{-3 \cdot m} = 23.5 \text{ \AA}$ the error is within 10%, which is suitable for a naked eye approximation.

6.10.2 Guinier regime

The Guinier regime is usually the crossover region, where the forward scattering is not dominant anymore and the slope of the scattering curve changes to the scattered intensity of the form factor. In this regime the overall size of the particle can be examined. This is similar to seeing something from far away: One may be able to discern the size of the particle but the distinct form remains hidden. Imagine a football and a pumpkin seen from 100 m away. They are close in size, you can properly judge it to be approximately 20 cm in diameter, but the exact form (ridges, stem of the pumpkin) remains hidden. A description that is only taking into account the scattered density of the particles as a whole, valid in that scattering regime is the Guinier Law:

$$I(Q) = \rho_0 v^2 \exp\left(-\frac{Q^2 R_g^2}{3}\right) \quad (6.58)$$

For details of derivation, which include a Taylor series expansion around zero of the scattered amplitude (Eq.6.36) and an averaging over all directions, please refer to the literature. [11,12] Another option is to develop a series expansion for the Debye Law (Eq.6.48) at low Q .

In order to evaluate the data using the Guinier Law, the data needs to be plotted as shown in Fig.6.17. The log-log representation and plotting versus Q^2 allow to directly read the inclination of the system, multiply by 3 and use the square root in order to retrieve the particle radius.

6.10.3 Debye regime

In contrast to the Guinier regime, where the data can be evaluated by the Guinier law, the Debye regime signifies the area, where the particulate form manifests in the scattering, which in general cannot be fitted by the Debye law. The Debye law is only valid for the scattering from Gaussian chains. As can be seen in the form factors section 6.8, there is a direct correlation to the dimensionality of the scattering particle (sphere, disc, rod) and the slope in log-log plot, since the scattering scales with $I(Q) \sim Q^{-D}$, where D is the dimensionality of the scattering object (sphere: $D = 3$; disc: $D = 2$; rod: $D = 1$). Also the scattering from fractal objects is possible, which then results in non-integer numbers for the slope. It should be noted that this is an approximation that is only valid for the case when $1/\text{particle radius} \ll Q \ll 1/\text{fundamental building block}$. The fundamental building block in this case can be for example atoms or single monomers of a chain.

6.10.4 Porod regime

The Porod regime, is the regime where the interface between the particle and the solvent dominates the scattered intensity. It is valid for large Q (before leveling out into the incoherent background) and therefore a good approach is extrapolating the sphere form factor to large Q . The decisive property of the scattered intensity is the scaling of $I(Q) \sim Q^{-4}$. This behavior can be derived from an extrapolation of the sphere form factor (Eq.6.33) to very large Q :

$$I(Q) \propto \left(\frac{4}{3}\pi R^3\right)^2 \frac{9(\sin QR - QR \cos QR)^2}{Q^6 R^6} \quad (6.59)$$

$$= 8\pi^2 \left(\frac{R^2(1 + \cos 2QR)}{Q^4} - \frac{2R \sin 2QR}{Q^5} + \frac{1 - \cos 2QR}{Q^6} \right) \quad (6.60)$$

The higher order terms vanish at large Q delivering the characteristic Q^{-4} behavior of the scattered intensity. Here only proportionality is claimed, which is strictly true in this case. If the scattered intensity is recorded in absolute intensities, here also information about the surface of the particles can be obtained. This then follows the form

$$\lim_{Q \rightarrow \infty} I(Q) = \frac{8\pi \Delta\rho S}{Q^4}. \quad (6.61)$$

$\Delta\rho$ is here the SLD difference between the particle and the surrounding medium and S the inter-facial area of the complete sample between particles and medium. This means, the absolute intensity of the Porod regime allows to determine the complete amount of surface in the sample.

6.10.5 Estimation of particle and feature Size

As described previously for low Q in most cases it is a good approximation to assume all particles in the sample have spherical symmetry (Section 6.10.2). The roots of the expression for the spherical form factor are in the locations $\tan(QR) = QR$, which is true for $QR \approx 4.49, 7.73, 10.90, \dots$. In many cases anyway only the first minimum of the form factor will be visible. This allows a fast approximation of the radius with $R \approx 4.5/Q_{min}$. Here it needs to be noted, that this is the rotational average of the particle, neglecting any structure of the particle whatsoever.

Another approach of determining the size or correlation of features is using Eq.6.3:

$$d = \frac{2\pi}{Q}$$

Although this is in general only strictly true for lamellar systems and the corresponding correlations, it is still a good approximation for a summary data examination during the experiment. With that restriction in mind it can be used for virtually any feature in the scattering curve and the size of the corresponding feature in the sample.

6.11 Further Reading

Most of the concepts shown in this manuscript are based on previous publications. The following selection of textbooks gives the reader a good overview of the principles of SAS.

6.11.1 A. Guinier: X-ray diffraction in crystals, imperfect crystals, and amorphous bodies

This early textbook concentrates on SAXS, as neutron scattering at the time of writing was still in its infancy. While some of the terminology may have changed slightly over time, in many aspects this book still gives a good fundamental overview of what can be done with small-angle scattering, and how to perform a solid data analysis. In addition, this is literally the book on the Guinier Law, and where some of the basic ideas of reading scattering curves were first collected.

6.11.2 R.J. Roe: Methods of x-ray and neutron scattering in polymer science

Here the author nicely manages to emphasize the commonalities and differences between x-ray and neutron scattering. An overview of the methods and technologies is given, as well as a helpful mathematical appendix, reiterating some of the concepts used in the book.

6.11.3 G. Strobl: The physics of polymers

For soft-matter researchers this book, even though not being focused on scattering as such, gives a good overview of applicable concepts for scattering with soft-matter samples. A wide range of helpful examples highlight in which particular area any evaluation concept of the data is applicable and useful.

References

- [1] A. Guinier, P. Lorrain, D. S.-M. Lorrain, and J. Gillis, "X-ray diffraction in crystals, imperfect crystals, and amorphous bodies," *Physics Today*, vol. 17, p. 70, 1964.
- [2] H. Stabinger and O. Kratky, "A new technique for the measurement of the absolute intensity of x-ray small angle scattering. the moving slit method," <https://iftex.fz-juelich.de/project/667ac3efb3b195385c5ff1a4> *Die Makromolekulare Chemie*, vol. 179, no. 6, pp. 1655–1659.
- [3] E. Kentzinger, M. Krutyeva, and U. Rücker, "Galaxi: Gallium anode low-angle x-ray instrument," *Journal of large-scale research facilities JLSRF*, vol. 2, p. 61, 2016.
- [4] H. Haubold, P. Hiller, H. Jungbluth, and T. Vad, "Characterization of electrocatalysts by in situ saxs and xas investigations," *JAPANESE JOURNAL OF APPLIED PHYSICS-SUPPLEMENT*, vol. 38, no. 1, pp. 36–39, 1999.
- [5] S. Roth, G. Herzog, V. Körstgens, A. Buffet, M. Schwartzkopf, J. Perlich, M. A. Kashem, R. Döhrmann, R. Gehrke, A. Rothkirch, *et al.*, "In situ observation of cluster formation during nanoparticle solution casting on a colloidal film," *Journal of Physics: Condensed Matter*, vol. 23, no. 25, p. 254208, 2011.
- [6] B. Hammouda, "A tutorial on small-angle neutron scattering from polymers," *Gaithersburg: National Institute of Standards and Technology*, 1995.
- [7] D. Tong, "Lectures on topics in quantum mechanics: Scattering theory," 2017.
- [8] B. Weyerich, J. Brunner-Popela, and O. Glatter, "Small-angle scattering of interacting particles. ii. generalized indirect fourier transformation under consideration of the effective structure factor for polydisperse systems," *Journal of Applied Crystallography*, vol. 32, no. 2, pp. 197–209, 1999.
- [9] A. Koutsioubas, S. Jaksch, and J. Pérez, "Denfert version 2: extension of ab initio structural modelling of hydrated biomolecules to the case of small-angle neutron scattering data," *Journal of applied crystallography*, vol. 49, no. 2, pp. 690–695, 2016.
- [10] T. D. Grant, "Ab initio electron density determination directly from solution scattering data," *Nature methods*, vol. 15, no. 3, p. 191, 2018.
- [11] A. Guinier, *X-ray diffraction in crystals, imperfect crystals and amorphous bodies*.
- [12] R. Roe, *Methods of x-ray and neutron scattering in polymer science*.

Exercises

- 1.) The resolution of a SANS experiment is determined by
 - The chosen wavelength
 - The proportion of elastic and inelastic scattering from the sample
 - The sample size

- 2.) Which components of a SANS instrument define the beam?
 - Monochromator/Choppers
 - Slits
 - Detector

- 3.) Which pairs are correct, when trying to understand a SANS curve?
 - Forward scattering: Aggregation
 - Guinier Regime: Size of particles
 - Porod Regime: Size of particles

- 4.) The difference between coherent and incoherent scattering in SANS and SAXS is
 - Core/neutron interactions do not allow for pure elastic scattering
 - Current SANS instruments are not developed enough to suppress incoherent scattering
 - For isotopically pure samples, there would be no difference

- 5.) Form Factors ...
 - ... are used to deal with the phase problem
 - ... are used because experimenters are lazy and like quick answers
 - ... do not render unique results

- 6.) Contrast matching experiments
 - are unique to neutron experiments
 - are possible because different isotopes give different contrasts
 - distort the results, because the sample chemistry is changed

- 7.) The Structure Factor
 - can be calculated by the experimental setup of the instrument

- () encodes the correlation between particles in the sample
- () shows the structure of the scattering particles

8.) Find the first two roots of the intensity scattered by a sphere. Use this value to create a sketch that:

- 1.) Shows the scattered intensity by a sphere
- 2.) Indicate a change happening by increased polydispersity
- 3.) Indicates aggregation of large particles in the sample

Bonus: What would this curve look like if there was no aggregation, but the particles would push away from each other?

9.) Decide and explain which properties of the scattering curve you need to evaluate if you are interested in

- a) the particle size
- b) the size distribution
- c) shape of the particle
- d) interaction between the particles

10.) At zero-th order, all particles can be approximated by a sphere. Conceptualize that thought. Using this knowledge, derive a solution for the Q-dependence of the Porod-Regime and the Guinier Regime.

7 Macromolecules (structure)

J. Stellbrink

Jülich Centre for Neutron Science 1

Forschungszentrum Jülich GmbH

Contents

7.1	Introduction	2
7.2	Polymers in dilute solution	2
7.2.1	Linear polymers.....	2
7.2.2	Branched polymers.....	6
7.2.3	In-situ experiments during polymerisation.....	9
7.3	Block copolymer Micelles	10
7.3.1	Form factor.....	11
7.3.2	Micellar exchange dynamics.....	12
7.3.3	Structure factor.....	13
	Appendices	15
A7.1	Scattering of a polymer	15
A7.2	The ultra-soft potential (Likos-Potential)	16
	References	18
	Exercises	19

Lecture Notes of the JCNS Laboratory Course Neutron Scattering. This is an Open Access publication distributed under the terms of the Creative Commons Attribution License 4.0, which permits unrestricted use, distribution, and reproduction in any medium, provided the original work is properly cited. (Forschungszentrum Jülich, 2024)

7.1 Introduction

Macromolecules are an integral part of Soft and Living Matter. In *Living Matter*, macromolecule-based functional systems are built from molecular units consisting of only a few different building blocks: amino acids are assembled into proteins, which in turn function individually, or cooperatively in nano- and micro-machines. The secret of success is the intrinsic hierarchical structuring over a large range of length scales. In *Soft Matter*, synthetic macromolecules are of much simpler structure. Nevertheless, there is a vast variety of material properties that can be realized with synthetic macromolecules. Theoretical concepts have been developed, and are essential for the rational design of soft materials, that are of paramount importance in a multitude of technical applications.

Synthetic polymers have crucially changed daily life since its development in the 1930ies. Modern polymers can be divided into two major classes (i) commodity polymers for daily life use which are produced in millions of tons per year and (ii) specialty polymers for high-performance applications which are niche products but highly profitable [1]. Typical commodity polymers are polyolefines like polyethylene (PE) or polypropylene (PP) used for packaging, films etc. Examples for specialty polymers are polydimethylsiloxane (PDMS) derivatives used in dental implants.

Currently, both classes of polymers in use are based on petrochemical feedstock, thus considered not “carbon-neutral” and “environment-friendly”. Due to changing global conditions and growing concerns about the mounting disposal problems, research on sustainable commodity polymers has been intensified during the last decade, both on the level of fundamental research and applied science [2]. To find the required balance between material properties and bioavailability/-degradability is the key for establishing sustainable polymers on a large scale industrial level and therefore a major challenge of future polymer science.

The development of new biomimetic specialty polymers is another major challenge. Biopolymers, like spider silk, are high-performance materials with material properties superior to any synthetic polymer. To transfer these properties to artificial biomimetic polymers, one has to fully understand, on the molecular level, the structure-property-relationships and enzymatic synthesis processes in living organisms.

In this lecture some recent applications of neutron scattering methods to characterize quantitatively on a microscopic length scale structure and interactions of synthetic macromolecules and its hierarchical structuring are given. A more comprehensive overview is found e.g. in [3].

7.2 Polymers in dilute solution

7.2.1 Linear polymers

A linear polymer is a sequence of molecular repetition units, the monomers, continuously linked by covalent bonds. The degree of polymerisation, D_p , i.e. the number of monomers constituting the polymer, the (weight average) molecular weight, $M_w = D_p M_m$, with M_m the molecular weight of the monomer, and the radius of gyration, $R_g \sim M_w^v$, are the most important structural parameters of a polymer. On a coarse-grained level, structural details arising from the explicit chemical composition of the polymer like bond lengths and angles can be neglected and what remains is the so-called scaling relation given above

that links molecular weight to size and which is generally valid for all polymers [4]. The numerical value of the scaling exponent ν depends on the strength of interactions. In the so called θ -state, when monomer-monomer interactions are as strong as monomer solvent interactions, the polymer structure can be described by a random walk, therefore Gaussian chain statistics are valid and $\nu=1/2$, see Appendix A7.1. When monomer solvent interactions are stronger than monomer-monomer interactions, so called excluded volume forces are effective, the polymer chain is “swollen” and $\nu=3/5$.

Here one has to emphasize that synthetic polymers, unlike biopolymers, always have an intrinsic polydispersity, i.e. there is a distribution of molecular weights. The polydispersity is given usually in terms of M_w/M_n , with M_n the number average molecular weight. Its precise number depends on the polymerisation reaction by which the polymer was synthesized. For a (theoretical) monodisperse polymer $M_w/M_n=1$ holds, the most monodisperse synthetic polymers with $M_w/M_n=1.02$ can be synthesized by “living” anionic polymerisation, classical polycondensation yields $M_w/M_n = 2$, radical polymerisation can even result in extremely broad distributions, $M_w/M_n > 10$.

Although in technical applications polymers are mostly used as bulk materials, polymer characterisation is usually performed in (dilute) solution. Historically, light scattering was the method of choice to characterise synthetic polymers [5], but nowadays size exclusion chromatography (SEC), also called gel permeation chromatography (GPC), is the standard technique to characterize routinely polymers [6].

Neutron scattering, due to its limited accessibility and high experimental costs, usually is found in basic academic research, but here it played a crucial role in confirming fundamental theoretical concepts of polymers [3].

For macromolecules the measured intensity $I(Q)$ can be expressed in first approximation as a product of particle form factor $P(Q)$ given by the *intramolecular* architecture, i.e. the particle geometry, and structure factor $S(Q)$ given by the *intermolecular* structure arising due to particle-particle interactions. Please note, that both $P(Q)$ and $S(Q)$ must be properly normalized, $P(Q)_{Q=0} = 1$ and $S(Q)_{QR \gg 1} = 1$, for details see chapter 6.9:

$$I(Q) = \frac{\Delta\rho^2}{N_a} \phi V_w P(Q) S(Q) \quad (7.1)$$

Here $\frac{\Delta\rho^2}{N_a}$ is the contrast factor, ϕ is the polymer volume fraction and $V_w = M_w/d$ is the molecular volume and d the polymer density in $[\text{g}/\text{cm}^3]$.

To characterize properly the *intramolecular* form factor $P(Q)$ one has therefore to investigate a concentration series in the dilute regime and extrapolate finally to infinite dilution. The form factor of a Gaussian chain (Debye function) is given by (for its derivation see Appendix A7.1).

$$f_D(x) = \frac{2}{x^2} (\exp(-x) - 1 + x) \quad (7.2)$$

With $x=Q^2 R_g^2$ and R_g the radius of gyration describing the overall dimension of the single polymer chain.

The Debye function describes the (ideal) polymer scattering well from length scales of the overall coil down to length scales where the polymer becomes locally rigid. The corresponding asymptotic limits are:

$$P(Q) \sim N \left(1 - \frac{1}{3} Q^2 R_g^2\right) \text{ for small } Q \quad (7.3)$$

$$\sim 2N / (Q^2 R_g^2) \text{ for large } Q \quad (7.4)$$

Equation 7.3 describes the conventional Guinier scattering of the overall polymer (compare chapter 6.10.2, equation 6.58), equation 7.4 describes a power law. At these length scales, the sub-chains of different lengths are self-similar and so they reveal a fractal behaviour. The prefactor is connected to the magnitude R_g^2/N that is the effective segment size. From this magnitude, one can calculate back to the local rigidity that is responsible for the effective segments.

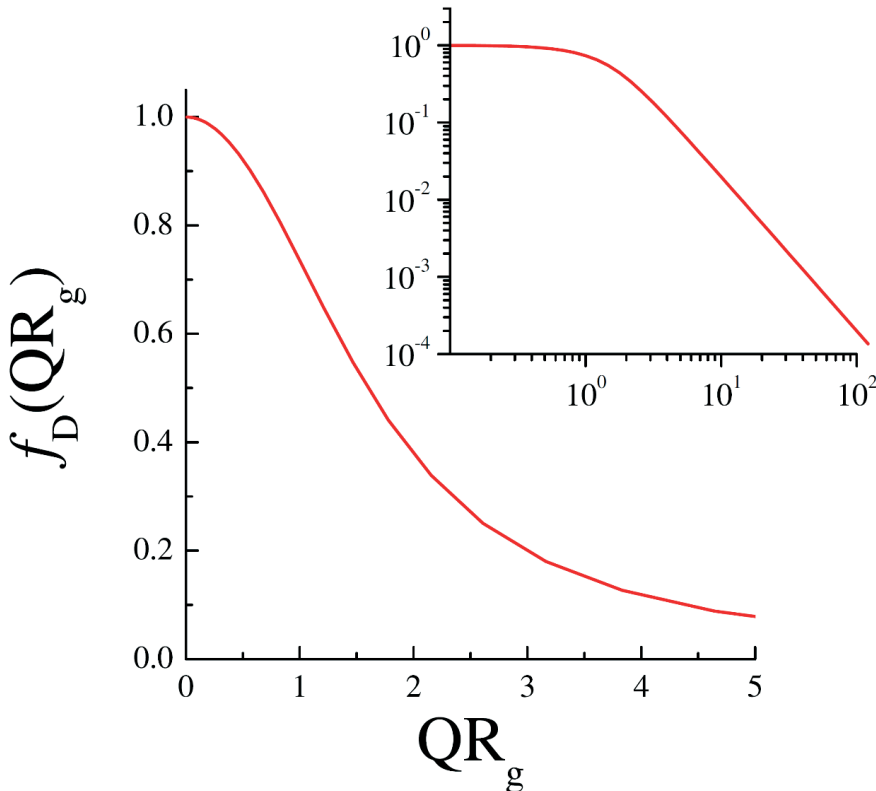


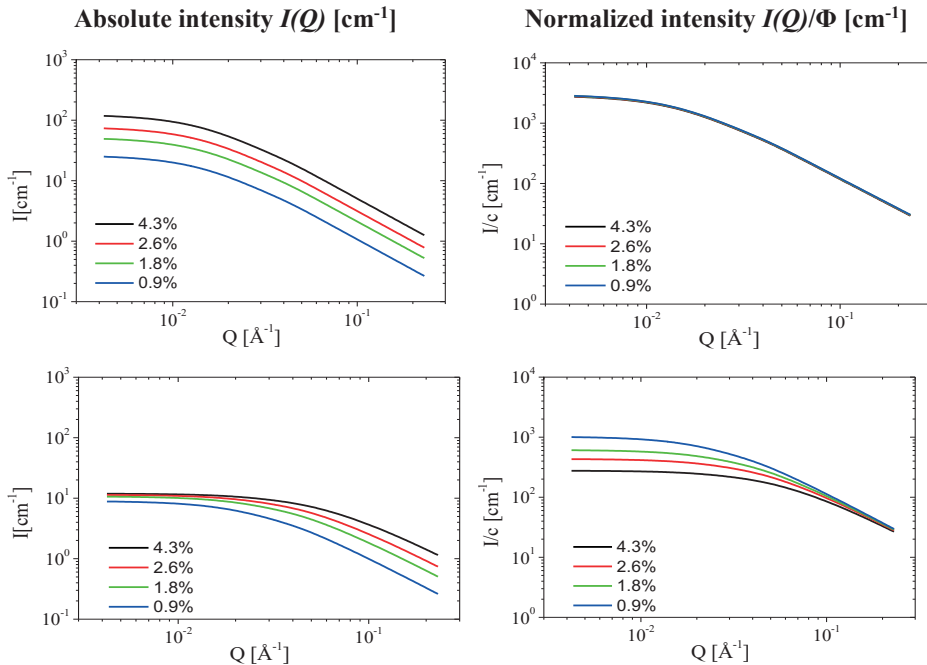
Figure 7.1: The theoretical Debye function, equation 7.2, describes the polymer scattering of independent polymers without interaction. The two plots show the function on a linear and double logarithmic scale.

Particle-particle interactions as seen in $S(Q)$ are weak in the dilute regime, but still effective, so that one can apply the virial expansion.

$$\phi / I(Q=0) = 1/V_w + 2A_2\phi + \dots \tag{7.5}$$

Equation 7.5 is formulated neglecting the contrast factor so it holds for all types of scattering experiments, i.e. SANS, SAXS and SLS. A crucial concentration separating dilute and semi-dilute regime is the so-called overlap concentration $\phi^* = (V_w/N_a) / (\frac{4}{3}\pi R_g^3)$, which describes the “internal concentration” per volume of a single polymer chain.

The value of the second virial coefficient A_2 directly reflects particle-particle interactions, i.e. a positive A_2 is found for repulsive interactions (good solvent i.e. excluded volume interactions), a negative one for attractive interactions (marginal/bad solvent) and finally $A_2=0$ characterizes no interactions (θ -solvent). Without any data fitting, this distinction can easily be made by plotting the intensity data $I(Q)$ of a concentration series normalized to the corresponding volume fractions $I(Q)/\phi$ (Since scattering arises due to an exchange of a volume element of solvent by a volume element of polymer with different scattering contrast, the natural concentration unit for any scattering experiment should be volume fraction ϕ). This is schematically shown in Figure 7.2. If no particle-particle interactions are present all data for all Q -vectors exactly fall on top of each other.



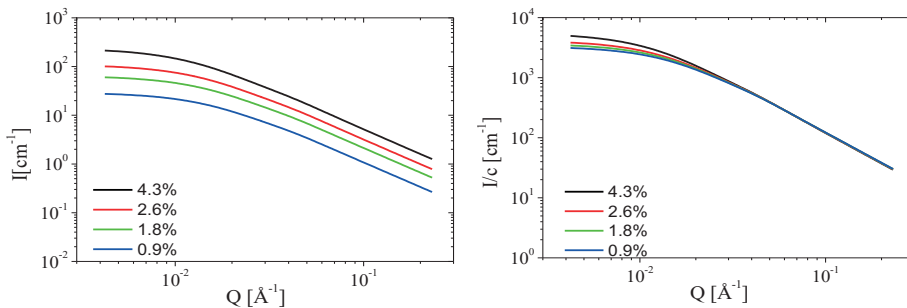


Figure 7.2: Calculated scattering intensities in absolute units $I(Q)$ (left) and normalized to polymer volume fraction $I(Q)/\phi$ (right) for solutions of a linear polymer at different volume fractions given in percent, see legends, assuming a virial ansatz for particle interactions. From top to bottom: No interactions $A_2=0$ (θ -solvent, repulsive interactions $A_2>0$ good solvent, attractive interactions $A_2<0$ marginal or bad solvent).

Irrespective what kind of interactions are present this also holds for high Q -vectors, since high Q -vectors mean small length scales and the local (*intramolecular*) structure is not affected by particle-particle interaction ($S(Q)=1$). In contrary, at low Q -vectors there are crucial differences between the individual concentrations in this representation. For repulsive interactions the forward scattering is reduced by $S(Q)$ therefore the lowest concentration shows the highest normalized intensity. For attractive interactions, on the other hand, the forward scattering is increased by $S(Q)$, therefore the lowest concentration shows the lowest normalized intensity. This sequence can be easily understood, because attractive interactions finally result in clustering of the individual particles.

For more details about synthesis and characterisation of macromolecules the interested reader is referred to standard textbooks e.g. [7], [8].

7.2.2 Branched polymers

Branching crucially influences the mechanical properties of polymers therefore characterisation and control of branching reactions during polymerisation processes are of vital interest not only for polymer industry to tune semi-empirically material properties, but also for fundamental research to derive a proper quantitative structure property relationship.

The simplest branched polymer is a regular star polymer, where f arms, each of same molecular weight $M_{w,arm}$, are emanating from a microscopic central branch point, the star core. Experimentally, such regular star polymers are nowadays most precisely realized by using chlorosilane dendrimers as branch points. The arms forming the star corona or shell are grafted to the dendrimer core by “living” anionic polymerisation [9]. The precise control of the dendrimer generation is reflected in the precise functionality of the final star polymer so that functionalities as high as $f=128$ can be achieved. However, with increasing functionality there is a polydispersity in functionality since the last arms are extremely difficult to graft since they have to diffuse through the already very crowded star polymer corona to react at the star core [10].

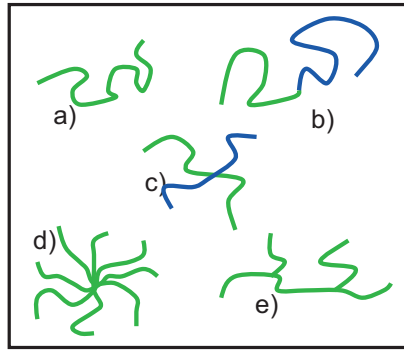


Figure 7.3: Schematic illustration of different polymer architectures: a) linear homopolymer, b) linear block copolymer, c) regular mikto-arm star polymer ($f=4$), d) regular star polymer ($f=8$), and e) comb polymer.

The form factor of a regular star polymer with Gaussian chain statistics has been derived by Benoit already in 1953 [11].

$$P_{star}(Q) = \frac{2}{f_w Q^4 R_{g,arm}^4} \times \left[Q^2 R_{g,arm}^2 - \left(1 - e^{-Q^2 R_{g,arm}^2}\right) + \frac{f_w - 1}{2} \left(1 - e^{-Q^2 R_{g,arm}^2}\right)^2 \right] \quad (7.6)$$

The overall size of the star polymer $R_{g,star}$ is related to the size of the individual arm by

$$R_{g,star} = \sqrt{\frac{(3f-2)}{f}} R_{g,arm}.$$

There is no rigorous analytical formula for a star polymer with swollen chain statistics, but experimental data for star polymers in a good solvent can be nicely described either by the Dozier function [12] or the approach derived by Beaucage [13]. His equation can be viewed as a "universal form factor" for an arbitrary mass fractal that can also be applied to many other polymeric systems:

$$P(Q) = G \cdot \exp(-Q^2 R_g^2 / 3) + B \left(\frac{1}{Q^*} \right)^P \quad (7.7)$$

with $Q^* = Q / [erf(QkR_g/\sqrt{6})]^3$. Here erf is the error function and G and B are amplitudes, which for mass fractals can be related to each other by $B = G \cdot P / R_g^P \cdot \Gamma(P)$ (polymeric constraint). P is the fractal dimension of the internal substructure, k an empirical constant found to be ≈ 1.06 and Γ is the Gamma function. The fractal dimension is related to the scaling exponent by $P=1/\nu$. The Beaucage expression can be nicely extended to describe hierarchical structures over multiple levels i $P(Q) = \sum_i P_i(Q)$ where $P_i(Q)$ are given by

Equation 7.7. Figure 7.4 shows form factors obtained for polybutadiene (PB) star polymers with varying functionality f but same $R_g \approx 50\text{nm}$ in *d*-cis-decalin.

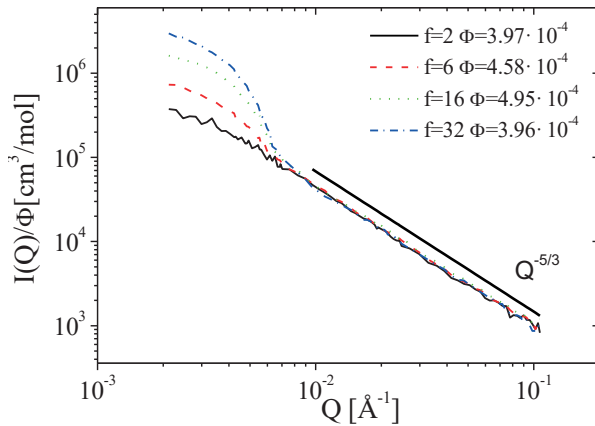


Figure 7.4: SANS intensity $I(Q)$ normalized by volume fraction ϕ for regular polybutadiene star polymers with varying functionality f but same radius of gyration $R_g \approx 50 \text{ nm}$. The asymptotic power law observed at high scattering vectors $I \sim Q^{-5/3}$ clearly indicates excluded volume interactions relevant in a good solvent, i.e. swollen chain statistics [14] (Reprinted by permission of Springer Nature: Springer, Appl. Physics A: Materials Science & Processing, partial structure factors in star polymer/colloid mixtures, J. Stellbrink et al., copyright 2007)

At low Q -vectors, $Q \leq 8 \times 10^{-3} \text{ \AA}^{-1}$, data could be modelled using the Benoit form factor, Equation 7.6 for a Gaussian star, which gives the explicit dependence on functionality f . For describing the complete data set we used the Beaucage form factor, Equation 7.7, which describes also the observed power law at high Q -vectors. One should note that this power law extends over more than one order of magnitude in Q and starts at the same Q -value of $\approx 8 \times 10^{-3} \text{ \AA}^{-1}$ for all f due to the same R_g . The observed power law slope of $I(Q) \sim Q^{-5/3}$ reflects the good solvent quality of cis-decalin for polybutadiene and decreases slightly with increasing f , indicating increasing arm stretching due to the increasing monomer density in the star corona.

The effect of branching becomes easily visible by using a so called Kratky representation, $I(Q) Q^2$ vs. Q . Whereas a linear polymer with Gaussian chain statistics reaches monotonically an asymptotic plateau, any branched structure shows a maximum. For the here discussed regular star polymer the height quantitatively depends on the arm number or functionality f , see figure 7.5.

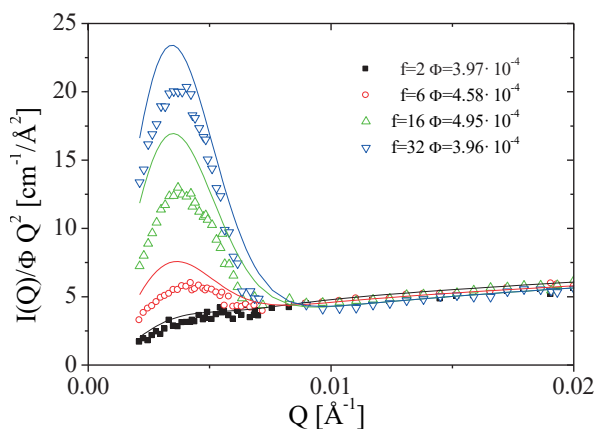


Figure 7.5: Kratky representation $I(Q) Q^2$ vs. Q for same data as in Figure 7.4. The increasing peak height with increasing functionality f due to branching becomes clearly visible as well as the discrepancy between experimental data (symbols) and Beaucage function used to model the data. The fact that no asymptotic plateau is observed results from the excluded volume interactions relevant in a good solvent, i.e. swollen chain statistics.

7.2.3 In-situ experiments during polymerisation

For understanding and controlling any chemical reaction a detailed understanding of reaction mechanism, type and role of intermediate species as well as reaction kinetics are prerequisite. How the microscopic structure of a growing polymer chain is evolving in the different steps of polymerisation reactions has to be resolved by non-invasive, real-time measurements. The ideal tool is small angle neutron scattering (SANS), since the microscopic structure of polymer-based materials can be resolved on a micrometer-to-nanometer-level by modern neutron scattering techniques. In addition, contrast variation, i.e. H/D exchange, can even “stain” certain parts of the polymers giving access to unprecedented structural information. So neutron scattering is a unique and outstanding technique to investigate polymerising systems in real-time, in particular since new, more powerful neutron sources became available worldwide (FRM-2, SNS, J-PARC). But for a complete description of the polymerisation process additional information in terms of reaction kinetics etc. are prerequisite. Thus, in-situ SANS experiments have to be supported by complementary methods like NMR, SEC, UV/VIS and IR spectroscopy, favourably also in real-time mode.

Recently we investigated reaction mechanism and kinetics of different polymerisation techniques like “living” anionic polymerisation [15] or post-metallocene catalyzed olefin polymerisation [16] by such an in-situ multi technique approach. Figure 7.6 shows time resolved SANS intensities $I(Q)$ in absolute units obtained during the polymerisation of 1-octene by a pyridylamidohafnium catalyst in toluene at 20°C. Experiments have been performed using the KWS-1 instruments at the former FRJ-2 reactor in Jülich which allowed a temporal resolution of about several minutes.

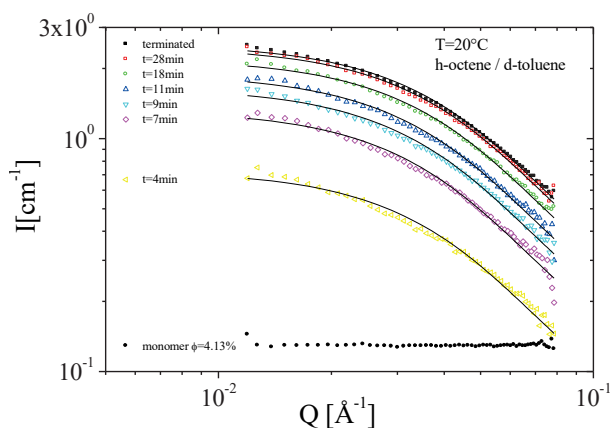


Figure 7.6: Time resolved SANS intensities $I(Q)$ in absolute units obtained during the polymerisation of 1-octene by a pyridylamidohafnium catalyst in toluene at 20°C [16] (reprinted with permission from *Macromolecules*, **42**, 1083, 2009. Copyright 2009, American Chemical Society)

The monomer solution shows a Q -independent intensity over the whole accessible SANS Q -range typical for small molecules, which act as “incoherent scatterers”. Note by: the actual incoherent background for all components, as described in Chapter 6, can be estimated by $\frac{d\Sigma(Q)^{inc}}{\Omega} = \frac{\Sigma\sigma_i^{inc} N_A}{4\pi V_w}$. After four minutes a polymer is already formed and the Q -dependence of the intensity can be described by a Beaucage form factor, equation 7.7. With ongoing polymerisation, increasing polymerisation time t the general shape of $I(Q)$ does not change any further, only the forward scattering $I(Q=0)$ is increasing due to the increasing molecular weight and concentration of the growing polymer chain. Finally, the polymerisation is almost finished after half an hour as can be seen by comparison with the terminated polymer. A detailed quantitative analysis of $I(Q,t)$ reveals that during this type of polymerisation reaction no aggregation phenomena of the growing polymer chain are relevant. Similar experiments at high flux sources allow today temporal resolutions smaller than 1 second if experiments are repetitively performed using a stopped flow mixer.

7.3 Block copolymer Micelles

When amphiphilic block copolymers are dissolved in a selective solvent, i.e. a solvent which is good for one block but a precipitant for the other, they spontaneously self-assemble into supramolecular aggregates known as micelles, in which the insoluble block forms the inner part or core, whereas the soluble block forms a solvent-rich shell or corona. The general behaviour of block copolymers in selective solvents has been subject of copious theoretical and experimental studies during the past decades. They are reviewed in several books [17] [18] and review articles [19][20] related to this topic. Extensive studies demonstrated that the micellar morphology can be tuned (going from spheres, cylinders, worms and vesicles) by varying the block-copolymer molecular weight, the chemical nature and the ratio of the blocks. One of the most extensively studied block-copolymers is poly(butadiene-ethylene oxide) (PB-PEO). As a function of

the hydrophilic block length (in term of PEO weight fraction w_{PEO}) spherical micelles ($w_{\text{PEO}} > 0.6$), worm-like micelles, WLM ($0.47 \leq w_{\text{PEO}} \leq 0.59$) or bilayers ($w_{\text{PEO}} < 0.47$) are formed. Different theoretical studies contributed to define the scaling laws for the parameters of equilibrium structures. Among them, a quantitative theory defining the thermodynamic stability of different morphologies in selective solvents has been recently developed [21]. The theory expresses the free energy contributions of the core, the corona and the interface as a function of the blocks structural parameters and the interfacial tension between the solvent and the insoluble block for different micellar morphologies. Solvent selectivity can be more easily tuned than the above mentioned parameters (molecular weight, block ratio etc) and moreover in a continuous way by varying the solvent composition. Therefore, solvent composition is a very natural and easy parameter to control the micellar structures. The change in the morphology of the self-assembled structures can be attributed to a change of solvent selectivity, which influences the different energy contributions responsible for the morphology: core-chain stretching, corona-chain repulsion and interfacial tension between the core and the solution.

The interest is to relate changes on the smallest relevant length scale, i.e. diameter and aggregation number per unit length, density profile in the corona, to changes in the macroscopic structure, i.e. the contour and persistence length of wormlike micelles and the transition from wormlike-to-spherical micelles etc. This molecular level understanding can help to elucidate the mechanisms involved in non-equilibrium conditions. Besides, it is expected that these quantities have a pronounced effect on the rheological behavior of the systems, and as such solvent composition could be used to tune the flow properties of micellar solutions.

7.3.1 Form factor

Figure 7.7 (left) shows the partial form factor normalized to volume fraction Φ , $P(Q)/\Phi$, in shell and core contrast for micelles formed by a symmetric amphiphilic block copolymer poly(ethylene-alt-propylene)-poly(ethylene oxide), h-PEP4-dh-PEO4 (the numbers denote the block molecular weight in kg/mol) [22]. Already, a qualitative discussion of the data reveals important features of the micellar architecture. First, the forward scatterings, $I(Q=0)$, in the two contrasts are the same. This is expected for micelles formed by a symmetric diblock copolymer in shell and core contrast (we should note that the two blocks have the same molar volume V_w) and is in this sense a proof of the applied contrast conditions. This means that the scattering profiles shown in figure 7.7 are directly reflecting pure shell and core properties. Second, both scattering profiles show well defined maxima and minima, up to four in core contrast, which arise from sharp interfaces typical for a monodisperse, compact spherical particle, see chapter 6, equation 6.33. These minima occur whenever $QR = \tan(QR)$, i.e. at $QR = 4.493, 7.725, \dots (n + 1/2) \pi$ (We should note that one has to consider that these oscillations are already smeared by the instrumental resolution function, so the data shown offer even more confirmation of the strong segregation between the core and corona and the low polydispersity of the micelles).

Also shown is Porod's law $I \sim Q^{-4}$, which describes the limiting envelope of all form factor oscillations. We should emphasize that in core contrast no *blob* scattering is visible [22]. This also corroborates the compact PEP core. A quantitative analysis in terms of a core-shell model gave the following micellar parameters: aggregation number $P = 1600$,

core radius $R_{\text{core}} = 145 \text{ \AA}$ and shell radius $R_{\text{m}} = 280 \text{ \AA}$ with a polydispersity of $\approx 5\%$. The solvent fraction in the swollen shell is $\Phi_{\text{solv}} = 60\%$.

Figure 7.7 (right) shows the corresponding partial form factor data, $P(Q)/\Phi$, in shell and core contrast for an asymmetric h-PEP1-dh-PEO20. The differences compared to figure 7.7 (left) are obvious: the difference in forward scattering of the two contrasts is reflecting the asymmetry of the block copolymer. Moreover, no maxima or minima are visible (also not at high Q in core contrast) and the power law observed in shell contrast has a slope of only $I \sim Q^{-5/3}$, which is typical for a polymer chain in a good solvent and arises from the swelling of the PEO in the shell (*blob* scattering). A quantitative analysis gives the following micellar parameters: aggregation number $P = 130$, core radius $R_{\text{core}} = 34 \text{ \AA}$ and shell radius $R_{\text{m}} = 260 \text{ \AA}$.

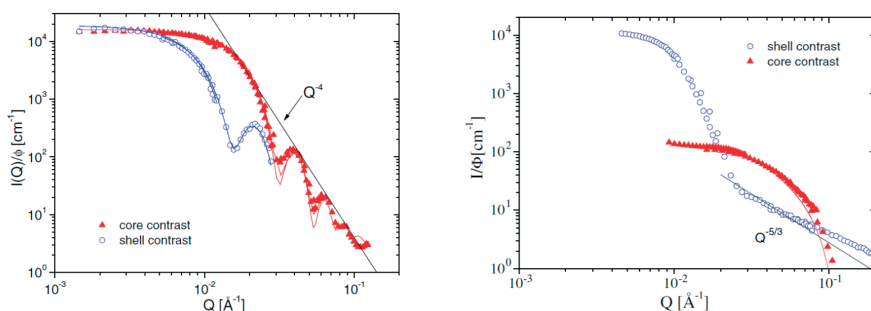


Figure 7.7: Form factors of block copolymer micelles with varying architecture in core (red) and shell contrast (blue). Left symmetric PEP4-PEO; right asymmetric PEP1-PEO20, the numbers denote the block molecular weight in kg/mole [22] (Reprinted by permission of IOP Publishing, copyright 2004).

7.3.2 Micellar exchange dynamics

Polymeric micelles are macromolecular analogues of well-known low-molecular surfactant micelles. As a consequence of random stochastic forces, the constituting chains will continuously exchange between the micelles. From the theory of Halperin and Alexander (HA), this exchange kinetics is expected to be dominated by a simple expulsion or insertion mechanism where single chains (unimers) are required to overcome a defined potential barrier [23]. Higher order kinetics including fusion and fission is not expected to take place since these mechanisms are neither favoured energetically nor entropically [24]. Experimentally, relatively few studies have been devoted to the exchange kinetics of polymeric micelles in equilibrium. This is most likely related to the associated experimental difficulties. Recently, we used a newly developed time resolved small angle neutron scattering (TR-SANS) technique [25]. This technique is perfectly suited for determination of exchange kinetics in equilibrium as, unlike other techniques; virtually no chemical or physical perturbations are imposed on the system. The labelling is restricted to a simple hydrogen/deuterium (H=D) substitution using fully hydrogenated (h) and fully deuterated (d) polymers with identical molar volumes and compositions. By mixing the corresponding H- and D-type micelles in a solvent with a scattering length corresponding to the average between the two, the kinetics can be determined. The average excess fraction of labelled chains residing inside the micelles is then simply

proportional to the square root of the excess SANS intensity. The corresponding correlation function is given by $R(t) = \{[I(t) - I_\infty]/[I(t=0) - I_\infty]\}^{1/2}$ was measured from a reference sample where the polymers have been completely randomized and $I(t=0)$ from the scattering of the reservoirs at low concentrations.

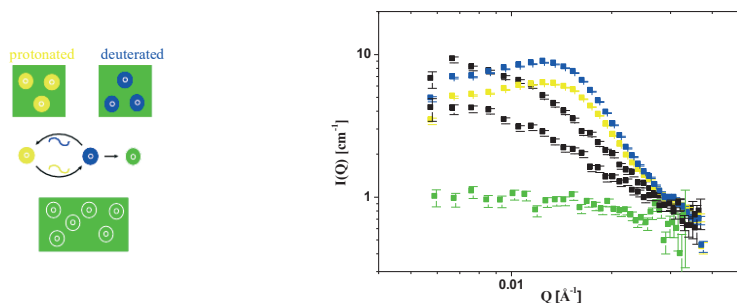


Figure 7.8: *Left: Schematic illustration of the TR-SANS technique to follow micellar exchange kinetics. Right: Corresponding time-resolved SANS data for PEP1-PEO20 micelles in H₂O/DMF 7:3 showing slow exchange (5min, 2h @ 50°C) (Reprinted by permission of Springer Nature: Adv. Polymer Sci., **184**, 1, 2013, Kinetics of Block Copolymer Micelles Studied by Small-Angle Scattering Methods, R. Lund et al., copyright 2013).*

7.3.3 Structure factor

How the structure factor $S(Q)$ can be derived from the pair correlation function $g(r)$ by liquid state theory has been shown in Chapter 6.9. $g(r)$ finally results from the effective pair potential $V(r)$, which describes the direct interactions between the solute only, after eliminating the rapidly moving degrees of freedom of the solvent molecules. From the position Q_{max} of the first peak in $S(Q)$ the average distance D between scattering particles can be derived by $D = 2\pi/Q_{max}$.

We recently showed that micelles formed by the amphiphilic block copolymer poly(ethylene-*alt*-propylene)–poly(ethylene oxide) (PEP–PEO) provide an interesting system to conveniently tune the ‘softness’ in terms of particle interactions (intermolecular softness) and the deformability of the individual particle (intramolecular softness). This is achieved by changing the ratio between hydrophobic and hydrophilic blocks from symmetric (1:1, Hard Sphere-like) to very asymmetric (1:20, star-like). One must emphasize that to approach the star-like regime is not a trivial task.

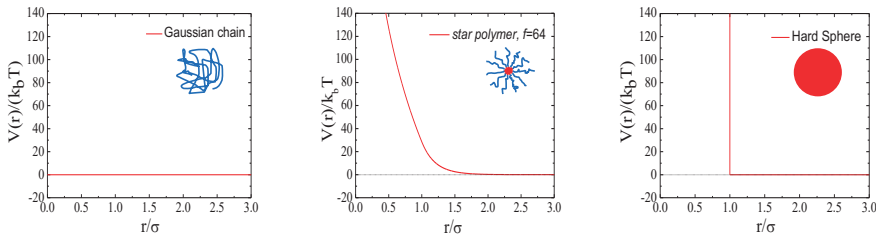


Figure 7.9: Different effective interaction potentials. The one for star polymers, i.e. soft colloids, is in-between the two limits Gaussian Chain (left) and Hard Spheres (right).

Figure 7.9 compares the effective interaction potential for soft colloids to those of the limiting cases Gaussian Chain, i.e. no interactions, and Hard Spheres, i.e. infinite strength of the potential at contact. The explicit form of $V(r)$ for star polymers, the limiting ultra-soft colloids, was derived by Likos et al. [26] and is explained in detail in Appendix 7.1.

Figure 7.10 shows the corresponding experimental structure factors $S(Q)$ for Hard Sphere and Soft interactions and its comparison with theoretical predictions.

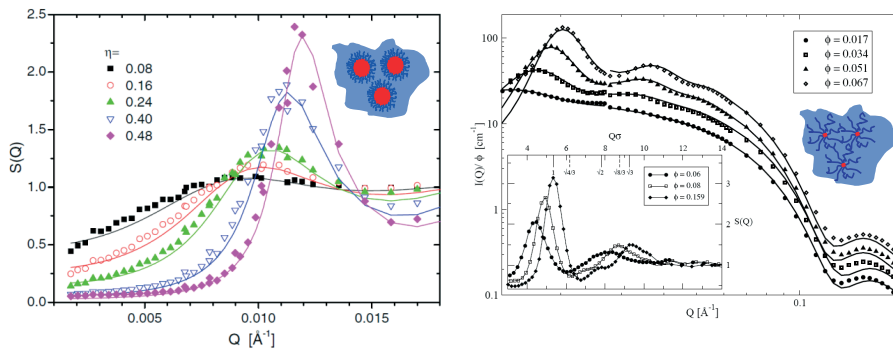


Figure 7.10: Experimental structure factor $S(Q)$ of block copolymer micelles with varying architecture obtained by SANS in core contrast (symbols) and the theoretical description (lines) resulting from the corresponding interaction potentials: Symmetric PEP4-PEO4 / Hard Sphere potential left, asymmetric PEP1-PEO20/ ultra soft potential right, see text and [22] (Reprinted by permission of IOP Publishing, copyright 2004) [28] (Reprinted by permission of American Physical Society, copyright 2005).

Appendices

A7.1 Scattering of a polymer

In this section we derive the scattering of a single (isolated) polymer coil. This model is the basis for many more complicated models of polymers in solution, polymeric micelles, polymer melts, diblock and multiblock copolymers and so on. So the understanding of these concepts is rather important for scattering experiments on any kind of polymer systems.

This example starts apart from many other calculations from point-like. These monomers are found along a random walk with an average step width of l_k . We try to argue for non-ideal chain segments, but finally will arrive at an expression for rather ideal polymers.

For the scattering function we obtain:

$$P(Q) \propto \frac{1}{N} \sum_{j,k=0}^N \langle \exp(iQ(R_j - R_k)) \rangle \quad (7.8)$$

$$\propto \frac{1}{N} \sum_{j,k=0}^N \exp\left(-\frac{1}{2} (Q(R_j - R_k))^2\right) \quad (7.9)$$

$$\propto \frac{1}{N} \sum_{j,k=0}^N \exp\left(-\frac{1}{6} Q^2 (R_j - R_k)^2\right) \quad (7.10)$$

At this stage, we use statistical arguments (i.e. statistical physics). The first rearrangement of terms (equation 7.8) moves the ensemble average of the monomer positions (and distances ΔR_{jk}) from the outside of the exponential to the inside. This is an elementary step which is true for polymers. The underlying idea is that the distance ΔR_{jk} arises from a sum of $|j-k|$ bond vectors which all have the same statistics. So each sub-chain with the indices jk is only distinguished by its number of bond vectors inside. The single bond vector b_j has a statistical average of $\langle b_j \rangle = 0$ because there is no preferred orientation. The next higher moment is the second moment $\langle b_j^2 \rangle = l_k^2$. This describes that each bond vector does a finite step with an average length of l_k . For the sub-chain we then find an average size $\langle \Delta R_{jk}^2 \rangle = |j-k| l_k^2$. The reason is that in the quadrature of the sub-chain only the diagonal terms contribute because two distinct bond vectors show no (or weak) correlations.

Back to the ensemble average: The original exponential can be seen as a Taylor expansion with all powers of the argument $iQ\Delta R_{jk}$. The odd powers do not contribute with similar arguments than for the single bond vector $b_j=0$. Thus, the quadratic term is the leading term. The reason why the higher order terms can be arranged that they finally fit to the

exponential expression given in equation 7.9 is the weak correlations of two distinct bond vectors. The next line equation 7.10 basically expresses the orientational average of the sub-chain vector ΔR_{jk} with respect to the Q -vector in three dimensions.

This derivation can be even simpler understood on the basis of a Gaussian chain. Then every bond vector follows a Gaussian distribution (with a centre of zero bond length). Then the ensemble average has the concrete meaning $\langle \dots \rangle = \int \dots \exp(\frac{3}{2} \Delta R_{jk}^2 / (|j-k| l_k^2)) d^3 \Delta R_{jk}$. This distribution immediately explains the rearrangement of equation 7.4. The principal argument is the central limit theorem: When embracing several segments as an effective segment any kind of distribution converges to yield a Gaussian distribution. This idea came from Kuhn who formed the term Kuhn segment. While elementary bonds still may have correlations at the stage of the Kuhn segment all correlations are lost, and the chain really behaves ideal. This is the reason why the Kuhn segment length l_K was already used in the above equations.

In the following we now use the average length of sub-chains (be it Kuhn segments or not), and replace the sums by integrals which is a good approximation for long chains with a large number of segments N .

$$P(Q) \propto \frac{1}{N} \int_0^N dj \int_0^N dk \exp\left(-\frac{1}{6} Q^2 (j-k) l_K^2\right) \quad (7.11)$$

$$= N f_D(Q^2 R_g^2) \quad (7.12)$$

$$f_D(x) = \frac{2}{x^2} (\exp(-x) - 1 + x) \quad (7.13)$$

In this integral one has to consider the symmetry of the modulus. The result is basically the Debye function which describes the polymer scattering well from length scales of the overall coil down to length scales where the polymer becomes locally rigid.

A7.2 The ultra-soft potential (Likos-Potential)

The effective potential $V(r)/k_b T$ between star polymers as a function of functionality f and interaction length σ was derived by by Likos et al. [26]. The interaction length σ is the distance between two star centres when the outermost blob overlaps. For larger distances two stars interact via a screened Yukawa-type potential whereas at distances smaller than σ when there is overlap of the star coronas, the potential has an ultra-soft logarithmic form.

$$\frac{V(r)}{k_b T} = \begin{cases} \frac{5}{18} f^{3/2} (1 + \sqrt{f}/2)^{-1} (\sigma/r) \exp\left[-\sqrt{f} (r - \sigma)/2\sigma\right] & (r > \sigma) \\ \frac{5}{18} f^{3/2} \left[-\ln(r/\sigma) + (1 + \sqrt{f}/2)^{-1}\right] & (r \leq \sigma) \end{cases} \quad (7.14)$$

All numerical factors have been chosen in such a way that the potential as well as its first derivative are smooth at crossover. Figure 7.12 shows the Likos-potential for different functionalities. At $f = \infty$ the Hard Sphere potential is recovered.

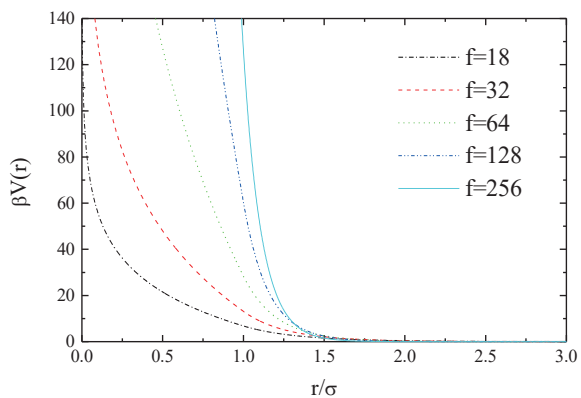


Figure 7.12: *Effective potential $V(r)/k_bT$ between star polymers with varying functionality f .*

References

- [1] C J.R. Severn and J.C. Chadwick, *Tailor-Made Polymers*, (Wiley-VCH, Weinheim, 2008)
- [2] G.W. Coates and M.A. Hillmyer, *Polymers from Renewable Resources*, *Macromolecules*, VI2, 7987 (2009); C.K. Williams, M.A. Hillmyer, *Polymer Rev.* 48, 1 (2008)
- [3] J. S. Higgins and H. C. Benoit, *Polymers and Neutron Scattering*; (Clarendon Press, Oxford, U.K., 1994).
- [4] P.G. De Gennes, *Scaling Concepts in Polymer Physics*, (Cornell University Press, 1979)
- [5] W. Brown, *Light Scattering: Principles and development*, (Oxford University Press, 1996)
- [6] S. Mori and H.G. Barth, *Size Exclusion Chromatography*, (Springer, 1999)
- [7] P.J. Flory, *Principles of Polymer Chemistry*, (Cornell University Press, 1953)
- [8] H.G. Elias, *Macromolecules*, (Wiley-VCH, Weinheim, 2009)
- [9] G. S. Grest, L. J. Fetters, J. S. Huang, and D. Richter, *Adv. Chem. Phys.* 94, 67 (1996)
- [10] J. Allgaier, K. Martin, H. J. Räder, and K. Müllen, *Macromolecules* 32, 3190 (1999)
- [11] H.J. Benoit, *J. Polym. Sci.*, 11, 507 (1953).
- [12] William D. Dozier, John S. Huang, Lewis J. Fetters, *Macromolecules* 24 2810 (1991)
- [13] G. Beaucage, *J. Appl. Crystallogr.* 28, 717(1995)
- [14] J. Stellbrink et al., *Applied Physics A* 74, S355 (2002)
- [15] J. Stellbrink et al. *Macromolecules*, 31, 4189 (1998)
- [16] A.Z. Niu et al., *Macromolecules* 42 1083 (2009)
- [17] I.W. Hamley, *The Physics of Block Copolymers*; (Oxford University Press: New York, 1998)
- [18] M. Antonietti and S. Förster, *Vesicles and Liposomes: A Self-Assembly Principle Beyond Lipids*, Vol. 15, (WILEY-VCH Weinheim, , 2003)
- [19] G. Riess, *Prog. Polym. Sci.* 28, 1107 (2003)
- [20] A. Halperin, M. Tirell and T.P. Lodge, *Adv. Polym. Sci.* 100, p31 (1990).
- [21] E.B. Zhulina, M. Adam, I. LaRue, S.S. Sheiko, M. Rubinstein, *Macromolecules* 38, 5330 (2005)
- [22] J. Stellbrink, G. Rother, M. Laurati, R. Lund, L. Willner and D. Richter, *J. Phys.: Cond. Matter*, 16, S3821 (2004)
- [23] A. Halperin and S. Alexander, *Macromolecules* 22, 2403 (1989)
- [24] E. Dormidontova, *Macromolecules* 32, 7630 (1999)
- [25] L. Willner, A. Poppe, J. Allgaier, M. Monkenbusch, and D. Richter, *Europhys. Lett.* 55, 667 (2001)
- [26] C.N. Likos et al., *Phys. Rev. Letters*, 80, 4450, (1998)
- [27] M. Watzlawek, C. N. Likos, and H. Lowen, *Phys. Rev. Lett.* 82, 5289 (1999).
- [28] M. Laurati, *Phys. Rev. Letters*, 94 195504 (2005)
- [29] B. Lonetti et al. *Phys. Rev. Letters*, 106, 228301 (2011)

Exercises

E7.1* Contrast or no contrast?

Due to synthetic (and financial) limitations only protonated material is available for a SANS experiment, for both polymer (poly(ethylene propylene), PEP, and solvent dimethylformamide, DMF).

a) Calculate the contrast factor $\frac{\Delta\rho^2}{N_A}$ following equation 5.16 and 7.1.

b) What is the necessary molecular weight M_w to achieve a signal-to-background ratio of 5 at $Q=0$ for a given polymer volume fraction $\phi=0.01$? (Remember: The incoherent scattering contributes to the background too and there is an empirical “rule of thumb” that the experimental incoherent scattering is twice the theoretical value due to inelastic and multiple scattering!)

c) At which Q -value the signal vanishes in the background?

(Assuming good-solvent conditions with a prefactor 0.01 [nm] for the R_g - M_w -relation and assuming the Guinier approximation for $P(Q)$)

d) For which combination of molecular weight and volume fraction ϕ the experiment could be performed in the dilute regime, i.e. $\phi \leq 0.1\phi^*$?

Given are sum formulae and densities

$$\text{h-PEP} = \text{C}_5\text{H}_{10}, \quad d_{\text{PEP}} = 0.84 \text{ g/cm}^3$$

$$\text{h-DMF} = \text{C}_3\text{H}_7\text{NO}, \quad d_{\text{PEO}} = 0.95 \text{ g/cm}^3$$

and coherent and incoherent scattering lengths b_{coh} and b_{inc} in units [cm]:

$$\text{C: } b_{coh} = 6.65\text{E-13}, \quad b_{inc} = 0$$

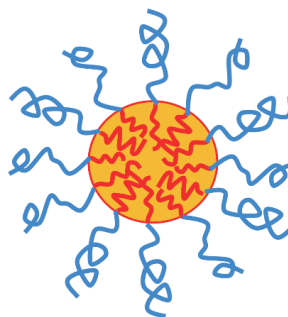
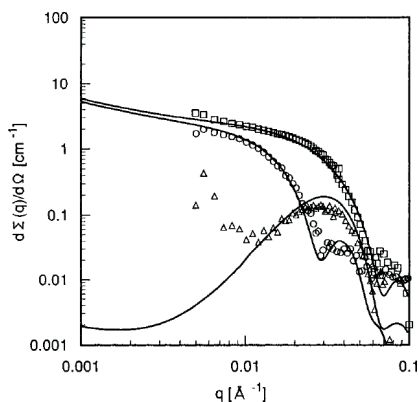
$$\text{H: } b_{coh} = -3.74\text{E-13}, \quad b_{inc} = 2.53\text{E-12}$$

$$\text{D: } b_{coh} = 6.67\text{E-13}, \quad b_{inc} = 4.04\text{E-13}$$

$$\text{O: } b_{coh} = 5.80\text{E-13}, \quad b_{inc} = 0$$

$$\text{N: } b_{coh} = 9.36\text{E-13}, \quad b_{inc} = 0$$

E7.2 Contrast Variation Experiment on Micelles



The three symbols \square , \circ and \triangle indicate the characteristic small angle scattering of spherical polymer micelles under different important contrast conditions. There are three conditions called: *shell contrast*, *core contrast* and *zero average contrast*. The *shell contrast* highlights the shell of the micelle (being hydrogenated) while the rest is deuterated. The *core contrast* highlights the core of the micelle (being hydrogenated) while the rest is deuterated. For the *zero average contrast* the average contrast of the deuterated core and the hydrogenated shell matches with the solvent.

Which condition can be connected to which symbol (or curve)?

- A \triangle -shell \circ -core and \square -zero
- B \circ -shell \square -core and \triangle -zero
- C \square -shell \triangle -core and \circ -zero

Why?

E7.3 Aggregation number of micelles

In aqueous solution, the diblock copolymer poly(ethylene propylene-block-ethylene oxide), PEP-PEO, forms spherical micelles, with PEP the non-soluble and PEO the soluble block. In dilute solution using core contrast, i.e. the scattering length density of the solvent is matched to the scattering length density of the micellar shell (formed by the soluble block PEO), the first form factor minimum is observed at $Q=0.12 \text{ \AA}^{-1}$.

Calculate

a.) the aggregation number N_{agg} , i.e. the number of diblock copolymers forming a single micelle, assuming full segregation, i.e. a non-swollen micellar core.

b.) How can N_{agg} derived in this way be cross-checked without performing another experiment?

Known are the monomer sum formulae and densities

h-PEP = C_5H_{10} , $d_{PEP}=0.84\text{g/cm}^3$

h-PEO = C_2H_4O , $d_{PEO}=1.12\text{g/cm}^3$

and the degree of polymerisation, D_p , of the blocks:

$D_{p,PEP} = 15$

$D_{p,PEO} = 40$

E7.4 Interactions of Gaussian chains

Calculate $S(Q)$ for Gaussian chains at a volume fraction $\phi = \phi^*$.

E7.5 Peak position in $S(Q)$

A solution of compact spherical colloids, $R=250\text{\AA}$, with volume fraction 0.25 should be characterised by SANS. At which Q -vector do you expect the first peak in the structure factor $S(Q)$ to appear?

E7.6 Structure factor contributions

Which type of particle interactions can be determined from the total scattering intensity $I(Q)$ at high scattering vectors only?

- A. Repulsive interactions
- B. Attractive interactions
- C. No interactions at all

8 Spin-dependent and Magnetic Scattering of Polarized Neutrons

W. Schweika

Jülich Centre for Neutron Science 2

Forschungszentrum Jülich GmbH

Contents

8.1	Introduction	2
8.2	Neutron spins in magnetic fields	2
8.2.1	Interaction of neutrons with magnetic fields	3
8.2.2	Experimental devices	4
8.3	Polarized neutron scattering and applications	9
8.3.1	Nuclear interaction of neutrons with matter	9
8.3.2	Magnetic interaction of neutrons with matter	13
8.3.3	Scattering and polarization analysis, the Blume-Maleyev equations	15
8.4	Final remarks and outlook	20
	References	22
	Exercises	24

8.1 Introduction

Among the properties that make the neutron a unique and valuable probe for condensed matter research, its spin and magnetic moment is of particular importance in the scattering process. There are two aspects to consider, firstly, the strong nuclear interaction of the neutron with an nucleus depends on the either parallel or antiparallel alignment of the spins of neutron and nucleus, and secondly, the neutron's magnetic moment interacts with the unfilled electron shells of atoms or ions in magnetic scattering. The scattering process will also have an impact on the spin state of the neutron probe. Hence, one may expect that controlling the neutron spin in a scattering experiment will provide further valuable information, which leads us to the subject of this lecture: polarized neutron scattering and polarization analysis. Indeed, it is possible by working with polarized neutron and polarization analysis to separate scattering terms with respect to their different structural or magnetic origins, and moreover, to uncover scattering contributions that remain hidden in usual unpolarized scattering experiments.

The method of polarized neutron scattering is mature and well developed. The theoretical description of magnetic neutron scattering by Halpern and Johnson 1939 [1] was essentially completed by the general theory by Blume and Maleyev, independently, in 1963 [2,3]. The first implementation of neutron polarization analysis by Moon, Riste and Koehler [4] laid the foundation for experimental work and some of their examples will be discussed in this lecture. In 1972, Mezei [5] developed the neutron spin echo technique, ten years later Schärpf accomplished the XYZ polarization analysis on a multidetector spectrometer, the D7 at ILL [6], and from 1988 Tasset and Brown developed neutron polarimetry [7,8].

This lecture will give an introduction first to polarized neutrons, how they interact with magnetic fields and upon experimental devices. The following sections will cover the scattering interaction of polarized neutrons with matter, the nuclear and magnetic scattering, followed by applications.

8.2 Neutron spins in magnetic fields

Basic properties

The neutron has a spin $S = \pm 1/2$ with angular momentum $\mathbf{L} = \hbar\mathbf{S}$. The magnetic moment of the neutron results from the spins of the individual quarks and their orbital motions, and the relation between spin and magnetic moment is given by the neutron g -factor, $g_n = -3.8260837(18)$, in units of the nuclear magneton $\mu_N = \frac{e\hbar}{2m_p} = 5.05078324(13) \cdot 10^{-27} \text{JT}^{-1}$

$$\mu_n = g_n S \mu_N \simeq \mp 1.913 \mu_N = \pm \gamma_n \mu_N,$$

where $\gamma_n = -g_n S$ is the gyromagnetic factor of the neutron (see Refs. [9]) . Because of the small ratio $\mu_n/\mu_B = m_e/m_p$, the neutron magnetic moment μ_n is small compared to the magnetic moment of the electron $\mu_e = g_e S \mu_B \approx 1 \mu_B$, with the Bohr magneton $\mu_B = \frac{e\hbar}{2m_e}$ and the Lande-factor $g_e = 2(1 + \alpha/2\pi - 0.328\alpha^2/\pi^2) \approx 2$ (see Refs. [10]), α is the fine structure constant. A peculiarity to note is that different to the electron and proton, the neutron magnetic moment is aligned opposite to its spin.

Polarization

Next we consider the many particle ensemble of neutrons in a neutron beam. Polarization of a neutron beam is defined by the normalized average over the neutron spins.

$$\mathbf{P} = 2\langle \mathbf{S} \rangle \quad (8.1)$$

Applying a magnetic field \mathbf{H} defines a quantization axis and the neutrons split in spin up and down states, n_\uparrow and n_\downarrow respectively. Measuring the beam polarization will take the projection of the spins in up- and down state states with proper normalization.

$$-1 < P = \frac{n_\uparrow - n_\downarrow}{n_\uparrow + n_\downarrow} < 1. \quad (8.2)$$

8.2.1 Interaction of neutrons with magnetic fields

Zeeman splitting

The dipolar interaction potential of a neutron with the magnetic field is given by

$$V_m = -\boldsymbol{\mu}_n \cdot \mathbf{B} \quad (8.3)$$

where \mathbf{B} is the magnetic induction. For neutrons passing from zero-field into a magnetic field the potential energy changes by the Zeeman term $\pm\mu_n B$ depending on the relative orientation of the magnetic moment. The according change in kinetic energy to conserve the total energy is small, $0.06 \mu\text{eV}/T$, which in experimental practice is of relevance only in rare cases.

Equation of motion and Larmor precession

The characteristic motion of the neutron magnetic moment in a magnetic field is Larmor precession, which for simplicity can be considered in a classical treatment. In fact, even the quantum mechanical treatment, which introduces Pauli spin matrices $\hat{\sigma}$ into the Schrödinger equation, is effectively a classical treatment considering the origin of these matrices. Originally [11], they result from the problem of mapping three dimensions onto two by introducing a complex component describing the classical problem of a spinning top. [12] The magnetic interaction tends to align the neutron moment with the magnetic induction in order to minimize the interaction energy. The magnetic moment is related to the angular momentum as

$$\boldsymbol{\mu} = \gamma \mathbf{L}, \quad (8.4)$$

where γ is the gyromagnetic ratio given by $\gamma = 2\mu_n/\hbar = 2\gamma_n\mu_N/\hbar = -1.83 \cdot 10^8 \text{ s}^{-1}\text{T}^{-1}$ or, in cgs units, $\gamma/2\pi = -2916 \text{ Hz/Oe}$. There is a torque $\boldsymbol{\mu} \times \mathbf{B} = \dot{\mathbf{L}}$ equal to the time derivative of the angular momentum, which leads to the Bloch equation of motion:

$$\dot{\boldsymbol{\mu}} = \gamma \boldsymbol{\mu} \times \mathbf{B}. \quad (8.5)$$

Because of the cross product, the time derivative of the magnetic moment is always perpendicular to the moment itself. Therefore, the resulting motion is a precession, where the angular momentum, the component L_z along the field, and the energy are constants of the motion, see Fig.8.1. The precession frequency is the *Larmor frequency* $\omega_L = -\gamma B$, and $\hbar\omega = 2\mu B$, the Zeeman splitting energy.

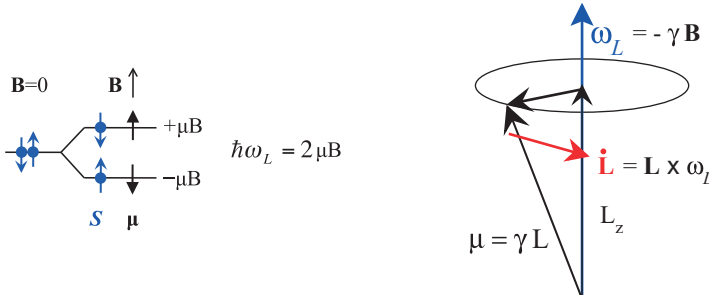


Fig. 8.1: Zeeman splitting (left) and Larmor precession (right). The motion of the neutron in a constant magnetic field conserves energy and angular momentum.

Motion in time dependent fields

The polarization will behave like the individual neutron spin in a constant magnetic field and will be a constant of motion. However, if we consider time-dependent fields, the finite velocity distribution in a neutron beam will result in a different time dependence. Hence de-phasing of neutrons spins and degrading of the polarization are possible experimental effects and have to be taken into account.

Thermal neutrons move with a speed of thousands of meters per second. When passing through spatially varying magnetic fields, the neutrons experience time-dependent field changes in their reference system. Replacing the constant \mathbf{B} by $\mathbf{B}(t)$, the differential equation Eq. (8.5) can be used to calculate numerically the effect of all relevant field variations in an experimental set-up.

Asymptotic cases

Usually, it is possible to work within two simple limiting cases of either (i) **slow adiabatic field variation**, in which the non-precessing spin component parallel to the field smoothly follows the field direction, or of (ii) **sudden field reversal**, in which the non-precessing spin component has no time to reorient itself, when traversing abruptly from a parallel to anti-parallel field or vice versa. Slow field variation means that the field \mathbf{B} changes or rotates in the coordinate system of the neutron with a frequency that is small compared to the Larmor frequency, see Fig. 8.2.

8.2.2 Experimental devices

Polarizer and polarization analyzer

The most common methods to polarize neutrons are (i) using the total reflection from magnetic multi-layers, (ii) using Bragg reflection of polarizing single crystals (typically Heusler crystals) and (iii) polarized He-3 filters, in which for anti-parallel spins the ($n, {}^3\text{He}$)-compound

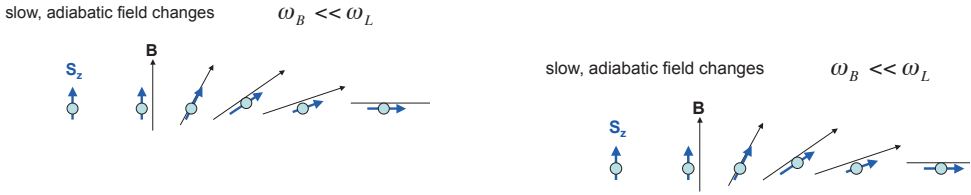


Fig. 8.2: Neutron polarization can be best preserved in the asymptotic cases of either slowly or suddenly varying fields. The second case is used in a cryoflipper to reverse the polarization with respect to the external field.

has a large absorption cross-section while all neutrons with parallel spins may pass the filter cell. The first two methods use an interference effect of nuclear and magnetic scattering amplitudes having the same absolute value as discussed below.

(i) Polarizing total reflecting supermirrors are an easy experimental tool to obtain a broad wavelength band of cold polarized neutrons. The angle of total reflection for a single ferromagnetic (FM) layer is given by

$$\Theta_c^\pm = \lambda \sqrt{n(b \pm p)/\pi}. \tag{8.6}$$

Hence, the critical angle may vanish for one orientation of the neutron spin and there is total reflection for the other one. Here n denotes the particle density and b and p the nuclear and magnetic scattering lengths, respectively. However, the critical angle can be further increased by artificial multi-layers (supermirrors) of alternating FM and non-magnetic layers of varying thickness [13], see Fig. 8.3. The λ dependence of the total reflectivity makes this type of polarizer less favorable for thermal neutrons of shorter wave length as it reduces the accepted divergence of the beam.

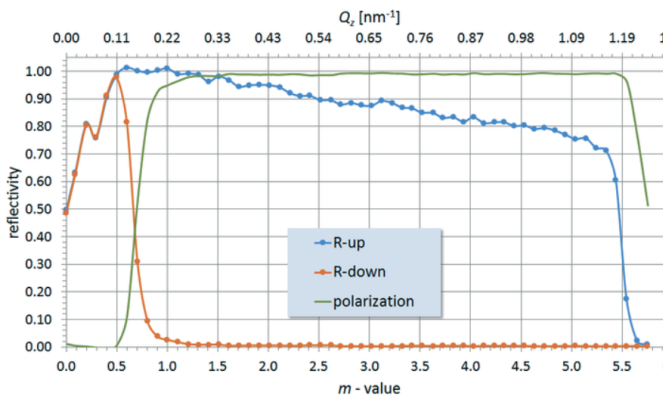


Fig. 8.3: Spin dependent reflectivity and polarisation of Fe/Si polarizing supermirror $m = 5.5$. $m=1$ corresponds to the total reflectivity of Ni. (from SwissNeutronics.ch [14])

(ii) Bragg reflection from a crystal monochromator with similar nuclear and magnetic scattering amplitudes b and p , which yields constructive interference $b + p$ for one spin state and destructive interference $b - p$ for the other. *E.g.* the (111) Bragg reflection of the Cu_2MnAl Heusler alloy gives 95 % polarization. However, the reflectivity of such crystals is low compared to usual non-polarizing monochromators and a saturating field is required over the entire monochromator, which makes it technically more complicated to combine with focusing though this is feasible.

(iii) ^3He filter cells, see Fig. 8.4, are of growing importance for polarizing neutrons, particularly for the more challenging case of thermal neutrons, although such cells are technically rather demanding and still under development. In case of spin-exchange optical pumping (SEOP) the spin polarization of ^3He gas is achieved in several steps. The cell is filled with additional Rb, K and N_2 vapor. Rb electrons are polarized with a circular polarized laser, by collisions the spin is exchanged with K, which most efficiently exchanges spin with ^3He . Since polarization results from absorption, such a device does not interfere with the beam divergence. One may note that requirements for field homogeneity are very high and it is a kind of art and glass alchemy to make cells with small depolarization all determining the lifetime of ^3He polarization. The neutron polarization P raises with increasing ^3He cell size or pressure, while the transmission T decreases. The optimum in efficiency is usually chosen by the maximum of a quality factor P^2T .

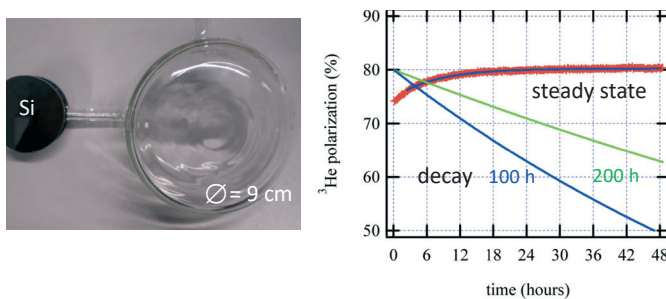


Fig. 8.4: (left) ^3He -cells made of Si-crystal (avoiding small angle scattering background) and of glass (for wide angle diffraction). ^3He in-situ polarization of a SEOP He-3 cell and measured polarization of neutron beam in transmission. (from Babcock et al. [15])

Guide-fields

A magnetic *guide field* is used to maintain the direction of the spin and the polarization of the neutron beam. The guide field preserves the quantization axis to which the neutron moments have to align either parallel or anti-parallel. Typical guide fields in the order of 10 G are strong compared to earth field and other possible stray fields and usually sufficient to prevent depolarization along the beam path. Such guide fields are usually too weak to have any significant impact on the sample magnetization.

Depolarization effects may occur for an inhomogeneous distribution of field directions over neutron beam cross-section, which is typically a few cm^2 . This can easily occur if a fer-

romagnetic material is used close to the beam or if the sample itself is ferromagnetic. A neutron beam passing through a ferromagnet is usually completely depolarized by differently oriented ferromagnetic domains in the beam path, unless a saturating magnetic field is used to align the domains. Depolarization will depend also on the path length through the sample, therefore, usually such effects are negligible in *neutron reflectometry* of thin ferromagnetic films.

XYZ-coils

In order to probe the orientation of the magnetic moments in the sample, it is desirable to align the polarization to any desired direction at the sample position. This can be done with a set-up of three orthogonal pairs of so-called xyz-coils. Fig. 8.5 illustrates the field setting along x-direction. In the example, one can see that the z-coil has been used to compensate the guide field at the sample position, and that the x-coils produce a field of a few Gauss. The field needs to be sufficiently strong so that the neutron polarization can follow the smooth variation of the field direction adiabatically, finally turning back into the z-direction of the guide field outside the xyz-coils.

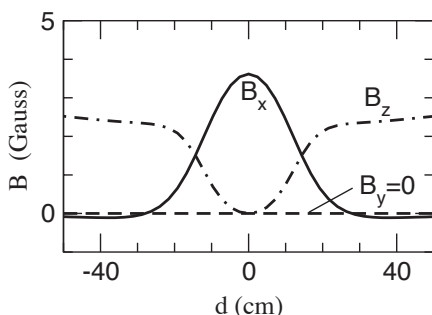


Fig. 8.5: (left) Magnetic field setting in a xyz-coil system for an adiabatic nutation of the polarization of cold neutrons in horizontal x-direction at the sample turning to a vertical (guide) field B_z at further distance from the sample. (right) A photo of the xyz-coil system in the DNS instrument at the FRM-2.

Flipper

The purpose of a π -flipper is to reverse the polarization and to detect whether the sample causes spin-flip scattering.

When applying a magnetic field perpendicular to the polarized neutron beam, the polarization immediately starts its Larmor precession. A flipper that reverses the neutron polarization with respect to the guide field has to induce a well-defined field pulse so that the polarization precesses by an angle π . For this purpose one can use the homogeneous field of a *Mezei* flipper, a long rectangular coil, see Fig. 8.6. Neutrons see a sudden field change when they enter and exit the coil, in between they precess around the perpendicular flipping field, whose

magnitude is tuned with respect to the time of flight that the neutrons spend inside the coil. Therefore, the device is λ -dependent and currents (fields) need to be properly tuned for a π -flip.

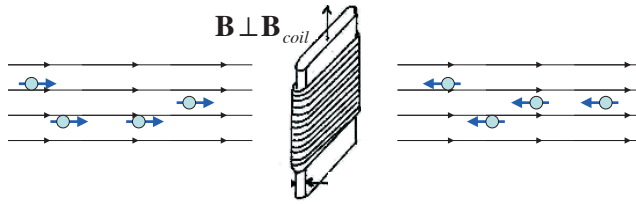


Fig. 8.6: Principle of a neutron π -spin flipper. The neutrons perform a Larmor-precession of 180° inside a long rectangular coil. The field B is perpendicular to spin orientation and adjusted to the speed of the neutrons.

The purpose of a $\pi/2$ -flipper is to set the polarization in precession mode by turning the polarization perpendicular to the guide field. A precessing polarization is used for instance in high resolution *Neutron Spin Echo spectroscopy* and for *Larmor diffraction*, see below. Both methods use the property of the neutron spin as an internal clock independent of the scattering process itself and achieve highest resolution.

The classical experimental set-up of Moon, Riste and Koehler (1969) combines the above discussed devices for polarized neutron scattering with so-called longitudinal polarization analysis. Principles and examples from this study [4] will be discussed in the following section.

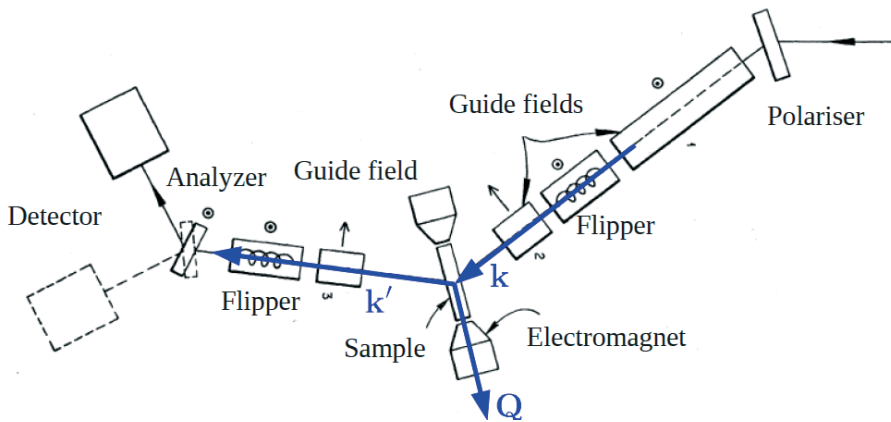


Fig. 8.7: The scheme of the triple axis instrument equipped for polarization analysis as used by Moon, Riste and Koehler (1969). Reprinted from [4]. Copyright (1969) by the American Physical Society.

8.3 Polarized neutron scattering and applications

8.3.1 Nuclear interaction of neutrons with matter

For thermal and cold neutrons, the range of the nuclear interaction is small compared to the neutron wavelength and can be described by a point-like and isotope-specific Fermi potential, which is proportional to the scattering length b ,

$$V(r) = \frac{2\pi\hbar^2}{m_n} b \delta(r - R) \quad (8.7)$$

The scattering amplitude $N_{\mathbf{Q}}$ for an ensemble of nuclei is determined by the transition matrix elements for the scattering potential $V_{\mathbf{Q}}$

$$N_{\mathbf{Q}} = \langle \mathbf{k}' \mathbf{S}' | V_{\mathbf{Q}} | \mathbf{k} \mathbf{S} \rangle \quad (8.8)$$

which in general depends on the scattering vector $\mathbf{k} - \mathbf{k}' = \mathbf{Q}$, the related energy transfer, and the spin states before and after the scattering process.

First, we consider the scattering of nuclei of one element only and assume further that these nuclei have zero spin (*e.g.* ^{12}C , ^{16}O ..., and typically "gg" isotopes with even number of protons and neutrons). The scattering length operator \hat{b} is a scalar and the scattering will be independent of the neutron spin orientation. This leads to the scattering intensity, where we replace the actual scattering length by the average \bar{b}_l and deviations, by including the mean square deviations

$$\frac{d\sigma}{d\Omega} = N \sum_w b_l b_{l'} e^{i\mathbf{Q}(\mathbf{R}_l - \mathbf{R}_{l'})} = N(\bar{b}^2 - \bar{b}^2) + \bar{b}^2 \sum_w e^{i\mathbf{Q}(\mathbf{R}_l - \mathbf{R}_{l'})}. \quad (8.9)$$

The first term on the right side is the isotopic incoherent scattering, it relates to random fluctuations in the scattering length. In contrast, the second term, the coherent nuclear scattering, is proportional to \bar{b}^2 and contains phase information.

Next we consider that scattering nuclei may have a spin $I \neq 0$ and that the interaction is spin-dependent. There are two possible spin states of the compound, coupling the neutron spin with the spin of a nucleus, which are either $J = J_+ = I + 1/2$ or $J = J_- = I - 1/2$, associated with different scattering lengths b_+ and b_- . The multiplicity of the spin states $2J + 1$ equal $2I + 2$ and $2I$ for parallel and anti-parallel spin alignment respectively. For an equiprobable occupation of all states, the probabilities for the J_+ and J_- states are

$$p_+ = \frac{I + 1}{2I + 1}, \quad p_- = \frac{I}{2I + 1}, \quad (8.10)$$

defining the weights for the average coherent scattering length and its mean square average

$$\bar{b} = p_+ b_+ + p_- b_-, \quad \bar{b}^2 = p_+ b_+^2 + p_- b_-^2. \quad (8.11)$$

Again this will lead to a scattering intensity as given by Eq.(8.9), only that the **spin-incoherent scattering** term is now related to the randomness of spin states.

In order to understand what will happen to the spin states of neutron and nuclei, we consider the transition matrix element Eq. (8.8) for the scattering length operator, which is the sum of the average, coherent part, $A (= \bar{b})$, and the fluctuating spin-dependent part, $B = \frac{b_+ - b_-}{2I+1}$,

$$\hat{\mathbf{b}} = A + B \hat{\boldsymbol{\sigma}} \cdot \hat{\mathbf{I}}. \quad (8.12)$$

Here, $\hat{\boldsymbol{\sigma}}$ is the Pauli spin operator given by **Pauli spin matrices**

$$\hat{\sigma}_x = \begin{pmatrix} 0 & 1 \\ 1 & 0 \end{pmatrix}, \quad \hat{\sigma}_y = \begin{pmatrix} 0 & -i \\ i & 0 \end{pmatrix}, \quad \hat{\sigma}_z = \begin{pmatrix} 1 & 0 \\ 0 & -1 \end{pmatrix}. \quad (8.13)$$

We choose the quantization axis z for the neutron polarization $\mathbf{P} = 2\langle \hat{\mathbf{S}} \rangle = \langle \hat{\boldsymbol{\sigma}} \rangle$, with spin-up states $|+\rangle = \begin{pmatrix} 1 \\ 0 \end{pmatrix}$ and spin-down states $|-\rangle = \begin{pmatrix} 0 \\ 1 \end{pmatrix}$. With

$$\begin{aligned} \hat{\sigma}_x|+\rangle &= |-\rangle, & \hat{\sigma}_y|+\rangle &= i|-\rangle, & \hat{\sigma}_z|+\rangle &= |+\rangle \\ \hat{\sigma}_x|-\rangle &= |+\rangle, & \hat{\sigma}_y|-\rangle &= -i|+\rangle, & \hat{\sigma}_z|-\rangle &= -|-\rangle \end{aligned} \quad (8.14)$$

we obtain the transition matrix elements

$$\begin{aligned} \langle +|\hat{\mathbf{b}}|+\rangle &= (A + BI_z) \langle +|+\rangle \quad \text{nsf} \\ \langle -|\hat{\mathbf{b}}|-\rangle &= (A - BI_z) \langle -|-\rangle \quad \text{nsf} \\ \langle +|\hat{\mathbf{b}}|-\rangle &= B(I_x - iI_y) \langle +|+\rangle \quad \text{sf} \\ \langle -|\hat{\mathbf{b}}|+\rangle &= B(I_x + iI_y) \langle -|-\rangle \quad \text{sf} \end{aligned} \quad (8.15)$$

for the non-spinflip (nsf) and spinflip (sf) scattering amplitudes, respectively. The non-spinflip scattering is given by the coherent scattering and one third of the spin-incoherent scattering, while two thirds of the spin-incoherent scattering is spinflip scattering. If we consider only coherent scattering, the final polarisation $\mathbf{P}' = \mathbf{P}$, whereas in case of only spin-incoherent scattering $\mathbf{P}' = -\frac{1}{3}\mathbf{P}$. The combination of coherent and spin-incoherent scattering may result in a change of magnitude and sign of polarization, however, the final polarization will not deviate from the initial polarization axis. Furthermore, the obtained result is simply independent of the direction of \mathbf{P} with respect to \mathbf{Q} . This is an important feature, which is in contrast to the dipolar magnetic interaction that will be discussed below.

In summary, we can distinguish three contributions to the nuclear scattering $|N_{\mathbf{Q}}|^2$ arising from the total nuclear scattering amplitude $N_{\mathbf{Q}} = \sum_j b_j e^{i\mathbf{Q}\cdot\mathbf{R}_j}$, the average coherent scattering, the isotopic, non-spin dependent part of the incoherent scattering, and the spin-incoherent scattering

$$\frac{d\sigma^N}{d\Omega_{\mathbf{Q}}} = |N_{\mathbf{Q}}|^2 = \frac{d\sigma^N}{d\Omega_{\text{spin-inc}}} + \frac{d\sigma^N}{d\Omega_{\text{isotope-inc}}} + \frac{d\sigma^N}{d\Omega_{\mathbf{Q},\text{coh}}}. \quad (8.16)$$

The sum of the coherent and isotopic incoherent nuclear scattering can be separated from the spin-incoherent scattering by measuring spin-flip and non-spin-flip scattering.

$$\frac{d\sigma}{d\Omega_{\text{spin-inc}}} = \frac{3}{2} \frac{d\sigma^{SF}}{d\Omega} \quad (8.17)$$

$$\frac{d\sigma^N}{d\Omega_{\mathbf{Q},\text{coh}}} + \frac{d\sigma^N}{d\Omega_{\text{isotope-inc}}} = \frac{d\sigma^{NSF}}{d\Omega} - \frac{1}{2} \frac{d\sigma^{SF}}{d\Omega} \quad (8.18)$$

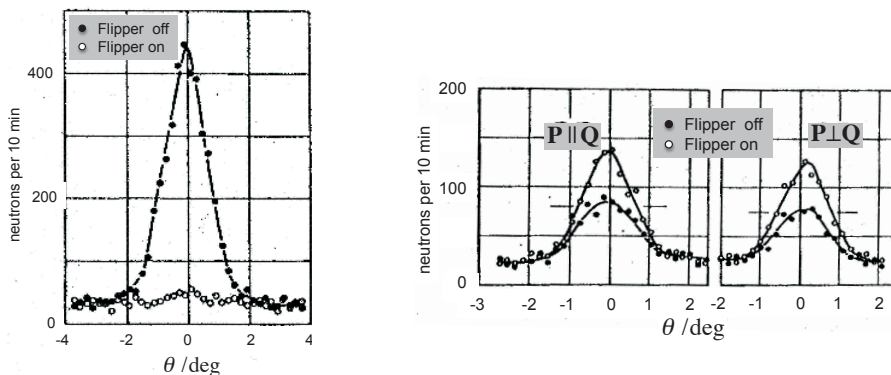


Fig. 8.8: Left: Nuclear isotopic incoherent scattering from nickel obtained by rocking the analyzer crystal through the elastic position, which is essentially all non-spin-flip scattering. Right: Nuclear spin-incoherent scattering from vanadium show $2/3$ and $1/3$ contributions in the spin-flip and non-spin-flip channel respectively. There is no dependence on the direction of \mathbf{P} relative to \mathbf{Q} for all nuclear scattering. Reprinted from [4]. Copyright (1969) by the American Physical Society.

There are two good examples of isotope and spin-incoherent scattering, Nickel and Vanadium respectively. Because Vanadium has essentially no coherent scattering, it is often used as a reference sample to calibrate data for detector efficiencies. It consists to 99.75% of the stable isotope ^{51}V with a nuclear spin $I = 7/2$. Polarization analysis reveals that $2/3$ of the spin-incoherent scattering is spinflip and $1/3$ is non-spinflip scattering, see Fig. 8.8. The second example Nickel consists of various isotopes, mostly with $I = 0$. As expected, the related isotope incoherent scattering is purely non-spinflip scattering, as also shown in Fig. 8.8. Note, the magnetic scattering vanishes for applying a saturating field $H \parallel Q$, see also Fig. 8.7.

Applications to local order in disordered hydrogenous materials

Typical soft matter samples contain hydrogen which causes a huge spin-incoherent background ($\sigma_{inc}(H) = 80 \text{ b}$) in the wide-angle scattering that contains information about local correlations ($\sigma_{coh}(H) = 1.76 \text{ b}$). Here, a precise determination of coherent scattering can be achieved by measuring spin-flip and non-spin-flip scattering. It is particularly valuable to combine this further with the method of contrast variation using H and D isotopes, having rather distinct scattering lengths, $b_{coh}(H) = -0.374 \cdot 10^{-12} \text{ cm}$ and $b_{coh}(D) = 0.667 \cdot 10^{-12} \text{ cm}$. Fig. 8.9 shows the separated coherent scattering of a polymer glass. Such results provide most useful information about local order that can be compared to molecular dynamics simulations of theoretical polymer models [17].

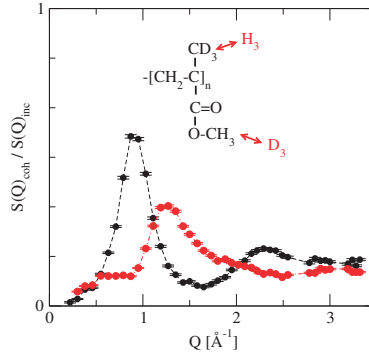


Fig. 8.9: Neutron polarisation analysis separates coherent scattering from spin-incoherent scattering, which is typically a disturbing large background in materials that contain hydrogen, while here it provides a precise intrinsic calibration. In addition, H/D contrast varies the coherent scattering of a polymer glass PMMA. [17]

Applications to dynamics in liquids

Since in a liquid all atoms are moving around, the scattering is not elastic as in the case of Bragg peaks from a solid, single crystal. Diffraction - the energy integrated scattering - provides us with structural properties from a snap-shot of typical atomic configurations. Since neutron energies are comparable to thermal energies involved in atomic motions, it is relatively simple to achieve an adequate energy resolution to study the dynamics for instance in liquids, see example in Fig. 8.10.

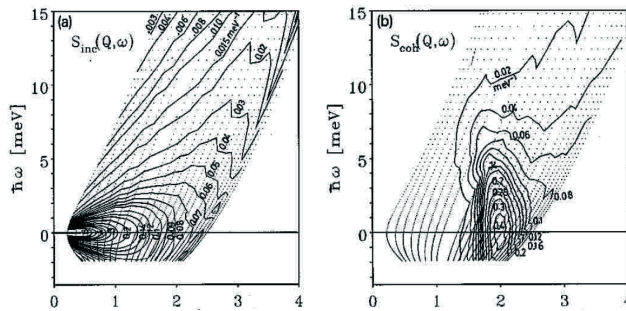


Fig. 8.10: Time-of-flight spectra of a) spin-incoherent and b) coherent scattering of liquid sodium at $T=840$ K separated by polarization analysis (from O. Schärpf. [18]). The dotted mesh corresponds to the coordinates of time-of-flight and scattering angles.

Therefore, a typical instrument set-up uses the time-of-flight technique: the monochromatic beam is pulsed by a mechanical chopper and the measured *time-of-flight* of the neutrons can be related to an energy transfer in the sample. Note, the separation by polarization analysis

in *coherent* scattering and *spin-incoherent* scattering distinguishes *pair-correlations* from *single particle correlations*, respectively. The study of liquid sodium [18], see Fig. 8.10, demonstrates instructively the complementary information that can be obtained. From simple liquid models one expects that the incoherent scattering has a Lorentzian shape in energy at constant Q , related to exponential relaxations in time, with a width that for the macroscopic limit, $Q \rightarrow 0$, is related to the diffusion constant. In contrast, the coherent scattering very differently exhibits a pronounced peak related to typical nearest neighbor distances reflecting precursors of Bragg peaks and crystalline order.

8.3.2 Magnetic interaction of neutrons with matter

Spin and orbital moments exert dipolar fields

$$\mathbf{B}_S = \nabla \times \left(\frac{\boldsymbol{\mu}_e \times \mathbf{R}}{R^3} \right), \quad \mathbf{B}_L = \frac{e}{c} \left(\frac{\mathbf{v}_e \times \mathbf{R}}{R^3} \right) \quad (8.19)$$

and result in a dipolar **magnetic interaction potential** for the neutron

$$V_m = -\boldsymbol{\mu} \cdot (\mathbf{B}_S + \mathbf{B}_L). \quad (8.20)$$

The derivation of the scattering law is lengthy and can be found in [16]; it leads to

$$\frac{d\sigma}{d\Omega_{\text{mag}}} = (\gamma_n r_0)^2 \left| \frac{1}{2\mu_B} \langle S'_Z | \hat{\boldsymbol{\sigma}} \cdot \hat{\mathbf{M}}_Q^\perp | S_Z \rangle \right|^2, \quad (8.21)$$

where r_0 is the classical electron radius. $\hat{\mathbf{M}}_Q^\perp$ is the operator of the magnetic interaction vector, defined in units of μ_B ,

$$\mathbf{M}_Q^\perp = \mathbf{e}_Q \times \mathbf{M}_Q \times \mathbf{e}_Q \quad (8.22)$$

which is reduced to only the perpendicular components of \mathbf{M}_Q with respect to \mathbf{Q} . \mathbf{M}_Q represents the total Fourier transform of the spin and orbital contribution to the magnetization density. Consequently, and in fundamental contrast to nuclear scattering, the magnetic scattering depends on a **form factor**, similarly to x-ray scattering. Because unpaired electrons are typically in the outer shells, such as the $3d$ or $4d$ shell of transition elements or the $4f$ shell of rare earth elements, the form factor drops typically faster than for the total electron cloud as seen in the x-ray form factor. Measuring the form factor in detail can reveal the relevant spin and orbital contributions to the magnetic moments.

The anisotropy of the interaction is due to the dipolar interaction of the neutron spin with the magnetic moments, which is illustrated in Fig. 8.11. The components of a magnetic dipole field parallel to the scattering vector \mathbf{Q} cancel out. Therefore, in contrast to the spin-incoherent scattering, magnetic scattering is anisotropic with respect to \mathbf{Q} and only \mathbf{M}_Q^\perp , the components perpendicular to \mathbf{Q} can be observed.

In analogy to the spin-dependent nuclear interaction, we obtain the transition matrix elements for the magnetic interaction, choosing z-polarization and x parallel to \mathbf{Q} , $\mathbf{M}_{x,\mathbf{Q}}^\perp = 0$, and

$$\begin{aligned} \langle + | \hat{\boldsymbol{\sigma}} \cdot \hat{\mathbf{M}}_Q^\perp | + \rangle &= M_{z,\mathbf{Q}}^\perp, \quad \text{nsf} \\ \langle - | \hat{\boldsymbol{\sigma}} \cdot \hat{\mathbf{M}}_Q^\perp | - \rangle &= -M_{z,\mathbf{Q}}^\perp, \quad \text{nsf} \\ \langle + | \hat{\boldsymbol{\sigma}} \cdot \hat{\mathbf{M}}_Q^\perp | - \rangle &= -iM_{y,\mathbf{Q}}^\perp, \quad \text{sf} \\ \langle - | \hat{\boldsymbol{\sigma}} \cdot \hat{\mathbf{M}}_Q^\perp | + \rangle &= iM_{y,\mathbf{Q}}^\perp, \quad \text{sf} \end{aligned} \quad (8.23)$$

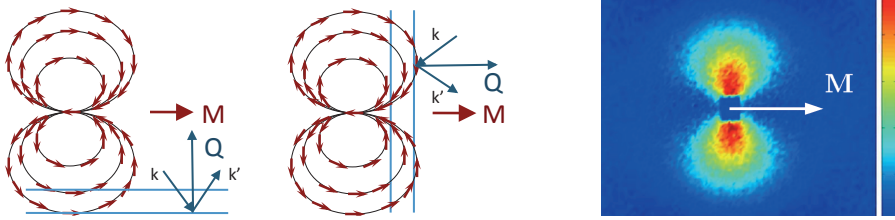


Fig. 8.11: Illustration why only M_Q^\perp is measured. For $M \perp Q$, magnetic dipole field amplitudes show constructive interference, for $M \parallel Q$ destructive interference. Right: Polarized small angle scattering ($Q = 0$ in centre) probing the magnetization of iron oxide nanoparticles. [19]

Hence, as illustrated in Fig. 8.12, the component of P parallel to M_Q^\perp remains unchanged,



Fig. 8.12: Change of initial polarization P to final polarization P' : the component perpendicular to M_Q^\perp reverses sign, the parallel component of P is invariant.

while the component of P perpendicular to M_Q^\perp reverses its sign. This selection rule combined with the Q -dependence provides another simple rule: If $P \parallel Q$, the total magnetic scattering will be spin-flip.

Therefore, as exemplified in Moon, Riste, Koehler’s seminal paper [4] nuclear and magnetic Bragg peaks can be separated from non-spin-flip and spin-flip scattering respectively by scanning with $P \parallel Q$, see the separation for Fe_2O_3 in Fig. 8.13.

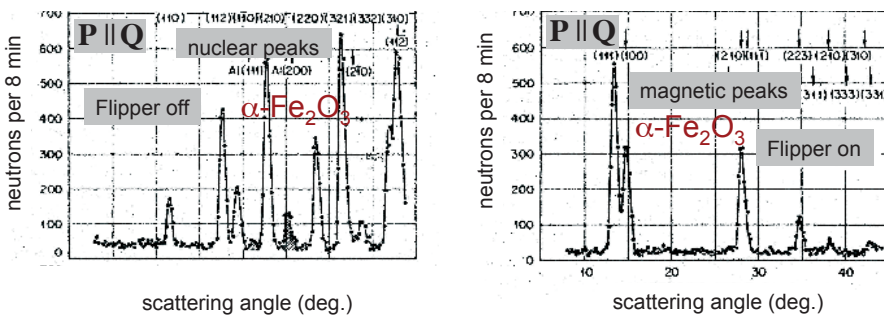


Fig. 8.13: Separation of magnetic and nuclear Bragg peaks for powder diffraction from Fe_2O_3 by non-spin-flip and spin-flip scattering with $P \parallel Q$. Reprinted from [4]. Copyright (1969) by the American Physical Society.

8.3.3 Scattering and polarization analysis, the Blume-Maleyev equations

However, turning from the individual expressions for the scattering amplitudes to scattering and interference of nuclear and magnetic scattering amplitudes, we have to face more complex expressions. A complete description of magnetic and nuclear neutron scattering has been given by Blume [2] and Maleyev [3] by two master equations. The first equation gives the scattering cross-section $\sigma_{\mathbf{Q}}$, the second one describes the final polarization \mathbf{P}' ,

$$\begin{aligned} \sigma_{\mathbf{Q}} = & |N_{\mathbf{Q}}|^2 + \sigma_{\text{isotope,inc}} + \sigma_{\text{spin,inc}} + |\mathbf{M}_{\mathbf{Q}}^{\perp}|^2 \\ & + \mathbf{P}(N_{-\mathbf{Q}}\mathbf{M}_{\mathbf{Q}}^{\perp} + \mathbf{M}_{-\mathbf{Q}}^{\perp}N_{\mathbf{Q}}) + i\mathbf{P}(\mathbf{M}_{-\mathbf{Q}}^{\perp} \times \mathbf{M}_{\mathbf{Q}}^{\perp}) \end{aligned} \quad (8.24)$$

$$\begin{aligned} \mathbf{P}'\sigma_{\mathbf{Q}} = & |N_{\mathbf{Q}}|^2\mathbf{P} + \sigma_{\text{isotope,inc}}\mathbf{P} - \frac{1}{3}\sigma_{\text{spin,inc}}\mathbf{P} \\ & + \mathbf{M}_{\mathbf{Q}}^{\perp}(\mathbf{P}\mathbf{M}_{-\mathbf{Q}}^{\perp}) + \mathbf{M}_{-\mathbf{Q}}^{\perp}(\mathbf{P}\mathbf{M}_{\mathbf{Q}}^{\perp}) - \mathbf{P}\mathbf{M}_{\mathbf{Q}}^{\perp}\mathbf{M}_{-\mathbf{Q}}^{\perp} \\ & + \mathbf{M}_{\mathbf{Q}}^{\perp}N_{-\mathbf{Q}} + \mathbf{M}_{-\mathbf{Q}}^{\perp}N_{\mathbf{Q}} + i\mathbf{M}_{\mathbf{Q}}^{\perp} \times \mathbf{M}_{-\mathbf{Q}}^{\perp} + i(\mathbf{M}_{\mathbf{Q}}^{\perp}N_{-\mathbf{Q}} - \mathbf{M}_{-\mathbf{Q}}^{\perp}N_{\mathbf{Q}}) \times \mathbf{P} \end{aligned} \quad (8.25)$$

The notation uses $-\mathbf{Q}$ to denote the complex conjugate. Here, for simplicity only the \mathbf{Q} -dependence is specified for Bragg scattering or diffuse scattering. However, in the more general form the scattering cross sections apply to inelastic scattering and can be related to van Hove correlation functions in space and time.

These equations readily show the different information that can be obtained from an unpolarized with respect to a polarized experiment. While unpolarized neutrons only measure the sum of nuclear and magnetic intensities, for polarized neutrons additional intensity may arise first, due to possible structural-magnetic (NM-terms) interference and second, due to cross products of the magnetic interaction vector $i\mathbf{M}_{\mathbf{Q}}^{\perp} \times \mathbf{M}_{-\mathbf{Q}}^{\perp}$ describing chiral correlations in non-collinear spin systems. A look at the second equation for the final polarization reveals that we can identify such terms "NM" and "M \times M" even with unpolarized neutrons, because they may create final polarization (set $\mathbf{P} = 0$).

Eq. 8.25 can be written as a tensor equation [8] (neglecting for brevity the incoherent parts)

$$\mathbf{P}'\sigma = (|N|^2\mathbf{1} + \mathcal{R})\mathbf{P} + \mathbf{P}'' \quad (8.26)$$

in which the first term $(|N|^2\mathbf{1} + \mathcal{R})\mathbf{P}$ consists of the scalar nuclear scattering $|N|^2$, $\mathbf{1}$ is the unity matrix, the matrix \mathcal{R} describes the rotation of \mathbf{P} , and \mathbf{P}'' is the created polarization.

Using the common convention for the specific orthogonal setting \mathbf{x} parallel to \mathbf{Q} , and \mathbf{y} and \mathbf{z} perpendicular to \mathbf{Q} , horizontally and vertically set to the scattering plane respectively, \mathcal{R} and \mathbf{P}'' are obtained as

$$\mathcal{R} = \begin{pmatrix} -|M_y|^2 - |M_z|^2 & 2 \operatorname{Im}[NM_z] & 2 \operatorname{Im}[NM_y] \\ -2 \operatorname{Im}[NM_z] & |M_y|^2 - |M_z|^2 & 2 \operatorname{Re}[M_yM_z] \\ -2 \operatorname{Im}[NM_y] & 2 \operatorname{Re}[M_zM_y] & -|M_y|^2 + |M_z|^2 \end{pmatrix} \quad (8.27)$$

$$\mathbf{P}'' = (-2 \operatorname{Im}[M_yM_z], 2 \operatorname{Re}[NM_y], 2 \operatorname{Re}[NM_z]) \quad (8.28)$$

The diagonal elements can be obtained by **longitudinal polarization analysis**, in which we consider spin-flip and non-spinflip for either x , y or z direction of initial and final polarization. For measuring the off-diagonal elements, for example R_{yz} obtained by $\mathbf{P} = (0, P_y, 0)$

and $\mathbf{P}' = (0, 0, P'_z)$, the magnetic field needs to switch from y to z -direction, which can be achieved by a zero-field at the sample. Alternatively, but so far not much used in practice, one can work with precessing neutron polarization [20,21]. The conventional approach, however, is to access all elements of the tensor \mathcal{R} by **spherical neutron polarimetry** (SNP). Experimentally, a zero-field can be achieved with a CryoPad or MuPad device [22] using superconducting material or a μ -metal [23] to shield the sample area from magnetic fields. In particular, SNP allows to distinguish a rotation of \mathbf{P}' from a depolarization of the beam. Depolarization may occur due to an incoherent superposition of intensities with different polarization, this includes spin-incoherent scattering, and more important for determining magnetic structures, intensity from different magnetic domains. See Ref. [8] for detailed examples and analysis. The interested reader is also referred to the recent user software Mag2Pol: a program for the analysis of spherical neutron polarimetry and flipping ratio data, see below [24].

It is noteworthy that the information in the off-diagonal elements, related to nuclear-magnetic interference and chirality, reappears in the diagonal elements in \mathbf{P}'' and can therefore also be obtained by conventional longitudinal polarization analysis. Polarization reversal and considering the sum and differences of intensities will separate \mathbf{P}'' from the trace of \mathcal{R} [25].

Next we consider two important cases, the so called (i) "flipping ratio" or "half-polarized" experiments to determine the magnetic structure or spin density, and (ii) XYZ polarization analysis with multi-detectors.

Magnetization and spin density distribution. The usual approach [26] is to measure the "flipping ratio" of Bragg reflection, defined as the intensity ratio between spin-up and spin-down neutrons with respect to a vertical applied magnetic field

and is given by

$$R = \frac{I^+}{I^-} = \frac{N_{\mathbf{Q}}N_{-\mathbf{Q}} + (N_{\mathbf{Q}}M_{-\mathbf{Q}}^{\perp} + N_{-\mathbf{Q}}M_{\mathbf{Q}}^{\perp}) + M_{\mathbf{Q}}^{\perp}M_{-\mathbf{Q}}^{\perp}}{N_{\mathbf{Q}}N_{-\mathbf{Q}} - (N_{\mathbf{Q}}M_{-\mathbf{Q}}^{\perp} + N_{-\mathbf{Q}}M_{\mathbf{Q}}^{\perp}) + M_{\mathbf{Q}}^{\perp}M_{-\mathbf{Q}}^{\perp}}. \quad (8.29)$$

To illustrate the advantage of polarized neutrons consider the case of a weak magnetic amplitude, $M_z = 0.1N$. For unpolarized neutrons the interference term NM_z vanishes. Therefore, the unpolarized intensity I is less interesting, but in contrast the ratio I^+/I^- is very sensitive:

$$I = 1.01|N|^2, \quad \text{and} \quad \frac{I^+}{I^-} = \frac{(1 + 0.1)N^2}{(1 - 0.1)N^2} = \frac{1.21}{0.81} \approx 1.5. \quad (8.30)$$

In order to solve Eq. 8.29 for the magnetic amplitudes and the magnetic structure, we need *a priori* an accurate crystallographic structure determination for the nuclear amplitudes N .

In the experiment a flipper is used to switch the polarization with respect to the applied field, which led to the name "flipping ratio". The term could be misleading, since the scattering process is purely non-spinflip as $\mathbf{P} \parallel \mathbf{M}_{\mathbf{Q}}^{\perp} \parallel z$. In such an experiment one uses polarized neutrons without polarization analysis, which has led to another deceptive term, describing this as a "half-polarized" set-up. Still, \mathbf{P} is favorably large, close to one, just \mathbf{P}' does not matter.

With respect to applications, the samples could be ferromagnets, where the magnetization is best near saturation using a strong field. However, one can also study paramagnets, and the induced magnetic moments will represent the spin density distribution. An example is given

in Figure 8.14 for the organic compound $[\text{Cu}_2(t\text{-Bupy})_4(\text{N}_3)_2](\text{ClO}_4)_2$. Here, the two Cu spins are the triplet ground state, and a part of the spin density is spreading from the Cu sites to ligands. The contours of the map start at a level of $0.01 \mu_B$, which nicely demonstrates the sensitivity of such measurements.

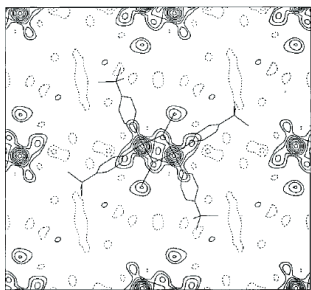


Fig. 8.14: $[\text{Cu}_2(t\text{-Bupy})_4(\text{N}_3)_2](\text{ClO}_4)_2$ spin density map (unit cell in ab , integration ± 0.25 in c), adapted with permission from [27]. Copyright 1998 American Chemical Society.

One may also study the response with respect to different field directions, which yields the susceptibility tensor on atomic scale. Strong anisotropies can be found for f -electrons of rare earth ions. It is noteworthy that such information can be obtained also from powder samples, when using a 2D detector which identifies the actual inclination of the Bragg planes with respect to the applied vertical magnetic field [28]. These are typical applications using Bragg intensities providing local information on atomic scale. If we turn to low Q and small angle neutron scattering, the intensities relate to the morphologies of magnetic structures, which refers to an example discussed already before: Fig. 8.11 shows the interference pattern $MN(\mathbf{Q})$ and contains the information on the magnetic morphology of iron oxide nanoparticles [19].

Chirality. The last term in Eq. 8.24 refers to the vector product of spin components perpendicular to \mathbf{Q} , and therefore, $i\mathbf{M}_{\perp\mathbf{Q}} \times \mathbf{M}_{\perp\mathbf{Q}}^{\perp}$ itself points in \mathbf{Q} -direction. The magnetic moments in real space are real quantities and the imaginary sign i says that this term is antisymmetric in \mathbf{Q} and relates to the sin-Fourier transform of chiral pair correlations $S_y(\mathbf{R})S_z(\mathbf{R}')$, which also implies the characteristic chiral feature of point inversion symmetry. A beautiful example depicted in Fig. 8.15 shows the antisymmetric chiral scattering from a spin liquid obtained by polarization reversal with respect to \mathbf{Q} and taking the difference of the intensi-

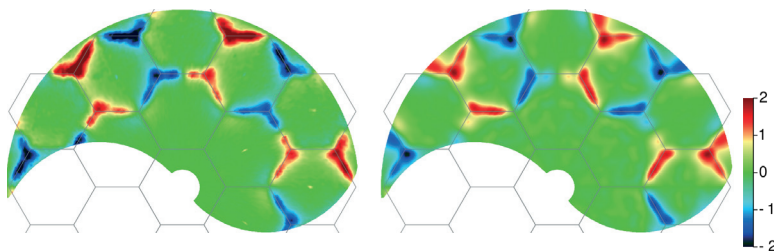


Fig. 8.15: Chiral spin liquid ground state in $\text{YBaCo}_3\text{FeO}_7$, Ref. Schweika et al. PRX 2020 . (left) Chiral scattering measured with polarization reversal along \mathbf{Q} . (right) Fourier analysis and model scattering based on purely cycloidal chiral correlations.

ties [29]. The antisymmetry perpendicular to \mathbf{Q} , reveals that $\mathbf{C} = \mathbf{S} \times \mathbf{S}'$ is perpendicular to the propagation, i.e. a cycloidal chirality. In contrast for a helix, the antisymmetry and \mathbf{C} would be in \mathbf{Q} direction.

Depending on the propagation direction parallel or perpendicular to \mathbf{Q} , we can distinguish a helix from a cycloid spin structure, respectively. The chiral intensity can be separated by polarized neutron scattering with measuring the intensity difference for \mathbf{P} parallel and antiparallel to \mathbf{Q} , which cancels out other nuclear and magnetic intensities, while there are no NM terms parallel to \mathbf{Q} . The chiral interference is purely spinflip scattering, however, it can be separated without applying polarization analysis like the NM interference.

XYZ Polarization analysis with multi detectors

So far it has been implicitly assumed that the data are measured with a single detector related to a single \mathbf{Q} set parallel to x . Multi-detector systems can collect scattering data in a much more efficient way and were used also for the previous example Fig. 8.15. The instrument D7 at ILL in Grenoble [30] was pioneering with covering a wide angle range with supermirror based polarization analyzers in front of a multi-detector. A similar instrument DNS [31] is operated by JCNS at the MLZ and FRM-2 in Munich, see Fig. 8.16.

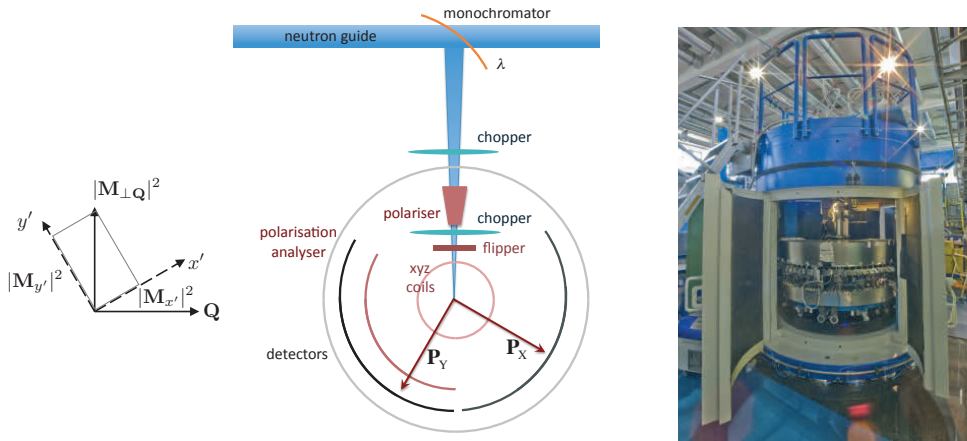


Fig. 8.16: Polarization analysis on a time-of-flight multi-detector instrument, the DNS instrument at FRM-2, see Ref. [25] for the specific setting of polarization.

Instead of measuring each data point with $\mathbf{P} \perp \mathbf{Q}$, using Pythagoras' theorem, we can construct the parallel and perpendicular components to \mathbf{Q} from any two orthogonal settings (x', y') in-plane and measure simultaneously with a multi-detector. Assuming isotropy, e.g. for powders and paramagnets, the pure magnetic scattering contribution separated from nuclear scattering can be obtained by either of the two combinations of spin flip and non-spinflip scattering, which is the "XYZ-method" introduced by Otto Schärpf [33]:

$$\frac{d\sigma}{d\Omega_{magn}} = 2 \left(\frac{d\sigma^{SF}}{d\Omega_x} + \frac{d\sigma^{SF}}{d\Omega_y} - 2 \frac{d\sigma^{SF}}{d\Omega_z} \right) = -2 \left(\frac{d\sigma^{NSF}}{d\Omega_x} + \frac{d\sigma^{NSF}}{d\Omega_y} - 2 \frac{d\sigma^{NSF}}{d\Omega_z} \right), \quad (8.31)$$

The magnetic contribution is separated by the directional dependence with respect to \mathbf{P} and identifies the magnetic contribution, while all nuclear scattering is independent of the direction of \mathbf{P} .

An application example for the XYZ-separation is given in Fig. 8.17 and identifies the weak magnetic diffuse scattering from a Keplerate, a molecular magnet $\text{Mo}_{72}\text{Fe}_{30}\text{X}$ of high symmetry with 30 magnetic vertex sites of Fe (X represents a larger number of H, C, and N atoms). The magnetic intensity (right figure) agrees favorably with the predicted structure resulting from a model with antiferromagnetic exchange between the Fe moments.

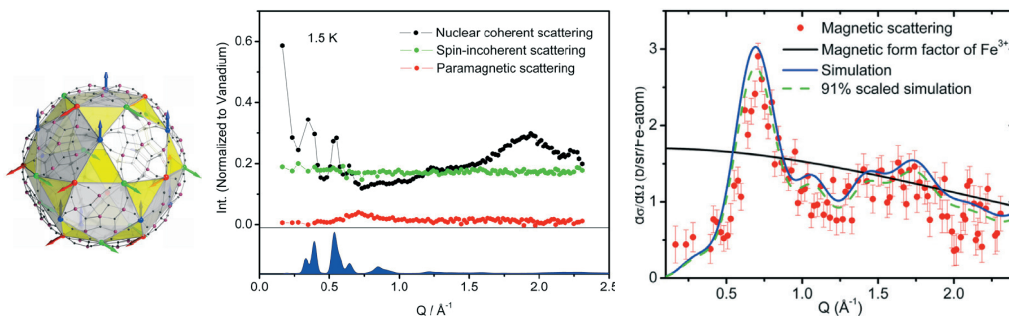


Fig. 8.17: $\text{Mo}_{72}\text{Fe}_{30}\text{X}$ molecule (magnetic Fe-ions at vertices, Mo-purple; X: O-black, H, C not shown) and a 3-sublattice non-collinear spin model resulting from AF Heisenberg exchange (left). XYZ-separation of weak magnetic intensities (middle). Comparison of the magnetic intensity and the spin-model calculation (right). [34]

Of course, single crystals can be also measured efficiently with multi-detectors by rotating the sample, *i.e.* by rotating the Ewald circle in the scattering plane. In the following example, see also Fig. 8.18, a study [35] on the "spin-ice" system $\text{Ho}_2\text{Ti}_2\text{O}_7$, a cubic pyrochlore structure, the horizontal scattering plane has been mapped with measuring spin flip scattering and \mathbf{P} vertical, obtaining the in-plane magnetic scattering (plus some weak flat background from spin-incoherent scattering). The tetrahedral network and Ising $\langle 111 \rangle$ spin-anisotropy leads to strong frustration for ferro-type exchange. In the ordered state the local spin-correlations can be described for each tetrahedra by a simple rule: two spins are pointing along the $\langle 111 \rangle$ cube diagonals towards the center of the tetrahedra and two spins point outwards. Actually this rule is the perfect analogue to the ice rules in hexagonal ice, describing the hydrogen bonds around the tetrahedral environment of the O ions.

Hence Pauling's famous ice model also explains why there should be a residual entropy due to remaining disorder in spin-ice, which is the origin of the broad diffuse scattering at low temperatures.

The extraordinary features of this diffuse scattering are so-called pinch-points, the saddle-points in intensity at (111) and (200) positions; on one hand the intensity variation radially, along the modulus of Q , is rather smooth, involving short-range correlations, on the other hand the transverse variation at constant Q is almost discontinuous and singular, which involves many Fourier coefficients and long-range correlations. The explanation is that the ice-topology creates effectively long-range interactions, – any local decision for a specific two-in two-out spin configuration imposes far-reaching constraints for the other tetrahedra –, an effective interaction that can be mapped to Coulomb interaction between monopoles and provides a picture, where the dipole moments in their local sums over four tetrahedral sites can be viewed as two separated monopoles. [35]

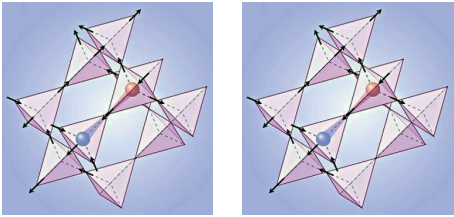


Fig. 8.18: *Spin-ice.* left: *Topological magnetic monopoles*, middle: *measured diffuse scattering from $\text{Ho}_2\text{Ti}_2\text{O}_7$ at $T=1.7\text{K}$ with $\mathbf{P} \parallel z$ in spin-flip mode; note pinch points at (002) and (111)* ; right: *Monte Carlo simulations of based on a nearest neighbor exchange model.* From [35]. Reprinted with permission from AAAS.

From the methodological point of view, for the case above, polarization analysis with measuring spin flip intensities for $\mathbf{P} = P_z$ is simple and most appropriate to access correlation of spin components in the scattering plane. However, for a rigorous and systematic separation the interested reader is referred to two important recent extensions of the classical XYZ-method of Schärpf [33]: (i) for single crystals and multi-detectors separating all magnetic and nuclear contributions by including polarization reversal [25], (ii) for a separation of out-of-plane scattering using 2D detector systems using two additional measurements with orthogonal in-plane polarizations. [36]

8.4 Final remarks and outlook

Polarized neutrons certainly prove to be very useful and may reveal structural and dynamic properties that are hidden to conventional neutron scattering. Applications are growing, slowly, since experimental techniques are more challenging and also because of the additional time requests for experiments. While there has been little gain in the average brightness of neutron sources since the early days, instrumentation has become much more efficient. Looking at count rates of Ni of MRK in Fig. 7.8 a comparison to the instrument DNS using multiple detectors shows a gain of about three orders of magnitude.

The most modern and intense neutron sources are the MW pulsed spallation sources SNS in the USA, JPARC in Japan and in near future the **European Spallation Source ESS**. There is a great challenge and potential gain in using a pulsed beam with wide wavelength band rather than a monochromatic beam.

At ESS, there is currently a dedicated polarized instrument under construction called MAGIC. Its scheme is depicted in Fig. 8.19. Based on a **time-of-flight Laue technique** combined with position sensitive area detectors, it gives access to large volumes in reciprocal space with favorable resolution. Characteristic features are a 1.7 \AA bandwidth of highly polarized neutrons within a spectrum of 0.6 to 6 \AA wavelength from the peak fluxes of the thermal and cold moderators.

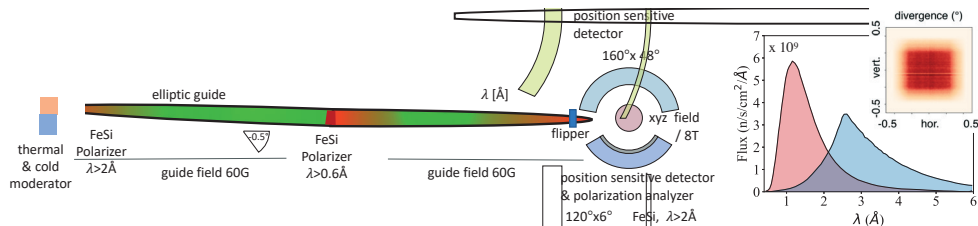


Fig. 8.19: Scheme of the ESS instrument MAGIC

In virtual experiments, simulating instrument, sample and scattering, the performance of this instrument has been studied and optimized. A few examples are shown in Fig. 8.20.

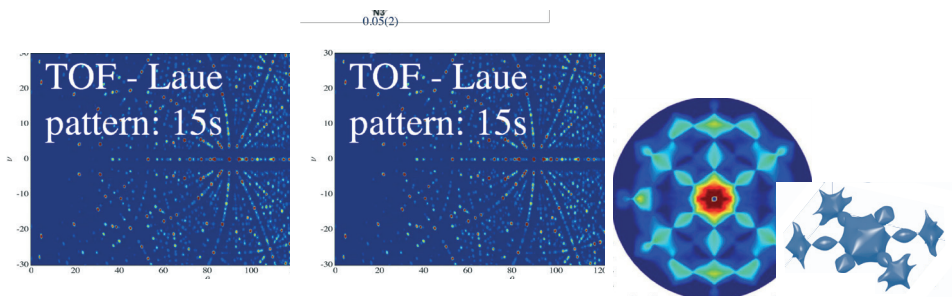


Fig. 8.20: Virtual experiments (McStas, Xavier Fabreges) on the ESS instrument MAGIC. left: time-of-flight Laue diagram from a 1mm³ sample of C₆₀; middle: reconstructed spin density map (in μ_B) from a molecular nano-magnet right: Ho₂Ti₂O₇ spin-ice scattering with 3 dim mapping in Q space..

The first one shows a Laue pattern from a small mm³ crystal (C₆₀). In contrast to normal Laue diffraction, with measuring the time-of-flight of the pulsed white beam all Bragg peaks are separated with a 3D access to reciprocal space. The gain compared to a conventional monochromatic instrument with a single detector is of course very high. Considering the determination magnetic structures with spin densities and weak moments, see Fig. 8.14 for comparison, it took two weeks counting with a single detector, while the best current instrumentation with a multi-detector and monochromatic beam would require two days, and the simulations, see middle of Fig. 8.20, show this will be possible with the same high quality already in 15 minutes. The example Fig. 8.20 (right) shows the simulation of the spin-ice scattering of Ho₂Ti₂O₇ based on the model of [37]. Here, with shorter wavelength a larger Q-range can be seen, compare Fig. 8.18 and again, with white beam and position sensitive detectors the Q-space is explored in 3D. The gain in efficiency, which is about three orders of magnitude will open capabilities to measure even very small samples and weak magnetic features.

References

- [1] Halpern and Johnson, Phys Rev **55**, 898 (1939).
- [2] M. Blume, Phys. Rev. **130**, 1670 (1963).
- [3] S. V. Maleyev, V. G. Baryakhtar P. A. and Suris, Fiz. Tv. Tela **4**, 3461 (1962); Soviet Phys. Solid State **4**, 2533 (1963).
- [4] R.M. Moon, T. Riste, W.C. Koehler, *Polarization analysis of thermal neutron scattering*, Phys. Rev. **181**, 920 (1969).
- [5] F. Mezei, Z. Phys. Rev. **255**, 146 (1972).
- [6] Otto Schärpf, AIP Conf. Proc. **89**, 175 (1982).
- [7] Tasset *et al.*, J. Appl. Phys. **63**, 3606 (1988).
- [8] P. J. Brown, J. B. Forsyth, and F. Tasset, Proc. Roy. Soc. London A **442**, 147 (1993); P.J. Brown, *Polarimetric Neutron Scattering*, in lecture notes on *Polarized Neutron Scattering* (Eds. Th. Brückel and W. Schweika), Schriften des Forschungszentrums Jülich, Series Matter and Materials Vol.**12**, Forschungszentrums Jülich (2002).
- [9] Alvarez, L. W., F. A. Bloch, *Quantitative determination of the neutron magnetic moment in absolute nuclear magnetons*, Phys. Rev. **57**, 111 (1940). negative sign of γ_n : P.N. Powers, *The magnetic scattering of neutrons*, Phys. Rev. **54**, 827 (1938).
- [10] Charles M. Sommerfield, Phys. Rev. **107**, 328 (1957). Magnetic Dipole Moment of the Electron: Julian Schwinger, Phys. Rev. **73**, 416 (1948).
- [11] O. Schärpf, in *Neutron Spin Echo Lecture Notes in Physics* **128**, Ed. F. Mezei, Springer, pp. 27-52 (1980).
- [12] F. Klein, *The mathematical theory of the top*, Princeton 1897; see also H. Goldstein, *Klassische Mechanik*, Akademische Verlagsges. Frankfurt am Main (1974).
- [13] O. Schärpf, J. Physics E: Sci. Instrum. **8**, 268 (1975); F. Mezei, Commun. Phys. **1**, 81 (1976); P. Böni, J. Neutron Research **5**, 63 (1996).
- [14] <http://www.swissneutronics.ch/products/coatings.html>
- [15] E. Babcock *et al.*, Journal of Physics: Conference Series 711 (2016) 012008.
- [16] G.L. Squires, *Introduction to the theory of thermal neutron scattering*, Cambridge University Press, Cambridge (1978).
- [17] A. C. Genix *et al.* Macromolecules **39**, 3947 (2006).
- [18] O. Schärpf, *The spin of the neutron as a measuring probe*, Chapter 11, p. 228, <http://82.135.31.182/neutronpol.pdf>
- [19] S. Disch, PhD thesis, RWTH Aachen (2010); New Journal of Physics **14**, 013025 (2012).

- [20] W. Schweika, *Physica B* **335** (1-4), 157 (2003).
- [21] W. Schweika, S. Easton, and K.-U. Neumann, *Neutron News* **16**, 14 (2005).
- [22] F. Tasset *et al.*, *Physica B* **267** (1-4) 69-74 (1999).
- [23] M. Janoschek *et al.* Spherical neutron polarimetry with MuPAD, *Physica B* **397** (1-2), 125-130 (2007).
- [24] N. Qureshi, arXiv:1801.08431v2 (2018).
- [25] W. Schweika, *J. Phys. Cons. Ser.* **211**, 012026 (2010).
- [26] J. Schweizer, *Magnetic Form Factors and Magnetization Densities Investigated by Polarized Neutron Diffraction* in lecture notes on *Polarized Neutron Scattering* (Eds. Th. Brückel and W. Schweika), Schriften des Forschungszentrums Jülich, Series Matter and Materials Vol. **12**, p. 291, Forschungszentrums Jülich (2002).
- [27] M. A. Aebersold *et al.* *J. Am. Chem. Soc.* **120**, 5238 (1998).
- [28] I. A. Kibalin and A. Gukasov, *Phys. Rev. Research* **1**, 033100 (2019).
- [29] . W. Schweika *et al.* *Phys. Rev. X* **12**, 021029 (2022).
- [30] O. Schärpf, *Physica B* **182**, 376 (1992).
- [31] W. Schweika and P. Böni, *Physica B* **297**, 155 (2001).
- [32] J. R. Stewart *et al.*, *J. Appl. Cryst.* **42**, 69 (2009).
- [33] O. Schärpf, H. Capellmann, *Phys. Stat. Sol. (a)* **135**, 359 (1993).
- [34] Z. Fu *et al.*, *New Journal of Physics* **12**, 083044 (2010).
- [35] T. Fennell *et al.* *Science* **326**, 415 (2009).
- [36] G. Ehlers *et al.* *EPJ Web of Conferences* **83**, 03004 (2015).
- [37] C. Henley, *The Coulomb phase in frustrated systems* *Ann. Rev. Condens Matter Phys.* **1** 179-210 (2010).

Exercises

Exercise 1: How good is the polarization? Consider a few cases:



(i) Spins are evenly distributed within a cone of $\pm\pi/4$ around z .
Make first a good estimate and calculate P_z .

(ii) An initially ideally polarized beam scatters from a Vanadium sample. What is the polarization after scattering? Next, looking more closely, if the sample is relatively thick and has a 20% scattering probability, calculate the polarization for two consecutive scattering events.

(iii) Among the isotopes of Ni (see <https://ncnr.nist.gov/resources/n-lengths/elements/ni.html>), you find few, which give spin-incoherent scattering causing a bit of spin-flip scattering. What is the polarization after scattering from natural Ni?

(iv) Actually, Ni is a ferromagnet, so how can we explain the figure 7.8 (left) and would one not expect also magnetic scattering and spin-flip scattering? However, by applying a magnetic field, how could you avoid magnetic scattering?

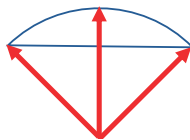
Exercise 2: Which is the required field in a flipper coil to rotate the polarization by π with respect to a external guide field H_z . Consider neutrons of 4 Å wavelength and a path of 1 cm in the flipper.

Exercise 3: Sprint competition of spin up and spin down neutrons. The course is 1 m and neutrons start with a speed of 4000 m/s. Immediately after the start a field of 1 T is switched on, when do the spin-up and spin-down neutrons arrive at the goal?

Exercise 4: Recall the rules about magnetic scattering:

- (i) which component of the magnetic moments with respect to Q are not scattering?
- (ii) which components with respect to P cause spinflip and non-spinflip scattering, respectively.

Exercise 5:



The unit cell displays two sites of different atoms, whose spins are antiferromagnetically ordered. This is an example of a so-called $q=0$ structure, where magnetic and the nuclear crystallographic Bragg peaks coincide. a) How to distinguish the contributions with polarization analysis and which Bragg peaks would you measure? b) Do you see a possibility to distinguish magnetic from nuclear scattering without polarization analysis?

9 Reflectometry and grazing incidence small angle scattering

E. Kentzinger

Jülich Centre for Neutron Science 2

Forschungszentrum Jülich GmbH

Contents

9.1	Introduction	2
9.2	Description of specular reflection	2
9.2.1	Wave equation in homogeneous medium. Optical index	3
9.2.2	Solution for a sharp surface. Fresnel's formulas	5
9.2.3	Total external reflection	6
9.2.4	Reflectivity from layered systems	7
9.2.5	Roughness and interdiffusion	9
9.3	Crystallography at the nanoscale: GISAXS from a nanoparticle assembly	11
9.4	Conclusion	13
9.5	Take-Home Message	14
	References	14
	Exercises	15

9.1 Introduction

Neutron reflectometry is a very efficient tool to determine the nuclear and magnetic density profiles along the depth of nanometric thin films. It has been used a lot to solve soft matter problems like the self organization of diblock copolymers, the structure of liquid-liquid interfaces or the structure of biomembranes [1]. Those studies benefit a lot from the possibility of contrast variation, i.e. the exchange of hydrogen by deuterium.

In the mid 1980's a new field of application of neutron reflectometry emerged. Following the discoveries of interlayer exchange coupling and giant magnetoresistance effect in magnetic multilayers [2], there has been an interest to determine, depth-resolved, the magnetic profile (see lecture 10 of this book).

More recently, the interest evolved towards the determination of the correlations of in-plane fluctuations in thin films. Those fluctuations can be nuclear or magnetic, in the bulk of the layers or at their interfaces, or nanometric objects deposited on a surface. The breaking of in-plane invariance introduced by those fluctuations produce scattering of radiation out of the specular direction, called grazing incidence small angle scattering (GISAS).

In this lecture, we will concentrate on neutron and x-ray reflectometry and GISAS for the determination of nuclear and chemical profiles. Section 9.2 shows the calculation of specular reflection at flat and homogeneous surfaces, introducing the concepts of scattering length density, index of refraction and total external reflection. It then describes the reflectivity from various types of layered structures and the effect of interfacial roughness and interdiffusion. Finally, an example of the application of grazing incidence small angle x-ray scattering (GISAXS) for the depth-resolved investigation of the lateral arrangement of nanoparticles is depicted (section 9.3).

9.2 Description of specular reflection¹

A monochromatic, well collimated beam impinges under a well defined, small angle $\alpha_i = \theta$ (in most cases $\theta \ll 5^\circ$) onto the surface of the sample. It is then partly reflected specularly from the surface, i.e. the outgoing angle $\alpha_f = \theta$ as well, and partly refracted into the material (See Fig. 9.1). As we will derive below, the reflection from a laterally homogeneous medium can be treated according to classical optics. Only the proper index of refraction n has to be used.

For most material, the index of refraction for neutrons is slightly smaller than 1, leading to total external reflection for small angles of incidence $\theta < \theta_c$, where θ_c depends on the material.

In the case of a single layer on the substrate, reflection and refraction take place at both the surface and the interface (Fig. 9.2). Then, the reflected beams from the different interfaces interfere with each other. Maximum intensity is received, when the path length difference between the two reflected beams is an integer multiple of the wavelength.

¹ A large part of this section is taken from Ref. [3–5].

For the case of perfectly smooth surface and interfaces, an exact description of the reflected and transmitted intensity can be deduced from quantum theory, as will be shown in the next subsections.

When the in-plane invariance of the layers or interfaces is broken, some diffuse signal can be observed out of the specular direction (Fig. 9.3). This is grazing incidence small angle scattering (GISAS). Its theoretical description goes beyond the scope of this lecture [6, 7].

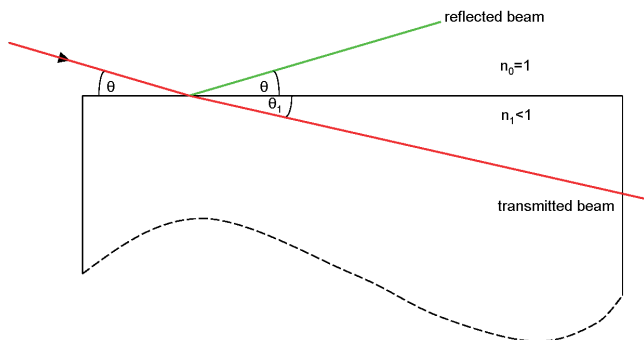


Fig. 9.1: Reflection and refraction from a free surface

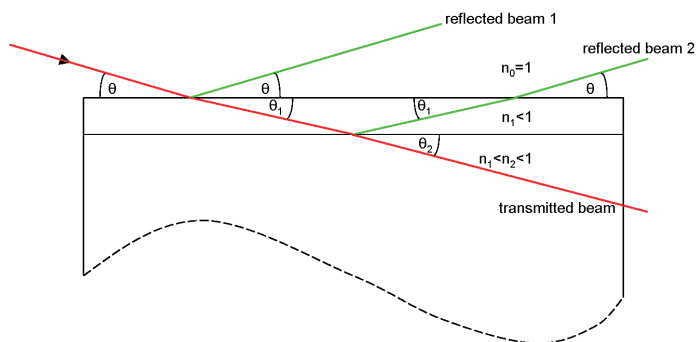


Fig. 9.2: Reflection and refraction from a single layer on a substrate

9.2.1 Wave equation in homogeneous medium. Optical index

The starting point is the Schrödinger equation for the wave function of the neutron:

$$\left[-\frac{\hbar^2}{2m} \Delta + V(\mathbf{r}) \right] \psi(\mathbf{r}) = E\psi(\mathbf{r}) \tag{9.1}$$

The kinetic energy of the neutron is given by $E = \hbar^2 k^2 / (2m)$ with the modulus $k = 2\pi / \lambda$ of the wave vector \mathbf{k} .

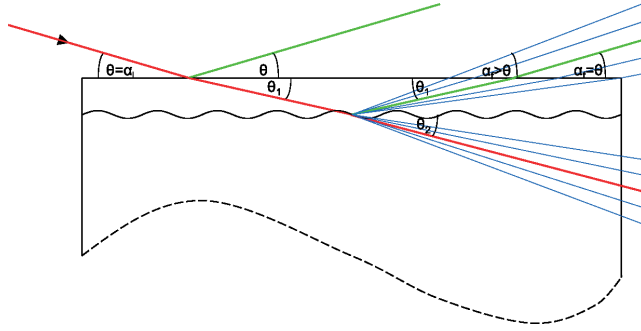


Fig. 9.3: Reflection, refraction and grazing incidence small angle scattering (GISAS) from a single layer on a substrate showing broken in-plane invariance

Due to the small $|\mathbf{Q}|$ values that are probed, a reflectometry experiment does not resolve the atomic structure of the sample in any of the three directions. Therefore, it is a valid approximation to describe the potential V_1 of the homogeneous material as

$$V_1 = \frac{2\pi\hbar^2}{m}\rho \quad (9.2)$$

where ρ is the scattering length density (SLD) defined by

$$\rho = \sum_j N_j b_j \quad (9.3)$$

where N_j is the number of nuclei per unit volume and b_j is the coherent scattering length of nucleus j . With that we receive

$$[\Delta + (k^2 - 4\pi\rho)] \psi(\mathbf{r}) = \left[\Delta + k^2 \left(1 - \frac{\lambda^2}{\pi} \rho \right) \right] \psi(\mathbf{r}) = [\Delta + k_1^2] \psi(\mathbf{r}) = 0 \quad (9.4)$$

with the wave vector k_1 inside the medium. From this equation, it is justified to introduce the index of refraction in the material

$$n = \frac{k_1}{k} \quad n \simeq 1 - \frac{\lambda^2}{2\pi} \rho \quad (9.5)$$

It is a number very close to 1 for thermal and cold neutrons. The quantity $1-n$ is of the order of 10^{-6} to 10^{-5} . For most materials it is positive (because the coherent scattering length b_j is positive for most isotopes), so that n is smaller than 1. This means that the transmitted beam is refracted towards the sample surface, which is opposite to the daily experience with light refracted at a glass or liquid surface.

9.2.2 Solution for a sharp surface. Fresnel's formulas

In analogy to classical optics, we can derive e.g. Fresnel's formulas. For the solution of the wave equation at a sharp surface between air and a semi-infinite medium, we assume the surface of the sample to be at $z = 0$. The potential is then

$$V(z) = \begin{cases} 0 & \text{for } z < 0 \\ V_1 & \text{for } z \geq 0 \end{cases} \quad (9.6)$$

As the potential V is independent of the in-plane coordinates x and y , the wave function in the Schrödinger equation (9.4) is of the form

$$\psi(\mathbf{r}) = e^{i(k_x x + k_y y)} \psi_z(z) \quad (9.7)$$

with the in plane components k_x and k_y of \mathbf{k} independent of z . The Schrödinger equation then reduces to the one dimensional equation

$$\frac{d^2 \psi_z(z)}{dz^2} + k_z^2(z) \psi_z(z) = 0 \quad (9.8)$$

with $k_z(z)$ depending on the medium. The general solution is given by

$$\psi_{zl}(z) = t_l e^{ik_{zl}z} + r_l e^{-ik_{zl}z}, \quad (9.9)$$

where the index l distinguishes between vacuum ($l=0$) and medium ($l=1$) and where

$$k_{z0} = \frac{2\pi}{\lambda} \sin(\theta) \quad \text{and} \quad k_{z1}^2 = k_{z0}^2 - 4\pi\rho. \quad (9.10)$$

The unique solution is determined by the boundary conditions. The incoming wave in the vacuum before interaction with the sample is a plane wave of norm 1, i.e. t_0 is equal to 1. In a half-infinite medium, there is no reflected wave, because there is nothing to reflect from, i.e. r_1 vanishes. In addition, the wave function and its first derivative must be continuous at the interface. So we receive the following boundary conditions:

$$t_0 = 1 \quad ; \quad r_1 = 0 \quad ; \quad \psi_{z0}(z=0) = \psi_{z1}(z=0) \quad ; \quad \frac{d\psi_{z0}}{dz}(z=0) = \frac{d\psi_{z1}}{dz}(z=0). \quad (9.11)$$

When we insert (9.9) into (9.11) we receive the continuity equations for the wave function:

$$1 + r_0 = t_1 \quad ; \quad k_{z0}(1 - r_0) = k_{z1}t_1. \quad (9.12)$$

t_1 is the amplitude of the transmitted wave and r_0 is the amplitude of the reflected wave. The reflectivity R is defined as the modulus squared of the ratio of the amplitudes or reflected and

incoming waves, the transmissivity T is defined as the modulus squared of the ratio of the amplitudes of transmitted and incoming waves.

$$R = |r_0|^2 \quad ; \quad T = |t_1|^2 \quad (9.13)$$

In conclusion, we arrive at the Fresnel's formulas for the reflection and the refraction at a flat interface

$$\text{Reflectivity :} \quad R = \left| \frac{k_{z0} - k_{z1}}{k_{z0} + k_{z1}} \right|^2 \quad (9.14)$$

$$\text{Transmissivity :} \quad T = \left| \frac{2k_{z0}}{k_{z0} + k_{z1}} \right|^2 \quad (9.15)$$

The reflectivity and transmissivity are plotted below as a function of θ .

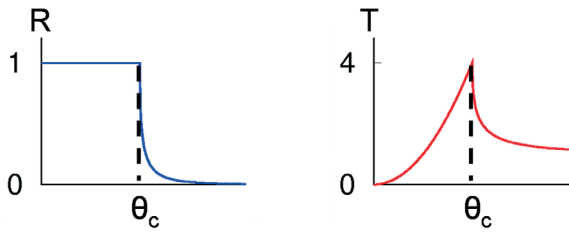


Fig. 9.4: Reflectivity and transmissivity of a substrate as a function of the angle of incidence

9.2.3 Total external reflection

For $k_{z1}^2 < 0$ in Eq. (9.10) i.e. for angles of incidence θ below the so called critical angle θ_c with

$$\theta_c \simeq \lambda \sqrt{\frac{\rho}{\pi}} \quad (9.16)$$

total reflection is observed, i.e. all intensity is reflected and no wave propagating in z -direction exists in the sample. Only an evanescent wave in the z -direction with propagation parallel to the surface is induced (k_{z1} is purely imaginary). For an angle of incidence above θ_c , the beam can partially penetrate the sample and is only partly reflected. Fig. 9.5 provides a calculation of the penetration depth Λ , defined as the inverse of the imaginary part of k_{z1} . Λ is equal to 10 nm at $\theta = 0$ and increases sharply (be attentive to the logarithmic scale) when θ crosses θ_c . It stays finite above θ_c because of absorption (ρ has actually an imaginary part).

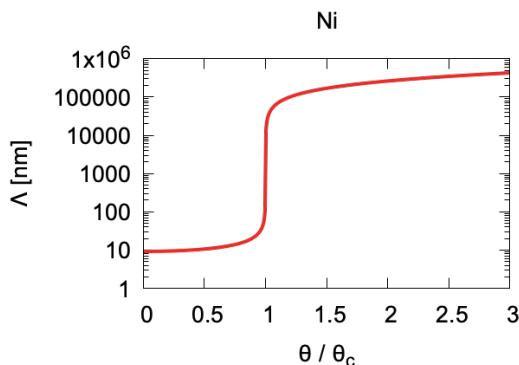


Fig. 9.5: Penetration depth of 6 Å wavelength neutrons in a nickel substrate

Note also in Fig. 9.4 that the transmissivity increases monotonously up to a value of 4 at θ_c and decreases to 1 at large angles. This result might look very surprising at first sight. The value of 4 for the transmissivity comes from the fact that the incident and the reflected waves in vacuum superpose to form a stationary wave of amplitude exactly equal to 2 at the interface with the medium. For the intensity, we obtain a factor of 4.

9.2.4 Reflectivity from layered systems

In a layered system, the same Ansatz as in Eq. (9.9) can be written in each layer l . The coefficients of reflection r_l and transmission t_l can be deduced recursively from the continuity relations of the wave function and its derivative at each interface. If N is the number of layers, and considering the vacuum on top of the multilayer and the substrate below, $2(N+2)$ coefficients have to be calculated. The number of interfaces being $N+1$, the continuity relations lead to $2(N+1)$ equations. Two other equations are obtained considering that the transmission into the vacuum is equal to one ($t_0 = 1$) and that, in the substrate, there is no reflected wave ($r_{N+1} = 0$), leading in total to a number of equations equal to the number of coefficients to determine. The calculation of the coefficients of reflection and transmission in each layer and, in particular, the calculation of the reflectivity in air are therefore possible [9].

Here we just want to demonstrate with very simple arguments how interference effects from layered structures arise and how the intensity modulations in Q-space are related to real space length scales.

Fig. (9.2) shows how interference can occur in a system composed of a single layer of thickness d deposited on a substrate. Interference occurs between beams reflected from the surface and those first transmitted in the layer, reflected from the interface between layer and substrate and then leaving the layer into vacuum. To a good approximation, refraction at the top surface can be neglected for incident angles twice the critical angle or total reflection. In this case $\theta = \theta_1$ in Fig. (9.2) holds. Since the index of refraction of the neutrons is very

close to one, this approximation is valid even for rather small angles of incidence. Then the optical path length difference between the two beams is:

$$\Delta = 2d \sin \theta \quad (9.17)$$

We can now determine the distance between interference maxima from the condition that the path length difference has to differ by one wavelength: $\lambda = 2d \cdot \delta(\sin \theta) \simeq 2d \cdot \delta\theta$. With $Q = \frac{4\pi}{\lambda} \sin \theta \simeq \frac{4\pi}{\lambda} \theta$ we finally obtain:

$$\delta Q \simeq \frac{2\pi}{d} \quad (9.18)$$

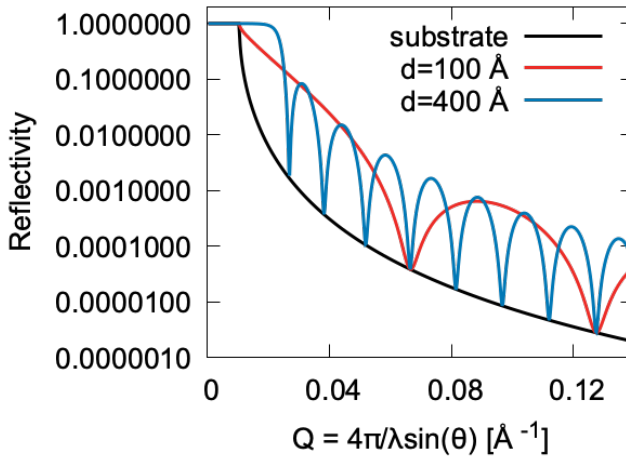


Fig. 9.6: Reflectivity of a Si substrate and reflectivity of a Ni layer ($\rho = 9.41 \times 10^{-6} \text{ \AA}^{-2}$) on Si substrate ($\rho = 2.15 \times 10^{-6} \text{ \AA}^{-2}$). Simulations are performed for two layer thicknesses d .

We can see that the interference phenomena in Q -space are connected with real space length scales in a reciprocal way. (9.18) tells us that there will be a number of interference maxima at a distance in Q of $\frac{2\pi}{d}$. These interference phenomena are called “Kiessig fringes”. Fig. 9.6 shows calculations of the reflectivity of a Ni layer deposited on a Si substrate. One observes that the reflectivities above the critical angle for total reflection decrease rapidly, therefore the ordinate is on a logarithmic scale. The oscillations of the reflectivity due to the above described interference effect can be observed. At small angles, due to the effect of refraction, the interference maxima are a bit denser distributed than at higher angles where formula (9.18) can be used to determine the layer thickness from the distance between the interference maxima. The thinner layer corresponds to an interference scheme with a bigger period. In both cases the minima of the interference scheme lay on the reflectivity of the Si substrate.

Note that for a 100 Å thick layer of Ni, that has a scattering length density (SLD) approximately 4 times larger than the one of Si, the critical angle of total reflection is determined by the SLD of Si and not by the one of Ni. This comes from the penetration depth of the neutrons that is bigger than 100 Å. For a 400 Å thick Ni layer, the θ_c approaches the one of Ni and the total reflection plateau is somewhat rounded.

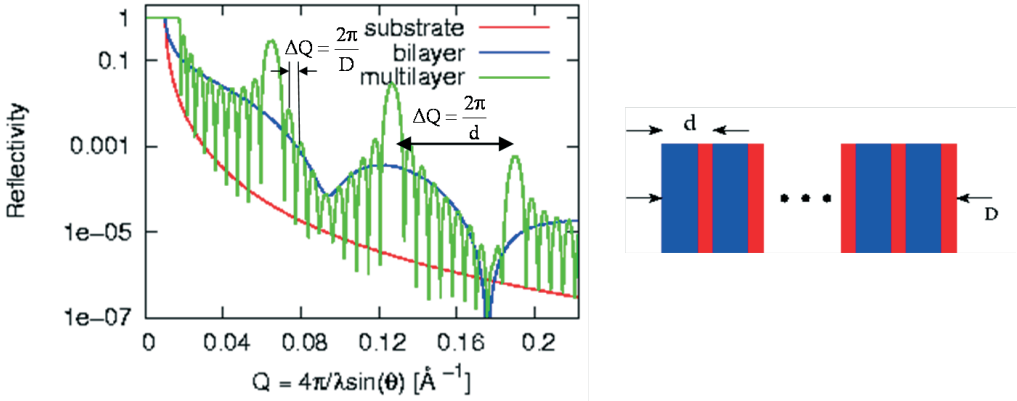


Fig. 9.7: Reflectivities of a Ni/Ti bilayer and of a Ni/Ti multilayer on Si substrate. Simulations are performed for Ni and Ti thicknesses of 70 and 30 Å respectively.

Fig. 9.7 shows the simulation of the neutron reflectivity from a multilayer on a Si substrate. This multilayer is composed of 10 double layers of 70 Å Ni and 30 Å Ti. One can clearly see the pronounced maxima due to the periodicity of the Ni/Ti double layer of thickness 100 Å. In between, one observes many weaker oscillations (be attentive to the logarithmic scale) with a period given by the total thickness of the multilayer.

9.2.5 Roughness and interdiffusion

Until now we assumed perfectly flat interfaces. A real interface will, however, always show a certain roughness at the atomic level, as shown in Fig. 9.8. The height profile of the interface is completely described by the parametrization $z(x, y)$. Such a detailed information is not at all interesting. Much more interesting are parameters that statistically describe the interface, such as the mean squared deviation from an ideally flat interface, or the lateral correlation length. Those parameters can be determined from reflectometry and scattering under grazing incidence [6].

As simplest model, we assume that the height coordinate z follows a random distribution of values around the nominal value z_j of the flat interface. The random distribution being described by a Gaussian function

$$P(\Delta z) = \frac{1}{\sigma\sqrt{2\pi}} \exp\left(-\frac{\Delta z^2}{2\sigma^2}\right), \quad (9.19)$$

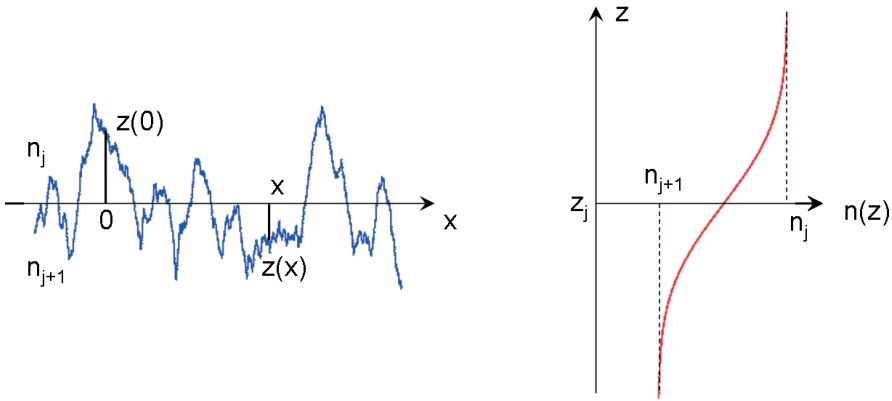


Fig. 9.8: Roughness of a real interface, characterized by the parametrization $z(x, y)$ and dependency of the refractive index on z .

the profile of index of refraction between layers j and $j + 1$ takes the form:

$$n(z) = \frac{n_j + n_{j+1}}{2} - \frac{n_j - n_{j+1}}{2} \operatorname{erf}\left(\frac{z - z_j}{\sqrt{2}\sigma_j}\right) \quad (9.20)$$

with the “Error” function:

$$\operatorname{erf}(z) = \frac{2}{\sqrt{\pi}} \int_0^z e^{-t^2} dt. \quad (9.21)$$

The reflectivity from such a rough interface is obtained from the average of the reflectivities from a sequence of layers that describe the profile of refraction index. This average is performed in detail in Ref. [10, 11]. As a result one obtains that the Fresnel coefficient for an ideally flat interface has to be modified by an exponential damping factor in the following way:

$$R_{\text{rough}} = R_{\text{flat}} \cdot \exp(-4\sigma_j^2 k_{zj} k_{zj+1}). \quad (9.22)$$

In this equation, σ_j is the root mean squared deviation from the nominal position of the flat interface.

The effects of interfacial roughness on the neutron reflectivity from a Si substrate and from a Ni layer on Si substrate have been simulated in Fig. 9.9. On the left side of Fig. 9.9 one can observe that the effect of roughness is to decrease the reflectivity at large wave vector transfers. The effect of roughness will be seen if the value of the scattering wave vector gets bigger than $1/\sigma$. Therefore, if one wants to determine very small roughness amplitudes, one has to measure the reflectivity till very large reflection angles and over a large dynamical range.

The right side of Fig. 9.9 shows the effect of the roughness of a single layer. The simulations have been performed for ideally flat interfaces, for a rough surface of the layer, for a rough interface between layer and substrate and for the case where both interfaces are rough. One can see that the four cases can be well differentiated. When only one of the two interfaces is rough, the interference pattern due to the reflection on the top and bottom interfaces is suppressed at large wave vectors. If both interfaces are rough, a faster decrease of the averaged reflectivity takes place.

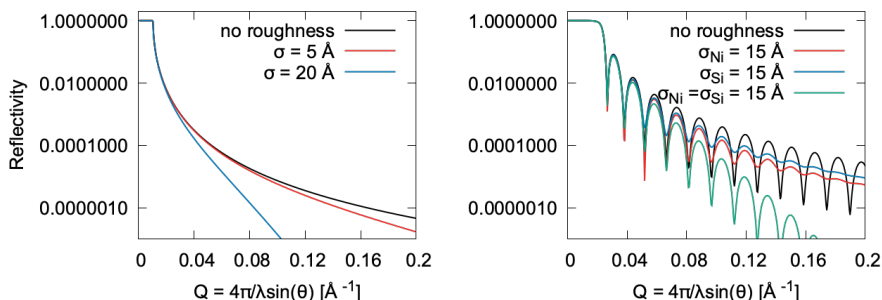


Fig. 9.9: *Left: Neutron reflectivity at the interface between vacuum and Si. Right: Neutron reflectivity from a 400 Å thick Ni layer on Si substrate. Effect of interfacial roughness.*

Finally, one should point out that a specular reflectivity measurement can only describe the profile of scattering length density normal to the interface. This means that a reflectivity measurement can not differentiate between interfacial roughness and interdiffusion, as interdiffusion will induce the same profile of refraction index as in Fig. 9.8. But what happens to the intensity loss described by the exponential factor of Eq. (9.22)? In the case of a diffuse interface, this intensity goes into the transmitted beam because there is no potential gradient in a direction different than the one normal to the interface. On the other hand, in the case of a rough interface, the intensity loss comes from scattering by lateral fluctuations of the potential, leading to intensities that can be observed in directions other than the specular direction: this is off-specular diffuse scattering. A statistical function like the height-height pair correlation function can be determined from the measurement of off-specular scattering [6].

9.3 Crystallography at the nanoscale: GISAXS from a nanoparticle assembly

The prime aim of this section is to emphasize on the added information provided by Grazing Incidence Small Angle Scattering (GISAS) with respect to other surface characterization techniques like Atomic Force Microscopy (AFM) and Scanning Electron Microscopy (SEM). AFM and SEM give information on the in-plane fluctuations of the order parameter, while GISAS allows a full 3 dimensional investigation, i.e. gives depth-resolved information on those in-plane fluctuations.

The study reported here [12] concerns the investigation of the ordering in an assembly of magnetic nanoparticles deposited on a surface. Those nanoparticles, of truncated cubic shape, were deposited under an applied magnetic field, leading to the formation of mesocrystals, i.e. columns (see Fig. 9.10), several hundreds nanometres high and several micrometres diameter, composed of a single crystalline arrangement of nanoparticles (see insert of Fig. 9.11). The whole assembly is a 2 dimensional orientational average of such mesocrystals.

The in-plane arrangement of the nanoparticles in each mesocrystal has been determined by SEM and consists of a square lattice (see insert of Fig. 9.11) of lattice parameter 13.1 nm. Only five different cubic and tetragonal Bravais lattices are compatible with this 2 dimensional arrangement: simple cubic (sc), simple tetragonal (st), body centred cubic (bcc), body centred tetragonal (bct) and face centred cubic (fcc). Two (bcc and fcc) of those five lattices can be excluded from packing and geometrical conditions.

The actual three-dimensional Bravais lattice has been determined by GISAXS, the geometry of the experiment being depicted in Fig. 9.10: a beam of x-rays, well collimated in both directions perpendicular to \mathbf{k}_i , impinges on the surface under an angle of incidence α_i and the scattered x-rays are collected on a position sensitive detector. Each detector pixel is defined by the values of the angles θ and α_f . Taking into account the smallness of those three angles, the components of the scattering wave vector along the three axes depicted in Fig. 9.10 are given by:

$$Q_x = k(\alpha_i^2 - \alpha_f^2 - \theta^2)/2, \quad Q_y = k\theta, \quad Q_z = k(\alpha_i + \alpha_f), \quad \text{with} \quad k = \frac{2\pi}{\lambda}. \quad (9.23)$$

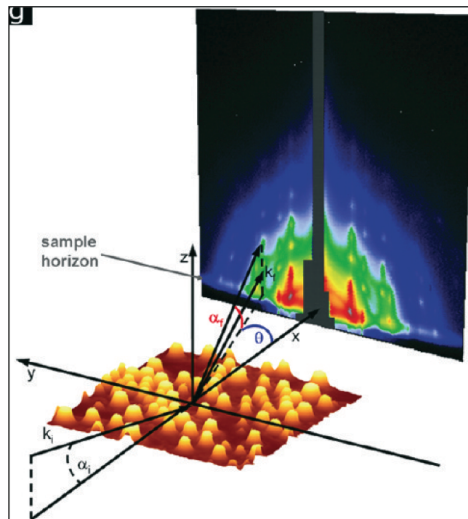


Fig. 9.10: Atomic Force Microscopy (AFM) image of the assembly of magnetic nanoparticles and geometry of the GISAXS experiment. GISAXS signal is collected on a 2 dimensional position sensitive detector. Taken from [12].

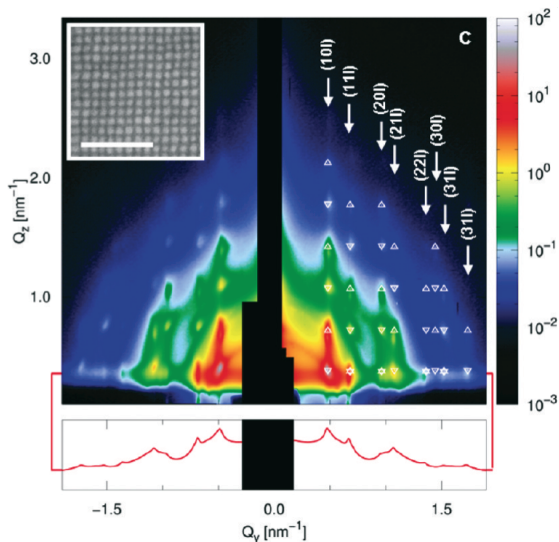


Fig. 9.11: GISAXS pattern of the assembly of magnetic nanoparticles. Insert: Scanning Electron Microscopy (SEM) image of the top of a mesocrystal of nanoparticles; scale bar represents 100 nm. Taken from [12].

The thus obtained GISAXS pattern at a certain angle of incidence α_i of the incoming beam close to the critical angle of total reflection is given in Fig. 9.11. This pattern shows a whole bunch of local intensity maxima at positions in Q_y and Q_z that are characteristic of the crystalline stacking respectively in-plane and out-of-plane. A relation connecting all the Q_z coordinates of the local maxima to their Q_y coordinates is obtained by a combination of Snell’s law and Bragg’s law leading to an extinction rule and an out-of-plane lattice parameter (17.8 nm) characteristic of a bct packing of the nanoparticle lattice.

9.4 Conclusion

This chapter has given an overview of reflectometry and GISAS as a tool for the investigation of thin films, their interfaces or mesoscopic objects deposited on a surface. We have presented a formalism which makes it possible to describe the specular reflectivity on non-magnetic systems. The formalism of neutron reflectometry for the investigation of the magnetic moment orientations in magnetic multilayers is presented in the next chapter of this book, together with several application examples.

9.5 Take-Home Message

Reflectometry of X-rays and neutrons from thin films with thicknesses in the mesoscopic range gives access to the scattering length density profile along their depth. The information is an average over the in-plane coordinates. With GISAS, in-plane correlations of the scattering length density can be investigated. Moreover, depth resolution is accessed by interpreting the GISAS signal as a function of α_i or α_f .

References

- [1] A special issue of *Langmuir* covers a broad range of applications of this technique for the characterization of surfaces and interfaces in the fields of soft matter and biology: *Langmuir* **25**(7), (2009).
- [2] P. Grünberg, *J. Phys. Condens. Matter* **13**, 7691 (2001). See also the web site of the European Magnetism Association, <https://magnetism.eu>
- [3] U.Rücker and E. Kentzinger in *Probing the Nanoworld, 38th IFF Springschool* (Schriften des Forschungszentrum Jülich, Materie und Material, Band 34, 2007). Lecture D4
- [4] Th. Brückel and E. Kentzinger in *Magnetische Schichtsysteme, 30. Ferienkurs des IFF* (Schriften des Forschungszentrum Jülich, Materie und Material, Band 2, 1999). Kapitel B3
- [5] Th. Brückel in *Laboratory course, Neutron Scattering* (Schriften des Forschungszentrum Jülich, Reihe Schlüsseltechnologien, Band 39, 2012). Lecture 14
- [6] S.K. Sinha, E.B. Sirota, S. Garoff, H.B. Stanley, *Phys. Rev. B* **38**:4, 2297 (1988).
- [7] G. Pospelov, W. Van Herck, J. Burle, J.M. Carmona Loaiza, C. Durniak, J.M. Fisher, M. Ganeva, D. Yurov and J. Wuttke, *J. Appl. Cryst.* **53**, 262 (2020). See also <https://www.bornagainproject.org>
- [8] M. Born and E. Wolf, *Principles of Optics* (Pergamon Press, Oxford, 1989).
- [9] L.G. Parratt, *Phys. Rev.* **95**, 359 (1954).
- [10] L. Névet, P. Croce, *Rev. de Phys. Appl.* **15**, 761 (1980).
- [11] J. Als-Nielsen and D. McMorrow, *Elements of Modern X-ray Physics. Second Edition* (Wiley, Chichester, 2011).
- [12] S. Disch, E. Wetterskog, R.P. Hermann, G. Salazar-Alvarez, P. Busch, Th. Brückel, L. Bergström, S. Kamali *Nano Letters* **11**, 1651 (2011). [dx.doi.org/10.1021/nl200126v](https://doi.org/10.1021/nl200126v)

Exercises

In the following the nuclear scattering length densities (in 10^{-6} \AA^{-2}) of several elements are displayed:

Cu: 6.53; Ag: 3.5; Si: 2.15; Au: 4.5

E9.1 * Reflection and transmission by a flat substrate

The following figure shows the neutron reflectivity from a flat substrate.

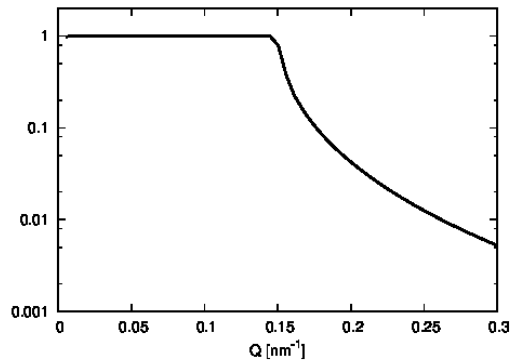


Fig. 9.12: Reflectivity from a substrate.

- Determine the element of which this substrate is made of
- Explain why the amplitude of the wave transmitted in the substrate is equal to 2 at an angle of incidence equal to the critical angle of total reflection

E9.2 * Layers on substrate

The figure below shows two simulations of reflectivity from a Cu layer deposited on Ag substrate. Determine for both cases (red and blue curves) the thickness of the Cu layer.

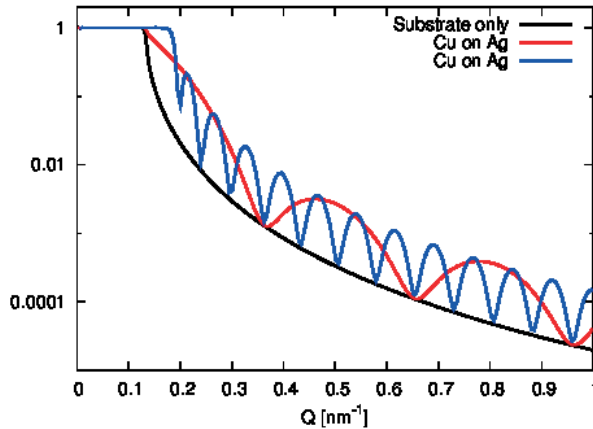


Fig. 9.13: Layer of Cu on Ag substrate

In the next figure, the reflectivity from a [Cu/Au] \times n multilayer is depicted. Determine the [Cu/Au] thickness, the total thickness of the multilayer and the number n of bilayers the multilayer is composed of.

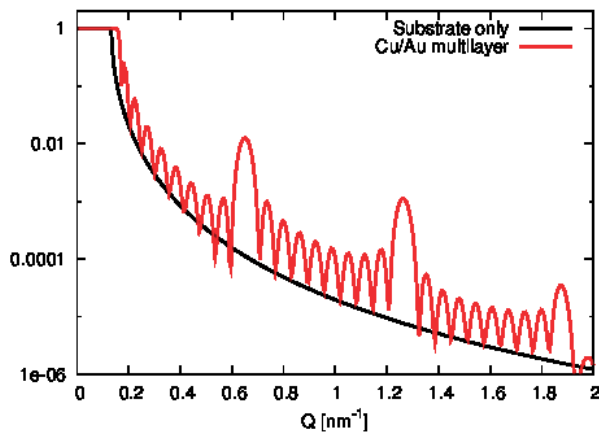


Fig. 9.14: Cu/Au multilayer on Ag substrate

E9.3 * GISAXS from nanoparticles on surface

The figure below shows a simulation of GISAXS from a square lattice of cubic nanoparticles of 5 nm edge length. The radiation wavelength is 1 Å and the plane of incidence of the X-rays is parallel to one edge of the cubes. Determine the lattice parameter.

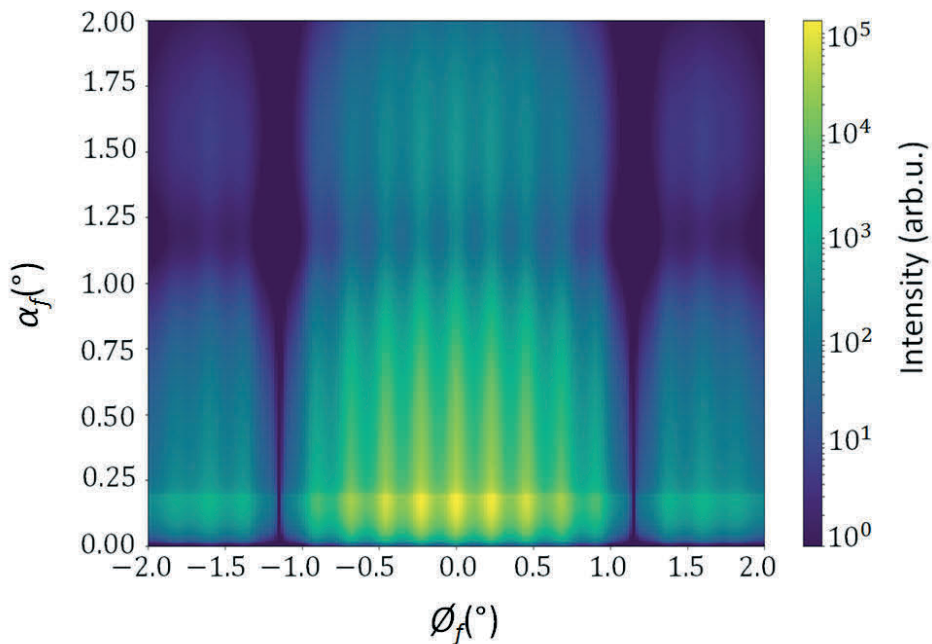


Fig. 9.15: GISAXS from a square lattice of cubic nanoparticles. The horizontal axis shows θ and the vertical one α_f as defined in Fig. 9.10. This simulation was performed by Asma Qdemat (JCNS-2) using the BornAgain software [7].

10 Magnetic Nanostructures

U. Rücker
Jülich Centre for Neutron Science
High Brilliance Source project group
Forschungszentrum Jülich GmbH

Contents

10.1 Introduction	2
10.2 Why are neutrons useful to investigate magnetic nanostructures?	4
10.3 Specular reflectivity of polarized neutrons.....	6
10.4 Layer-by-layer magnetometry	9
10.5 Vector magnetometry	11
10.6 Conclusion.....	16
References	17
Exercises	18

Lecture Notes of the JCNS Laboratory Course Neutron Scattering. This is an Open Access publication distributed under the terms of the Creative Commons Attribution License 4.0, which permits unrestricted use, distribution, and reproduction in any medium, provided the original work is properly cited. (Forschungszentrum Jülich, 2024)

10.1 Introduction

The physical properties of a layered structure of nanometer size, as it is shown schematically in Fig. 10.1, differ from the bulk properties of the constituents. There are several origins of new effects due to miniaturization:

The ratio between surface and volume is much higher than in bulk. Therefore, the number of atoms with reduced coordination is significant and can change the crystalline structure as well as the electronic structure of the whole layer. Boundary conditions, e.g. for the magnetic induction \mathbf{B} become important, introducing shape anisotropies. The magnetization tends to align along the long edges of the magnetic nanostructure because the dipolar fields are smaller then. At the interface between two layers, the electronic structures and the crystal lattices have to be matched, which leads to structural stress, interfacial disorder and electronically to charge transfer (e.g. a Shottky barrier in semiconductor heterostructures) or splitting of the layers' bandstructures.

Nanostructures can be prepared in several dimensions: thin films with a thickness in the nm range are 2D nanostructures, stripes with thickness and width in the nm range are 1D nanostructures, and dots or nanoparticles with all three dimensions in the nm range are 0D nanostructures. The dimension number indicates, in how many directions the dimension remains macroscopic.

Magnetic nanostructures are nanostructures which contain at least one magnetic constituent. Typical systems are layered structures with ferromagnetic and nonmagnetic layers or arrays of ferromagnetic dots on a nonmagnetic substrate. The interesting aspect of 2D magnetic nanostructures is the fact that two ferromagnetic (FM) layers with a nonmagnetic (NM) spacer in between have a connection between their electronic systems across the spacer layer. This connection influences as well the magnetic behaviour as the electron transport through the system.

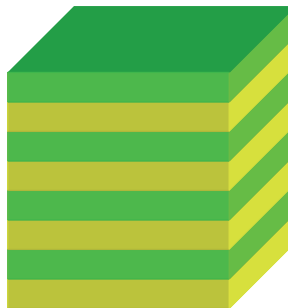


Fig. 10.1: *Sketch of a layered structure of two materials*

The first fundamental phenomenon found in magnetic layered structures has been the oscillating magnetic interlayer coupling in FM / NM / FM trilayer structures. Depending on the NM interlayer thickness, the magnetizations of the two FM layers tend to align parallel or antiparallel to each other [1]. It turned out that the coupling is mediated by electronic states in the NM interlayer close to the Fermi surface [2].

Subsequently, the most important discovery followed, the Giant Magnetoresistance Effect (GMR) [3] [4]. For this discovery, P. Grünberg and A. Fert were honoured with the Nobel Prize for Physics 2007. They have found out that the resistivity of a layered structure containing more than one ferromagnetic layer depends on the mutual orientation of the magnetization directions, see Fig. 10.2. They used the antiferromagnetic coupling in Fe / Cr / Fe trilayer structures to be able to influence the mutual orientation of the magnetization of the Fe layers by changing the applied magnetic field.

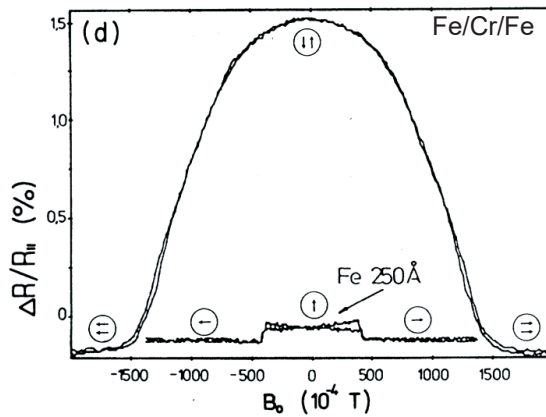


Fig. 10.2: *Giant Magnetoresistance effect in an Fe / Cr / Fe trilayer compared to the anisotropic magnetoresistance effect in a single Fe layer. Reprinted figure with permission from G. Binasch et al., Phys. Rev. B. 39 (1989), 4828 [3]. Copyright 1989 by the American Physical Society.*

It turns out that the resistivity is highest in the case of antiparallel alignment of the two magnetization directions. This effect is much stronger and much more sensitive to changes in the magnetization direction of each ferromagnetic layer than the anisotropic magnetoresistance effect in single ferromagnetic layers, which was known before. The microscopic origin of the GMR effect is the matching between the spin-split bandstructures of the two ferromagnetic layers. The conductivity of the entire structure is the sum of the conductivities for the two spin channels. As the Fermi surface is different for the two spin channels, the matching between the FM and the NM layer is different.

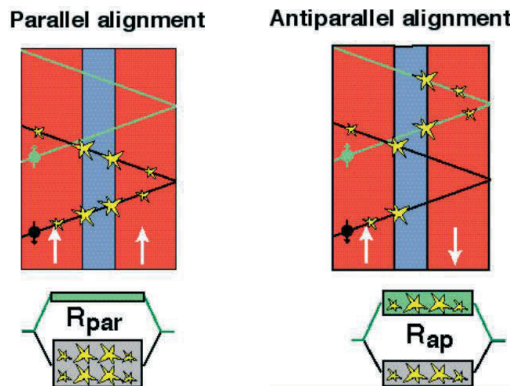


Fig. 10.3: *Different matching of the bandstructures between ferromagnetic and non-magnetic layers changes the resistivity for the different spin channels*

As shown in Fig. 10.3, in the case of parallel alignment, the scattering probability of a conduction electron is the same at both interfaces. For one spin channel, the scattering probability is high while for the other one it is low. The conductivity is then dominated by the spin channel with the smaller scattering probability. The resistivity of the entire structure, which can be described as a parallel wiring of the two resistors for the two spin channels, is small.

In the case of antiparallel alignment, the scattering probability for each spin channel is high in one of the FM layers. This results in a relatively low conductivity for both spin channel, so that the resulting resistivity is much higher compared to the case of parallel magnetization.

As GMR structures are easy to prepare and easy to use, the sensor technology based on this effect quickly became standard in the readout system of computer harddisks and many other applications. Today, it has been replaced by Tunneling Magnetoresistance (TMR), where the nonmagnetic interlayer is insulating and electrons travel across this tunneling barrier while preserving their spin state. Then, the height of the tunneling barrier depends on the spin of the electron and the magnetization direction of both ferromagnetic layers. A detailed overview over the field of spin transport in layered systems is given in Ref. [5].

10.2 Why are neutrons useful to investigate magnetic nano-structures?

For the investigation of magnetism, many methods are well known. In most cases the magnetization of a sample is measured. A different, but more indirect approach is the measurement of spin-dependent bandstructures by absorption and photoemission spectroscopy of polarized light or x-rays.

The first (and oldest) approach is to measure the integral magnetization of a sample by classical magnetometry, e.g. by using a Vibrating Sample Magnetometer (which measures the induction when moving the magnetic sample in a coil), a Faraday balance (which measures the force on

the magnetic sample in a field gradient), or more recently a SQUID magnetometer (which measures the magnetic flux inside a superconducting loop). In case of magnetic nanostructures deposited on any macroscopic substrate, the small signal coming from the nanostructure is always superimposed by the signal from the substrate which is typically 10000 times larger in volume. Even if the nanostructure is ferromagnetic and the substrate only diamagnetic, the correction due to the substrate is in most cases much stronger than the signal itself.

Better adapted to thin structures are methods that are surface sensitive. The magneto-optical Kerr effect (MOKE) measures magnetization with polarized light reflected from a magnetic surface. Due to the magnetization of the sample the polarization direction of the light is modified. This method is surface sensitive in the range of the penetration depth of the light used (typically some 10 nanometers). At synchrotron x-ray sources one can use X-ray Magnetic Circular Dichroism (XMCD). The energy dependence of the absorption of circularly polarized (soft) x-rays is measured at the absorption edges of the magnetic materials. Again, the information is integrated over the penetration depth of the x-ray photons used, but it is element specific due to the choice of the x-ray energy in resonance with the magnetic orbitals of a certain element.

Magnetic domains can be imaged using e.g. Magnetic Force Microscopy (surface sensitive, measuring the stray fields above the sample), Lorentz microscopy (the transmission of electrons through a very thin sample is observed; due to the Lorentz forces the electrons are deviated according to the magnetization strength and direction), or Kerr microscopy (observing the MOKE using an optical microscope; again it integrates over the penetration depth of the light, with the lateral resolution of the optical microscope). Photoemission electron microscopy (PEEM) with soft x-rays can give an overview about the density of certain electronic states with a lateral resolution in the nanometer range and time resolution down to nanoseconds. In combination with XMCD, XMCD-PEEM can visualize the evolution of magnetic domains under variable magnetic fields. But again, the depth resolution is only determined by the penetration depth and the element specific absorption of the x-rays.

What is missing is a method that can access the magnetism of buried layers using the depth information. Here, we need a probe that is sensitive to magnetic fields while having a spatial resolution (at least in depth) in the nm regime. Cold neutrons have a wavelength appropriate for resolving nm length scales and they carry a spin that interacts with the magnetic fields. For most of the magnetic investigations, the neutron's spin has to be prepared in a certain state, so we use polarized neutrons for the investigation of magnetic nanostructures.

Polarized neutron reflectometry with polarization analysis is a method for depth-resolved investigation of magnetic layered structures; I will introduce this method in the following chapter. Together with the analysis of off-specular scattering, lateral structures in the μm range can be investigated, allowing to access magnetic domains in buried layers. Polarized SANS reveals information about magnetic structures in the nm range perpendicular to the beam direction, while polarized GISANS (Grazing Incidence Small Angle Neutron Scattering) combines the possibilities of both methods and allows to access lateral magnetic structures in the nm range in buried layers.

10.3 Specular reflectivity of polarized neutrons

In the previous lecture, you have learned about specular reflectivity of neutrons on layered structures with nuclear scattering contrast. For the investigation of magnetic layered structures, we have to remind that the neutron is a spin $\frac{1}{2}$ particle and therefore interacts with the magnetic induction \mathbf{B} .

To treat the neutron's spin properly, we have to work with wave functions in the 2-dimensional quantum mechanical spin space, where the usual space-dependent functions, e.g. the potential, become operators on the neutron's spin.

In analogy to eq. (9.2), the potential of a homogeneous magnetic material in layer number l can be separated into two parts

$$\hat{V}_l = V_l^N \hat{1} + \hat{V}_l^M \quad (10.1)$$

where V_l^N is the nuclear interaction known from eq. (9.2), and $\hat{1}$ is the unity operator, which does not affect the spin state, so that the nuclear interaction is described independently on the neutron's spin. The magnetic dipole interaction is described by the operator $\hat{V}_l^M = -\mu_n \hat{\boldsymbol{\sigma}} \cdot \mathbf{B}_l$ which is a scalar product of the neutron magnetic moment operator $\mu_n \hat{\boldsymbol{\sigma}}$ and the magnetic induction \mathbf{B}_l inside the material.

For the description in coordinates, we need to define a coordinate system which is convenient to describe the experiment. Typically, the magnetic field \mathbf{H} is applied in the plane of the sample. We choose this direction to be the x-direction of the coordinate system $\mathbf{H} = H\mathbf{e}_x$ and also as the quantization axis for the neutron spin. Under this assumption, the spin operator $\hat{\boldsymbol{\sigma}} = (\sigma_x, \sigma_y, \sigma_z)$ is the following:

$$\sigma_x = \begin{pmatrix} 1 & 0 \\ 0 & -1 \end{pmatrix} \quad \sigma_y = \begin{pmatrix} 0 & 1 \\ 1 & 0 \end{pmatrix} \quad \sigma_z = \begin{pmatrix} 0 & -i \\ i & 0 \end{pmatrix} \quad (10.2)$$

In analogy to chapter 9.2, the Schrödinger equation can be solved in coordinate and spin space, where the eigenvectors $|+\rangle$ and $|-\rangle$ of the operator $\hat{\boldsymbol{\sigma}} \cdot \mathbf{b}_0 = \sigma_x$ with the eigenvalues $+1$ and -1 , respectively, define states of the neutron with "spin up" and "spin down". The solution of the Schrödinger equation is the neutron wave function $|\Psi(\mathbf{r})\rangle$, which is again a linear combination of those two spin states.

$$|\Psi(\mathbf{r})\rangle = \Psi^+(\mathbf{r})|+\rangle + \Psi^-(\mathbf{r})|-\rangle = \begin{pmatrix} \Psi^+(\mathbf{r}) \\ \Psi^-(\mathbf{r}) \end{pmatrix} \quad (10.3)$$

After some calculation which you can find in Ref [6] we end up with a set of two coupled one-dimensional linear differential equations for every layer, which are the analogue to equation (9.8).

$$\frac{\partial^2 \Psi_l^+(z)}{\partial z^2} + [k_{zl}^2 - 4\pi(\rho_l^N + \rho_l^M m_{xl})] \Psi_l^+(z) - 4\pi \rho_l^M m_{yl} \Psi_l^-(z) = 0 \quad (10.4)$$

$$\frac{\partial^2 \Psi_l^-(z)}{\partial z^2} + [k_{zl}^2 - 4\pi(\rho_l^N - \rho_l^M m_{xl})] \Psi_l^-(z) - 4\pi \rho_l^M m_{yl} \Psi_l^+(z) = 0 \quad (10.5)$$

In these formulae, you find the nuclear scattering length density ρ^N that you know from eq. (9.3) together with its magnetic analogue ρ^M , the magnetic scattering length density. It is proportional to the net magnetization M of the material. In case of a ferromagnetic material, the magnetization vector \mathbf{M} typically is aligned in some direction, which is described by the unit vector $\mathbf{m} = \mathbf{M} / M$.

Now, we can have a closer look at the different terms in equation (10.4) and (10.5). As Non-Spinflip (NSF) interaction, one finds in (10.4) for spin + (“spin up”) the sum of the nuclear interaction and the magnetic interaction with the magnetization along the quantization direction and in (10.5) for spin – (“spin down”) the difference. In case of a magnetically saturated layer (all the magnetization is aligned with the external field), the scattering length density for spin + neutrons is enhanced and for spin – neutrons reduced compared to the nonmagnetic case.

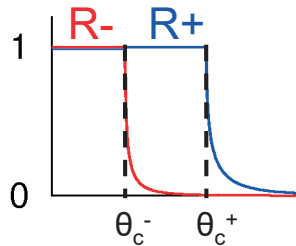


Fig. 10.4: *The total reflection angle θ_c of the surface of a magnetized material is different for both spin directions*

This has an influence on the index of refraction, on the total reflection angle, and of course on the reflectivity, which is a function of the change of the index of refraction at a certain interface. Fig. 10.4 shows schematically the splitting of the total reflection angle.

In case that the magnetization is not fully aligned with the field, the component along the field direction influences the scattering length density for NSF. The in-plane magnetization component perpendicular to the field induces a spin-flip (SF) interaction that is equally strong for both spin-flip channels $+-$ and $-+$, as is described in the last term of eq. (10.5) or (10.4), respectively.

Specular reflectivity of polarized neutrons is not sensitive to any magnetization component perpendicular to the layer plane. This agrees with the statement in lecture 8 (eq. (8.22) f.) that only the magnetization component \mathbf{M}_\perp perpendicular to \mathbf{Q} contributes to the magnetic interaction with the neutron’s spin.

As an example, I would like to show the polarized neutron reflectivity of a [Co / Cu] multilayer. The respective nuclear and magnetic scattering length densities are

$$\text{Co: } \rho_N = 2.30 \cdot 10^{-6} \text{ \AA}^{-2} \quad \rho_M = 4.24 \cdot 10^{-6} \text{ \AA}^{-2}$$

$$\text{Cu: } \rho_N = 6.53 \cdot 10^{-6} \text{ \AA}^{-2} \quad \rho_M = 0.$$

Obviously, the sum of the magnetic and the nuclear scattering length density of Co is almost equal to the scattering length density of Cu. In the case of magnetic saturation, spin + neutrons will not feel any contrast at the Co / Cu interfaces because they see the sum of nuclear and magnetic scattering length density in the Co layer. The multilayer structure is invisible for spin + neutrons. In contrast, spin – neutrons experience the difference of nuclear and magnetic scattering length density (which is in fact negative), so that the contrast is huge.

Fig. 10.5 makes the contrast situation visible by using colours representing the different scattering length densities.

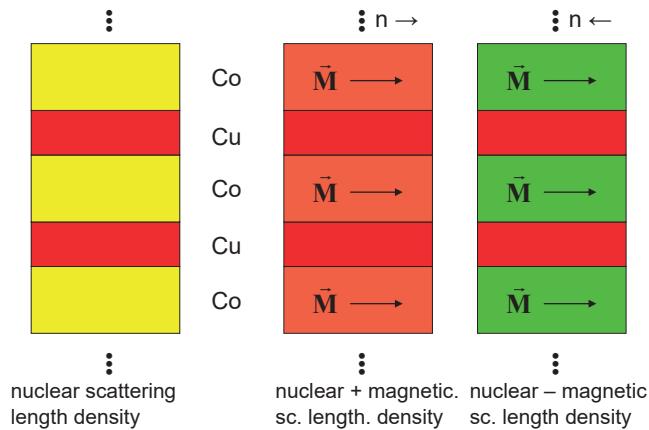


Fig. 10.5: *The contrast between Co and Cu depends on the magnetization state. It almost vanishes for spin up neutrons, but is strong for spin down.*

Fig. 10.6 shows the measured polarized neutron reflectivity of such a multilayer. The total reflection edge is identical for both spin channels, because the biggest scattering length density in the layered structure is the one of Cu, which is not magnetic. But the multilayer Bragg peaks at $2\theta = 3^\circ$ and $2\theta = 6^\circ$ are strongly spin split. For spin – neutrons, the Bragg peak is about 30 times stronger than for spin + neutrons. Here, one can see that the contrast is responsible for the reflectivity, not the strength of the scattering potential, as the scattering length density (which describes the scattering potential) is higher for spin +, but the contrast between the layers is much stronger for spin –.

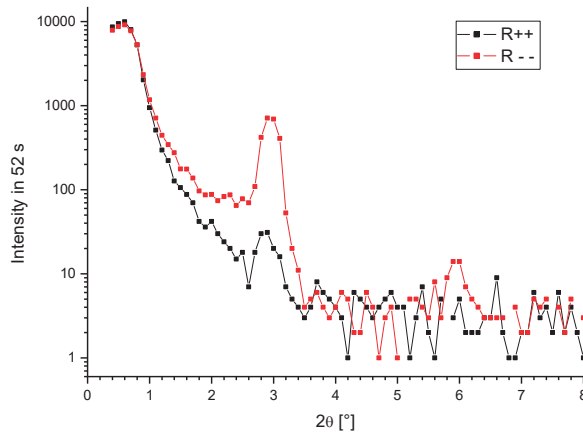


Fig. 10.6: *Specular reflectivity of polarized neutrons from a [Co / Cu] multilayer with 20 periods at magnetic saturation*

10.4 Layer-by-layer magnetometry

One important application of polarized neutron reflectometry with polarization analysis is layer-by-layer magnetometry. As an example, I present the magnetization evolution in exchange bias multilayers of the type $[\text{IrMn} / \text{CoFe}]_N$ with the number of periods [7]. The exchange bias effect is the coupling between a ferromagnetic layer and a neighbouring antiferromagnetic layer. If the antiferromagnet has been cooled below its Néel temperature with the ferromagnet being saturated, it conserves the interface magnetization without being sensitive to the applied magnetic field. This induces an additional unidirectional anisotropy on the ferromagnetic layer, i.e. the original magnetization direction is preferred over all others. The hysteresis loop is shifted away from $H = 0$.

The green curve in Fig. 10.7 shows the exchange biased magnetization curve of an IrMn / CoFe double layer shifted left together with the magnetization loop of the NiFe buffer layer, which is not affected by exchange bias and therefore symmetric around $H = 0$ field. The CoFe layer shows a nice square hysteresis loop, indicating spontaneous magnetization flip at the coercive field.

Strangely, the shape of the magnetization loop of the exchange biased CoFe layers changes, when the number of $[\text{IrMn} / \text{CoFe}]_N$ bilayers is increased. In addition, the strength of the exchange bias is increased.

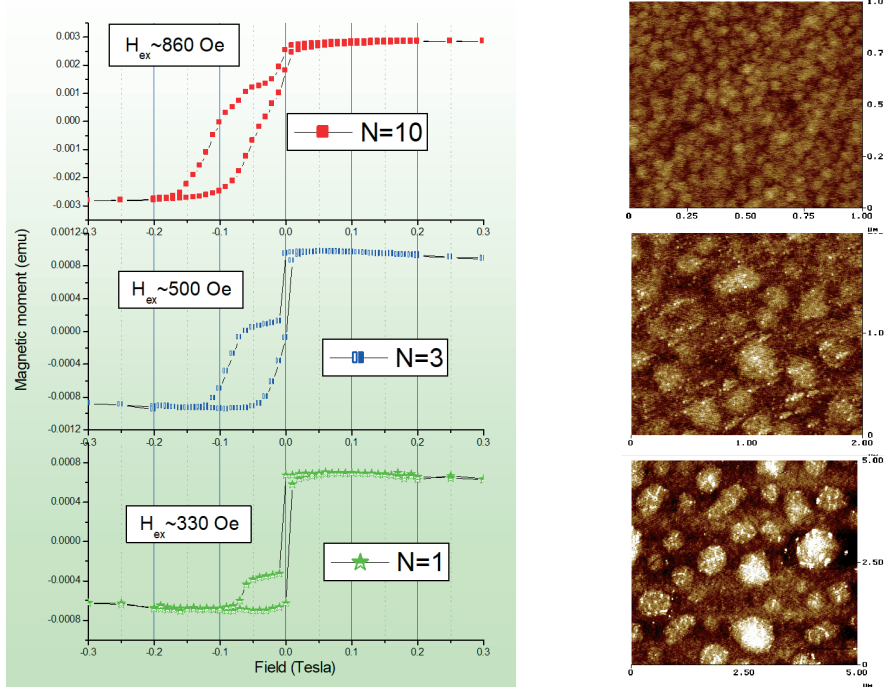


Fig. 10.7: SQUID magnetization measurements (at room temperature, left) and AFM micrographs of the surface (right) of polycrystalline multilayers of the type $\text{SiO}_2 / 10 \text{ nm NiFe} / [5 \text{ nm IrMn} / 3 \text{ nm CoFe}]_N$ with $N = 1, 3$, or 10 , resp.

An AFM study of the surfaces shows that the grain size of the polycrystalline layers is reduced from layer to layer during the preparation procedure, but no information could be found that justifies the slope of the magnetization curves and that could eventually explain the origin of a magnetization rotation process responsible for the gradual evolution of the magnetization as a function of the applied field.

Therefore, a polarized neutron reflectivity study was performed, to investigate the individual behaviour of the ferromagnetic layers in the multilayer structure. As an example, Fig. 10.8 shows the specular polarized neutron reflectivity at one of the coercive fields (i.e. the net magnetization vanishes) together with the fit.

The polarized neutron measurement shows no spin flip signal at all, immediately excluding the idea of a magnetization rotation process. Furthermore, the fit of the measured data shows that the magnetization of the upper 5 CoFe layers is aligned antiparallel to the field while the magnetization of the lower 5 CoFe layers is still aligned along to the field. I.e., the exchange bias on the upper layers (with smaller grains) still can hold the magnetization in the preferred direction, while the magnetization of the lower layers already has followed the field.

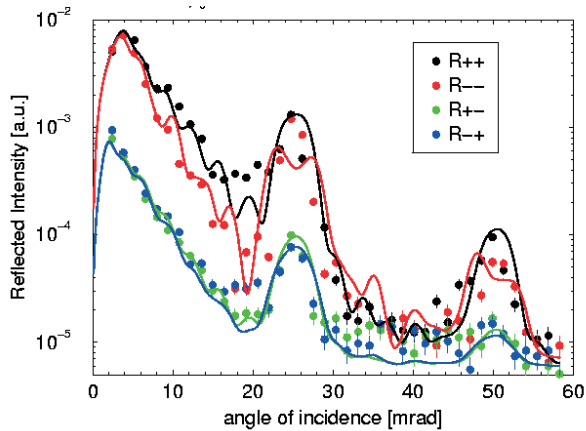


Fig. 10.8: Polarized neutron reflectivity of the sample with $N = 10$ at $\mu_0 H = -0.1$ mT after positive saturation

Together with measurements at several other magnetic field values on both branches of the hysteresis loop it turned out that every single layer has a square magnetization loop, but the strength of the exchange bias effect (i.e. the shift of the centre of the loop away from $H = 0$) increases with reduced grain size. The overlaying of the differently shifted square loops then results in the inclined net magnetization loop measured with magnetometry.

10.5 Vector magnetometry

The second important application of polarized neutron reflectometry with polarization analysis is vector magnetometry in layered structures. The ability to distinguish between SF and NSF channels offers an independent access to the in-plane magnetization components perpendicular and parallel to the field direction. As a magnetization direction perpendicular to the sample surface is rare (due to the shape anisotropy) one can determine the full magnetization vector in most cases.

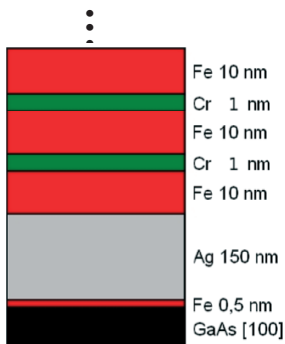


Fig. 10.9: Layer sequence of an epitaxially grown and antiferromagnetically coupled $[Fe/Cr]_N$ multilayer

I would like to explain the power of vector magnetometry using the example of an epitaxially grown and antiferromagnetically (AF) coupled $[Fe/Cr]_N$ multilayer with an odd number of Fe layers [8]. Fig. 10.9 shows the layer sequence of such a sample grown on a GaAs single crystal with a Ag buffer layer to improve

the surface quality. The magnetic behaviour is determined by the competition between 3 different interactions (see Fig. 10.10): The crystalline anisotropy in the single crystalline Fe layers tries to align the magnetization in every Fe layer along one of the in-plane $[100]$ directions. This results in 4 equivalent easy axes. The antiferromagnetic coupling (mediated by the Cr interlayer) has the tendency to align the magnetization of two neighbouring Fe layers antiparallel to each other. The Zeeman term tries to align the magnetization of every ferromagnetic layer along the applied field.

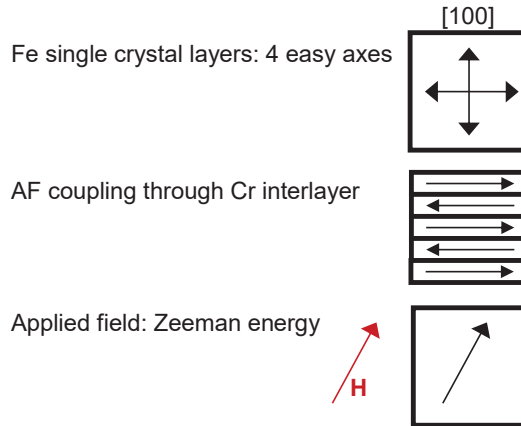


Fig. 10.10: *The magnetic behaviour in an applied magnetic field is governed by 3 competing interactions*

As the multilayer under investigation has an odd number of Fe layers, the antiparallel orientation of the magnetization in remanence (where the Zeeman term is weak) will leave the magnetization of one layer uncompensated, so that the Zeeman energy does not vanish even at very small fields. This effect is supposed to align the remanent magnetization of all layers along or antiparallel to the field direction.

Fig. 10.11 shows MOKE measurements of such a sample with $N = 7$ Fe layers in the multilayer sequence. The MOKE signal is a function of the magnetization, but not proportional to it, because it is a superposition of the longitudinal Kerr effect (proportional to the magnetization along the field) and the transverse Kerr effect (proportional to the magnetization perpendicular to the field). Furthermore, the weight of the layers close to the surface is much higher than the weight of lower lying layers due to the limited penetration depth of the light. Therefore, one should not worry about the MOKE curve not being monotonous. Nevertheless, a jump in the MOKE curve always indicates a spontaneous change of the magnetization state.

In addition, Fig. 10.11 shows a simulation of the integral magnetization component along the field based on a numerical minimization of the three energy terms mentioned above. This kind of simulation cannot reproduce effects of activation barriers leading to hysteresis.

The simulation and the MOKE measurement have a good qualitative agreement. In saturation, the magnetic moment of every layer is aligned with the field. In the intermediate field range, the magnetization is alternatingly pointing left or right from the field direction, so that the

magnetization component along the field is almost equal for every layer and the magnetization components perpendicular to the field fulfil as much as possible the AF coupling.

At remanence, the magnetization of all layers is turned by 90° , so that 4 layers have the magnetization along the field and 3 layers antiparallel to the field. This configuration fulfils as well the AF coupling condition as the alignment of the net magnetization along the applied field.

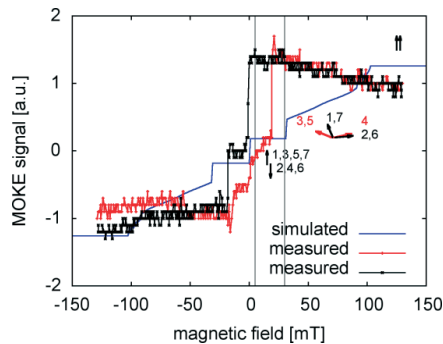


Fig. 10.11: MOKE measurement of $[Fe / Cr]_N$ multilayers with $N = 7$ Fe layers. The simulation of the magnetization curve is based on minimization of the total energy.

Fig. 10.12 shows the polarized neutron reflectivity together with the offspecular scattering at saturation field. One can see a structured signal with total reflection and several Bragg peaks according to the periodicity in the multilayer structure only in the R^{++} channel. For spin – neutrons the contrast between fully magnetized Fe and Cr vanishes, so the R^{--} shows only the total reflection (with a reduced critical angle compared to R^{++}), but no Bragg peaks. As no magnetization component perpendicular to the field direction exists, there is no real spin flip signal. What you see in R^{+-} and R^{-+} is a parasitic signal due to the limited efficiency of the polarizing equipment of the instrument. The Bragg sheets crossing the specular Bragg peaks are due to vertically correlated roughness of the Fe / Cr interfaces.

Fig. 10.13 shows the same in the intermediate field range. Additional Bragg peaks of half order appear, which are stronger in SF compared to NSF. This is the indication of the alternation of the magnetization directions due to the antiferromagnetic coupling. Mainly the magnetization component perpendicular to the field oscillates while the component remaining along the field is modulated less. As the sample is no more saturated, the magnetization component in field direction is reduced, so that the contrast for spin – neutrons does not vanish any more. Therefore, the full order Bragg peaks also come up in R^{--} . They are now mainly induced by the nuclear structure while the magnetic contribution is collected in the half order signal. The strong off-specular signal around the half order Bragg peaks in the SF channels is a signature of magnetic domains.

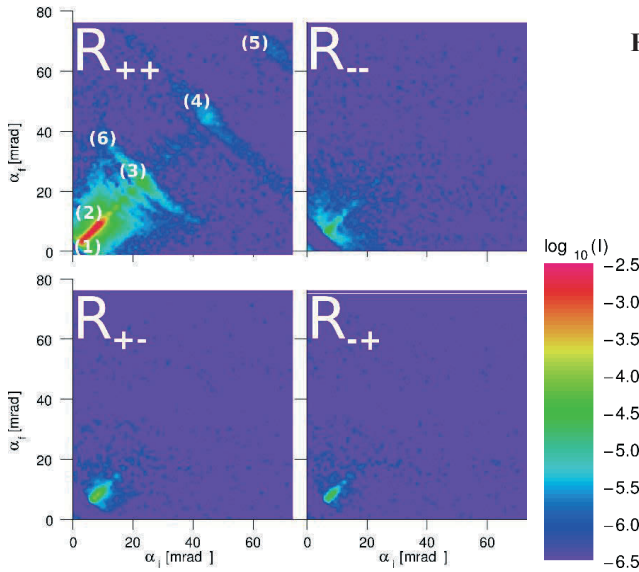


Fig. 10.12: Polarized neutron reflectivity and offspecular scattering of an AF-coupled $[Fe/Cr]_7$ multilayer in saturation field of 300 mT.

Indicated are the primary beam (1) blocked by the beamstop, the plateau of total reflection (2), the first (3), second (4) and third order (5) Bragg peak (giving information about the layer structure), and the Bragg sheets (6) (giving information about correlated roughness).

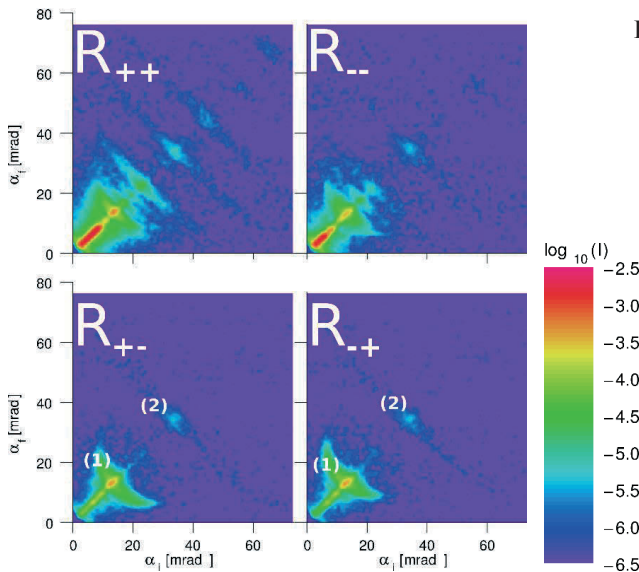


Fig. 10.13: Polarized neutron reflectivity and offspecular scattering of an AF-coupled $[Fe/Cr]_7$ multilayer in intermediate field of 30 mT.

Indicated are the AF superstructure Bragg peaks of the order $1/2$ (1) and $1\frac{1}{2}$ (2).

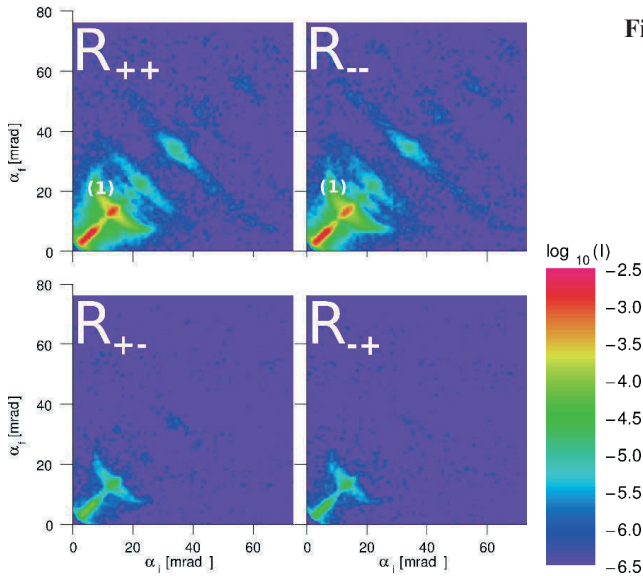


Fig. 10.14: Polarized neutron reflectivity and offspecular scattering of an AF-coupled $[\text{Fe} / \text{Cr}]_7$ multilayers in remanence field of 5 mT.

Indicated are the AF superstructure Bragg peaks of order $\frac{1}{2}$ (1).

At remanence, as shown in Fig. 10.14, all half order peaks appear only in the NSF channels. The small contribution in the SF channels can be explained due to the limited polarization of the neutron beam. This shows that the magnetization of all layers of the $[\text{Fe} / \text{Cr}]_7$ sample is aligned alternately parallel and antiparallel to the field direction, as has been proposed by the simulation for the MOKE measurement.

In addition to the qualitative description presented here, a quantitative analysis of the measurements allows to determine the angle of the magnetization vector of every layer independently. This analysis is presented in Ref. [8].

10.6 Conclusion

Neutron reflectometry with polarized neutrons and polarization analysis is a tool to determine depth-dependent magnetization in layered magnetic nanostructures.

Non-Spinflip (NSF) reflectivity contains information about the magnetization components along the field direction of the different layers inside the structure. As (in magnetic saturation) the spin + neutrons are sensitive to $\rho^N + \rho^M$ and the spin - neutrons to $\rho^N - \rho^M$, the contrast seen by the neutrons with different spin is different due to the magnetized layers.

Spinflip (SF) reflectivity is purely induced by magnetization components perpendicular to the field direction. This is a very sensitive tool to determine magnetization rotation or tilting processes in magnetic structures.

Together with a quantitative modeling of the 4 reflectivity components, the user can determine size and direction of the in-plane components of the magnetization vector in all layers in a layered magnetic structure.

References

- [1] P. Grünberg, R. Schreiber, Y. Pang, M.B. Brodsky, and H. Sowers, *Phys. Rev. Lett.* **57** (1986), 2442
- [2] P.H. Dederichs, “Interlayer Exchange Coupling“, chapter C 3 in “Magnetism goes Nano“, 36th IFF Spring School, Forschungszentrum Jülich, series Matter and Materials, Vol. 26 (2005)
- [3] G. Binasch, P. Grünberg, F. Saurenbach, and W. Zinn, *Phys. Rev. B* **39** (1989), 4828
- [4] M.N. Baibich, J.M. Broto, A. Fert, F. Nguyen Van Dau, F. Petroff, P. Etienne, G. Creuzet, A. Friedrich, and J. Chazelas, *Phys. Rev. Lett.* **61** (1988), 2472
- [5] D.E. Bürgler, “Spin-Transport in Layered Systems“, chapter E 5 in “Magnetism goes Nano“, 36th IFF Spring School, Forschungszentrum Jülich, series Matter and Materials, Vol. 26 (2005)
- [6] U. Rücker, E. Kentzinger, “Thin Film Systems: Scattering under Grazing Incidence“, chapter D4 in “Probing the Nanoworld“, 38th IFF Spring School, Forschungszentrum Jülich, series Matter and Materials, Vol. 34 (2007)
- [7] A. Paul, E. Kentzinger, U. Rücker, D.E. Bürgler, and P. Grünberg, *Phys. Rev. B* **70** (2004), 224410
- [8] E. Josten, U. Rücker, S. Mattauch, D. Korolkov, A. Glavic, and Th. Brückel, *J. Phys: Conf. Ser.* **211** (2010), 012023

Exercises

E10.1 Magnetic contrast

We measure the polarized neutron reflectivity of a $[\text{Ni}_2\text{Fe} / \text{Pt}]_N$ multilayer structure in magnetic saturation. The Ni_2Fe alloy is ferromagnetic.

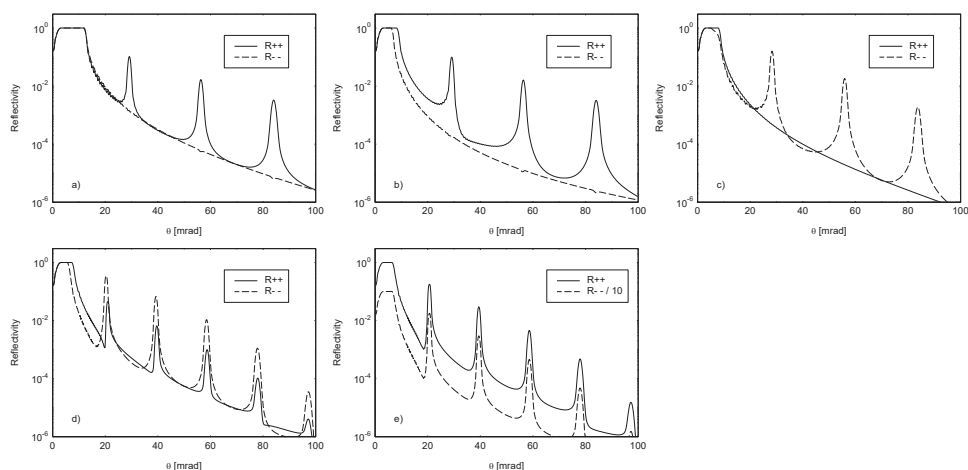
- * a) Calculate the nuclear and magnetic scattering length densities for the two constituents of the multilayer:

	Ni	Fe	Pt
density [g/cm^3]	8.90	7.86	21.4
atomic weight [g/mol]	58.71	55.85	195.09
nuclear scattering length [$1\text{E}-14 \text{ m}$]	1.03	0.954	0.95
magnetic scattering length density [$1\text{E}-6 \text{ \AA}^{-2}$]	1.52	5.12	0

If you don't want to calculate all the values yourself, you may continue with the tabulated values of the nuclear scattering length densities:

Ni: $9.41\text{E}-6 \text{ \AA}^{-2}$, Fe: $8.09\text{E}-6 \text{ \AA}^{-2}$, Pt: $6.29\text{E}-6 \text{ \AA}^{-2}$.

- ** b) Which of the 5 reflectivity curves presented below is the one measured on this alloy? Think about the critical angle (has to do with the highest scattering length density in all layers) and the contrast between adjacent layers (influences the height of the diffraction peaks) for both spin directions parallel (R_{++}) and antiparallel (R_{--}) to the applied magnetic field (saturation!).



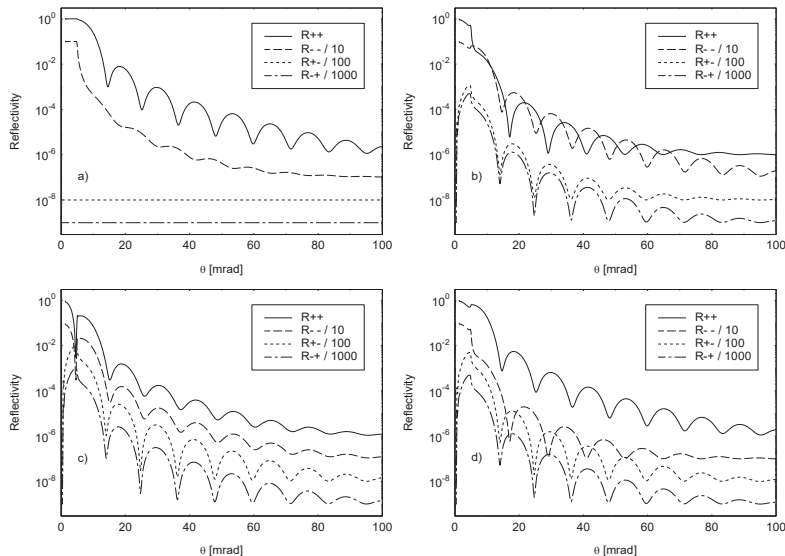
** c) The other 4 curves have been measured on different samples. Which curve belongs to which sample?

- I. The sum of nuclear and magnetic scattering length density of the magnetic layers is equal to the nuclear scattering length density of the nonmagnetic layers
- II. The sample contains an additional nonmagnetic layer with a scattering length density higher than the sum of the magnetic and nuclear scattering length densities of Ni_2Fe on top of the $[\text{Ni}_2\text{Fe} / \text{Pt}]_N$ multilayer
- III. No layer is magnetic
- IV. The nuclear scattering length density of the nonmagnetic layers is somewhere between the sum and the difference of nuclear and magnetic scattering length density of the magnetic layers

E10.2 Vector magnetometry

** The following figures show polarized neutron reflectivity measurements with polarization analysis from a ferromagnetic single layer on a nonmagnetic substrate. Find out which figure belongs to which magnetization state:

- I. The sample is magnetized perpendicular to the field direction
- II. The sample is magnetized parallel to the field direction
- III. The magnetization of the sample is inclined by 45° against the field direction
- IV. This set of curves is wrong. (Why?)



11 Inelastic Neutron Scattering

R. Zorn

Jülich Centre for Neutron Science 1

Forschungszentrum Jülich GmbH

Contents

11.1 Introduction	2
11.2 Theory	2
11.2.1 Kinematics of neutron scattering	2
11.2.2 Scattering from vibrating atoms	3
11.2.3 Scattering from diffusive processes	8
11.3 Instrumentation	17
11.3.1 Triple axis spectrometer	17
11.3.2 Time-of-flight spectrometer	18
11.3.3 Backscattering spectrometer	19
11.3.4 Inverse TOF spectrometer	21
11.3.5 Neutron spin echo spectrometer	22
References	27
Exercises	29

11.1 Introduction

One of the most important benefits of neutron scattering is the possibility to do inelastic scattering and by this way gain insight into the dynamics of materials as well as the structure. Neutrons tell us where the atoms are *and how they move* [1]. Although this feature is shared with inelastic x-ray scattering and dynamic light scattering, there is still a considerable range of slow dynamics in molecular systems which can be studied exclusively by inelastic neutron scattering.

This lecture can only present a short glimpse on the theoretical foundations and instrumental possibilities of inelastic neutron scattering. For those who are interested in more details, several textbooks can be recommended [2–6]. Also supplementary information on correlation functions [7] and Fourier transforms [8] may be found in earlier editions of this school.

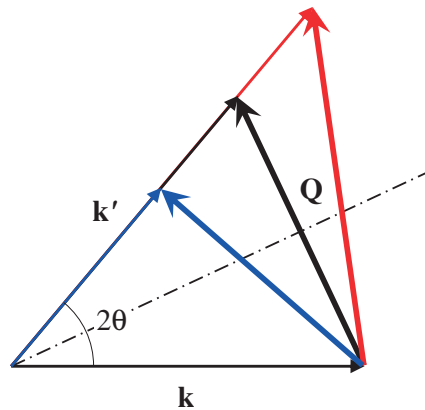


Fig. 11.1: Definition of the scattering vector Q in terms of the incident and final wave vectors k and k' . The black (isosceles) triangle corresponds to elastic scattering. The blue and red ones correspond to inelastic scattering with energy loss or gain of the scattered neutron, respectively.

11.2 Theory

11.2.1 Kinematics of neutron scattering

Up to this lecture it has always been tacitly assumed that the wavelength (or wave vector, or energy) of the neutrons is the same before and after scattering. The defining quality of *inelastic neutron scattering* is that this is not anymore the case. The neutrons may lose or gain energy in the collision with the nuclei. The characteristic quantity for the inelasticity is the energy transfer,

$$\hbar\omega = \Delta E = E' - E. \quad (11.1)$$

Here, E and E' are the energies of the neutron before and after the scattering. In the following the notation $\hbar\omega$ will be used preferentially because it reveals the meaning of the energy

transfer controlling the time scale of the observed dynamics, $1/\omega$.

Note that in some books E and E' represent the energy of the scattering system. This leads to a change of sign in ΔE . Even the wording “energy gain/loss” becomes ambiguous and should always be supplemented by “of the neutron” or “of the system”. Also, some authors prefer to write $E = E_{\text{final}} - E_{\text{initial}}$. So, it should always be checked whether E denotes the incident energy or the energy transfer.

$\hbar\omega \neq 0$ implies $k' \neq k$. As a consequence, Q now does not anymore result from the isosceles construction drafted in black in Fig. 11.1 but from scattering triangles as those in blue and red. Application of the cosine theorem leads to the following expression for Q in the inelastic situation:

$$Q = \sqrt{k^2 + k'^2 - 2kk' \cos(2\theta)} \quad (11.2)$$

$$= \sqrt{\frac{8\pi^2}{\lambda^2} + \frac{2m\omega}{\hbar} - \frac{4\pi}{\lambda} \sqrt{\frac{4\pi^2}{\lambda^2} + \frac{2m\omega}{\hbar}} \cos(2\theta)}. \quad (11.3)$$

Note that there is a fundamental difference to the simpler expression for elastic scattering,

$$Q_{\text{el}} = \frac{4\pi}{\lambda} \sin \theta, \quad (11.4)$$

used in the preceding lectures. Q now also depends on the energy transfer $\hbar\omega$ implying that Q is not anymore constant for a single scattering angle. Fig. 11.2 shows the magnitude of this effect for typical parameters of a neutron scattering experiment. It can be seen that it is by no means negligible for typical thermal energies of the sample even at temperatures as low as 100 K.

The other fundamental difference to elastic scattering to be considered is that the total scattering cross section is not identical anymore to the bound scattering cross section read from tables. In the extreme case of a free nucleus the scattering cross section is reduced to [2]

$$\sigma = \frac{4\pi b^2}{(1 + m/M)^2} \quad (11.5)$$

where M is the mass of the scattering nucleus. It can be seen that in the worst case (scattering from a gas of atomic hydrogen) this is a reduction by $1/4$.

11.2.2 Scattering from vibrating atoms

The most important case of inelastic neutron scattering from vibrating atoms is that of scattering from phonons in crystals. In this field, inelastic neutron scattering is the most important tool of research. At first, a short recapitulation of the phonon picture will be presented [9,10].

As a simplified model for the crystal one can consider a chain of N atoms with mass M regularly spaced by a distance a and connected by springs with the spring constant K . For this system the equations of motion can readily be written down:

$$\frac{d^2 u_j}{dt^2} = \frac{K}{M} (u_{j+1} - 2u_j + u_{j-1}). \quad (11.6)$$

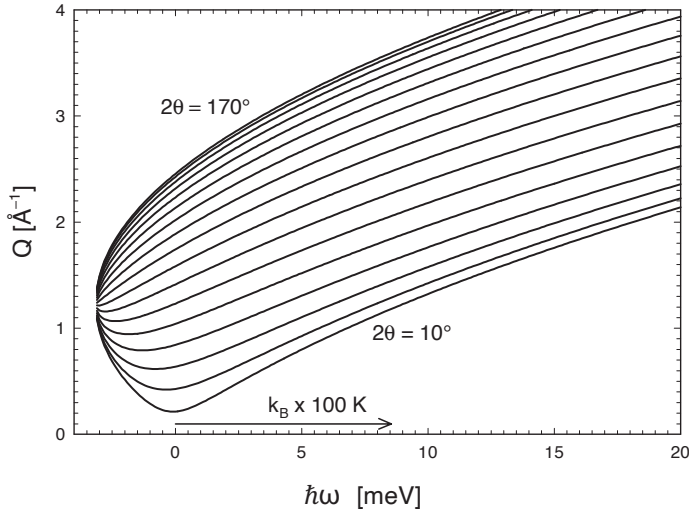


Fig. 11.2: Scattering vectors Q accessed by a neutron scattering experiment with the detector at scattering angles $2\theta = 10 \dots 170^\circ$ vs. the energy transfer $\hbar\omega$ (incident wavelength $\lambda = 5.1 \text{ \AA}$). For comparison the thermal energy $k_B T$ corresponding to 100 K is indicated by an arrow.

In addition, it has to be specified what the equations of motions are for the first and the last atom (boundary condition). This is usually done by identifying the left neighbour of the first atom with the last and vice versa, $u_0 = u_N$ and $u_{N+1} = u_1$, as in a closed necklace rather than an open chain. This is the most natural choice for large N and called the Born-von-Kármán boundary condition. The equation system (11.6) can be solved by the ansatz

$$u_j(t) = \sum_k U_k(t) \exp\left(i \frac{kj}{N}\right) \quad (11.7)$$

with integer k ($k \in \mathbb{Z}$). Here, U_k are the *normal coordinates* and each of them fulfils the equation of motion of a single harmonic oscillator:

$$\frac{d^2 U_k}{dt^2} = \frac{2K}{M} \left(\cos \frac{2\pi k}{N} - 1 \right) U_k. \quad (11.8)$$

By introducing these *normal coordinates*, the system of differential equations (11.6) can be *decoupled* into a set of differential equations which can be solved separately. The solutions are

$$U_k(t) = A_k \exp(i\Omega_k t) \text{ with} \quad (11.9)$$

$$\Omega_k = \sqrt{\frac{2K}{M} \left(1 - \cos \frac{2\pi k}{N} \right)} = 2\sqrt{\frac{K}{M}} \left| \sin \frac{\pi k}{N} \right|. \quad (11.10)$$

The second equation gives a relation between the index of the oscillator k and the frequency. On the other hand, the index determines via equation (11.7) the wavelength of the vibration.

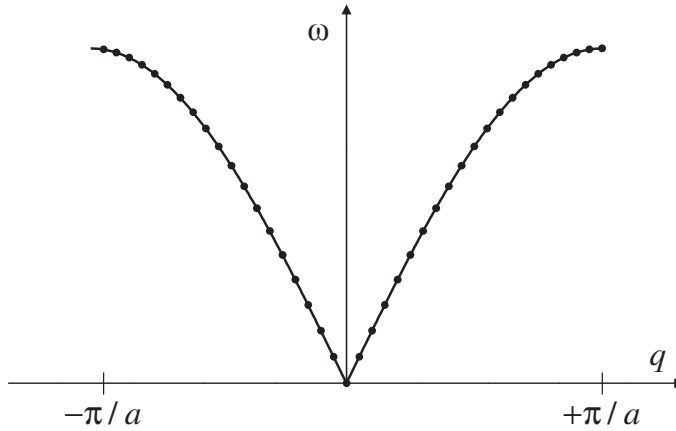


Fig. 11.3: Dispersion relation in a linear chain with $N = 40$ atoms (Born-von-Kármán boundary condition).

One wavelength covers N/k lattice positions, corresponding to $\lambda_{\text{vib}} = Na/k$ in actual length. The corresponding wave ‘vector’ is $q = 2\pi/\lambda_{\text{vib}} = 2\pi k/Na$ ¹. This implies that there is a relation between the wave vector and the frequency called the *dispersion relation* (Fig. 11.3):

$$\Omega(q) = 2\sqrt{\frac{K}{M}} \left| \sin \frac{qa}{2} \right|. \quad (11.11)$$

This relation does not contain the number of atoms anymore. For large N the points constituting the curve in Fig. 11.3 will get closer and closer, finally leading to the continuous function (11.11). The individual positions of these points depend on the boundary condition. But because they are getting infinitely dense for $N \rightarrow \infty$ the exact boundary conditions do not matter for a large system.

It can be seen that the dispersion relation (11.11) is periodic in q . On the other hand, there are only N normal coordinates necessary to solve the N original equations of motion. This is exactly the number of wave vectors found in a q interval of length $2\pi/a$. The usual choice is $-\pi/a \dots \pi/a$ as a representative zone for the dispersion relation.

There are two modifications necessary when considering a real three-dimensional crystal instead of this simplified model: (1) The crystal is periodic in three dimensions. (2) The vibrations are governed by quantum mechanics. The first requirement leads to the consequence that instead of a scalar, one has to use a real wave *vector*, $q \rightarrow \mathbf{q} = (q_x, q_y, q_z)$ in reciprocal space. The interval defined in Fig. 11.3 changes into a polyhedron called the first Brillouin zone (Fig. 11.4) [9, 10]. It is constructed in the same way as the Wigner-Seitz cell in real space: The Brillouin zone contains all points which are closer to the origin than to any other lattice point. Its surfaces are the bisecting planes between the origin and its neighbours (in reciprocal space).

¹ As will be seen later, there is a close connection between this lower case q and the scattering vector upper case Q . Nevertheless, they are not the same and care has to be taken not to mix up both q -s.

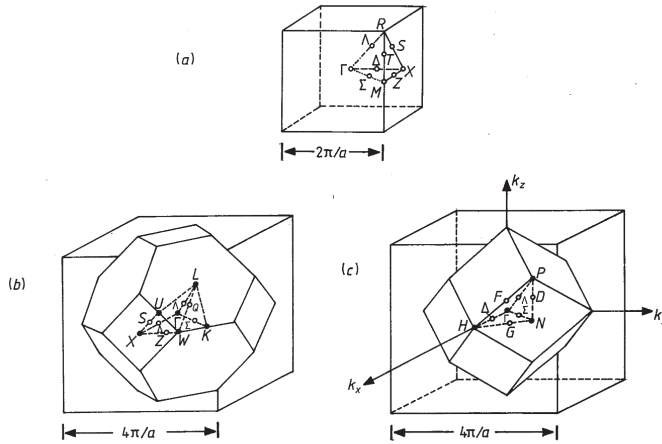


Fig. 11.4: Brillouin zones for cubic lattices: (a) simple cubic, (b) face-centred cubic, (c) body-centred cubic. From [10].

For every amplitude A_k equation (11.9) gives a valid solution of the equations of motion. This means that in the classical picture the vibrations can have any energy. The quantum mechanical treatment (which is too complex to be treated here in detail) leads to the result that only certain energies with a distance of $\hbar\Omega_k$ are allowed. This quantisation implies that the vibrations can be treated as *quasiparticles* with the energy $\hbar\Omega_k$ called *phonons*. The increase of the vibrational amplitude corresponding to an energy change of $+\hbar\Omega_k$ is then seen as a creation, the inverse process as an annihilation of a phonon. Then it makes sense to define $\hbar\mathbf{q}$ as the momentum of the phonon. In this way the dispersion relation $\Omega(\mathbf{q})$ is similar to the relations shown in Fig. 4.2 of lecture 4 for real particles.

The introduction of the quasiparticle (phonon) concept leads to the simple interpretation of inelastic neutron scattering by vibrating lattices: The scattering process can be viewed as a collision between phonons and neutrons. In this process the energy as well as the momentum has to be conserved:

$$E' - E = \hbar\omega = \pm\hbar\Omega(\mathbf{q}), \quad (11.12)$$

$$\mathbf{k}' - \mathbf{k} = \mathbf{Q} = \pm\mathbf{q} + \boldsymbol{\tau}. \quad (11.13)$$

The second equation shows that the analogy with a two-particle collision is not complete. A wave vector, changed by a lattice vector $\boldsymbol{\tau}$ in reciprocal space, corresponds to the *same* phonon. In the one-dimensional case, this can be seen from equation (11.7): If one adds an integer multiple of N to k (corresponding to a multiple of $2\pi/a$ in q) all values of the complex exponential remain the same. Analogously, in the three dimensional case adding a lattice vector

$$\boldsymbol{\tau} = h\boldsymbol{\tau}_1 + k\boldsymbol{\tau}_2 + l\boldsymbol{\tau}_3 \quad (h, k, l \in \mathbb{Z}) \quad (11.14)$$

does not change anything and momentum has only to be conserved up to an arbitrary reciprocal lattice vector. The condition (11.13) can also be visualised by the Ewald construction as done in lecture 4 for elastic scattering.

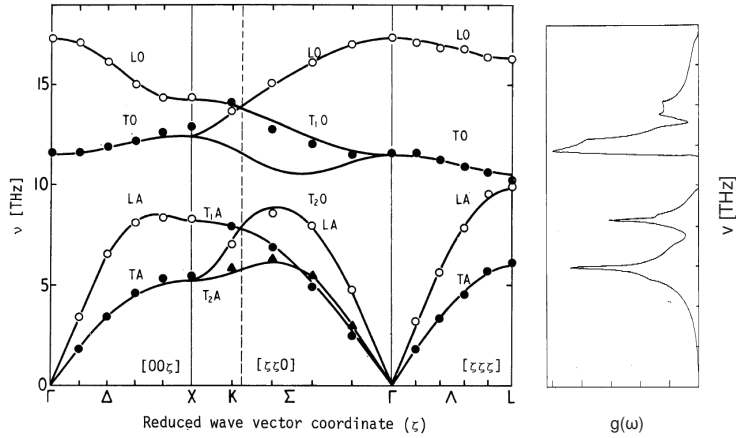


Fig. 11.5: *Left: Phonon dispersion of NiO measured by inelastic neutron scattering. Frequencies are expressed as $\nu = \omega/2\pi$ and the wave vector is expressed in units of $\zeta = \pi/a$. The lattice is simple cubic, thus the symbols below the abscissa correspond to those in Fig. 11.4(a). Right: Phonon density of states (see section 11.2.3) of NiO plotted to the same scale in frequency. From [11].*

From the conservation laws (11.12) and (11.13) one expects that the scattering intensity has sharp peaks at the positions where both conditions are fulfilled and is zero everywhere else. This is indeed so for coherent scattering, unless effects as multi-phonon scattering and anharmonicity are strong (usually at higher temperatures). Therefore, inelastic scattering allows the straightforward determination of the phonon dispersion relation as shown in Fig. 11.5.

In this figure, it can be seen that some of the phonon ‘branches’ start at the origin (*acoustic phonons*), as in the simple calculation of the one-dimensional chain. Others are ‘floating’ around high frequencies (*optical phonons*). The latter occur in materials with atoms of different weight or bond potential. (The one-dimensional chain would also produce these solutions if the masses were chosen differently for even and odd j .) In this case, a mode where all atoms of a unit cell move roughly in phase has the usual behaviour expected from the monatomic chain. In particular the dispersion relation at low q is a proportionality:

$$\Omega(q) = vq. \quad (11.15)$$

This relation is typical for sound waves. v is the sound velocity, longitudinal or transverse according to the type of phonons considered. In the polyatomic crystal or chain, there are additional modes where the atoms move in anti-phase. This implies a much higher deformation of the bonds. These vibrations constitute the optical phonon branches.

There is another difference between the one-dimensional chain and the three-dimensional crystal visible. The atomic displacements are not simply scalars u_j but vectors \mathbf{u}_j which have a direction. This direction can be either parallel or perpendicular to the wave vector \mathbf{q} . Depending on this, one speaks of *longitudinal* and *transverse* phonons. The usual notation is LA, TA, LO, TO, where the first letter indicates the phonon polarisation and the second whether it is acoustic or optical. An additional index as T_1A is used for \mathbf{q} directions

where the symmetry allows a distinction between the perpendicular orientations of \mathbf{u}_j . The full mathematical expression for the phonon scattering [2] includes an intensity factor proportional to $|\mathbf{Q} \cdot \mathbf{u}_j|^2$. This factor obviously vanishes if \mathbf{Q} and \mathbf{u}_j are perpendicular, implying that purely transverse modes are unobservable in the first Brillouin zone where $\mathbf{Q} = \mathbf{q}$.

It has to be noted, that the above arguments only hold for *coherent neutron scattering* (see equation (11.22) below) from crystalline materials. If the material is amorphous the coherent scattering will be diffuse (as it is for incoherent scattering always). The readily understandable reason for this is that the definition of the phonon wave vector \mathbf{q} requires a lattice.

Finally, an indirect effect of vibrations on the elastic scattering should be mentioned. The elastic scattering (also for x-ray scattering) is reduced by the *Debye-Waller factor*. This reduction can be understood from a ‘hand-waving’ argument: Due to the thermal vibrations, atoms are displaced by \mathbf{u}_j from their nominal lattice position. Although on the average $\langle \mathbf{u} \rangle$ is zero, there will be a finite *mean-square displacement* $\langle u^2 \rangle$. The Debye-Waller factor can be shown [2, 9] to be

$$\exp(-\langle (\mathbf{Q} \cdot \mathbf{u}) \rangle) = \exp(-Q^2 \langle u^2 \rangle / 3) \quad (11.16)$$

where the second expression is only valid for isotropic conditions. It can be seen that the attenuation of diffraction peaks increases with increasing Q and increasing mean-square displacement, that is at higher temperature. Note, that this does *not* mean that elastic scattering can observe dynamics, because a permanent static displacement of the atoms would have the same effect.

The treatment of inelastic scattering by spin waves is very similar to that of deformation waves above. In analogy to the phonon the quasiparticle ‘magnon’ is introduced. Thereby, the displacement \mathbf{u}_j is replaced by the orientation of the spin. The construction of normal modes (Bloch waves) and the quantisation proceeds in the same way as for phonons. As explained in lecture 7 neutrons interact with the nuclei as well as with the magnetic moments of nuclei and electrons. Therefore, inelastic neutron scattering is also a tool for the detection of magnons and this has been one of its first applications [12].

11.2.3 Scattering from diffusive processes

For the inelastic scattering from vibrational motions it was practical to consider the scattering as a process between (quasi)particles, neutrons and phonons/magnons. But there are many types of molecular motions, mostly irregular and only statistically defined, which cannot be treated in this concept, e.g. thermally activated jumps or Brownian motion. For these motions it is more adequate to use a concept of *correlation functions* to calculate the scattering.

Because these ‘diffusive’ processes are usually much slower than phonon frequencies it is in most cases not necessary to treat them quantum-mechanically. Therefore, in this section, a picture of the scattering material will be used where the positions of all scatterers are given as functions of time $\mathbf{r}_j(t)$ (trajectories)². In this picture the *double differential cross-section*, defined as the probability density that a neutron is scattered into a solid angle element $d\Omega$

² This treatment also ignores that in the scattering process the trajectories of the scattering particles are modified, i.e. recoil effects. The consequences of this approximation are outlined by the end of this section.

with an energy transfer $\hbar\omega \dots \hbar(\omega + d\omega)$, is

$$\frac{d\sigma}{d\Omega d\omega} = \frac{1}{2\pi} \frac{k'}{k} \int_{-\infty}^{\infty} e^{-i\omega t} dt \sum_{j,k=1}^N b_j^* b_k \langle e^{i\mathbf{Q}\cdot(\mathbf{r}_k(t) - \mathbf{r}_j(0))} \rangle. \quad (11.17)$$

In order to derive a quantity similar to the structure factor $S(\mathbf{Q})$ in lectures 4 and 5, one assumes again a system of N *chemically* identical particles. Because the neutron scattering length is a nuclear property, there may still be a variance of scattering lengths. And even in monoisotopic systems, there may be such a variance due to disorder of the nuclear spin orientations, since the scattering length also depends on the combined spin state of the scattered neutron and the scattering nucleus³. Therefore, it is assumed that scattering lengths are randomly distributed with the average $\bar{b} = (1/N) \sum_j b_j$ and the variance $|\bar{b}|^2 - |\bar{b}|^2 = \overline{|b - \bar{b}|^2} = (1/N) \sum_i |b_i - \bar{b}|^2$. As will be seen later, this gives rise to the *incoherent scattering* contribution which is usually found in neutron scattering (in contrast to x-ray scattering). The sum in expression (11.17) can be decomposed into one over different indices and one over identical indices:

$$\sum_{j,k=1}^N b_j^* b_k e^{i\mathbf{Q}\cdot(\mathbf{r}_k(t) - \mathbf{r}_j(0))} = \sum_{j \neq k=1}^N b_j^* b_k e^{i\mathbf{Q}\cdot(\mathbf{r}_k(t) - \mathbf{r}_j(0))} + \sum_{j=1}^N |b_j|^2 e^{i\mathbf{Q}\cdot(\mathbf{r}_j(t) - \mathbf{r}_j(0))}. \quad (11.18)$$

They have to be averaged in different ways with respect to the distribution of scattering lengths. In the first term b_j^* and b_k can be averaged separately because the different particle scattering lengths are uncorrelated: $\overline{b^* b} = \overline{b^*} \overline{b} = |\bar{b}|^2$. In the second term one has to average *after* taking the absolute square:

$$= \sum_{j \neq k=1}^N |\bar{b}|^2 e^{i\mathbf{Q}\cdot(\mathbf{r}_k(t) - \mathbf{r}_j(0))} + \sum_{j=1}^N \overline{|b|^2} e^{i\mathbf{Q}\cdot(\mathbf{r}_j(t) - \mathbf{r}_j(0))}. \quad (11.19)$$

In order to avoid the sum over distinct particles, the first sum is complemented by the $j = k$ terms, $|\bar{b}|^2 e^{i\mathbf{Q}\cdot(\mathbf{r}_j(t) - \mathbf{r}_j(0))}$, and to compensate, these terms are subtracted in the second sum:

$$= \sum_{j,k=1}^N |\bar{b}|^2 e^{i\mathbf{Q}\cdot(\mathbf{r}_k(t) - \mathbf{r}_j(0))} + \sum_{j=1}^N \left(\overline{|b|^2} - |\bar{b}|^2 \right) e^{i\mathbf{Q}\cdot(\mathbf{r}_j(t) - \mathbf{r}_j(0))}. \quad (11.20)$$

With this result it is possible to express the double differential cross section as

$$\frac{\partial \sigma}{\partial \Omega \partial \omega} = N \frac{k'}{k} \left(|\bar{b}|^2 S_{\text{coh}}(\mathbf{Q}, \omega) + \left(\overline{|b|^2} - |\bar{b}|^2 \right) S_{\text{inc}}(\mathbf{Q}, \omega) \right) \quad (11.21)$$

with

$$S_{\text{coh}}(\mathbf{Q}, \omega) = \frac{1}{2\pi N} \int_{-\infty}^{\infty} e^{-i\omega t} dt \sum_{j,k=1}^N \langle e^{i\mathbf{Q}\cdot(\mathbf{r}_k(t) - \mathbf{r}_j(0))} \rangle \quad (11.22)$$

and

$$S_{\text{inc}}(\mathbf{Q}, \omega) = \frac{1}{2\pi N} \int_{-\infty}^{\infty} e^{-i\omega t} dt \sum_{j=1}^N \langle e^{i\mathbf{Q}\cdot(\mathbf{r}_j(t) - \mathbf{r}_j(0))} \rangle. \quad (11.23)$$

³ In this section only nuclear non-magnetic scattering will be considered. For a full treatment of magnetic scattering see lecture 7 or vol. 2 of ref. 2.

The quantities defined by (11.22) and (11.23) are called *coherent* and *incoherent scattering function* or *dynamic structure factors*. It is a peculiarity of neutron scattering that there is also the incoherent term, which solely depends on the *single particle dynamics* due to the variance of the scattering lengths.

The prefactors of the scattering functions in expression (11.21) are often replaced by the scattering cross sections

$$\sigma_{\text{coh}} = 4\pi |\bar{b}|^2, \quad \sigma_{\text{inc}} = 4\pi \left(|\bar{b}|^2 - |\bar{b}|^2 \right). \quad (11.24)$$

They give the scattering into all directions, i.e. the solid angle 4π (for the incoherent part in general and for the coherent in the limit $Q \rightarrow \infty$).

As demonstrated in ref. 2, it is also possible to use the concept of correlation functions for phonons. In this way it is possible to calculate the scattering from phonons in terms of $S_{\text{coh}}(\mathbf{Q}, \omega)$ and $S_{\text{inc}}(\mathbf{Q}, \omega)$. The result for the coherent scattering gives non-vanishing contributions only for (\mathbf{Q}, ω) combinations which fulfil the conservation laws (11.12) and (11.13). This was already shown in section 11.2.2 but the explicit calculation gives also the intensity of the phonon peaks, e.g. the mentioned result that transverse phonon peaks vanish in the first Brillouin zone. But with this mathematical approach it is also possible to calculate the incoherent scattering which is not bound to the momentum conservation (11.13). The result is for inelastic incoherent neutron scattering from cubic crystals in the one-phonon approximation [2]:

$$S_{\text{inc}}(\mathbf{Q}, \omega \neq 0) = \frac{\hbar Q^2}{2M} \exp(-2W(\mathbf{Q})) \frac{g(|\omega|)}{\omega} \frac{1}{\exp(\hbar\omega/k_{\text{B}}T) - 1} \quad (11.25)$$

$$\xrightarrow{\text{high } T \text{ limit}} \exp(-2W(\mathbf{Q})) \frac{Q^2 k_{\text{B}}T}{2M} \frac{g(|\omega|)}{\omega^2}. \quad (11.26)$$

(Here, $\exp(-2W(\mathbf{Q}))$ is a shorthand for the Debye-Waller factor (11.16).) From this expression it can be seen that the incoherent scattering is determined by the *phonon density of states* $g(\omega)$ alone and does not depend on the full details of the phonon dispersion. The density of states $g(\omega)$ is the projection of the phonon dispersion curves onto the frequency axis, as demonstrated in Fig. 11.5. Besides nuclear inelastic scattering, which requires Mößbauer-active nuclei, inelastic incoherent neutron scattering is the most important method to determine $g(\omega)$.

In some cases it is interesting to consider the part of expression (11.22) before the time-frequency Fourier transform, called *intermediate coherent scattering function*:

$$I_{\text{coh}}(\mathbf{Q}, t) = \frac{1}{N} \sum_{jk} \langle e^{i\mathbf{Q} \cdot (\mathbf{r}_k(t) - \mathbf{r}_j(0))} \rangle. \quad (11.27)$$

Its value for $t = 0$ expresses the correlation between atoms *at equal times*. A theorem on Fourier transforms tells that this is identical to the integral of the scattering function over all energy transfers:

$$I_{\text{coh}}(\mathbf{Q}, 0) = \frac{1}{N} \sum_{jk} \langle e^{i\mathbf{Q} \cdot (\mathbf{r}_k - \mathbf{r}_j)} \rangle = S(\mathbf{Q}) = \int_{-\infty}^{\infty} S_{\text{coh}}(\mathbf{Q}, \omega) d\omega. \quad (11.28)$$

($S(\mathbf{Q})$ is the structure factor as derived in lectures 4 and 5 for the static situation.) This integral relation has a concrete relevance in diffraction experiments. There, the energy of the neutrons is not discriminated: The diffraction experiment implicitly integrates over all $\hbar\omega$ ⁴. Equation (11.28) shows that this integral corresponds to the instantaneous correlation of the atoms. The diffraction experiment performs a ‘snapshot’ of the structure. All dynamic information is lost in the integration process and therefore it is invisible in a diffraction experiment.

Similarly the *incoherent intermediate scattering function* is

$$I_{\text{inc}}(\mathbf{Q}, t) = \frac{1}{N} \sum_{j=1}^N \langle e^{i\mathbf{Q} \cdot (\mathbf{r}_j(t) - \mathbf{r}_j(0))} \rangle \quad (11.29)$$

with

$$I_{\text{inc}}(\mathbf{Q}, 0) = \frac{1}{N} \sum_{j=1}^N \langle e^{i\mathbf{Q} \cdot (\mathbf{r}_j - \mathbf{r}_j)} \rangle = 1 = \int_{-\infty}^{\infty} S_{\text{inc}}(\mathbf{Q}, \omega) d\omega. \quad (11.30)$$

Note that this result is independent of the actual structure of the sample. Integration of the double-differential cross section (11.21) over ω shows that also the static scattering contains an incoherent contribution. But because of (11.30), this term is constant in Q . It contributes as a flat background in addition to the $S(Q)$ -dependent scattering. In some cases (e.g. small-angle scattering) it may be necessary to correct for this, in other cases (e.g. diffraction with polarisation analysis) it may even be helpful to normalise the coherent scattering.

In the paragraphs before it was shown, that the value of the intermediate scattering functions at $t = 0$ corresponds to the integral of the scattering function over an infinite interval. This is a consequence of a general property of the Fourier transform. There is also the inverse relation that the value of $S(\mathbf{Q}, \omega)$ at $\omega = 0$ is related to the integral of $I(\mathbf{Q}, t)$ over all times. The most important case is here when $I(\mathbf{Q}, t)$ does not decay to zero for infinite time, but to a finite value $f(\mathbf{Q})$. In that case the integral is infinite, implying that $S(\mathbf{Q}, \omega)$ has a delta function contribution at $\omega = 0$. This means that the scattering contains a strictly elastic component. Its strength can be calculated by decomposing the intermediate scattering function into a completely decaying part and a constant for the coherent and the incoherent scattering:

$$I_{[\text{coh}|\text{inc}]}(\mathbf{Q}, t) = I_{[\text{coh}|\text{inc}]}^{\text{inel}}(\mathbf{Q}, t) + f_{[\text{coh}|\text{inc}]}(\mathbf{Q}). \quad (11.31)$$

Because the Fourier transform of constant one is the delta function this corresponds to

$$S_{[\text{coh}|\text{inc}]}(\mathbf{Q}, \omega) = S_{[\text{coh}|\text{inc}]}^{\text{inel}}(\mathbf{Q}, \omega) + S_{[\text{coh}|\text{inc}]}^{\text{el}}(\mathbf{Q})\delta(\omega), \quad (11.32)$$

where $S_{[\text{coh}|\text{inc}]}^{\text{el}}(\mathbf{Q}) = f_{[\text{coh}|\text{inc}]}(\mathbf{Q})$, the *elastic coherent/incoherent structure factor* (EISF), can

⁴ Strictly speaking, this is only an approximation. There are several reasons why the integration in the diffraction experiment is not the ‘mathematical’ one of (11.28): (1) On the instrument the integral is taken along a curve of constant 2θ in Fig. 11.2 while constant Q would correspond to a horizontal line. (2) The double differential cross-section (11.21) contains a factor k'/k which depends on ω via (11.2). (3) The detector may have an efficiency depending on wavelength which will introduce another ω -dependent weight in the experimental integration. All these effects have been taken into account in the so-called Placzek corrections [8, 13, 14].

be written as

$$S_{\text{coh}}^{\text{el}}(\mathbf{Q}) = \frac{1}{N} \sum_{j,k=1}^N \langle e^{i\mathbf{Q} \cdot (\mathbf{r}_k(\infty) - \mathbf{r}_j(0))} \rangle, \quad (11.33)$$

$$S_{\text{inc}}^{\text{el}}(\mathbf{Q}) = \frac{1}{N} \sum_{j=1}^N \langle e^{i\mathbf{Q} \cdot (\mathbf{r}_j(\infty) - \mathbf{r}_j(0))} \rangle. \quad (11.34)$$

Here, $t = \infty$ indicates a time which is sufficiently long that the correlation with the position at $t = 0$ is lost. For the EISF this lack of correlation implies that the terms with initial and final positions can be averaged separately:

$$\begin{aligned} S_{\text{inc}}^{\text{el}}(\mathbf{Q}) &= \frac{1}{N} \sum_{j=1}^N \langle e^{i\mathbf{Q} \cdot \mathbf{r}_j} \rangle \langle e^{-i\mathbf{Q} \cdot \mathbf{r}_j} \rangle \\ &= \frac{1}{N} \sum_{j=1}^N |e^{-i\mathbf{Q} \cdot \mathbf{r}_j}|^2 \end{aligned} \quad (11.35)$$

$$= \frac{1}{N} \sum_{j=1}^N \left| \int_V d^3r \exp(i\mathbf{Q} \cdot \mathbf{r}) \rho_j(\mathbf{r}) \right|^2. \quad (11.36)$$

Here, $\rho_j(\mathbf{r})$ denotes the ‘density of particle j ’, i.e. the probability density of the individual particle j being at \mathbf{r} . From (11.35) one can see that the normalisation of the EISF is $S_{\text{inc}}^{\text{el}}(0) = 1$ (in contrast to that of the structure factor, $\lim_{Q \rightarrow \infty} S(Q) = 1$). One can say that the EISF is the form factor of the volume confining the motion of the particles. E.g. for particles performing any kind of motion within a sphere, the EISF would be $S_{\text{inc}}^{\text{el}}(Q) = 9(\sin(QR) - QR \cos(QR))^2 / Q^6 R^6$ as derived in lecture 5.

As in the static situation, the scattering law can be traced back to distance distribution functions. These are now (in the treatment of inelastic scattering) time-dependent. They are called *van Hove correlation functions*:

$$G(\mathbf{r}, t) = \frac{1}{N} \left\langle \sum_{j,k=1}^N \delta(\mathbf{r} - \mathbf{r}_k(t) + \mathbf{r}_j(0)) \right\rangle, \quad (11.37)$$

$$G_{\text{s}}(\mathbf{r}, t) = \frac{1}{N} \left\langle \sum_{j=1}^N \delta(\mathbf{r} - \mathbf{r}_j(t) + \mathbf{r}_j(0)) \right\rangle. \quad (11.38)$$

Insertion into

$$I_{[\text{coh}|\text{inc}]} = \int_{V_d} G_{[\text{s}]}(\mathbf{r}, t) \exp(i\mathbf{Q} \cdot \mathbf{r}) d^3r \quad (11.39)$$

directly proves that the spatial Fourier transforms of the van Hove correlation function are the intermediate scattering functions.

The two particle version can be reduced to the microscopic density,

$$\rho(\mathbf{r}, t) = \sum_{j=1}^N \delta(\mathbf{r} - \mathbf{r}_j(t)). \quad (11.40)$$

Its autocorrelation function in space and time is

$$\langle \rho(\mathbf{0}, 0) \rho(\mathbf{r}, t) \rangle. \quad (11.41)$$

The $\mathbf{0}$ is showing that translational symmetry is assumed. So the correlation function can be replaced by its average over all starting points \mathbf{r}_1 in the sample volume:

$$\langle \rho(\mathbf{0}, 0) \rho(\mathbf{r}, t) \rangle = \frac{1}{V} \int_V d^3 r_1 \langle \rho(\mathbf{r}_1, 0) \rho(\mathbf{r}_1 + \mathbf{r}, t) \rangle. \quad (11.42)$$

Insertion of (11.40) gives

$$\langle \rho(\mathbf{0}, 0) \rho(\mathbf{r}, t) \rangle = \frac{1}{V} \left\langle \sum_{j,k=1}^N \int_V d^3 r_1 \delta(\mathbf{r}_1 - \mathbf{r}_k(t)) \delta(\mathbf{r}_1 + \mathbf{r} - \mathbf{r}_j(t)) \right\rangle \quad (11.43)$$

$$= \frac{1}{V} \left\langle \sum_{j,k=1}^N \delta(\mathbf{r}_k(t) + \mathbf{r} - \mathbf{r}_j(t)) \right\rangle. \quad (11.44)$$

Together with (11.37) this implies

$$G(\mathbf{r}, t) = \frac{1}{\rho_0} \langle \rho(\mathbf{0}, 0) \rho(\mathbf{r}, t) \rangle. \quad (11.45)$$

Again setting $t = 0$ results in the static scattering situation:

$$G(\mathbf{r}, 0) = \frac{\langle \rho(\mathbf{0}, 0) \rho(\mathbf{r}, 0) \rangle}{\rho_0} = \delta(\mathbf{r}) + \rho_0 g(\mathbf{r}) \quad (11.46)$$

with $g(\mathbf{r})$ as defined in lecture 5.

As in the case of static scattering there is an alternative way to derive the scattering function by Fourier-transforming the density

$$\rho_{\mathbf{Q}}(t) = \int d^3 r e^{i\mathbf{Q}\cdot\mathbf{r}} \rho(\mathbf{r}, t) = \sum_{j=1}^N e^{i\mathbf{Q}\cdot\mathbf{r}_j(t)} \quad (11.47)$$

and then multiplying its conjugated value at $t = 0$ with that at t :

$$I_{\text{coh}}(\mathbf{Q}, t) = \frac{1}{N} \langle \rho_{\mathbf{Q}}^*(0) \rho_{\mathbf{Q}}(t) \rangle \quad (11.48)$$

and

$$S_{\text{coh}}(\mathbf{Q}, \omega) = \frac{1}{2\pi N} \int_{-\infty}^{\infty} e^{-i\omega t} \langle \rho_{\mathbf{Q}}^*(0) \rho_{\mathbf{Q}}(t) \rangle dt. \quad (11.49)$$

(This is a consequence of the *cross-correlation theorem* of Fourier transform which is the generalisation of the Wiener-Khinchine theorem for two different correlated quantities.)

Note that a reduction of the self correlation function $G_s(\mathbf{r}, t)$ to the density is *not* possible in the same way. The multiplication $\rho(\mathbf{0}, 0) \rho(\mathbf{r}, t)$ in equation (11.45) inevitably includes all combinations of particles j, k and not only the terms for identical particles j, j . Therefore, the incoherent scattering cannot be derived from the density alone but requires the knowledge of the motion of the individual particles.

From the definitions (11.37) and (11.38) it is immediately clear that the van Hove correlation functions (as defined here) are symmetric in time

$$G_{[\text{s}]}(\mathbf{r}, -t) = G_{[\text{s}]}(\mathbf{r}, t). \quad (11.50)$$

if the system is dynamically symmetric to an inversion of space. From (11.50) and general properties of the Fourier transform it follows that $I(\mathbf{Q}, t)$ is real and that it is also symmetric in time:

$$I(\mathbf{Q}, -t) = I(\mathbf{Q}, t). \quad (11.51)$$

In turn this implies that the scattering functions are real and symmetric in energy transfer $\hbar\omega$:

$$S(\mathbf{Q}, -\omega) = S(\mathbf{Q}, \omega). \quad (11.52)$$

It can be seen that this identity violates the principle of detailed balance. Up- and downscattering should rather be related by

$$S(\mathbf{Q}, -\omega) = \exp\left(\frac{\hbar\omega}{k_{\text{B}}T}\right) S(\mathbf{Q}, \omega). \quad (11.53)$$

The reason for this is that (as mentioned in footnote 2) the influence of the neutron's impact on the motion of the system particles is neglected. This would be included in a full quantum-mechanical treatment as carried out in ref. 2 or ref. 8 where the detailed balance relation (11.53) emerges in a natural way. Note that equation (11.53) implies that both $I(\mathbf{Q}, t)$ and $G_{[\text{s}]}(\mathbf{r}, t)$ are complex functions. (This is not 'unphysical' because they are no directly measurable quantities in contrast to $S(\mathbf{Q}, \omega)$ which is proportional to $d\sigma/d\Omega d\omega$. Even neutron spin-echo measures only the real part of $I(\mathbf{Q}, t)$, see equation (11.70).)

Because the detailed balance relation (11.53) is also valid in classical thermodynamics (and also recoil can be understood in the framework of classical mechanics) there should be a way to derive a correct result from a classical treatment of the system too. This task is important because only rather simple systems can be treated quantum-mechanically. Especially, results from molecular dynamics computer simulations are classical results. The result for $S(\mathbf{Q}, \omega)$ derived here is obviously only a crude approximation. Better approximations can be obtained by applying correction factors restoring (11.53) [16–18]. The exact classical calculation is rather complicated [19] and requires knowledge of the system beyond just the trajectories of the particles.

Inelastic scattering is often also called neutron (scattering) spectroscopy. That there is indeed a relation to better-known spectroscopic methods as light spectroscopy, can be seen from the dependence of the scattering function on a frequency ω . It can be said that inelastic neutron scattering, for every \mathbf{Q} , produces a spectrum, understood as the frequency dependence of a quantity, here the scattering cross section. The optical methods Raman- and Brillouin spectroscopy are completely analogous in this respect, yielding the same $S(\mathbf{Q}, \omega)$ but different measured double-differential cross-sections because photons interact with matter differently. Other methods, as absorption spectroscopy, impedance spectroscopy or rheology do not yield a \mathbf{Q} dependence and are thus insensitive to the molecular structure. They provide only information about the overall dynamics. The deeper reason for this analogy is that scattering experiments as well as 'ordinary' spectroscopy can be explained by linear response theory (appendix B of ref. 2 or ref. 15).

Example: diffusion

For simple diffusion the density develops in time following Fick's second law,

$$\frac{\partial \rho}{\partial t} = D \Delta \rho \equiv D \left(\frac{\partial^2 \rho}{\partial x^2} + \frac{\partial^2 \rho}{\partial y^2} + \frac{\partial^2 \rho}{\partial z^2} \right). \quad (11.54)$$

The underlying mechanism is Brownian motion, i.e. random collisions with solvent molecules. Therefore, it can be concluded from the central limit theorem of statistics that the density of particles initially assembled at the origin is a Gaussian in all coordinates:

$$\begin{aligned} \rho_1 &= \frac{1}{\sqrt{2\pi}\sigma} \exp\left(-\frac{x^2}{2\sigma^2}\right) \frac{1}{\sqrt{2\pi}\sigma} \exp\left(-\frac{y^2}{2\sigma^2}\right) \frac{1}{\sqrt{2\pi}\sigma} \exp\left(-\frac{z^2}{2\sigma^2}\right) \\ &= \frac{1}{(2\pi)^{3/2}\sigma^3} \exp\left(-\frac{r^2}{2\sigma^2}\right). \end{aligned} \quad (11.55)$$

The index 1 should remind that the prefactor is chosen such that the total particle number $\int \rho_1 d^3r$ is normalised to one. The width of the distribution, σ has the dimension length. The only way to construct a length out of D (dimension length²/time) and time is $\sigma = c\sqrt{Dt}$ where c is a dimensionless constant. Inserting this into (11.55) yields:

$$\rho_1 = \frac{1}{c^3(2\pi Dt)^{3/2}} \exp\left(-\frac{r^2}{2c^2 Dt}\right). \quad (11.56)$$

The derivatives of this expression with respect to t and x, y, z can be calculated and inserted into (11.54):

$$\frac{\sqrt{2}(r^2 - 3c^2 Dt)}{8\pi^{3/2}c^5 D^{5/2}t^{7/2}} \exp\left(-\frac{r^2}{2c^2 Dt}\right) = \frac{\sqrt{2}(r^2 - 3c^2 Dt)}{4\pi^{3/2}c^7 D^{7/2}t^{7/2}} \exp\left(-\frac{r^2}{2c^2 Dt}\right). \quad (11.57)$$

One can see that the right- and left-hand side are identical if $c = \sqrt{2}$. This proves that the 'guess' (11.55) is indeed a solution of Fick's second law and also determines the unknown c . With the value of c substituted, the 'single particle density' is

$$\rho_1 = \frac{1}{(8\pi Dt)^{3/2}} \exp\left(-\frac{r^2}{4Dt}\right). \quad (11.58)$$

Diffusion-like processes are often characterised by the *mean-square displacement* $\langle r^2 \rangle$ ⁵. Because of the statistical isotropy, the average displacement $\langle r \rangle$ is always zero. Therefore, the characterisation of the mobility of a diffusional process has to be done using the second moment, which is the average of the square of the displacement. For the simple Fickian diffusion this can be calculated from (11.58):

$$\langle r^2 \rangle = \int \rho_1 r^2 4\pi r^2 d^3r = 6Dt. \quad (11.59)$$

⁵ Here, the definition is "displacement from the position at $t = 0$ " rather than "displacement from a potential minimum" on page 8. This is an obvious choice because the diffusing particle is not subjected to a potential as the atom in a crystal. Therefore, there is nothing like an 'equilibrium position'. This difference is indicated by the usage of $\langle r^2 \rangle$ instead of $\langle u^2 \rangle$. Because in the case of motion in a potential the displacement between time zero and time t can be understood as the difference of the displacements at time zero from the equilibrium position and that at time t , it follows that $\langle r^2 \rangle = 2\langle u^2 \rangle$

For incoherent scattering the starting position $\mathbf{r}(0)$ is irrelevant. Therefore, expression (11.58) is also $G_s(r, t)$. Because the Fourier transform of a Gaussian function is a Gaussian itself, the corresponding incoherent intermediate scattering function is

$$I_{\text{inc}}(Q, t) = \exp(-DQ^2t), \quad (11.60)$$

and because the Fourier transform of an exponential decay is a Lorentzian the incoherent scattering function is

$$S_{\text{inc}}(Q, \omega) = \frac{1}{\pi} \frac{DQ^2}{\omega^2 + (DQ^2)^2}. \quad (11.61)$$

This function is centred around $\omega = 0$, and for that reason the scattering is called *quasielastic*. This is typical for diffusionlike processes in contrast to vibrational processes which yield (phonon) peaks at finite energy transfers. For this reason, many textbook authors distinguish between inelastic and quasielastic neutron scattering instead of subsuming the latter under the former as done here⁶.

From expression (11.60) one can see that $I_{\text{inc}}(Q, t)$ decays faster with time for larger Q and from (11.61) that $S_{\text{inc}}(Q, \omega)$ is getting broader. This is understandable because Q defines the spatial resolution of a neutron scattering experiment in a reciprocal way. So a larger Q means observation on shorter distances which can be travelled faster by the diffusing particle.

Finally, one can see that

$$I_{\text{inc}}(Q, t) = \exp\left(-\frac{Q^2 \langle r^2 \rangle}{6}\right). \quad (11.62)$$

Because this expression is derived independently of the specific form of $\sigma(t)$ in (11.55) it is generally valid if the distribution of displacements $G_s(r, t)$ is a Gaussian. Even if this is not the case, equation (11.62) is often a good low- Q approximation called the *Gaussian approximation*⁷ and is the dynamical analogue of to the Guinier approximation of static scattering.

In general, the incoherent intermediate scattering function cannot be derived from the mean-square displacement alone. Because equation (11.62) is the first term of the cumulant expansion $\exp(aQ^2 + bQ^4 + \dots)$ of $I_{\text{inc}}(Q, t)$ [20] the mean-square displacement can be calculated as

$$\langle r^2 \rangle = -\lim_{Q \rightarrow 0} \frac{6}{Q^2} \ln I_{\text{inc}}(Q, t) \quad \text{or} \quad (11.63)$$

$$\langle r^2 \rangle = -\left. \frac{d \ln I_{\text{inc}}(Q, t)}{dQ^2} \right|_{Q=0}. \quad (11.64)$$

By replacing $I_{\text{inc}}(Q, t)$ by its value at infinite time, the EISF $S_{\text{inc}}^{\text{el}}(Q)$, the limiting mean-square displacement of a confined motion can be obtained. This is the principle of the *elastic scan* technique often used on neutron backscattering spectrometers [21].

⁶ There are two reasons for the choice made here: (1) The correlation function approach is also applicable to phonons. So, if this method is used, there is no conceptual difference between the treatment of vibrations and diffusion. (2) There are models as the damped harmonic oscillator which yield a continuous transition between inelastic scattering in the underdamped case and quasielastic scattering in the overdamped case.

⁷ In the literature, denominators 1, 2, and 3 are also found in this expression. Most of these formulae are nevertheless correct. Some authors use $\langle r^2 \rangle$ as mean-square displacement from an average position (what is called $\langle u^2 \rangle$ here). Then, 3 is the correct denominator because of $\langle r^2 \rangle = 2\langle u^2 \rangle$ (footnote 5). If the displacement is considered only in one coordinate ($\langle x^2 \rangle$), then 2 is the right denominator.

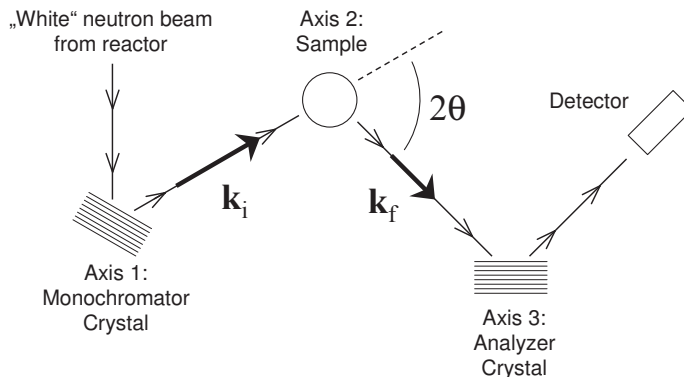


Fig. 11.6: Schematic setup of a triple-axis spectrometer.

11.3 Instrumentation

11.3.1 Triple axis spectrometer

The basic objective of inelastic neutron scattering is to measure the momentum transfer $\mathbf{q} = \mathbf{k}' - \mathbf{k}$ and the energy transfer $\hbar\omega = E' - E$. This task in general requires a monochromator for the incoming neutron beam and an analyzer for the scattered neutrons. In the most straightforward setup, the triple-axis spectrometer (3AX), one uses the Bragg planes of crystals similar to the diffracting grids in an optical spectrometer (figure 11.6).

Axis 1 turns the monochromator crystal. By doing this the neutron wavelength fulfilling the Bragg condition can be changed. In this way the wave vector $k = 2\pi/\lambda$ of the neutrons impinging on the sample is determined. Axis 2 turns the arm carrying the analyser crystal around the sample position. This defines the scattering angle 2θ . Finally, axis 3 turns the analyser crystal around its own axis such that only the desired k' is admitted to the detector.

For a given setting of axis 1 all points in the kinematically allowed (Q, ω) area (see Fig. 11.2) can be addressed by suitable settings of axis 2 and 3. E.g., for the study of phonons usually a 'constant- Q scan' is performed where $\mathbf{Q} = \mathbf{k}' - \mathbf{k}$ is held constant and only $\hbar\omega = E' - E$ is varied. For this purpose a coordinated change of the angles of axis 2 and 3 is required which is accomplished by computer control.

Historically, the triple-axis spectrometer is the first inelastic neutron scattering instrument. The first prototype was constructed in 1955 by Bertram N. Brockhouse. In 1994, Brockhouse received the Nobel prize for this accomplishment (together with Clifford G. Shull for the development of neutron diffraction).

The 3AX spectrometer is still widely in use for purposes where a high Q resolution is necessary and only a small region in the (Q, ω) plane has to be examined. This is mostly the study of phonons and magnons in crystals. In other fields, e.g. for 'soft matter' systems, it has been replaced by instruments showing better performance. The most important ones will be discussed here: time-of-flight (TOF) spectrometer, backscattering (BS) spectrometer,

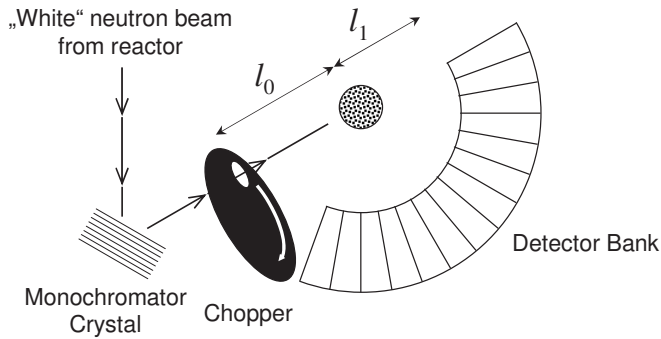


Fig. 11.7: Schematic setup of a time-of-flight spectrometer with crystal monochromator.

inverse TOF spectrometer, and neutron spin echo (NSE) spectrometer.

11.3.2 Time-of-flight spectrometer

The main disadvantage of the 3AX spectrometer is that it can only observe one (Q, ω) point at a time. While for samples where the scattering is concentrated into Bragg peaks this may be acceptable, for systems with diffuse scattering a simultaneous observation of a range of Q vectors and energy transfers $\hbar\omega$ is desired. This is accomplished by surrounding the sample position with an array of detectors (figure 11.7). In addition the energy of the scattered neutrons E' is here measured by their time of flight: A chopper in the incident beam defines the start time of the neutrons. The electronic pulse from their registration in the detector gives the end of their flight through the spectrometer. From the time difference the velocity of the neutrons can be calculated and from this in turn the energy transfer. The relation between time-of-flight and energy transfer is given by

$$\hbar\omega = \left(\frac{l_1^2}{(l_0 - \sqrt{2E/m_n} t_{\text{flight}})^2} - 1 \right) E. \quad (11.65)$$

As in all inelastic neutron scattering experiments, the lower limit of the energy transfer is $-E$. (The neutrons cannot lose more than their incident energy.) Because scattered neutrons with arbitrary high energies arrive at the detector in a finite time there is no principal upper limit. Nevertheless, at high energy transfers the time-of-flight scale gets so compressed that energy resolution worsens. This sets a practical upper limit at $5 \dots 10 E$.

The monochromatization of the incoming neutron beam can either be done by Bragg reflection from a crystal or by a sequence of choppers which are phased in order to transmit a single wavelength only. The former principle usually yields higher intensities while the latter is more flexible for the selection of the incident energy E and attains better energy resolution.

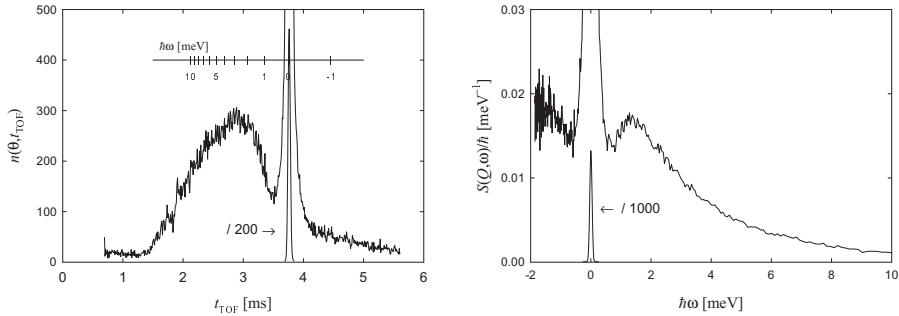


Fig. 11.8: Left: raw data from TOF spectrometer: neutron counts in a time channel of $10 \mu\text{s}$ during one hour registration time. The sample is a mesoscopically confined glass-forming liquid. The floating non-linear axis indicates the energy transfers calculated by equation (11.65). Because of the strength of the elastic scattering that part of the spectrum has been reduced by a factor of 200. Right: the same TOF data converted to $S(Q, \omega)$, elastic line reduced by factor 1000. The characteristic vibrational modes of the material at $\hbar\omega \approx 1.7 \text{ meV}$ (14 cm^{-1}) become only visible after the transformation.

Instrument	Type	λ_i [\AA]	Q_{max} [\AA^{-1}]	$\Delta\hbar\omega$ [meV]
PANTHER (ILL)	TX	0.86–3.3	3.5–14	0.4–6
IN5 (ILL)	CC	2–15	0.8–5.7	0.01–6
SHARP (ILL)	CX	4.1–5.9	1.8–2.6	0.05–0.17
TOFTOF (MLZ)	CC	1.5–5	2.0–6.5	0.1–3

Table 11.1: Basic specifications of representative neutron time-of-flight spectrometers. Instrument types: TX—thermal, crystal; CX—cold, crystal; CC—cold, chopper. The maximal Q and the energy resolution $\Delta\hbar\omega$ depend on the incident wavelength; the upper limits of their ranges correspond to the lower limit of the incident wavelength λ_i and vice versa. Institutions: ILL—Institut Laue-Langevin, MLZ—Maier-Leibnitz Zentrum.

Table 11.1 shows some representative TOF instruments with their basic specifications. Depending on the desired incident wavelength the instruments are constructed either using neutrons directly from the reactor moderator (thermal neutrons, $\lambda_{\text{max}} \approx 1.8 \text{ \AA}$) or a cold source, where an additional moderation, e.g. by liquid hydrogen, takes place ($\lambda_{\text{max}} \approx 4 \text{ \AA}$). Thermal neutrons make a larger Q range accessible while cold neutrons yield better energy resolution. Therefore, the choice of the instrument depends on the system to be observed but in general ‘cold neutron’ instruments are preferred for inelastic neutron scattering in soft matter systems while ‘thermal neutron’ instruments are used for studies of phonons and magnetism.

11.3.3 Backscattering spectrometer

A recurring problem of inelastic neutron scattering investigations is that processes are too slow to be observed. Without resorting to extreme setups which lead to a loss of intensity, the energy resolution of TOF spectrometers is limited to about $10 \mu\text{eV}$, which corresponds to

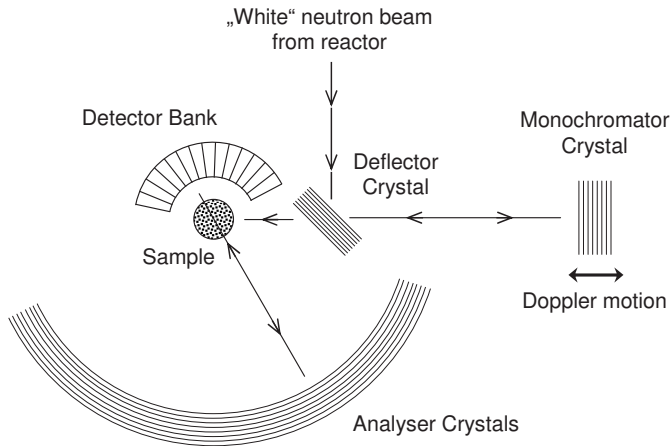


Fig. 11.9: Schematic setup of a backscattering spectrometer.

a maximal timescale of 200 ps. This is often not sufficient for e.g. the large scale motions in polymers, biological systems, or glass-forming materials. Therefore, instruments with highest energy resolution are often needed, the backscattering (BS) and neutron spin echo (NSE) spectrometer.

The energy resolution of a TOF spectrometer is limited by the selectivity of the monochromator crystal⁸. If perfect crystals are used the spread of the selected wavelengths $\Delta\lambda/\lambda$ is determined by the uncertainty of the scattering angle α at the monochromator and analyser, $\Delta\alpha$. Differentiating the Bragg condition $\lambda = 2 \sin(\alpha/2)/d$ one obtains

$$\Delta\lambda/\lambda = \cot \alpha \cdot \Delta\alpha/2. \quad (11.66)$$

This expression becomes zero for $\alpha = 180^\circ$. In practice this means that the wavelength spread becomes minimal if the neutron beam is reflected by 180° , i.e. in backscattering condition.

Figure 11.9 shows schematically the instrument based on this principle. The first crystal in the beam is only a deflector with low wavelength selectivity. The actual monochromatization takes place upon the second reflection by the crystal in backscattering position. The monochromatized neutrons are then scattered by the sample which is surrounded by analyzer crystals placed on a spherical surface. There they are again scattered under backscattering condition. The reflected neutrons pass once more through the sample and finally reach the detector.

It can be seen that the backscattering condition leads to technical problems in several places: (1) The deflector must not accept all neutrons otherwise the monochromatized beam would be scattered back into the source. This can be solved by reducing its size deliberately below

⁸ For chopper spectrometers the limit is given by the pulse length which could in principle be arbitrary small. But since the counted intensity decreases quadratically with pulse length the resolution limit of an efficient experiment is in the same range.

Instrument	Type	λ [Å]	Q_{\max} [Å ⁻¹]	$\Delta\hbar\omega$ [μeV]	$\hbar\omega_{\max}$ [μeV]
SPHERES (JCNS)	CD	6.27	1.8	0.7	30
HFBS (NIST)	CD	6.27	1.7	0.9	30
IN16B (ILL)	CD	3.23–6.27	1.8–3.5	0.3–2.0	31–59
IN13 (ILL)	TH	2.23	5.5	8	300

Table 11.2: Basic specifications of representative neutron time-of-flight spectrometers. Instrument types: CD—cold, Doppler monochromator; TH—thermal, heated monochromator. The maximal Q and the energy resolution $\Delta\hbar\omega$ depend on the incident wavelength; the upper limits of their ranges correspond to the lower limit of the incident wavelength λ_i and vice versa. Institutions: JCNS—Jülich Centre for Neutron Science, NIST—National Institute of Standards and Technology, ILL—Institut Laue-Langevin

the neutron beam area or putting it on a rotating disk which removes it at the moment when the neutrons come back from the monochromator. Of course all these measures are taken at the expense of intensity. (2) The second passage of the scattered neutrons through the sample causes additional multiple scattering and absorption. Both problems can be avoided by leaving exact backscattering condition but with the consequence that the energy resolution degrades.

So far it seems that the backscattering instrument can only observe elastic scattering ($E' = E$) if the same crystals are used for monochromator and analyzer. In order to do inelastic scattering one has to change either E or E' . It turns out that this is much easier for the incident energy by either using a moving monochromator (Doppler effect) or a heated monochromator (thermal expansion modifying the lattice plane distance d). The latter technique usually allows larger energy transfers. For very large energy transfers, different crystals are used for monochromator and analyzer, yielding an offset of the whole $\hbar\omega$ range. Table 11.2 comprises specifications of representative BS spectrometers.

11.3.4 Inverse TOF spectrometer

The inverse TOF spectrometer is a kind of hybrid between the TOF spectrometer and the backscattering spectrometer. Usually, such instruments are built at spallation sources which produce short pulses of neutrons. If the neutrons are produced in pulses one can use their creation time to start the TOF clock and in principle there is no need for a chopper. In this way, on a pulsed source, all neutrons can be used in contrast to conventional TOF spectrometers which use only a few percent. The principle can also be realised by chopping a continuous beam into pulses on reactors with a loss of intensity comparable to that of an ordinary TOF instrument (e.g. BATS in Table 11.3). Because the energy resolution depends on the length of the pulses this ‘pulse shaping’ may also be necessary on a long-pulse spallation source.

For inverse TOF instruments, the incident energy E is variable and measured by the time-of-flight and the final energy E' is kept constant by a fixed set of analyser crystals. This is often called “inverse geometry” or “inverse time-of-flight”. By putting the analyser crystals into near backscattering position it is possible to obtain a very good energy resolution already

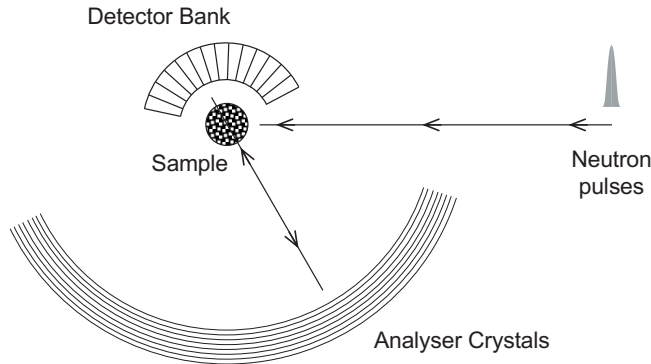


Fig. 11.10: Schematic setup of a inverse time-of-flight spectrometer.

Instrument	Source	λ [Å]	Q_{\max} [Å ⁻¹]	$\Delta\hbar\omega$ [μeV]	$\hbar\omega_{\max}$ [meV]
IRIS (RAL)	S	6.7–20	0.6–1.9	1–18	0.4
BATS (ILL)	R	3.3–6.3	1.8–3.5	1.2–59	0.34–1.1
DNA (J-PARC)	S	3.3–6.3	2.0–3.4	1.4–19	0.08–1.5

Table 11.3: Basic specifications of representative inverse time-of-flight spectrometers. The maximal Q and the energy resolution $\Delta\hbar\omega$ depend on the incident wavelength; the upper limits of their ranges correspond to the lower limit of the incident wavelength λ_i and vice versa. R–reactor source, S–pulsed spallation source. Institutions: RAL–Rutherford-Appleton Laboratory, ILL–Institut Laue-Langevin, J-PARC–Japan Proton Accelerator Research Complex.

close to true backscattering spectrometers and combine it with the large energy range of a TOF instrument. Because of the analyser positioning these instruments are sometimes also called “backscattering” although the way the energy transfer is measured is completely different from that of the instruments described in section 11.3.3.

11.3.5 Neutron spin echo spectrometer

In order to access even slower processes a very high resolution technique is needed allowing to reach more than 100 nanoseconds corresponding to energy transfers in the neV range. Such a technique is provided by neutron spin echo (NSE) spectrometers [22] which are able to measure directly energy *changes* of the neutron due to scattering.

This distinguishes NSE from conventional inelastic neutron scattering techniques which proceed in two steps: (1) monochromatization of the incident beam to E , (2) analysis of the scattered beam (E'). The energy transfer is then determined by taking the difference $E' - E$. In order to achieve high energy resolutions with these conventional techniques a very narrow energy interval must be selected from the relatively low-intensity neutron spectrum of the

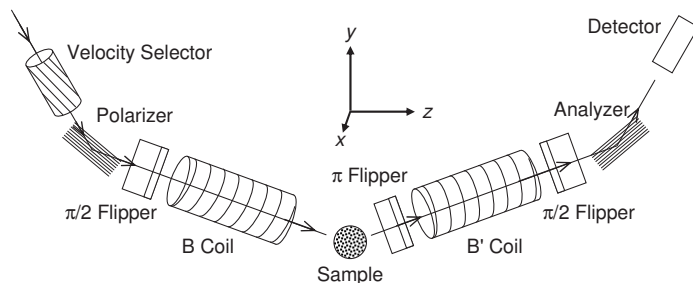


Fig. 11.11: Schematic setup of a neutron spin echo spectrometer.

source. Conventional high-resolution techniques therefore inevitably run into the problem of low count rates at the detector.

Unlike these methods, NSE measures the individual velocities of the incident and scattered neutrons using the Larmor precession of the neutron spin in a magnetic field. The neutron spin vector acts as the hand of an internal clock, which is linked to each neutron and connects the result of the velocity measurement to the neutron itself. Thereby the velocities before and after scattering on one and the same neutron can be compared and a direct measurement of the velocity difference becomes possible. The energy resolution is thus decoupled from the monochromatization of the incident beam. Relative energy resolutions in the order of 10^{-5} can be achieved with an incident neutron spectrum of 20% bandwidth.

The motion of the neutron polarization $\mathbf{P}(t)$ —which is the quantum mechanical expectancy value of the neutron spin—is described by the Bloch equation

$$\frac{d\mathbf{P}}{dt} = \frac{\gamma\mu}{\hbar}(\mathbf{P} \times \mathbf{B}) \tag{11.67}$$

where γ is the gyromagnetic ratio ($\gamma = -3.82$) of the neutron, μ the nuclear magneton and \mathbf{B} the magnetic field. Equation (11.67) is the basis for manipulation of the neutron polarization by external fields. In particular, if a neutron of wavelength λ is exposed to a magnetic field B over a length l of its flight path, its spin is rotated by

$$\phi = \left(\frac{2\pi|\gamma|\mu\lambda m}{h^2} \right) Bl. \tag{11.68}$$

The basic setup of an NSE spectrometer is shown in figure 11.11. A velocity selector in the primary neutron beam selects a wavelength interval of 10–20% width. In the primary and secondary flight path of the instrument precession fields B and B' parallel to the respective path are generated by cylindrical coils. Before entering the first flight path the neutron beam is polarized in forward direction⁹. Firstly, a $\pi/2$ flipper rotates the polarization to the x direction perpendicular to the direction of propagation (z). This is done by exposing the neutrons to a well defined field for a time defined by their speed and the thickness of a

⁹ This is done by a “polarizing supermirror” which only reflects neutrons of that spin—similar to the Nicol prism in optics.

flat coil (Mezei coil). Beginning with this well-defined initial condition the neutrons start their precession in the field B . After being scattered by the sample the neutrons pass a π flipper and then pass the second precession field B' . Finally, the neutrons pass another $\pi/2$ coil which, under certain conditions, restores their initial polarization parallel to their flight direction. In order to understand what that condition is, one has to trace the changes of the spin vector (z always denoting the direction parallel to neutron propagation):

(n_x, n_y, n_z)	neutronic device
(0,0,1)	
(1,0,0)	$\pi/2$ flipper
$(\cos \phi, \sin \phi, 0)$	field B
$(\cos \phi, -\sin \phi, 0) =$ $(\cos(-\phi), \sin(-\phi), 0)$	π flipper
$(\cos(\phi' - \phi), \sin(\phi' - \phi), 0)$	field B'
$(0, \sin(\phi - \phi'), \cos(\phi - \phi'))$	$\pi/2$ flipper

In total, the spin is rotated by $\phi - \phi'$ around the x axis when a neutron passes through the spectrometer. This means that the final polarization is identical to the incident if $\phi = \phi' (+2\pi n)$, especially if $\lambda_i = \lambda_f$ (elastic scattering) and $\int_0^l B dz = \int_0^{l'} B' dz$ (for homogeneous fields: $B l = B' l'$) as follows from (11.68). This condition is called “spin echo” and is independent of the individual velocities of the neutrons because their difference alone determines $\phi - \phi'$.

Leaving spin echo condition the probability of a single neutron to reach the detector is reduced due to the polarization analyzer by $\cos(\phi' - \phi)$. If we keep the symmetry of the instrument, $B l = B' l'$, but consider inelastic scattering the precession angle mismatch can be approximated by

$$\begin{aligned} \phi' - \phi &= \left(\frac{2\pi |\gamma| \mu m}{h^2} \right) B l (\lambda_f - \lambda_i) \\ &\approx \underbrace{\frac{|\gamma| \mu m_n^2 \lambda^3 B l}{h^3}}_{=t_{\text{NSE}}(B)} \omega \end{aligned} \quad (11.69)$$

for small energy transfers where $\Delta \lambda \approx \hbar \omega / \frac{dE}{d\lambda}$ can be used. Because the energy transfer for inelastic scattering is not fixed but distributed as determined by the scattering function $S(Q, \omega)$ we have to average the factor $\cos(\phi' - \phi)$ weighted by $S(Q, \omega)$ to get the reduction of count rate at the detector, the effective polarization

$$P(Q, t_{\text{NSE}}) = \frac{\int_{-\infty}^{\infty} S(Q, \omega) \cos(\omega t_{\text{NSE}}) d\omega}{\int_{-\infty}^{\infty} S(Q, \omega) d\omega}. \quad (11.70)$$

Expression (11.70) reverses the temporal Fourier transform of equation (11.22) and therefore the result of the NSE experiment

$$P(Q, t_{\text{NSE}}(B)) = \frac{I(Q, t_{\text{NSE}}(B))}{I(Q, 0)} \quad (11.71)$$

is the normalised *intermediate* scattering function. This function is often more understandable and easier to interpret than the frequency dependent scattering function.

In order to estimate typical Fourier times t_{NSE} which can be accessed by NSE we consider maximum fields of $B = B' = 500$ Gauss in precession coils of $l = l' = 2$ m length operating at $\lambda = 8 \text{ \AA}$. Then (11.69) results in a time of about 10 ns which can be reached.

From this equation it also becomes clear that the most efficient way to enlarge this time is to use longer wavelengths because λ enters in the third power. This in turn reduces the accessible Q range which constitutes a drawback for studies on low molecular materials but not for the large scale properties of polymers which have to be observed at low Q anyway.

Because NSE works in time domain, there is no well-defined way to relate the maximum Fourier time t_{max} of an NSE spectrometer to the resolution $\Delta\hbar\omega$ of one of the instruments mentioned before. A rule of thumb would be that 1 ns corresponds to $1 \mu\text{eV}$, thus $\Delta\hbar\omega/\mu\text{eV} = \text{ns}/t_{\text{max}}$. Because of the inverse relation between time and frequency, the corresponding limit to $\hbar\omega_{\text{max}}$ on backscattering and inverse TOF, on an NSE spectrometer is the smallest time accessible, t_{min} . This time depends strongly on the technical set-up of the spectrometer. In most cases it is about three orders of magnitude below t_{max} .

There are two restrictions of the application of NSE which may impede its use even if the dynamical range is adequate for the system to be studied:

- If the sample changes the polarisation of the beam the information encoded in the neutron spins gets ‘scrambled’. This is the case for magnetic samples but also for systems with spin-incoherent scattering. Because ^1H hydrogen is a spin-incoherent scatterer this often makes chemical deuteration necessary. Nowadays, NSE experiments are often still feasible because there may be a stochastic relation between the numbers of neutrons scattered. This would be 1/3 ‘up’ and 2/3 ‘down’ in the case of pure spin-incoherent scattering. Nevertheless, there are combinations of nuclei which bring the probabilities close to 1/2 or uncontrollable situations as in ferromagnets where NSE measurements are impossible.
- Because the value of λ in equation (11.69) varies by 10...20% from neutron to neutron the relation between the phase difference and the energy transfer is somewhat ‘blurred’. For processes like diffusion which have a broad distribution of ω (see (11.61)) this is usually not important. But for mechanisms which produce well-defined energy transfers $\hbar\omega$ this is problematic and neutron backscattering is preferable.

Exemplary NSE spectrometers with their specifications are listed in table 11.4. NSE spectrometers are very flexible instruments often used with different setups of which only “typical” ones have been included. As special features have to be mentioned that IN11 and WASP have one-dimensional detector arrays which span 60° and 130° degrees respectively, allowing the simultaneous observation of a range of Q values. The instruments IN15 and J-NSE have two-dimensional detector arrays which can be used for studying anisotropies but cover a smaller angular range. IN15 uses a focusing mirror in order to increase neutron flux which would be otherwise very low due to its long precession coils.

A straightforward optimisation is the use of multidetectors covering a large angular range as in TOF or BS spectrometers. This is indeed possible by adopting a radial magnetic field

Instrument	λ [Å]	Q_{\max} [Å ⁻¹]	t_{\max} [ns]	features	options
IN11 [†] (ILL)	4.5–12	0.9–2.4	2–45		multidetector, three-axes
J-NSE (JCNS)	4.5–16	0.4–1.5	10–350	multidetector, superconducting coils	
IN15 (ILL)	8–25	0.13–0.4	30–1000	mirror optics	time-of-flight
WASP (ILL)	3–12	1.0–3.9	0.6–18	radial geometry	
NSE (ORNL)	2–14	0.4–3.1	1–280	time-of-flight, superconducting coils	

Table 11.4: Basic specifications of representative neutron spin echo spectrometers. The maximal Q and the maximal Fourier time t_{\max} depend on the incident wavelength; the upper limit of the Q range and the lower limit of t_{\max} correspond to the lower limit of the incident wavelength λ and vice versa. Institutions: ILL–Institut Laue-Langevin, JCNS–Jülich Centre for Neutron Science, ORNL–Oak Ridge National Laboratory. [†]IN11 is not in operation anymore but included for historical reasons.

configuration. The drawback is that the field integral is less well defined in this setup. This leads to a reduction of the time range by a factor of about 10 compared to a conventional NSE spectrometer.

Also for NSE it is possible to optimise the instrument for pulsed sources by using time-of-flight. The idea is that one omits the velocity selector and uses the fact that the neutrons arrive ‘sorted’ by velocity at the instrument. So one works with a very large wavelength range. But still individual wavelengths can be identified from the time of registration in the detector. The different wavelengths generate different Q values at the same detection angle. This saves the often necessary step to vary either the scattering angle or the wavelength to collect several Q values.

References

- [1] This dictum is usually attributed to the Nobel prize winners B. N. Brockhouse and/or C. G. Shull. But to the knowledge of the author, no reliable quotation clarifying its true origin exists.
- [2] S. W. Lovesey: “Theory of Neutron Scattering from Condensed Matter” (Clarendon Press, Oxford, 1984).
- [3] G. L. Squires: “Introduction to the theory of thermal neutron scattering” (Cambridge University Press, Cambridge, 1978).
- [4] G. E. Bacon: “Neutron Diffraction” (Clarendon Press, Oxford, 1975).
- [5] G. E. Bacon (ed.): “Fifty Years Of Neutron Diffraction: The Advent Of Neutron Scattering” (Adam Hilger, Bristol, 1986).
- [6] M. Bée: “Quasielastic neutron scattering” (Adam Hilger, Bristol, 1988).
- [7] R. Zorn: “Fourier Transforms” in T. Brückel, G. Heger, D. Richter, R. Zorn (eds.): “Neutron Scattering” (Forschungszentrum Jülich, 2008, <http://hdl.handle.net/2128/37180>), chapter I.
- [8] R. Zorn, D. Richter: “Correlation Functions Measured by Scattering Experiments”, *ibidem*, chapter 4.
- [9] N. W. Ashcroft, N. D. Mermin: “Solid State Physics” (Holt-Saunders, New York, 1976).
- [10] G. P. Srivastava: “The physics of phonons” (Adama Hilger, Bristol, 1990).
- [11] H. Bilz, W. Kress: “Phonon dispersion relations in insulators”, *Solid-state sciences*, Vol. 10 (Springer, Berlin, 1979).
- [12] B. N. Brockhouse, *Phys. Rev.* **106** 859 (1957).
- [13] G. Placzek, *Phys. Rev.* **86** 377 (1952).
- [14] J. L. Yarnell, M. J. Katz, R. G. Wenzel, S. H. Koenig, *Phys. Rev. A* **7** 2130 (1973).
- [15] R. Zorn: “Correlations and Response of Matter to Probes” in K. Urban, C. M. Schneider, T. Brückel, S. Blügel, K. Tillmann, W. Schweika, M. Lentzen, L. Baumgarten: “Probing the Nanoworld” (Forschungszentrum Jülich, 2008).
- [16] P. Schofield, *Phys. Rev. Lett.* **4** 239 (1958)
- [17] R. Aamodt, K. M. Case, M. Rosenbaum, P. F. Zweifel, *Phys. Rev.* **126** 1165 (1962)
- [18] Eq. 5.98 in volume 1 of ref. 2.
- [19] Chapter 3.5 in volume 1 of ref. 2.
- [20] A. Rahman, K. S. Singwi, A. Sjölander, *Phys. Rev.* **126**, 986 (1962).

[21] R. Zorn, *Nucl. Instr. Meth. A* **603**, 439 (2009)

[22] Mezei, F. (ed.) (1980): *Neutron spin echo*, Springer, Heidelberg.

Exercises

Note: Exercises are labelled by stars (* through ***) indicating the level of difficulty. Try to solve the easier ones first.

E11.1 Scattering triangle*

For the feasibility of an inelastic neutron scattering experiment it is essential that the desired $Q, \hbar\omega$ combination (in the scattering function $S(Q, \omega)$) can be reached at a certain combination of incident neutron wavelength λ and angle 2θ .

1. $\lambda = 5.1 \text{ \AA}$, $2\theta = 90^\circ$ and $\hbar\omega = 5 \text{ meV}$, which value has Q ? Which value would Q have calculated from the formula for elastic scattering?
2. $\lambda = 5.1 \text{ \AA}$, $Q = 1 \text{ \AA}^{-1}$, what is the largest energy gain and largest absolute energy loss one can reach? What do you have to do if you need larger values of $|\hbar\omega|$?

Hints: $\hbar = 1.0546 \times 10^{-34} \text{ Js}$, neutron mass: $m = 1.6749 \times 10^{-27} \text{ kg}$, $1 \text{ eV} = 1.6022 \times 10^{-19} \text{ J}$.

E11.2 Q dependence of characteristic time***

In many cases, the incoherent intermediate scattering function can be written in the form $I_{\text{inc}}(Q, t) = \exp(-(t/\tau(Q))^\beta)$ with $\tau(Q) \propto Q^{-x}$. E.g. in the lecture diffusion ($x = 2$, $\beta = 1$) and the ideal gas ($x = 1$, $\beta = 2$) were presented. In a later lecture you will learn that for polymers in the melt $x = 4$, $\beta = 1/2$ holds. For polymers in solution the Zimm model predicts $x = 3$, $\beta = 2/3$. In all cases $x \cdot \beta = 2$. What is the reason for this nearly universal relation?

E11.3 Choice of instruments**

The most important aspect of planning an inelastic neutron scattering experiment is the choice of the right instrument matching the time scale of the process to be observed.

1. What is the range of energy transfers corresponding to the right-hand side of Fig. 11.5 in meV? Which instrument would you chose?
2. The diffusion coefficient of benzene at room temperature is about $2 \times 10^{-5} \text{ cm}^2/\text{s}$. Which instrument would you use to study this diffusion on the length scale of 0.5 nm ? (Hints: As you may know from the lectures of diffraction and SANS, the lengths are related roughly roughly by $Q = 2\pi/l$. From that value calculate the width of the quasielastic scattering in (11.61) and convert it to meV.)
3. The diffusion coefficient of the protein alcohol dehydrogenase in water is $23.5 \mu\text{m}^2/\text{s}$. Which instrument would you use to study this diffusion on the length scale of 3 nm ?

4. When molecules containing methyl groups are cooled down to near absolute zero, their rotation does not completely stop because quantum tunnelling between the energy minima is possible. This leads to a splitting of the ground state, which can be very different in chemically similar molecules: methane (CH_4): $142 \mu\text{eV}$, methyl fluoride (CH_3F): $23.1 \mu\text{eV}$, methyl iodide (CH_3I): $2.44 \mu\text{eV}$. Which instrument may be used for which compound?

12 Virtual Neutron Scattering Experiments

K. Lieutenant

Jülich Centre for Neutron Science 2

Forschungszentrum Jülich GmbH

Contents

12.1	Introduction.....	2
12.2	Simulation of neutron scattering instruments.....	2
12.2.1	Monte Carlo simulations	2
12.2.2	Instrument design	4
12.2.3	Example: A diffractometer for the High Brilliance neutron Source (HBS)	4
12.3	Virtual experiments	5
12.4	Digital twins	6
12.5	Applications of virtual experiments	7
12.5.1	Training and experiment preparation.....	7
12.5.2	Teaching	8
12.5.3	Test of data evaluation software	8
	References	9
	Exercises.....	10

Lecture Notes of the JCNS Laboratory Course Neutron Scattering. This is an Open Access publication distributed under the terms of the Creative Commons Attribution License 4.0, which permits unrestricted use, distribution, and reproduction in any medium, provided the original work is properly cited. (Forschungszentrum Jülich, 2024)

12.1 Introduction

Mankind faces several challenges these days: it is necessary to stop the climate change, fight diseases, keep the biodiversity and reach a sustainable economy and ecological food and water supply for everybody. To achieve all that, new technologies and materials are needed, which require research to understand the processes underlying the problem and to find and test new materials. This requires a variety of methods to investigate matter.

Neutron scattering is an important method for this research, especially to study biological systems, magnetic materials and energy materials, because it makes magnetic structures and light atoms visible (especially H atoms) and can distinguish atoms close to each other in the periodic system and is even isotope sensitive.

Dedicated instruments were built to determine atomic structures or structures in the nm-scale, to study inelastic processes in a certain time and length range, to take images of the interior of an object or to analyse its atomic composition.

Practically all instruments are prototypes, adapted to the source and the planned scientific applications. The construction is expensive, and the flux is lower than that of other beams. This results in long measuring times and makes beam time precious. As a consequence, it is necessary to build optimized instruments and use beamtime efficiently. To build optimized instruments, they are first designed analytically and then simulated by Monte Carlo simulations. This allows comparing different setups and parameter choices and even enables numerical optimization.

Usually, the simulations include scattering of neutrons in known samples and determining the distribution of neutrons on the detector. They are then called virtual experiments. Often, the simulated spectra are evaluated using the data evaluation software foreseen for the real experiments.

Virtual experiments also useful for teaching purposes, training to handle the instrument, preparation of the real experiment and even for testing the data evaluation software.

12.2 Simulation of neutron scattering instruments

12.2.1 Monte Carlo simulations

Monte Carlo (MC) simulations are used in many fields, e.g. traffic simulations, telecommunication or physics. The basic idea is to create a large number of events by random number choices. As an example, in a simulation of the traffic in a town, an 'event' is the ride from point A to B in the town, e.g. a commute to work in the morning. The random number choices would be: the home address (mainly in living area), work address (usually in the city centre or a business park) and the starting time.

Similarly, in neutron scattering, the events are the possible trajectories of a neutron through the instrument including the scattering possibilities in the sample. Accordingly, the

parameters determined by random choices for each event are: the starting position (on the moderator surface), the flight direction from the moderator, the neutron wavelength and the starting time at the moderator for time-of-flight instruments (see 0). Dependent on the instrument, additional choices may be needed, e.g. for the scattering in the sample or the detection process in the detector.

The trajectory of each neutron through the instrument is then calculated treating them as classical particles usually under the influence of gravity until they are absorbed, missing a component or reaching the sample. Here they are scattered into a chosen solid angle and counted, if they reach the detector. Each trajectory is given a weight in neutrons per second, which enable to monitor the neutron intensity at any point of the instrument and in any monitor channel or detector cell.

Why not scanning the parameters? A 'dense' distribution of each parameter is only possible in 1- or 2-dimensional parameter space, not in 6 or more dimension. As an example, if there are 6 parameters and 1 million events, there can be only 10 different values for each parameter. For the instrument simulation described above, only 10 different wavelength values, e.g. 1, 2, ... 10 Å. So, peaks generated by neutrons of e.g. 2.45 or 3.6 Å will not be visible.

Name and history: First Monte Carlo simulations were performed within the Manhattan Project to develop the atomic bomb; they called it Monte Carlo method as it reminded them on gambling in a casino. It was also the start of the MCNP program, which is still used today. It is one of a few programs to simulate shielding and the target-moderator-reflector system, where neutrons are generated and slowed down.

A branch of the MCNP program was converted to NISP [1] to simulate neutron scattering instruments with the idea to accelerate simulation by only considering neutrons on their way to sample and detector. As it was difficult to use, it was only continued as long as the author supported the simulations. In the late 90s, new programs were developed (e.g. VITESS [2], McStas [6]). They were designed for a broad user community, are easy to use and can be employed for all kinds of instruments at all kinds of neutron sources.

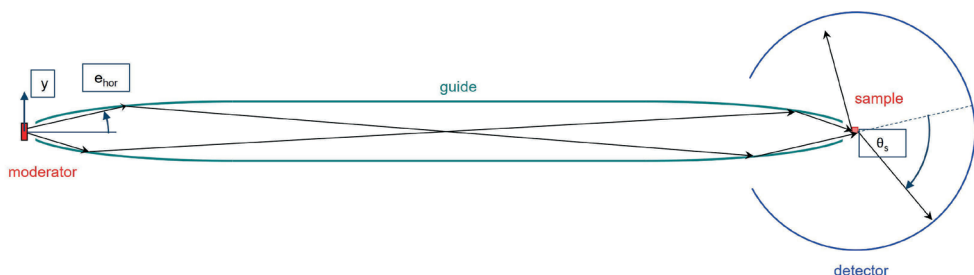


Fig. 12.1: Concept of Monte Carlo simulations as used in virtual experiments on neutron scattering instruments showing 3 of the 6 parameters determined by random choices: y , e_{hor} , Θ_s . In the other dimension (not shown here), there are 3 more: z , e_{vert} , Φ_s .

12.2.2 Instrument design

A new instrument first needs a design concept and analytical calculations starting from the scientific applications foreseen for the instrument. The analytical calculations allow already an estimation of its resolution and the flux at the sample.

Then it is simulated to see the beam properties (at the sample) and get more precise values for flux and resolution. It can be optimized for highest flux, highest resolution, best peak shape, highest signal to noise ratio or any other figure-of-merit. Therefore, many simulations are necessary comparing different parameter settings or even using numerical optimisation to find the best parameter set.

When instruments are upgraded, both, the old and the new setup are simulated and compared. The simulation of the old version should reflect the experimental results. If that is the case and the simulation of the new setup gives a better figure-of-merit, an improved instrument performance can be expected (see e.g. [4]).

12.2.3 Example: A diffractometer for the High Brilliance neutron Source (HBS)

As an alternative to fission or spallation neutron sources, Compact Accelerator-driven Neutron Sources (CANS) have been developed, in which protons with energies of the order 10 MeV cause the release of neutrons by nuclear reactions in neutron-rich isotopes of some elements (e.g. ${}^7\text{Li}$, ${}^9\text{Be}$, or ${}^{181}\text{Ta}$). CANS sources are scalable by adapting proton energy and current to the needed source strength. At the upper end, High-Current Accelerator-driven Neutron Sources (HiCANS) allow instrument performances as offered by current medium reactor and spallation sources.

The Jülich High Brilliance neutron Source (HBS) is one of these HiCANS sources. It has been developed over the last years at Forschungszentrum Jülich. The Technical Design Report, released in 2023 contains not only a description of the facility as a whole, of the accelerator and the target-moderator-reflector system, but also a suggestion for the instrument suite, which covers all scientific applications studied using neutrons [5]. It comprises SANS instruments and reflectometers for large scale structure studies, spectrometers to study dynamics of materials, imaging instruments for 'photos' of the interior of objects and analytics instruments for the determination of element or isotope composition by analytics instruments and six diffractometers to determine atomic positions.

One of them is the Thermal Powder Diffractometer (TPD), a time-of-flight powder diffractometer. It allows a large variation in flux and resolution so that it can be used for high-resolution measurements as well as low-resolution time-resolved measurements **Fehler! Verweisquelle konnte nicht gefunden werden..** It has been simulated in detail for the three different setups - high resolution, medium resolution and high intensity. The results show promising beam properties at the sample (see 0).

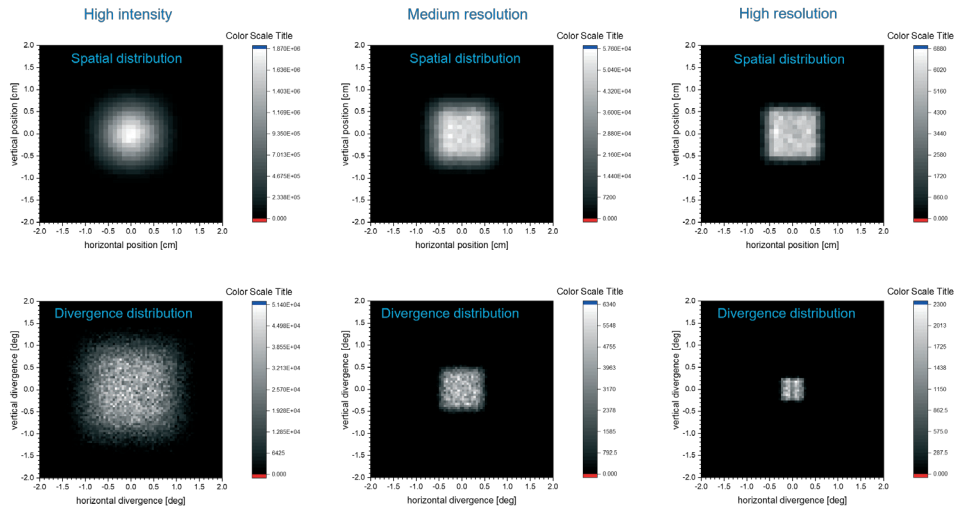


Fig. 12.2 *Spatial (top) and divergence (bottom) distribution of the beam of the thermal powder diffractometer of the HBS at the sample position for the three different setups obtained by MC simulations using the VITESS program [1]*

12.3 Virtual experiments

In the next step, a sample is added to the simulation. The sample scatters the neutrons, and their distribution on the detector is simulated – this is the diffraction pattern. For time-of-flight instruments, it is converted into a function $I(Q)$ or $I(d)$, the intensity as a function of the momentum transfer Q or the d -spacing d . (see 0). This allows calculating the linewidth and checking the line shape. The diffraction pattern can now be used for data evaluation, e.g. by using the same software as for real experiments. This enables to check the instrument performance in terms of the final output.

In our example, a virtual experiment of the Thermal Powder Diffractometer was performed using the standard sample $\text{Na}_2\text{Ca}_3\text{Al}_2\text{F}_{14}$ (NAC) for powder diffractometer. It revealed a symmetric linewidth and a resolution and detector count rate comparable to diffractometers on current neutron sources (see 0)

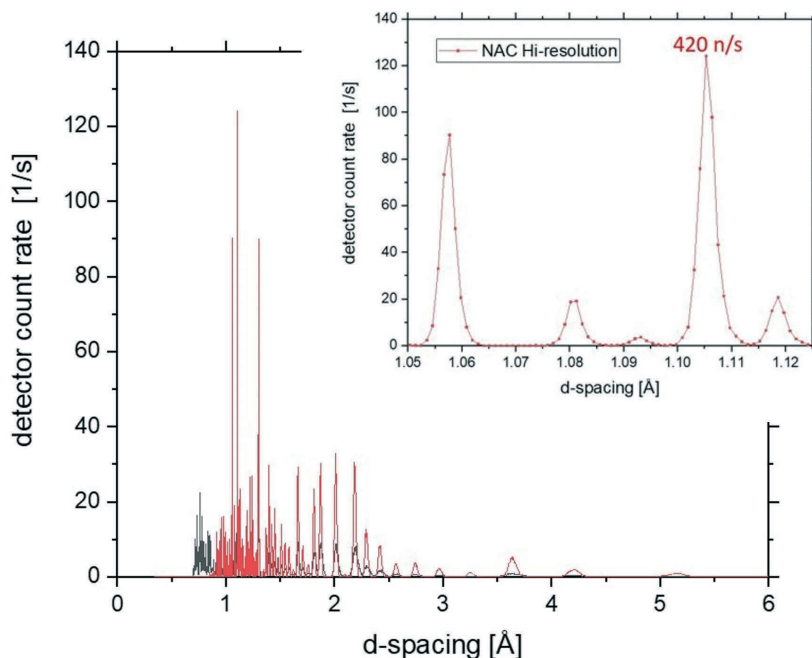


Fig. 12.3: Diffraction pattern of a NAC sample obtained by simulation of the thermal powder diffractometer of the HBS in the high-resolution setup. The red curve shows the pattern of the long wavelength frame (1.65 – 2.7 Å), the black curve that of the short wavelength frame (0. - 1.65 Å). The inset shows the range around 1.1 Å of the red curve stretched by a factor of about 50.

12.4 Digital twins

Simulations of the diffraction patterns have been performed for many years already. Now we want to emulate the real neutron scattering experiment by a simulation, in which the simulated system reacts just like the real system. Ideally, the graphical user interface that is used for the real instrument is also used for the virtual experiments. We then have a so-called digital twin of the instrument. This is realized in several of the experiments in the JCNS lab course to enable virtual experiments, when the real experiments cannot be performed.

While most components in a real instrument have their counterpart in the virtual experiment, the neutron beam is usually treated differently: So far, it has been common practice to take all neutrons out of the consideration that are not on the way to sample and detector anymore. In a digital twin, we have to treat also neutrons scattered in the sample environment, passing through the sample without reacting with it, or interacting with the sample support (cf. 0).

In a second step, the absorption of neutrons in the different components could be used to simulate the background radiation.

It is also required for the simulation to enable visualization of the detector screen or the monitors and to update this output every few seconds in order to show the advance of the (virtual) measurement.

For some instruments, it is a challenge to get the simulation as fast as the experiment. Then it may be necessary to store events after the fixed part of the instrument and read them to simulate the variable part of the instrument.

The final step to a digital twin is then to have an 'endless' simulation that reacts instantaneously on parameter changes. This has not been realized - presently a parameter change causes a restart of the simulation with the new parameter set – but this feature is currently in the works.

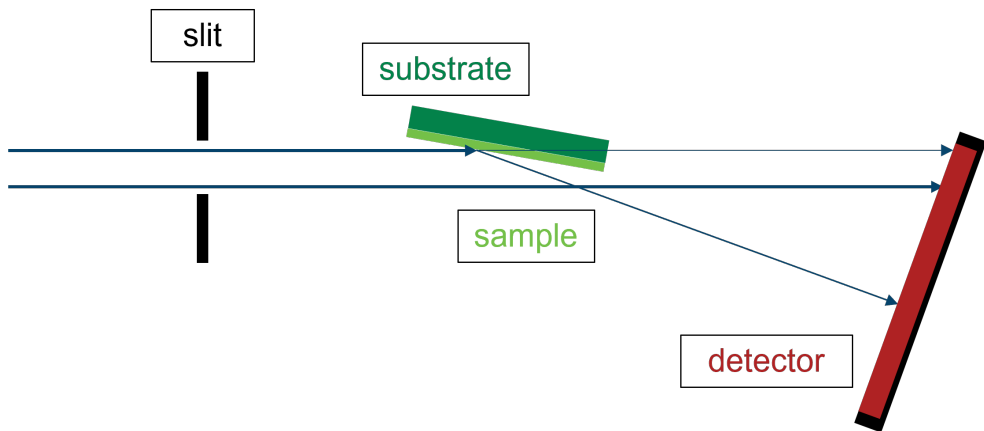


Fig. 12.4: Trajectories of neutrons passing through or by the sample in a simulation of a digital twin of a neutron reflectometer.

12.5 Applications of virtual experiments

12.5.1 Training and experiment preparation

If a digital twin with the same GUI exists, it can be used to learn how to set up the instrument and to conduct an experiment. For this purpose, the simulation should be available as a web application enabling the scientist to control the instrument before his beamtime starts (cf. 0). That will save him time at the facility so that he can use the beamtime more efficiently.

Even without the same GUI, virtual experiments can be used to prepare experiments. Using a sample similar to the one to be measured, instrument settings can be varied to find out the best compromise between needed resolution and high counting rate. It also gives an estimation of the beamtime needed for each experiment, which will enable to make a realistic measurement plan.

12.5.2 Teaching

Virtual experiments can also be used to learn about neutron scattering. Independent of a real measurement, one can exchange samples and vary instrument settings and view the results. One only needs a simple PC for that, install a freely available software (VITESS, McStas, ...) and get results after some seconds or a few minutes of simulation time.

12.5.3 Test of data evaluation software

One advantage of virtual experiments over real experiments is that the sample parameters are exactly known, because they are input parameters. So, it is possible to compare the result of the data evaluation with the true parameters.

This does not only allow checking the influence of the instrument on the final result, but also to check the data evaluation software.

Another possibility is to mark neutron trajectories in the simulation, e.g. where they are scattered. Thus, you can separate contributions from the sample environment or from multiple scattering from the real signal.

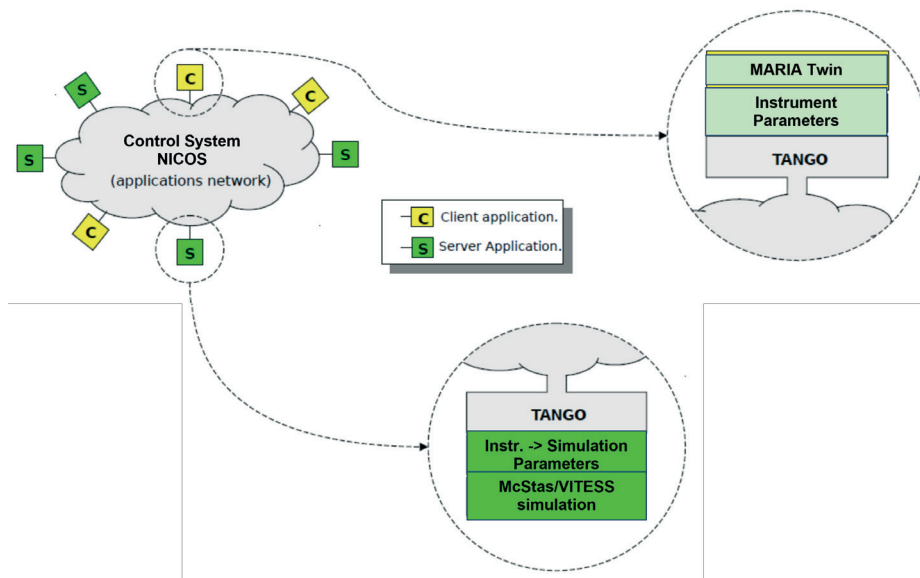


Fig. 12.5: Integration of a program for virtual neutron scattering instruments into the NICOS operating system for instrument control of the MLZ instruments in a client-server-application giving a digital twin of the real instrument.

References

- [1] P.A. Seeger and L.L. Daemen, *Proc. SPIE* **5536**, 109 (2004).
- [2] C. Zendler et al., *J. Phys.:Conf.Ser.* **528**, 012036 (2014).
<https://viteess.fz-juelich.de/>
- [3] P. K. Willendrup and K. Lefmann, *J. Neutron Res.* **22**, 1 (2020).
mcstas.org
- [4] K. Lieutenant et al., *J. Appl. Cryst.* **40**, 1056 (2007).
- [5] Th. Brückel, Th. Gutberlet, eds., *Technical Design Report HBS*, Vol. 9 of *Schriften des Forschungszentrums Jülich*, General (Forschungszentrum Jülich GmbH, Jülich, 2023).
- [6] K. Lieutenant et al., submitted for publication

Exercises

Preparation

- Download the current version of the program VITESS from the website: <https://viteess.fz-juelich.de>
- Start the program and prepare a new instrument simulation by defining the parameter directory, where the simulation is executed

E12.1 Source and sample illumination*

- Use 'source' as the first module and create neutrons in the wavelength range 4.5 to 5.5 Ang.
- Choose a cold moderator of the FRM-II source (from InstallDirectory/FILES/moderators/...)
- Illuminate a 2 x 2 cm² large area in 10 meters distance.
- Put a 2D monitor there to show the divergence distribution
- Put a 1D monitor there to show the wavelength distribution
- Run the simulation using 1 Mio and 100 Mio 'trajectories' (=events) and compare

E12.2 SANS spectrum**

- Add a 2 x 2 x 0.1 cm SANS sample of spheres of 100 nm diameter shortly behind the monitors
- Add a 1 m² detector of 5 x 5 mm² cell size (using the modules 'screen') in 4 m distance from the sample
- Run the simulation and monitor the intensity distribution on the detector
- Use the module 'eval_sans' to generate the spectrum I(Q)

E12.3 Resolution***

- Look at the spectrum I(q). Is it in agreement with your expectations for a spherical sample?
- Which parameters contribute to the Q resolution?
- Which parameters is dominating here?
- What can be done to improve the resolution e.g. to half the value in $\delta Q/Q$?

13 Strongly correlated electrons

M. Angst

Jülich Centre for Neutron Science 2

Forschungszentrum Jülich GmbH

Contents

13.1 Introduction	2
13.2 Electronic structure of solids	3
13.3 Strong electronic correlations: the Mott transition	6
13.4 Complex ordering phenomena: perovskite manganites as example	9
13.5 Probing correlated electrons by scattering methods	13
13.6 Summary	17
References	18
Exercises	19

13.1 Introduction

Materials with *strong electronic correlations* are materials, in which the movement of one electron depends on the positions and movements of all other electrons due to the long-range Coulomb interaction. With this definition, one would naively think that all materials show strong electronic correlations. However, in purely ionic systems, the electrons are confined to the immediate neighborhood of the respective atomic nucleus. On the other hand, in ideal metallic systems, the other conduction electrons screen the long-range Coulomb interaction. Therefore, while electronic correlations are also present in these systems and lead for example to magnetism, the main properties of the systems can be explained in simple models, where electronic correlations are either entirely neglected (e.g. the free electron Fermi gas) or taken into account only in low order approximations (Fermi liquid, exchange interactions in magnetism etc.). In highly correlated electron systems, simple approximations break down and entirely new phenomena and functionalities can appear. These so-called *emergent* phenomena cannot be anticipated from the local interactions among the electrons and between the electrons and the lattice [1]. This is a typical example of *complexity*: the laws that describe the behavior of a complex system are qualitatively different from those that govern its units [2]. This is what makes highly correlated electron systems a research field at the very forefront of condensed matter research. The current challenge in condensed matter physics is that we cannot reliably predict the properties of these materials. There is no theory, which can handle this huge number of interacting degrees of freedom. While the underlying fundamental principles of quantum mechanics (Schrödinger equation or relativistic Dirac equation) and statistical mechanics (maximization of entropy) are well known, there is no way at present to solve the many-body problem for some 10^{23} particles. Some of the exotic properties of strongly correlated electron systems and examples of emergent phenomena and novel functionalities are:

- *High temperature superconductivity*; while this phenomenon was discovered in 1986 by Bednorz and Müller [3], who received the Nobel Prize for this discovery, and since then has continually attracted the attention of a large number of researchers, there is still no commonly accepted mechanism for the coupling of electrons into Cooper pairs, let alone a theory which can predict high temperature superconductivity or its transition temperatures. High temperature superconductivity has already some applications such as highly sensitive magnetic field sensors, high field magnets, and power lines, and more are likely in the future.
- *Colossal magnetoresistance* effect CMR, which was discovered in transition metal oxide manganites and describes a large change of the electrical resistance in an applied magnetic field [4]. This effect can be used in magnetic field sensors and could eventually replace the giant magnetoresistance [5, 6] field sensors, which are employed for example in the read heads of magnetic hard discs.
- The *magnetocaloric* effect [7], a temperature change of a material upon applying a magnetic field, can be used for magnetic refrigeration without moving parts or cooling fluids.
- *Metal-insulator-transitions* as observed e.g. in magnetite (Verwey transition [8]) or certain vanadites are due to strong electronic correlations and could be employed as electronic switches.

- *Multiferroicity* [9], the simultaneous occurring of various ferroic orders, e.g. ferromagnetism and ferroelectricity, in one material. If the respective degrees of freedom are strongly coupled, one can switch one of the orders by applying the conjugate field of the other order. Interesting for potential applications in information technology is particularly the switching of magnetization by an electric field, which has been proposed to be used for easier switching of magnetic non-volatile memories [10]. Future applications of multiferroic materials in computer storage elements are apparent. One could either imagine elements, which store several bits in form of a magnetic- and electric polarization, or one could apply the multiferroic properties for an easier switching of the memory element.
- *Negative thermal expansion* [11] is just another example of the novel and exotic properties that these materials exhibit.

It is likely that many more such emergent phenomena will be discovered in the near future. This huge potential is what makes research on highly correlated electron systems so interesting and challenging: this area of research is located right at the intersection between fundamental science investigations, striving for basic understanding of the electronic correlations, and technological applications, connected to the new functionalities [12].

13.2 Electronic structure of solids

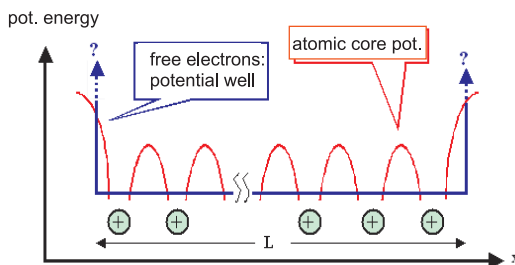


Fig. 13.1: *Potential energy of an electron in a solid.*

In order to be able to discuss the effects of strong electronic correlations, let us first recapitulate the textbook knowledge of the electronic structure of solids [13, 14]. The description of the electron system of solids usually starts with the adiabatic or Born-Oppenheimer approximation: The argument is made that the lighter electrons are moving so quickly compared to the nuclei that the electrons can instantaneously follow the movement of the much heavier nuclei and thus see the instantaneous nuclear potential. This approximation serves to separate the lattice- and electronic degrees of freedom. Often one makes the further approximation to consider the nuclei to be at rest in their equilibrium positions. The potential energy seen by a single electron in the averaged field of all other electrons and the atomic core potential is depicted schematically for a one dimensional system in Fig. 13.1.

The following simple models are used to describe the electrons in a crystalline solid:

- *Free electron Fermi gas*: here a single electron moves in a 3D potential well with infinitely high walls corresponding to the crystal surfaces. All electrons move completely independent, i.e. the interaction between the electrons is considered only indirectly by the Pauli exclusion principle.
- *Fermi liquid*: here the electron-electron interaction is accounted for in a first approximation by introducing *quasiparticles*, so-called dressed electrons, which have a charge e , and a spin $\frac{1}{2}$ like the free electron, but an effective mass m^* , which can differ from the free electron mass m . Other than this renormalization, interactions are still neglected.
- *Band structure model*: this model takes into account the periodic potential of the atomic cores at rest, i.e. the electron moves in the average potential from the atomic cores and from the other electrons.

Considering the strength of the long-range Coulomb interaction, it is surprising that the simple models of Fermi gas – or better Fermi liquid – already are very successful in describing some basic properties of simple metals. The *band structure model* is particularly successful in describing semiconductors. But all three models have in common that the electron is described with a single particle wave function and electronic correlations are only taken into account indirectly, to describe phenomena like magnetism due to the exchange interaction between the electrons or BCS superconductivity [15], where an interaction between electrons is mediated through lattice vibrations and leads to Cooper pairs, which undergo a Bose-Einstein condensation.

What we have sketched so far is the textbook knowledge of introductory solid state physics courses. Of course there exist more advanced theoretical descriptions, which try to take into account the electronic correlations. The strong Coulomb interaction between the electrons is taken into account in density functional theory in the so-called “LDA+U” approximation or in the so-called dynamical mean field theory DMFT or a combination of the two in various degrees of sophistication [16]. Still, all these extremely powerful and complex theories often fail to predict even the simplest physical properties, such as whether a material is a conductor or an insulator.

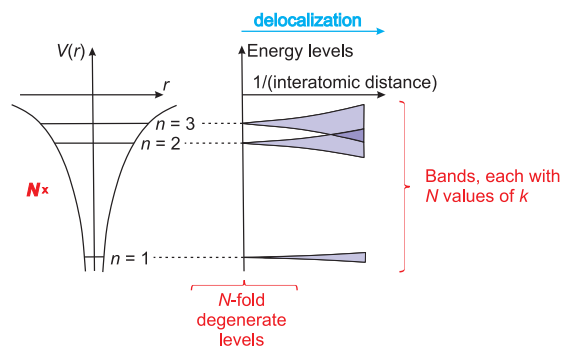


Fig. 13.2: Left: Atomic potential of an electron interacting with the atomic core and the corresponding level scheme of sharp energy levels. Right: Broadening of these levels into bands upon increase of the overlap of the wave functions of neighboring atoms. After [13]

Let us come back to the *band structure* of solids. In the so-called tight-binding model one starts from isolated atoms, where the energy levels of the electrons in the Coulomb potential of the corresponding nucleus can be calculated. If N such atoms are brought together, the wave functions of the electrons from different sites start to overlap so that electrons can hop between neighboring atoms. This leads to a broadening of the atomic energy levels, which eventually will give rise to the electronic bands in solids, each of which is a quasi-continuum of $2N$ electronic states (N possible values of \mathbf{k} , spin $\sigma = \uparrow$ or \downarrow). The closer the atoms are brought together, the more the wave functions overlap, the more the electrons will be delocalized, and the broader in energy are the corresponding bands (Fig. 13.2).

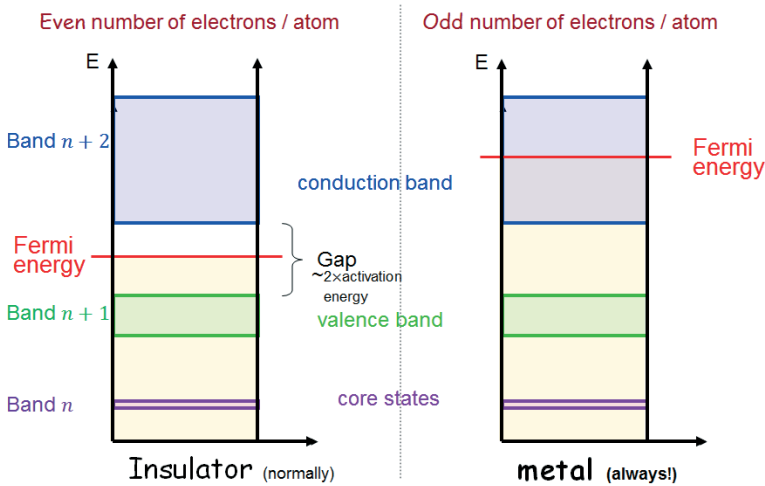


Fig. 13.3: *Band structure of insulators and metals.*

If electronic correlations are not too strong, the electronic properties can be described by a band structure, which allows one to predict whether a material is an insulator or a metal. This is shown in Fig. 13.3. At $T = 0$ all electronic states are being filled up to the Fermi energy, taking into account the Pauli principle. If there is an even number of electrons per atom (or more generally per primitive unit cell), say $2m$, these will fill up exactly the first m bands, and the higher energy bands are empty. Unless there is band-overlap between the highest occupied (valence) band and the lowest unoccupied (conduction) band (which may accidentally happen in 3D) any electron transport would require the bump of an electron from the valence to the conduction band, and consequently the material is an insulator (at non-zero T some electrons may be thermally excited to the conduction band if the band gap is small, one calls the material then a semi-conductor rather than an insulator). If there is an odd number of electrons per primitive unit cell, say $2m + 1$, the first $2m$ bands will be completely full, but the band $2m + 1$ will be half-filled. In a partially filled band electrons easily move in response to a voltage, hence the material is a metal – within the model described so far always. However, as mentioned above this *band structure model* describes the electrons with single particle wave functions. Where are the electronic correlations?

13.3 Strong electronic correlations: the Mott transition

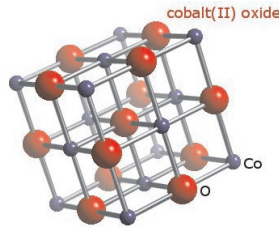


Fig. 13.4: Rock-salt (NaCl)-type structure of CoO.

It turns out that *electronic correlations* are particularly important in materials, which have some very narrow bands. This occurs for example in transition metal oxides or transition metal chalcogenides as well as in some light rare earth intermetallics (heavy fermion systems). Consider CoO as a typical and simple example of a transition metal oxide. CoO has the rock-salt structure shown in Fig. 13.4, with a face-centered cubic (fcc) unit cell containing four formula units. The primitive unit cell of the fcc lattice, however, is spanned by the basis vectors $\mathbf{a}' = \frac{1}{2}a(\mathbf{e}_x + \mathbf{e}_y)$, $\mathbf{b}' = \frac{1}{2}a(\mathbf{e}_y + \mathbf{e}_z)$, and $\mathbf{c}' = \frac{1}{2}a(\mathbf{e}_z + \mathbf{e}_x)$, where a is the lattice constant, and \mathbf{e}_x , \mathbf{e}_y , and \mathbf{e}_z , are the unit basis vectors of the original fcc unit cell. The primitive unit cell contains only one cobalt and one oxygen atom. The electronic configurations of these atoms are: Co: $[\text{Ar}]3d^74s^2$; O: $[\text{He}]2s^22p^4$. In the solid, the atomic cores of Co and O have the electronic configuration of Ar and He, respectively. These electrons are very strongly bound to the nucleus and we need not consider them on the usual energy scales for excitations in the solid state. We are left with nine outer electrons for the Co and six outer electrons for the O atom in the solid, so that the total number of electrons per primitive unit cell is $9 + 6 = 15$, i.e. an odd number. According to our considerations in the last section, we must have at least one partially filled band and CoO *should* be a metal.

What does the experiment tell us? Well, in fact, CoO is a very good insulator with a room-temperature resistivity $\rho(300\text{ K}) \sim 10^8 \Omega\text{cm}$ (For comparison, the good conductor iron has $\rho(300\text{ K}) \sim 10^{-7} \Omega\text{cm}$. The resistivity of CoO is exponentially decreasing with increasing temperature T , and the T -dependence corresponds to activation energies of about 0.6 eV or a temperature equivalent of 7000 K, which means there is a huge band gap making CoO a very good insulator. To summarize these considerations: the band theory breaks down already for a very simple oxide consisting of only one transition metal and one oxygen atom!

In order to understand the reason for this dramatic breakdown of band theory, let us consider an even simpler example: the alkali metal sodium (Na) with the electronic configuration $[\text{Ne}]3s^1=1s^22s^22p^63s^1$. Following our argumentation for CoO, sodium obviously has a half-filled 3s band and is therefore a metal. This time our prediction was correct: $\rho(300\text{ K}) \sim 5 \times 10^{-6} \Omega\text{cm}$. However, what happens if, hypothetically, we pull the atoms further apart and increase the lattice constant continuously? Band theory predicts that for all distances sodium remains a metal, since the 3s band will always be half-filled. This contradicts our intuition: at a certain critical separation of the sodium atoms, there must be a transition from a metal to an insulator. This metal-to-insulator transition was predicted by Sir Nevill Mott (physics Nobel price 1977); it is therefore called the *Mott transition* [17]. The physical principle is illustrated in Fig.

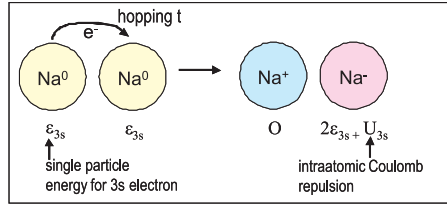


Fig. 13.5: Illustration of (electron) hopping between two neutral Na atoms - involving charge fluctuations.

13.5: On the left, two neutral Na atoms are depicted. The atomic energy levels of the outer electrons correspond to an energy ε_{3s} . The wave functions of the 3s electrons will overlap giving rise to a finite probability that an electron can hop from one sodium atom to the other one. Such a delocalization of the electrons arising from their possibility to hop is favored because it lowers their kinetic energy. This can be seen for example by generalizing the “particle in a box” problem: $E_{\text{kin}} \propto p^2 = \hbar^2/\lambda^2$ (de Broglie) and $\lambda \sim$ box size, and it is consistent with the uncertainty principle $\Delta p \cdot \Delta x \geq \frac{\hbar}{2}$. Fig. 13.5 on the right shows the situation after the electron transfer. Instead of neutral atoms, we have one Na^+ and one Na^- ion. However, we have to pay a price for the double occupation of the 3s states on the Na^- ion, namely the intra-atomic Coulomb repulsion between the two electrons denoted as U_{3s} . While this is a very simplistic picture, where we assume that the electron is either located on one or the other Na atom, this model describes the two main energy terms by just two parameters: the hopping matrix element t , connected to the kinetic energy, and the intra-atomic Coulomb repulsion U , connected with the potential energy due to the Coulomb interaction between the two electrons on one site. In this simple model, we have replaced the long range Coulomb potential proportional to $1/r$ with its leading term, an on-site Coulomb repulsion U . More realistic models would have to take higher order terms into account but already such a simple consideration leads to very rich physics. We can see from Fig. 13.5 that electronic conductivity is connected with charge fluctuations and that such charge transfer costs energy, where U is typically of the order of 1 or 10 eV. Only if the gain in kinetic energy due to the hopping t is larger than the penalty in potential energy U can we expect metallic behavior. If the sodium atoms are now being separated more and more, the intra-atomic Coulomb repulsion U will maintain its value while the hopping matrix element t , which depends on the overlap of the wave functions, will diminish. At a certain critical value of the lattice parameter a , potential energy will win over kinetic energy and conductivity will be suppressed. This is the physical principle behind the *Mott transition*.

More formally, this model can be cast into a model Hamiltonian, the so-called *Hubbard model* [18]. In second quantization of quantum-field theory, the corresponding Hamiltonian is

$$\hat{\mathcal{H}} = -t \sum_{j,l,\sigma} (\hat{c}_{j\sigma}^\dagger \hat{c}_{l\sigma} + \hat{c}_{l\sigma}^\dagger \hat{c}_{j\sigma}) + U \sum_j \hat{n}_{j\uparrow} \hat{n}_{j\downarrow}, \quad (13.1)$$

where the operator $\hat{c}_{j\sigma}^\dagger$ creates an electron in the atomic orbital $\Phi(\mathbf{r} - \mathbf{R}_j)|\sigma\rangle$. The first term is nothing but the tight-binding model of band structure (in second quantization), where t is the hopping amplitude depending on the overlap of the wavefunctions from nearest-neighbor atoms at \mathbf{R}_1 and \mathbf{R}_2 :

$$t = \int \Phi(\mathbf{r} - \mathbf{R}_1) \frac{e^2}{4\pi\varepsilon_0 |\mathbf{r} - \mathbf{R}_2|} \Phi(\mathbf{r} - \mathbf{R}_2) d\mathbf{r}. \quad (13.2)$$

It describes the kinetic energy gain due to electron hopping.

The second term is the potential energy due to doubly-occupied orbitals. Here, $\hat{n}_{j\sigma} = \hat{c}_{j\sigma}^\dagger \hat{c}_{j\sigma}$ is the occupation operator of the orbital $\Phi(\mathbf{r} - \mathbf{R}_j)|\sigma\rangle$ and U is the Coulomb repulsion between two electrons in this orbital,

$$U = \int \frac{e^2 |\Phi(\mathbf{r}_1 - \mathbf{R}_j)|^2 |\Phi(\mathbf{r}_2 - \mathbf{R}_j)|^2}{4\pi\epsilon_0 |\mathbf{r}_1 - \mathbf{r}_2|} d\mathbf{r}_1 d\mathbf{r}_2, \quad (13.3)$$

The *Hubbard model* is a so-called *lattice fermion model*, since only discrete lattice sites are being considered. It is the simplest way to incorporate correlations due to the Coulomb interaction since it takes into account only the strongest contribution, the on-site Coulomb interaction. Still there is very rich physics contained in this simple Hamiltonian like the physics of ferromagnetic- or antiferromagnetic metals and insulators, charge- and spin density waves and so on [18]. A realistic Hamiltonian should contain many more inter-site terms due to the long-range Coulomb interaction likely to contain additional new physics.

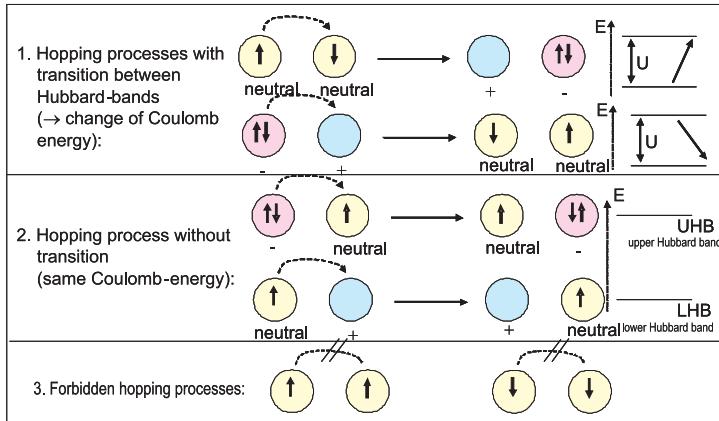


Fig. 13.6: Illustration of hopping processes between neighboring atoms together with their corresponding energy scales.

The most direct consequence of the on-site Coulomb interaction is that additional so-called Hubbard bands are created due to possible hopping processes, illustrated in Fig. 13.6: The first row shows hopping processes involving a change of the total Coulomb energy. The second row shows hopping processes without energy change. The last row shows hopping processes forbidden due to the Pauli principle (here, the spin enters the model, giving rise to magnetic order). From Fig. 13.6 we can identify two different energy states. Configurations for which the on-site Coulomb repulsion comes into play have an energy which is higher by the on-site Coulomb repulsion U as compared to such configurations where the electrons are not on the same atom. In a solid these two energy levels will broaden into bands (due to the delocalization of the electrons on many atoms driven by the hopping matrix element t), which are called the lower Hubbard band and the upper Hubbard band. If these bands are well separated, i.e. the Coulomb repulsion U dominates over the hopping term t , we will have in insulating state (only the lower Hubbard band is occupied). If the bands overlap, we will have a metallic state. Note that lower and upper Hubbard band are totally different from the usual band structure

of solids as they do not arise due to the interaction of the electrons with the atomic cores but due to electronic correlations. As a result the existence of the Hubbard bands depends on the electronic occupation: the energy terms for simple hopping processes depend on the occupation of neighboring sites. The apparently simple single electron operator gets complex many body aspects.

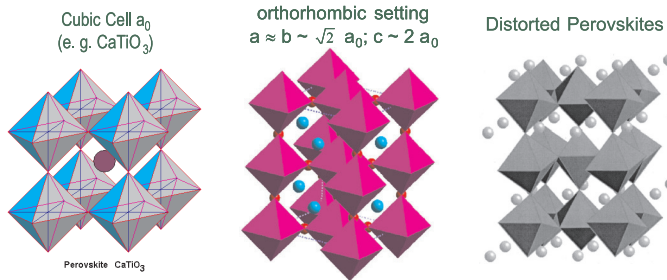


Fig. 13.7: Perovskite structures. The A -site atoms are shown as spheres, octahedra have Mn (or Ti) at their center and O at their corners. Left: Ideal (cubic) structure. Middle: cubic structure in orthorhombic setting. Right: distorted structure with rotated and tilted oxygen octahedra.

13.4 Complex ordering phenomena: perovskite manganites as example

The correlation-induced localization leads to atomic-like *electronic degrees of freedom* that can (because the possible hopping of electrons between sites means that different sites interact with one another) order in complex ways. The electronic degrees of freedom include charge (or ion valence), orbital (which atomic orbitals are occupied, what is the shape of the electron cloud), and magnetic moment. In the following we will discuss these ordering processes, taking as an example, because of their particularly simple basic structure, *perovskite manganites* (see e.g. [19]). Their stoichiometric formula is $A_{1-x}B_xMnO_3$, where A is a trivalent cation (e.g. $A = La, Gd, Tb, Er, Y, Bi$) and B is a divalent cation ($B = Sr, Ca, Ba, Pb$). The doping with divalent cations leads to a mixed valence on the manganese sites. In a purely ionic model (neglecting covalency) charge neutrality requires that manganese exists in two valence states: Mn^{3+} (electronic configuration $[Ar]3d^4$, note that the $4s$ electrons are lost first upon positive ionization in a solid; the reason is that the $4s$ orbitals have electron density extending much further from the nucleus, which leads to a Coulomb penalty given nearby negative ions) and Mn^{4+} ($[Ar]3d^3$) according to the respective doping levels: $A_{1-x}B_xMnO_3 \rightarrow [A_{1-x}^{3+}B_x^{2+}] [Mn_{1-x}^{3+}Mn_x^{4+}] O_3^-$. The structure of these mixed valence manganites is related to the perovskite structure (Fig. 13.7). Perovskite $CaTiO_3$ is a mineral, which has a cubic crystal structure, where the smaller Ca^{2+} metal cation is surrounded by six oxygen atoms forming an octahedron; these corner sharing octahedra are centered on the corners of a simple cubic unit cell and the larger Ti^{4+} metal cation is filling the interstice in the center of the cube. This ideal cubic perovskite structure is extremely rare. It only occurs when the sizes of the metal ions match to fill the spaces between the oxygen atoms ideally. Usually there is a misfit of the mean ionic radii of the A and B ions, which leads to sizeable tilts of the oxygen octahedra, described in larger cells (see Fig. 13.7).

These tilt distortions are, however, not important for the following general considerations of the electronic degrees of freedom.

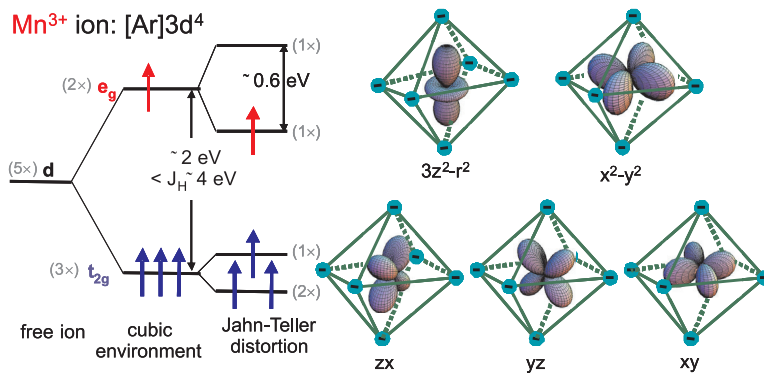


Fig. 13.8: Energy level diagram for a Mn^{3+} ion in an oxygen octahedron. For the free ion, the five 3d electron levels are degenerate. They split in a cubic environment into t_{2g} and e_g levels. If Hund's rule coupling is stronger than crystal field splitting, a high-spin state results. The degeneracy of the e_g level is lifted by a Jahn-Teller distortion resulting in an elongation of the oxygen octahedra. On the right of the figure, the a basis set of 5 real 3d orbitals are depicted.

For an isolated manganese, or other transition metal, ion, the electrons are filled into the five d orbitals according to *Hund's rules*. The first, and dominant, Hund rule implies that electrons tend to maximize their total spin $S = \sum_j s_j$, avoiding in particular double occupation of any d orbital. In other words, the electrons occupy the orbitals in such a way that the spins of all electrons are parallel as far as the Pauli principle permits. This is a consequence of the intra-atomic Coulomb repulsion between electrons, in particular the exchange contribution to the Coulomb repulsion. The energy gained by fulfilling the first Hund rule is called the Hund's rule energy J_H . The second Hund rule, originating from direct intra-atomic Coulomb repulsion, states that the total angular momentum L is maximized, as far as consistent with the first Hund rule, i.e. orbitals are filled from high to low angular momentum. Finally, the third Hund rule, due to spin-orbit coupling, states that total spin and orbital momentum are (anti-)parallel for more (less) than half-filled shells. For the manganites the octahedral surrounding of the Mn ions leads to so-called *crystal field effects*. To explain these we stay in the ionic model and describe the oxygen atoms as O^{2-} ions. The outer electrons of the Mn ions, the 3d electrons, experience the electric field created by the surrounding O^{2-} ions of the octahedral environment. This so-called crystal field leads to a splitting of the electronic levels by the crystal field as depicted in Fig. 13.8: The 3d orbitals with lobes of the electron density pointing towards the negatively charged oxygen ions ($3z^2 - r^2$ and $x^2 - y^2$; so-called e_g orbitals) will have higher energies compared to the orbitals with the lobes pointing in-between the oxygen atoms (zx , yz , and xy ; so-called t_{2g} orbitals). For the manganites this crystal-field splitting is typically $\sim 2 \text{ eV}$. If we now consider a Mn^{3+} ion, how the electrons will occupy these crystal field levels depends on the ratio between the crystal-field splitting and the intra-atomic exchange J_H : If the crystal field splitting is much larger than Hund's coupling, a *low-spin state* results, where all electrons are in the lower t_{2g} level and two of these t_{2g} orbitals are singly occupied and one is doubly occupied. Due to the Pauli principle the spins in the doubly occupied orbital have to be antiparallel, giving rise to a total spin $S = 1$ for this low-spin state. Usually, however, in the manganites Hund's rule

coupling amounts to $\sim 4\text{eV}$, stronger than the crystal field splitting. In this case the *high spin state* shown in Fig. 13.8 is realized, where four electrons with parallel spin occupy the three t_{2g} orbitals plus one of the two e_g orbitals. The high spin state has a total spin of $S = 2$ and the orbital angular momentum is quenched, i.e. $L = 0$. This state has an orbital degree of freedom: the e_g electron can either occupy the $3z^2 - r^2$ or the $x^2 - y^2$ orbital. The overall energy can (and thus will) be lowered by a geometrical distortion of the oxygen octahedra that shifts the e_g levels, lifting their degeneracy. This so-called *Jahn-Teller effect* (Fig. 13.8) further splits the d-electron levels. For the case shown, the c -axis of the octahedron has been elongated, thus lowering the energy of the $3z^2 - r^2$ orbital with respect to the energy level of the $x^2 - y^2$ orbital. The Jahn-Teller splitting in the manganites has a magnitude of typically $\sim 0.6\text{eV}$.

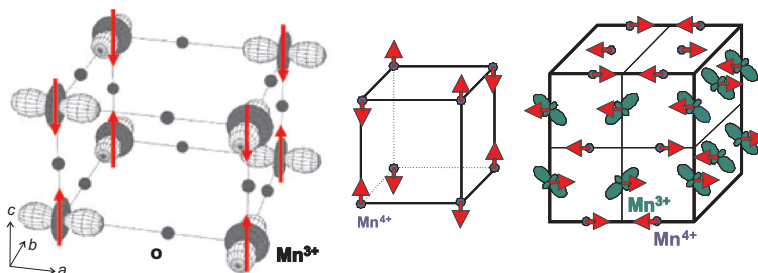


Fig. 13.9: Left: *Orbital order in LaMnO_3 .* Below the Jahn-Teller transition temperature of 780 K, a distinct long range ordered pattern of Jahn-Teller distortions of the oxygen octahedra occurs leading to orbital order of the e_g orbitals of the Mn^{3+} ions as shown. Also shown is the antiferromagnetic spin order which sets in below the Néel temperature $T_N \sim 145\text{K}$. Oxygen atoms are represented by filled circles, La is not shown. Center: *Distinct spin order of CaMnO_3 .* Right: *Charge-, orbital- and spin-order in half-doped manganite $\text{La}_{0.5}^{3+}\text{Sr}_{0.5}^{2+}\text{Mn}_{0.5}^{3+}\text{Mn}_{0.5}^{2+}\text{O}_3$.*

The Jahn-Teller effect demonstrates nicely how in these transition metal oxides electronic and lattice degrees of freedom are coupled. Only the Mn^{3+} with a single electron in the e_g orbitals exhibits the Jahn-Teller effect, whereas the Mn^{4+} ion does not. A transfer of charge between neighboring manganese ions is accompanied with a change of the local distortion of the oxygen octahedron: a so-called lattice polaron. Due to the Jahn-Teller effect, charge fluctuations and lattice distortions become coupled in these mixed-valence oxides.

Having explained the Jahn-Teller effect, we can now introduce an important type of electronic order occurring in these materials: *orbital order*. Consider the structure of LaMnO_3 : All manganese are trivalent and are expected to undergo a Jahn-Teller distortion. In order to minimize the elastic energy of the lattice, the Jahn-Teller distortions on neighboring sites are correlated. Below a certain temperature $T_{JT} \sim 780\text{K}$, a cooperative Jahn-Teller transition takes place, with a distinct pattern of distortions of the oxygen octahedra throughout the crystal lattice as shown in Fig. 13.9 left. This corresponds to a long-range orbital order of the e_g electrons, not to be confused with magnetic order of an orbital magnetic moment. In fact, the orbital magnetic moment is quenched, i.e. totally suppressed, by the crystal field surrounding the Mn^{3+} ions (this is always the case for non-degenerate states with real wave functions because such functions have pure-imaginary expectation values for an angular momentum operator). *Orbital ordering* instead denotes a long-range ordering of an anisotropic charge distribution around the nuclei. As the temperature is further lowered, magnetic order sets in at $T_N \sim 145\text{K}$. In LaMnO_3 the

spin degree of freedom of the Mn^{3+} ion orders antiferromagnetically in so-called A-type order: spins within the a - b plane are parallel, while spins along c are coupled antiferromagnetically. The depicted antiferromagnetic ordering results from a complex interplay between structural-, orbital- and spin degrees of freedom and the relative strengths of the different coupling mechanisms in LaMnO_3 , as can be seen by comparing with the different magnetic order of CaMnO_3 , which does not have an orbital degree of freedom (Fig. 13.9 center).

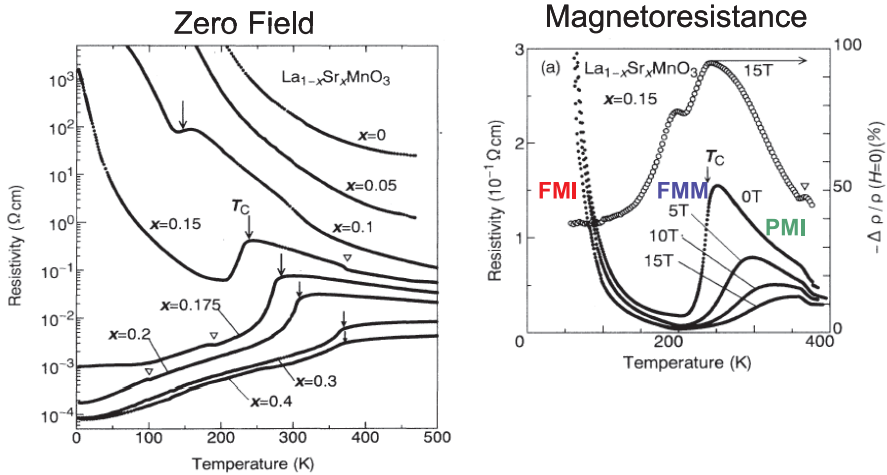


Fig. 13.10: Resistivity in the $\text{La}_{1-x}\text{Sr}_x\text{MnO}_3$ series [20]. Left: resistivity in zero field for various compositions from $x = 0$ to $x = 0.5$. Right: resistivity for $x = 0.15$ in different magnetic fields H , and magnetoresistance, defined as the change in resistivity relative to its value for $H = 0$. Reprinted with permission from [20]. © 1995 by the American Physical Society.

Doped manganites are even more complex, because the charge on the Mn site becomes an additional degree of freedom due to the two possible manganese valences Mn^{3+} and Mn^{4+} . In order to minimize the Coulomb interaction between neighboring manganese sites, so-called *charge order* (or *ion valence order*) can develop. This is shown for the example of half-doped manganites in Fig. 13.9 on the right: These half-doped manganites show antiferromagnetic spin order, a checkerboard-type charge order with alternating Mn^{3+} and Mn^{4+} sites and a zig-zag orbital order of the additional e_g electron present on the Mn^{3+} sites. This is only one example of the complex ordering phenomena that can occur in doped mixed valence manganites. These ordering phenomena result from a subtle interplay between lattice-, charge-, orbital-, and spin degrees of freedom and can have as a consequence novel phenomena and functionalities such as *colossal magnetoresistance*.

How are these ordering phenomena related with the macroscopic properties of the system? To answer this question, let us look at the resistivity of doped Lanthanum-Strontium-Manganites (Fig. 13.10): The zero field resistance changes dramatically with composition. The $x = 0$ compound shows insulating behavior: the resistivity ρ increases with decreasing temperature T . The higher doped compounds, e.g. $x = 0.4$, are metallic with $\rho(T)$ decreasing. Note, however, that the resistivity of these compounds is still about three orders of magnitude higher than for typical good metals. At an intermediate composition $x = 0.15$, the samples are insulators at

higher T down to about 250 K, then a dramatic drop of the resistivity indicating an insulator-to-metal transition and again an upturn below about 210 K with typical insulating behavior. The metal-insulator transition occurs at the temperature where ferromagnetic long-range order sets in. Around this temperature we also observe a very strong dependence of resistivity on external magnetic field. This is the so-called *colossal magnetoresistance* effect. In order to appreciate the large shift in the maximum of the resistivity curve with field (Fig. 13.10 right) one should remember that the energy scales connected with the Zeeman interaction of the spin $\frac{1}{2}$ electron in an applied magnetic field are very small: the energy equivalent of 1 Tesla for a spin $\frac{1}{2}$ system corresponds to 0.12 meV, which in turn corresponds to a temperature equivalent of 1.3 K. The strong dependence of the resistance on an external field is partly due to the so-called *double exchange* mechanism: the electron hopping from Mn^{3+} to Mn^{4+} (associated with metallicity) can occur only if the t_{2g} spins are parallel, which is automatically fulfilled (only) in the ferromagnetic state. This phase competition and consequent tunability by external parameters, such as temperature and field, is typical for correlated-electron systems.

It is clear that our entire discussion starting from ionic states is only a crude approximation to the real system. Therefore we now have to pose the question how can we determine the true valence state? Or more general, which experimental methods exist to study the complex ordering and excitations of the charge-, orbital-, spin- and lattice- degrees of freedom in these complex transition metal oxides?

13.5 Probing correlated electrons by scattering methods

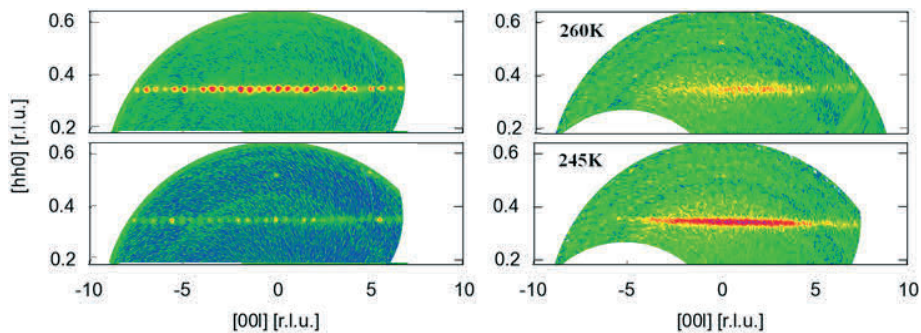


Fig. 13.11: Polarized single crystal neutron diffraction on LuFe_2O_4 . The $(\frac{1}{3}, \frac{1}{3}, l)$ line of spin and charge order superstructure reflections is shown. Left: magnetic reflections in the spin-flip channel (top) and charge order reflections in the non-spin-flip channel (bottom) at 220 K. Right: diffuse scattering in the spin-flip channel at two temperatures above T_N , revealing short-range magnetic correlations [21].

How can these various ordering phenomena be studied experimentally? Obviously we need probes with atomic resolution, which interact with the spins as well as with the charges in the system. Therefore neutron and x-ray scattering are the ideal microscopic probes to study the complex ordering phenomena and their excitation spectra. The lattice and spin structure can be studied with neutron diffraction from a polycrystalline or single crystalline sample as detailed

Ions	La ³⁺	Pr ³⁺	Nd ³⁺	Sm ³⁺	Eu ³⁺	Gd ³⁺	Tb ³⁺	Dy ³⁺	Er ³⁺
R_0	2.172	2.138	2.105	2.090	2.074	2.058	2.032	2.001	1.988
Ions	Tm ³⁺	Yb ³⁺	Y ³⁺	Ca ²⁺	Sr ²⁺	Ba ²⁺	Mn ³⁺	Mn ⁴⁺	
R_0	1.978	1.965	2.019	1.967	2.118	2.285	1.760	1.753	

Table 13.1: R_0 values of cation-oxygen bonds [22] in manganese perovskites needed for the bond valence calculation (13.4).

in chapter 8 of this course, “Structural analysis”. Fig. 13.11 shows as an example of more recent research on a material with more complex (rhombohedral) crystal structure polarized neutron diffraction on a single crystal of LuFe_2O_4 , a once-proposed charge-order-based multiferroic. Periodic arrangements of spins and/or Fe valence states in this material can be described by an enlarged cell, which corresponds to a smaller cell in reciprocal space and therefore leads to the emergence of *superstructure reflections* between the main nuclear reflections. Magnetic reflections in the spin-flip channel yield the spin structure, while the charge-order reflections show up in the non-spin-flip channel (c.f. chapter 7). For charge order and small structural distortions complementary synchrotron x-ray diffraction data is often useful because of the higher achievable q -resolution. It is beyond the scope of this lecture to discuss the experimental and methodological details of such a structure analysis or to present detailed results on specific model compounds. For this we refer to the literature, e.g. [21]. For the above example, we just want to mention that the refinement of spin and charge order showed strong spin-charge coupling, but the absence of a polar charge order, negating the proposed multiferroicity. At first sight it might be surprising that neutron diffraction is able to give us information about *charge order*. We have learnt in the introductory chapters that neutrons interact mainly through the strong interaction with the nuclei and through the magnetic dipole interaction with the magnetic induction in the sample. So how can neutrons give information about charge order? Obviously charge order is not determined directly with neutrons. However, the length of the transition metal-oxygen bond will depend on the charge (valence state) of the transition metal ion. The higher the positive charge of the transition metal, the shorter will be the bond to the neighboring oxygen, just due to Coulomb attraction. This qualitative argument can be quantified in the so-called *bond-valence sum*. There is an empirical correlation between the valence V_i of an ion and the bond lengths R_{ij} to its neighbors:

$$V_i = \sum_{ij} s_{ij} = V_i = \sum_{ij} e^{\frac{R_0 - R_{ij}}{B}}. \quad (13.4)$$

Here, the R_{ij} are the experimentally determined bond lengths, $B = 0.37$ is a constant, and R_0 are tabulated values for the cation-oxygen bonds, see, e.g., [22]. Table 13.1 reproduces some of these values. The sum over the partial “bond-valences” s_{ij} gives the valence state of the ion.

Even though this method to determine the valence state is purely empirical, it is rather precise compared to other techniques. The values of the valences found with this method differ significantly from a purely ionic model. Instead of integer differences between charges on different transition metal ions, one finds more likely differences of a few tenth of a charge of an electron, though rare exceptions, where near-integer valence differences were observed, exist [23].

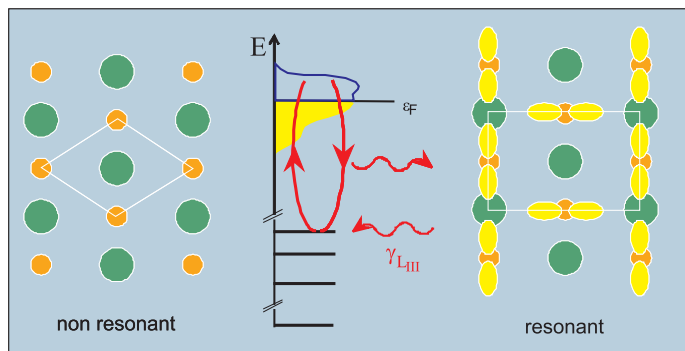


Fig. 13.12: *Anisotropic anomalous x-ray scattering for a hypothetical diatomic 2D compound. Left: Reconstruction of the charge distribution from a laboratory x-ray source, sensitive mainly to the spherical charge distribution and corresponding unit cell (white lines). Middle: Principles of resonance x-ray scattering in an energy level diagram (see text). Right: Charge distribution deduced from such an anomalous x-ray scattering experiment. An orbital ordering pattern is apparent, which could not be detected with non-resonant x-ray scattering. The evidently larger unit cell gives rise to superstructure reflections (at resonance).*

Just like *charge order*, *orbital order* is not directly accessible to neutron diffraction since orbital order represents an anisotropic charge distribution and neutrons do not directly interact with the charge of the electron. However, we have seen in the discussion of the Jahn-Teller effect (Figs. 13.8 and 13.9) that an orbital order is linked to a distortion of the local environment visible in different bond lengths within the anion complex surrounding the cation. Thus, by a precise determination of the structural parameters from diffraction, one can determine in favorable cases the ordering patterns of all four degrees of freedom: lattice, spin, charge and orbitals.

Is there a more direct way to determine charge- and orbital order? The scattering cross section of x-rays contains the atomic form factors, which are Fourier transforms of the charge density around an atom. Therefore, one might think that charge and orbital order can be easily determined with x-ray scattering. However, as discussed in the last paragraph, usually only a fraction of an elementary charge contributes to charge- or orbital ordering. Consider the Mn atom: the atomic core has the Ar electron configuration, i.e. 18 electrons are in closed shells with spherical charge distributions. For the Mn^{4+} ion, three further electrons are in t_{2g} levels. Since in scattering, we measure intensities, not amplitudes, these 21 electrons contribute $21^2 r_0^2$ to the scattered intensity (the classical electron radius r_0 is the natural unit of x-ray scattering). If the difference in charge between neighboring Mn ions is $0.2e$, this will give an additional contribution to the scattered intensity of $0.2^2 r_0^2$. The relative effect of *charge order* in x-ray scattering is therefore only a tiny fraction $\frac{0.2^2}{21^2} \sim 10^{-4}$, even ignoring that scattering from all other atoms makes the situation worse. There is, however, a way to enhance the scattering from non-spherical charge distributions, the so-called *anisotropic anomalous x-ray scattering*, first applied for *orbital order* in manganites by Murakami *et al.* [24]. The principle of this technique is depicted in Fig. 13.12, showing scattering from a hypothetical diatomic 2D compound. Non resonant x-ray scattering is sensitive mainly to the spherical charge distribution. A reconstruction of the charge distribution done from such an experiment might look schematically as shown on the left. The corresponding crystal structure can be described with a primitive unit cell (white

lines). To enhance the scattering from the non-spherical part of the charge distribution, an experiment can be done at a synchrotron source, with the energy of the x-rays tuned to the energy of an absorption edge (middle). Now, second order perturbation processes can occur, where a photon induces virtual transitions of an electron from a core level to empty states above the Fermi energy and back with re-emission of a photon of the same energy. As second-order perturbation processes have a resonant denominator, this scattering will be strongly enhanced near an absorption edge. If the intermediate states in this resonant scattering process are somehow connected to orbital ordering, scattering from orbital ordering will be enhanced. Thus in the resonant scattering experiment, orbital order can become visible as indicated on the right. With the shown arrangement of orbitals, the true primitive unit cell of this hypothetical compound is obviously larger than the unit cell that was deduced from the non resonant scattering experiment (left), which was not sensitive enough to determine the fine details of the structure. An increase of the unit cell dimensions in real space is connected with a decrease of the distance of the reciprocal lattice points, leading to additional *superstructure reflections*. The intensity of these reflections has the strong energy dependence expected for a second-order perturbation process. This type of experiment is called *anisotropic anomalous x-ray scattering*, because it is sensitive to the anisotropic charge distribution around an atom.

So far we have discussed some powerful experimental techniques to determine the various ordering phenomena in complex transition metal oxides. Scattering can give much more information than just on the time averaged structure. Quasi-elastic diffuse scattering gives us information on fluctuations and short range correlations persisting above the transitions, e.g. short range correlations of polarons, magnetic correlations in the paramagnetic state (Fig. 13.11), local dynamic Jahn-Teller distortions etc. Studying these correlations and fluctuations helps to understand what drives the respective phase transitions into long-range order. The relevant interactions, which give rise to these ordering phenomena, can be determined from inelastic scattering experiments as learnt in the chapter “Inelastic neutron scattering”. For example, in a new class of iron-based high-temperature superconductors, the involvement in Cooper pairing of lattice vibrations or alternatively magnetic fluctuations is controversial, and both of these can be probed in-depth by inelastic neutron scattering (see, e.g., [25]). Since there is a huge amount of scattering experiments on highly correlated transition metal oxides and chalcogenides, a review of these experiments definitely goes far beyond the scope of this introductory lecture.

13.6 Summary

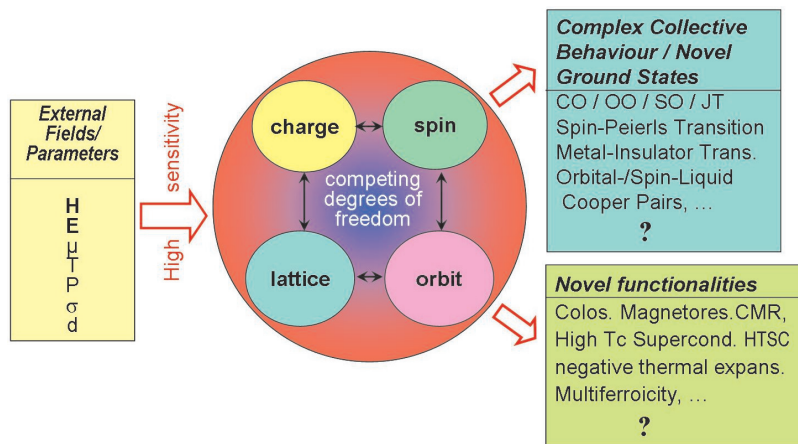


Fig. 13.13: Illustration of complexity in correlated electron systems. **H, E:** magnetic and electric field, respectively; μ : chemical potential (doping); T : temperature; P : pressure; σ : strain (epitaxial growth); d : dimensionality (e.g. bulk versus thin film systems); *CO*: charge order; *OO*: orbital order; *SO*: spin order; *JT*: Jahn-Teller transition.

This chapter gave a first introduction into the exciting physics of highly correlated electron systems, exemplified by transition metal oxides and chalcogenides. The main message is summarized in Fig. 13.13. The complexity in these correlated electron systems arises from the competing *degrees of freedom*: charge, lattice, orbit and spin. The ground state is a result of a detailed balance between these different degrees of freedom. This balance can be easily disturbed by external fields or other thermodynamical parameters, giving rise to new ground states or complex collective behavior. Examples are the various ordering phenomena discussed, Cooper pairing in superconductors, so-called spin-Peierls transitions in 1D systems etc. This high sensitivity to external parameters as well as the novel ground states of the systems gives rise to novel functionalities, such as the colossal magnetoresistance effect, high temperature superconductivity, multiferroicity, and many more. A theoretical description of these complex systems starting from first principles, like Schrödinger equation in quantum mechanics or the maximization of entropy in statistical physics, is bound to fail due to the large number of strongly interacting particles. Entirely new approaches have to be found to describe the emergent behavior of these complex systems. Therefore highly correlated electron systems are a truly outstanding challenge in modern condensed matter physics. We have shown in this lecture that neutron and x-ray scattering are indispensable tools to disentangle this complexity experimentally. They are able to determine the various ordering phenomena as well as the fluctuations and excitations corresponding to the relevant degrees of freedom. No other experimental probe can give so much detailed information on a microscopic level as scattering experiments.

Acknowledgement

I thank Th. Brückel for much of the materials from previous lectures that are used in this chapter.

References

- [1] R. B. Laughlin and D. Pines, *Proc. Natl. Acad. Sci. USA* **97**, 28 (2000).
- [2] T. Vicsek, *Nature* **418**, 131 (2002).
- [3] J. G. Bednorz and K. A. Müller, *Z. Phys. B* **64**, 189 (1986).
- [4] A.-M. Haghiri-Gosnet and J.-P., *J. Phys. D: Appl. Phys.* **36**, R127 (2003).
- [5] G. Binasch, P. Grünberg, F. Saurenbach, and W. Zinn *Phys. Rev. B* **39**, 4828 (1989).
- [6] M. N. Baibich *et al.*, *Phys. Rev. Lett.* **61**, 2472 (1988).
- [7] M. H. Phan and S. C. Yu, *J. Magn. Magn. Mater.* **308**, 325 (2007).
- [8] E. J. W. Verwey, *Nature* **144**, 327 (1939).
- [9] M. Fiebig, *J. Phys. D.: Appl. Phys.* **38**, R123 (2005).
- [10] M. Bibes and A. Barthélémy, *Nat.* **7**, 425 (2008).
- [11] G. D. Barrera *et al.*, *J. Phys.: Condens. Mat.* **17**, R217 (2005).
- [12] E. Dagotto, *Science* **309**, 257 (2005).
- [13] N. W. Ashcroft and N. D. Mermin, *Solid State Physics* (Thomson Brooks/Cole, New York, 1976).
- [14] H. Ibach and H. Lüth, *Solid State Physics: An introduction to principles of materials science* (Springer, Berlin, 2010).
- [15] J. Bardeen, L. N. Cooper, and J. R. Schrieffer, *Nobel Prize in Physics in 1972 for a microscopic theory of superconductivity (nowadays called BCS-theory.)*
- [16] K. Held *et al.*, *J. Phys.: Condens. Mat.* **20**, 064202 (2008).
- [17] N. F. Mott, *Rev. Mod. Phys.* **40**, 677 (1968).
- [18] P. Fazekas, *Lecture notes on electron correlation and magnetism* (World Scientific, Singapore, 2003).
- [19] T. Chatterji (Ed.), *Colossal magnetoresistive manganites* (Kluwer Academic Publishers, Dordrecht, 2004).
- [20] A. Urushibara *et al.*, *Phys. Rev. B* **51**, 14103 (1995).
- [21] J. de Groot *et al.*, *Phys. Rev. Lett.* **108**, 037206 (2012). *ibid.* **108**, 187601 (2012). For a general review see also M. Angst, *Phys. Status Solidi RRL* **7**, 383 (2013).
- [22] G. H. Rao, K. Bärner, and I. D. Brown, *J. Phys.: Condens. Mat.* **309**, 257 (2005).
- [23] M. Angst *et al.*, *Phys. Rev. Lett.* **99**, 086403 (2007).
- [24] Y. Murakami *et al.*, *Phys. Rev. Lett.* **81**, 582 (1998).
- [25] R. Mittal *et al.*, *Phys. Rev. Lett.* **102**, 217001 (2009).

Exercises

Note: * indicates an increased difficulty. Solve the easier problems first.

E13.1 Electronic structure and Mott transition

- In modeling the electronic structure of crystalline solids, what is the typical starting assumption to separate the electronic structure from the lattice dynamics, and why does it work?
- In which of the three simplest models of electrons in a solid are the electronic correlations taken into account at least approximately?
- Neglecting electronic correlations, would you predict NaCl to be an insulator or a metal? Why?
- The competition of which two contributions to the total energy of the electrons is crucial for the Mott-transition? Which further contributions to the total energy are neglected in the simplest model?
- Assume that a particular material is a Mott-insulator, but just barely so (i.e. the relevant energy contributions are almost equal). What would you predict to happen when sufficiently high pressure is applied, and why?

E13.2 Electronic ordering in correlated-electron materials

- List and very briefly explain three “electronic degrees of freedom”, which can become ordered.
- To order of which of the electronic degrees of freedom is neutron scattering *directly* sensitive, and to which not?
- For those electronic degrees of freedom, to which neutron is *not* directly sensitive, neutron scattering can still be used to deduce an ordered arrangement: How and why? Is there a more direct scattering method than neutron scattering?
- * What, if any, connection is there between orbital order and orbital magnetic momentum?
- * Discuss why electronic correlations favor ordering processes of electronic degrees of freedom.

E13.3 Crystal field

Fe has atomic number 26 and in oxides typically has valence states 2+ or 3+.

- Determine the electronic configuration of free Fe^{2+} and Fe^{3+} ions (hint: as for Mn the outermost s -electrons are lost first upon ionization).
- From Hund’s rules determine the values of the spin S , orbital angular momentum L , and total angular momentum J of Fe^{2+} and Fe^{3+} ions.

(Hund's rules:

1. S max.
2. L max consistent with 1.
3. $J = |L - S|$ for a less than half filled shell,
 $J = |L + S|$ for a more than half filled shell).

c) * The effective moment μ_{eff} of a magnetic ion can be determined experimentally by the Curie-Weiss law, and is given by $\mu_{\text{eff}} = g_J \sqrt{J(J+1)} \mu_B$, where the Landé factor is

$$g_J = \frac{3}{2} + \frac{S(S+1) - L(L+1)}{2J(J+1)}. \quad (13.5)$$

Calculate the expected effective moment in units of μ_B of Fe^{2+} and Fe^{3+} ions, i) assuming S , L , and J as determined in b) and ii) setting $L = 0$ ('quenched orbital momentum'). Compare with the experimental values of $\sim 5.88 \mu_B$ for Fe^{3+} and $\sim 5.25 - 5.53 \mu_B$ for Fe^{2+} .

d) * The negatively charged oxygen ions surrounding the Fe ions in an oxide solid influence the energy of the different orbitals. Plot the expected energy level diagram for the case of an octahedral environment of nearest-neighbor O^{2-} (corresponding to the example in the lecture). How does the total spin moment of Fe^{2+} change between weak and strong crystal field splittings (relative to intra-atomic "Hund's" exchange)?

e) (optional) ** In a tetrahedral environment the energy levels of the orbitals are reversed compared to an octahedral environment. Determine the spin moment of Fe^{2+} in a tetrahedral environment with strong crystal field splitting. Is an orbital angular momentum possible in this case?

E13.4 Orbital and Magnetic order in LaMnO_3 (Optional!)

The orbital and magnetic order in LaMnO_3 is sketched in Fig. 13.9 (page 11 of the chapter) on the left. One crystallographic unit cell $a \times b \times c$ is shown.

- a) Why is there no charge order in LaMnO_3 ?
- b) What are the smallest unit cells (sketch in relation to the crystallographic cell) that can describe i) magnetic order, ii) * orbital order (*Hint: consider also centered cells, where the centering symmetry is broken by the orbital order*), iii) both magnetic and orbital order.
- c) Make a plot of reciprocal space in the a^*-c^* -plane indicating the positions, where you expect nuclear, orbital, and magnetic Bragg peaks to occur.
- d) * As c), but for the a^*-b^* -plane.

14 Dynamics of Polymers and Biological Macromolecules

R. Biehl

Jülich Centre for Neutron Science 1

Forschungszentrum Jülich GmbH

Contents

14.1	Introduction	2
14.2	Coarse graining	2
14.3	Conformation of linear chains	3
14.4	Separation of global and internal dynamics	4
14.5	Linear polymers in melt	6
14.6	Linear polymers in solution	9
14.7	Protein domain motions	10
14.8	Between chain dynamics and domain motions: intrinsically disordered proteins	11
14.9	Domain dynamics of antibodies	13
14.10	Summary	16
	Appendices	17
	References	19
	Exercises	22

14.1 Introduction

A polymer is a chain of several polyatomic units called monomers covalent bonded together. Since virtual all kinds of molecules can act as a monomeric unit, thereby only differing in the ways in which they can be bound together, a wealth of synthetic and naturally occurring biopolymers with enormous diversity in properties is nowadays known. They all belong to the class of polymers. Synthetic polymers are materials without which modern technology cannot be imagined. In many places they have supplanted traditional materials as metals. One of the reasons for this is that polymers show unique mechanical properties which are desirable for engineering, e.g. high impact resistance at low specific mass. The polymer composition (specific monomers) and architecture (linear, branched ring) influence the material properties.

Biopolymers as proteins or DNA determine life. Biopolymers, in particular proteins, share similarities with polymers which allow to use polymer models to describe their structure and dynamics. Proteins are polymers with a specific sequence of 20 amino acids which are charged, hydrophobic or hydrophilic. Intrinsically unfolded proteins (IDP) sample a large conformational space similar to above polymers. The structure of globular proteins is mainly stabilized by hydrophobic interactions but additionally via a hydrogen bond network and crosslinking by disulfide bonds. The protein structure and related conformational changes are often related to the function of the protein e.g. by arranging the active center after substrate binding or allowing transport and release of products. As larger domains contribute to the configurational changes the timescale of the involved motions is slowed down. More and more the role of slow domain dynamics is recognized as essential to understand the function of proteins.

14.2 Coarse graining

The complexity of polymers/biopolymers can nowadays covered by all-atom MD simulations requiring a huge amount of resources and computation time. The essential structure and dynamics can be examined since long time [24, 29, 32, 35] by coarse grained models that successfully describe all essential features of polymers within analytical theories and allow to understand all basic properties.

The basic assumption of simplest bead-and-spring models is that beads do not interact with each other except over springs with next neighbors. For linear polymers the result is a Gaussian chain as the simplest model for chain relaxation. The building blocks of such a chain are N segments each consisting of sufficient monomers so that their end-to-end distance follows a Gaussian distribution with the average segment length l . Coarse graining includes that the segments may consist of several monomers that segments are longer than the Kuhn length describing the local stiffness of chain structure. While the Rouse model assumes only friction with the surrounding like a melt the Zimm model includes additional friction between beads mediated by hydrodynamic interactions between all beads. Assuming friction between monomers leads to additional internal friction in the chain. More structured objects like proteins or double stranded DNA can be described by networks of connected beads in a similar way describing also the 3D structure. Neutron scattering allows to study the microscopic

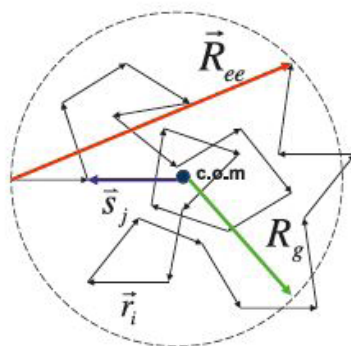


Fig. 14.1: A freely jointed chain and definitions: end-to-end distance \vec{R}_{ee} , gyration radii R_g , segment vector \vec{r}_i and \vec{s}_j is a vector between the segment and centre-of-mass.

structure and dynamics of polymer chains based on the existing theories.

14.3 Conformation of linear chains

Polymers can often be imagined as spaghetti-like or coiled molecules. Their stiffness varies from very flexible to rigid in the case of rods. Their configuration *i.e.* their spatial distribution of monomer units or segments changes all the time as the result of Brownian dynamics which leads to a sampling over a huge configurational space. The simplest model to deal with is the freely jointed chain (FJC). An example for such a configuration is shown in Fig. 14.1 and illustrates the idea that polymer chains consisted of equivalent segments are performing random walks. With this, the ensemble of systems can be characterized by average quantities. One is the so-called end-to-end vector and its square

$$\vec{R}_{ee} = \sum_{i=1}^N \vec{r}_i, \quad R_{ee}^2 = \sum_{i,j=1}^N \vec{r}_i \vec{r}_j \quad (14.1)$$

which is the scalar quantity. N is the number of segments in the polymer chain. The bond vector length (or step) $|\vec{r}_i|$, connecting 2 beads is l . A further important parameter which has its counterpart in classical mechanics is the radius of gyration R_g with

$$R_g^2 = \frac{1}{N} \sum (\vec{r}_i - \langle \vec{r}_i \rangle)^2 \quad (14.2)$$

where $\langle \vec{r}_i \rangle$ is the center of mass averaged over all i . The FJC model assumes an equal probability in all directions of all bond vectors, random bond rotation angles while keeping the bond length constant. The mean radius of gyration can then be obtained - using random walk statistics

$$\langle R_g^2 \rangle = \frac{1}{6} N l^2 \quad (14.3)$$

From both end-to-end distance and radius of gyration an important statement which applies to polymer chain is already observed: the size depends on the square root of the number of

basic steps (number of segments), \sqrt{N} . Real polymer chains are not connected in this freely jointed way. Instead, bond angles θ_{ij} assume well-defined values and correlations between bonds within the chain as well as from the environment will affect the size. Intuitively it can be understood that these correlations will vanish with increasing separation distance. Also, the flexibility of polymer chains is restricted by the fact that rotations with the so-called bond rotation angle are enabled within a certain range only due to steric reasons.

An important polymer model to include interactions is the Flory theory [24] that includes intermolecular and solvent interactions. If the monomers like the solvent, they try to have more contact and the polymer will swell (good solvent). This corresponds to repulsive interaction between monomers and includes non-overlapping volumes. If the monomers doesn't like the solvent the polymer try to avoid solvent contact and collapse (bad solvent) corresponding to attractive monomer interaction. Between both cases, when interactions are balanced the interactions cancel and we find an ideal configuration without interaction (theta solvent) close to the FJC. The end-to-end distance is here

$$\langle R_{ee}^2 \rangle = N^\nu l^{2\nu} \quad (14.4)$$

The Flory exponent ν is 0.5 for ideal solvents and 0.6 for good solvent (actually 0.588). Often the range of ν is increased to span from collapsed chains $\nu = 1/3$ to highly swollen chains $\nu < 1$ with repulsive interactions between monomers.

The size of a polymer chain can be measured by various scattering experiments (light scattering, SAXS, SANS). The single chain normalized formfactor $P(Q)$ is:

$$P(Q) = \frac{1}{N^2} \sum_{k,j=1}^N \langle \exp(i\vec{Q} \cdot (\vec{r}_k - \vec{r}_j)) \rangle = \frac{1}{N^2} \sum_{k,j=1}^N \exp\left(-\frac{1}{6}Q^2 l^2 |k-j|^{2\nu}\right) \quad (14.5)$$

using $\langle r_k - r_j \rangle = l^2 |k-j|^{2\nu}$ [10]. For long chains ($Q^2 l^2 / 6 \ll 1$ and $N \gg 1$) and $\nu = 1/2$ $P(Q)$ is described by the Debye function [12] with

$$g_D(x) = \frac{2}{x^2} (\exp(-x) - 1 + x) \quad (14.6)$$

and the argument $x = (QR_g)^2$. A SANS experiment with fit to the Debye function is presented in Fig. 14.2 in a linear scale and in the form of a second moment Kratky representation achieved when $g_D(x)$ is multiplied by Q^2 . The Kratky representation emphasises the high Q -regime. For Gaussian chains with an asymptotic Q^{-2} behaviour the high Q regime then assumes a plateau. As shown the data are in perfect agreement with the Gaussian chain results derived above.

14.4 Separation of global and internal dynamics

The intermediate scattering function (ISF) measured e.g. by NSE has contributions from overall translational and rotational diffusion and from motions within the molecule that we call internal dynamics. In the general case, all motions might be coupled. In a simplifying assumption known as decoupling approximation we assume that the internal dynamics (int) does not alter the overall diffusion and that translational (trans) and rotational (rot) diffusion

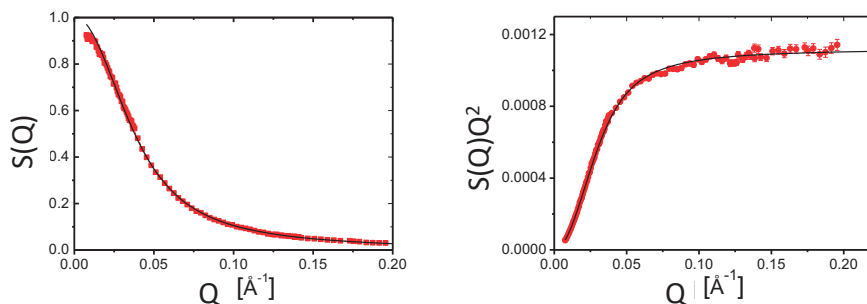


Fig. 14.2: SANS scattering intensity obtained for a poly(alkylene oxide) polymer and described by the Debye function (lines) [11]. On the left, the Debye curve fits ideally and the high Q -dependence shows Q^{-2} . On the right, the Kratky region (plateau) is highlighted.

are decoupled too. For the single particle pair correlation function or coherent scattering function we assume

$$F(Q, t) = F_{\text{trans}}(Q, t) \cdot F_{\text{rot}}(Q, t) \cdot F_{\text{int}}(Q, t) \quad (14.7)$$

For spherical symmetric objects like spheres or Gaussian chains rotational contributions cannot be observed as there is no contrast change during rotation. On the other side proteins and DNA are asymmetric and have significant rotational contributions.

Diffusion of rigid objects

The diffusional term contributing to equation (14.7) for a rigid object has contributions from translational and rotational diffusion characterized by the respective diffusion coefficients D_T and D_R . These can be calculated from the atomic coordinates r_α or coarse grained bead models by HYDROPRO on basis of a PDB conformation [22] or measured in dilute solutions. We yield

$$F_{\text{trans}}(Q, t) = \exp(-Q^2 D_T t) \quad (14.8)$$

$$F_{\text{rot}}(Q, t) = \sum_{l=0}^{\infty} S_l(Q) \exp(-l(l+1)D_R t) \quad (14.9)$$

$$\text{with } S_l(Q) = \sum_m \left| \sum_\alpha b_\alpha j_l(Qr_\alpha) Y_{l,m}(\Omega_\alpha) \right|^2 \quad (14.10)$$

where $S_l(Q)$ are the coefficients of a multipole expansion of the asymmetric form factor with scattering length b_α of the atom α at position r_α and orientation Ω_α , $j_l(Qr)$ are the spherical Bessel functions and $Y_{l,m}(\Omega_\alpha)$ the spherical harmonics [4, 19].

Concentration effects

At infinite dilution the measured signal $I(Q, t)$ is independent of direct concentration effects as $I(Q, t)/I(Q, 0) = F(Q, t)/F(Q, 0)$. For larger concentrations the interaction depends on the type of polymer and the solvent. Polymer in theta-solvent or in melt have virtually no interaction. Dependent on the solvent quality, as good or bad solvent, the interactions can be attractive or repulsive. Additional charges and excluded volume for globular particles contribute to the overall interaction. This leads to a spatial distribution describing spatial correlations between objects subsumed in the structure factor $S(Q)$. The translational diffusion coefficient D_T is influenced by these direct interactions and hydrodynamic interactions (HI) described by the hydrodynamic function $H_T(Q)$. This is described by $D_T(Q) = D_{T0}H_T(Q, c)/S(Q, c)$ where the index 0 indicates the dilute limit (single particle limit). [19, 26].

The hydrodynamic function $H_T(Q)$ can be calculated within the $\delta\gamma$ expansion of Beenakker and Mazur [1, 2] for spherical objects which approximately holds also for polymers with a HI screening radius R_{HI} . [6] or proteins [4, 5, 15] and reduces the translational diffusion coefficient with $H_T(Q = \infty) = \eta_0/\eta < 1$ [1, 2, 8, 20]. η_0/η is measured as the ratio between solvent viscosity η_0 and protein solution viscosity at the measured concentration η . At low Q $H(Q)$ has similarities to $S(Q)$ and as a rule of thumb is approximately $H(Q) - H(\infty) \approx 0.5(S(Q) - 1)$ for hard spheres. Hydrodynamic effects also influence the rotational diffusion coefficient subsumed in the hydrodynamic factor H_R for rotational diffusion with $D_R = D_{R0}H_R$. According to ref. 32 for spherical particles this effect can be estimated as $1 - H_R = (1 - H_T(Q = \infty))/3$.

14.5 Linear polymers in melt

To describe the motion of a polymer, we start with the bead and spring model. Each bead undergoes friction $\zeta = 6\pi\eta l$ with the surrounding which can be a polymer melt or solvent of viscosity η . Hydrodynamic interactions are assumed screened and therefore neglected. Harmonic springs between the beads of spring constant $\kappa = (k_B T)/l^2$ are assumed. We can write down a Langevin equation for the segmental motion using $f_n(t)$ for the thermal random force acting on bead “ n ” within the Rouse model [29]:

$$\zeta \frac{dr_n}{dt} = \kappa (r_{n+1} - 2r_n + r_{n-1}) + f_n(t) \quad (14.11)$$

$$\zeta \frac{d\mathbf{r}}{dt} = \kappa \mathbf{k} \mathbf{r} + \mathbf{f}(t) \quad (14.12)$$

using vector notation $\mathbf{r} = (r_1, \dots, r_N)$ with the tri-diagonal connectivity matrix

$$\mathbf{k} = \begin{pmatrix} -1 & 1 & 0 & 0 & \dots \\ 1 & -2 & 1 & 0 & \dots \\ 0 & 1 & -2 & 1 & \dots \\ 0 & 0 & 1 & -2 & \dots \\ \dots & \dots & \dots & \dots & \dots \end{pmatrix} \quad (14.13)$$

Microscopic dynamics on scales shorter than the segment or Kuhn length like dihedral rotations of bonds can lead to internal friction ζ_i between beads which can be included in the RIF model (Rouse with internal friction) as [7] :

$$\zeta \frac{d\mathbf{r}}{dt} = \kappa \mathbf{k}\mathbf{r} + \zeta_i \frac{d}{dt} \mathbf{k}\mathbf{r} + \mathbf{f}(t) \quad (14.14)$$

The coupled differential equations (14.12) and (14.14) can be solved using the eigenbasis of the connectivity matrix (14.13), i.e. normal mode decomposition. With the proper boundary conditions of force free ends $\partial r_n / \partial n (n = 0, N) = 0$ the eigenmodes turn out as

$$\phi_p(n) = \frac{1}{N} \cos\left(\frac{p\pi}{N}n\right) \quad (14.15)$$

with a wavelength $\lambda_p = lN/p$ along the chain. The eigenmode p relaxes with the characteristic time τ_p where

$$\tau_p = \tau_R/p^2 + \tau_i, \quad \tau_R = \frac{N^2 l^2 \zeta}{3\pi^2 k_B T} = \frac{N^2 \zeta}{3\pi^2 \kappa} = \tau_0 N^2, \quad \tau_i = \zeta_i / \kappa \quad (14.16)$$

τ_R is the longest relaxation time also called the Rouse time without internal friction in the Rouse model. $\tau_0 = \frac{l^2 \zeta}{3\pi^2 k_B T} = \frac{1}{W\pi^2}$ is the segmental relaxation time where W is the Rouse rate which is related to monomer (bead) friction ζ . τ_i is the additional relaxation time due to internal friction ζ_i . At the time τ_p the chain subsection with N/p monomers moves over its own distance. Thus the mean square displacement msd ,

$$msd = \langle (r_n(\tau_p) - r_n(0))^2 \rangle = l^2 \frac{N}{p} = l^2 \left(\frac{\tau_p}{\tau_0}\right)^{\frac{1}{2}} \quad (14.17)$$

Since (14.17) holds for all p , the chain segments at times shorter than τ_R move in a subdiffusive way with $msd \propto t^{1/2}$. This is a basic prediction of the Rouse model. Performing the full calculation starting from (14.11)-(14.12), the final result for the time dependent msd is:

$$msd = \langle r_n^2(t) \rangle = \sqrt{\frac{12l^2 k_B T}{\pi \zeta}} t \quad (14.18)$$

For the single chain dynamic structure factor, where we look on a labelled e.g. protonated chain in a deuterated environment, we have to deal with the interference of scattered waves originating from the different atoms or monomers of the chain. The detailed calculations are given in reference [10]. The result may be expressed in terms of the Rouse modes Eq. (14.15) and corresponding relaxation times $\tau_p = \tau_R/p^2$ and amplitude factors $a_p = 1/p^2$.

$$S(q, t) = \frac{1}{N} e^{-q^2 D_R t} \sum_{n,m} e^{-\frac{1}{6} q^2 B(n,m,t)} \quad (14.19)$$

$$B(n, m, t, \tau_p) = |n - m|^{2\nu} l^2 + \frac{4R_e^2}{\pi^2} \sum_{p=1}^{N-1} a_p \cos(\pi p n / N) \cos(\pi p m / N) (1 - e^{-t/\tau_p})$$

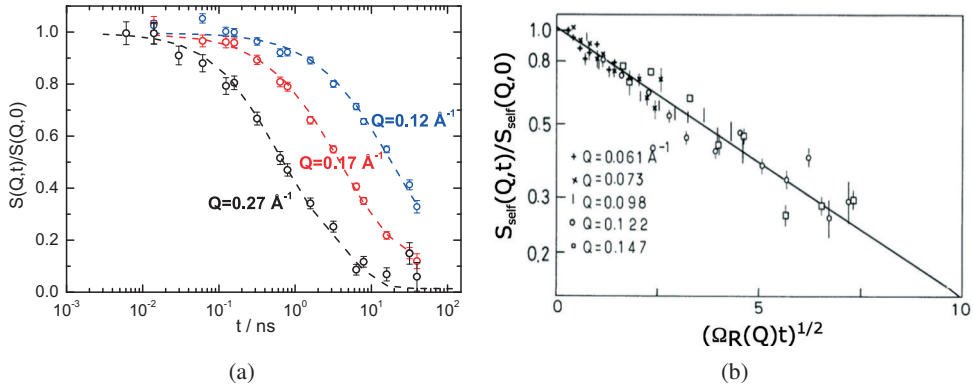


Fig. 14.3: (a) NSE data for the polydimethylsiloxane (PDMS) melt measured at different values of the momentum transfer Q [18]. Dashed lines present fitting curves obtained by using (14.19); (b) Dynamic structure factor for the segmental self motion in a PDMS melt at 100°C [27]. The data are scaled with the Rouse variable (14.21). The solid line shows the predicted $t^{1/2}$ relaxation by the Rouse model.

for small Q ($QR_{ee} < 1$) $B(n, m, t)$ becomes negligible and $S(Q, t)$ describes the centre-of-mass self diffusion of the chain with $D_R = k_B T / N\zeta$.

$$S_{self}(Q, t) = \frac{1}{N} S(Q, t) = \exp(Q^2 D_R t) \quad (14.20)$$

For $QR_{ee} > 1$ and $t < \tau_R$ the internal relaxation processes dominate. For $t = 0$ we have $S(Q, t) = S(Q)$; *i.e.* the structure factor corresponds to a snapshot of the chain structure (14.2). By using a mixture of protonated ($\approx 10\%$) and deuterated chains, neutron spin echo (NSE) directly measures the coherent single chain dynamic structure factor $S(Q, t)$ that is the spatial Fourier transform of the monomer-monomer dynamic pair correlation function. As an example, the NSE data for the bulk PDMS melt are shown in Fig. 14.3a.

Quasielastic incoherent neutron scattering directly measures the segment self correlation function with $n = m$ in (14.19). In Gaussian approximation we have for pure Rouse:

$$S_{self}(Q, t) = \exp\left(-\frac{Q^2}{6} \langle r^2(t) \rangle\right) = \exp(-D_R Q^2 t) \exp\left(-\frac{2}{\sqrt{\pi}} (\Omega_R(Q)t)^{\frac{1}{2}}\right) \quad (14.21)$$

$$\Omega_R(Q) = \frac{k_B T l^2}{12\zeta} Q^4$$

The second part of this equation is obtained by inserting of Eq.(14.18). $\Omega_R(Q)$ is the characteristic relaxation rate, that increases with the momentum transfer as Q^4 .

Even though a clear cut prediction, experimentally the observation of the self correlation function of a Rouse chain is an important challenge. The necessary resolution at the low momentum transfers requires, neutron spin echo spectroscopy [21, 28]. Here, incoherent experiments are difficult, since incoherent scattering depolarises the neutron beam to a large extend (2/3 spin flip scattering). Therefore, using a trick the first successful experiments were carried out. The chemists produced deuterated PDMS where randomly short protonated

sections were copolymerised. These protonated sections in a generally deuterated environment gave rise to coherent scattering, however, since the scattering from different labels was uncorrelated the self correlation function was measured.

Fig. 14.3b displays the obtained self correlation function for PDMS [27] in a presentation where the logarithm of the scattering function is plotted versus $(\Omega_R(Q)t)^{\frac{1}{2}}$, the scaling variable of Eq.(14.21). In this way all the data collapse on one single master curve that according to Eq.(14.21) should be a straight line. The experimental results beautifully verify the major prediction of the Rouse model and show that the simple approximation of the bead - spring model properly accounts for the segmental dynamics of the PDMS chain on the space time frame investigated.

14.6 Linear polymers in solution

In typical solutions like water or organic solvents hydrodynamic interactions (HI) need to be taken into account. In the the Zimm model [35] this is done by using a preaveraging approximation using the equilibrium average

$$\mathbf{H}_{nm} \longrightarrow \langle \mathbf{H}_{nm} \rangle = \frac{\mathbf{I}}{2\pi^2 \zeta |n - m|^{1/2}} \quad (14.22)$$

The above equation (14.14) changes to

$$\frac{d\mathbf{r}}{dt} = \langle \mathbf{H} \rangle (\kappa \mathbf{k}\mathbf{r} + \zeta_i \frac{d}{dt} \mathbf{k}\mathbf{r} + \mathbf{f}(t)) \quad (14.23)$$

For $N \gg 1$ $\langle \mathbf{H} \rangle$ becomes diagonal in the eigenbasis of the connectivity matrix (14.13). The eigenmode p relaxes with the characteristic time τ_p where

$$\tau_p = \tau_Z / p^{3\nu} + \tau_i, \quad \tau_Z = \frac{\eta R_e^3}{(3\pi)^{1/2} k_b T} = \frac{N^{3\nu} \zeta}{6\pi(3\pi)^{1/2} \kappa}, \quad \tau_i = \zeta_i / \kappa \quad (14.24)$$

τ_Z is the longest relaxation time also called the Zimm time without internal friction in the Zimm model. τ_i is the additional relaxation time due to internal friction ζ_i in the corresponding ZIF model (Zimm with internal friction).

The single chain dynamic structure factor $S(Q, t)$ for the Zimm model is the same as (14.19) with the amplitude factor $a_p = 1/p^{3\nu+1}$ and the mode relaxation time τ_p of the Zimm respectively the ZIF model. Here $R_e = N^\nu l$ and $D_Z = \frac{8}{3(6\pi^3)^{1/2}} \frac{k_b T}{\eta R_e} = 0.196 \frac{k_b T}{\eta R_e}$ for $\nu = 0.5$. For $\nu = 0.6$ the prefactor is 0.203.

Fig. 14.4 shows an example for the polyelectrolyte (PE) polystyrene sulfonic acid (PSS) [6]. The SAXS data Fig. 14.4a decrease at low Q is due to the structure factor $S(Q)$ with increasing concentration. $S(Q)$ effects are reduced with increasing charge screening due to added salt. PE formfactor shows a more expanded chain with $\nu \gtrsim 0.6$ due to repulsion between charges. The minima around $Q = 3 - 4nm^{-1}$ are related to a disc like cross section of the chain from counter ion condensation. NSE spectra were fitted with a ZIF model complemented by $H(Q)/S(Q)$ correction for D_Z . Fig. 14.4b show effective diffusion extracted by fitting $exp(= Q^2 D_{eff} t)$ to model and data to get an easier overview. At low Q

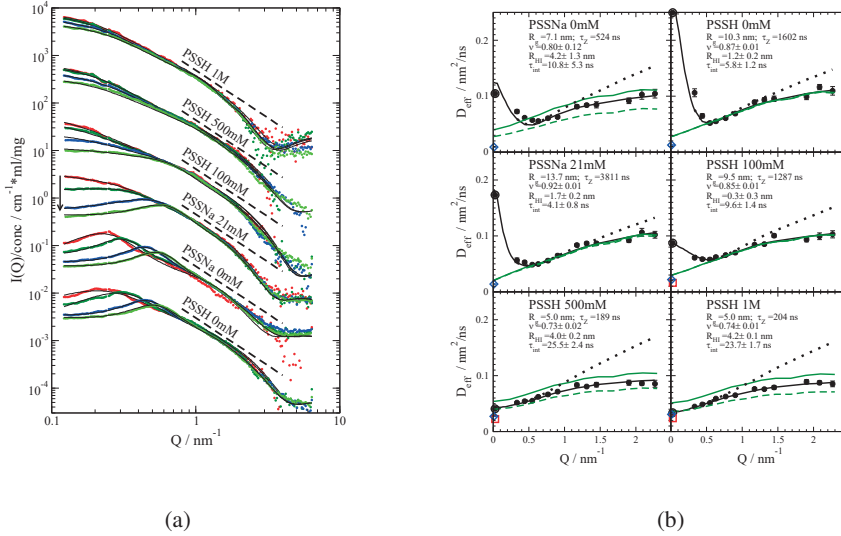


Fig. 14.4: (a) SAXS data for PSS MW=39k (c_{NaCl} shifted consecutively). A stronger $S(Q)$ with increasing c_p results mainly in the decreased intensity at a low Q . Concentrations were 5, 10, 20, 30 mg/mL except for 21 mM with 8.3, 16.6, 33.2 and 50 mg/mL (colors red to green, along arrow). Black lines correspond to fits using a generalised Gaussian worm as formfactor and a 2-Yukawa potential with attractive and repulsive components. Broken lines indicate the extension of a Q^{-2} power law to a high Q to demonstrate the deviation from a Gaussian chain. (b) Effective diffusion coefficients D_{eff} for PSS 39k $c_p M_w = 30$ mg/ml with respective parameters: experimental (points); ZIF with full $H(Q)/S(Q)$ correction (black line); ZIF only with self-part correction D_s/D_0 (green dashed); same but $\tau_{int} = 0$ (Zimm) (dotted); ZIF without correction (green line); DLS extrapolated concentration 0 mg/mL (red square), 30 mg/mL (circle); PFG-NMR self-diffusion D_s (blue diamond). It should be noted that the self-part corrected ZIF (green dashed line) fits well to D_s . The self-part D_s/D_0 correction is noticeable as a difference between solid and dashed green lines. Reprinted from ref [6] Licensed under CC-BY 4.0

the collective D_{eff} increases due to $H(Q)/S(Q)$ correction reflecting $S(Q)$ and hydrodynamic interactions. At larger Q above 0.5 nm^{-1} we observe self diffusion ($S(Q) \approx 1$) with an approximate linear increase as predicted for Zimm dynamics $D_{eff} \propto kT/\eta$ [10] of neutral chains. Above 1 nm^{-1} dynamics slows down due to internal friction. The charged chain behaves on segment length scale independently of charge or screening salt like a neutral chain expanded according to ν .

14.7 Protein domain motions

To explore the internal dynamics of fragments or domains we use a Langevin equation similar to (14.12). Different to the polymer models we have to take into account all neighbours

in the direct vicinity of beads, representing e.g. amino acids, which have e.g. hydrophobic contacts. The connectivity matrix (14.13) contains more off-diagonal elements representing interacting beads. Tirion has shown that a simplified elastic force field is enough to describe the slowest large scale motions [32]. With this in mind we assume Brownian motion of the protein atoms in a harmonic potential around the equilibrium positions, a problem described by the Ornstein-Uhlenbeck process [33, 34]. The coherent intermediate scattering function is (for details see appendix A14.2)

$$F_{\text{int}}(Q, t) = \left\langle \sum_{\alpha, \beta} b_{\alpha} b_{\beta} \exp(i\mathbf{Q} \cdot \mathbf{R}_{\beta}^{\text{eq}}) \exp(-i\mathbf{Q} \cdot \mathbf{R}_{\alpha}^{\text{eq}}) \cdot f_{\alpha\beta}(Q, \infty) \cdot f'_{\alpha\beta}(Q, t) \right\rangle. \quad (14.25)$$

Here $f_{\alpha\beta}(Q, \infty)$ is a time independent factor determined by the internal forces. The time dependent part is

$$f'_{\alpha\beta}(Q, t) = \exp\left(\sum_{j=1 \dots 3N} (\mathbf{v}_{\alpha} \cdot \mathbf{Q})(\mathbf{v}_{\beta} \cdot \mathbf{Q}) \exp(-\lambda_j t)\right) \quad (14.26)$$

with displacements $v_{j\alpha} = \sqrt{k_{\text{B}}T/(\lambda_j \Gamma_j)} \hat{b}_{j\alpha}$ in Brownian normal mode j with relaxation time $1/\lambda_j$ and friction Γ_j . The contribution of internal dynamics to the NSE signal is $F_{\text{int}}(Q, t)/F_{\text{int}}(Q, 0)$. The dynamics of single independent particles or subunits can be described by the much simpler function

$$F_{\text{int}}(Q, t) = \exp(-Q^2 \langle u^2 \rangle (1 - \exp(-\lambda t))) \quad (14.27)$$

with the mean square displacement $\langle u^2 \rangle$ in the harmonic potential [17]. Nevertheless, in this simplification, the specific arrangement of the conformation is lost.

Looking at the time dependence we find again the pattern $\exp(\dots(1 - e^{-\lambda t}))$ observed in Rouse. Expanding the first exponential in equation (14.26) as $\exp(x) = 1 + x$ we get a simplification for small displacements

$$f'_{\alpha\beta}(Q, t) = 1 + \sum_{j=1 \dots 3N} (\mathbf{v}_{\alpha} \cdot \mathbf{Q})(\mathbf{v}_{\beta} \cdot \mathbf{Q}) \exp(-\lambda_j t) \quad (14.28)$$

showing that the amplitude is directly related to the displacements of the modes. Using $F(Q, t)/F(Q, 0)$ for the measured NSE signal we find with $B = \sum_{j=1 \dots 3N} (\mathbf{v}_{\alpha} \cdot \mathbf{Q})(\mathbf{v}_{\beta} \cdot \mathbf{Q})$ and $A = B/(1 + B)$ assuming a single relaxation rate λ

$$\frac{F(Q, t)}{F(Q, 0)} = [(1 - A) + Ae^{-\lambda t}] \frac{F_{\text{trans}}(Q, t) \cdot F_{\text{rot}}(Q, t)}{F_{\text{trans}}(Q, 0) \cdot F_{\text{rot}}(Q, 0)} \quad (14.29)$$

14.8 Between chain dynamics and domain motions: intrinsically disordered proteins

The biological role of the IPD is founded in their high conformational adaptivity, enabling them to respond rapidly to environmental changes, in the flexibility of their associative properties allowing them to fold into different states depending on partner molecules. For these

properties the dynamics is essential. Myelin basic protein (MBP) is a major component of the Myelin sheets in the central nervous system [13]. Among the several isoforms the major human and bovine isoform the 18.5 kDa form with 170 amino acids was investigated. In the human body MBP is of significant importance as there are many neurological disorders such as multiple sclerosis that are related to MBP malfunction. Lipid free MBP is not completely unfolded but retains some elements of the alpha helix and beta sheet (about 60 % of the protein is unfolded) [25].

Since the intrinsic disorder prevents crystallographic structure determination, only low-resolution SANS and SAXS information about the average structure in the disordered state exists. Figure 14.5A and B display X-ray and neutron form factors of MBP. Both data show a power law decay at $Q > 1.0 \text{ nm}^{-1}$ with power law coefficients of ≈ -2 , which is characteristic for Gaussian chain polymers in theta solvents. Figure 14.6 displays NSE spectra from 54 mg/ml solutions. Inspecting Figure 14.6A already with a naked eye the two-component structure of the NSE spectra at Q -values above 0.9 nm^{-1} is visible. Thus, we deal with long time rigid body motion augmented by internal dynamics with relaxation times below 10 ns.

As the SAS data could be reasonably well described by a Debye form factor, Gaussian chain statistics with $\nu = 0.5$ and an end-to-end distance $R_e = \sqrt{6}R_g = 8.08 \text{ nm}$ was employed. With this approach the first Zimm mode corresponding to the rotational relaxation time equals to $\tau_1 = 73.9 \text{ ns}$. Fig. 14.6B display the results of the ZIF description – the translational diffusion coefficient was adapted to the experimental values from DLS. The solid lines in Figure Fig. 14.6B show the improved result of ZIF compared to Zimm model. A large value for the internal friction $\tau_1 = 81.6 \pm 4 \text{ ns}$ is imposed, that is longer than the first mode relaxation time. The internal friction dominates all higher relaxation times to such an extent that the limiting value τ_1 is quickly approached and the $\tau_p \sim p^{-3/2}$ signature of the Zimm model is lost. As a second approach a structural ensemble evaluated from a inverse Monte Carlo simulation (EOM [3]) was used to interpret the full NSE spectra. We found elongated structures with a relatively compact core and flexible ends on both sites similar to Figure 14.5C. The most probable structure was used for normal mode analysis as rigid protein. On this basis the Q -dependent effective diffusion coefficient D_0 was calculated. For the translational and rotational diffusion coefficients $D_T = 3.7 \pm 0.2 \text{ \AA}^2/\text{ns}$ and $D_R = 2.35 \pm 0.36 \times 10^6 \text{ s}^{-1}$ were found. The corresponding average rotational correlation time $\tau_R = 1/(6D_{R0}) = 70.9 \text{ ns}$. The calculated translational diffusion coefficients agree well with the DLS results at infinite dilution.

Using equation (14.29), a Q -dependent motional amplitude $A(Q)$ and an internal mode relaxation time were evaluated. The fit results from the structural model to the NSE spectra are displayed in Figure Fig. 14.6A up to 40 ns. The contribution of the internal protein motion to the spectra becomes directly visible. The results for the Q -dependent amplitude are displayed in Figure 14.5D. For the characteristic internal relaxation time $1/\lambda_{\text{int}} = 8.4 \pm 2.0 \text{ ns}$ is found for the whole structural ensemble.

Given the structural information as well as the spectral line shapes it is not surprising that the polymer approach does not work. The motions of MBP are significantly slower than that of a Gaussian polymer of the same size in solution. Thus, for MBP the structural ensemble gives a significantly better realization of the dynamics as the polymer model. The lowest soft collective excitations of the structural model, as they are revealed by the normal mode analysis, are displayed in Figure 14.5C. Normal mode 7 and 8 correspond to bending and

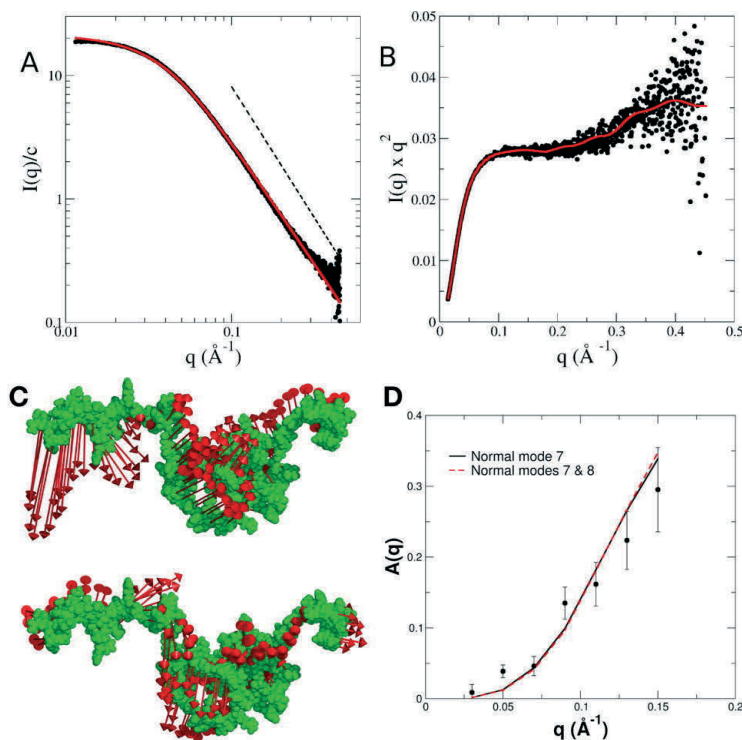


Fig. 14.5: Small angle scattering data from MBP (A) SAXS data at 4.5 mg/ml. (B) SANS results extrapolated to infinite dilution. The solid lines in (A) are fits with the Debye equation for a Gaussian chain with $R_g = 3.38$ nm. Power law scattering is indicated above $Q > 1$ nm $^{-1}$ by dashed lines. (C) Kratky plot of the SAXS data. The line is a result of the scattering from the most probable conformational ensembles. (C) Displacement pattern of the normal modes 7 (upper part) and 8 (lower part) from a structural model. The lengths of the vectors are increased for better visibility. (C) Amplitude of the internal protein dynamics as obtained from the fit. The solid and dashed lines are the calculated mode amplitude according to equation 4. Reprinted with permission from ref. 30.

stretching motions of the structural model. With these modes the internal dynamics amplitude $A(Q)$ was calculated and is compared with the experimental values in Figure 14.5D. As may be seen mode 7 is dominating and fully reproduces the observed $A(Q)$. The displacement patterns indicate that the center part of MBP remains rather rigid, while the termini are flexible.

14.9 Domain dynamics of antibodies

Specificity and constancy cause the high potential of antibodies to be used in immunotherapy or to develop new specific drugs targeting specific cells for inhibition/activation of cell processes. IgG are the major antibody class, large molecules of 150 kDa composed of four pep-

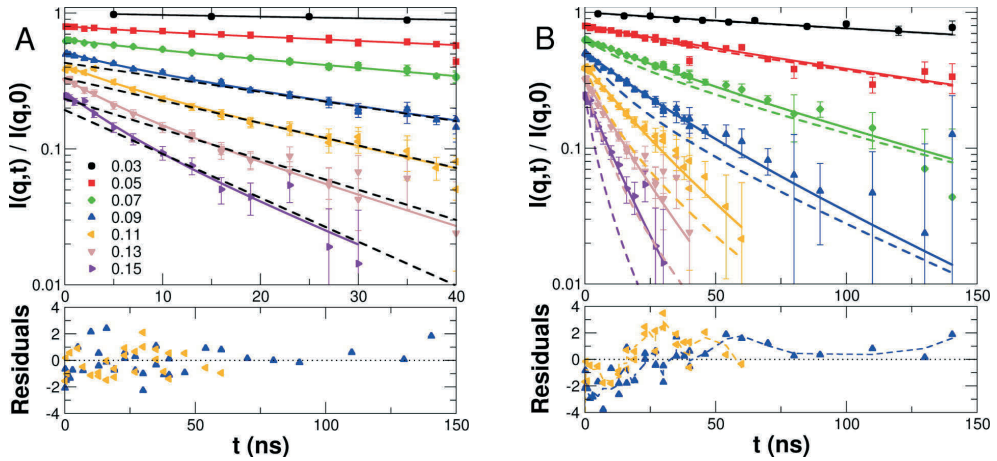


Fig. 14.6: NSE Data for MBP: All spectra start at unity but are shifted consecutively by a factor of 0.8 for clarity. The residuals of the displayed fits are given for $Q=0.9$ and 1.1 nm^{-1} below the graphs. (A) Solid lines are fits to the NSE data with the structural model. The dashed lines are exponential fits for $t > 20 \text{ ns}$ to extrapolate the long time rigid body dynamics. A clear separation between the internal and the global dynamics is obvious. (B) The dashed lines are a result of the Zimm model. The solid lines represent a fit with a ZIF model. Reprinted with permission from ref. 30.

tide chains: two identical heavy chains of 50 kDa and two identical light chains of 25 kDa, in a Y-shaped structure (Figure 14.7). The conformational dynamics of IgG results from a functional important hinge region as a loose section of the polypeptide chain that links the Fc and Fab domains.

We used X-ray scattering to investigate the configurations of IgG in solution in a concentration range between 3 and 26.4 mg/ml as shown in Figure 14.7 right [31]. As approved by analytical ultracentrifugation the solution contains monomer and dimers, which is common for antibodies in solution as there is a tendency to build oligomers. Dimers with a head-head configuration are proposed [9]. Modelling of mixtures between monomers and dimers, including a flexible hinge region in the centre, allows to fit the SAXS form factor as shown in Figure 14.7, right. The dimers show still flexibility in the hinge. Figure 14.8 displays the intermediate scattering function $I(Q,t)/I(Q,t=0)$ as measured by NSE. Already by simple inspection, a clear deviation from a simple diffusion process is observed on short times. Fitting the data by the corresponding single exponential decay $I(Q,t)/I(Q,t=0) = \exp(-D_{\text{eff}}Q^2t)$ one can see a proper fit for long times t with an effective diffusion coefficient D_{eff} . The effective diffusion is shown on the right. On a ten-nanosecond scale, clear indications for a faster relaxation can be observed, which we attribute to motions within the molecule.

The 6×6 diffusion tensor \mathbf{D} was calculated by HYDROPRO on basis of a valid PDB conformation [22]. As result we get additionally the scalar diffusion coefficients D_{T0} and D_{R0} for the monomer and dimer. The rotational correlation times $\tau_r = 1/6D_{R0}$ for the monomer and dimer are on a scale of 260 ns^{-1} respectively 500 ns^{-1} and are longer than the translational

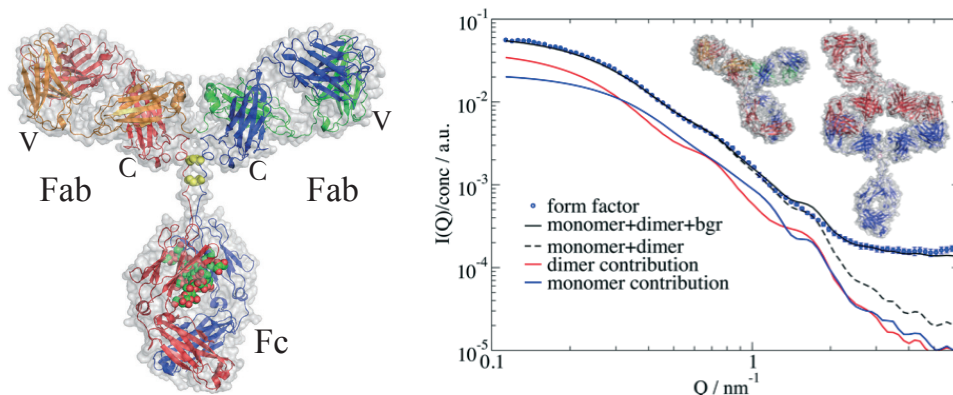


Fig. 14.7: Left: Immunoglobulin G1 with Fc and two Fab fragments with the van der Waals surface in grey. The Fc fragment is built from parts of the heavy chains (red and blue cartoon) and the glycans (red and green spheres) between the two heavy chains. Fab fragments are built from heavy and light chains (orange and green cartoon) with a hinge between the variable region (V) and the constant region (C) of the Fab fragment. The heavy chains are connected in the linker region by two disulfide bonds (yellow spheres). The structure displayed is based on the human IgG1 structure IgG-ALL.pdb of Padlan [23]. Right: The SAXS form factor with the fit result. The form factor fit includes $52 \pm 4\%$ monomer as monomer and $48 \pm 4\%$ monomer in dimers and a background contribution (bgr). The dashed line shows the combined monomer-dimer scattering, the red line shows the contribution of the dimer, while the blue line shows the monomer; all without the residual background. Reprinted from ref. 31 Licensed under CC-BY 4.0

diffusion times. Therefore, we can extract the effective diffusion $D_{\text{eff}}(Q)$ comprising translational and rotational contributions of the overall protein by applying a single exponential fit for times $t > 15$ ns. The result is shown in Figure 14.8 together with the DLS result for the same concentration as used for NSE measurement. We use equation (14.30) and the 6×6 diffusion tensor \mathbf{D} together with the monomer and dimer structure to calculate $D_0(Q)$ of the rigid structures (see inset in Figure 14.8). The increase from low Q to the higher Q values results from the stronger visibility of the rotational diffusion if the observation length scale $2\pi/Q$ reaches the size of the protein. At low Q we see only the translational diffusion as measured by DLS. The expected diffusion $D_{\text{eff}}(Q)$ of the monomer/dimer mixture can be calculated as the average of monomer and dimer diffusion weighted by the scattering contribution to the form factor as shown in Figure 14.7. To include the hydrodynamic effects, the translational contribution $D_{\text{eff}}(Q=0)$ is corrected by $H_t(Q=\infty) = 0.66$ as calculated from viscosity and correspondingly the rotational diffusion contribution $D_{\text{eff}}(Q) - D_{\text{eff}}(Q=0)$ as described above by H_r . It needs to be emphasised that the excellent agreement is not a fit but based on additional measurement and model calculations. The specific structure of IgG with three nearly equal sized fragments connected by flexible linkers suggests a simple model of three fragments within a harmonic potential. The flexible linkers may act as springs fixing the relative equilibrium position of the fragments but allowing fluctuations around the equilibrium position.

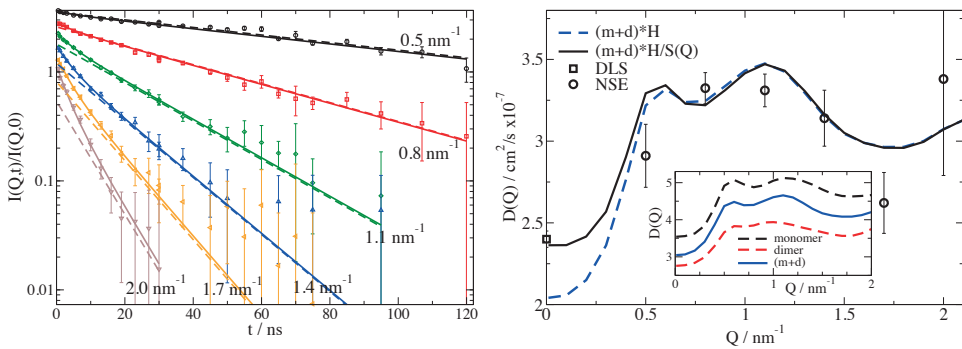


Fig. 14.8: $I(Q, t)/I(Q, 0)$ of IgG. Spectra were shifted for clarity. Solid lines represent the fit by (14.7) with contributions from translational and rotational diffusion from (14.8) and internal dynamics described in section (14.7) using 3 degrees of freedom for each domain. Dashed lines correspond to the contribution of translational and rotational diffusion and are close to a single exponential for $t > 15$ ns. Right: Effective diffusion coefficient D_{eff} for long Fourier times at a concentration of 29 mg/ml for NSE and DLS. The dashed blue line shows the result for $D_{\text{eff}}(Q)$ as a mixture between monomer and dimer including $H(Q)$. The black solid line includes additionally the $1/S(Q)$ correction. The inset shows the diffusion coefficients for monomer and dimer with the intensity averaged $D_{\text{eff}}(Q)$. Reprinted from ref. 31 Licensed under CC-BY 4.0

We use a reduced set of obvious displacements patterns and consider three perpendicular vectors of unit length for each of the three fragments. One is aligned parallel to the linker from the IgG centre of mass to a fragment centre of mass and two further aligned perpendicular to this. Overall this represents nine degrees of freedom. Using equation (14.25)ff we find an excellent description of the data as shown in Figure 14.8 left. The additional information beyond the amplitude and the relaxation time are the force constant of the harmonic potential and the relevant friction for the Ornstein-Uhlenbeck process. We find a force constant of about 10 pN/nm and a friction of about 40000 g/ps/mol. The friction corresponds to the friction exerted from the water on a single free fragment. The force constant is comparable to the force of an entropic spring of the same length as the linker from the centre to the fragment (about 8 amino acids). Concluding, we observe that even short linkers act as an entropic spring for the fragments allowing the highest degree of mobility with a large configurational freedom.

14.10 Summary

The macroscopic properties of polymers and the function of biopolymers can be explained on the basis of their microscopic dynamics. To explore the latter, inelastic neutron scattering is the most important experimental technique as it covers the necessary length- and time scales. Especially, neutron spin echo spectroscopy is useful as its time range allows observing the slow motions of polymer chains. A further advantage of neutron scattering is that it allows the selective study of regions of the polymer chain by means of isotopic labelling.

Appendices

A14.1 Diffusion of rigid globular macromolecules

The effective diffusion of rigid macromolecules like proteins can be calculated by

$$D_0(Q) = \frac{1}{Q^2 F(Q)} \sum_{j,k} \langle b_j e^{-iQr_j} \begin{pmatrix} Q \\ r_j \times Q \end{pmatrix} D_{6 \times 6} \begin{pmatrix} Q \\ r_j \times Q \end{pmatrix} b_k e^{-iQr_k} \rangle \quad (14.30)$$

with $F(Q) = \langle \sum_{j,k} b_j b_k e^{-Q(r_j - r_k)} \rangle$ as formfactor of a atomic configuration with atom positions r_i and coherent scattering length b_i . $D_{6 \times 6} = \begin{pmatrix} D_{TT} & D_{TR} \\ D_{TR} & D_{RR} \end{pmatrix}$ is the 6×6 diffusion matrix.

A14.2 Brownian motion of the fragments in a harmonic potential

In the following, we consider Brownian motion in a harmonic potential around the equilibrium position, a problem described by the Ornstein-Uhlenbeck process [33, 34] and follow refs. [16, 17] in the derivation of the corresponding correlation function for coherent neutron scattering $F_{\text{coh}}(Q, t)$. Restricting the analysis to the internal coordinates of the protein, the translational and rotational degrees of freedom are separated. The rotational and translational degrees of freedom are described by rotational and translational diffusion, which can be treated within the decoupling approximation according to equation (2) and equation (3). The coherent intermediate scattering function $F_{\text{coh}}(Q, t)$ of atoms or subunits α with coherent scattering length b_α at positions b_α describing our internal dynamics can be written as

$$F_{\text{int}}(Q, t) = \left\langle \sum_{\alpha, \beta} b_\alpha b_\beta \exp(i\mathbf{Q} \cdot \mathbf{R}_\beta^{\text{eq}}) \exp(-i\mathbf{Q} \cdot \mathbf{R}_\alpha^{\text{eq}}) \right\rangle \quad (14.31)$$

For larger subunits or coarse graining, the scattering amplitude can be substituted by Q dependent scattering amplitude. With displacements \mathbf{u}_α from the time independent equilibrium position $\mathbf{R}_\alpha^{\text{eq}}$ we can use $\mathbf{R}_\alpha = \mathbf{R}_\alpha^{\text{eq}} + \mathbf{u}_\alpha(t)$ and $f_{\alpha\beta}(Q, t) = \langle \exp(-i\mathbf{Q} \cdot (\mathbf{u}_\alpha(0) - \mathbf{u}_\beta(t))) \rangle$ resulting in

$$F_{\text{int}}(Q, t) = \left\langle \sum_{\alpha, \beta} b_\alpha b_\beta \exp(i\mathbf{Q} \cdot \mathbf{R}_\beta^{\text{eq}}) \exp(-i\mathbf{Q} \cdot \mathbf{R}_\alpha^{\text{eq}}) \cdot f_{\alpha\beta}(Q, t) \right\rangle. \quad (14.32)$$

We describe the internal dynamics by a Langevin type equation $\ddot{x} + \gamma\dot{x} + \kappa x = f_s(t)$ as with position vector x , friction matrix γ , force constant matrix κ and random acceleration $f_s(t)$ in mass weighted coordinates and mass weighted friction and force constants [17]. In the case of vanishing friction ($\gamma = 0$), normal mode analysis with the eigenequation

$\kappa \hat{e}_j = \omega_j^2 \hat{e}_j$ of eigenvalues ω_j^2 and eigenvectors \hat{e}_j results in oscillating solutions describing vibrational motion. Here, we restrict ourselves to the highly overdamped case of high friction with a negligible acceleration term \ddot{x} . The high friction solution of Smoluchowski dynamics is solved by the eigenequation $\gamma^{-1} \kappa \hat{b}_i = \lambda_j \hat{b}_i$ of eigenvalues λ_j and eigenvectors \hat{b}_j with characteristic exponentially decaying solutions. For details about the derivation of low and high friction limits see Kneller et al. [16]. According to the nature of the modes, the \hat{e}_i are called elastic or vibrational normal modes, while the \hat{b}_i are called brownian normal modes indicating that the Brownian motion characterizes the modes and eigenvalues.

Using the normal modes we may decompose the last term $f_{\alpha\beta}(Q, t)$ in equation (14) in a constant term and a term describing the time dependence

$$f_{\alpha\beta}(Q, t) = f_{\alpha\beta}(Q, \infty) \cdot f'_{\alpha\beta}(Q, t). \quad (14.33)$$

The constant term is related to the vibrational modes and only dependent on the harmonic potential as

$$f_{\alpha\beta}(Q, \infty) = \exp\left(-\sum_{j=1\dots 3N} \frac{1}{2} ((d_{j\alpha}Q)^2 + (d_{j\beta}Q)^2)\right) \quad (14.34)$$

$$f_{\alpha\beta}(Q, 0) = \exp\left(-\sum_{j=1\dots 3N} \frac{1}{2} ((d_{j\alpha} - d_{j\beta})Q)^2\right) \quad (14.35)$$

with vibrational displacement $d_{j\alpha} = \sqrt{\frac{k_B T}{m_\alpha \Gamma_j}} \hat{e}_{j\alpha}$ of subunit α in normal mode j . $d_{j\alpha}$ is the displacement vector that corresponds to the width in a Gaussian distribution around equilibrium configuration R_α^{eq} in the harmonic potential with force constant $k_j = m\omega_j^2$ along normal mode j .

In the high friction limit the time dependent part within Smoluchowski dynamics is described by

$$f'_{\alpha\beta}(Q, t) = \exp\left(\sum_{j=1\dots 3N} (v_\alpha Q)(v_\beta Q) \exp(-\lambda_j t)\right) \quad (14.36)$$

with displacements $v_{j\alpha} = \sqrt{\frac{k_B T}{\lambda_j \Gamma_j}} \hat{b}_{j\alpha}$ of subunit α in Brownian normal mode j and friction $\Gamma_j = \hat{b}_j^T \gamma \hat{b}_j$. v_j is the displacement vector within relaxation time $1/\lambda_j$. A force constant can be estimated by $k_j = \lambda_j \Gamma_j$. We assume the friction matrix γ to be diagonal and zero off diagonal terms [14]. For equal valued diagonal friction matrix, the vibrational and Brownian modes are equal and mode displacements can be used to calculate the displacement between the fragments. Friction with the solvent may be attributed to surface subunits but can also be equally distributed for rigid domains for simplicity. For independent relaxing modes the mean square displacement is $msd = \sum_j \frac{1}{N} \sum_\alpha v_\alpha^2$.

The coherent intermediate scattering function describing the internal dynamics is finally

$$F_{\text{int}}(Q, t) = \left\langle \sum_{\alpha, \beta} b_\alpha b_\beta \exp(i\mathbf{Q} \cdot \mathbf{R}_\beta^{\text{eq}}) \exp(-i\mathbf{Q} \cdot \mathbf{R}_\alpha^{\text{eq}}) \cdot f_{\alpha\beta}(Q, \infty) \cdot f'_{\alpha\beta}(Q, t) \right\rangle. \quad (14.37)$$

The contribution of internal dynamics to the NSE signal can be calculated accordingly by

$$\frac{F_{\text{int}}(Q, t)}{F_{\text{int}}(Q, 0)} = \frac{\left\langle \sum_{\alpha, \beta} b_{\alpha} b_{\beta} \exp(i\mathbf{Q} \cdot \mathbf{R}_{\beta}^{\text{eq}}) \exp(-i\mathbf{Q} \cdot \mathbf{R}_{\alpha}^{\text{eq}}) \cdot f_{\alpha\beta}(Q, \infty) \cdot f'_{\alpha\beta}(Q, t) \right\rangle}{\left\langle \sum_{\alpha, \beta} b_{\alpha} b_{\beta} \exp(i\mathbf{Q} \cdot \mathbf{R}_{\beta}^{\text{eq}}) \exp(-i\mathbf{Q} \cdot \mathbf{R}_{\alpha}^{\text{eq}}) \cdot f_{\alpha\beta}(Q, \infty) \cdot f'_{\alpha\beta}(Q, 0) \right\rangle}. \quad (14.38)$$

The close similarity of numerator and denominator let us perceive that the dominating term describing the time evolution is of the form $\exp(\dots \exp(-\dots t))$. In fact, for the case of a single independent particle in a harmonic trap, the dynamics can be described by the much simpler function shown in equation 14.27.

References

- [1] C W J Beenakker and P Mazur. Self-diffusion of spheres in a concentrated suspension. *Physica A: Statistical Mechanics and its Applications*, 120(3):388–410, 1983.
- [2] C.W.J. Beenakker and P. Mazur. Diffusion of spheres in a concentrated suspension II. *Physica A: Statistical Mechanics and its Applications*, 126(3):349–370, jul 1984.
- [3] Pau Bernadó, Efstratios Mylonas, Maxim V Petoukhov, Martin Blackledge, and Dmitri I Svergun. Structural Characterization of Flexible Proteins Using Small-Angle X-ray Scattering. *Journal of the American Chemical Society*, 129(17):5656–5664, 2007.
- [4] R Biehl and D Richter. Slow internal protein dynamics in solution. *Journal of Physics: Condensed Matter*, 26(50):503103, nov 2014.
- [5] Ralf Biehl, Bernd Hoffmann, Michael Monkenbusch, Peter Falus, Sylvain Prévost, Rudolf Merkel, and Dieter Richter. Direct Observation of Correlated Interdomain Motion in Alcohol Dehydrogenase. *Physical Review Letters*, 101(13):138102, sep 2008.
- [6] Ekaterina Buvalaia, Margarita Kruteva, Ingo Hoffmann, Aurel Radulescu, Stephan Förster, and Ralf Biehl. Interchain Hydrodynamic Interaction and Internal Friction of Polyelectrolytes. *ACS Macro Letters*, 22:1218–1223, 8 2023.
- [7] Ryan R Cheng, Alexander T Hawk, and Dmitrii E Makarov. Exploring the role of internal friction in the dynamics of unfolded proteins using simple polymer models. *The Journal of chemical physics*, 138(7):074112, 2013.
- [8] Vittorio Degiorgio, Roberto Piazza, and Robert B Jones. Rotational diffusion in concentrated colloidal dispersions of hard spheres. *Phys. Rev. E*, 52(3):2707—2717, sep 1995.
- [9] Galahad Deperalta, Melissa Alvarez, Charity Bechtel, Ken Dong, Ross McDonald, and Victor Ling. Structural analysis of a therapeutic monoclonal antibody dimer by hydroxyl radical footprinting. *mAbs*, 5(1):86–101, jan 2012.
- [10] M. Doi and S. F. Edwards. *The theory of polymer dynamics*. Clarendon Press, 1988.

- [11] Christine Gerstl, Gerald J. Schneider, Wim Pyckhout-Hintzen, Jürgen Allgaier, Sabine Willbold, Diana Hofmann, Ulrich Disko, Henrich Frielinghaus, and Dieter Richter. Chain conformation of poly(alkylene oxide)s studied by small-angle neutron scattering. *Macromolecules*, 44(15):6077–6084, 8 2011.
- [12] Boualem Hammouda. SANS from homogeneous polymer mixtures: A unified overview, 1993.
- [13] George Harauz, Noboru Ishiyama, Christopher M.D Hill, Ian R. Bates, David S. Li-bich, and Christophe Farès. Myelin basic protein—diverse conformational states of an intrinsically unstructured protein and its roles in myelin assembly and multiple sclerosis. *Micron*, 35(7):503–542, oct 2004.
- [14] Konrad Hinsén, Andrei-Jose Petrescu, Serge Dellerue, Marie-Claire Bellissent-Funel, and Gerald R. Kneller. Harmonicity in slow protein dynamics. *Chemical Physics*, 261(1-2):25–37, nov 2000.
- [15] R. Inoue, R. Biehl, T. Rosenkranz, J. Fitter, M. Monkenbusch, A. Radulescu, B. Farago, and D. Richter. Large domain fluctuations on 50-ns timescale enable catalytic activity in phosphoglycerate kinase. *Biophysical Journal*, 99(7):2309–2317, 2010.
- [16] Gerald R. Kneller. Inelastic neutron scattering from damped collective vibrations of macromolecules. *Chemical Physics*, 261(1):1–24, 2000.
- [17] Gerald R. Kneller. Quasielastic neutron scattering and relaxation processes in proteins: analytical and simulation-based models. *Physical chemistry chemical physics : PCCP*, 7(13):2641–55, jul 2005.
- [18] M. Krutyeva, A. Wischnewski, M. Monkenbusch, L. Willner, J. Maiz, C. Mijangos, A. Arbe, J. Colmenero, A. Radulescu, O. Holderer, M. Ohl, and D. Richter. Effect of nanoconfinement on polymer dynamics: Surface layers and interphases. *Physical Review Letters*, 110(10):108303, 3 2013.
- [19] HM Lindsay, R Klein, DA Weitz, MY Lin, and P Meakin. Effect of rotational diffusion on quasielastic light scattering from fractal colloid aggregates. *Physical Review A*, 38(5):2614–2626, 1988.
- [20] P Mazur and W Van Saarloos. Many-sphere hydrodynamic interactions and mobilities in a suspension. *Physica A: Statistical Mechanics and its Applications*, 115:21–57, sep 1982.
- [21] F. Mezei, C. (Catherine) Pappas, and T. (Thomas) Gutberlet. *Neutron spin echo spectroscopy : basics, trends, and applications*. Springer, 2003.
- [22] A Ortega, D Amorós, JG de la Torre, and J García de la Torre. Prediction of Hydrodynamic and Other Solution Properties of Rigid Proteins from Atomic- and Residue-Level Models. *Biophysical Journal*, 101(4):892–898, 2011.
- [23] Eduardo A. Padlan. Anatomy of the antibody molecule. *Molecular Immunology*, 31(3):169–217, feb 1994.

- [24] Paul J. Flory. *Statistical Mechanics of Chain Molecules*. Interscience, New York, 1969.
- [25] Eugenia Polverini, Anna Fasano, Francesco Zito, Paolo Riccio, and Paolo Cavatorta. Conformation of bovine myelin basic protein purified with bound lipids. *European Biophysics Journal*, 28:351–355, 1999.
- [26] P N Pusey. The dynamics of interacting Brownian particles. *Journal of Physics A: Mathematical and General*, 8(9):1433–1440, 1975.
- [27] D. Richter, B. Ewen, B. Farago, and T. Wagner. Microscopic dynamics and topological constraints in polymer melts: A neutron-spin-echo study. *Physical Review Letters*, 62(18):2140, 5 1989.
- [28] D Richter, • M Monkenbusch, •a Arbe, • J Colmenero, • M Monkenbusch, • A Arbe, and • J Colmenero. Neutron Spin Echo in Polymer Systems. *Advances in Polymer Science*, 174:1–221, 2005.
- [29] Prince E. Rouse. A theory of the linear viscoelastic properties of dilute solutions of coiling polymers. *The Journal of Chemical Physics*, 21(7):1272–1280, 7 1953.
- [30] Andreas M Stadler, Laura Stingaciu, Aurel Radulescu, Olaf Holderer, Michael Monkenbusch, Ralf Biehl, and Dieter Richter. Internal nanosecond dynamics in the intrinsically disordered myelin basic protein. *Journal of the American Chemical Society*, 136(19):6987–94, may 2014.
- [31] Laura R. Stingaciu, Oxana Ivanova, Michael Ohl, Ralf Biehl, and Dieter Richter. Fast antibody fragment motion: flexible linkers act as entropic spring. *Scientific Reports*, 6:22148, mar 2016.
- [32] Tirion and Monique M Tirion. Large Amplitude Elastic Motions in Proteins from a Single-Parameter, Atomic Analysis. *Phys Rev Lett*, 77(9):1905–1908, aug 1996.
- [33] G. Uhlenbeck and L. Ornstein. On the Theory of the Brownian Motion. *Physical Review*, 36(5):823–841, sep 1930.
- [34] Ming Wang and G. Uhlenbeck. On the Theory of the Brownian Motion II. *Reviews of Modern Physics*, 17(2-3):323–342, apr 1945.
- [35] Bruno H. Zimm. Dynamics of Polymer Molecules in Dilute Solution: Viscoelasticity, Flow Birefringence and Dielectric Loss. *The Journal of Chemical Physics*, 24(2):269–278, 2 1956.

Exercises

Note: Exercises are labelled by stars (* through ***) indicating the level of difficulty. Try to solve the easier ones first.

E14.1 Scaling arguments

(a **) You may have noticed that no firm definition of the average segment length l has been given. Related to this, there is no fixed relation between the number of segments N and well-defined quantities as the degree of polymerisation or the molecular weight. On the first thought, this casts some doubts on results as (14.39).

$$\eta = \frac{\zeta l^2 \rho N}{36} \propto N \quad (14.39)$$

$$D = \frac{k_B T}{\zeta N} \propto N^{-1} \quad (14.40)$$

But on a closer look it turns out that the limiting results of the Rouse model are independent of the choice of l . When l is replaced by $l' = \alpha l$, one can replace N , ζ , and ρ in such a way that all macroscopic results remain unchanged. Show this for the end-to-end distance $R_e^2 = Nl^2$ and equations (14.39), (14.40), and (14.18).

(b *) In the pre-CGI days of King Kong and Godzilla filmmakers sometimes used scaled-down mechanised models of the monsters for the scenes where these deal out destruction, e.g. by tearing down houses. These scenes were often taken in slow motion to make them look more realistic. Why? What slow-motion factor would be (theoretically) appropriate if the monster is scaled down 1 : 25.

E14.2 Internal friction

(c *) Assume we find in the ZIF model an internal friction time τ_i roughly equal to the Zimm time τ_Z for MBP with 170 residues and $\nu \approx 0.5$. Calculate the ratio of internal and solvent friction of a bead ζ_i/ζ for $\nu = 0.5$.

Discuss the case when $\zeta_i/\zeta = 1$. Can the internal friction time be measured? If yes where and why is this difficult?

E14.3 R_g/R_h

(d *) Dynamic light scattering measures the low Q diffusion coefficient which is often interpreted as hydrodynamic radius R_h of a sphere with same diffusion coefficient $D = k_B T / 6\pi\eta R_h$. SAXS or SANS result in R_g . What is R_h/R_g for a Gaussian chain in solvent? What is the ratio for a sphere with $R_g^2 = 3/5 R^2$. Are conclusions from R_h/R_g e.g. from DLS and SAXS unambiguous? How do you substantiate a statement?

15 Applications of Neutron Scattering - an Overview

Th. Brückel
Jülich Centre for Neutron Science 2
Forschungszentrum Jülich GmbH

Contents

15.1	Introduction	2
15.2	Scattering and correlation functions	4
15.3	The generic scattering experiment	8
15.4	Diffractometers	9
15.4.1	Wide angle diffraction versus small angle scattering	10
15.4.2	Small angle neutron scattering SANS	11
15.4.3	Large scale structures: Reflectometry	18
15.4.4	Atomic structures: Single crystal and powder neutron diffraction.....	24
15.5	Spectroscopy	27
15.5.1	Time-of-Flight or TOF spectroscopy	27
15.5.2	Triple axis spectroscopy	30
15.5.3	High resolution spectroscopy	32
15.6	Summary and conclusions	34
	References	37
	Exercises	38

15.1 Introduction

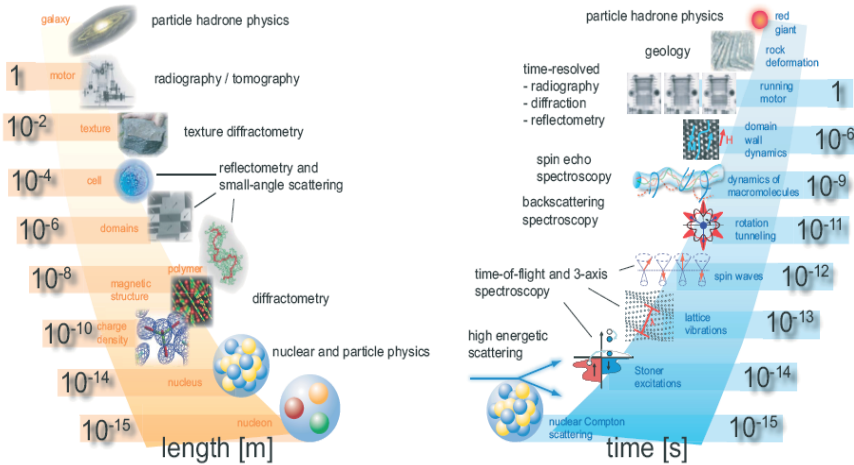


Fig. 15.1: Length- and time scales covered by research with neutrons giving examples for applications and neutron techniques [1].

Research with neutrons covers an extraordinary range of length- and time scales as depicted in figure 15.1. The very extremes of length scales - below 10^{-12} m - are the domain of nuclear and particle physics, where e. g. measurements of the charge or electric dipole moment of the neutron provide stringent tests of the standard model of particle physics without the need of huge and costly accelerators. On the other extreme, neutrons also provide information on length- and time scales relevant for astronomical dimensions, e. g. the decay series of radioactive isotopes produced by neutron bombardment give information on the creation of elements in the early universe. In this course, however, we are only concerned with neutrons as a probe for condensed matter research and therefore restrict ourselves to a discussion of neutron scattering. Still, the various neutron scattering and imaging techniques cover an area in phase space from picometers pm up to meters and femtoseconds fs up to hours, a range, which probably no other probe can cover to such an extent.

Different specialized neutron scattering techniques are required to obtain structural information on different length scales:

- With *wide angle neutron diffractometry*, magnetization densities can be determined within single atoms on a length scale of about 10 pm^1 . The position of

¹ In this sense, neutrons are not only nanometer nm probes, but even picometer pm probes!

atoms can be determined on a similar length scale, while distances between atoms lie in the 0.1 nm range².

- The sizes of large macromolecules, magnetic domains or biological cells lie in the range of nm to μm or even mm. For such studies of large scale structures, one applies *reflectometry* or *small angle scattering* techniques.
- Most materials relevant for engineering or geo-science occur neither in form of single crystals, nor in form of fine powders. Instead they have a grainy structure, often with preferred orientation of the grains. This so-called texture determines the macroscopic strength of the material along different directions. *Texture diffractometry* as a specialized technique allows one to determine this grainy structure on length scales of up to mm.
- Finally, for even larger structures, one uses imaging techniques, such as neutron *radiography* or *tomography*, which give a two-dimensional projection and full 3-dimensional view, respectively, into the interior of a sample due to the attenuation of the neutron beam, the phase shift or other contrast mechanisms.

In a similar way, different specialized neutron scattering techniques are required to obtain information on the system's dynamics on different time scales:

- *Neutron Compton scattering*, where a high energy neutron in the eV energy range makes a deep inelastic collision with a nucleus in so-called impulse approximation, gives us the momentum distribution of the atoms within the solid. Interaction times are in the femtosecond fs time range.
- In magnetic metals, there exist single particle magnetic excitations, so-called Stoner excitations, which can be observed with inelastic scattering of high energy neutrons using the so-called *time-of-flight spectroscopy* or the *triple axis spectroscopy* technique. Typically, these processes range from fs to several hundred fs.
- Lattice vibrations (phonons) or spin waves in magnetic systems (magnons) have frequencies corresponding to periods in the picosecond ps time range. Again, these excitations can be observed with *time-of-flight* or *triple axis spectroscopy*.
- Slower processes in condensed matter are the tunneling of atoms, for example in molecular crystals or the slow dynamics of macromolecules. Characteristic time scales for these processes lie in the nanosecond ns time range. They can be observed with specialized techniques such as *backscattering spectroscopy* or *spin-echo spectroscopy*.
- Even slower processes occur in condensed matter on an ever-increasing range of lengths scales. One example is the growth of domains in magnetic systems, where domain walls are pinned by impurities. These processes may occur with typical time constants of microseconds μs . Periodic processes on such time scales can be observed with *stroboscopic neutron scattering* techniques.
- Finally, *kinematic neutron scattering* or imaging techniques, where data is taken in consecutive time slots, allow one to observe processes from the millisecond ms to the hour h range.

In this chapter, we will overview the various techniques used in neutron scattering and provide some examples for their application. We will start by repeating the properties of

² In what follows, we use as “natural atomic unit” the Ångström, with $1 \text{ \AA} = 0.1 \text{ nm}$.

the different correlation functions, in order to be able to judge what kind of information we can obtain from a certain neutron scattering experiment. We will introduce neutron scattering techniques used to obtain information on “where the atoms are” (diffractometry) and “what the atoms do” (spectroscopy). We will finish by reviewing the range of applicability of various neutron scattering methods and compare them to other experimental techniques.

15.2 Scattering and correlation functions

This somewhat advanced section can be skipped during first reading, but is given here for completeness.

The neutron scattering cross section for nuclear scattering can be expressed in the following form (for simplicity, we restrict ourselves to a mono-atomic system):

$$\frac{\partial^2 \sigma}{\partial \Omega \partial \omega} = \frac{k'}{k} \cdot N \cdot \left[\left(|\bar{b}|^2 - |\bar{b}'|^2 \right) S_{inc}(\mathbf{Q}, \omega) + |\bar{b}'|^2 S_{coh}(\mathbf{Q}, \omega) \right] \quad (15.1)$$

The cross section is proportional to the number N of atoms. It contains a kinematical factor k'/k , i. e. the magnitude of the final wave vector versus the magnitude of the incident wave vector, which results from phase-space density consideration. The scattering cross section contains two summands: one is the incoherent scattering cross section, which depends on the variance of the scattering length $\left(|\bar{b}|^2 - |\bar{b}'|^2 \right)$, and the other one is the coherent scattering cross section, which depends on the magnitude square of the average scattering length density $|\bar{b}'|^2$. The cross section (15.1) has a very convenient form: it separates the interaction strength between probe (here: the neutrons) and sample from the properties of the system studied. The latter is given by the so-called scattering functions $S_{inc}(\mathbf{Q}, \omega)$ and $S_{coh}(\mathbf{Q}, \omega)$, which are completely independent of the probe and solely a property of the system under investigation [2]. The *coherent scattering function* $S_{coh}(\mathbf{Q}, \omega)$ (also called *dynamical structure factor* or *scattering law*) is a Fourier transform in space and time of the pair correlation function:

$$S_{coh}(\mathbf{Q}, \omega) = \frac{1}{2\pi\hbar} \int G(\mathbf{r}, t) e^{i(\mathbf{Q}\cdot\mathbf{r} - \omega t)} d^3r dt \quad (15.2)$$

Here the *pair correlation function* $G(\mathbf{r}, t)$ depends on the time dependent positions of the atoms in the sample:

$$\begin{aligned} G(\mathbf{r}, t) &= \frac{1}{N} \sum_{ij} \int \langle \delta(\mathbf{r}' - \mathbf{r}_i(0)) \cdot \delta(\mathbf{r}' + \mathbf{r} - \mathbf{r}_j(t)) \rangle d^3r' \\ &= \frac{1}{N} \int \langle \rho(\mathbf{r}', 0) \cdot \rho(\mathbf{r}' + \mathbf{r}, t) \rangle d^3r' \end{aligned} \quad (15.3)$$

$\mathbf{r}_i(0)$ denotes the position of atom i at time 0 , while $\mathbf{r}_j(t)$ denotes the position of atom j at time t . The angle brackets denote the thermodynamic ensemble average, the integral extends over the entire sample volume and the sum runs over all atom pairs in the sample.

Instead of correlating the positions of two point-like scatterers at different times, one can rewrite the pair correlation function in terms of the particle density as given in the second line of (15.3). Coherent scattering arises from the superposition of the amplitudes of waves scattered from one particle at time θ and a second particle at time t , averaged over the entire sample volume and the thermodynamic state of the sample. In contrast, incoherent scattering arises from the superposition of waves scattered from the same particle at different times. Therefore, the *incoherent scattering function* $S_{inc}(\mathbf{Q}, \omega)$ is given in the following form:

$$S_{inc}(\mathbf{Q}, \omega) = \frac{1}{2\pi\hbar} \int G_s(\mathbf{r}, t) e^{i(\mathbf{Q}\cdot\mathbf{r} - \omega t)} d^3r dt \quad (15.4)$$

which is the Fourier transform in space and time of the *self-correlation function* $G_s(\mathbf{r}, t)$:

$$G_s(\mathbf{r}, t) = \frac{1}{N} \sum_j \int \langle \delta(\mathbf{r}' - \mathbf{r}_j(0)) \cdot \delta(\mathbf{r}' + \mathbf{r} - \mathbf{r}_j(t)) \rangle d^3r' \quad (15.5)$$

We next define the *intermediate scattering function* $S(\mathbf{Q}, t)$ as the purely spatial Fourier transform of the correlation function (here we have dropped the index “coh” and “inc”, respectively, as the intermediate scattering function can be defined for coherent as well as for incoherent scattering similarly):

$$\begin{aligned} S(\mathbf{Q}, t) &:= \int G(\mathbf{r}, t) e^{i\mathbf{Q}\cdot\mathbf{r}} d^3r \\ &= S(\mathbf{Q}, \infty) + S'(\mathbf{Q}, t) \end{aligned} \quad (15.6)$$

For reasons, which will become apparent below, we have separated in the second line the intermediate scattering function for infinite time

$$S(\mathbf{Q}, \infty) = \lim_{t \rightarrow \infty} S(\mathbf{Q}, t) \quad (15.7)$$

from the time development at intermediate times. Given this form of the intermediate scattering function $S(\mathbf{Q}, t)$, we can now calculate the scattering function as the temporal Fourier transform of the intermediate scattering function:

$$\begin{aligned} S(\mathbf{Q}, \omega) &= \frac{1}{2\pi\hbar} \int_{-\infty}^{+\infty} S(\mathbf{Q}, t) e^{-i\omega t} dt = \frac{1}{2\pi\hbar} \int_{-\infty}^{+\infty} [S(\mathbf{Q}, \infty) + S'(\mathbf{Q}, t)] e^{-i\omega t} dt \\ &= \underbrace{\frac{1}{\hbar} \delta(\omega) S(\mathbf{Q}, \infty)}_{\text{elastic scattering}} + \underbrace{\frac{1}{2\pi\hbar} \int_{-\infty}^{+\infty} S'(\mathbf{Q}, t) e^{-i\omega t} dt}_{\text{inelastic scattering}} \end{aligned} \quad (15.8)$$

In this way, the scattering function has been separated into one term for frequency θ , i. e. vanishing energy transfer $\Delta E = \hbar\omega = 0$ and one term for non-vanishing energy transfer. The first term is the purely elastic scattering, which is given by the correlation function at infinite times. Correlation at infinite times is obtained for particles at rest. A prominent example is the Bragg scattering from a crystalline material, which is purely elastic, while

the scattering from liquids is purely quasi-elastic³ since the atoms in liquids are moving around freely and thus the correlation function vanishes in the limit of infinite time differences.

Often times the energy of the scattered neutron is not discriminated in the detector. In such experiments, where the detector is set at a given scattering angle, but does not resolve the energies of the scattered neutrons, we measure an *integral cross section* for a fixed direction $\hat{\mathbf{k}}'$ of \mathbf{k}' :

$$\left(\frac{d\sigma}{d\Omega}\right)_{coh,int} = \int \frac{\partial^2 \sigma}{\partial \Omega \partial \omega} \Big|_{\hat{\mathbf{k}}'=const} \cdot d\omega \quad (15.9)$$

Momentum and energy conservation are expressed by the following kinematic equations of scattering:

$$\mathbf{Q} = \mathbf{k}' - \mathbf{k} \ ; \ \hbar\omega = E - E' = \frac{\hbar^2}{2m} (k^2 - k'^2) \quad (15.10)$$

Due to these kinematic conditions, the scattering vector \mathbf{Q} will vary with the energy of the scattered neutrons E' or the energy transfer $\hbar\omega$ as the integral in (15.9) is performed. The so-called *quasi-static approximation* neglects this variation and uses the scattering vector \mathbf{Q}_0 for elastic scattering ($\hbar\omega = 0$) in (15.9). This approximation is valid only if the energy transfer is small compared to the initial energy. This means that the movements of the atoms are negligible during the propagation of the radiation wave front from one atom to the other. In this case, the above integral can be approximated as follows:

$$\begin{aligned} \left(\frac{d\sigma}{d\Omega}\right)_{coh,QSA} &= \frac{k'}{k} \frac{N}{2\pi\hbar} \int \left(\int G(\mathbf{r}, t) e^{i(\mathbf{Q}_0 \cdot \mathbf{r} - \omega t)} d^3 r dt \right) d\omega \\ &= \frac{k'}{k} \frac{N}{2\pi\hbar} \int G(\mathbf{r}, t) e^{i\mathbf{Q}_0 \cdot \mathbf{r}} \delta(t) d^3 r dt = \frac{k'}{k} \frac{N}{2\pi\hbar} \int G(\mathbf{r}, 0) e^{i\mathbf{Q}_0 \cdot \mathbf{r}} d^3 r \end{aligned} \quad (15.11)$$

which shows that the integral scattering in quasi-static approximation depends on the *instantaneous spatial correlation function* only, i.e. it measures a snapshot of the arrangement of atoms within the sample. This technique is e.g. very important for the determination of short-range order in liquids, where no elastic scattering occurs (see above).

Our discussion on correlation functions can be summarized in a schematic diagrammatic form, see figure 15.2.

³ Inelastic scattering usually denotes scattering from an excitation with well-defined energy transfer, while quasi-elastic scattering denotes scattering which is not elastic, but has a broad energy distribution, centered around an energy transfer of zero.

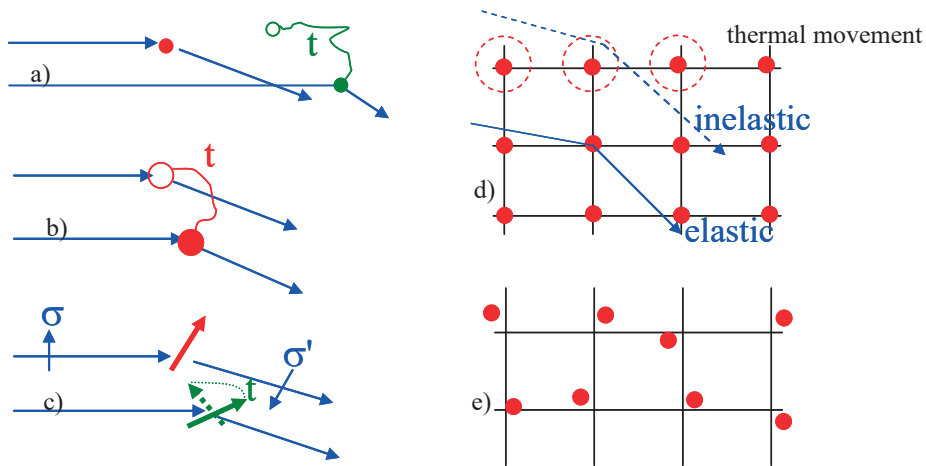


Fig. 15.2: Schematic diagrams depicting the various scattering processes: a) coherent scattering is connected with the pair correlation function in space-and time; b) incoherent scattering is connected with the self-correlation function; c) magnetic scattering is connected with the spin pair correlation function; d) elastic and inelastic scattering from a crystal measures average positions and movements of the atoms, respectively, e) inelastic scattering in quasi-static approximation sees a snapshot of the sample.

Figure 15.2 shows that coherent scattering is related to the pair correlation between atoms at different times (15.2a), while (quasi-elastic) incoherent scattering relates to the one particle self-correlation function at (different) times (e.g. diffusion of atoms) (15.2b). In analogy to nuclear scattering, magnetic scattering depends on the correlation function between magnetic moments of the atoms. If the magnetic moment is due to spin only, it measures the *spin pair correlation function*. Since the magnetic moment is a vector quantity, this correlation function strongly depends on the neutron polarization. For this reason, in magnetic scattering we often perform a polarization analysis as discussed in the corresponding chapter. Figure 15.2d depicts elastic and inelastic scattering from atoms on a regular lattice. Elastic scattering depends on the infinite time correlation and thus gives us information on the time averaged structure. Excursions of the atoms from their time averaged positions due to the thermal movement will give rise to inelastic or quasi-elastic scattering, which allows one e.g. to determine the spectrum of lattice vibrations, see chapter on “inelastic neutron scattering”. Finally, an experiment without energy analysis in quasi-static approximation will give us the instantaneous correlations between the atoms, see figure 15.2e. This schematic picture shows a snapshot of the atoms on a regular lattice. Their positions differ from the time averaged positions due to thermal movement.

15.3 The generic scattering experiment

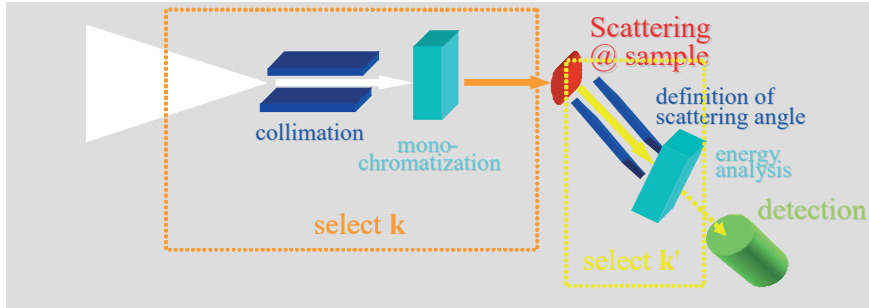


Fig. 15.3: Schematic diagram of a generic scattering experiment; the primary spectrometer in front of the sample serves to select an incident wave vector distribution by means of collimation and monochromatization; the secondary spectrometer after the sample selects a final wave vector; the number of neutrons for a given distribution of incident wave vector \mathbf{k} and final wave vector \mathbf{k}' is counted in the detector.

A generic scattering experiment is depicted schematically in figure 15.3. The incident beam is prepared by collimators, which define the direction of the beam and monochromators, which define the energy of the incident neutrons. Together these optical elements select an incident wave vector \mathbf{k} . In reality, since these neutron-optical elements are never perfect, a certain distribution of incident wave vectors around an average wave vector is selected in the primary spectrometer. In an analogous manner, a final wave vector \mathbf{k}' - or better a distribution of final wave vectors - is being selected from all scattered waves after the sample by the secondary spectrometer. Finally, the scattered neutrons are being counted in the detector. Since our neutron-optical elements are never perfect, the measured intensity in the detector is not simply proportional to the scattering function $S(\mathbf{Q}, \omega)$ (or more precisely, the cross section), but it is proportional to the convolution of the scattering function (or cross section) with the *experimental resolution function* R :

$$I(\mathbf{Q}_0, \omega_0) \propto \iint S(\mathbf{Q}, \omega) R(\mathbf{Q}_0 - \mathbf{Q}, \omega_0 - \omega) d^3Q d\omega \quad (15.12)$$

Here, the resolution function R appears due to the limited ability of any experimental setup to define an incident or final wave vector \mathbf{k} or \mathbf{k}' , respectively. R therefore depends purely on the instrumental parameters and not on the scattering system under investigation. The art of any neutron scattering experiment is to adjust the instrument - and with it the resolution function - to the problem under investigation. If the resolution of the instrument is too tight, the intensity in the detector becomes too small and counting statistics will limit the precision of the measurement. If, however, the resolution is too relaxed, the intensity will be smeared out and will not allow one to determine the scattering function properly.

The simplest way to collimate an incident beam is to put two slits with given openings in a certain distance in the beam path and thus define the angular spread of the incident

beam. For monochromatization of a neutron beam, usually one of two different methods is applied:

- One can use the wave property of the neutron and diffract the neutron beam from a single crystal. According to Bragg's law $2d \sin \theta = \lambda$, a certain wave length λ is being selected for a given lattice d -spacing under a scattering angle 2θ .
- One can use the particle property of the neutron and use the neutron time-of-flight to determine its velocity and thus its kinetic energy. How this is being done technically is discussed in the corresponding section of this course.

Following our discussion of the correlation functions, we will now distinguish two principally different types of neutron scattering instruments:

- **Diffractometers:** these are scattering instruments, which either perform no energy analysis at all, or which measure only the truly elastic scattering. As discussed in chapter 15.2, the truly elastic scattering allows one to determine the time averaged structure. The prominent example is Bragg scattering from single crystals. If, however, no energy analysis is performed, one usually makes sure that one works in quasi-static approximation to facilitate the interpretation of the scattered intensity distribution. Quasi-static approximation corresponds to a snapshot of the scatterers in the sample and is important for example to determine short-range order in a liquid. Be it elastic scattering or integral scattering in quasi-static approximation, a diffraction experiment allows one to determine the position of the scatterers only. The movement of the scatterers is not (directly) accessible with such a diffraction experiment. Similarly, in a diffraction experiment for magnetic scattering, the arrangement of magnetic moments within the sample, i.e. its magnetic structure, can be determined, while the spin dynamics is not accessible in a diffraction experiment⁴.

- **Spectrometers:** a neutron spectrometer is dedicated to measure inelastic scattering, i.e. to determine the change of the neutrons' kinetic energy $E = \frac{\hbar^2 k^2}{2m}$ during

the scattering process. Such an experiment requires the analysis of the energy of the scattered neutrons, in contrast to a conventional diffractometer. Now the intensity measured in the detector depends on momentum- and energy- transfer and is proportional to the convolution of the double differential scattering cross section (15.1) with the resolution function of the instrument (15.12). Therefore, a neutron spectrometer gives us information on the scattering functions (coherent or incoherent) and thus on the truly time dependent pair- or self-correlation functions. This is why spectrometers are used to determine the dynamics of a system after its structure has been determined in a previous diffraction experiment⁵.

15.4 Diffractometers

⁴ In fact, there is a way to access also spin- or lattice- dynamics in a diffraction experiment: lattice vibrations will give rise to diffuse scattering around Bragg peaks, so-called thermal diffuse scattering, which can be modelled and thus the spectrum of excitations can be determined in an indirect, but not model-free direct way.

⁵ Of course, spectrometers could also be used to determine the structure, but usually their resolution is not at all adapted to this purpose.

15.4.1 Wide angle diffraction versus small angle scattering

According to (15.10) and de Broglie, the momentum transfer during a scattering experiment is given by $\hbar\mathbf{Q} = \hbar\mathbf{k}' - \hbar\mathbf{k}$. Remembering that $k = \frac{2\pi}{\lambda}$, the magnitude Q of the scattering vector \mathbf{Q} can be expressed in terms of wavelength λ and scattering angle 2θ as:

$$Q = \frac{4\pi}{\lambda} \sin \theta \quad (15.13)$$

As we have seen in chapter 15.2, the scattering cross section is related to the Fourier transform of the spatial correlation function and therefore a reciprocal relation exists between characteristic real space distances d and the magnitude of the scattering vector Q , for which intensity maxima appear:

$$\Delta Q \sim \frac{2\pi}{d} \quad (15.14)$$

Bragg scattering from crystals provides an example for this equation (compare corresponding introductory chapter): the distance between maxima of the Laue function is determined by $\Delta Q \cdot d = 2\pi$, where d is the corresponding real space periodicity. Reflectometry provides another example (see below): the Q -distance between Kiessig fringes is given by the relation $\Delta Q \cdot d \sim 2\pi$ (compare (15.19)), where d is the layer thickness.

(15.14) is central for the choice of an instrument or experimental set-up, since it tells us which Q -range we have to cover in order to get information on a certain length range in real space. (15.13) tells us at which angles we will observe the corresponding intensity maxima for a given wavelength. This angle has to be large enough in order to separate the scattering event clearly from the primary beam. This is why we need different instruments to study materials on different length scales. Table 15.1 gives two examples.

Example	d	ΔQ	2θ ($\lambda=1$)	2θ ($\lambda=10 \text{ \AA}$)	Technique
Distance between atoms in crystals	2 \AA	3.14 \AA^{-1}	29°	"cut-off"	wide angle diffraction
Precipitates in metals (e.g. Co in Cu)	400 \AA	0.016 \AA^{-1}	0.14°	1.46°	small angle scattering

Tab. 15.1: Examples for scattering from structures on different characteristic real space length scales d . ΔQ is the corresponding characteristic scattering vector according to (15.14), 2θ the scattering angle according to (15.13), calculated for two different wavelengths λ .

1. The study of structures on atomic length scales is typically done with a wavelength of around 1 \AA (comparable to the distance between the atoms) and the scattered intensity is observed at rather large angles between 5° and 175°. Therefore one speaks of *wide angle diffraction*, which is employed for the study of atomic structures.
2. For the study of large-scale structures (precipitates, magnetic domains, macromolecules in solution or melt) on length scales of 10 up to 10,000 \AA (1 up to 1000 nm), the magnitude of the relevant scattering vectors as well as the corresponding scattering angles are small. Therefore one chooses a longer wavelength in order to expand the diffractogram. The suitable technique is *small angle scattering*, which is employed to study large scale structures.

In what follows we will first focus on the study of large-scale structures. In the corresponding conceptually very simple instruments, some typical considerations for the design of an instrument can be exemplified. We will distinguish between small angle neutron scattering instruments and reflectometers, discuss the basic instrument concepts and list some possible applications. After having discussed how large-scale structures can be studied with neutron diffraction, we will then introduce instruments for wide angle scattering and their possible applications.

15.4.2 Small Angle Neutron Scattering (SANS)

As mentioned in chapter 15.4.1, small angle scattering is employed whenever structures on length scales between typically 10 \AA and 10,000 \AA (1 nm and 1,000 nm) are of interest. This range of real space lengths corresponds to a scattering vector of magnitude between about 10^{-1}\AA^{-1} and 10^{-4}\AA^{-1} (1 nm^{-1} and 10^{-3}nm^{-1}). In order to observe the scattering events under reasonable scattering angles, one chooses a rather long wavelength. However, due to the moderator spectrum (see chapter on neutron sources), there is very little neutron flux at wavelengths above 20 \AA . Therefore typically neutrons of wavelength between 5 and 15 \AA are employed for small angle neutron scattering.

Two different principles of small angle neutron scattering will be distinguished in this chapter: the pinhole SANS and the focusing SANS depicted in figures 15.4 and 15.5, respectively. Other types of instruments, e.g. with multi-pinhole grid collimation, are variants of these techniques and will not be discussed here.

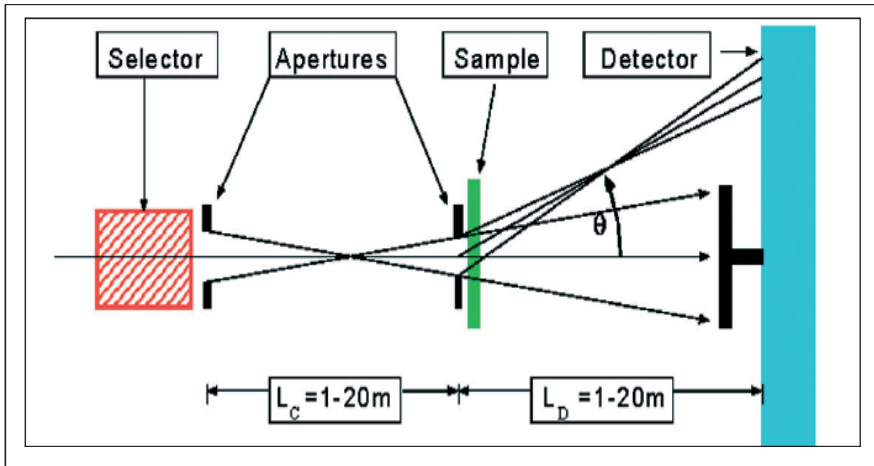


Fig. 15.4: Schematics of a pinhole SANS, where the incident wave vector is defined through distant apertures (KWS-1 or KWS-2 of JCNS [3]).

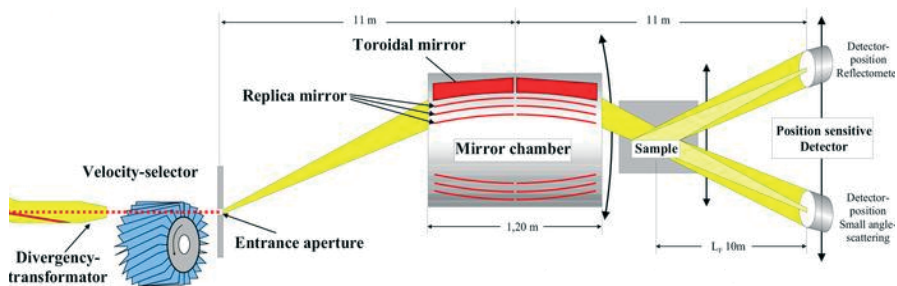


Fig. 15.5: Schematics of a focusing SANS, where an image of the entrance aperture is produced on the detector by a focusing mirror (KWS-3 of JCNS [3]).

For both instrument concepts, the wavelength band is usually defined by a so-called velocity selector. Figure 15.6 shows a photo of a velocity selector drum build in Jülich for the instrument KWS-3.



Fig. 15.6: *Photo of the velocity selector drum of the JCMS instrument KWS-3 showing the screw-like twisted channels separated by absorbing walls, which only neutrons of a certain wavelength band can pass when the drum is turning.*

In the pinhole SANS, the direction of the incident wave vector k is defined by two distant apertures of comparable size. The longer the distance between the diaphragms, the higher is the collimation for a given cross section of the beam. The sample is placed right next to the second aperture and the scattered neutrons are being recorded in a detector, which is at a large distance from the sample; typically, the sample-detector distance is comparable to the collimation distance. The overall length of such an instrument can amount to 40 m, up to 80 m.

In contrast to the pinhole SANS, the focusing SANS uses a divergent incident beam and a focusing optical element produces an image of the entrance aperture on the detector. The sample is positioned directly behind the focusing element. Small angle scattering from the sample appears on the position-sensitive area detector around the primary beam spot. Such a set-up with a focusing element would be the natural solution in light optics, where focusing lenses are readily available. Due to the weak interaction of neutrons with matter, the index of refraction for neutrons is very close to one, and it is difficult to produce efficient focusing elements. In case of the focusing SANS realized by Forschungszentrum Jülich [4], a toroidal⁶ mirror is employed as focusing element. Locally, the toroidal shape is a good approximation to an ellipsoid with its well-known focusing properties. The challenge in realizing such a device lies in the fact that small angle scattering from the focusing element has to be avoided i.e. the mirror has to be flat on an atomic scale (root-mean square roughness of about 3 Å!), which became possible due to the developments of optical industry for x-ray satellites.⁷

⁶ A torus is a surface of revolution generated by revolving a circle about an axis coplanar with the circle, which does not touch the circle (examples: doughnuts, inner tubes).

⁷ It should be mentioned that nowadays focusing lenses for neutron scattering have also been realised. These have a very long focal distance, but can be employed to improve intensity or resolution in pinhole SANS.

As an example of the considerations leading to the design of a neutron scattering instrument, we will now discuss the resolution of a pinhole SANS machine. In general terms, the resolution of an instrument denotes the smearing of the signal due to the instruments' finite performance (15.12). As neutron scattering is a flux limited technique, there is need for optimization: the better the resolution of the instrument, i.e. the better the angular collimation $\Delta\theta$ and the smaller the wavelength spread $\Delta\lambda$, the smaller is the intensity recorded on the detector. Therefore, resolution has to be relaxed to such an extent that the features of interest are still measurable and not smeared out entirely by the resolution of the instrument, while at the same time the intensity is maximized. In order to determine the resolution of a SANS instrument, we start from (15.13): $Q = \frac{4\pi}{\lambda} \sin \theta$. The influence of angular- and wavelength spread can be determined by differentiation of this equation, where the different contributions have to be added quadratically according to Gauss:

$$\begin{aligned} \Delta Q^2 &= \left(\frac{\partial Q}{\partial \theta} \right)^2 (\Delta \theta)^2 + \left(\frac{\partial Q}{\partial \lambda} \right)^2 (\Delta \lambda)^2 = \left(\frac{4\pi}{\lambda} \right)^2 \cos^2 \theta (\Delta \theta)^2 + \left(\frac{4\pi \sin \theta}{\lambda^2} \right)^2 \Delta \lambda^2 \\ &\stackrel{\theta \rightarrow 0}{=} \left(\frac{4\pi}{\lambda} \right)^2 \left[(\Delta \theta)^2 + \theta^2 \left(\frac{\Delta \lambda}{\lambda} \right)^2 \right] = \frac{k^2}{12} \left[\left(\frac{d_D}{L_D} \right)^2 + \left(\frac{d_E}{L_C} \right)^2 + \left(\frac{d_S}{L_C} + \frac{d_S}{L_D} \right)^2 + \theta^2 \left(\frac{\Delta \lambda}{\lambda} \right)^2 \right] \end{aligned} \quad (15.15)$$

ΔQ^2 is the variance of the scattering vector due to the finite collimation and monochromatization. d_E and d_S are the diameters of the entrance and sample aperture, respectively. d_D denotes the detector pixel size. L_C and L_D are collimation length and sample-detector distance, respectively. An optimization can be achieved, if all terms in (15.15) contribute the same amount, which leads to the condition

$$L_D = L_C, \quad d_E = d_D = 2d_S \quad (15.16)$$

(15.16) shows that a pinhole SANS has to be designed such that sample-to-detector distance L_D is equal to the collimation length L_C . Typical values are $L_D = L_C = 10$ m with openings of $d_E = 3$ cm for the entrance- and $d_S = 1.5$ cm for the sample aperture. Note that one can chose the opening of the entrance aperture to be twice as large as the opening of the sample aperture - or sample size - without sacrificing markedly in resolution, while gaining in neutron count rate! The detector needs a minimum pixel resolution $d_D \approx d_E$; a detector with a radius of about $R_D \approx 30$ cm is necessary to cover the required Q-range up to 0.05 \AA^{-1} at $L_D = 10$ m and for $\lambda = 8 \text{ \AA}$. Having defined the incident collimation, we can now determine the appropriate wavelength spread with the same argument as above: the last term in the sum in (15.15), corresponding to the wavelength spread, should contribute the same amount to the variance of the scattering vector as the corresponding terms for the collimation, i. e.:

$$\frac{\Delta \lambda}{\lambda} = \frac{d_E}{L_C} \cdot \frac{L_D}{r_D} \approx \frac{d_E}{r_D} \approx \frac{1}{10} = 10\% \quad (15.17)$$

(15.17) demonstrates that in general for small angle scattering we don't need a very high degree of monochromatization. A 10 % wavelength band is acceptable, since for small angles the smearing due to the wavelength spread is quite comparable to the smearing due to the incident divergence. This is the reason why usually a velocity selector is employed as monochromatizing element for small angle scattering, as it lets a wavelength band of typically 10 % pass.

Let us give a short introduction into the analysis of small angle scattering experiments. As in any scattering experiment, the detected intensity is proportional to the scattering cross section, which in the SANS case is usually normalized to the sample volume and therefore has the unit [cm^{-1}]:

$$\frac{d\Sigma}{d\Omega} = \frac{1}{V_{\text{sample}}} \cdot \frac{d\sigma}{d\Omega} \quad (15.18)$$

Here we discuss the so-called “two phase model” only, where homogeneous particles are dispersed in a matrix (e. g. precipitates in metals or nanoparticles in solution etc.). The cross section will then be proportional to the contrast between particles and solution

$$\Delta b = \sum_j b_j (\rho_{j,P} - \rho_{j,M}) \quad (15.19)$$

where j labels atom species j of scattering length b_j with number density $\rho_{j,P}$ in the particle and $\rho_{j,M}$ in the matrix, respectively. The differential cross section per particle is given by the interference term (note: we use a continuum description for the small Q limit):

$$\begin{aligned} \frac{d\Sigma}{d\Omega}(\mathbf{Q}) &= \left| \int_V \Delta b \cdot e^{i\mathbf{Q}\cdot\mathbf{r}} d^3r \right|^2 \\ &= \Delta b^2 V^2 \underbrace{\left| \frac{1}{V} \int_V e^{i\mathbf{Q}\cdot\mathbf{r}} d^3r \right|^2}_{f(\mathbf{Q})} \end{aligned} \quad (15.20)$$

Here $f(\mathbf{Q})$ denotes the *particle form factor* for a homogeneous particle of volume V :

$$f(\mathbf{Q}) = \frac{1}{V} \int_V e^{i\mathbf{Q}\cdot\mathbf{r}} d^3r \quad (15.21)$$

(15.20) is the differential cross section for a single particle. For very dilute solutions of identical particles, the cross section will be given by (15.20) times the number N of particles (“single particle approximation”). However, in more concentrated solutions, there will be additional interference effects between the particles, which are described by the so-called *structure factor* S and we obtain the modified cross section for dense solutions:

$$\frac{d\sigma}{d\Omega} = N \cdot \Delta b^2 \cdot V^2 \cdot |f(\mathbf{Q})|^2 \cdot S(\mathbf{Q}) \quad (15.22)$$

where $S(\mathbf{Q})$ is related to the Fourier transform of the pair correlation function $g(\mathbf{R})$ between the single particles at distance \mathbf{R} :

$$S(\mathbf{Q}) = 1 + \frac{1}{V_{\text{sample}}} \int_{V_{\text{sample}}} g(\mathbf{R}) e^{i\mathbf{Q}\cdot\mathbf{R}} d^3r \quad (15.23)$$

(Note: for vanishing pair correlations $g(\mathbf{R}) \equiv 0$, i.e. random distributed particles, the structure factor has to be unity: $S(\mathbf{Q}) \equiv 1$).

The isotropic form factor of a homogeneous sphere of radius R can be calculated by Fourier transform and is introduced elsewhere in this course:

$$f(Q) = 3 \frac{\sin QR - QR \cos QR}{(QR)^3} \quad (15.24)$$

For forward scattering $f(Q=0)=1$ per definition. For small values of the scattering vector, this expression can be approximated by:

“Guinier Law” for $QR \leq 2$:

$$|f(Q)|^2 \approx e^{-\frac{(QR_G)^2}{3}} \approx 1 - \frac{Q^2 R_G^2}{3} \quad (15.25)$$

Here the quantity R_G is the so-called *radius of gyration* of the particle. For a spherical particle $R_G^2 = \frac{3}{5} R^2$, but R_G can be defined in a more general way also for non-spherical particles.

For $QR=3$ the form factor squared has dropped to about 10 %. In the larger Q region - neglecting the sharp minima of the form factor (15.24), which are often not visible due to particle size distribution and instrumental resolution - the form factor follows the behavior:

“Porod Law” for $QR \geq 4.5$:

$$|f(Q)|^2 \approx 2\pi \frac{A}{V^2} Q^{-4} \quad (15.26)$$

where $A=4\pi R^2$ is the surface, and $V = \frac{4\pi}{3} R^3$ the volume of the sphere of radius R . In small angle scattering, often times one does not deal with simple geometrically smooth particles in a second phase. In stochastic growth processes or soft matter system, irregular *fractal* structures can appear, which show self-similarity on multiple length scales. For such structures, power laws with other exponents are observed:

$$\begin{aligned} \frac{d\sigma}{d\Omega}(\text{mass fractal}) &\sim Q^{-D} = Q^{-1} \dots Q^{-3} \\ \frac{d\sigma}{d\Omega}(\text{surface fractal}) &\sim Q^{D_s-6} = Q^{-3} \dots Q^{-4} \end{aligned} \quad (15.27)$$

where D denotes the so-called *fractal dimension* for porous objects. D is in general smaller than 3 and non-integer. If the particles have a dense core, but a rough self-similar surface, they are called *surface fractals* with a surface area of $A \sim R^{D_s}$. From the above discussion we see that characteristic regions can be distinguished in a small angle scattering experiment:

1. Close to forward direction in the very small Q limit and for dilute solutions, we observe constant scattering proportional to the number of particles N , the square of the particle volume V^2 and contrast (15.19). For known contrast, we can deduce the product $N \cdot V^2$, if the scattering is measured in absolute units by comparing to a

known scatterer e. g. water. For dense solutions, the structure factor from correlations between particles becomes apparent.

2. In the region up to $QR \leq 2$, the Guinier Law (15.25) holds for compact particles.

From a *Guinier-Plot* $\ln \frac{d\sigma}{d\Omega}$ versus Q^2 one can determine the radius of gyration

$$R_G = \frac{\int_V r^2 \Delta b(r) d^3 r}{\int_V \Delta b(r) d^3 r} \quad (15.28)$$

3. In the Porod-region $QR \geq 4.5$

$$\frac{d\sigma}{d\Omega} = \Delta b^2 2\pi N A Q^{-4} \quad (15.29)$$

we can, independent of particle shape, determine the total surface area $N \cdot A$ of all particles with sharp surfaces from a *Porod Plot* $\frac{d\sigma}{d\Omega} \cdot Q^4$ versus Q .

4. Finally, if Q approaches the value $1/a$ where a corresponds to typical atomic distances, we approach the region of Bragg scattering from atomic structures (wide angle scattering).

Let us now turn to applications of small angle scattering. One example is given in figure 15.7, which is concerned with the self-organization of crystalline amorphous diblock-copolymers [4]. Combining three different instruments, small angle scattering has been observed over ten orders of magnitude in cross section and nearly four orders of magnitude in momentum transfer. In different regions, different power laws apply, corresponding to different structures: the Q^{-2} power law corresponds to $2d$ structures on the shortest length scale, the Q^{-1} power law corresponds to the organization of rods in bundles, while the Q^{-3} power law corresponds to a network of bundles with a mass fractal aspect and finally, correlations become visible in the very low Q -range.

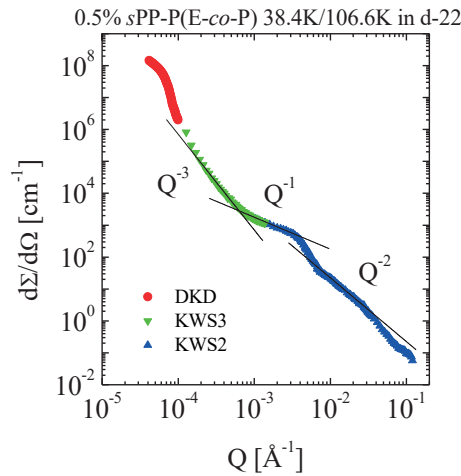


Fig. 15.7: *SANS investigation of the self-organization of a crystalline-amorphous diblock-copolymer measured with three different instruments of different resolution: double crystal diffractometer, focussing SANS and pinhole SANS for the low, medium and larger Q range, respectively. Plotted is the cross section in absolute units versus the magnitude of the scattering vector. For details see [4].*

We will end this short introduction into the principles of small angle scattering by listing some examples for applications of small angle scattering in different fields of science:

- *soft matter*: polymers and colloids, e. g. micelles, dendrimers, liquid crystals, gels, reaction kinetics of mixed systems, ...
- *materials science*: phase separation in alloys and glasses, morphologies of superalloys, micro-porosity in ceramics, interfaces and surfaces of catalysts
- *biological macromolecules*: size and shape of proteins, nucleic acids and of macromolecular complexes, bio-membranes, drug vectors
- *magnetism*: ferromagnetic correlations and domains, flux line lattices in superconductors, ...

15.4.3 Large scale structures: Reflectometry

As elaborated in chapter 15.4.2, neutron small angle scattering is applied to determine large-scale structures, e. g. scattering length density fluctuations on length scales of some 100 Å in bulk material. There is another type of instrument, which is dedicated to the study of large-scale structures in thin film systems, on surfaces and in multilayers. Such an instrument is called a *neutron reflectometer*. This conceptually simple instrument is depicted schematically in figure 15.8.

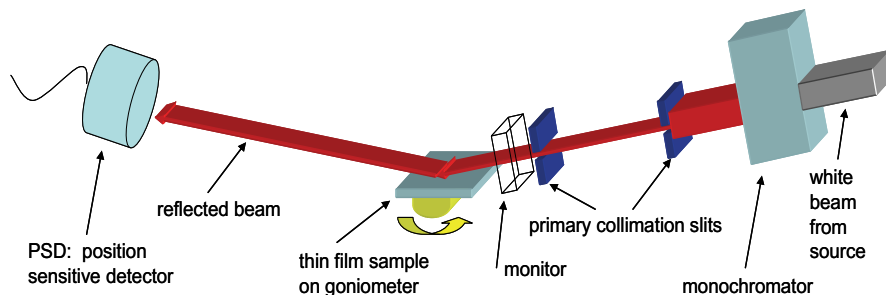


Fig. 15.8: *Schematics of a neutron reflectometer. Monochromatization can be done in many different ways: by a velocity selector, by a crystal monochromator, or by a chopper in a time-of-flight instrument. Collimation slits define the direction of the incident beam. The monitor is a low efficient detector of high transmission, which measures the incident flux on the sample. The reflected neutrons are either detected in a position sensitive detector, or a secondary collimation in front of a point detector selects the direction of the reflected beam. For magnetic samples, a polarizer, a polarization analyzer and guide fields can be inserted for polarization analysis experiments.*

Similar to a pinhole SANS instrument, the incident beam is collimated through a set of two well separated slits. However, since in reflectometry, one is mainly interested in the momentum transfer perpendicular to the planar sample surface, the collimation of a reflectometer is tight only in this direction. Along the sample surface the beam can be wide and have a larger divergence in order to gain intensity. This collimated beam impinges on the sample under a grazing angle (typically fractions of a degree up to a few degrees) and is reflected into a single point detector or a position sensitive detector. To define the angle of exit for a point detector, a secondary collimation is needed between sample and detector. The incident beam is monochromatized using different techniques, depending on the resolution requirements: velocity selector, time-of-flight chopper or crystal monochromator.

With such an instrument, the layer structure of a sample can be determined, such as layer composition, layer thickness and surface- or interfacial roughness. This information is obtained in so-called specular reflection, for which the incident angle is equal to the final angle like in a reflection from a perfect optical mirror. In this case, the momentum transfer of the neutrons is perpendicular to the surface of the sample and thus only laterally averaged information can be obtained. In order to determine lateral correlations within the layers, for example magnetic domain sizes, a momentum transfer within the layer has to occur, which implies that angle of incidence and final angle have to be different. Short range correlation within the layers will then give rise to so-called off specular diffuse scattering as well known in optics from a bad optical mirror.

The scattering geometry is shown in figure 15.9.

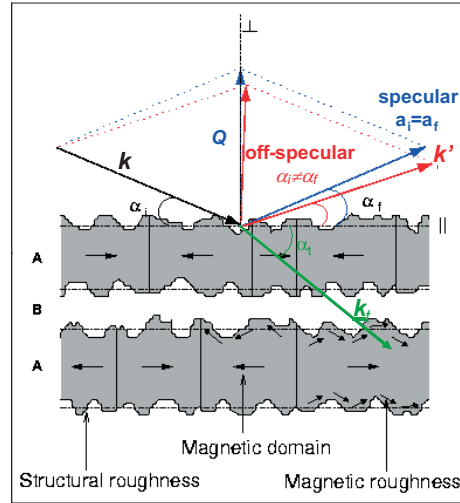


Fig. 15.9: Scattering geometry for grazing incidence neutron scattering. Specular reflections are obtained, if the angle of incidence equals the final angle $\alpha_i = \alpha_f$. Off-specular scattering is observed at $\alpha_i \neq \alpha_f$.

In fact, the theoretical description of neutron reflectometry follows exactly along the lines of conventional optics, except that for neutrons in most cases the index of refraction is smaller than one and thus external total reflection occurs for neutrons coming from vacuum towards matter⁸. The index of refraction n of neutrons of wavelength λ from a layer composed of elements with scattering length b_j and number density ρ_j and linear absorption coefficient μ_n is given by:

$$n = 1 - \frac{\lambda^2}{2\pi} \sum_j b_j \rho_j - i \frac{\lambda}{4\pi} \mu_n =: 1 - \delta - i\beta \quad (15.30)$$

Refraction and total reflection are described by the well-known *Snell's Law* of optics:

$$\text{Snell's law: } \frac{\cos \alpha_i}{\cos \alpha_f} = \frac{k_f}{k_i} = n \quad (15.31)$$

$$\text{angle of total reflection: } \cos \theta_c = n \quad (15.32)$$

⁸ This is exactly what happens in neutron guides, evacuated tubes of usually rectangular cross section, where neutrons are totally reflected from the smooth glass side walls, often coated, e.g. with ⁵⁸Ni, to enhance the angle of total reflection. Since for total reflection conditions, reflectivity is close to 100%, neutrons are transported over large distances (some 10 to above 100 m) nearly without loss from the source to the instruments by bouncing back- and forth from the guide side walls.

The intensities of reflected and transmitted beam can be determined from the optical *Fresnel equation* (A_0 , A_1 , B_0 : amplitudes of incident, transmitted and reflected waves, respectively; k_z , k_{tz} : component of wavevector \mathbf{k} and \mathbf{k}_z , respectively, perpendicular to average surface):

Fresnel equation:

$$\text{Reflectivity } R = \left| \frac{B_0}{A_0} \right|^2 = \left| \frac{k_z - k_{tz}}{k_z + k_{tz}} \right|^2 = \left| \frac{\alpha_i - n \cdot \alpha_t}{\alpha_i + n \cdot \alpha_t} \right|^2 \quad (15.33)$$

$$\text{Transmissivity } T = \left| \frac{A_1}{A_0} \right|^2 = \left| \frac{2k_z}{k_z + k_{tz}} \right|^2 = \left| \frac{2\alpha_i}{\alpha_i + n \cdot \alpha_t} \right|^2 \quad (15.34)$$

Figure 15.10 shows as an example the reflectivity and transmissivity of a Ni layer.

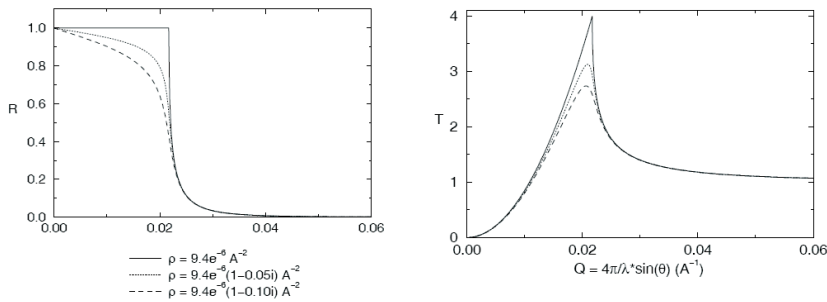


Fig. 15.10: Reflectivity and transmissivity of neutrons from a Ni surface.

Here we just want to demonstrate with very simple arguments how interference effects from layered structures arise and how the intensity modulation in Q -space are related to real space length scales. Figure 15.11 shows how interference can occur from a beam being reflected at the surface and at the internal interface of a double layer stack.

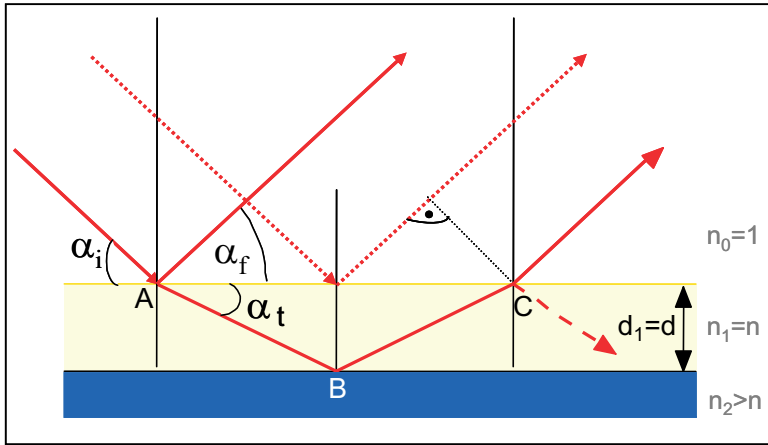


Fig. 15.11: Schematics of the reflection of a neutron beam from a single layer on a substrate. There exists an optical path length difference Δ between the rays drawn with a solid line and those drawn with a dotted line.

For simplicity we consider only the case of a specular reflection, i.e. the incident angle α_i is equal to the angle of exit α_f : $\alpha_i = \alpha_f = \alpha$. Interference occurs between beams reflected from the surface (dotted line in figure 15.11) and those first transmitted into the layer, reflected from the interface between layer 1 and substrate and then leaving the layer into vacuum (solid line). To a good approximation, refraction at the top surface can be neglected for incident angles larger than about twice the critical angle of total reflection. In this case $\alpha_i = \alpha = \alpha_f = \alpha$ holds. Since the index of refraction for neutrons is very close to one, this approximation is valid even for rather small angles of incidence. Then the optical path length difference for the two beams is:

$$\Delta = 2d \sin \alpha \quad (15.35)$$

Here d is the thickness of layer 1. We can now determine the distance between interference maxima from the condition that the path length difference has to differ by one wavelength: $\lambda = 2d \cdot \Delta(\sin \alpha) \approx 2d \cdot \Delta \alpha$. With $Q = \frac{4\pi}{\lambda} \sin \alpha \approx \frac{4\pi}{\lambda} \alpha$ we finally obtain:

$$\Delta Q \approx \frac{2\pi}{d} \quad (15.36)$$

Again, we can see that the interference phenomena in Q -space are connected with real space length scales in a reciprocal way. (15.36) tells us that there will be a number of interference maxima at distances in Q of $\frac{2\pi}{d}$. These interference phenomena are called “Kiessig fringes” and are well known to us in conventional optics for example as the beautiful colors observed in soap bubbles. Figure 15.12 shows as an example the reflectivity of neutrons from a thin nickel layer on a glass substrate, which is nothing else but a section of a neutron guide employed to transport the neutrons from the source to the

instrument over long distances by multiple total reflections. The Kiessig fringes are nicely visible in this example and the thickness of the nickel layer can be determined from the distance between adjacent intensity maxima.

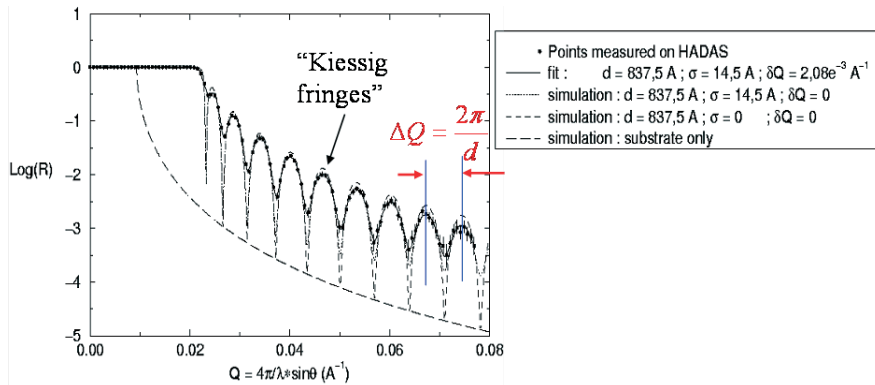


Fig. 15.12: Reflectivity of neutrons from a nickel layer on glass substrate on a logarithmic scale. Data points were measured on the HADAS reflectometer of the late FRJ-2 reactor. The solid line shows a fit, where the layer thickness was determined to be 837.5 Å with a root mean square roughness of 14.5 Å and where the resolution of the instrument of $\delta Q = 2.08 \cdot 10^{-3} \text{ \AA}^{-1}$ has been taken into account; the dotted line shows a simulation for the same structural parameters, but for an ideal instrument without resolution broadening; the short dashed line shows the simulation for the same layer thickness but without roughness; the long dashed line shows the simulation for the glass substrate only.

Neutron reflectometry has many applications in different fields of science of which we can only list a few:

- *soft matter science*: thin films e. g. polymer films; self-organization of diblock copolymers; surfactants; liquid-liquid-interfaces, ...
- *life science*: structure of bio-membranes
- *materials science*: surface of catalysts; kinetic studies of interface evolution; structure of buried interfaces
- *magnetism*: thin film magnetism e. g. exchange bias, laterally structured systems for magnetic data storage, multilayers of highly correlated electron systems, ...

15.4.4 Atomic structures: Single crystal and powder neutron diffraction

As explained in chapter 15.4.1, wide angle scattering with neutrons of wavelength typically 1 \AA is applied for the determination of atomic structures. Due to the periodicity of the lattice, Bragg peaks appear under diffraction angles given by the Bragg equation (compare reflectometry: (15.35) and (15.36)!):

$$2d \sin \theta = \lambda \quad (15.37)$$

The intensity of the Bragg peaks is governed by the arrangement of the atoms within the unit cell (structure factor) and the scattering from the single atom (form factor). By collecting a large set of scattered intensities for many Bragg peaks, modeling the atomic structure and refining the parameters in order to get an optimum agreement between calculated and observed intensities, the arrangement of atoms within the unit cell as well as the arrangements of spins for magnetic samples can be determined. Figure 15.13 shows the schematics of a single crystal diffractometer.

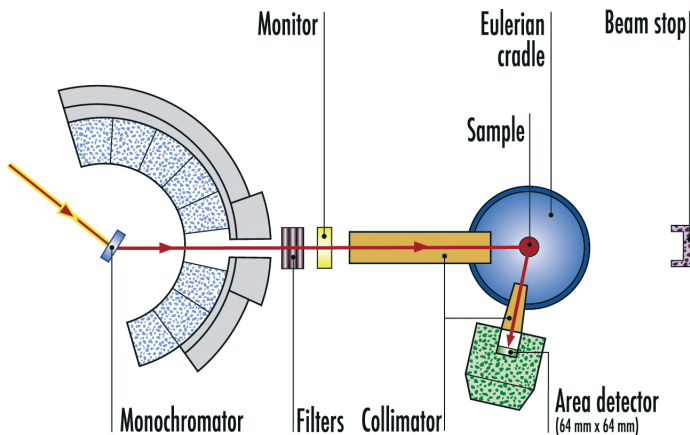


Fig. 15.13: *Schematics of a single crystal diffractometer. The drawing shows the layout of the diffractometer D9 at the Institute Laue-Langevin and has been taken from <http://www.ill.eu/>.*

In contrast to small angle scattering, where a broad wavelength band is employed to enhance the scattered intensity, a better monochromatization of typically $\frac{\Delta\lambda}{\lambda} \sim 1\%$ has to be achieved for wide angle scattering to avoid the broadening of the Bragg reflections due to the wavelength spread according to (15.37). This monochromatization is typically done by Bragg diffraction from a single crystal. The direction of the incident beam is determined by a set of slits. As Bragg reflections only occur when the corresponding lattice planes have a definite orientation with respect to the incident beam, the single

crystal sample is usually mounted on a so-called Eulerian cradle, which allows one to orient the sample using the three Eulerian angles ω , χ and ϕ . Finally, the scattered beam is detected in a point- or small area detector. Care must be taken to collect the entire integrated intensity for a scan through the Bragg reflection.

A conceptually simpler experiment for the determination of atomic structures is the neutron powder diffractometer. In this case, since the powder grains in the sample usually have random orientations with respect to the incident beam, there is no need for orienting the sample with respect to the beam. Scattering will always occur for some of the grains, which fulfill the Bragg condition by chance. As scattering occurs for all allowed Bragg reflections simultaneously, it would be very inefficient to detect scattered intensities by a single point detector, which would have to be positioned recursively for the correct 2θ values. Therefore, in powder diffraction one usually uses a large linear - or even better area - position sensitive detector, which is arranged on a circular arch around the sample position.

While neutron powder diffraction is conceptually simple, it poses the problem that Bragg reflections will overlap for larger unit cells, e.g. due to finite peak width. Among other factors, the peak width is determined by the resolution of the instrument. One can show that the resolution function for a neutron powder diffractometer on a beam being monochromized by a Bragg reflection from a monochromator crystal⁹ is given by:

$$(\Delta 2\theta)^2 = U \tan^2 \theta + V \tan \theta + W \quad (15.38)$$

For overlapping reflections, one cannot determine the intensities of the various Bragg reflections separately. The solution to the problem is the so-called *Rietveldt*- or profile refinement, where structural parameters (unit cell metric $a, b, c, \alpha, \beta, \gamma$, atom positions and site occupations, the Debye-Waller-factors, etc.) are refined together with the instrumental parameters (zero point of the scattering angle $2\theta_0$, parameters of the resolution function U, V, W , etc). Assuming a certain peak shape function, this allows one to model the entire powder diffractogram and determine the corresponding parameters from a refinement, which aims at minimizing the weighted sum of the quadratic deviations of calculated and observed intensities for all data points. Figure 15.14 shows an example of such a Rietveldt analysis for data taken from a colossal magnetoresistance manganite.

⁹ Alternatively, one can chop the incoming white beam, so that the different wavelengths arrive at different times at the sample; from the arrival time of elastically scattered neutrons at the detector, one can deduce the wavelengths of the scattered neutrons. Using large area detectors, which cover most of the solid angle 4π , this time-of-flight technique, typically applied at pulsed sources, can be very efficient.

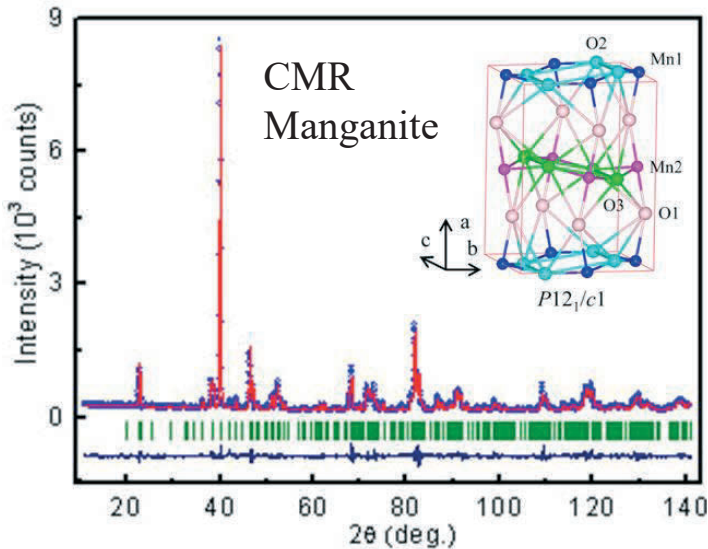


Fig. 15.14: Powder neutron diffraction from a colossal magnetoresistance manganite. Points represent the measured intensities, the solid line the calculated profile function. The green bars below the diffractogram indicate the positions of the Bragg reflections and the line beneath shows the difference between observed and calculated intensities [5].

As one can see, there is a very strong overlap of Bragg reflections, especially at larger scattering angles. Still, by using the above-mentioned profile refinement technique, the atomic structure of the compound could be determined to a high precision.

Applications of wide angle diffractions are manifold:

- *life-sciences*: structure of biological macromolecules, e. g. Hydrogen (crystal water!) in protein structures
- *chemistry*: structure determination of new compounds, position of light atoms; time resolved reaction kinetics
- *materials science*: stress-strain determination; texture of materials
- *geo-science*: phase and texture analysis
- *solid state physics*: structure - function relations e. g. in high T_C superconductors; magnetic structures and spin densities, e. g. in molecular magnets

15.5 Spectroscopy

So far, we have only explored the purely elastic - or the quasi-static correlation functions, which give us structural information on various length scales only. We will now turn to the general case of correlation functions in space and time, which allow us to determine in addition the microscopic dynamics of the sample under investigation. Again, different instrument types exist for different applications. First of all, if we consider the neutron as a particle, we can determine the time-of-flight it needs to travel from the sample to the detector and thus its velocity or energy after the scattering process. With the knowledge of the incident energy, the energy transfer during the scattering process can be determined. This kind of neutron spectrometer is called a *time-of-flight or TOF spectrometer*. A special case of the TOF spectrometer is the so-called *neutron spin-echo spectrometer*, where the time-of-flight of the neutrons is being determined through the Larmor precession of the nuclear spin of neutrons in an external magnetic field. Neutron spin-echo spectroscopy has the highest energy resolution and measures the intermediate scattering function directly. Therefore, it is well suited to study slow relaxation processes. An alternative approach to spectroscopy is to determine the energy of scattered neutrons by means of Bragg reflection from an analyzer crystal. Such an instrument is called a *crystal spectrometer* and if the selection of the incident wavelength is done by a crystal monochromator, it is called a *triple axis spectrometer*. A variant of a crystal spectrometer is the high-resolution *backscattering spectrometer*. Of course, there are various combinations of these techniques, which exist in particular at spallation sources. A discussion of all of the various instrument concepts goes well beyond the scope of this introductory course.

15.5.1 Time-of-Flight or TOF spectroscopy

Figure 15.15 depicts schematically a generic time-of-flight spectrometer. Neutrons are being monochromatized either by reflection from a monochromator crystal or by time-of-flight techniques (X-TOF or TOF-TOF instruments, respectively). Monochromatic neutron pulses are produced by a chopper, which can be a fast rotating (up to e.g. 600 Hz) disc or drum made from neutron absorbing material, which has a slit that lets neutron pass only during a short time interval of typically some microseconds. This pulsed neutron beam impinges on the sample and is scattered under all possible scattering angles. Neutrons are recorded on a two dimensional position sensitive detector (nowadays, this is often an array of linear position sensitive ^3He detector tubes) surrounding the sample typically on the surface of a cylinder. From the arrival time of the neutrons in the detector with respect to the starting time given by the opening of the chopper, an intensity spectrum can be recorded for each scattering angle separately as a function of the arrival time of the neutrons in the detector. Using simple kinematic equations for the neutron as a particle and a calibration obtained by measuring a reference sample, this time-of-flight spectrum can be converted into the scattering function $S(\mathbf{Q}, \omega)$. Figure 15.16 illustrates the scattering process in a flight-path-versus-time diagram.

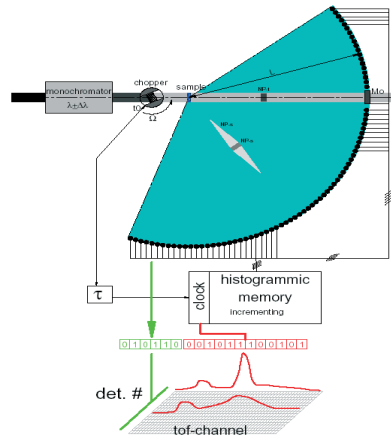


Fig. 15.15: *Generic TOF spectrometer. The neutron beam is monochromatized, either by a crystal monochromator (X-TOF) or by time-of-flight (TOF-TOF) with choppers and / or the pulse from a spallation source. A chopper creates monochromatic neutron beam pulses incident on the sample. The scattered neutrons are collected in an array of detectors surrounding the sample. For each detector pixel, the neutrons are counted into a histogram as a function of their arrival time. These intensity – time histograms can be converted into the scattering function $S(\mathbf{Q},\omega)$ by using a reference sample for absolute calibration and simple kinematic relations between scattering angle and flight time on one hand and scattering vector and energy on the other hand.*

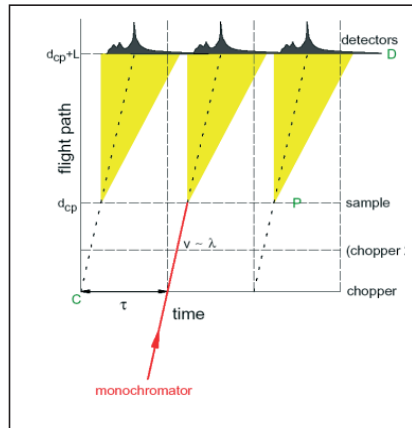


Fig. 15.16: *Flight-path-versus-time-diagram for a generic time-of-flight instrument (see text). (Courtesy of Dr. M. Monkenbusch).*

In such a diagram, a monochromatic neutron beam has a certain slope, which can be derived from the de Broglie equation $p = \frac{h}{\lambda} = m \cdot v = m \cdot \frac{s}{t}$:

$$t = \frac{m}{h} \cdot s \cdot \lambda \quad (15.39)$$

Typical velocities for thermal neutrons lie in the range of meter per millisecond. In figure 15.16 the neutrons coming from a monochromator enter the chopper with a certain slope in the path-vs.-time diagram corresponding to the velocity of the monochromatic neutrons. With a repetition rate of $\frac{1}{\tau}$ given by the chopper frequency, pulses of monochromatic neutrons leave the chopper. A second chopper can be applied to suppress higher order reflections. The neutron scattered from the sample can either gain energy, resulting in a steeper slope in the path-vs.-time diagram or lose energy resulting in a shallower slope. The number of neutrons entering the detector in a certain time interval is counted into a histogram with the elastic line usually being strongest and inelastic events being visible in neutron energy gain or -loss.

A nice example for a powder neutron time-of-flight spectrum is given by the excitation spectrum of a molecular magnet, namely Mn_{12} acetat, see figure 15.17 [6]. Here the time-of-flight axis has been converted into an energy scale. Clearly visible are nicely separated excitations, which result in the energy level diagram depicted on the middle of figure 15.17. Transitions between these levels correspond to transitions between different values of the magnetic quantum number of the total spin of the molecule. Modeling this energy level spectrum allows one to determine the magnetic interaction parameters, here mainly the magnetic anisotropy.

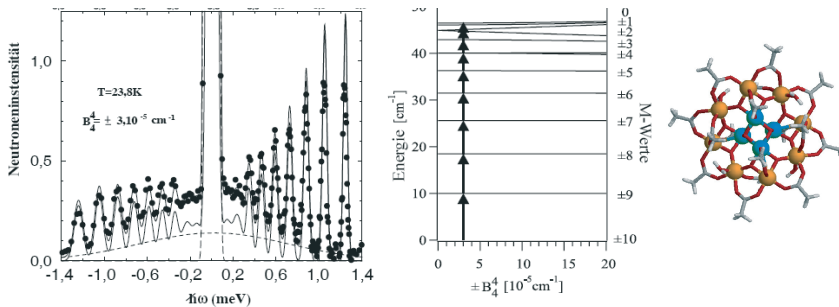


Fig. 15.17: *Left: Time-of-flight spectrum of the molecular magnet Mn_{12} acetat converted into an energy scale; middle: the corresponding energy level diagram; right: the magnetic molecule consisting of an outer ring of 8 Mn atoms (orange) with parallel coupled spins and an inner ring of 4 Mn atoms (blue) with opposite spin orientation. Taken from [6].*

Typical applications of time-of-flight spectroscopy can be found in various fields of science:

- *soft matter and biology*: dynamics of gels, proteins and biological membranes; diffusion of liquids, polymers; dynamics in confinement
- *chemistry*: vibrational states in solids and adsorbed molecules on surfaces; rotational tunneling in molecular crystals
- *materials science*: molecular excitations in materials of technological interest (e. g. zeolites) and especially in diluted systems (matrix isolation); local and long range diffusion in superionic glasses, hydrogen-metal systems, ionic conductors
- *solid state physics*: quantum liquids; crystal field splitting in magnetic systems; spin dynamics in high T_C superconductors; phase transitions and quantum critical phenomena; phonon density of states.

15.5.2 Triple axis spectroscopy

An alternative approach for the study of dynamics of condensed matter systems is the so-called *triple axis spectroscopy*. The schematic of a triple axis spectrometer is depicted in figure 15.18.

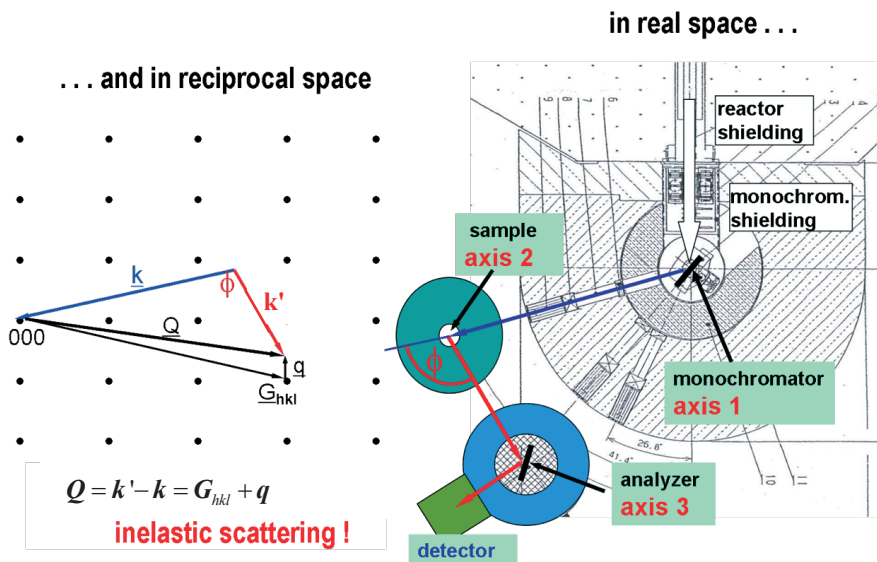


Fig. 15.18: *right*: schematics of a triple axis spectrometer showing the three axes; *left*: scattering diagram in reciprocal space. (Courtesy Dr. H. Conrad).

In this case the energies of the incident and scattered neutrons are selected by means of a single crystal monochromator and - analyzer, respectively. Also, the sample is usually in single crystalline form. These crystals (monochromator, sample, analyser) are on rotation tables, which form axis 1, axis 2 and axis 3 of the triple axis spectrometer. If we compare this instrument with the time-of-flight spectrometer shown in figure 15.15, one difference becomes immediately clear: while the time-of-flight spectrometer with its large detector

bank allows one to obtain an overview over the excitation spectrum in reciprocal space, the triple axis spectrometer is the instrument of choice, if a certain narrow region in \mathbf{Q} and ω is of interest. This is the case, if sharp excitations like lattice vibrations (phonons) or spin waves (magnons) are being investigated. A propagation vector of such an excitation together with a certain energy transfer can be selected by setting monochromator, sample and analyzer to the corresponding values as depicted in the scattering diagram of figure 15.18, left. Here the energy transfer is given by $\Delta E = \frac{\hbar^2}{2m}(k'^2 - k^2)$, while the momentum transfer is given as $\hbar\mathbf{Q} = \hbar\mathbf{k}' - \hbar\mathbf{k} = \hbar\mathbf{G}_{hkl} + \hbar\mathbf{q}$.

As an example, Figure 15.19 shows spin wave dispersion relations determined for the garnet $\text{Fe}_2\text{Ca}_3\text{Ge}_3\text{O}_{12}$ by triple axis spectroscopy.

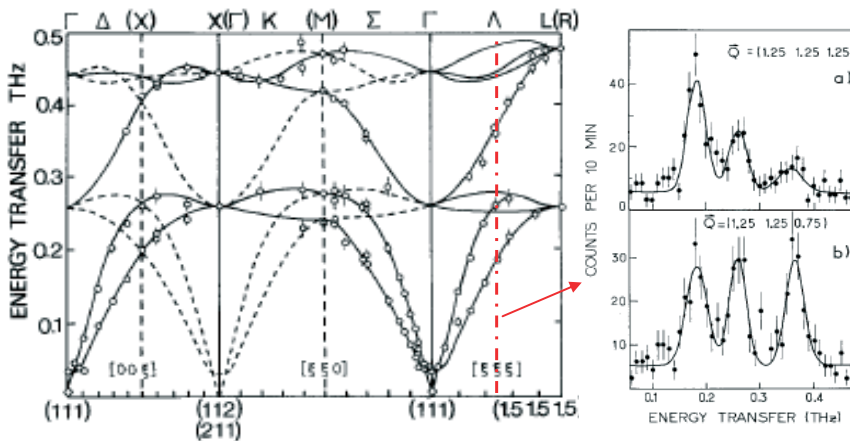


Fig. 15.19: Spin wave dispersion relations for the garnet $\text{Fe}_2\text{Ca}_3\text{Ge}_3\text{O}_{12}$ along main symmetry directions in reciprocal space. The data points are obtained from scans keeping the momentum transfer $\hbar\mathbf{Q}$ constant. The figure on the right shows examples of such “constant \mathbf{Q} scans”. The solid lines are model calculations, from which the interaction (exchange) parameters between the spins in the unit cells can be determined; figure taken from [7].

Typical examples of triple axis spectroscopy lie mainly in solid state physics:

- phonon dispersions in crystalline material, from which the interatomic forces can be determined
- spin wave dispersions, which allow one to determine exchange and anisotropy parameters
- dynamics of biological model membranes
- lattice and spin excitations in quantum magnets, superconductors, ...
- phase transitions: critical behavior.

15.5.3 High resolution spectroscopy

Both, time-of-flight and triple axis spectroscopy, have typical energy resolutions of a few percent of the incident neutron energy. While such energy resolutions are sufficient in many cases, there is need for higher energy resolutions, for example to investigate the rather slow movements of large macromolecules, the slow spin dynamics of frustrated spin systems, diffusion of atoms or tunneling processes in molecular crystals. In order to improve the energy resolution, one could just narrow the energy band width of the neutrons incident on the sample. However, such an improvement of resolution goes hand-in-hand with the decrease of the signal in the detector and is therefore not practicable beyond certain limits. There are, however, alternative approaches to increase the energy resolution: *neutron spin echo spectroscopy* and *backscattering spectroscopy*.

Neutron spin echo spectroscopy can be understood as a further development of the time-of-flight spectroscopy, where the flight times of individual neutrons are encoded and thus a broad wavelength band of incident neutron energies can be used. Encoding of the flight-time is done by the Larmor precession of the nuclear spin of the neutrons in an external magnetic field. Loosely speaking "each neutron carries its own clock" to measure its individual time-of-flight. Figure 15.20 demonstrates the principle of neutron spin echo spectroscopy: the incident neutron beam with a broad wavelength band of typically 10 %

is being polarized with the polarization along the neutron flight direction. A so-called $\frac{\pi}{2}$ -flipper turns the neutron polarization into the vertical direction, just before the neutrons enter a strong magnetic field, which is designed in such a way that the field integral $\int \mathbf{B}(s)ds$ is identical for all neutron flight paths (an absolute non-trivial requirement!!).

In the external field, the nuclear magnetic moment of the neutron starts to precess in this field with a Larmor precession frequency determined by:

$$\frac{d\mathbf{s}}{dt} = \gamma \mathbf{s} \times \mathbf{B} \quad (15.40)$$

Due to the different neutron velocities and thus different flight times in the magnetic field area, the neutron beam reaching the sample is entirely depolarized. Typical field integrals are in the range of $0.5 \text{ T}\cdot\text{m}$ giving rise to some 10,000 precessions of the neutron spin. At the sample, the polarization of each neutron is inverted by a so-called π -flipper. In the second arm of the neutron spin echo spectrometer, the scattered neutrons travel through an identical solenoid as on the incident side. If the neutrons are scattered elastically and the field integrals in the two coils are precisely identical, then the full polarization of the neutron beam will be restored and a full intensity will be recorded in the detector after a

further $\frac{\pi}{2}$ flip and a polarization analyzer. This maximum intensity is called the spin echo. This spin echo is due to the fact that in the second coil, each neutron performs as many revolutions as in the first coil and thus has to end up with the initial spin direction. If an inelastic scattering event happens at the sample, the spin echo will be destroyed, i.e. the intensity in the detector will be lowered. The echo signal can be measured by scanning the field of the second coil with respect to the field of the first coil. Since the echo signal depends directly on the time-of-flight which neutrons need to travel through the magnetic

field region, the spin echo technique directly measures the intermediate scattering function $I(\mathbf{Q}, t)$ instead of $S(\mathbf{Q}, \omega)$. This type of spectroscopy is therefore well suited to measure slow relaxation processes like the magnetization dynamics in spin glasses or the dynamics of large macromolecules.

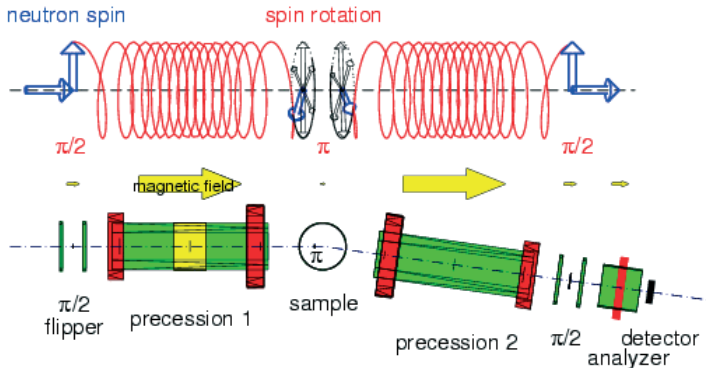


Fig. 15.20: Schematics of the neutron spin echo spectrometer of JCMS at the Heinz Maier-Leibnitz Zentrum MLZ in Munich [3]. The incident neutron beam has a wavelength – or energy band of $\Delta\lambda/\lambda = 10\%$.

Another instrument for high resolution spectroscopy, based on a crystal analyzer and thus related to the triple axis spectrometer, is the so-called neutron *backscattering instrument*. Starting from the Bragg equation $\lambda = 2d \sin \theta$ one can derive the wavelength spread of a Bragg reflection from a monochromator or analyzer crystal by simple derivation:

$$\Delta\lambda = \left(\frac{\partial\lambda}{\partial d}\right)^2 (\Delta d)^2 + \left(\frac{\partial\lambda}{\partial\theta}\right)^2 (\Delta\theta)^2 \Rightarrow \left(\frac{\Delta\lambda}{\lambda}\right)^2 = \left(\frac{\Delta d}{d}\right)^2 + \cot^2 \theta \cdot (\Delta\theta)^2 \quad (15.41)$$

(15.41) shows that the wavelength spread results from two factors: an uncertainty in the lattice d-spacing, which can be minimized for perfect crystals such as silicon or germanium and a term resulting from the divergence of the beam. For backscattering, i.e. $2\theta = 180^\circ$ or $\theta = 90^\circ$ this latter contribution vanishes due to the $\cot(\theta)$ dependence. Thus, in backscattering one can work with a very divergent beam and still achieve a very good wavelength- or energy- resolution – of course at the prize of a poor angular resolution. This principle is applied for backscattering instruments. An example of such a spectrometer from a neutron spallation source is shown in figure 15.21.

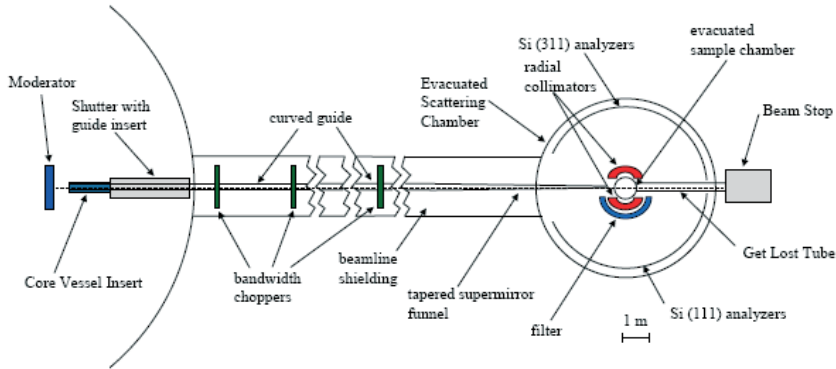


Fig. 15.21: Schematics of the neutron backscattering spectrometer BASIS at the Spallation Neutron Source SNS in Oak Ridge, USA, taken from [8].

Neutron pulses are produced in the supercritical hydrogen moderator. These pulses have a width of about $45 \mu\text{s}$ for $\lambda = 6.267 \text{ \AA}$ wavelength neutrons (this wavelength corresponds with silicon (111) backscattering analyzers). Bandwidth choppers are used to select a certain wavelength band from the pulsed white neutron beam. A long incident flight path of 84 m between moderator and sample allows one to define with great precision the wavelength of the incident neutrons arriving at the sample at a certain time after the initial neutron pulse. Neutrons are scattered from the sample onto Si (111) analyzers, reflected from these analyzers into detectors in a close-to-backscattering geometry. In this way the final neutron wavelength is fixed to 6.267 \AA , while the incident neutron wavelength varies with time after the pulse and thus the energy transfer can be determined like in a time-of-flight instrument¹⁰. An energy resolution of about $2.2 \mu\text{eV}$ can be achieved with the dynamic range of $\pm 250 \mu\text{eV}$. Typical applications of such a backscattering spectrometer lie in the investigation of tunneling in molecular crystals, spin diffusion or slow spin relaxation in frustrated spin systems, or atomic diffusion processes.

15.6 Summary and conclusions

In this chapter we have given a rough overview over the different neutron scattering techniques and their applications. Many details will be discussed in the practical part of this course. In addition to the instrument concepts presented, there are many variants, which could not be discussed within the scope of this introduction. Besides neutron scattering there are of course many other techniques, which cover similar lengths- and time- scales for research in condensed matter. All these techniques are complementary since all of

¹⁰ The BASIS spectrometer is an example of a so-called *inverse TOF spectrometer*, where the final velocity of neutrons is fixed and the incident velocity varies. This is in contrast to a *direct TOF spectrometer*, where the incident velocity is fixed and the final velocity varies.

them can only access a certain phase space region and since the contrast mechanisms are quite different for the different techniques. Figures 15.22 and 15.23 depict the relevant lengths- and time- scales accessible with various neutron- and non-neutron techniques.

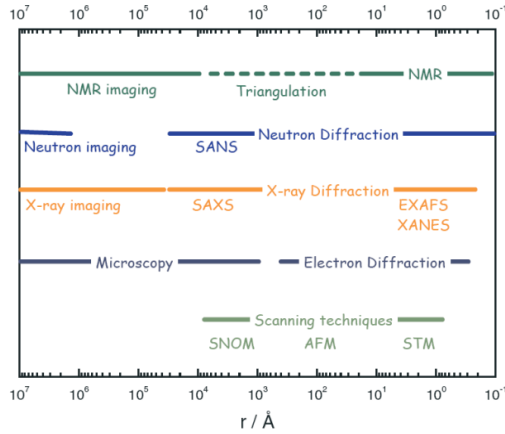


Fig. 15.22: *Experimental techniques with spatial resolution: neutron diffraction compared to other experimental techniques; taken from [9].*

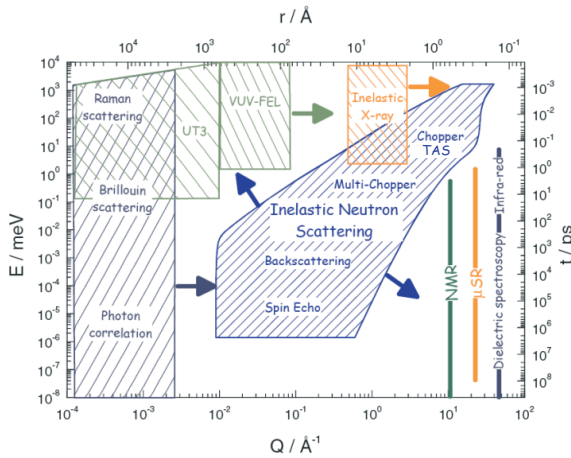


Fig. 15.23: *Experimental techniques with time and energy resolution, respectively: neutron spectroscopy compared to other experimental techniques; taken from [9].*

As these figures clearly demonstrate, neutron techniques cover a very large range of lengths- and time- scales relevant for research on condensed matter systems. Together with the typical assets of neutrons - sensitivity to magnetism, gentle non-destructive probe, sensitivity to light elements, contrast for neighboring elements etc. - it is clear why neutrons are such an important probe in many research fields. Figure 15.24 shows how research with neutrons is relevant in many areas of fundamental research and how this in turn is highly relevant for many developments of modern technologies, which are the basis to solve current challenges of mankind.

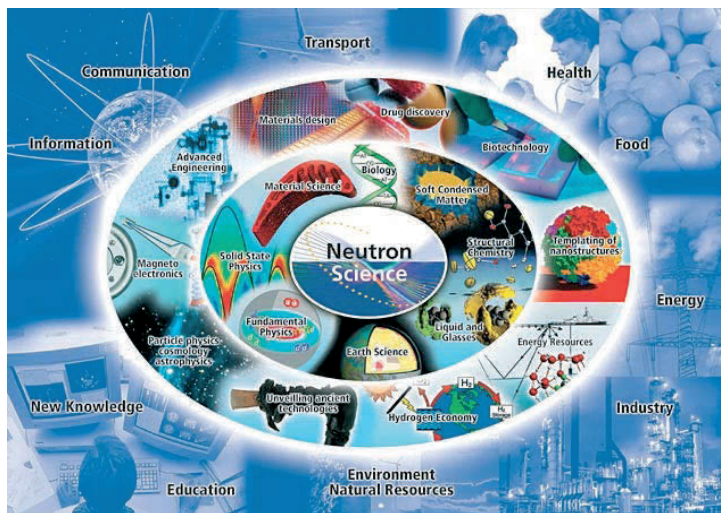


Fig. 15.24: *Significance of research with neutrons in fundamental research and modern technologies, which finally shape our environment and help solve pressing problems of modern societies, like energy supply, transport or communication; taken from [9].*

References

- [1] Th. Brückel (Ed.) *Forschung mit Neutronen in Deutschland - Status und Perspektiven* Brochure of the German Committee for Research with Neutrons KFN; 2005
see also <http://www.neutronenforschung.de>
- [2] G.L. Squires *Introduction to the Theory of Thermal Neutron Scattering* Dover Publications Inc.; Reprint 1997 or S.W. Lovesey *Theory of Neutron Scattering from Condensed Matter: Vol. 1 & 2* (International Series of Monographs of Physics) Clarendon Press; 1986
- [3] http://www.jcms.info/jcms_instruments/
- [4] A. Radulescu, E. Kentzinger, J. Stellbrink, L. Dohmen, B. Alefeld, U. Rucker, M. Heiderich, D. Schwahn, Th. Brückel, D. Richter; *KWS-3: The New (Very) Small-Angle Neutron Scattering Instrument Based on Focusing-Mirror-Optics*; *Neutron News* **16** (2005), 18 - 21
- [5] H. F. Li, Y. Su, Y. Xiao, J. Perbon, P. Meuffels, Th. Brückel; “*Crystal and Magnetic Structure of Single Crystal $La_{1-x}Sr_xMnO_3$ ($x \sim 1/8$)*”; *European Physical Journal B* **67** (2009), 149 - 157
- [6] R. Bircher, G. Chaboussant, A. Sieber, H.U. Güdel and H. Mutka; *Transverse magnetic anisotropy in Mn_{12} acetate: Direct determination by inelastic neutron scattering*; *Phys. Rev. B* **70** (2004), 212413-6
- [7] Th. Brückel, B. Dorner, A. Gukasov, V. Plakhty, W. Prandl, E. Shender, O. Smirnow; *Dynamical interaction of antiferromagnetic subsystems: a neutron scattering study of the spinwave spectrum of the garnet $Fe_2Ca_3(GeO_4)_3$* ; *Z. Phys. B* **72** (1988), 477 - 485
- [8] <http://neutrons.ornl.gov/> ; http://neutrons.ornl.gov/instrument_systems/beamline_02_basis/index.shtml
- [9] ESS project reports 2003 and update 2004;
http://neutron.neutron-eu.net/n_documentation/n_reports/n_ess_reports_and_more

Exercises

Multiple choice

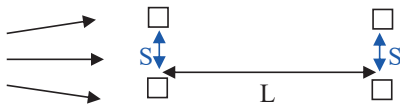
- Thermal neutrons have typical energies of
 - 0.2 meV
 - 20 meV
 - 2000 meV
 - 20000 meV
- In 1 sec, thermal neutrons cover a distance of
 - 10 m
 - 100 m
 - 1000 m
 - 100000 m
- Neutron choppers rotate with frequencies up to
 - 5 Hz
 - 600 Hz
 - 60000 Hz
- Phonon- and Magnon-dispersions are usually measured at
 - small angle scattering instruments
 - triple axis spectrometers
 - backscattering spectrometers
 - neutron spin echo spectrometers
- Interface structure in thin film systems is usually studied at
 - powder diffractometers
 - time-of-flight spectrometers
 - reflectometers
- Polymer reptation has been extensively studied at
 - thermal time-of-flight spectrometers
 - triple axis spectrometers
 - spin-echo spectrometers
- Incoherent scattering (e.g. of hydrogen) is very useful to
 - reduce the background
 - study magnetic properties
 - study diffusive motions

8. The scattering vector Q is directly related to
- the momentum transfer of neutrons to the sample
 - the coherence of the neutron beam
 - the phase shift during scattering
9. The resolution function of an instrument is directly related to
- the Fourier transform of the pair correlation function of the atoms in the sample
 - the coherence volume of the neutron beam
 - the collimation and monochromatization of the beam

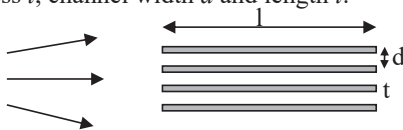
E15.1 Collimation

Assume you have to define the direction of a neutron beam by collimation. The incident beam has a flat angular distribution over an angular range much wider than needed. Employ the following three methods, plot the intensity distribution after your collimating device, comparing shape, width and transmission:

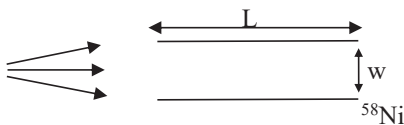
1. two slits with opening S in distance L



2. a “Soller Collimator” consisting of N neutron absorbing plane-parallel plates of thickness t , channel width d and length l :



3. a neutron guide of length $L \gg$ width w coated with ^{58}Ni ($b = 14.4 \text{ fm}$; fcc-structure; $a_0 = 3.520 \text{ \AA}$)



What is the principle difference between method 3 and methods 1 and 2?

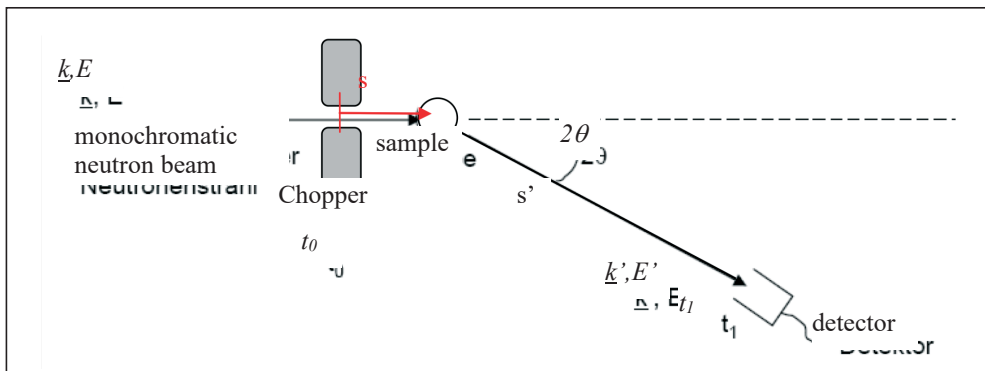
E15.2 Monochromatization

You have now the task to monochromatize your ideally collimated neutron beam (neglect any angular divergence). Again, three methods are offered:

- a) A velocity selector, see figure 15.6. Take as parameters the thickness of the drums of 10 cm , an inner radius of the lamella of 6 cm , a distance between the lamella of 1 cm and an inclination angle of 10° . How fast does this selector have to turn to monochromatize neutrons of wavelength 10 \AA ? Estimate the wavelength spread in percent.
- b) A crystal monochromator made from pyrolytic graphite $PG(002)$ reflection with a lattice d -spacing of 3.343 \AA . PG is not an ideal crystal, but a mosaic crystal consisting of many small crystalline blocks slightly canted against each other within an angular width of say $40'$. Calculate the Bragg angle for a wavelength of 2.4 \AA and 10 \AA , respectively, and estimate the wavelength spread in percent.
- c) A sequence of two disk choppers with radius R and opening d in a distance L . Take $L = 3\text{ m}$, $R = 20\text{ cm}$, $d = 1\text{ cm}$. Which wavelength is selected, if the choppers rotate at 200 Hz with a phase shift of 100° ?

E15.3 TOF-Spectroscopy (optional!)

In a time-of-flight spectrometer, the energy change of the neutrons during scattering is being determined by the neutron time-of-flight:



- a) Calculate the time-of-flight between chopper and detector for a flight path length $s+s'=3\text{ m}$ for neutrons of wavelength 1 \AA for an elastic scattering process.
- b) Determine the relation between the delayed arrival time of neutrons at the detector and the energy loss during inelastic scattering at the sample.
- c) Determine the relation between energy transfer $\hbar\omega = E - E'$ and the magnitude of the momentum transfer $|\hbar\mathbf{Q}| = \hbar|\mathbf{k}' - \mathbf{k}|$ for a detector with fixed scattering angle 2θ .

Which factors determine the energy resolution of a TOF spectrometer? How does this affect the design of such an instrument?

Band / Volume 273

Analysis of the signal transduction cascade tuning the 2-oxoglutarate dehydrogenase activity in *Corynebacterium glutamicum*

L. Sundermeyer (2023), VI, 119 pp

ISBN: 978-3-95806-722-6

Band / Volume 274

Multicellular defense against phage infection in *Streptomyces* – impact of secondary metabolites and mycelial development

L. Kever (2023), iv, 246 pp

ISBN: 978-3-95806-724-0

Band / Volume 275

Investigation of the electronic band structure of 2D transition metal dichalcogenides via angle-resolved photoemission spectroscopy

B. Parashar (2023), xvii, 156 pp

ISBN: 978-3-95806-725-7

Band / Volume 276

Strain- and process engineering for polyketides production with *Pseudomonas taiwanensis* VLB120 in two-phase cultivations

T. P. Schwanemann (2023), 230 pp

ISBN: 978-3-95806-726-4

Band / Volume 277

Quantitative atomic-level investigation of solid materials through multidimensional electron diffraction measurements

H. L. Lalandec-Robert (2024), xxi, 152 pp

ISBN: 978-3-95806-735-6

Band / Volume 278

Studies on the cAMP-responsive regulatory network of *Corynebacterium glutamicum*

N. Wolf (2024), iii, 122 pp

ISBN: 978-3-95806-736-3

Band / Volume 279

Rare-earth atoms on two-dimensional materials: ab initio investigation of magnetic properties

J. P. Carbone (2024), 235 pp

ISBN: 978-3-95806-740-0

Band / Volume 280

Communities of Niche-optimized Strains (CoNoS) – a novel concept for improving biotechnological production

R. Zuchowski (2024), VIII, 168 pp

ISBN: 978-3-95806-743-1

Band / Volume 281

Enabling mixed microbial upcycling of plastic monomers

Y. S. Ackermann (2024), XVI, 203 pp

ISBN: 978-3-95806-749-3

Band / Volume 282

Folding and structural studies of *saccharomyces cerevisiae*

Phosphoglycerate Kinase

N. Bustorff (2024), xxvi, 126 pp

ISBN: 978-3-95806-754-7

Band / Volume 283

**The role of cellular development in multicellular antiphage
defense of *Streptomyces***

T. Luthe (2024), vi, 173 pp

ISBN: 978-3-95806-768-4

Band / Volume 284

**Probing the Transformation from Transition Metal Complexes to Extended
Two-Dimensional Nanostructures**

D. Baranowski (2024), XII, 103 pp

ISBN: 978-3-95806-772-1

Band / Volume 285

Neutron Scattering

Lectures of the JCNS Laboratory Course held at Forschungszentrum Jülich
and at the Heinz-Maier-Leibnitz Zentrum Garching

edited by S. Förster, K. Friese, M. Kruteva, S. Nandi, M. Zobel, R. Zorn (2024),
ca. 365 pp

ISBN: 978-3-95806-774-5

Weitere **Schriften des Verlags im Forschungszentrum Jülich** unter
<http://wwwzb1.fz-juelich.de/verlagextern1/index.asp>

Schlüsseltechnologien / Key Technologies

Band / Volume 285

ISBN 978-3-95806-774-5